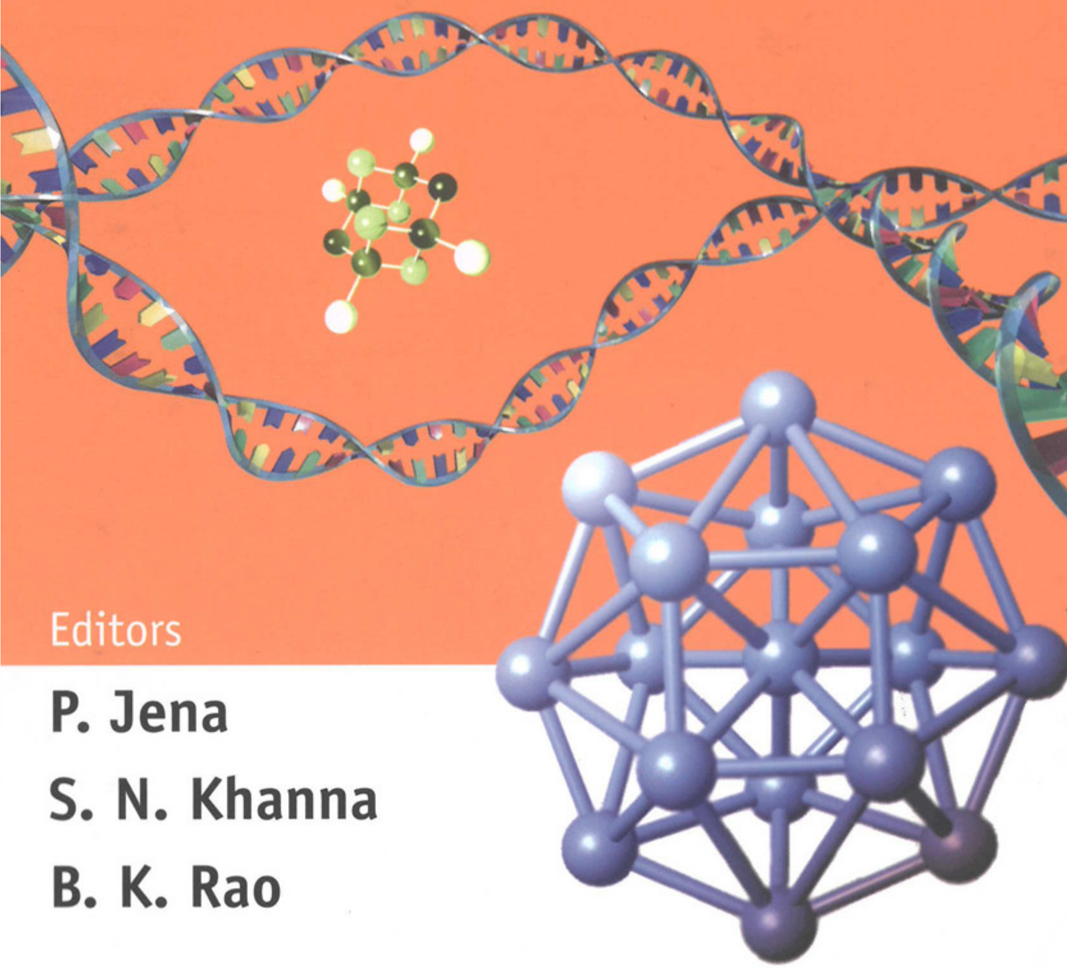

Editors

P. Jena

S. N. Khanna

B. K. Rao

Clusters and Nano-Assemblies

Physical and Biological Systems

Clusters and Nano-Assemblies

Physical and Biological Systems

This page intentionally left blank

Editors

P. Jena

S. N. Khanna

B. K. Rao*

Virginia Commonwealth University, USA

*Deceased**

Clusters and Nano-Assemblies

Physical and Biological Systems

Richmond, Virginia, USA 10–13 November, 2003

World Scientific

NEW JERSEY • LONDON • SINGAPORE • BEIJING • SHANGHAI • HONG KONG • TAIPEI • CHENNAI

Published by

World Scientific Publishing Co. Pte. Ltd.
5 Toh Tuck Link, Singapore 596224
USA office: 27 Warren Street, Suite 401-402, Hackensack, NJ 07601
UK office: 57 Shelton Street, Covent Garden, London WC2H 9HE

British Library Cataloguing-in-Publication Data
A catalogue record for this book is available from the British Library.

CLUSTERS AND NANO-ASSEMBLIES
Physical and Biological Systems

ISBN 981-256-331-8

This book is printed on acid-free paper.

Printed in Singapore by Mainland Press

Preface

The International Symposium on "Clusters and Nano-Assemblies: Physical and Biological Systems" was held in Richmond, Virginia from November 10-13, 2003. The symposium dealt with the fundamental science and technology of atomic clusters, nano-structures and their assemblies in physical and biological systems. The manner in which finite size, low dimensionality and reduced symmetry affect the properties of nano-assemblies was explored. While the field of clusters and nano-structures in physical sciences has been actively pursued over the past two decades, nature has known the benefit of nano-scale for a very long time. The focus of this symposium was to explore ways by which an understanding of unique properties of nano-scale biological systems such as proteins, enzyme reactions, RNA, and DNA can help us design novel materials composed of inorganic nano-scale systems in physical sciences. Similarly, how the techniques developed in physical sciences can lead to a fundamental understanding of biological systems was explored. The study of proteins in the gas phase through electrospray ionization mass spectroscopy, for which Professor John Fenn of Virginia Commonwealth University won the 2002 Nobel Prize in Chemistry, is an example of how the interface between the physical and biological sciences can lead to major breakthroughs.

In addition to assessing current understanding of these fields, outstanding problems and future directions were brought into focus. For example, how does one proceed from knowing the novel properties of isolated clusters and nano-particles to materials where these constitute the building blocks? How does one make use of the nature's creation such as enzymes to synthesize inorganic nano-structures with unique functionality that never existed in nature? The synergism produced by bringing together researchers working on surfaces, interfaces, clusters, and nano-structures in physical and biological sciences helped to answer some of these questions. The impact of these materials on technology was also discussed.

The topics included:

Synthesis, nucleation, growth, characterization, atomic and electronic structure, dynamics, ultra-fast spectroscopy, stability, electrical, magnetic, optical, thermodynamic, and catalytic properties of:

Clusters:	Free and supported
Cluster Materials:	Self-assembled, ligated, and embedded
Nano-structures:	Quantum dots, wells, and corrals; nano-tubes and wires
Bio-systems:	Protein, Enzyme reactions, RNA, DNA, Supra-molecular assemblies, bio-interfaces, bio-hybrid devices
Nano-Technology:	Spintronics; magnetic, optical, and bio-sensors; catalysts; molecular electronics; drug delivery, bio-chips

This interdisciplinary symposium drew participants and speakers from Physics, Chemistry, Biology, Materials Science, and Chemical and Electrical Engineering. Nearly --- participants from --- countries attended this symposium. A total of 157 papers (42 invited and 115 contributed) were presented. The keynote session was addressed by two Nobel Laureates: Prof. John B. Fenn of Virginia Commonwealth University and Dr. William D. Phillips of National Institute of Standards and Technology. This symposium was sponsored by the American Physical Society, ASM international, IEEE, Materials Research Society, The Minerals, Metals & Materials Society and as a topical meeting.

This symposium would not have been possible without the tireless efforts of the members of the Local Organizing Committee, the input from the International Advisory Board, and the financial support of Air Force Office of Scientific Research, Army Research Office, Center for Innovative Technology of Virginia, Department of Energy, National Science Foundation, NanoVa, National Aeronautics and Space Administration, Philip Morris USA, and Virginia Commonwealth University. Our special thanks go to the graduate and undergraduate students and postdoctoral fellows of in the Physics and Engineering Departments of Virginia Commonwealth University for volunteering their services during the symposium, to the conferees for the high quality of their participation, and last but not the list to Mrs. Barbara martin for her assistance throughout the two year period this symposium was in the making.

On May 7, 2004 we lost our dear friend and colleague, Bijan K. Rao. He was an integral part of the Richmond symposia series and our group. His presence will be missed for ever and we dedicate the proceedings of this symposium to his memory.

Richmond, Virginia
September, 2004

P. Jena
S. N. Khanna
B. K. Rao*

*Deceased

CONTENTS

Atomic Clusters

Organic and Molecular Clusters

Catalysis

Quantum Dots/Rings

Nano-Wires and Tubes

Magnetic Properties

Electrical and Optical Properties

Clusters on Support

Nano-Growth on Strained Surfaces/Nano-Assemblies

Biology at Molecular Level

Biotechnology

CATALYSIS WITH SMALL FREE NOBLE METAL CLUSTERS

THORSTEN M. BERNHARDT, LIANA D. SOCACIU, JAN HAGEN,
DENISIA POPOLAN, JÉRÔME LE ROUX, ULRICH HEIZ,[†]
LUDGER WÖSTE

Institut fürExperimentalphysik, Freie Universität Berlin, Arnimallee 14
D-14195 Berlin, Germany

In general, reaction mechanisms in heterogeneous catalysis are difficult to reveal, because of the complexity of the reaction system. Our approach employs mass-selected metal clusters as well-defined model reaction centers. Chemical reactions on these clusters are investigated in a temperature controlled radio frequency (rf)-ion trap setup. Product ion concentrations as a function of storage time enable the determination of reaction kinetics and reaction mechanisms of free clusters. As an example, the CO combustion reaction on small gold clusters is studied. It is known that supported gold clusters with few atoms up to nm size exhibit relevant catalytic properties. Our ion trap measurements reveal catalytic activity already for negatively charged gold dimers. When the reaction kinetics are investigated as a function of temperature, an intermediate product with CO and O_2 coadsorbed can be isolated. In contrast, small atomic silver clusters have not been found relevant for catalytic oxidation processes so far. Our investigations show for the first time evidence for a strongly size dependent catalytic activity of Ag_n^-.

1. Introduction

Although it is well known that bulk gold material and extended clean gold surfaces are inert under ambient reaction conditions, there is currently a strong interest in the catalytic activity of this noble metal. This originates in the discovery that dispersed nano-sized gold particles very effectively catalyze oxidation processes even at low temperatures [1]. Of particular interest and importance is the recent finding that mass-selected supported gold clusters actively facilitate the oxidation of CO to CO_2 even at cryogenic temperatures, if their size is eight or more atoms and if a charge transfer from the surface (F-center) to the cluster is present [2]. However, the reason for this strong size dependence and the mechanism of the oxidation reaction is still unresolved. This clearly demonstrates the need for further investigations of the reactions of small gold clusters, in particular at low temperatures, in order to identify in detail the role of cluster charge as well as reaction temperature on the reaction mechanism of small mass-selected gold clusters.

[†] Present address: Institut für Oberflächenchemie und Katalyse, Universität Ulm, D-89069 Berlin, Germany.

In the next step we extend the investigations to negatively charged silver clusters. Silver with μm particle size is used commercially in large scale as oxidation catalyst in the ethylene epoxidation process [3]. However, nano-size or even atomic silver clusters have not been recognized as active oxidation catalysts so far. Employing low energy guided ion beam technique in conjunction with an rf-octupole ion trap for reaction studies, we are able to reveal the detailed catalytic reaction cycle of free gold dimer ions. Furthermore, we will present evidence that certain silver cluster sizes are indeed catalytically active.

2. Experiment

The reactions of free mass-selected gold and silver clusters are investigated in a variable temperature rf-octopole ion trap inserted into a tandem quadrupole mass spectrometer. The use of an rf-ion trap to investigate gas phase metal cluster reactions has the advantage that the experimental conditions, i. e., reaction temperature, reactant partial pressures, total pressure, and reaction time, can be precisely determined. The general experimental setup has been described in detail elsewhere [4]. Only a brief outline will be given here. The gold cluster anions are produced by an ion sputtering source (CORDIS [5]). Mass selection is achieved via a first quadrupole mass filter Q1 (Fig. 1). The mass-selected cluster ion beam then enters the octupole ion trap which is filled up to space charge limit with metal cluster ions (about 10^4 clusters per mm^3). The trap is prefilled with a helium partial pressure on the order of 1 Pa and the clusters are thermalized to the temperature of the background helium gas in the trap within few milliseconds. A closed cycle helium cryostat attached to the trap allows temperature adjustment in the range between 20 and 350 K. Time-resolved kinetic measurements on the time scale of seconds are performed with small, well defined partial pressures of the reactants O_2 and CO present in the trap. For this purpose all ions are extracted from the trap after defined storage time by means of a pulsed electrostatic field and are subsequently mass-analyzed by a second quadrupole mass filter.

3. Results and Discussion

The reactions of free negatively charged gold and silver clusters with O_2 and CO have been investigated previously [6-9]. Also coadsorption of both reactant molecules onto small gold clusters has been reported recently [9, 10]. The possible catalytic activity of Au_2^- in the CO combustion reaction was first predicted by Häkkinen and Landman [11]. A subsequent experimental investigation indeed revealed the catalytic reaction of the gold dimer and, in conjunction with theory, a detailed reaction cycle could be formulated [12]. Also for particular larger gold clusters evidence for catalytic CO_2 formation has been reported [10]. In this contribution first the experimental determination of the catalytic reaction cycle of Au_2^- will be described. Second, we will report on coadsorption of O_2 and CO onto small silver cluster anions before we take the example of Ag_{11}^- to demonstrate that particular silver clusters sizes show evidence to be active oxidation catalysts in the CO combustion reaction.

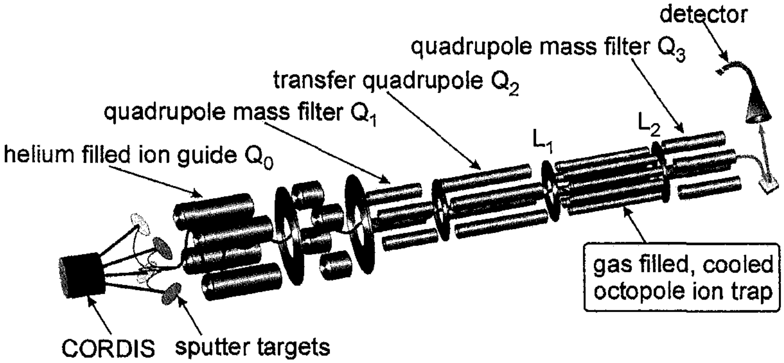

Figure 1. Experimental setup for the investigation of catalytic reactions of free mass-selected metal clusters. The cluster ions are sputtered from solid targets with a cold reflex discharge ion source (CORDIS), mass-selected (Q_1), and guided at low energies (Q_0 and Q_2) into the rf-octopole ion trap which is attached to a closed cycle helium-cryostat. By means of appropriate switching of the lenses L_1 and L_2 the reaction products are extracted and subsequently mass-analyzed by another quadrupole mass filter (Q_3).

3.1. *Catalytic carbon monoxide oxidation by Au_2^-*

When Au_2^- is reacted with solely O_2 in the rf-ion trap the single product ion observed is $Au_2O_2^-$. Analysis of the reaction kinetics depicted in Fig. 2a reveals a straight forward association reaction mechanism with Au_2^- completely reacting to yield the oxide product within several seconds at room temperature. A fit of the integrated rate equations of this association reaction mechanism to the experimental data is represented by the solid lines in Fig. 2a. If CO is added to the trap, no new reaction products besides Au_2^- and $Au_2O_2^-$ are formed as can be seen from the mass spectrum in Fig. 2c. However, Au_2^- is no longer completely transformed into oxide, but an offset appears in the gold cluster concentration at long reaction times which is apparent from the corresponding kinetics depicted in Fig. 2b. The most simple reaction mechanism that fits this data is the equilibrium reaction in which oxide is formed but bare gold dimer is reformed to a certain extent. The solid lines in Fig. 2b are obtained by fitting the equilibrium mechanism to the experimental data. However, the extent to which the gold dimer is reformed increases with increasing CO concentration. Thus, the reaction mechanism must involve more intermediate steps representing the influence of CO.

The next step to reveal the complete reaction mechanism consists in cooling down the ion trap to cryogenic temperatures. The product ion mass spectrum recorded at 100 K (Fig. 2e) shows the appearance of an additional mass peak. This peak can be assigned to the complex $Au_2(CO)O_2^-$ which apparently represents an intermediate in the reaction mechanism. The experimental evidence obtained so far demonstrates that O_2 adsorption is the first step in the observed reaction mechanism. Subsequent CO coadsorption yields the observed intermediate and finally the bare gold dimer ion must be reformed. The further strategy to reveal the full reaction mechanism consists in varying the available experimental parameters, i. e., temperature and reactant partial pressures. This procedure leads to a series of kinetic traces similar to the one shown in Fig. 2d. The goal then is to find one reaction mechanism that is able to fit all experimental kinetic data obtained under the various reaction conditions. This kinetic evaluation method results in the most simple mechanism which is able to fit the experimental data and it is very sensitive with respect to the reaction details [12]. In this way it is possible to rule out all but one possible reaction mechanism which is displayed in Fig. 3. The solid lines in Fig. 2d represent the fit of this mechanism to the experimental data. It equally well fits all other obtained kinetic data [12]. In this catalytic reaction cycle $Au_2O_2^-$ reacts with CO to form $Au_2(CO)O_2^-$ which will either redissociate to the oxide or further react with a second CO molecule to reform Au2- while liberating two CO_2 molecules.

Because the ion trap operates in the kinetic low pressure regime, the elementary steps of this reaction cycle must be viewed in the framework of the Lindemann energy transfer model for association reactions [13] which considers third body collisions with helium buffer gas atoms to accommodate the excess energy liberated in the bimolecular reaction steps [12]. All but one reaction steps show a negative dependence of the corresponding termolecular rate constants on the reaction temperature. Within the Lindemann model this negative temperature dependence is indicative of a barrierless reaction. Only the last reaction step representing the reformation of Au_2^- and liberation of CO_2 displays a positive temperature dependence of the rate constant. This demonstrates the presence of an activation barrier in this particular reaction step. This experimental information on the reaction energetics is also in excellent agreement with theoretical modeling of the reaction pathway [12]. Additional details of the reaction mechanism are obtained by complementary theoretical simulations revealing that the bonding of O_2 to Au_2^- is characterized by partial electron transfer (0.4e) from the metal cluster to the antibonding π-orbital of the oxygen molecule, making the oxygen molecule a superoxo-like species [11].

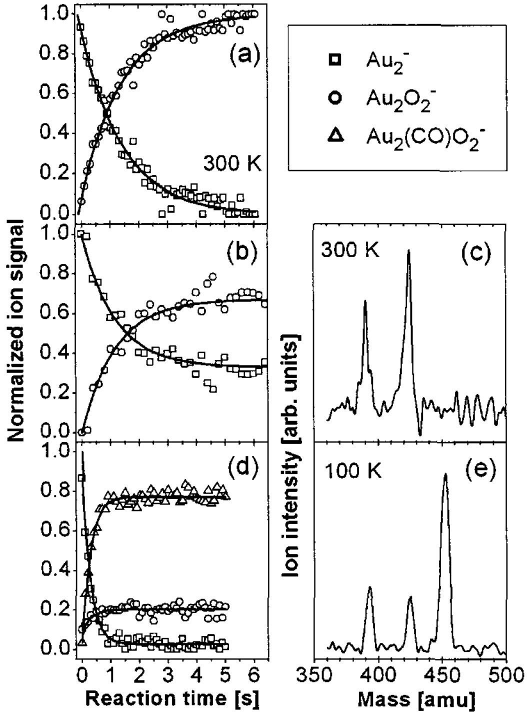

Figure 2. Product ion mass spectra (c) and (e) and kinetic traces (a), (b), (d) under different reaction conditions. (a) 300 K; O_2 only (0.12 Pa); (b) and (c) 300 K; O_2 and CO ((b) 0.02 Pa O_2; 0.05 Pa CO; (c) 0.12 Pa O_2; 0.12 Pa CO); (d) and (e) 100 K; O_2 and CO (0.02 Pa O_2; 0.04 Pa CO).

Furthermore it is possible to deduce the CO_2 production rate from the kinetic fit and thus to obtain the turn-over-frequency (TOF) of the catalytic reaction. The calculated TOF amounts to 0.5 CO_2 molecules per gold cluster per second. This is in the same order of magnitude as the catalytic activity of oxide supported gold cluster particles with a size of a few nanometers, which ranges between 0.2 s^{-1} per Au atom (~2 nm diameter particles at 273 K) and 4 s^{-1} per Au atom (3.5 nm particles at 350 K) [1, 14].

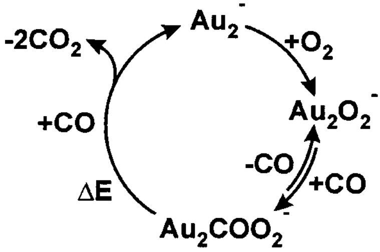

Figure 3. Reaction mechanism for the catalytic CO oxidation with free Au_2^- obtained from the kinetic evaluation method.

In conclusion of this part, through measurement of the temperature dependent reaction kinetics of Au_2^- with O_2 and CO in an rf-ion trap it is possible to reveal the details of the catalytic reaction mechanism leading to gas phase oxidation of CO at low temperatures.

3.2. *Ag_n^- reactions with molecular oxygen and carbon monoxide*

Anionic free silver clusters are found to readily react with molecular oxygen. In contrast, no reactions with carbon monoxide are observed for clusters with up to 13 atoms over the whole temperature range between 100 and 300 K [7, 15]. Therefore it is most surprising to detect the coadsorption complex $Ag_4(CO)O_2^-$ in the product ion mass spectrum obtained after reaction of Ag_4^- with a mixture of O_2 and CO at 100 K (Fig. 4). This observation points toward the prevalence of cooperative effects in the adsorption behavior of the molecules onto this silver cluster.

It is also interesting to note that unlike anionic gold clusters, where no reaction products with molecular oxygen are observed for clusters with an odd size of atoms [7-9], our recent experiments show adsorption of two or in selected cases even three O_2 molecules onto small odd size silver cluster anions [16].

Complementary theoretical results provide evidence for cooperative adsorption effects also in theses cases: A weakly bound first O_2 promotes the adsorption of a second oxygen molecule which is in turn differently bound (bridge position) with the O_2 bond elongated and is thus activated for further reactions [16]. In particular, cluster complexes of the general structure $Ag_nO_4^-$ (odd n) therefore have been proposed to be potentially active in catalytic oxidation reactions with silver cluster anions involved [16].

Fig. 5 shows the example of Ag_{11}^- first in reaction with only O_2 in the ion trap (upper trace of Fig. 5). The bare silver cluster is almost completely reacted and forms the product ion $Ag_{11}O_4^-$. If, however, CO is introduced into the trap in addition to O_2, the most surprising result is observed: The oxide signal is depleted and the bare Ag_{11}^- cluster signal reappears (lower trace of Fig. 5). This observation leads to the conclusion that CO reacts with the $Ag_{11}O_4^-$ oxide cluster. In this reaction it is likely to assume that CO_2 is liberated, in particular as the reappearance of the bare metal cluster has also been an indication for a catalytic reaction in the case of Au_2^- [15].

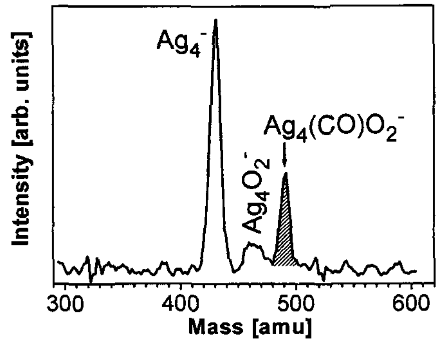

Figure 4. Product ion mass spectrum after reaction of Ag_4^- with O_2 and CO at 100 K (recorded with trace amounts of O_2 and 0.03 Pa CO in the trap). Reaction time is 2 s.

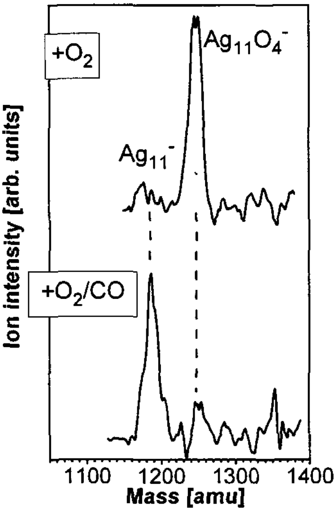

Figure 5. Product ion mass spectra of Ag_{11}^- clusters in reaction with solely O_2 (0.01 Pa O_2, upper trace) and a mixture of 0.01 Pa O_2 and 0.03 Pa CO (lower trace) at 100 K. Reaction times are 0.1 s.

In conclusion, the ion trap measurements of the reaction of selected silver cluster anions with a mixture of O_2 and CO demonstrate the importance of cooperative effects in the adsorption of these molecules. Furthermore, the example of Ag_{11}^- identifies $Ag_nO_4^-$ oxide complexes as key intermediates in potential oxidation reactions with silver clusters involved and provides evidence for catalytic CO oxidation reaction by this particular cluster.

Acknowledgments

Financial support by the Deutsche Forschungsgemeinschaft through SFB 450 is gratefully acknowledged. The authors thank Hannu Häkkinen and Uzi Landman for theoretical support and fruitful discussion concerning the gold cluster experiments. In the case of the silver cluster reactions support and helpful discussions with Vlasta Bonačić-Koutecký are acknowledged. We also would like to thank Štefan Vajda for support and discussions.

References

1. M. Haruta, *Catal. Today* **36**, 153 (1997); M. Valden, X. Lai, and D. W. Goodman, *Science* **281**, 1647 (1998).
2. A. Sanchez, S. Abbet, U. Heiz, W.-D. Schneider, H. Häkkinen, R. N. Barnett, U. Landmann, *J. Phys. Chem. A* **103**, 9573 (1999).
3. B. C. Gates, "Catalytic Chemistry." John Wiley & Sons, Inc., New York, Singapore, 1992.
4. L. D. Socaciu, J. Hagen, U. Heiz, T. M. Bernhardt, T. Leisner, L. Wöste, *Chem. Phys. Lett.* **340**, 282 (2001).
5. R. Keller, F. Nöhmeier, P. Spädtke, M. H. Schönenberg, *Vacuum* **34**, 31 (1984).
6. D. M. Cox, R. Brickman, K. Creegan, A. Kaldor, *Z.Phys. D* **19**, 353 (1991); W. T. Wallace, R. L. Whetten, *J. Phys. Chem. B* **104**, 10964 (2000); W. T. Wallace, R. L. Whetten, *Eur. J. Phys. D* **16**, 123 (2001); J. Hagen, L. D. Socaciu, U. Heiz, T. M. Bernhardt, L. Wöste, *Eur. J. Phys. D*, **24**, 327 (2003); D. Stolcic, M. Fischer, G. Ganteför, Y. D. Kim, Q. Sun, P. Jena, *J. Am. Chem. Soc.* **125**, 2848 (2003); Y. D. Kim, M. Fischer, and G. Ganteför, *Chem. Phys. Lett.* **377**, 170 (2003).
7. T. H. Lee, K. M. Ervin, *J. Phys. Chem.* **98**, 10023 (1994).
8. B. E. Salisbury, W. T. Wallace, R. L. Whetten, *Chem. Phys.* **262**, 131 (2000).
9. J. Hagen, L. D. Socaciu, M. Elijazyfer, U. Heiz, T. M. Bernhardt, L. Wöste, *Phys. Chem. Chem. Phys.* **4**, 1707 (2002).
10. W. T. Wallace, R. L. Whetten, *J. Am. Chem. Soc.* **124**, 7499 (2002).
11. H. Häkkinen, U. Landman, *J. Am. Chem. Soc.* **123**, 9704 (2001).
12. L. D. Socaciu, J. Hagen, T. M. Bernhardt, L. Wöste, U. Heiz, H. Häkkinen, U. Landman, *J. Am. Chem. Soc.* **125**, 10437 (2003).
13. K. J. Laidler, "Chemical Kinetics." HarperCollins, New York, 1987.

14. M. Haruta, *Appl. Catal. A* **222**, 427 (2001).
15. L. D. Socaciu, J. Hagen, J. Le Roux, D. Popolan, T. M. Bernhardt, L. Wöste, Š. Vajda, *J. Chem. Phys.*, submitted.
16. J. Hagen, L. D. Socaciu, J. Le Roux, D. Popolan, T. M. Bernhardt, L. Wöste, R. Mitrić, H. Noack, V. Bonačić-Koutecký, *J. Am. Chem. Soc.*, submitted.

ACTIVATED DIATOMIC SPECIES AS IMPORTANT REACTION INTERMEDIATES OF NANOCATALYSIS

YOUNG DOK KIM AND GERD GANTEFÖR
Department of Physics, University of Konstanz D-78457 Konstanz, Germany

In the present work, evidences are provided that diatomic molecules such as oxygen and nitrogen tend to adsorb molecularly at room temperature on metal nanoclusters. These results imply that the catalytic reactions on nanoclusters are mediated by the formation of activated diatomic molecules instead of the dissociative chemisorption, which generally takes place on metal single crystal surfaces. Our results demonstrate that molecular-level understanding on nanocatalysis can be obtained by means of experimental techniques of cluster science.

1. Introduction

The most important steps of the heterogeneously catalyzed reactions are generally believed to be dissociation of reactants such as oxygen, nitrogen and hydrogen. The dissociative chemisorption of N_2 is the rate determining step of the ammonia synthesis [1,2]. The dissociation of oxygen molecules is required to catalyze CO to CO_2 via the Langmuir-Hinshelwood mechanism or Mars-van Krevelen mechanism [3,4].

The chemical properties of nanomaterials are of particular interest, since chemical activities change significantly as a function of cluster size [5-8]. Even though various examples for interesting catalytic properties of nanomaterials are recently provided, the molecular-level understanding on nanocatalysis is still missing. To shed light on chemisorption structure on nanoparticles, we have previously performed UPS studies on H/Ti-cluster systems, in which the pattern of UPS spectra of the Ti anion clusters reacted with H_2 completely change as the number of Ti atoms in a cluster exceeds 4 [9]. This result was interpreted in terms of the molecule to atom transition, i.e. hydrogen is molecularly bound on Ti_n^- with n<4, whereas hydrogen dissociates for n > 4 [10]. Indications for the atom to molecule transition were also found in the mass-spectroscopy experiments [9].

2. Experiments and Results

To obtain a deeper understanding on the chemisorption on small nanoclusters, N_2 adsorption on Nb and W anion clusters and O_2 adsorption on Au and Ag cluster are tackled using UPS. M_n^- anions (M = W, Nb, Au and Ag) are produced with a pulsed arc cluster ion source. The temperature of the clusters is estimated to be about room temperature. The mass of the metal anion clusters reacted with an H_2, N_2 or O_2 molecule is selected using Time-of-Flight mass spectrometer (mass resolution $m/\Delta m$=400). A selected bunch is irradiated by a UV laser pulse (hv = 4.66eV) and the kinetic energies of the detached electrons are measured using a "magnetic bottle"- type time-of-flight electron spectrometer with an energy resolution of about 2%. For more detailed description of the experimental set-up [see ref. 10].

The early transition metals such as W, Nb and Ti exhibit very high propensity towards the dissociation of diatomic molecules such as H_2, N_2, and O_2 [1]. However, on W and Nb anion clusters consisting of less than about 10 atoms, N_2 molecularly adsorbs (Fig. 1). In the UPS spectra, the molecular adsorption of N_2 on W anion clusters consisting of 6-8 atoms is evident by the vibrational fine structures of about 200 meV, which correspond to the N-N stretching frequency with end-on or lying-down geometries (Fig. 1) [1]. The vibrational fine structures in the UPS spectrum of an anion correspond to the vibrational frequency of the neutral counterpart with an identical geometry as the anion. In our mass spectroscopy experiments, W anion clusters smaller than W_5^- turned out to be much less reactive towards N_2 adsorption with respect to the larger clusters. For the Nb anion clusters consisting of less than 7 Nb atoms, the N-N stretching frequency corresponds to the end-on adsorption, i.e. only one N atom is attached to the metal (Fig. 1). Only for larger clusters with n > 7, the N-N frequency of about 150 – 180 meV corresponding the more activated lying-down species can be observed.

Besides N_2 adsorption, molecular adsorption can be observed for O_2 adsorption on Au and Ag anion clusters. It was previously shown that O_2 molecularly bound on even numbered Au anion clusters, whereas odd-numbered clusters do not react (Fig. 2) [11,12]. Similar even/odd-relation towards oxygen adsorption is also visible for Ag anion clusters (Fig. 2). In the UPS spectra for $Ag_2O_2^-$ and $Ag_8O_2^-$, the vibrational frequencies corresponding to O-O are observed, indicating that O_2 does not dissociate on Ag_2^- and Ag_8^- (Fig. 2). For other Ag anion clusters reacted with O_2, no vibrational structure can be identified in UPS. Appearance of the O-O vibrational structure in UPS indicates that the additional charge in the anion is localized in oxygen, since then the photoelectron detachment changes the O-O bond length significantly, yielding the Franck-Condon profile, which is the vibrational fine structures. Therefore, absence of the O-O vibrational structure in the UPS spectrum implies less Ag to O_2 charge transfer than Ag_2^- and Ag_8^-. The electron affinities (EA) of Ag_2^- and

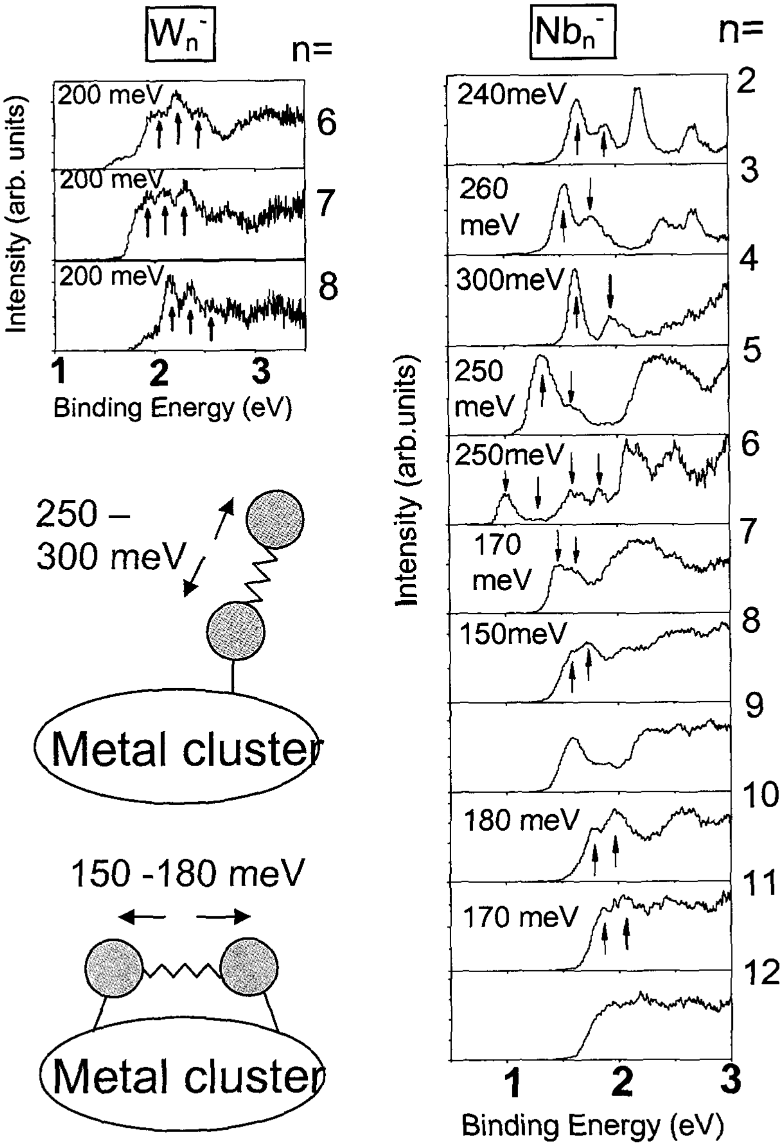

Figure 1. Nitrogen adsorption on W and Nb anion clusters is studied using UPS. The arrows indicate vibrational fine structure assigned to stretching vibration of N_2. The photon energy is 4.66eV.

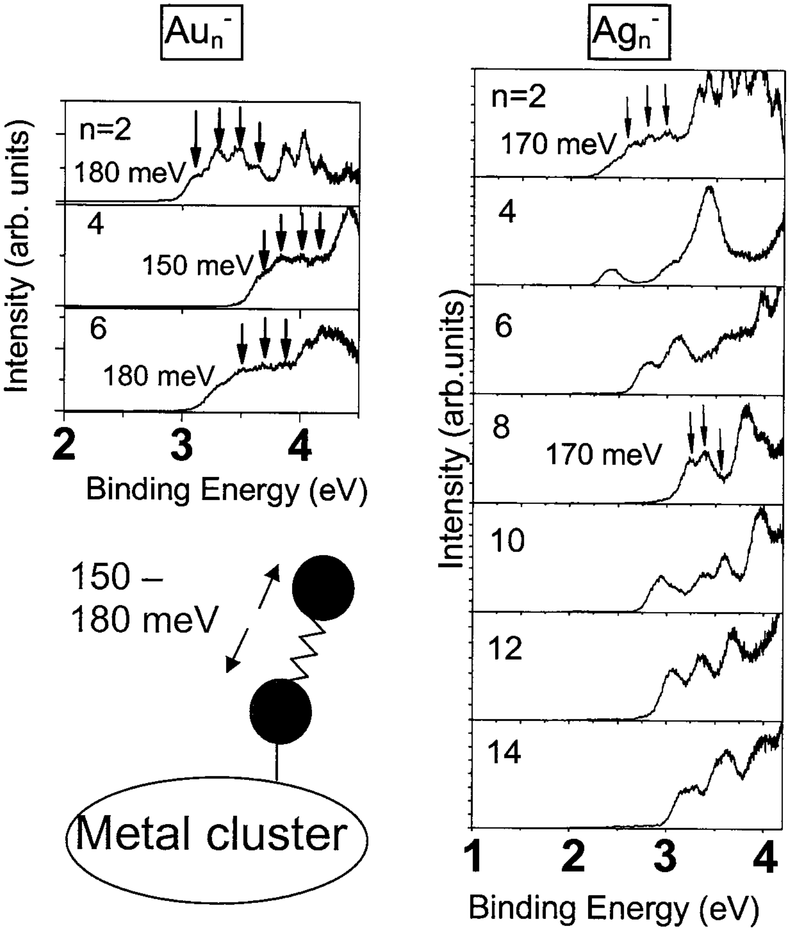

Figure 2. Oxygen adsorption on Au and Ag anion clusters. Oxygen molecularly adsorbs on these clusters, which is evident from the vibrational fine structures corresponding to the O-O stretching mode. Detailed analysis indicates that even those clusters without the vibrational fine structures yield non-dissociative adsorption of oxygen.

Ag_8^- increase by about 1.3 eV upon O_2 adsorption, which is significantly higher than the values for other Ag anion clusters in Fig. 2 (for other Ag clusters, increase of EA upon O_2 adsorption is below 1 eV), also suggesting much larger Ag to O_2 charge transfer for Ag_2^- and Ag_8^-. Considering that the dissociative adsorption of the oxygen requires much larger charge transfers from metal to O_2, one can suggest that O_2 also molecularly adsorbs on the Ag anion clusters in Fig. 2. The larger Ag to oxygen charge transfer for Ag_2^- and Ag_8^- with respect to other Ag anion clusters can be rationalized in terms of the electronic shell model, since one electron transfer from Ag_2^- and Ag_8^- to oxygen yields closed shell configurations ($1s^2$ or $1s^2 1p^6$) [13].

The molecular adsorption of O_2 on Au anion clusters might be not very surprising considering that the dissociative chemisorption of O_2 is energetically less stable than the molecular adsorption, i.e. the chemisorption pattern of the Au bulk crystal is also reflected in the corresponding nanoclusters [14]. However, for H_2/Ti, N_2/Nb, N_2/W and O_2/Ag systems, the chemisorption pattern is completely changed on nanoclusters with respect to the bulk crystals [1,2,15]. It seems that there should be the same physical origin for the non-dissociative adsorption for these systems studied in the present work. Considering that charge transfer from metal to adsorbate is generally crucial for the dissociative adsorption [16], the nondissociative adsorption on nanoclusters may be related to the lower electron densities in nanoclusters with respect to the bulk counterparts.

It should be mentioned that the metal clusters studied in the present work are in the anionic states. The excess electron in the anionic state (partially) occupies the antibonding orbitals of the N_2 or O_2, and therefore the dissociation probability of anions should be higher than those of the respective neutral clusters. However, our result shows that even anions do not dissociate O_2 and N_2. As mentioned above, the dissociative chemisorption of O_2 and N_2 requires more than 4 electrons within a simple electronic model, and it is possible that one additional electron in these small clusters is not sufficient to yield the dissociative chemisorption.

Considering that the efficient dissociation of gas phase reagents is generally required to increase the catalytic activities as mentioned in the introduction, do our results indicate that nanoclusters should be generally catalytically much less reactive than the bulk counterparts? It is interesting to note that Au nanoclusters are much more reactive than other hitherto known catalysts for CO-oxidation. On Au nanoclusters, the CO-oxidation was suggested to be operating via non-dissociative adsorption of O_2 followed by the formation of CO_3 species [11,17]. The CO_3 can then be decomposed to O and CO_2. This mechanism is much different from the CO-oxidation mechanisms for the bulk metal surfaces, proceeding via the dissociative chemsiorption of O_2. It is also important to note that the ammonia synthesis on a single molybdenum centre proceeds through the reaction of di-nitrogen species and hydrogen [18]. This result is much different from the observations on metal single crystal surfaces, on which dissociation of nitrogen is necessary for the ammonia synthesis. Accordingly, even though small nanoclusters can often less efficiently dissociate diatomic molecules, the formation of the activated diatomic molecules can open new reaction channels, resulting in superior catalytic activities of the nanoclusters.

3. Concluding Remarks

In the present work, ample evidences are provided that molecular adsorption of diatomic molecules is favoured on nanoclusters consisting of less than 10-20 atoms. It is likely that the catalytic process on nanoclusters generally includes non-dissociatively adsorbed activated species, which hardly form on larger particles or bulk crystal surfaces under reaction conditions. We demonstrate that studies of the reactions between gas molecules and mass-selected clusters can open new insights into the characteristics of nanoclusters.

Acknowledgments

We acknowledge DFG (Deutsche Forschungsgemeinschaft) for the financial supports.

References

1. The Chemical Physics of Solid Surfaces and Heterogeneous Catalysis, edited by King and Woodruff. Vol 3A 1990.
2. Somorjai G.A. Introduction to Surface Chemistry and Catalysis, Wiley, New York, 1994.
3. H. Over et al. Science 287 (2000) 1474.
4. Engel T.; Ertl G. Adv. Catal. 28 (1979) 1.
5. M. B. Knickelbein, Annu. Rev. Phys. Chem. 50 (1999) 79.
6. A. Kaldor, D. M. Cox, and M. R. Zakin, Adv. Chem. Phys. 70 (1988) 211.
7. M. Valden, X. Lai, D.W: Goodman, Science 281 (1998)1647.
8. A.T. Bell, Science 200 (2003) 1688.
9. S. Buckart, N. Blessing, and G. Ganteför, Phys. Rev. B 60 (1999) 15639.
10. C.-Y. Cha, G. Ganteför, and W. Eberhardt, Rev. Sci. Instrm. 63 (1992) 5661.
11. D. Stolcic, M. Fischer, G. Ganteför, Y.D. Kim, Q Sun, P. Jena J. Am. Chem. Soc. 125 (2003) 2848.
12. T.H. Lee, K.M. Ervin. J. Phys. Chem. 98 (1994) 10023.
13. W.A. Heer, Rev. Mod. Phys. 65 (1993) 611.
14. N. Saliba, D. Holmes-Parker, and B.E. Koel, Surf. Sci. 410 (1998) 270.

15. C.T. Campbell and M. Paffett, Surf. Sci. 143 (1984) 517.
16. R. Hoffman, Rev. Mod. Phys. 60 (1988) 601.
17. A. Sanchez, S. Abbet, U. Heiz, W.D. Schneider, H. Häkkinen, R.N. Barnett, U. Landman,J. Phys. Chem. A 103 (1999) 9573.
18. D.V. Yandulov, and R.R, Schrock, Science 301 (2003) 76.

RELATIVISTIC DENSITY FUNCTIONAL CALCULATIONS FOR OPEN–SHELL SYSTEMS

S. VARGA AND A. ROSÉN
Department of Experimental Physics
Chalmers University of Technology and Göteborg University
SE-41296 Göteborg
Sweden
E-mail: varga@fy.chalmers.se

J. ANTON AND B. FRICKE
Fachbereich Naturwissenschaften
Abteilung Physik
Universität Kassel
D-34132 Kassel
Germany

We report on results of four–component moment-polarized relativistic density functional calculations for open shell systems. Especially, in this contribution we focus on atoms with open shells. The results obtained so far show, that atomic ground state energies can be calculated with good accuracy. Thus, more accurate binding energies for molecules and clusters can be estimated.

1. Introduction

Accurate values of binding energies of molecules and clusters are an important basis for determining the stability and trends in bonding character of polyatomic systems. A general way for obtaining such energies is to subtract the total energy of the compound from the total energies of its constituents. Using a relativistic density functional theory (RDFT) method [1,2] we are able to calculate those values accurately enough, especially in the presence of atoms with nuclear charges at the upper end of the periodic table.

However, depending on the occupation of the electronic spin states, different values are possible which are clearly distinguished in the nonrelativistic (spin unrestricted) regime by spin-up and spin-down orbitals. In fact, the differences between total energies of polarized versus unpolarized treatment can be significant, e.g. for the gold atom it is approximately 0.15 eV.

To account for the 'correct' atomic reference energies the treatment of the electron spin was included into the moment–polarized [a] version [3] of the RDFT [4].

2. Method

The method is based on the inclusion of the magnetization density into the relativistic density functional formalism [3,5]. In this approach the total energy functional is given by

$$E[n] = T_s + E^{ext}[n] + E^{H}[n] + E^{xc}[n, \mathbf{m}] \tag{1}$$

with the functionals of the kinetic energy, the external potential energy, the Hartree energy and the exchange–correlation energy (in sequence of occurence). The basic ingredients, the electronic density n and the magnetization density $\mathbf{m}$,

$$n(\mathbf{r}) = \sum_{k}^{occ} \psi_k^\dagger(\mathbf{r})\psi_k(\mathbf{r}) \; ; \tag{2}$$

$$\mathbf{m}(\mathbf{r}) = -\mu_B \sum_{k}^{occ} \psi_k^\dagger(\mathbf{r})\beta\mathbf{\Sigma}\psi_k(\mathbf{r}) \tag{3}$$

are expressed by a set of N auxiliary four-component spinors $\psi_k(\mathbf{r})$, given numerically on a three-dimensional point mesh. The total energy is then derived by the solution of the corresponding relativistic Kohn-Sham equations (RKS) in their non-collinear form [3]

$$\left(\hat{t} + V^{ext} + V^{H} + \frac{\delta E^{xc}[n,\mathbf{m}]}{\delta n} - \mu_B\beta\mathbf{\Sigma}\cdot\frac{\delta E^{xc}[n,\mathbf{m}]}{\delta \mathbf{m}}\right)\psi_k(\mathbf{r}) = \epsilon\psi_k(\mathbf{r}) \, . \tag{4}$$

This general form can be transformed into the collinear form in which the alignement of $\mathbf{m}(\mathbf{r})$ is parallel to the symmetry axis and the density is expressed by the generalized spin densities

$$n_{\pm}(\mathbf{r}) = \frac{1}{2}\left(n(\mathbf{r}) \mp \frac{1}{\mu_B}\mathbf{m}_z(\mathbf{r})\right) = \sum_{k}^{occ} \psi_k^\dagger(\mathbf{r})\frac{1 \pm \beta\Sigma_Z}{2}\psi_k(\mathbf{r}) \quad . \tag{5}$$

---

[a] i.e. the relativistic extension of the spin–polarization, since the electron spin is not well defined in the relativistic case.

A brief discussion of the two different approaches, the collinear and non-collinear form, can be found in the Reference [3].

3. Results

In this section some results of polarized calculations for atoms are shown.

First, we start from a pure nonrelativistic treatment using the nonrelativistic limit of the RDFT. In Table 1 and Table 2 the calculated energy eigenvalues (ϵ) and the total energies E_{tot} obtained from spin-polarized nonrelativistic Hartree-Fock-Slater calculations are listed for the atomic ground states of nitrogen (^4S) and oxygen (^3P), respectively. The data show excellent agreement with the reference values obtained by the highly accurate finite element method (FEM) [6] as well as those of the Amsterdam density functional code (ADF) [7].

Table 1. Energy eigenvalues and total energy from spin-polarized Hartree-Fock-Slater calculations for the atomic ground state ^4S of nitrogen. In the column 'occ' the occupation numbers of the electronic spin states are given.

	occ	RDFT	FEM	ADF
ϵ(1s-up)	1	-14.0011	-14.0011	
ϵ(1s-down)	1	-13.9328	-13.9328	
ϵ(2s-up)	1	-0.7071	-0.7071	-0.7068
ϵ(2s-down)	1	-0.4902	-0.4902	-0.4909
ϵ(2p-up)	3	-0.2941	-0.2941	-0.2937
ϵ(2p-down)	0	-0.0932	-0.0931	-0.0926
E_{tot}		-54.0018	-54.0018	

Table 2. As Table 1 for the ^3P ground state of oxygen.

	occ	RDFT	FEM	ADF
ϵ(1s-up)	1	-18.7973	-18.7972	
ϵ(1s-down)	1	-18.7333	-18.7332	
ϵ(2s-up)	1	-0.8985	-0.8985	-0.8982
ϵ(2s-down)	1	-0.7497	-0.7497	-0.7504
ϵ(2p-up)	3	-0.3626	-0.3626	-0.3627
ϵ(2p-down)	1	-0.2213	-0.2213	-0.2217
E_{tot}		-74.3565	-74.3565	

In a next step we have applied the RKS for some atoms with different nuclear charges which are distributed over a wide region of the periodic table.

The results are shown in Table 3. These atomic calculations are performed with the molecular code (in this context denoted as molecular one-center calculations, MOC). In order to test our approach we have performed the calculations using the relativistic local density approximation [8] (RLDA) in the nonrelativistic form for the exchange–correlation potential as it has been done in the reference [10]. We have chosen different combinations of j and m_j values in order to determine the ground state. As can be seen, the calculated total energies are in very good accordance with the reference data. In the third column those occupied atomic valence states are listed which determine the highest occupied molecular orbitals in the MOC.

Table 3. Values of the total energies for some atoms (in Hartree): results of relativisitic moment-polarzed calculations in the collinear form using the local density approximation.

element	calculated	reference [10]	occupied valence (j, m_j)
N	-54.16437	-54.16817	2p(3/2,3/2)
O	-74.58410	-74.58346	2p(3/2,±3/2)
Cu	-1652.33482	-1652.33534	4s(1/2,-1/2)
Pt	-18436.49817	-18436.49930	5d (5/2,±5/2),(5/2,±3/2),(5/2,+1/2)
Au	-19037.57605	-19037.57646	6s(1/2,-1/2))
Tl	-20277.88576	-20277.88468	6p(1/2,+1/2)
Bi	-21570.04069	-21570.04178	6p(3/2,-3/2)

As a final example we have explicitly calculated the 'spin-polarization' energy for the bismuth atom in its ground state configuration ($6p_{1/2}^2$,$6p_{3/2}^1$) for different exchange–correlation functionals. Besides the RLDA, also the semilocal Becke88/Perdew86 scheme of the generalized gradient approximation in its relativistic [9] (RGGA) extension was applied. The amounts of the polarization energies were determined to 0.11 eV and 0.14 eV for the RLDA and RGGA, respectively. This can be compared with the values from scalar relativistic calculations [7].

Table 4. Values of the total energies for the bismuth atom: Δ denotes the difference between polarized and unpolarized calculations. All values are given in eV.

method	RLDA	RGGA
a) unpolarized	-585694.90293	-586487.28828
b) polarized, coll	-585695.01346	-586487.43276
$\Delta^{b)-a)}$	0.1105	0.1444
Δ Ref.[7]	0.1212	0.1543

4. Summary

The results of moment-polarized calculations of the ground states for atoms show good agreement with reference data. A problem up to now is the determination of the correct ground state because many configurations have to be calculated. However, it is notable, that the recent development of the RDFT not only offers the possibility of determining binding energies accurately but also treating multiplet splitting of atomic levels and considering magnetic effects.

Acknowledgments

S. V. would like to thank the members of the molecular physics group at Chalmers University of Technology and the REUTERS AG, Germany.

References

1. T. Baştuğ, K. Rashid, W.-D. Sepp, D. Kolb and B. Fricke, *Phys. Rev. A* **55**, 1760 (1997)
2. S. Varga, E. Engel, W.-D. Sepp and B. Fricke, *Phys. Rev. A* **59**, 4288 (1999)
3. J. Anton, T. Jacob, B. Fricke and E. Engel, *Phys. Rev. Lett.* **89**, 213001 (2002)
4. A. K. Rajagopal and J. Callaway, *Phys. Rev. B* **10**, 1 (1973)
5. E. Engel, R. M. Dreizler, S. Varga and B. Fricke, "Relativistic Density Functional Theory" in "Relativistic Effects in Chemistry and Physics of heavy elements", John Wiley and Sons (Ed. B. A. Hess) (2003)
6. D. Heinemann, A. Rosén and B. Fricke, *Chem. Phys. Lett.* **166**, 627 (1988)
7. ADF 2.3.0, Theoretical Chemistry, Vrije Universiteit, Amsterdam (1997)
8. E. Engel, S. Keller, A. Facco-Bonetti, H. Müller and R. M. Dreizler, *Phys. Rev. A* **52**, 2750 (1995).
9. E. Engel, S. Keller and R. M. Dreizler, *Phys. Rev. A* **53**, 1367 (1996)
10. E. Engel, T. Auth and R. M. Dreizler; *Phys. Rev. B* **64**, 235126 (2001)

ELECTRONIC STRUCTURE AND STABILITY OF THE $As@Ni_{12}@As_{20}$ AND As CAGES

TUNNA BARUAH
Department of Physics, Georgetown University, Washington DC, 20057

RAJENDRA R. ZOPE
School of Computational Sciences, George Mason University, Fairfax, VA 22030

MARK R.PEDERSON
Center for Computational Materials Science, Naval Research Laboratory, Washington DC 20375-534

The recent synthesis of the $[As@Ni_{12}@As_{20}]^{-3}$ clusters with near perfect icosahedral symmetry [Science, 300, 778 (2003)], points to the possibility of forming As based fullerenes. Here we first examine the electronic structure, vibrational stability and bonding of the $As@Ni_{12}@As_{20}$ cluster and then examine possibilities of forming other As cages by all-electron density functional total energy calculations. We show that the As-As σ bonds are weakened and strong As-Ni bonding occurs in the $As@Ni_{12}@As_{20}$ cluster. Our calculations show that although the As cages are vibrationally stable, only the dodecahedral As_{20} is stable against dissociation into As4 clusters. Finally, the infrared and Raman spectra of the $As@Ni_{12}@As_{20}$ and the As clusters are presented.

1. Introduction

The recent synthesis of $As@Ni_{12}@As_{20}$ cluster by Eichhorn and co-workers [1] marks an important step in the search of inorganic fullerenes that is triggered by the discovery of the C_{60} molecule [2, 3]. The $As@Ni_{12}@As_{20}$ cluster is like an onion, where after peeling off one layer of atoms one can arrive at an inside cage made up of different kind of atoms. The molecule in the crystalline form has nearly perfect icosahedral symmetry. The outer cage is made up of twenty As atoms in the form of a dodecahedron where each As atom is 3-fold coordinated. The structure of the $As@Ni_{12}@As_{20}$ is shown in Fig.1.The outer As cage consists of 12 pentagonal faces and each face is capped from inside by a Ni atom. The As_{20} outer cage has dodecahedral symmetry and the inner Ni cage has icosahedral symmetry. In the crystalline structure, this molecule forms a salt as $[As@Ni_{12}@As_{20}]^{-3}[(C_4H_9)_4P]_3^{+}$.

In this article, we present our density functional calculation of the electronic stricture, vibrational frequencies and calculated infrared and Raman spectra of the As@Ni_{12}@As_{20} cluster. Based on the electronic density and the vibrational modes, we analyze the bonding between the inner and the outer cages. The synthesis of the As@Ni_{12}@As_{20} molecule points to the possibility of synthesizing other As based fullerene-like molecules. We have optimized the structures of various possible As cages and examine their stability. We show that As_{20} cluster is particularly stable and the predicted Raman spectra of As cages can help in identifying these clusters in As vapor.

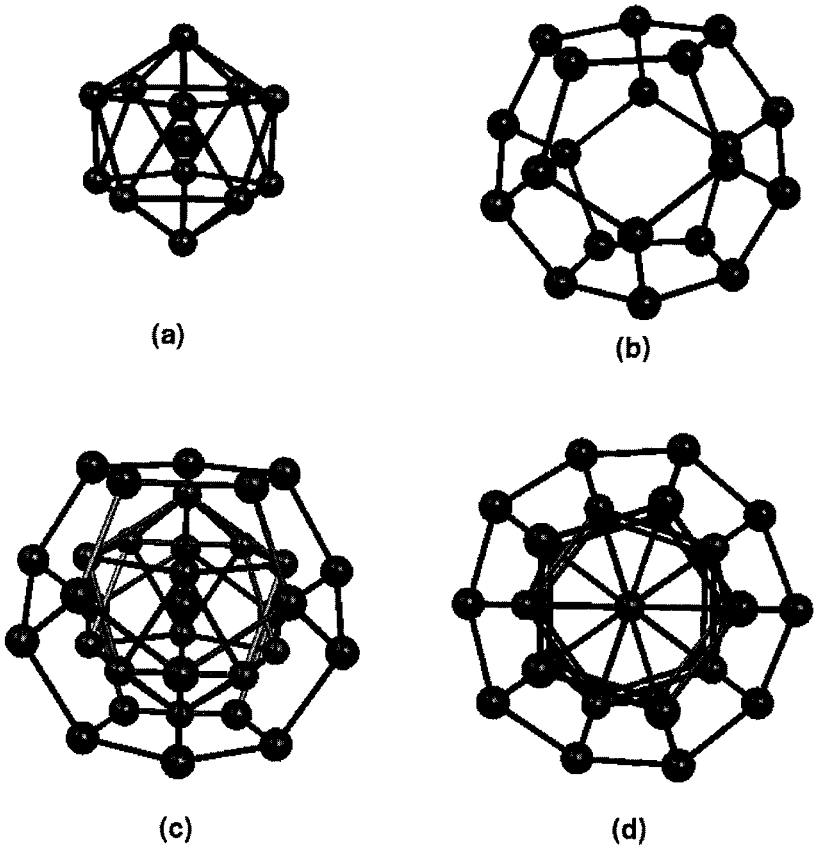

Figure 1. The optimized geometries of the a) As@Ni_{12}, b) As_{20} and c) As@Ni_{12}@As_{20} cages. Another view of As@Ni_{12}@As_{20} is shown in (d).

In the following section we briefly describe the computational methods. The next section contains results and discussion on the As@Ni_{12}@As_{20} cluster. The subsequent section describes the possibilities of existence of As_n clusters.

2. Computational Details

Our all-electron density functional [4] calculations were carried out using the Naval Research Laboratory Molecular Orbital Library (NRLMOL) package [5]. This package uses a linear combination of atomic and molecular orbitals which are expanded in a set of Gaussians. The Gaussian exponents are optimized for each atom [6]. The basis for the As and Ni atoms consists of 7s, 6p and 4d type contracted Gaussians. In the present calculation the exchange-correlation effect was described within the generalized gradient approximation due to Perdew, Burke, and Ernzerhof [7]. The geometry optimization was carried out using the LBFGS method.

For the As_n clusters, we have restricted our study to those cage structures which may break up into an integral number of tetramers. This is because the As tetramer is a highly stable cluster [8]. The focus is on finding vibrationally stable symmetric cages and on obtaining the energies of dissociation into tetramers. Also we have restricted the cage structures to the ones with 3-fold coordination as seen in the experimentally achieved As shell of the $As@Ni_{12}@As_{20}$ cluster.

The optimized structures were further examined for vibrational instabilities. The vibrational frequencies were calculated by displacing each atom from its equilibrium positions and calculating the forces. The dynamical matrix is constructed from the energies of the perturbed system and from this matrix the frequencies are calculated. The infrared and Raman spectra are calculated by applying a small electric field of 0.005 a. u.. The details of these methods can be found in Ref. [9].

3. Results and Discussion

3.1. $As@Ni_{12}@As_{20}$

The optimized geometries of the $As@Ni_{12}@As_{20}$ cluster and its two subunits As_{20} and $As@Ni_{12}$ are shown in Fig. 1. The atomization energy, electron affinity, ionization potential, and gap between the highest occupied and lowest unoccupied molecular orbitals (HOMO-LUMO) of these three clusters are presented in Table 1. The geometry of the As_{20} cage is shown in Fig. 1. It has dodecahedral symmetry and consists of 12 pentagonal rings. The As atoms are sp^3 hybridized and each As atom is 3-fold coordinated. The cage is formed by 30 sigma bonds between the As atoms. The radius of the isolated As cage is 3.5 Å. It is a closed shell system with a gap of 1.44 eV between the highest occupied and lowest unoccupied molecular orbitals (HOMO-LUMO).

The As@Ni_{12} cage has an onion-like structure with one As atom at the center of Ni icosahedral cage. The radius of the isolated As@Ni_{12} is 2.36 A which is much smaller then the As_{20} cage. This cluster has a magnetic moment of 3 μ_B. This cluster has a small HOMO-LUMO gap of 0.17 eV.

The encapsulation of the As@Ni_{12} by As_{20} to form the As@Ni_{12}@As_{20} (cf. Fig.1(c)) leads to an expansion of both the cages by about 10-12%. The atomic coordinates of the onion-like molecule satisfies the golden rule of the icosahedral symmetry. The molecule is stable by 26 eV with respect to its two isolated subunits. The encapsulated molecule has a magnetic moment of 3 μ_B.

Table 1. The atomization energy (AE), electron affinity (EA), ionization potential (IP), and HOMO-LUMO gap (ΔE) in eV for the As_{20}, As@Ni_{12} and As@Ni_{12}@As_{20} are presented.

System	AE	EA	IP	ΔE
As_{20}	2.79	2.45	6.75	1.44
As@Ni_{12}	3.05	2.44	5.56	0.17
As@Ni_{12}@As_{20}	3.70	3.47	6.4	0.11

The vibrational frequencies of the As_{20}, As@Ni_{12} and the AsNi_{12}@As_{20} confirm the clusters to be local minima on the potential energy surface. One of the main interesting points of this molecule is its high symmetry and therefore the nature of bonding between the Ni and the As cage is therefore of great importance. The IR and Raman spectra of the As@Ni_{12}@As_{20} and its subunits are calculated to discern the strength of bonding between them. The IR and Raman spectra are shown in Fig. 2 and in Fig. 3 respectively. The As_{20} shows Raman active modes at 73, 79, and 152 cm^{-1}. The low frequency Raman active modes are symmetry breaking H_g modes while the mode at 152 cm^{-1} is a breathing mode. The IR spectra of As_{20} shows only a single peak at 167 cm^{-1}. The vibrational modes of As@Ni_{12} at 123, 144, 188, and 305 cm^{-1} have T_{1u} symmetry and are IR active whereas the five-fold degenerate modes at 109 and 217-221 cm^{-1} along with the A_g mode at 262 cm^{-1} are Raman active.

The IR spectrum of As@Ni_{12}@As_{20} is dominated by a large peak at 265 cm^{-1} with three smaller peaks at 84, 163, and 212 cm^{-1}. The low frequency IR mode of As@Ni_{12}@As_{20} at 84 cm^{-1} appears to be due to the rocking motion of the As@Ni_{12} in which the As_{20} cage also gets mildly distorted. This rocking motion can be correlated with the mode at 143 cm^{-1} in the spectrum of As@Ni_{12}. The small peak at 163 cm^{-1} in the IR of As@Ni_{12}@As_{20} is due to the three-fold vibration of the central As atom. The most dominant peak in the spectrum of As@Ni_{12}@As_{20} at 265 cm^{-1} is caused by torsional motion mostly of the Ni cage.

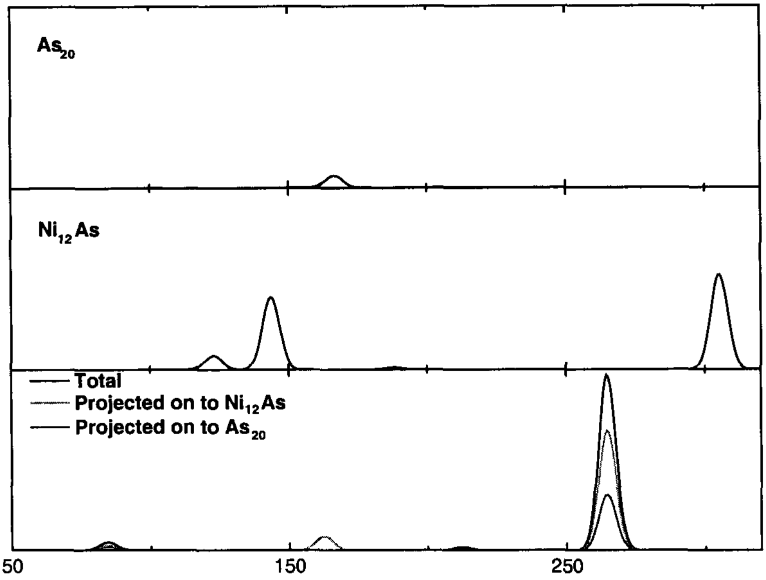

Figure 2. The IR spectrum for the As@Ni_{12}@As_{20} molecule and its projections on its subunits are shown in the bottom panel. The top two panels show the IR spectra of the isolated As_{20} and As@Ni_{12} cages respectively.

The highest Raman peak of the As@Ni_{12}@As_{20} is seen at 67 cm^{-1} followed be a small peak at 102 cm^{-1}. These modes have H_g symmetry. The increased intensity of the lowest Raman peak in As@Ni_{12}@As_{20} is due to an increase in polarizability derivative upon encapsulation. In fact, we find that the ratio of the intensities of the highest Raman peak in As@Ni_{12}@As_{20} and its subunits scales exactly as the square of the ratio of their radii. The mode at 142 cm^{-1} is a breathing mode and correlates to the breathing mode of As@Ni_{12}@As_{20} at 152 cm^{-1}. The mode at 227 cm^{-1} which is basically an asynchronous breathing motion with motions of the Ni and As cage being in opposite phase.

From both the IR and Raman spectra we find that there is no one-to-one mapping between the peaks in the IR spectrum of As@Ni_{12}@As_{20} with those of its isolated subunits. We do not see any pure "rattling" motion of As@Ni_{12} inside the As_{20} cage and therefore there must be a strong coupling of the vibrational modes between the As@Ni_{12} and the As_{20} cages [11].

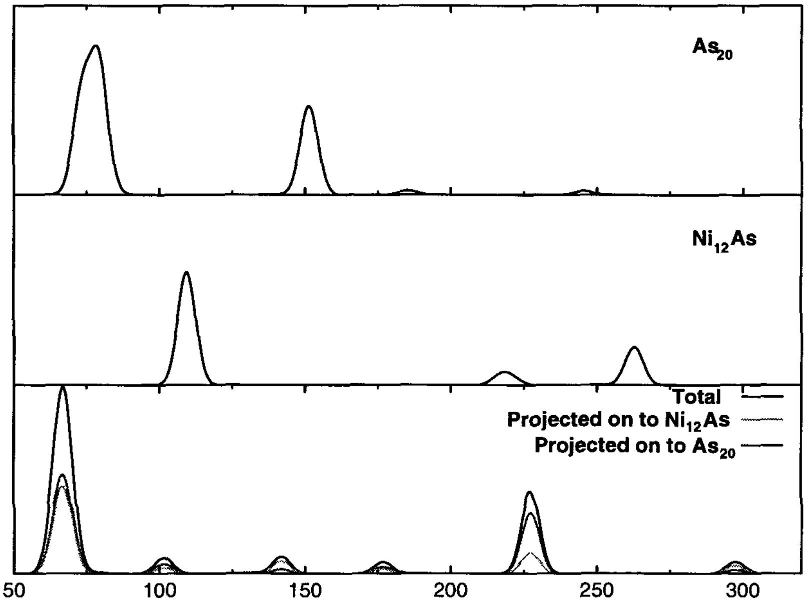

Figure 3. The Raman spectrum for the $As@Ni_{12}@As_{20}$ molecule and its sub-units.

The isovalued surfaces of the charge densities in isolated As_{20}, $As@Ni_{12}$, and the $As@Ni_{12}@As_{20}$ cage are shown in Fig. 4. The values of the charge density surfaces were chosen to bring out the relative strengths of various bonds. In the isolated $As@Ni_{12}@As_{20}$, the As-As bonds are σ bonds formed due to the overlap of the half-filled sp^3 hybridized orbitals. The As atoms also possess a lone pair of electrons in the fourth orbital which do not take part in the bonding. Thus there are 30 pairs of σ bonds which hold the cage together. The second figure in Fig. 4 shows the isosurface of density in $As@Ni_{12}@As_{20}$ cage. The interesting point in this cage is that the As-As bonds become much weaker compared to the As_{20} cage and As atoms form strong bonds with the inner Ni atoms. In the encapsulated form, instead of forming σ bonds with the nearest As atoms, the As atoms form three σ bonds with the d orbitals from three nearest Ni atoms. This way the octet rule is satisfied for each of the As atoms. Each Ni forms bonds with five nearest As atoms and Ni atoms lie very close to the center of the pentagonal faces of the As cage. However, they lie below the pentagonal face and give the $As@Ni_{12}@As_{20}$ cluster a dimpled golf-ball like appearance. The strong bonding between the As and the Ni atoms on the surface makes the Ni cage expand and the outer As cage also expands due to kinetic energy repulsion [12].

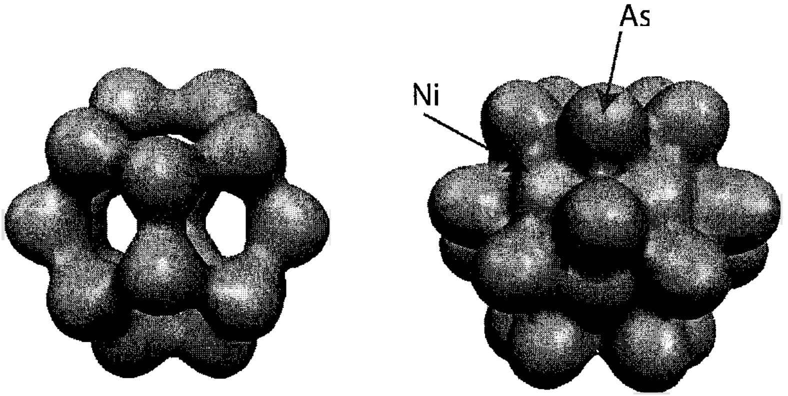

Figure 4. The isosurfaces of the charge densities of isolated As_{20} , and the $As@Ni_{12}@As_{20}$ cluster.

3.2. *As cages*

We have examined the stability of fullerene-like As cages where the As atoms are 3-fold coordinated. The optimized geometries of the of the $As_{4,8,20,28,32,36,60}$ cages are shown in Figs. 5 and 6.

The As_4 and As_8 clusters have T_d and O_h point symmetry. The bond lengths and angles do not vary in these structures due to their symmetry. A tetrahedral structure for the tetramer was predicted by Morino *et al.* [10] and was shown to be stable by Shen and Schaefer [8]. The As_{20} has a dodecahedral structure made up of 12 pentagons. The 28-atom cluster also has T_d symmetry and has three inequivalent atoms. The 32-atom cluster has an unusual cage-like structure which has an elongated structure. The symmetry for the As_{32} cluster allows for cyclic permutations plus non cyclic permutations followed by inversion. The As_{36} has D_{6h} symmetry while the 60-atom cluster has a structure similar to the C_{60} structure. However, the As_{60} cluster is much larger than the C_{60} in size. Apart from the As_{32}, all the clusters from n = 20 onward are spherical in shape. While As_{20} is made up of pentagons, the 28-, 32-, 36-, 60-atom clusters have both pentagonal and hexagonal faces.

The symmetry, atomization energy, energy gap between the HOMO-LUMO gap, the dissociation energies with respect to As_4, vertical ionization potential and electron affinities are presented in Table 2 The binding energies per atom of the As clusters are centered around 2.7 eV. All the clusters considered here have close shell structures and are Jahn-Teller stable. We have also confirmed the vibrational stability of the As clusters. Although the atomization energies and vibrational frequencies indicate the clusters to be stable, apart from the As_{20} cluster, all the other cages are unstable with respect to As_4. It may be pointed out that Shen and Schraefer have predicted that As_{20} is unstable with respect to dissociation into As_4 clusters [8].

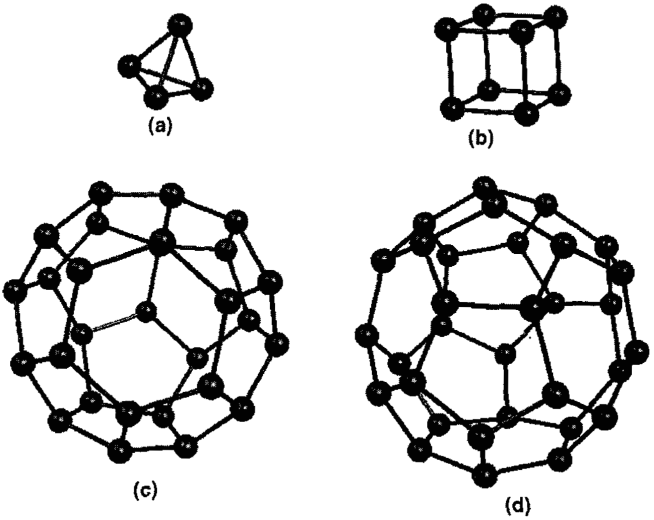

Figure 5. Structures of (a) As_4, (b) As_8, (c) As_{28}, and (d) As_{32} cages.

We have also checked the possible dissociation channels for the As_{20} cage. The monomer dissociation costs 55.8 eV, the dimer costs 13.90 eV and the tetramer dissociation costs 0.54 eV. The above values show that the tetramer dissociation is the most favored channel for the As_{20} cage. This feature was also predicted by Shen and Schaefer [8].

We find that the binding energy of the As_{20} is slightly higher than the most stable As_4 cluster. The As_4 clusters are highly unreactive as evident from the large HOMO-LUMO gap and large vertical ionization potential (vIP) and negative vertical electron affinity (vEA) (cf. Table 2). The instability of the clusters increases towards the larger sizes [13].

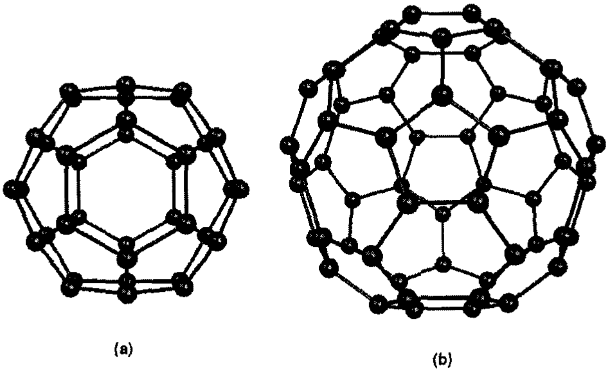

Figure 6. Structures of As_{36} and As_{60}.

Table 2. The atomization energies (AE), vertical ionization potentials (vIP), vertical electron affinities (vEA), HOMO-LUMO Gaps and dissociation energies (DE) for the tetramer channel are presented for As_n where n = 4, 8, 20, 32, 36, and 60. All values are in eV.

Cage	Symmetry	AE (eV)	VIP (eV)	vEA (eV)	HOMO-LUMO gap (eV)	DE (eV)
As_4	T_d	2.76	8.68	-0.32	4.10	0.00
As_8	O_h	2.62	7.15	1.78	1.38	1.12
As_{20}	I_h	2.79	6.83	2.45	1.44	-0.54
As_{28}	T_d	2.70	6.74	2.19	1.50	1.68
As_{32}	D_3	2.69	6.65	2.61	1.41	2.23
As_{36}	D_{6h}	2.67	6.19	2.84	1.31	3.14
As_{60}	I_h	2.57	6.30	3.18	1.28	11.29

The calculated Raman spectra of the As cages are plotted in the frequency ranges of 0 - 120 cm^{-1} and 120 - 400 cm^{-1} in Figs. 7 and 8 respectively. The larger clusters show high peaks in the low frequency region which are several order of magnitude larger than that of the As_4 cluster. The Raman intensity which depends on the polarizability increases for larger clusters. Due to the large radii of the higher order clusters, the polarizability and its derivative increases which in turn influences the Raman intensity. This trend is seen across the series. The As_{60} shows an intense Raman peak at 18 cm^{-1} which is several times larger than those for As_{28}, As_{32}, and As_{36}. This peak corresponds to a H_g mode of vibration. The scattering cross section is inversely proportional to the frequency of the vibrational mode and therefore at low frequencies the Raman intensity increases as can be seen from Fig. 7.

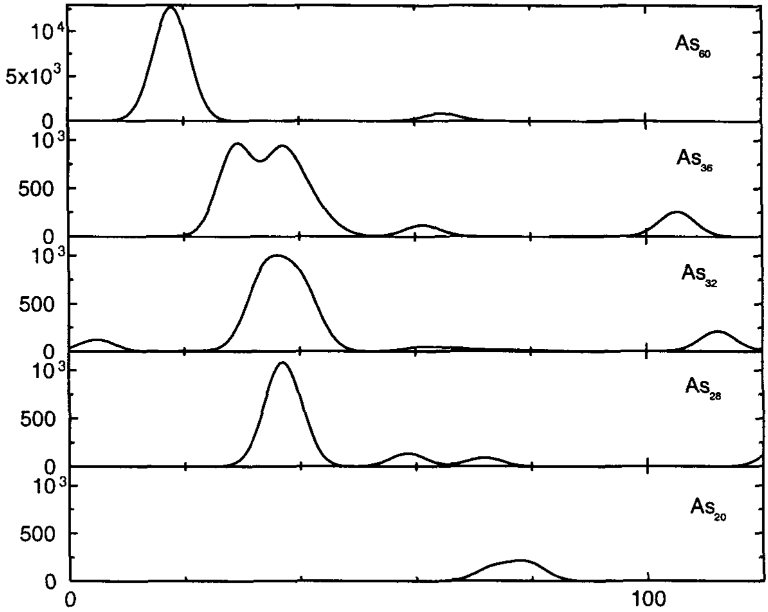

Figure 7. Raman spectra of As_{20}, As_{28}, As_{32}, As_{36}, and As_{60} clusters in the frequency range 0-120 cm^{-1}. The Raman spectra of the As_4 and As_8 clusters do not have any peak in this range. The Raman intensity of the As_{60} is much larger compared to the other clusters and therefore is plotted in a different scale.

The Raman intensities are much lower for the smaller clusters and peaks are seen at higher frequencies (Fig. 8). The Raman scattering intensities in the frequency range 120- 400 cm^{-1} are shown in Fig. 8. All the modes of As_4 show Raman activity since they are respectively of A_1, T_2 and E symmetry. The highest peak for As_4 occurs at 344 cm^{-1}. The experimental Raman spectra of As vapor shows a strong peak at 356 cm^{-1} [15]. The As_4 shows other peaks at 201 and 256 cm^{-1}. The experimental spectrum displays a broad peak at around 250 cm^{-1} which becomes much broader at high temperature. A weighted Raman spectrum of the most stable species, namely As_4 and As_{20} shows an asymmetric peak around 250 cm^{-1} similar to the experimental profile. The next peak at 200 cm^{-1} is much smaller in intensity but is still visible in the experimental spectrum. The calculated As_{20} Raman spectrum shows prominent peaks at lower frequencies of 185, 151, and 79 cm^{-1}. Since the experimental Raman spectrum is measured between 120 to 450 cm^{-1}, the large signatures of the As_{20} can not be discerned from the experimental spectrum. An experimental measurement of the Raman spectra in the low frequency region can be helpful in identifying the existence of As_{20}.

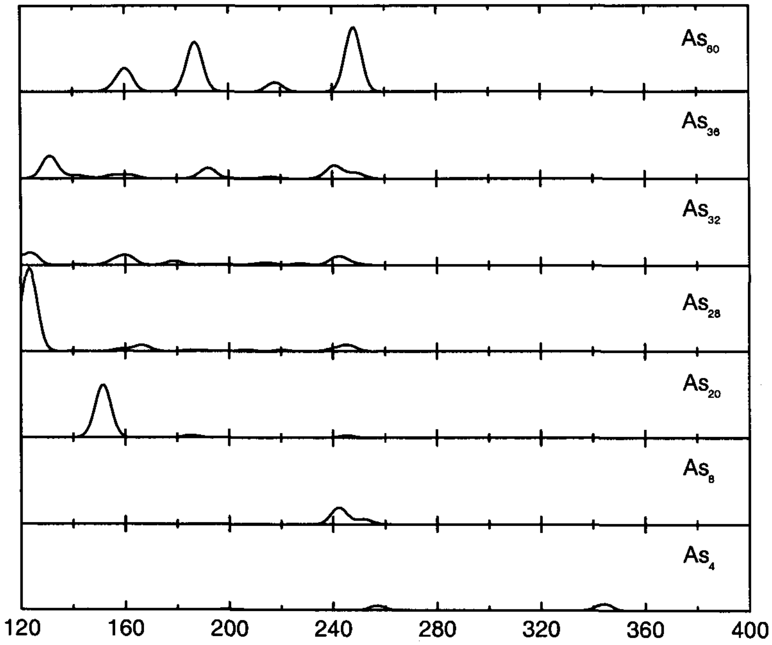

Figure 8. Raman spectra of As_4, As_8, As_{20}, As_{28}, As_{32} , As_{36}, and As_{60} clusters in the frequency range 120 - 400 cm^{-1}. All the panels show Raman intensity in the same scale.

4. Summary

We have carried out an all-electron density functional study on the geometry, electronic structure, and vibrational stability of As_{20}, As@Ni_{12}, and As@Ni_{12}@As_{20} clusters. We find that the encapsulated cluster has icosahedral symmetry in the gas-phase. We also predict the vibrational frequencies of all the three clusters considered and predict their IR and Raman spectra. The lack of a one to one mapping between the IR and Raman spectra of the $As@Ni_{12}@As_{20}$ and As_{20} and $As@Ni_{12}$ shows that there exists strong interaction between the two cages. The isodensity surface of the As_{20} and $As@Ni_{12}@As_{20}$ shows that the As-As bonding undergoes drastic change in the encapsulated form and becomes much weaker. Each As in $As@Ni_{12}@As_{20}$ forms strong bonds with the three nearest neighbor Ni atoms.

We have also examined the possibility of existence of As cage structures in gas-phase. We have studied the geometry, vibrational stability, energetics and Raman spectra of As cages of size n = 4, 8, 20, 28, 32, 36, and 60. In this work we have restricted search for caged clusters with 3-fold coordination and also the ones with relatively high symmetry. We find that all the clusters except As20 are unstable against dissociation into As4 units. The vibrational stability of the clusters are determined and we also predict theoretically the Raman spectra of the cages studied here. We find that the larger clusters possess high polarizability. We expect our study will inspire experimental search for such metastable clusters.

Acknowledgments

TB and MRP acknowledges financial assistance from ONR (Grant No. N000140211046) and by the DoD High Performance Computing CHSSI Program. RRZ acknowledges support from the GMU. The authors thank S.L. Richardson and M. R. Beltran for helpful discussions.

References

1. M. J. Moses, J. C. Fettinger, and B. W. Eichhorn, Science **300**, 778 (2003).
2. H. W. Kroto, J. R. Heath, S. C. O'Brien, R. F. Curl, and R. E. Smalley, Nature (London) **318**, 162 (1985).
3. W. Kratschmer, L. D. Lamb, K. Fostiropoulous, and D. R. Huffman, Nature (London) **347**, 254 (1990).
4. P. Hohenberg and W. Kohn, Phys. Rev. **136**, B864 (1964);W. Kohn and L.J. Sham, Phys. Rev. **140**, A1133 (1965).
5. M. R. Pederson and K. A. Jackson, Phys. Rev. B. **41**, 7453 (1990); K.A. Jackson and M. R. Pederson, Phys. Rev. B. **42**, 3276 (1990); M. R. Pederson and K. A. Jackson, Phys. Rev. B. **43**, 7312 (1991).
6. D. V. Porezag and M. R. Pederson, Phys. Rev. A **60**, 9566 (1999).
7. J. P. Perdew, K. Burke and M. Ernzerhof, Phys. Rev. Lett. **77**, 3865(1996).

8. M. Shen and H. F. Schaefer, J. Chem. Phys., **101**, 2261 (1994).
9. D. V. Porezag and M. R. Pederson, Phys. Rev. B. **54**, 7830 (1996);
10. Y. Morino, T. Ukaji, and T. Ito, Bull. Chem. Soc. Jpn. **39**, 64 (1966).
11. T. Baruah, R. R. Zope, S. L. Richardson, and M. R. Pederson, Phys. Rev B, in press.
12. T. Baruah, R. R. Zope, S. L. Richardson, and M. R. Pederson, to be published.
13. T. Baruah, R. R. Zope, M. R. Pederson, and M. R. Beltran, to be published.
14. M. R. Pederson and A. A. Quong, Phys. Rev. B **46**, 13584 (1992).
15. K. Roth, J. Kortus, M. Herms, D. Porezag, and M. R. Pederson, Jpn. J. Appl. Phys. **38**, 989.

STRUCTURAL AND ELECTRONIC PROPERTIES OF CDTE CLUSTERS

JEFFREY RUFINUS[†]
Widener University, Science Division, 1 University Place
Chester, PA 19013, USA

We present a density functional study on the structural and electronic properties of small (up to 16 atoms) CdTe semiconductor clusters. The lowest energy structures as well as HOMO-LUMO orbital gaps and binding energies are calculated with the Gaussian 03 program. The clusters with N = 8 to 12 atoms have relatively higher energy gaps with local minima at N = 10. We found that N = 10 cluster is relatively stable and can be a magic number for CdTe clusters. We also find a strong correlation between the HOMO-LUMO gaps and binding energies.

1. Introduction

Due to their great importance in the microelectronics industry, semiconductor clusters have been studied extensively. The majority of semiconductor clusters studied to date, however, have focused on groups III-V (e.g. GaAs [1], InAs [2]) and IV-IV (e.g. Ge [3, 4], Si [5, 6], SiGe [7]) semiconductors. Recently, the interests in other groups of semiconductor clusters have arisen. Some groups have investigated the properties of II-VI (e.g. CdS, CdSe) [8,9] as well as IV-VI (e.g. GeTe) [10] clusters. To our best knowledge there have been no similar studies on the structural and electronic properties of CdTe clusters, even though this compound has been extensively studies in their solid state (see, e.g. [11]).

Among II-VI semiconductors, CdTe is of a great interest to the technological industry. It has been an attractive candidate for use in various optoelectronic devices, high-performance infrared detectors, and room temperature radiation detectors [12]. It is also the most promising material for the next generation of soft x-ray detectors [13].

Here we report a density functional study of structural and electronic properties of Cd_nTe_n clusters with n = 1 to 8. The study includes finding the lowest energy structures of the CdTe clusters as well as their binding energies and highest occupied molecular orbital (HOMO) to lowest unoccupied molecular orbital (LUMO) energy gaps. We found some interesting properties of

---

[†] E-mail: rufinus@cs.widener.edu

this cluster and we compare our results with the previous studies on other II-VI clusters, such. such as CdS and CdSe clusters [8].

2. Computational Method

All of our computations were performed with a Gaussian 03 program [14]. The Kohn-Sham equations are solved in the framework of the density functional theory (DFT). The three-parameter hybrid functional of Becke, Lee, Yang and Parr (B3LYP) was employed. B3LYP functional includes a mixture of Hartree-Fock exchange with DFT exchange-correlation. We used the standard Los Alamos LANL2DZ in Gaussian 03 as the basis set.

3. Results and Discussions

3.1. *Atomic Structure*

Geometry optimizations were performed to obtain the structures of CdTe clusters. In Fig. 1 we show some of the structures that we found. We tried a variety of different initial configurations to obtain the lowest energy structures for these clusters. The simplest structure of Cd_1Te_1 has a bond length of ~ 2.65 Angstrom. There is only one ground state structure found for both Cd_2Te_2 cluster (with C_{2V} symmetry) and Cd_3Te_3 cluster (also with C_{2V} symmetry). These two lowest energy structures look very similar to those of Cd_nS_n/Cd_nSe_n (n = 2, 3) clusters calculated in Ref. [8]. For n > 3, however, for the same number of atoms, we obtained more than one ground state structure with several eV of energy differences among one another. For example, we found two ground state structures for Cd_4Te_4, one structure with C_s symmetry, and another structure with D_{2D} symmetry. The difference in energy between these two structures is ~ 1.4 eV. The cluster with D_{2D} symmetry has lower energy than the one with C_S symmetry. Fig. 1 shows only the lowest energy structures for Cd_nTe_n (n = 1 to 8) clusters.

The structures for these II-VI clusters do not resemble their solid phase. Smaller clusters tend to adopt high symmetry arrangements. For Cd_2Te_2, the cluster forms a rhombus. For Cd_3Te_3, the cluster forms an equilateral triangle. The lowest energy Cd_4Te_4 structure, as mentioned above, has D_{2D} symmetry, while Cd_5Te_5 and Cd_6Te_6 have C_{2V} and C_{2h} symmetries, respectively. The geometries for N = 7 and 8 are less regular.

3.2. *Stability and the Magic Number*

The binding energy per atom of CdTe clusters is shown in Fig. 2. The binding energy increases monotonically as the size of the cluster increases. Clusters with 8 and 12 atoms are the local maxima. The CdS/CdSe clusters have local maxima at N = 6 and N = 12 [8]. In our calculations, the difference of binding energies between N = 8 and N = 6 is ~0.05 eV/atom.

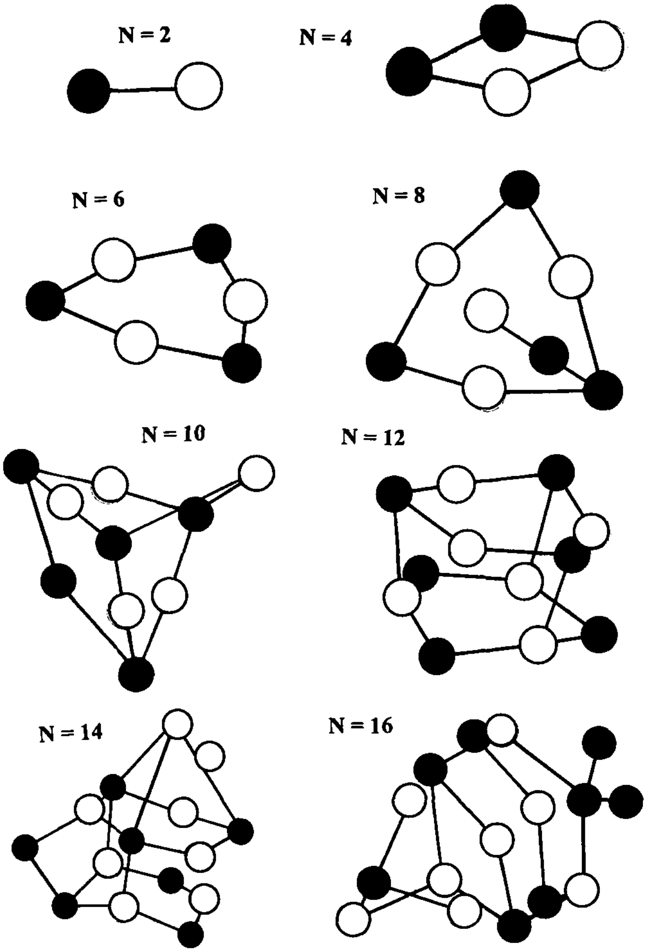

Figure 1. The lowest energy structures of CdTe clusters. The filled circles represent Te and the empty circles represent Cd atoms.

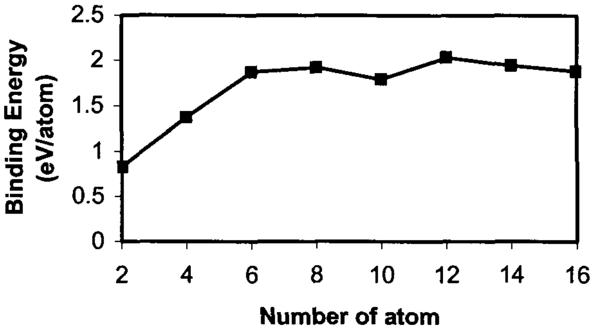

Figure 2. Binding energy (eV/atom) versus the number of atom.

There is, however, a local minimum for 10 number of atoms (Cd_5Te_5). This may indicate that the Cd_5Te_5 cluster is more stable than its neighbors. In order to determine whether this is the case, we calculated the second order binding energy difference using the following formula [15]:

$$\Delta E'(N) = E(N+1) + E(N-1) - 2\,E(N), \qquad (1)$$

where E(N) is the binding energy with N total number of atoms and Δ E'(N) is the second order difference of the binding energy. The calculated energy difference Δ E'(N) is shown in Fig. 3 (solid line). From this figure we know that the N = 10 atom is the local maximum, which indicates that Cd_5Te_5 cluster is more stable than its neighboring clusters.

We further calculated the increment in energy of adding one atom to the preceding cluster using the following simple formula [15]:

$$\Delta E(N) = -\,[E(N) - E(N-1)]. \qquad (2)$$

The information on the stability of the clusters can also be obtained from formula (2). The calculated result of Δ E(N) versus the cluster size is shown in Fig. 3 (dotted line). Δ E(N) increases monotonically from N = 4 to N = 10. Again we find that N = 10 is the local maximum, which indicates that the Cd_5Te_5 cluster is more stable than its neighboring clusters. Thus, according to our calculation, the cluster Cd_5Te_5 with 10 atoms and C_{2V} symmetry can be a magic number for CdTe clusters.

3.3. *Electronic Structure: HOMO-LUMO gap*

Clusters of certain sizes have special properties compared to other clusters. In the previous subsection it was mentioned that Cd_5Te_5 cluster with 10 atoms is more stable than other clusters with different sizes. It is also interesting to see the HOMO-LUMO gaps of CdTe clusters and whether these gaps have some correlation with their binding energies.

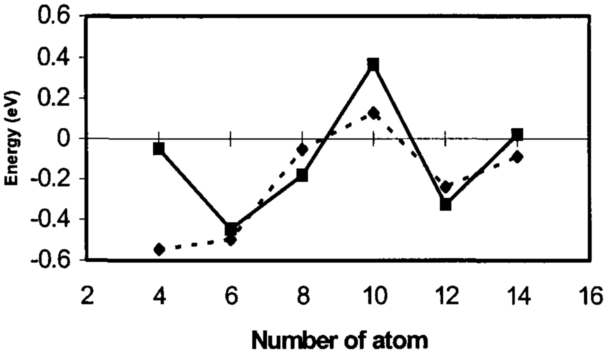

Figure 3. The second energy difference Δ E'(N) (solid line) and the increment in energy Δ E(N) (dotted line) versus the number of atom.

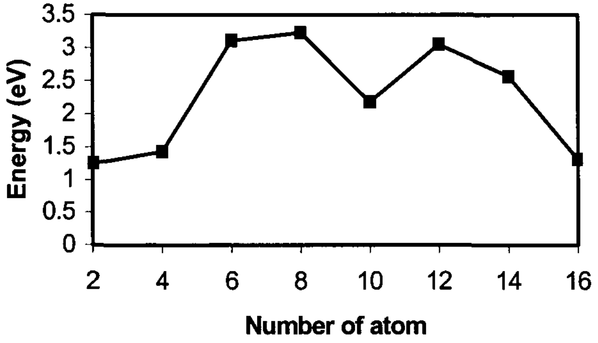

Figure 4. HOMO-LUMO gaps versus the number of atom.

The calculated HOMO-LUMO gaps for CdTe clusters are shown in Fig. 4. We find that the HOMO-LUMO gaps do correlate strongly with the binding energies (Fig. 2). The gaps increase monotonically and have local maxima for cluster sizes of N = 8 and N = 12. (Ref. [8] found that N = 6 and N = 12 as the local maxima for CdS and CdSe clusters. In our calculations, the HOMO-LUMO gap for N = 8 is ~ 0.12 eV higher than N = 6.) Thus, the clusters with 8 and 12 atoms have relatively higher energy gaps than the rest of the cluster, and they also exhibit local maxima in their binding energies (see Fig. 2).

4. Conclusion

We have done a density functional calculations of Cd_nTe_n clusters with n = 1 to 8. We report our results on the lowest energy structures as well as the HOMO-LUMO gaps and binding energies. The lowest energy structures of CdTe clusters do not resemble the bulk phase. We found some resemblance in electronic properties between CdTe clusters and other II-VI semiconductor clusters such as CdS and CdSe. The binding energies as well as the HOMO-LUMO gaps curve as the function of cluster size do have similar shapes with the curves for CdS and CdSe clusters. We found strong correlation between the HOMO-LUMO gaps and the binding energies. We also found that Cd_5Te_5 is a relatively stable cluster and N = 10 is a possible magic number for CdTe clusters.

Acknowledgement

The author acknowledges support from the National Science Foundation (Grant number DMR-0304429) and Widener University grants.

References

1. H. E. Ruda and J. G. Ping, *Phys. Rev.* **B46**, 15936 (1992).
2. A. Costales and R. Pandey, *Chem. Phys. Letters* **362**, 210 (2002).
3. B.-X Li and P.-L Cao, *Phys. Rev.* **B62**, 15788 (2000).
4. J. Wang, G. Wang and J. Zhao, *Phys. Rev.* **B64**, 205411 (2001).
5. E. Kaxiras and K. Jackson, *Phys. Rev. Letters* **71**, 727 (1993).
6. K.-M. Ho, A. A. Shvartsburg, B. Pan, Z.-Y Lu, C.-Z Wang, J. G. Wacker, J. L. Fye and M. F. Jarrold, *Nature* **392**, 582 (1998).
7. S.-D. Li, Z.-G. Zhao, X.-F. Zhao, H.-S. Wu and Z.-H Jin, *Phys. Rev.* **B64**, 195312 (2001).
8. M. C. Troparevsky and J. R. Chelikowsky, *J. Chem. Phys.* **114**, 943 (2001).
9. J. Joswig, M. Springborg and G. Seifert, *J. Phy. Chem.* **B2000**, 2617 (2000).
10. R. Natarajan and S. Ogut, *Phys. Rev.* **B67**, 235326 (2003).
11. S.-H. Wei and S. B. Zhang, *Phys. Rev.* **B62**, 6944 (2000).
12. V. V. Godlevsky, M. Jain, J. J. Derby and J. R. Chelikowsky, *Phys. Rev.* **B60**, 8640 (1999).

13. C. C. Kim, M. Daraselia, J. W. Garland and S. Sivananthan, *Phys. Rev.* **B56**, 4786 (1997).
14. M. J. Frisch et. al., Gaussian 03, Revision B. 03, Gaussian Inc., Pittsburgh, PA (2003).
15. S. H. Wei, Z. Zeng, J. Q. You, X. H. Yan and X. G. Gong, *J. Chem. Phys.* **113**, 11127 (2000).

SPIN EXCITATIONS INDUCED BY PROJECTILE IN FERROMAGNETIC CLUSTER

R.-J. TARENTO, P. JOYES
Laboratoire de Physique des Solides ,bât 510, Université de Paris-Sud, Orsay, 91405, Fr

R. LAHRECHE, D.E. MEKKI
Faculté des Sciences, Département de Physique, Université d'Annaba Annaba, B.P12, Al

We investigate the diffusion of a spin polarized projectile on a ferromagnetic linear cluster. The interaction between the projectile and the target is described with a Heisenberg Hamiltonian which excludes the charge degree of freedom during the process. Our calculation is based on a real time description of the spins of the two interacting systems. The spin excitations induced by the spin of a projectile-atom are investigated versus the cluster size, the trajectory parameters(projectile velocity, impact parameter..). Non adiabatic behaviour during the collision has been characterized by the spin temperature at the end of the collision process. The effects of the phonons on the spin excitations will be discussed.

1. Introduction

A lot of experimental[1] and theoretical[2] studies have been devoted to interaction between a fast atomic particle with a metallic cluster showing various kinds of non-atomic effects like electronic excitations, ionisation and capture.

Other experiments have been performed on the spin diffusion on bulk magnetic targets like the spin depolarisation of low energy polarized electrons through ferromagnetic films[3]. Though, up to now, only bulk targets are employed, similar experiments could be made in the next future on finite media.

We will use a time dependent Heisenberg formalism which will be presented in Sec 2. We discuss our results on the spin diffusion on cluster, on the nonadiabic effects and on the phonon magnon coupling effect.in Sec.3.

2. The Heisenberg Hamiltonian

The most simple Hamiltonian describing the time-dependent behavior of spin excitations is a spin-polarized nanostructure is the Heisenberg Hamiltonian.

$$H^{(Heis)}=-\sum_{i,j} J\,(r_{ij})\,\mathrm{S}_{\mathrm{i}}\,\mathrm{S}_{\mathrm{j}} \qquad (1)$$

where S_i refer to the spin of particle i. In the present study one of the sites, say site 1, is moving along a given trajectory, while the others are assumed fixed. Between two close target atoms the J_{ij} interaction term remains constant and is J_o. The dependence of J_{1i} on the r_{1i} distance between the target atom i and the incident atom 1 can be taken as

$$J_{1i}=J_{i1}=J(r_{1i})=J_o^{'}\exp\left(-\frac{r_{1i}}{r_o}\right) \qquad (2)$$

$J_o^{'}$ has been chosen in our calculation such that for r_{1i} equal to the nearest target distance, J_{1i} is equal to J_o. r_o ($r_o \cong 1$Å) is a typical interaction length. The distance r_{1i} between the incident and the target particles depends on time t. It is assumed that in the studied speed range the motion of the particle 1 does not depend on spin evolution during interaction. Only linear trajectories with constant V velocities will be considered.

$H^{(Heis)}$ has been widely used in various solid state problems, for instance, in the aggregate case to investigate π electron magnetic properties in polyenes[4]. But the use of $H^{(Heis)}$ implies no electron transfer: i.e no charge exchange between the incident particle and the target during the collision and no electron population changes in the target during collision either.

3. Results for Small Linear Cluster

We consider the collision of an up incident spin on a ferromagnetic down spin target both initially polarized along the Z-axis. Therefore we take a J_o=0.1eV positive value so that the initial target is the ground state. The target , called C_n is a linear chain of n atoms which are located along the Y-axis (the atoms are located at sites 2, 4 ... ,2 n (Å)).

The wave function $|\Psi\rangle$ is written as $|\Psi\rangle=\sum_i \alpha_i|\phi_i\rangle$

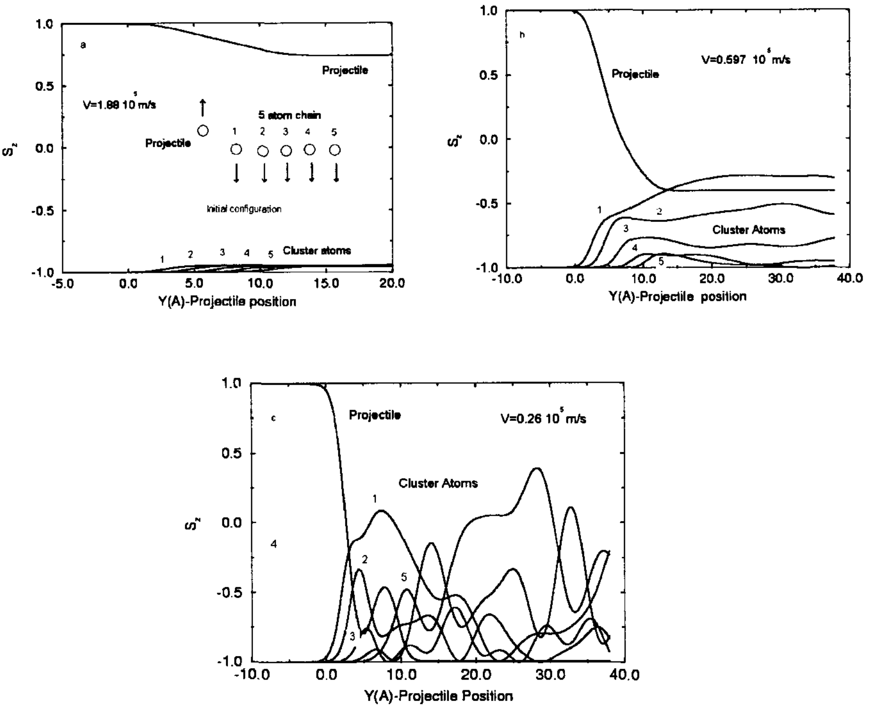

Figure 1. Evolution of the z spin component S_z for the projectile and 5 atom chains atoms versus the projectile velocity V. Y is the projectile position for an arbitrary trajectory parallel to the y-axis with an impact parameter b=2Å.The initial spin configuration is displayed in Fig.1.a.

$\{|\phi_i\rangle\}$ are the states $|\uparrow;\downarrow,\ldots,\downarrow\rangle, |\downarrow;\uparrow,\ldots,\downarrow\rangle$, with only one up spin for the projectile and cluster system (the first spin is referred to the projectile one). The time dependence α_i are obtained by solving numerically the Schrödinger equation with for the initial configuration $|\uparrow;\downarrow,\ldots,\downarrow\rangle$. At every time of the dynamics the conservation of the total spin S_z and S^2 of the system has been checked.

In Figure.1., we report 3 different behaviours of S_z^i for the projectile and atom cluster spin versus the projectile velocity V corresponding to an energy for a silver atom of 20Kev,2KeV and 400eV. During a first phase T1, the projectile spin is varying like the cluster ones. In a second phase T2 only the excited cluster has its spins varying. Notice that for this velocity range, during

T1 the cluster atom positions are frozen. The projectile trajectory is parallel to the cluster axis and the impact parameter b=2Å. The evolution depends on the two characteristic time $\tau=\hbar/J$ which describes the intra spin in the chain and $\tau'(V)$ the travelling time along one atomic distance. For $\tau'<\tau$ (Fig.1.a), the target spins vary significantly when the projectile is above them. Each site behave as if it were isolated. For $\tau'\approx\tau$ (Fig.1.b), The spin amplitudes of variation are larger due to a larger projectile-site interaction. For $\tau'>\tau$(Fig.1.c), the incident spin flip almost completely. The target spin has a complex evolution. The projectile is interacting with a fully excited target

The excitation energy Ex is defined as $E\text{-}E_{ad}$ where the system energy E is given by $<\Psi| H^{Heis}| \Psi>$ and E_{ad} is the energy of the adiabatic state associated to the initial state. In Fig.2. Ex is display during the phase T1 and the beginning of the phase T2. At the beginning of the collision, Ex is increasing with V. We can see that the energy transfer at the end of the collision (i.e T1 phase) is small at low and high velocity and displays a maximum for V=0.6 10^4 m/s. The time evolution of Ex is quite complex. Ex is not only increasing with time. This effect is linked the non adiabatic process involved during the collision. What is happening during the phase T2 is discussed below.

The spin temperature in the cluster at the end of the phase T1 or the beginning of T2 is another way of characterizing the excitation in the system. In Fig.3. the spin temperature is displayed versus the impact parameter. The spin temperature is increasing when b is decreasing. At high velocity, as the energy transfer is small, the spin temperature is also small. In the case of the 10 atom chain the temperature is significant for b<4.5Å but for the 3 atom chain it is for b<10Å.

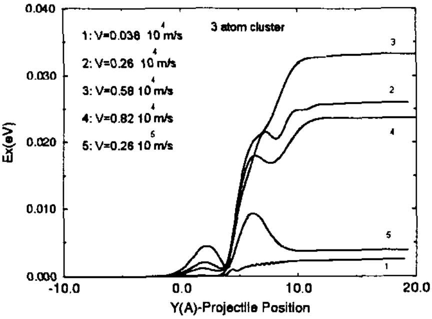

Figure 2. Excitation energy evolution during collision between a 3 atom chains cluster and a projectile with velocity V. The initial spin configuration is displayed in Fig.1

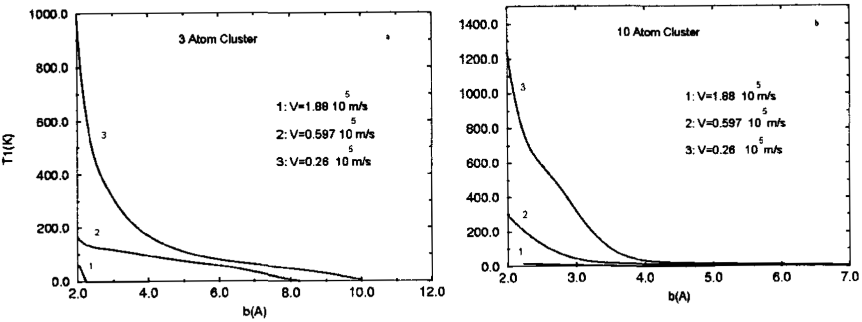

Figure 3. Spin temperature in the cluster at the end of the collision in the 3 or 10 atom chains atoms versus the impact parameter b versus the projectile velocity V. The initial spin configuration is displayed in Fig.1.a

For small b the temperature is large for intermediate velocity. For larger time we can see below that the cluster could excite other degrees of freedom.

At the end of phase T_1, the cluster is only spin exited if the projectile speed is not too small (the atom nucleus are still nearly frozen). The set of excitations produced in the cluster just after the collision are reported in Fig.4. versus the cluster size. Increasing n, the excitation spectra forms a band varying between 0 et $8\omega_o$ ($\omega_o=\frac{J}{4\hbar}$) which is associated to the classical chain spin wave dispersion.

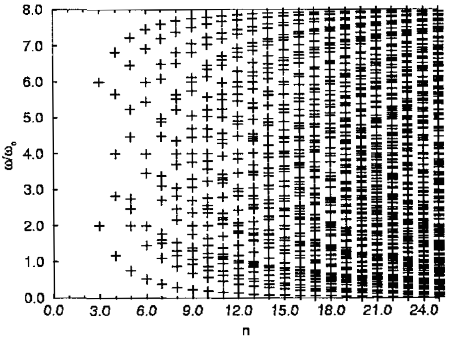

Figure 4. Set of the excitation frequencies in the cluster just after the collision (i.e at the beginning of the phase T2) versus the size of the cluster. $\omega_o=\frac{J}{4\hbar}$

In fact Fig.4 gives for a given size all the possible excitation frequencies. But only the collision conditions control if a frequency is really excited. Illustrate this fact on the 3 atom cluster. In this case 2 frequencies are possible: $\omega_2=2\omega_0$ and $\omega_6=6\omega_0$ for the spin excitations of the two atoms located at the beginning and end of the chain and only one frequency (ω_6) for the atom at the chain centre. The ratio of the excitation frequencies ω_6/ω_2 for the atom located at the chain end is highly dependent on the projectile trajectory. For a trajectory in the cluster median plane only ω_6 is excited.. In Tale.1. the ratio ω_6/ω_2 is reported versus the collision impact parameter b and the projectile velocity V (either for a trajectory along the chain axis or perpendicular but in the cluster plane). In the case where the trajectory is along the chain axis: We note that for large V the ratio is zero meaning that only ω_2 is involved and if we decrease V, ω_6 is excited and the ratio ω_6/ω_2 is increasing when b is decreasing. In the other case where the trajectory is perpendicular at large V the ratio is slowly decreasing with b.

Let us discuss what is happening in the cluster during the phase T2. During the phase T1 the cluster is spin-excited. Its excitation has been previously characterized by Ex or the spin temperature. During the phase T2 the excess of excitation energy for the spins is distributed to the vibration degrees of freedom i.e: the nucleus are no more frozen. This phenomena generate a coupling between the magnon and the phonon. In our calculation the nucleus have been treated classically like in the Carr Parrinello procedure. A part of the spin excitation is transformed into vibration excitation. In Table.2 the spin temperature $T2^{in}$ ($T2^{f}$) at the beginning

Table 1. Ratio of the excitation frequencies ω_6/ω_2 appearing just after the collision in the 3 atom chain cluster versus the impact parameter b and the projectile velocity V (in x 10^5m/s unit). The collision trajectory is parallel to the cluster axis (perpendicular but in the same plan) in Table.1.a(b).

Table 1.a

ω_6/ω_2	b=2Å	b=3Å	b=4Å	b=5Å	b=6Å
V=0.26	0.52	0.57	0.23	0.15	0.11
V=0.597	0.35	0.52	0.30	0.25	0.23
V=1.88	0	0	0	0	0

Table 1.b

ω_6/ω_2	b=2Å	b=3Å	b=4Å	b=5Å	b=6Å
V=0.26	0.20	0.10	0.09	0.05	0.00
V=0.597	0.22	0.21	0.18	0.17	0.16
V=1.88	0.24	0.24	0.29	0.24	0.21

Table 2. Phonon pulsation ω_{ph} (x10^{12} s^{-1}) and Spin temperatures $T2^{in}$($T2^{f}$) just at the beginning (at the end) of the phase T2 following the collision between of a projectile and the 3 atom chain cluster versus the impact parameter b with the projectile velocity V=0.44 10^5m/s. The initial collision trajectory conditions are reported in Fig.1.

	b=2Å	b=3Å	b=4Å	b=5Å	b=6Å
$T2^{in}$(K)	293	172	121	87.5	65.5
$T2^{f}$(K)	268.5	166	118.5	86	64
ω_{ph}	1.39	01.46	01.49	1.495	1.5

(at the end) of the phase T2 which follows the collision. $T2^{in}$ and $T2^{f}$ are increasing when b is decreasing. But the difference $T2^{in}$-$T2^{f}$ is decreasing with b meaning that the vibration amplitude are smaller when is decreasing..

For a projectile trajectory parallel to the chain axis only the stretching vibration mode is exited The effect of the phonon-magnon coupling decreases the stretching vibration mode ω_{ph} (Table.2) from its free value when b is decreasing.

3. Conclusions

The calculation has shown the importance of the spin excitation during the collision phase which induce vibration excitations coupled to them after the collision

Acknowledgements

The authors thank the Egide for the support (Procope:03196UB)

References

1. Bréchignac C., Cahuzac Ph, Concina B., Leygnier J. and Tignières I., *Eur. Phys.* **D12** (2000), 185-192.
2. Martin F., Politis M.F., Zarour B. and Hervieux P.A., *Phys. Rev.* **A60** (1999), 4701-4705.

3. Oberli D., Burgermeister R., Riesen S., Weber W. and Siegmann P.A., *Phys. Rev. Lett.* **81** (1998), 4228-4231.
4. Maynaud D., Durand Ph, Daudey J.P. and Malrieu J.P., *Phys. Rev.* **A28** (1983), 3193-3206.

TIME-DEPENDENT CHARGE DYNAMICS IN C_{60} AND A PROPOSAL FOR NANOSTRUCTURE-BASED COMPUTING TECHNOLOGY

G. P. ZHANG
Department of Physics, Indiana State Univeristy, Terre Haute, IN 47809, USA

Thomas F. George
Office of the Chancellor / Departments of Chemistry & Biochemistry and Physics & Astronomy, University of Missouri-St. Louis, St. Louis, MO 63121, USA

DANIEL A. JELSKI
Department of Chemistry, Rose-Hulman Institute of Technology, 5500 Wabash Avenue, Terre Haute, IN 47803, USA

In this paper, we investigate the ultrafast charge dynamics in C_{60}. In particular, the ultrafast charge redistribution after laser excitation is computed as a function of time. We find that the charge relaxation is site-specific. The maximal change is at the top and bottom pentagons. Based on these results, we propose a nanostructure-based computing technology. We argue that it can be controlled both optically and electrically. This may become an emerging frontier.

1. Introduction

Ultrafast dynamics in nanostructured materials is of technological importance. In this paper, we investigate how C_{60} responds to the laser radiation and how the charges on the ball redistribute themselves. The technical details and initial results have already been presented in our recent publications [1]. We will focus on some basic effects of those dynamical processes to shine new light on those ultrafast phenomena.

2. Time-Reversal Invariance in Ultrafast Dynamics

Before we introduce the ultrafast dynamics in C_{60}, we want to investigate the time-reversal invariance in the Rabi oscillations. Such oscillations are very attractive since they represent one of the few problems, which can be solved analytically under the rotating-wave approximation (RWA). In a two-level system, the Rabi Hamiltonian is [2]

$$H_0 = E_1|1\rangle\langle 1| + E_2|2\rangle\langle 2|, \tag{1}$$

where $E_2 > E_1$. The interaction between the laser and the system is

$$V(t) = \gamma e^{i\omega t}|1\rangle\langle 2| + \gamma e^{-i\omega t}|2\rangle\langle 1|, \tag{2}$$

where γ and ω are real and positive. γ represents the strength of the interaction, and ω is the frequency of the external field. The time-dependent density matrix can be computed by solving the following equation:

$$i\hbar\dot{\rho} = [H,\rho] = [H_0 + V(t), \rho]. \tag{3}$$

An exact solution to this problem was worked out by Rabi. The initial condition is that at $t = 0$, only the lower level is populated, so that $\rho_{11}(0) = 1$ and $\rho_{22}(0) = 0$. For any later time,

$$\rho_{22}(t) = \frac{\gamma^2/\hbar^2}{\gamma^2/\hbar^2 + (\omega - \omega_{12})^2/4} \sin^2(\Omega t), \tag{4}$$

where

$$\Omega = \sqrt{\frac{\gamma^2}{\hbar^2} + \frac{(\omega - \omega_{12})^2}{4}}. \tag{5}$$

In the meantime,

$$\rho_{11}(t) = 1 - \rho_{22}(t), \tag{6}$$

where $\omega_{12} = (E_2 - E_1)/\hbar$. It is interesting to note that if we change t by $-t$, the results remain the same. This time-reversal symmetry is directly connected to the interaction term $V(t)$. In experiments, such symmetry is determined by laser pulses. Consider a common laser pulse shape like $|\vec{E}(t)| = A\cos(\omega t)$ exp $[-(t-t_0)^2/\tau^2]$. Here A is the amplitude of the field, ω is the laser frequency, τ is the pulse duration or width, e is the electron charge, t is the time, and t_0 is the time delay. If we transform from t to $-t$, then the whole process of interest depends on whether the delay time t_0 is zero or not. If the delay time is zero, then we still have this symmetry. Otherwise, the symmetry is broken. To be more precise, the laser pulse determines the direction of time evolution of the dynamics. In the case where more than two pulses are involved, the results depend on the delays of those pulses.

3. Charge Dynamics in C_{60}

We orient C_{60} in such a way that the z-axis goes through two pentagons, one behind the other (see Fig. 1). The laser polarization is chosen along the z-axis.

Ninety bonds can be categorized into 13 distinctive layers from the top pentagon to the one behind. We label those layers by layer number n from 1 to 7. The other six layers from 8-13 on the back are symmetric with respect to the central layer, layer 7. All the atoms are denoted from a to e. Neutral C_{60} has 60 π electrons, where its inter-ball hopping and therefore is neglected here. The Hamiltonian for the system can then be written as [1]

$$H_0 = -\sum_{i,j,\sigma} t_{ij}\left(c_{i,\sigma}^{+} c_{j,\sigma} + h.c.\right) + \frac{K}{2}\sum_{i,j}(r_{ij} - d_0)^2, \tag{7}$$

where all the electron operators are standard [3].

$t_{ij} = t_0 - \alpha\left(|\vec{r}_i - \vec{r}_j| - d_0\right)$ is the hopping integral between nearest-neighbor atoms at $\vec{r}_i$ and $\vec{r}_j$, and $r_{ij} = |\vec{r}_i - \vec{r}_j|$. Here t_0 is the average hopping constant, α

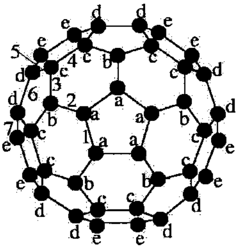

Fig. 1. C_{60} is oriented such that one pentagon is directly behind the other. The numbers, referred to as layer numbers, denote distinctive locations. The letters from *a* to *e* specify the different carbon atoms.

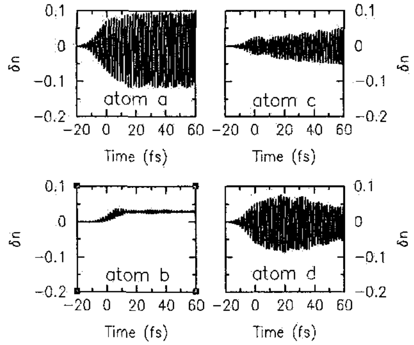

Fig. 2. Charge fluctuations on different carbon atoms. The atoms from *a* to *d* refer to those in Fig. 1.

is the electron-lattice coupling constant, and $d_0 = 1.54\text{A}$. The second term in Eq. (7) is the lattice elastic energy, and K is the spring constant. By fitting the energy gap and bond lengths, we have determined the above parameters as $t_0 = 1.8eV, \alpha = 3.5eV/A$ and $K = 30.0eV/A^2$ [1].

The dynamical simulation is done by numerically solving Eq. 3. We note that although all carbon atoms are equivalent, in the presence of a laser field, they are not. In particular, in our current polarization, the charge fluctuation is different and symmetric with respect to the equatorial line on layer 7. We define the charge change as $\delta n = \rho_{ii}(t) - \rho_{ii}(0)$, where the results are shown in Fig. 2. It is amazing that the respective changes are very different. For instance, for atoms *a*, the amplitude is very large with very rapid oscillations. Note that since our laser pulse width is 10 fs, the dynamics after 20 fs proceeds without laser influence, but one still sees a net charge change on atom *a*. The reason why the charge change is maximal at atom *a* is simply because the polarization is directly through the center of the pentagon formed by those *a* atoms. However, in contrast to atom *a*, atom *b* shows a saturation behavior, which increases at first and then saturates at about 0.05. This means that all the *b* atoms gain electrons. This is a very unique layer, where it is known the Jahn-Teller distortion starts from this layer to the equatorial region. For atom *c*, we see that its amplitude is small initially but gradually in creases with time. Atom *d* is on the equatorial line. Our previous study [4,5] shows that such charge fluctuation substantially affects the overall dynamics. All the charge dynamics on the back are symmetric with respect to the equatorial line.

4. A Proposal for Nanostructure Based Computing Technology

Based on our above results, we propose a nanostructure-based computing technology. Such technology meets two important criteria: (a) fast communication and (b) structure miniaturization. The nanostructure virtually plays the same role as optical fiber but operates on a nanoscale level. There are several nonparallel features connected with this technology: (i) There is no space constraint on the information passage, in contrast to the current electronic based bus line where one has to wait to send the information until the line is cleared off. (ii) Multiple transmissions of signals are possible, which is essentially infinite.

Figure 3 schematically shows the essential feature of this technology. Light enters the nanotube from the left nanotube and after reflection reaches C_{60}. C_{60} plays a role like central processing units (CPU) and controls all the reflected light entering another channels. The light inside the nanotube is completely reflected from the inner wall of the tubes. If the light frequency is detuned away from the main absorption band, the optical loss is very small. In addition, one can use many incident lights at the same time, so that the computing process is intrinsically parallel. Our idea is that buckyballs and nanotubes will form a two-dimensional mesh, and each of the balls can be either controlled electrically or optically by the external field. We can view this overall process in terms of two stages, where in the first stage one can use polarization to control the light transmission in a nanotube. Since the nanotube is linked to C_{60}, then at the second stage, one can use light to control the dynamics of C_{60}, and subsequently the structure and electronic change in C_{60} will affect the light transmitted from the nanotube.

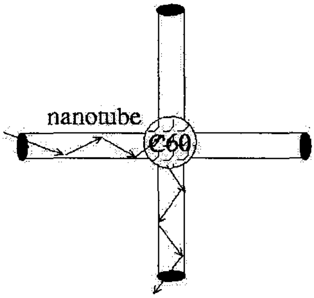

Fig. 3. Proposed nanotube and C_{60}-based central process unit. This can be controlled by either the light or current, or both.

References

[1] G. P. Zhang, R. T. Fu, X. Sun, D. L. Lin and Thomas F. George, *Phys. Rev.* B **50**, 11976 (1994); X. Sun, G. P. Zhang, Y. S. Ma, K. H. Lee, T. Y. Park, T. F. George and L. Pandey, *ibid.* **53**, 15 481 (1996); G. P. Zhang, X. Sun, T. F. George and L. N. Pandey, *J. Chem. Phys.* **106**, 6398 (1997).

[2] I. I. Rabi, Phys. Rev. **49**, 324 (1936); J. J. Sakurai, *Modern Quantum Mechanics,* page 320, [Addison-Wesley Publishing Company (1994)].

[3] G. P. Zhang, T. A. Callcott, G. T. Woods, L. Lin, Brian Sales, D. Mandrus and J. He, *Phys. Rev. Lett.* **88**, 189902 (2002).

[4] G. P. Zhang, Phys. *Rev. Lett.* **91**, 176801 (2003).

[5] G. P. Zhang, X. Sun, and T. F. George, *Phys Rev.* B, **68**, 165410 (2003).

MOLECULAR DYNAMICS STUDY OF IRON CLUSTER COALESCENCE AT SUB-MELTING POINT TEMPERATURES

FENG DING, KIM BOLTON, ARNE ROSÉN
Department of Experimental Physics, School of Physics and Engineering Physics, Göteborg University and Chalmers University of Technology, SE-412 96, Göteborg, Sweden
(Email: fengding@fy.chalmers.se)

The coalescence of two iron clusters (Fe_{300}+Fe_{300} ⟶ Fe_{600}) at temperatures below the cluster melting points has been studied by molecular dynamics (MD). At temperatures ≈200°C below the melting point phase change from the icosahedral Fe_{300} structure to the face centered cubic (fcc) Fe_{600} structure occurs even though the clusters are not molten. Moreover, surface melting is not required for the coalescence or the phase change. At lower temperatures elongated Fe_{600} clusters that are not fcc, and that may be metastable, are formed.

1. Introduction

Nano-clusters and nanowires are of great interest due to their potential applications in designing new materials, novel sensors and other nanodevices. Properties of these nanodevices at elevated temperatures will depend, among other things, on their thermal characteristics. Although there have been many studies of the thermal properties of nanoclusters and nanowires[1-3], most of them have focused on the liquid-solid phase transition. These studies include, for example, the cluster size and structure dependence of the melting point and the importance of surface melting on the phase transition[1, 3]. Far less attention has been paid to the coalescence of clusters at temperatures below the cluster melting point, even though it is known that this process may have important ramifications in growth and design of nanodevices. For example, it is not clear whether the coalescing clusters will keep their original (crystalline) structures and form grains in the larger cluster, or whether a new (crystalline) phase can be formed at these low temperatures. Hence, studies of the mechanism of sub-melting point coalescence is of both fundamental scientific and technological interest.

In this paper we present molecular dynamics (MD) simulation results of the coalescence of two Fe_{300} clusters, Fe_{300}+ Fe_{300} ⟶ Fe_{600}, at temperatures below their melting points. At temperatures ≈200°C below the melting points there is a phase change from the icosahedral Fe_{300} to the face centered cubic (fcc) Fe_{600} structure, whereas at lower temperatures the Fe_{600} cluster is elongated. The mechanism of the sub-melting point phase transition is also investigated.

2. Potential Energy Surface and Simulation Methods

Previous investigations have shown that the many-body interaction potential, which is based on the second moment approximation of the tight binding model [4], is good for studying the thermal properties of the pure [5] and alloy [6] transition metal systems. The parameters for the iron cluster studied here are obtained by fitting the cohesive energy, lattice parameter and elastic constants of γ -Fe (fcc structure) to experimental data[7].

Annealed Fe_{300} and Fe_{600} structures were obtained from MD simulations where the initial geometries of the clusters were selected by randomly placing the iron atoms in a sphere and then annealing to 0 K[8]. These structures were used to obtain the cluster melting points by ramping the temperature of the clusters (initially in their annealed geometries) from 600 to 1300 K in steps of 50 K. At each temperature a 500 ps canonical simulation was run to obtain the Lindemann index at that temperature, and the temperature where there is a sudden increase in the Lindemann index is the melting point [9,10].

Simulations of the coalescence of two Fe_{300} clusters were initialized by placing them, in their annealed geometries, 2.2 nm apart. Constant temperature coalescence was studied by canonical MD simulations using the Berendsen velocity scaling method[11]. To investigate the effect of a bath gas, constant energy trajectories – which simulate coalescence in vacuum – were run under similar conditions. In both types of simulations a 1fs integration step size was used. Simulations were terminated when a (meta)stable Fe_{600} cluster was obtained.

3. Results and Discussion

Figure 1 shows the annealed Fe_{300} and Fe_{600} structures. The annealed Fe_{300} structure is icosahedral, which is the same as the known structure for the magic number Fe_{309} cluster of similar size [12]. The difference between the annealed Fe_{300} and known Fe_{309} structures is that the high energy Fe atoms at the icosahedral vortices are missing in the Fe_{300} structure. The annealed Fe_{600} structure is fcc with a twin boundary. Although it is not known if this is the global minimum energy structure (which may be single crystal fcc), it is expected that this annealed structure is very similar in geometry and energy to the global minimum energy structure (several annealing simulations with significantly different initial conditions yielded similar fcc structures with twin boundaries).

Figure 2 shows the Lindemann index obtained for Fe_{300} and Fe_{600} clusters at temperatures between 600 and 1300 K. The melting points are 1100 K for Fe_{300} and 1150-1200 K for the Fe_{600} cluster.

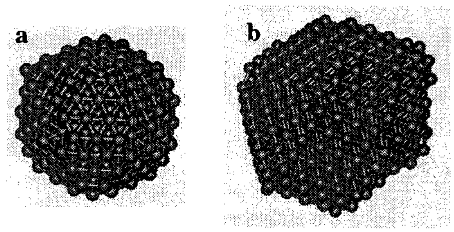

Figure 1. Annealed structures of the Fe_{300} (a) and Fe_{600} (b) clusters. Fe_{300} is icosahedral and Fe_{600} is fcc with a twin boundary.

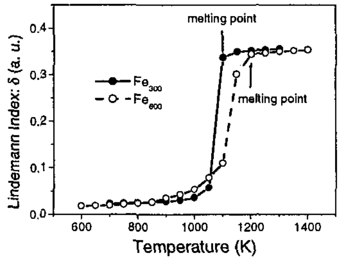

Figure 2. Melting process of Fe_{300} and Fe_{600} clusters. The sharp increase in the Lindmann index is due to melting of the clusters.

Figure 3 shows the energy relaxation and final structures during the coalescence of two Fe_{300} clusters at 900, 700, 500, 200 and 2 K. It is evident that the shape of the final (meta)stable Fe_{600} cluster depends on the temperature. At 900 K the stable Fe_{600} cluster is essentially spherical and has an fcc structure, which is similar to its annealed structure shown in Figure 1. At lower temperatures the Fe_{600} cluster is elongated, having a rod-like shape with an aspect ratio of about 1.5 at 700 K and a peanut shape at temperatures lower than 500 K.

It is also evident from Figure 3 that there is a large, approximately 20 eV, energy decrease when the two Fe_{300} clusters impact with each other (between ≈10-40 ps) and that there is a rapid restructuring of the Fe atoms at the cluster-cluster interface. This is observed at all temperatures, including the lowest temperature of 2 K. Considering the fact that scaling to this temperature was done at each time step during the simulation, which means that increased kinetic energy due to cluster-cluster attraction and impact does not facilitate this structural reorganization, it appears that the rapid reorganization of the Fe atoms at the cluster-cluster interface is due to a local change in the potential energy felt by the interfacial atoms. That is, due to the contact between the two clusters, the cohesive energy of the atoms at the interface decreases and the cluster restructures.

As shown in Fig. 3, coalescence at 900 K occurs over two distinct stages. During the first stage, 0-20 ps, the Fe_{300} clusters impact and coalesce into a spherical, non-crystalline (glass-like) structure (see the line graph in Fig. 3). As discussed above, the energy decreases by about 20 eV during this stage. This non-crystalline Fe_{600} cluster is metastable, and requires ≈60-80 ps to relax to the lower energy crystalline fcc structure (similar to its annealed structure in Figure 1). Additional evidence that there is no melting during coalescence is that the Fe atoms that originate from the different Fe_{300} clusters do not mix and are still well separated in the final Fe_{600} structure. This is in contrast to previous studies of the coalescence of clusters and nanorods that indicate that diffusion of surface atoms is the dominant driving force in the solid state coalescence process [13-15]. Extensive surface diffusion, which requires high thermal activation energies and long time, is not observed during the coalescence in our simulations.

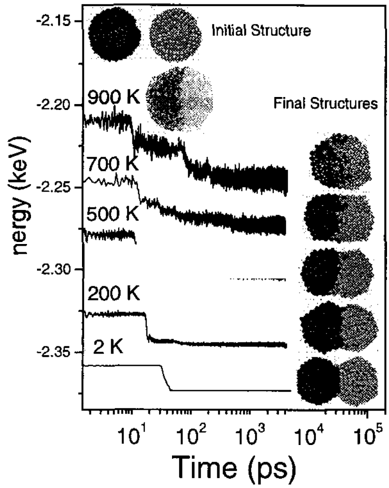

Figure 3. Energy relaxation during the coalescence of two Fe_{300} clusters at different temperatures. The inserted pictures are the initial and final structures obtained at different temperature. The inserted line graph shows the glass-like metastable structure at 900 K. Different gray scales denote iron atoms that originate from the different Fe_{300} clusters.

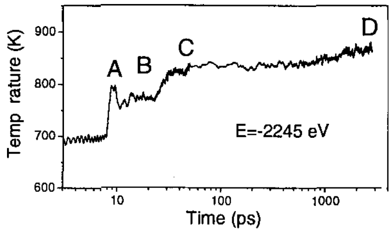

Figure 4. The time dependence of the temperature during the coalescence of two Fe_{300} clusters at a constant energy of −2245 eV. The cluster geometries at points A—D are shown in Figure. 5.

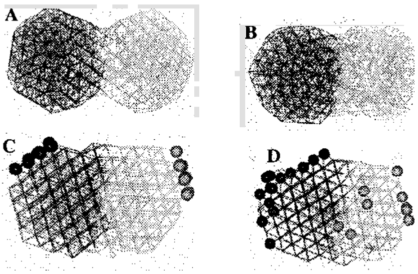

Figure 5. Four snapshots of the coalescence shown in Fig. 4. At sub-melting point temperatures, the coalescing Fe_{300} clusters undergo a phase transition to an fcc Fe_{600} cluster.

As discussed above, elongated Fe_{600} clusters are found at the lower temperatures (2 – 700 K). These structures do not have the fcc structure of the annealed Fe_{600} cluster and, even though they are stable on our several ns simulation timescale and on an experimental timescale, they may be metastable (i.e., kinetically stable). However, it is important to note that the fcc Fe_{600} structure formed at 900 K was formed from a disordered, non-crystalline intermediate at an energy of ≈-2240 eV (see Figure 3). The metastable intermediates at the lower temperatures are crystalline (essentially having the isocosahedral structures of the Fe_{300} clusters) and their energies are much less than -2240 eV (see Figure 3). Hence, if these elongated, low temperature Fe_{600} clusters are indeed metastable intermediates for the fcc structure, the mechanism for the transition to the fcc geometry may be different from that at 900 K.

The constant temperature trajectories discussed above simulate coalescence in a high pressure gas environment. To investigate the effect of the bath gas, the velocity scaling was omitted, i.e., constant energy trajectories were propagated. This simulates cluster coalescence in vacuum. Figure 4 shows the results when the initial temperature of the separated clusters was 700 K (i.e., it corresponds to the 700 K trajectory shown in Figure 3). The total energy is -2245 eV. Since the total energy is held constant, the reduction in potential energy during coalescence leads to an increase in the kinetic energy and hence the temperature. This is shown in Figure 4. However, it is important to note that, even though there is an increase in temperature, it never exceeds the clusters' melting points.

Figure 5 shows four snapshots of the cluster geometries during coalescence. These snapshots are taken from the times marked A-D in Figure 4. Panel A shows the icosahedral structures of the two Fe_{300} clusters shortly after impact. Since there is no temperature scaling, the kinetic energy increases by about 20 eV and can accelerate coalescence. This leads to a disordered intermediate (B), which undergoes a phase transition to the fcc structure shown in panel C. This is very similar to the dynamics observed for coalescence at 900 K (see Figure 3). Thus, the presence of an ambient gas may have a large effect on the (meta)stable cluster that is formed and/or the time that is required to form a stable structure.

Panels C and D in Figure 5 show the Fe_{600} structure at 60 ps and 2.2 ns. The balls in panel C clarify the atoms that form two small islands on the surface of the cluster. These islands are not stable and are substantially reduced in size or disappear at 2.2 ns (see panel D). Hence, small islands on the cluster surface are less stable than the larger ones or, alternatively, the surface atoms at high curvature positions are not stable. The aspect ratio of the Fe_{600} cluster decreases from 1.4 (panel C) to 1.2 (panel D) and the structure in panel D is thus more 'spherical' than that in panel C. Although diffusion of the atoms in the islands reduces the aspect ratio of the Fe_{600} cluster, the atoms that originate from the two Fe_{300} clusters are well separated in the final structure, supporting the fact that surface melting is not extensive and is not required for cluster coalescence.

4. Conclusion

The coalescence of two Fe_{300} clusters below their melting point is studied by molecular dynamics (MD). In contrast to grains found in bulk materials, two clusters can coalesce into a stable structure at temperatures lower than their melting points. The simulations show that the cluster shape depends on the temperature. When two or more clusters come into contact there is a change in the local environment for the atoms in the cluster-cluster interface region. This can be seen as a change in their local potential energy environment, and this leads to a structuring of these atoms in the coalesced cluster. At higher temperatures (which are still below the melting point) this can lead to a disordered phase that is intermediate to a stable crystalline phase. Hence, phase change can occur below the melting point. At low temperatures elongated structures, that may be metastable, are formed. It is also clear from the simulations that extensive surface melting is not required to explain the fabrication of larger devices from nanoclusters.

Acknowledgments

This work is funded by the Swedish Research Council and the Swedish Foundation for Structure Research (The CARAMEL Consortium). We are also grateful to the Swedish National Allocations Committee for High Performance Computing for the allocated computer time at the national supercomputing facilities.

References

1 J. L. Young, E-K Lee, and S. Kim, *Phys. Rev. Lett.* **86**, 999 (2001)
2 S. L. Lai, J. R. A. Carlsson, L. H. Allen, *Appl. Phys. Lett.*, **72** 1098 (1998)
3 Ph. Buffat and J-P. Borel, *Phys. Rev.* **A13**, 2287 (1976)
4 V. Rosato, M. Guillope, and B. Legrand, *Philos. Mag.* **A59**, 321 (1989)
5 L. J. Lewis, P. Jensen, and J-L. Barrat, *Phys. Rev.* **B56,** 2248 (1997)
6 J. Stanek, G. Marest, H. Jaffrezic, *et. al.*, *Phys. Rev.* **B52**, 8414, (1995)
7 M. Guillope and B. Legrand, *Surf. Sci.* **215**, 577 (1989)
8 S. Kirkpatrick, C. D. Gelatt, Jr., M.P. Vecchi *Science*, **220**, 671 (1983)
9 R. S. Berry, T. L. Beck, H. L. Beck, *et. al.*, *Adv. Chem. Phys.* **52**, 75 (1988)
10 F. A. Lindemann, Physik Z. **11**, 609 (1910)
11 H. J. C. Berendsen, J. P. M. Postma, *et. Al.*, *J. Chem. Phys.*, **81**, 3684.(1984)
12 W. Miehle, O. Kandler, T. Leisner, O. Echt, *J. Chem. Phys.* **91,** 5940 (1989)
13 C. R. Stoldt, A. M. Cadilhe, *et. al. Phys. Rev. Lett.*, **81**, 2950 (1998)
14 A. Bogicevic, S. Liu, J. Jacobsen, *et. al. Phys. Rev.* **B57**, R9459 (1998)
15 P. Jensen, N. Larralde, J. L. Barrat, *et. Al.* Euro. Phys. J. **B11**, 497 (1999)

USING IDEAL PES MODEL TO STUDY KINETICS OF COMPLEX SYSTEM

JUN LU
Department of Chemistry, The University of Chicago
5735 South Ellis Avenue, Chicago, IL 60637

R. STEPHEN BERRY†
Department of Chemistry and The James Frank Institute, The University of Chicago
5735 South Ellis Avenue, Chicago, IL 60637

Ideal PES models with master equation dynamics are used to study the possibility and the robustness for statistical sample PES to predict the fundamental kinetic information on a full PES. To compare the kinetics of full and sample PES, eigenvalue spectra from master equation are examined together with the relaxation of total potential energy. Results show that under special circumstances of some simple and symmetric PES model, perfect PES's can always exist and they have exactly the same kinetics as the full one. Generally, good sample PES's are those which have the similar topological structure and cover the high saddle barriers region of the full PES.

1. Introduction

One challenge of applying master equations [1] to kinetics is the increasing complexity of the potential energy surface (PES) with the size of the system. Solving the master equation involves diagonalizing a transition matrix whose dimension is the number of configuration states of the PES [2-4]. For example in atomic clusters, the number of energy minima of the PES increases at least exponentially with the number of atoms [5]. Therefore it is impractical to construct a full PES and the corresponding master equation, even of a noble gas cluster of more than 20 particles.

Thus an important question is: how can one construct a manageable statistical sample of a very large complex PES, and then use master equation dynamics to solve the sample PES to draw reliable inferences about the kinetics on the full many-dimensional surface? Ball and Berry firstly addressed this problem by using "sequence sampling" method to obtain samples of the full PES of Ar_{11} and Ar_{13} [6]. The authors have shown that with sequence sampling, the sample PES can be used to predict the slowest relaxation mode within better than a factor of two.

---

† The corresponding author, email: berry@uchicago.edu

In this paper, we study the possibilities and robustness of sample PES in depicting the kinetics of full one via the ideal PES model. The ideal PES model provides us the convenience and freedom in manipulating the topology of PES to simplify the problem. We construct two ideal PES's and their samples, apply master equation dynamics to them, compare the kinetics of full and sample PES's by comparing the eigenvalue spectra as well as the relaxation of potential energy.

2. Construction of Master Equation

The first step to construct a master equation is to calculate the rate coefficients for inter-well transitions. We use the following coarse-grained Arrhenius equation to calculate the rate coefficient for the transition from energy minimum j to adjacent minimum i, k_{ij}:

$$k_{ij} = \frac{k_B T}{h} \exp[-\frac{E(i,j) - E(j)}{k_B T}] \tag{1}$$

where k_B is the Boltzmann constant, h is the Planck constant, and T is temperature. $E(i,j)$ is the energy of the saddle point which connects minima i and j, $E(j)$ is the energy of minimum j. This formula does not consider the partition functions of stationary points as some other methods, e.g. RRKM theory [7,8], but it is already sufficient for the purpose of this work. To obtain a better, precise formula for calculating rate coefficient is not our aim here.

Following the standard procedure of solving master equation [2,4], we obtain the time-dependant population probability for the system to reside in energy minima i:

$$P_i(t) = \sqrt{P_i^{eq}} \sum_{j=1}^{N_{min}} \widetilde{u}_i^{(j)} e^{\lambda_j t} [\sum_{m=1}^{N_{min}} \widetilde{u}_m^{(j)} \frac{P_m(0)}{\sqrt{P_m^{eq}}}] \tag{2}$$

In the above expression of multi-exponential relaxation, **P(0)** and $\mathbf{P}^{eq}$ are the vectors of initial and equilibrium population probabilities, respectively. λ's are the eigenvalues of the transition matrix [2,4] which is composed of the rate coefficients of inter-state transitions. $\widetilde{\mathbf{u}}^{(j)}$ is the *j-th* eigenvector of the transition matrix. Eigenvalues and eigenvectors are important in explaining the kinetic relaxation since the former determine the timescale of the relaxation rates and the latter describe the population flows in terms of changes among individual states. If labeling all the λ's in decreasing order, then $\lambda_1=0$ and $\lambda_j<0$ for $j \geq 2$. The eigenvector with $\lambda_1=0$ defines the $\mathbf{P}^{eq}$ vector since all other terms vanish when $t \to \infty$ in Eq.(2). Among all other $N_{min}-1$ relaxation modes, the ones with larger eigenvalues (or less negative ones, corresponding to slower relaxation) dominate the relaxation. Therefore, if one wants to use a sample PES to infer dynamics on the complete PES, the eigenvalue spectrum of the sample PES should represent well the larger eigenvalues and their eigenvectors.

With the knowledge of the time dependent population probabilities of each minimum, $P_i(t)$, we can look at the evolution toward equilibrium for any thermodynamic property A, if it has a well defined value A_i for each minimum i in the master equation. The result is a weighted average:

$$\langle A(t)\rangle = \sum_{i}^{N_{\min}} A_i P_i(t) \tag{3}$$

3. Relaxation on a Simple Ideal PES Model and Its Sample PES's

3.1. *Constructing Full and Sample PES*

Our first ideal PES model is composed of m "monotonic sequences" [9,10]. Each monotonic sequence is a "Min-Sad-Min-...-Sad-Min" sequence with monotonically increasing energy values for the minima. In our model, each sequence has n linked energy minima via $(n-1)$ energy saddles.

Fig. 1 is a topological description of this ideal PES. All the $(n\times m)$ minima are distributed in n energy levels and each level has m minima with one from each of the m sequences. All the m minima in the same energy level are linked with each other by $m\times(m-1)/2$ energy saddle points.

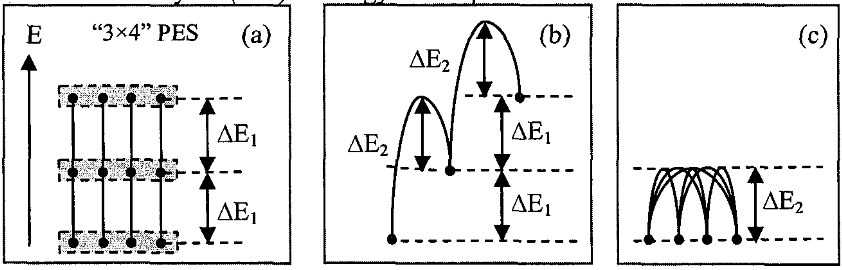

Figure 1. Illustration of the first ideal PES model. (a) An example of "3×4" PES with 3 energy levels and 4 monotonic sequences. Energy minima are denoted by dots, energy saddles are denoted by lines. All minima in each shaded area are all linked by saddle points. (b) Schematic description of minima and saddles in one monotonic sequence. (c) Schematic description of minima and saddles at one energy level.

A typical ideal PES model in this section has following parameters:

$$n=10,\ m=10,\ \Delta E_1=\Delta E_2=4\ \text{kcal/mol}. \tag{4}$$

We call this "10×10 PES" in this paper and take it here as the full PES. Then we take subsets of the minima and all related saddles to form different sample PES's. We constructed three sample PES's with different topologies.

1)"**10×k" sample PES** (*k<m*): This series sample PES keeps *k* of the *m* monotonic sequences from the full PES. In the later testing sample PES, *k=4*.
2)"**10×10-UT" sample PES**: This sample PES has an "up-triangular" shaped topology. See Fig. 2(a).
3)"**10×10-DT" sample PES**: This sample PES has a "down-triangular" shaped topology. See Fig. 2(b).

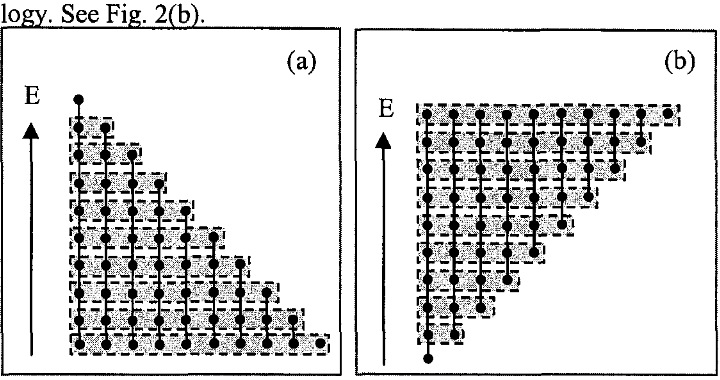

Figure 2. Illustration of (a) "10×10-UT" sample PES and (b) "10×10-DT" sample PES. Energy minima are denoted by dots, energy saddles are denoted by lines. All minima in each shaded area are all linked by saddle points.

3.2. *Results*

We plot the eigenvalue spectra for the full PES and the sample PES's in Fig. 3. The 10×4 PES (Fig. 3(b)) has exactly the same largest 10 eigenvalues (including $\lambda_1=0$) as the 10×10 PES (Fig. 3(a)). A detailed eigenvector analysis shows, all these and only these largest 10 eigenvalues are responsible for the population transition among those minima along the same monotonic sequences. Therefore for these two PES's, the population relaxation along the direction of energy axis must be exactly the same (See Fig. 4.). Both 10×10 and 10×4 PES's have another group of eigenvalues corresponding to the population transition among the minima in the same energy levels. These 90 (for 10×10) and 30 (for 10×4) eigenvalues are both distributed among 10 distinctive values with degeneracy of 9 and 3 each. This degeneracy is brought by the symmetry of the topologies of the two PES's.

For the two triangular-shaped PES's, the 10×10-UT PES (Fig. 3(c)) still preserves similar values for the group of eigenvalues of slow kinetic processes. However with the 10×10-DT PES (Fig. 3(d)), several of the largest eigenvalues have comparative large discrepancies from those of the full 10×10 PES. We find later (Fig.4) that the 10×10-UT PES has relaxation behavior similar to that of the full PES, but the relaxation on the 10×10 DT PES is significantly slower. It is also worth noting that since both of these triangular-shaped PES's break part of the symmetry in their topologies, the degeneracies of some small eigenvalues are lost.

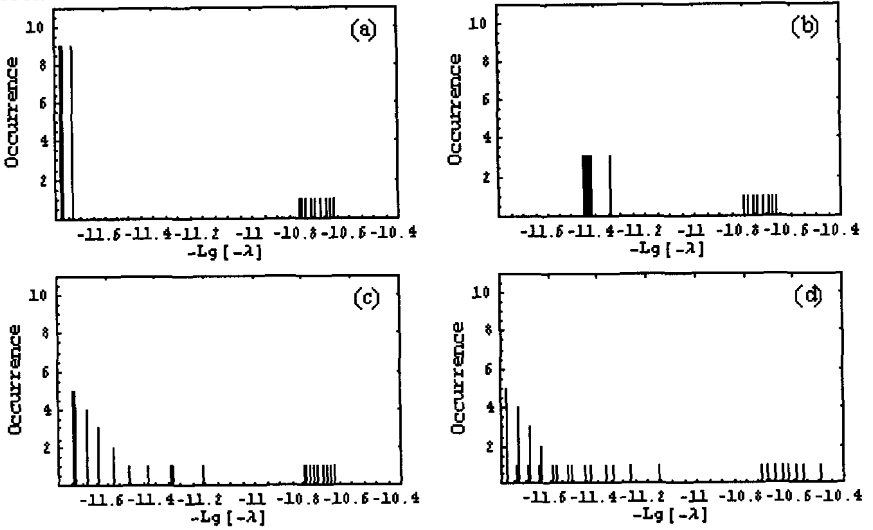

Figure 3. Line spectra of (a) "10×10" PES and its three sample PES's: (b) "10×4" PES, (c) "10×10-UT" PES and (d) "10×10-DT" PES, for all the non-zero eigenvalues of the master equation.

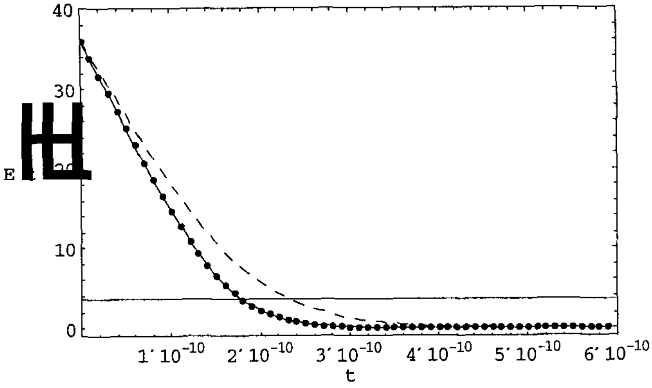

Figure 4. Relaxations of total potential energy for the full 10×10 PES (continuous line) and its three samples: 10×4 PES (completely overlapped with the 10×10 PES), 10×10-UT PES (dotted line) and 10×10-DT PES (dashed line). All the relaxations start from the initial population with a uniform distribution among the energy minima of the highest energy level. The horizontal line marks 90% completion of the relaxation.

Relaxation of total potential energy for the full PES and its three samples are plotted in Fig. 4. All the relaxations start from the initial population with a uniform distribution among the energy minima of the highest energy level. As predicted above, the 10×4 sample PES has exactly the same relaxation profile as the 10×10 full PES; the relaxation of 10×10-UT PES also precisely match the full PES; however, the relaxation of 10×10-DT PES is significantly slower than the full PES. For 90% of complete relaxation, the 10×10-UT PES is only 0.14% faster than the full PES, but the 10×10-DT PES is 29% slower. The reason of this delay in the relaxation of potential energy for 10×10-DT PES can be accounted by the fact that, for each energy level in this PES (Fig. 2(b)), there is always one minimum that has no pathway to lead its population to flow directly downstream. This phenomenon of topology-induced dynamic delay has also been observed by Doye and Wales in their work [11].

4. Relaxation on a More Complicated Ideal PES Model and Its Sample PES's

4.1. *Constructing Full and Sample PES*

In our second model PES, we completely break the symmetry of the previous 10×10 PES and also vary the height of saddle barriers according to the energy of the minima the saddles connect. We build a 50×50 full PES by following steps. (i) First build a symmetric 50×50 PES as the same method in Section 3.1. (ii) Increase the saddle barrier height (ΔE_2 in Fig.1) linearly with the decrease of energy levels: (This reflects the general situation of the PES of atomic clusters or proteins.)

$$\Delta E_2 = b\{1 + c[L_{tot} - L(\max[E_i, E_j])]\} \tag{5}$$

where L_{tot} is the total energy levels (L_{tot}=50 in this case), $L(\max[E_i, E_j])$ is the energy level of the higher energy minimum of the two minima the saddle connects. b and c are constants and in this case, b=4 kcal/mol and c=0.02. (iii) To further break the symmetry, small fluctuations are made to all energy minima and saddles according to a Gaussian distribution with the standard deviation of 0.5 kcal/mol and the range of $-1.0 \sim 1.0$ kcal/mol.

We then construct four series of sample PES's.

1) **"50×N-Series" samples**: in this series, the sample PES's randomly keep several entire monotonic sequences of the full PES, so the samples span the entire energy levels as the full PES. These sample PES's include "50×40", "50×30", "50×20", and "50×10" PES's.
2) **"N×50-Series" Samples**: in this series, the sample PES's keep N lowest energy levels of minima, so they span all the monotonic sequences. These sample PES's include "40×50", "30×50", "20×50", and "10×50" PES's.
3) **"N×N-Series" Samples**: in this series, the sample PES's keep N lowest energy levels of minima from randomly selected N monotonic

sequences. These sample PES's include "40×40", "30×30", "20×20", and "10×10" PES's.

4) **"N×50(up)-Series" Samples**: in this series, the sample PES's keep N highest energy levels of minima, this is just the opposite of N×50 samples. These sample PES's include "40×50(up)", "30×50(up)", "20×50(up)", and "10×50(up)" PES's.

4.2. ***Results***

Densities of eigenvalues against their logarithmic value are plotted in Fig. 5. It shows that the N×50-series sample PES's (Fig. 5(b)) have the best representation for eigenvalue spectrum of full PES in large eigenvalues region. This is due to the fact that N×50 PES's cover the full PES region of the highest saddle barriers, which actually determine the relaxation rates of the slowest kinetic transitions. These slow relaxation rates are associated with the large eigenvalues.

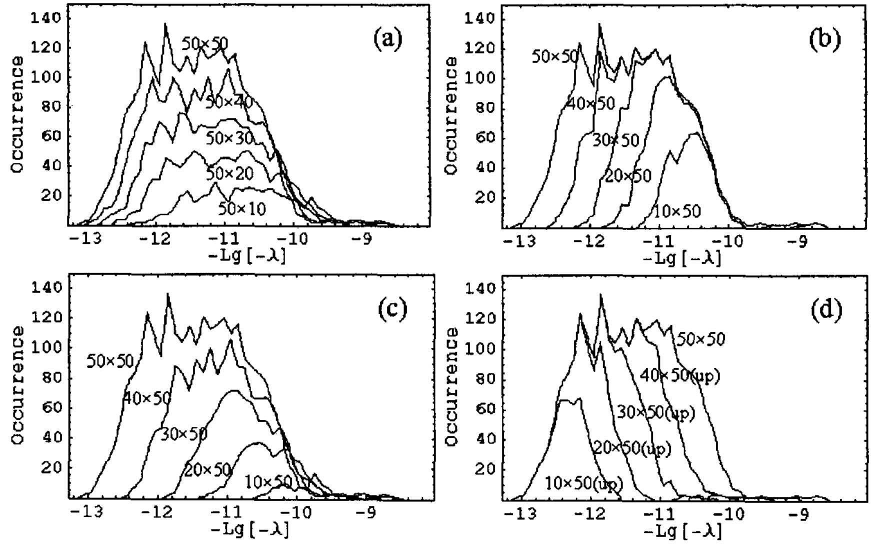

Figure 5. Eigenvalue spectra of the 50×50 full PES and its four series of sample PES's: (a)50×N sample PES's, (b)N×50 sample PES's, (c)N×N sample PES's and (d)N×50(up) sample PES's. Plotted are the densities of eigenvalues against their logarithmic value for each sample and full PES's. The names of the PES's are labeled accordingly.

Both 50×N and N×N-series sample PES's (Fig. 5(a) and 5(c), respectively) still keep most of the large eigenvalues of the full PES in their eigenvalue density spectra. But there is a little over-representation of large eigenvalues. This happens especially on the small samples of those two series samples. The difference between 50×N and N×N series sample PES's is that, since 50×N-series samples span all the energy regions of both high and low energy barriers, they also preserve part of the small eigenvalues of the full PES, corresponding to the slow kinetic processes.

In contrast to N×50 PES's, the N×50(up) PES's (Fig. 5(d)) have a very poor representation for large eigenvalues but on the contrary a good representation for small ones of the full PES. This is easy to understand since the N×50(up) PES's cover most of the full PES region of low saddle barriers where kinetics is fast.

5. Conclusions

From this study, several useful conclusions can be drawn to direct further work in simplifying PES. First, from the 10×10 PES and its samples, the close correlation between the kinetic relaxation and the eigenvalue spectrum of the master equation suggests that we may use eigenvalue spectrum as an important criterion to judge the robustness of a sample PES. Second, according to both 10×10 and 50×50 PES's, behaviors of various sample PES's indicate that a good sample PES usually (1) has similar topology as the full PES; (2) covers as much as possible the "rough" area of the full PES.

References

1. N. G. van Kampen, *Stochastic Processes in Physics and Chemistry.* (North-Holland, Amsterdam, 1981).
2. K. D. Ball and R. S. Berry, *J. Chem. Phys.* **109**, 8557 (1998).
3. Y. Levy, J. Jortner, and R. S. Berry, *Phys. Chem. Chem. Phys.* **4**, 5052 (2002).
4. O. M. Becker and M. Karplus, *J. Chem. Phys.* **106**, 1495 (1997).
5. C. J. Tsai and K. D. Jordan, *J. Phys. Chem.* **97**, 11227 (1993).
6. K. D. Ball and R. S. Berry, *J. Chem. Phys.* **111**, 2060 (1999).
7. P. J. Robinson and K. A. Holbrook, *Unimolecular Reactions.* (Wiley-Interscience, London, 1972).
8. R. G. Gilbert and S. C. Smith, *Theory of Unimolecularand Recombination Reactions.* (Blackwell Scientific, Oxford, 1990).
9. K. D. Ball, R. S. Berry, R. E. Kunz, F. Y. Li, A. Proykova, and D. J. Wales, *Science* **271**, 963 (1996).
10. R. E. Kunz and R. S. Berry, *J. Chem. Phys.* **103**, 1904 (1995).
11. J. P. K. Doye and D. J. Wales, *J. Chem. Phys.* **105**, 8428 (1996).

THE Z=82 SHELL EFFECT NEAR THE PROTON DRIP-LINE

C. SAMANTA and S. ADHIKARI
Saha Institute of Nuclear Physics, 1/AF Bidhan Nagar, Calcutta 700064, India
Physics Department, Virginia Commonwealth University, Richmond, VA 23284-2000

Variation of the shell effect near the Pb nucleus is studied through a comparison between the experimental and theoretical binding energies and one-proton separation energies. The theoretical binding energies are computed using a recently developed mass formula (called, BWM) which reproduces the general trend of the binding energy versus neutron number curves for all the nuclei from Li to Bi. As BWM has no shell effect incorporated, it shows marked deviation near a magic number. When the shell effect diminishes, the difference between the BWM predictions and experimental mass diminishes. The shell effect in isotopes of Pb (Z=82) peaks at neutron number N=126 and, approaches zero near N=106 which suggests that the magic nucleus Lead might lose its magicity when its neutron number content reduces to 106. The shell effect again increases gradually for N<106, indicating considerable shell effect in Pb near the proton drip-line.

The unusual stability of nuclei with "magic" numbers of neutrons and protons was explained to be due to nuclear shell structure. A discovery in 1984 showed that similar magic numbers also appears in small clusters of Na-atoms [1]. In analogy with the stability of magic nuclei, the magic numbers in Na-clusters were explained due to electronic shell closure. However, due to different nature of the potentials in atomic and nuclear domain, the two sets of magic numbers do not exactly coincide such as, the magic numbers in the Na-clusters are 2, 8, 20, 40, 58, 92...[1, 2] whereas, the nuclear magic numbers are 2, 8, 20, 28, 50, 82 and 126. Recently, atomic clusters have been found whose stabilities are not ruled by the electronic shell closure. For example, Na_8Mg cluster [3] which contains 10 valence electrons should not be magic, but it is. Similarly, Al_{13}^- and $Al_{13}K$ [4], which contain 40 electrons each, are magic while, $Al_{13}Cu$ which also contains 40 electrons is not [5]. The same phenomenon also appeared in nuclei. Recently, the neutron number N = 6 and 16 have been found to be new nuclear magic numbers [6, 7] in only a few neutron-rich nuclei. On the other hand, the known magicities at N = 8 and 20 are found to disappear in ^{12}Be and ^{32}Mg nuclei [7].

The central question then arises: why do some nuclei and atomic clusters deviate from the magic numbers prescribed by the shell structures and, is there a convenient way to identify the occurrence and disappearance of magic numbers in atomic clusters as well as in nuclei. While such analysis may be easier in atomic clusters because of the interaction (Coulomb) being well known, similar analysis in nuclei in microscopic framework poses difficulties as the nucleon-nucleon interaction is very complicated.

In atomic mixed clusters, movements of single particle levels causes appearance of new magic numbers and disappearance of some old ones. Similarly, in nuclei away from the β-stability line, the rearrangements of nuclear shells cause drifting of magic numbers from the known to unexpected values. Recently, in an experiment at RIKEN, Japan we found that in the neutron-rich ^{23}O nucleus the $2s_{1/2}$ state comes down very close to (or, possibly even below) the $1d_{5/2}$ state, giving rise to the N=16 magic shell gap [8].The observed ground state spin parity of ^{11}Be is $½^+$ (instead of $½^-$) which indicates lowering of the $2S_{1/2}$ state below $1p_{1/2}$ [7].

About six thousand combinations of protons and neutrons are possible to form a nucleus within the neutron- and proton-drip lines. Beyond the drip-lines no nucleus can be formed as the one-nucleon separation energy becomes zero on these lines. Due to large diffuseness of neutron density and central potential the single-particle, the spectrum of neutron-drip-line nuclei resembles that of the harmonic oscillator with the spin-orbit term. Theory predicts that the magic shell gap at neutron number N=82 will be quenched in neutron-rich nuclei far from the β-stability line and, may eventually disappear completely at the neutron-drip line [9].

While one may expect similar quenching of the Z=82 shell gap near the proton-drip line, controversy exists for the Z=82 shell gap quenching. From the analysis of some α-decay studies it was predicted that the shell closure effect at Z=82 may disappear in the vicinity of N=112-114 [10, 11]. But, later on from the alpha decay of several even-even nuclei it was suggested that the large variation in the hindrance factors of the alpha decay to the excited 0^+ state is a proof for the persistence of the Z=82 shell closure at the neutron deficient side [12].

The purpose of this study is not to calculate the so-called "shell gaps" microscopically, but to present an overall "shell effects" in a macroscopic framework for the different isotopes of Pb. This shell effect is extracted by comparing the experimental masses with a liquid drop type mass formula, called BWM [7], which has no shell effect incorporated. The BWM was formulated by modifying the pairing and the asymmetry terms of the Bethe-Weizsäcker (BW) mass formula to fit the gross properties of the binding energy versus neutron number curves for all the nuclei from Li to Bi with a fixed set of parameters [7]. The BW, originally designed for medium and heavy mass nuclei, fails miserably for light nuclei, especially for the recently discovered rare-isotopes existing near the drip lines. In BWM, the expression for the binding energy is [7],

$$BE(A,Z) = 15.777A - 18.34A^{2/3} - 0.71\frac{Z(Z-1)}{A^{1/3}} - 23.21\frac{(A-2Z)^2}{A(1+e^{-A/17})} + (1-e^{-A/30})\delta$$

where, the term $\delta = +12\ A^{-1/2}$ for even Z-even N nuclei, and $-12\ A^{-1/2}$ for odd Z-odd N nuclei and 0 for odd A nuclei. The detail of the parameter evaluation and their physical significane is given in ref. [7]. It is pertinent to note that, this formula is applicable only for the spherical nuclei having negligible shell effects and it shows marked deviation for nuclei with shell effects. As the shell effect in a nucleus decreases, the discrepancy between the experimental data and the predictions of BWM diminishes. In the following we study the shell effect in the isotopes of Pb by comparing the binding energies and separation energies computed from BWM as well as from the experimental masses [13-15], which include the recently found ones away from the line of β-stability.

Fig.1 shows the single-proton separation energy (S_p) from Pb and nearby elements, plotted against the proton number (Z). For N=126 (Z=82) a large break in the experimental value of the separation energies indicates strong magicity of the doubly magic ^{208}Pb nucleus, and as expected, there is a large discrepancy between the experimental values and the BWM predictions. Interestingly, this discrepancy at Z=82 (as well as at some nearby Z values) almost disappears at N=106, but a considerable discrepancy appears again at Z=82, N=104.

In Fig.2, the difference ΔB (=EXP-BWM) between the binding energies computed from the experimental masses (EXP) and the BWM is plotted against the proton number around the Z=82 region, in the range of N=100 to 114. The binding energies computed by BWM and experimental mass data of different isotopes of Pb are given in Table 1 which shows close agreement near N=106 and increasing discrepancies away from it. As the neutron number decreases from N=126, ΔB value is found to decrease and becomes almost zero (~56 keV) at N=106, but it increases again for N<106. The rise happens due to the mutual support of shell effects as the neutron magic number N=82 is approached.

In summary we have studied the shell effect in Pb nuclei near the proton drip line by comparing the binding energies and separation energies computed from the experimental mass and a liquid drop type mass formula called, BWM [7]. As BWM has no shell effect incorporated it cannot reproduce the masses of magic nuclei, but can delineate their positions through sharp contrast to experimental binding energy/one-nucleon separation energy data. When the shell effect quenches, the difference between the experimental mass and BWM predictions diminishes.

The binding energy of the doubly magic nucleus ^{208}Pb is grossly under predicted (by about 9.75 MeV) by BWM, as expected. Nevertheless, in the range of N=105-109, the experimental binding energies of Pb and some of its nearby elements are very close to the values calculated by BWM (Table 1). The most interesting finding in this work is that the shell effect in Pb approaches almost zero (~56 keV) at N=106 and then rises again for N<106 whereas the masses of some nearby lower Z nuclei remain close to the BWM predictions.

The "shell effect" in conventional terminology encompasses the magicity and deformation effects in nuclei. As all the even-even isotopes of Pb have spherical ground states, the reduction of shell effect near the neutron number N=106 indicates reduced magicity or, quenching of the Z=82 shell gap. This conclusion awaits verification by microscopic calculations and experimental measurements. In this context it is pertinent to note that in moving away for the neutron shell closure at N=126, the number of valence neutrons increases up to the mid-shell configuration and this may bring in an important energy correlation that may contribute to nuclear masses. The large amount of valence neutrons may induce a polarization of the closed proton core. In a microscopic theory these specific and important correlations should first be removed in order to be able to deduce results on a changing spherical Z=82 shell gap but, such a microscopic calculation is beyond the scope of this work. On the experimental side, data on knockout and pickup cross sections with isotopes of Pb are needed to extract the spectroscopic factors and to establish in some acceptable approximation the so-called shell gaps and positions of the spherical j-shells.

Reference

[1] W.D.Knight et al., Phys. Rev. Lett. **52**, 2141(1984)
[2] C.Yannouleas, P.Jena, S.N.Khanna, Phys. Rev. **B46**, 9751 (1992)
[3] M.M.Kappes et al., Phys. Lett. **119**, 11(1985)
[4] B.K.Rao, S.N.Khanna, P.Jena, Phys. Rev. **B62**, 4666 (2000)
[5] S.N.Khanna, C.Ashman, B.K.Rao, and P.Jena, J. Chem. Phys. **114**, 9792 (2001)
[6] A.Ozawa et al., Phys. Rev. Lett. **84**, 5493 (2000)
[7] C.Samanta and S.Adhikari, Phys.Rev. **C65**, 037301 (2002); *see references there in.*
[8] R.Kanungo et al., Phys. Rev. Lett. **88**, 142502 (2002)
[9] B.Chen et al, Phys. Lett. **B355**, 37 (1995)
[10] K.Toth et al., Phys. Rev. Lett. **53**, 1623 (1984)
[11] B.A.Brown, Phys. Rev. **C46**, 811 (1992)
[12] J.Wauters et al., Phys. Rev. Lett. **72**, 1329 (1994)
[13] Nuclear Wallet Cards, Brookhaven National Laboratory, 2000
[14] S.Schwarz et al., Nucl. Phys. **A693**, 533 (2001)
[15] Yu.N.Novikov et al., Nucl. Phys. **A697**, 92 (2002)

Table 1. Binding energy of Pb isotopes computed from experimental (EXP) mass data [13-15] and the mass formula BWM [7] and, their difference ΔB (all in MeV) at different neutron number (N).

N	EXP	BWM	ΔB	N	EXP	BWM	ΔB
99	1399.827	1398.064	1.763	116	1560.007	1557.059	2.948
100	1411.618	1409.840	1.779	117	1567.235	1563.879	3.356
101	1420.369	1419.624	0.745	118	1576.326	1572.235	4.091
102	1431.980	1430.969	1.010	119	1583.437	1578.734	4.703
103	1440.611	1440.341	0.270	120	1592.166	1586.764	5.402
104	1451.712	1451.270	0.442	121	1599.090	1592.951	6.139
105	1460.053	1460.242	-0.189	122	1607.480	1600.666	6.814
106	1470.824	1470.768	0.056	123	1614.215	1606.551	7.664
107	1479.095	1479.352	-0.257	124	1622.303	1613.959	8.344
108	1489.666	1489.488	0.178	125	1629.040	1619.550	9.490
109	1497.737	1497.697	0.040	126	1636.408	1626.661	9.747
110	1508.108	1507.454	0.654	127	1640.344	1631.966	8.378
111	1515.879	1515.299	0.580	128	1645.529	1638.789	6.740
112	1525.950	1524.690	1.260	129	1649.354	1643.817	5.537
113	1533.521	1532.183	1.338	130	1654.485	1650.358	4.127
114	1543.163	1541.218	1.945	131	1658.299	1655.117	3.182
115	1550.663	1548.369	2.294	132	1663.258	1661.385	1.873

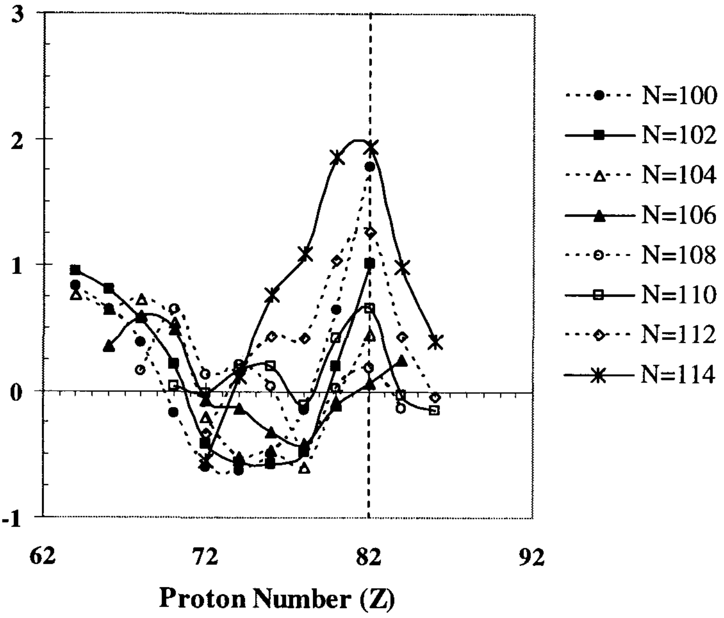

Figure 1 The difference (ΔB) between the binding energies computed from the experimental masses [13-15] and BWM [7] is plotted against the proton number (Z) for N=100-114. The plot shows quenching of Z=82 shell effect near N=106 and rise of shell effect for N<106.

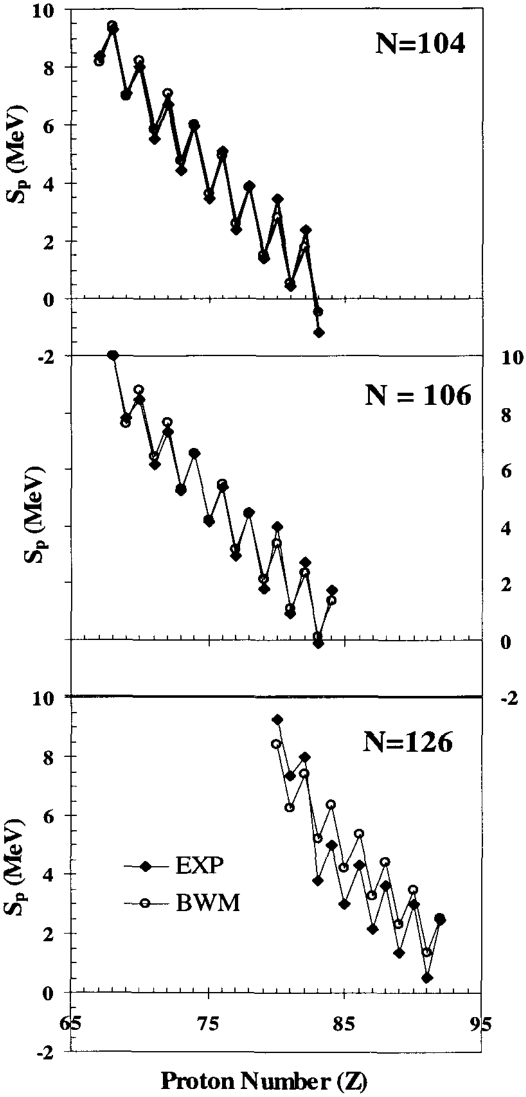

Figure 2 Plot of one-proton separation energy(Sp) versus proton number(Z) curve from measured masses [13-15] and BWM [7] to delineate the shell effect at Z=82 for N=104,126 and its near disappearance at N=106.

FUNDAMENTAL CLUSTER STUDIES OF MATERIALS AND ATMOSPHERIC CHEMISTRY

D. P. HYDUTSKY, D. E. BERGERON, T. E. DERMOTA, J. R. STAIRS, K. L. KNAPPENBERGER, JR., K. M. DAVIS, C. E. JONES, JR., M. A. SOBHY, N. J. BIANCO, S. J. PEPPERNICK, AND A. W. CASTLEMAN, JR.
Chemistry and Physics Department, Pennsylvania State University, 128 Davey Laboratory, University Park, PA 16802, U.S.A

This paper discusses several current research areas in fundamental cluster science. Delayed ionization of the Met-Car, the study and synthesis of novel cluster materials, and solvation of atmospherically relevant clusters with water are all currently under investigation. The delayed ionization experiments show good agreement with a thermionic emission model. Supermagic Al_{13}^- clusters are found to react with CH_3I to form new stable clusters. The effects of water solvation on excited SO_2 and HBr clusters are examined with the pump-probe technique. All of these topics give insight into the fundamental physics and chemistry of clusters and provide relevant information to real world problems.

1. Introduction

Gas phase clusters have long been studied because of their interesting properties that differ from both a single molecule or atom and the bulk quantities of the material. Many fundamental processes can be critically interrogated in this unique size regime. The quantum nature of such small systems permits experimentation at a molecule by molecule level, such that the transition from lone atoms and molecules to the bulk can be explored in great detail.

The structure of this paper is as follows: clusters mimicking bulk thermionic emission like behavior are discussed in the delayed ionization section, the synthesis of new aluminum clusters is covered in the novel materials section, and the excited state dynamics of self solvated SO_2 clusters and HBr clusters solvated in water are presented in the solvation section.

2. Delayed Ionization

Delayed ionization has been observed in several systems [1-3], including the Metallocarbohedrene (Met-Car) family, M_8C_{12}, where M is an early transition metal. Delayed ionization is often observed in clusters when the binding energy is higher than the ionization potential. In order for the delayed ionization to be thermionic, the cluster must have vibrational modes where it can store energy that is in excess of its ionization potential. When a cluster meets these requirements, the ionization process often occurs on a time-scale billions of times slower than that predicted by the photoelectric effect. In this section, we display the delayed ionization phenomena as they occur in the zirconium Met-Car, and we model this cluster's delayed ionization with the thermionic emission model.

A detailed description of the experimental setup used for these investigations has been described elsewhere [4], hence, only a brief discussion is given here. The metal-carbon clusters are produced in a laser vaporization source, where the second harmonic of a Nd:YAG (532 nm) ablates a metal rod while ~25% methane seeded in helium gas is pulsed over the rod. The metal plasma surrounding the rod reacts with the carbon and the clusters form as the gas is expanded into a vacuum. The clusters are then skimmed, producing a pulsed molecular beam of metal-carbon clusters. The clusters travel between two time-of-flight grids where they are ionized with a nanosecond ultraviolet XeCl excimer laser (308 nm). The time-of-flight grid that is farthest from the detector is equipped with a fast high-voltage transistor switch (Behlke switch HTS 31). This switch pulses the voltage from 1000 V to 4500 V, while the other time-of-flight grid is held constant at 3500 V. The time at which the switch changes the voltage is varied in 50 ns steps from the time before the ionization laser interacts with the molecular beam until there are no more ions created. This allows for the removal of prompt ions and the detection of only delayed ions. Once ionized, the molecules travel through a time-of-flight tube and, after being reflected, are detected with microchannel plates.

As published in Stairs *et al.*[5] and shown graphically in Fig. 1, we have modeled the delayed ionization of the zirconium Met-Car with the thermionic emission model. This model assumes that the energy imparted onto the cluster by the ionization laser is stored in vibrational modes of the cluster rather than utilizing the energy to ionize promptly. These vibrational modes are excited for a time on the order of microseconds, and then the energy is transferred back to the electronic modes causing the cluster to ionize.

Modeling the delayed ionization of the clusters with the thermionic emission model allows one to obtain knowledge of the average number of photons absorbed by the clusters as well as the internal energy of the cluster prior to being ionized. In the case of the zirconium Met-Car, the model gave the average number of 308 nm photons absorbed as 1.99, and the initial internal energy as 0.14 eV. Calculations of the density of states of the Met-Car are also under way for the various geometries that have been proposed. These calculations will serve as a starting point for future delayed ionization experiments as well as photo electron spectroscopy (PES) experiments.

3. Novel Cluster Materials

Aluminum clusters are studied extensively, partially due to their compatibility with the Jellium description. In the anionic cluster series, Al_{13}^-, Al_{23}^-, and Al_{37}^- have closed electronic shells and have been studied in some detail. Simultaneous closures of geometric and electronic shells provide these clusters with remarkable chemical nobility, and it is widely believed that similar species may provide the building blocks for novel nanostructured materials. In this vein, doped clusters have often been studied in order to synthesize neutral species that are isoelectronic with the closed shell, stable entities.

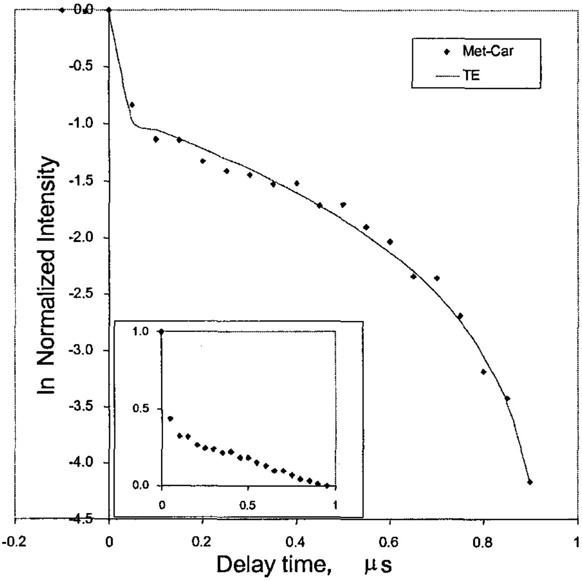

Figure 1. Natural log-linear plot of the delayed ionization of the Zr Met-Car shown with the thermionic emission model fit. Due to the long extraction time (50 μs), each data point represents the summation of ions created at that time step and thereafter. *Inset*: Linear-linear plot of data.

Recently, we reported on the chemical formation of neutral Al_nCH_3 clusters via reaction of cluster anions with methyl iodide [6]. As a side product of the neutralization reaction, we noted that Al_nI^- clusters were formed. Current studies are aimed specifically at the properties of halogentaed aluminum clusters. We are probing relative stabilities of clusters of various sizes, and composition.

Particular attention has been paid to the interactions of closed-shell Jellium clusters with halogen atoms, and the dependence of the nature of these interactions on relative electron affinities (EAs). Al_{13}^-, for example, has an EA close to that of Br. We have observed that the preservation of the cluster core is highly dependent on the cluster's ability to retain its preferred charge state, so that while interaction with iodine might be favorable, interaction with chlorine can de-stabilize a cluster. These studies have important implications with respect to salt-like cluster assembled materials, as we believe cluster-halide interactions to be ionic in nature. In addition, multiple halogenated clusters may actually prove to have characteristics desirable in the synthesis of new complex salt-like materials analogous to the complex organic salts that feature I_3^- ions.

4. Solvation

Solvation of atmospherically relevant species, such as SO_2 and HBr, have been studied to investigate the changes to the excited state dynamics following a photo excitation. These systems can probe the initial steps of molecules dissolving into a solvent and reveal relevant information on possesses in the atmosphere. For example, HBr is known to attach to the surface of ice particles in the stratosphere and if enough water molecules are free to solvated HBr, it dissociates into H^+ and Br^-. The bromine anion can then participate in various reactions, ultimately leading to the destruction of ozone [7]. This process cannot take place unless the initial dissolution of the HBr molecules occurs. Thus, a detailed understanding of how many water molecule this requires would be useful.

A study of $(SO_2)_m$ clusters excited to the coupled $^1A_2$, $^1B_1$ states by a 265 nm photon and to the F band by two 265 nm photons has been performed. The measured decay rates for clusters are significantly slower than the value of < 0.1 ps which has been determined computationally for the SO_2 molecule [8]. Solvation of the excited state SO_2 molecule apparently retards the movement of the excited state wave packet from the $^1B_1$ state into the $^1A_2$ state. Further experiments are underway to examine these effects.

Excitation of the F band of SO_2 solvated in SO_2 molecules leads to a rather complex temporal behavior [9]. The signal intensity is found to first increase with a time constant of about 1 ps for all clusters. The 1 ps growth is followed by a slow decay that is strongly influenced by cluster size. Self-solvation results in a substantial decrease in the decay rate from the F band, for example the measured decay rates increase from about 13 ps to 65 ps for clusters of 1 to 5 SO_2 molecules, respectively. The exact nature of this decay process has not yet been determined but it is believed to be the result of energy relaxation or redistribution from the excited state molecule to solvent molecules in the cluster.

The oxygen loss process that follows the excitation of the SO_2 E state has also been investigated. The monomer transient rapidly decays, exhibiting an excited state lifetime of 230 fs. The corresponding SO product displays a growth of 225 fs which agrees well with the proposed mechanism for the loss of an oxygen atom from the SO_2 molecule. *Ab initio* calculations [10] of the potential energy surface of states falling in this energy range indicate that the wavepacket evolves through a bending mode prior to dissociation and our studies of the monomer are in good agreement with this interpretation.

Initial finding in our studies of the E state evolution of homogeneous SO_2 clusters suggest we are observing a "caging" mechanism. The caging of SO_2 does not appear to proceed as the direct dissociative recombination previously reported for many linear molecules [11]; rather, the dissociation appears to be prevented by a steric effect. Our interpretation of the E state requires the chromophore to become linear prior to dissociating. The data indicates that incorporating additional SO_2 molecules causes an unfavorable steric restriction of this bending mechanism, as is reflected by the slower rate constant for larger cluster species.

An investigation of the solvation of HBr with water, leading to the formation of a dissociated ionic species, also has been performed recently in our laboratory [12]. These studies elucidated the number of water molecules necessary for the dissociation event to occur in the ground state and measured the temporal behavior of the excited dissociated species. When more than 4 water molecules are present in the $HBr(H_2O)_n$ clusters, solvation occurs in the ground state. $HBr(H_2O)_{1-4}$ clusters were excited to the C state by two photons of 271.5 nm light and probed with one photon of 407 nm light. Upon excitation, the clusters dissociate as the valence state has been lowered by solvation, making the transition favorable (Fig. 2). The time dynamics of the $H^+(H_2O)_{1-4}$ species show a growth ranging from 0.5 ps to 2.3 ps for the $H^+(H_2O)$ to the $H^+(H_2O)_4$ clusters respectively. These protonated water clusters reflect the neutral species $HBr(H_2O)_n$; upon ionization of each cluster, a Br atom evaporates because of its low binding energy. This growth was interpreted to be solvent reorganization around the excited state contact ion pair as the growth time increases with the addition of more solvent molecules.

Further findings indicate that other HBr molecules can act as a solvent, leading to the formation of the ion pair as long as at least one water molecule is present [13]. However, if no water molecules are present, HBr cannot self-solvate. This interesting phenomenon is explained as follows. HBr is a linear diatomic molecule, and as a result, it can only simultaneously interact with two other molecules, one at each end. Thus, no matter how many HBr molecules are present in a cluster, each is only solvated by two other HBr molecules. However, when one molecule of water is introduced into the cluster, multiple interactions between the molecules of the cluster can occur because the bent geometry of H_2O allows interaction of the water molecule with four other molecules in the cluster. The result of this increased interaction between molecules in the cluster is stabilization of the ion pair. Our findings indicate that in an $(HBr)_m(H_2O)_n$ cluster, the ion-pair is formed for any combination of $m + n \geq 5$ as long as $n \geq 1$.

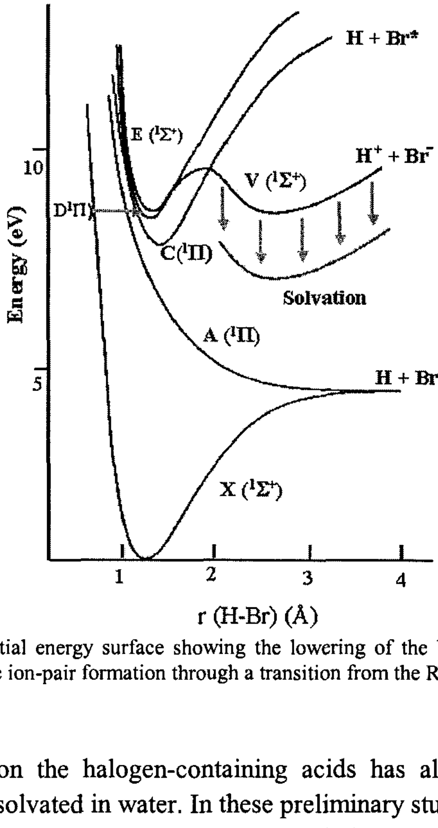

Figure 2. HBr potential energy surface showing the lowering of the V state by solvation, allowing excited state ion-pair formation through a transition from the Rydberg C state.

Further work on the halogen-containing acids has also begun, with the investigation of HI solvated in water. In these preliminary studies, HI clusters are excited to the A state by one photon of 265 nm light, and then ionized at later times by the 400 nm probe pulse for detection in a typical pump-probe scheme. It is evident that significantly more work is needed before the results can be fully interpreted.

5. Conclusion

These studies increase our understanding of cluster phenomena. Delayed ionization studies probe the nature of energy redistribution and ionization. Clusters such as the salt-like Al_nI^- have important implications to cluster assembled materials. Finally, solvation has far reaching effects in many aspects of chemistry, thus it is important to gain further understanding of this very fundamental topic.

Acknowledgements

We gratefully acknowledge financial support from the United States Air Force Office of Scientific Research Grant Number F49620-01-1-0380 and F49620-01-1-0122, the Department of Energy Grant Number DE-FG02-02ER46009, and the Atmospheric Sciences and Experimental Physical Chemistry Divisions of the U.S. National Science Foundation, Grant Number NSF-0089233.

References

1. P. D. Dao and A. W. Castleman, Jr., *J. Chem. Phys.* **84,** 1435 (1986).
2. E. E. B. Campbell and R. D. Levine, *Annu. Rev. Phys. Chem.* **51,** 65 (2000).
3. T. Leisner, K. Athanassenas, D. Kreisle, E. Recknagel, and O. Echt, *J. Chem. Phys.* **99,** 9670 (1993).
4. J. R. Stairs and A. W. Castleman, Jr., *Int. J. Mass Spectrom.* **216,** 75 (2002).
5. J. R. Stairs, K. M. Davis, S. J. Peppernick, and A. W. Castleman, Jr., *J. Chem. Phys.* **119,** 7857 (2003).
6. D. E. Bergeron and A.W. Castleman, Jr., *Chem. Phys. Lett.* **381,** 189 (2003).
7. U. Platt and G. Hönninger, *Chemosphere* **52,** 325 (2003).
8. H. Muller, and H. Koppel, *Chem. Phys.* **183,** 107 (1994).
9. T. E. Dermota, D. P. Hydutsky, N. J. Bianco, and A. W. Castleman, Jr., *Femtochemistry VI Proceedings* (in press).
10. K. Kamiya, H. Matsui, *Bull. Chem. Soc. Jpn.* **64,** 2792 (1991).
11. A. Sanov, S. Nandi, W. C. Lineberger, *J. Chem. Phys.* **108,** 5155 (1998).
12. S. M. Hurley, T. E. Dermota, D. P. Hydutsky and A. W. Castleman, Jr. *Science* **298,** 202 (2002).
13. S. M. Hurley, T. E. Dermota, D. P. Hydutsky, and A. W. Castleman, Jr., *J. Chem. Phys.* **118,** 9272 (2003).

EXCITED STATE CHARGE TRANSFER AND DISSOCIATION OF Mg^+-CH_3I COMPLEX

FUMINORI MISAIZU[†], ARI FURUYA, HIRONORI TSUNOYAMA,
AND KOICHI OHNO

*Department of Chemistry, Graduate School of Science, Tohoku University, Aramaki,
Aoba-ku, Sendai 980-8578, Japan*

Photodissociation of Mg^+-CH_3I has been studied in the UV region using a reflectron time-of-flight mass spectrometer. Three bands were observed in a dissociation spectrum peaking at about 27200, 29600, and 38100 cm^{-1}, which were assigned to the bands originating from $^2P \leftarrow ^2S$ transition of Mg^+. Five kinds of ions, CH_3^+, Mg^+, I^+, CH_3I^+, and MgI^+, were observed as fragment ions. Dissociation processes were discussed from the consideration of potential energy curves including charge transfer states obtained by CIS calculation.

1. Introduction

Intermolecular charge transfer (CT) and charge separation have been one of the central interest in gas-phase cluster studies [1, 2]. Especially as models of solvation processes in electrolyte solution, clusters consisting of a metal atom with solvent molecules have been investigated widely by photoionization mass spectrometry [1]. In addition, excited CT states of clusters are also examined by laser spectroscopy in order to obtain dynamical information on the intermediate state of bimolecular reactions [2, 3]. One of the spectroscopic techniques widely used in such studies is photodissociation spectroscopy of mass-selected cluster ions. Clusters containing a magnesium monocation, Mg^+, have been studied extensively, because allowed transitions lie in UV region due to the atomic $^2P \leftarrow ^2S$ transition. There are several reports on the observation that the fragment ions are produced via CT in the photodissociation of Mg^+-molecule clusters, such as $MgC_2H_4^+$ [4] and $MgNH_3^+$ [5]. Furthermore, in the photodissociation study of $MgCH_3X^+$ (X=F and Cl) [6], CH_3^+ ion produced by intracluster reaction and CT was observed as a major product.

In this study, excited electronic states and photoinduced dissociation processes have been investigated for Mg^+-CH_3I complex. A variety of dissociation pathways are observed including CT and chemical bond rupture.

[†] Electronic mail: misaizu@qpcrkk.chem.tohoku.ac.jp.

Photodissociation spectrum and dissociation processes are discussed from theoretical calculation based on density functional theory.

2. Experimental Setup and Calculation

Details of the experimental setup have been described elsewhere [7]. The apparatus consists of three-stage differentially evacuated chambers. Clusters containing Mg^+ and CH_3I were generated by a combination of laser vaporization and supersonic expansion. A magnesium rod was irradiated with a visible laser to produce Mg^+, and binary cluster ions were produced after collision between Mg^+ and CH_3I clusters formed by pulsed expansion. Product ions were then accelerated by pulsed electric fields in a time-of-flight mass spectrometer (TOF-MS). Selected Mg^+-CH_3I complex ion by a pulsed mass gate in the drift region was photolyzed by another pulsed laser, which was irradiated perpendicularly with the cluster-ion beam direction in front of the reflection region of the reflectron TOF-MS. Remaining parent and fragment ions were then mass-analyzed in the reflector and in the second field free region of the reflectron, and were detected by microchannel plates. A pulsed Nd:YAG-pumped dye laser was used as a photolysis laser with wavelengths of 380-415 nm. Second harmonic of the dye laser was also used for the shorter wavelength region of 225-380 nm. The photolysis laser fluence was kept under 7 mJ/cm^2 in order to prevent saturation or nonresonant multiphoton processes.

Geometrical structures of $MgCH_3I^+$ complex was optimized by a density functional theory (DFT) program of the Gaussian 98 package with the 6-31+G* basis set for Mg, C, and H, and 6-311G* basis set for I. The B3LYP functional was utilized in the present calculations. We used configuration interaction singles (CIS) approach [8] for calculation of excitation energies.

3. Results and Discussion

3.1. *Photodissociation Spectrum*

Fig. 1(a) shows a typical photofragment ion mass spectrum from $MgCH_3I^+$ at a photolysis wavelength of 266 nm. Five ions, CH_3^+, Mg^+, I^+, CH_3I^+, and MgI^+ are found as photofragment (daughter) ions. Although CH_3^+ and Mg^+ are overlapped in this mass spectrum, we observed these ions separately under a different ion-focusing condition. All of these ions are confirmed to be produced by one photon absorption from the dissociation laser power dependence. Fig. 1(b) shows a photodissociation spectrum of $MgCH_3I^+$ obtained by monitoring total fragment ion intensities vs. photolysis energy. There are three peaks at about

27200 (band I), 29600 (band II), and 38100 cm^{-1} (band III), while the band I and II may be energetically overlapped each other. Sharp peaks come from fluctuations of experimental conditions, although each point is determined by the average of repeated measurements. Band III is found to have fairly broad bandwidth of about 4000 cm^{-1} (FWHM), in contrast to the bands I and II. Fraction of each fragment ion is also shown for band I-III in Fig. 1(e). Fragment ions of Mg^+ and MgI^+ are predominantly observed in all bands. In addition, intensity of CH_3I^+ is rather high in band II, and the I^+ ion is only produced in band III. Small amount of CH_3^+ ion is also observed only at band III, which is not shown in the spectrum because of small abundance.

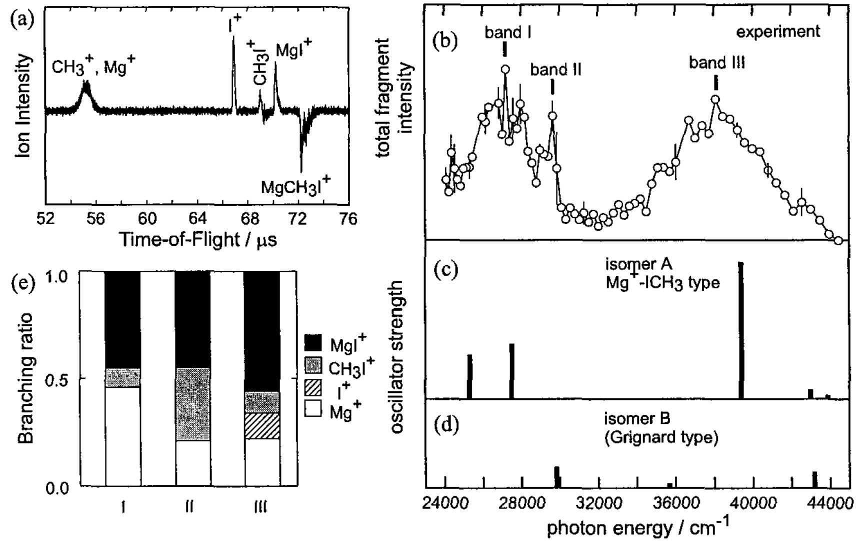

Figure 1. (a) Mass spectrum of photofragment ions from Mg^+-CH_3I by photolysis laser on-minus-off at 266 nm. (b)-(d) Photodissociation spectrum of Mg^+-CH_3I obtained by (b) experiment, (c) calculation for isomer A, and (d) calculation for isomer B. (e) Branching fractions of fragment ions observed for band I-III.

3.2. *Geometrical Structure and Electronic States of Mg^+-CH_3I*

Fig. 2 shows optimized structures and natural charges of Mg^+-CH_3I obtained by DFT calculation. One isomer (A) has a bent geometry in which Mg lies next to the I atom of CH_3I. We also found another isomer (B) having a structure of a reaction product in which Mg is inserted in C-I bond, which is about 0.17 eV less stable than the most stable isomer. Although the isomer B is regarded as an ion from a Grignard reagent, CH_3MgI, we concluded that the isomer A is predominant in the present experiment, from the comparison of the obtained dissociation spectrum with the CIS calculation result as shown below. For this isomer A, natural population analysis indicates that the positive charge is almost localized on Mg in the ground state.

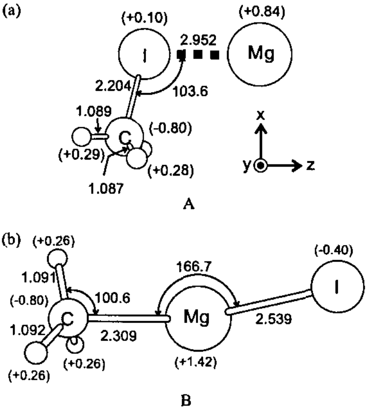

Figure 2. Optimized structures and natural charges (in parenthesis) of (a) isomer A and (b) isomer B.

The CIS approach was performed to predict vertical transition energies of Mg$^+$-CH$_3$I from the ground state structures. Calculated vertical transition energies are shown in Fig. 1(c) and 1(d). Because predicted absorption bands of isomer A well reproduce the experimental spectrum, this isomer is expected to be predominant in the cluster ion beam. In the calculated absorption spectrum of isomer A, low-lying three excited electronic states are found to originate from splitting of 3p orbitals of Mg$^+$ as a result of interaction with the CH$_3$I molecule. Transition energies for these excited states are 25300 (2^2A'←1^2A'), 27500 (1^2A" ←1^2A'), and 39400 cm^{-1} (3^2A'←1^2A'). Among these, the first and second excited states originate from 3p$_x$ and 3p$_y$ orbitals of Mg$^+$, respectively, whose orientations are both perpendicular to the Mg-I bond axis. On the other hand, the third excited state is caused by 3p$_z$ orbital having parallel orientation with Mg-I axis. Energy splitting of these three excited states can be explained by repulsion between the excited electron and non-bonding electrons of the I atom. The 2^2A' and 1^2A" states have lower energies than ^{2}P←^{2}S of free Mg$^+$ because of reduced electron density in the Mg$^+$-I direction, whereas the 3^2A' state has higher energy due to repulsive interaction along the axis.

3.3. *Dissociation Processes*

A variety of processes including intracluster charge transfer (CT) and chemical reactions in the excited state of Mg^+-CH_3I produce five fragment ions, CH_3^+, Mg^+, I^+, CH_3I^+, and MgI^+. Because of the calculation result that the positive charge is almost localized on Mg atom in the ground state, Mg^+ daughter ion is produced by 'evaporation' (intermolecular bond breaking) of CH_3I molecule. On the other hand, CH_3I^+ and MgI^+ ions are produced by intracluster CT and an intracluster chemical reaction (chemical bond breaking), respectively. Furthermore, CH_3^+ and I^+ ions are expected to be produced by intracluster reaction after CT in the excited states. Observed dissociation processes are summarized as follows:

$MgCH_3I^+$	$\rightarrow$	CH_3^+	+	MgI	(CT + reaction)	3.55 eV	(1)
	$\rightarrow$	Mg^+	+	CH_3I	(evaporation)	1.01 eV	(2)
	$\rightarrow$	I^+	+	$MgCH_3$	(CT + reaction)	5.51 eV	(3)
	$\rightarrow$	CH_3I^+	+	Mg	(CT)	3.01 eV	(4)
	$\rightarrow$	MgI^+	+	CH_3	(reaction)	1.27 eV	(5)

Although neutral fragments are not identified in the present experiments, neutrals shown above are expected to be formed from an energetic point of view. Calculated appearance energies of each daughter ions are also listed in above equations. From these values, observed daughter ions except for I^+ can be produced with one photon absorption in the present spectral region. Although calculated I^+ appearance energy is higher than photon energy used in this study, we confirmed that I^+ is produced by one photon absorption from measurement of laser power dependence at a wavelength of 266 nm which corresponds to the excitation to the third excited state (band III). One explanation for this discrepancy is that the parent Mg^+-CH_3I ions may have sufficient internal energy, because of the lacking of collisional cooling processes in the present pickup source. It should also be pointed out that iodine atom has strong spin-orbit interaction which is not treated in our calculation. Thus the discrepancy of experimental and calculated appearance energy for I^+ may be caused both by the ion internal energy and by the uncertainty in the present calculation.

Potential energy curves of the ground and excited states were also calculated along the Mg-I bond distance by CIS approach as shown in Fig. 3. The curves of initially photoexcited states, i.e., three excited states originating from Mg^+ 3p orbitals, are found to be all bound with respect to this coordinate. The first two excited states, 2^2A' and 1^2A", show attractive interactions, whereas the third 3^2A' state has a potential well of only 0.39 eV. Observed band width of 4000 cm^{-1} at band III in the dissociation spectrum [Fig. 1(b)] is partly due to the excitation to repulsive part of the third 3^2A' state, because Mg-I equilibrium nuclear distance of the state is longer than that of the ground state. From the bound nature of potential energy curves for the three excited states along the Mg-I bond axis, Mg^+ is expected to be formed after internal conversion from the excited states to higher vibrational levels of the ground state. Furthermore, CT states having both A' and A" symmetry, corresponding to excitation from I 5p orbital to Mg^+ 3s, are found to be crossed with these three excited states at about 3.5-4 Å of Mg-I bond length. Thus the CH_3I^+ fragment ion is expected to be produced from the CT states via these potential crossings, although the observation that CH_3I^+ is produced exclusively at band II cannot be explained at present. Additional excited states corresponding to electron excitation from non-bonding I 5p to $\sigma^*_{C\text{-}I}$ are found to be crossed with the 3^2A' state. These excited states may be repulsive along the C-I bond distance, because of the electron population to the $\sigma^*_{C\text{-}I}$ orbital. Thus the MgI^+ fragment ions produced by C-I bond rupture are expected to be produced from these excited states. Although these states converge more than 0.4 eV higher in energy than 3^2A' state along the Mg-I bond axis in Fig. 4, it is expected that the energy should be much lower along the C-I bond axis. Potential crossings of initially excited states with either of the two kinds of excited states mentioned above are also expected to contribute to the formation of CH_3^+ and I^+, because these ions are produced by both intracluster CT and by chemical bond breaking. For further discussion on these fragmentation processes, it is necessary to calculate potential curves along the C-I coodinate, although we found it rather difficult to obtain quantitative results under the present calculation level.

Acknowledgments

This work is supported by a Grant-in-Aid for Scientific Research from the Japanese Ministry of Education, Culture, Sports, Science and Technology. Calculations were partly done by using Fujitsu VPP5000 computer of the Research Center for Computational Science, Okazaki National Research Institutes. H. T. is supported by the Research Fellowship of the Japan Society for the Promotion of Science for Young Scientists.

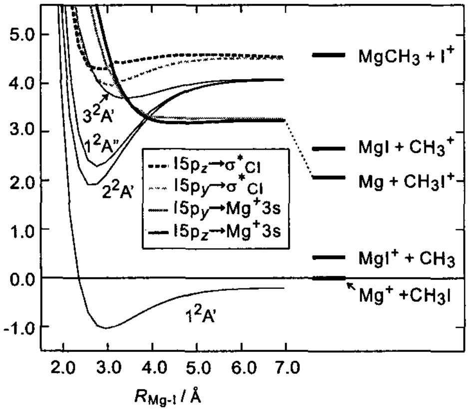

Figure 3. Calculated potential energy curves of Mg^+-CH_3I along Mg-I bond length.

References

1. C. Dedonder-Lardeux, G. Grégoire, C. Jouvet, S. Martrenchard, and D. Solgadi, Chem. Rev. 100, 4023 (2000).
2. C. E. H. Dessent, M. A. Johnson, I. Becker, and O. Cheshnovsky, Adv. Chem. Phys. 106, 265 (1999) .
3. X. Y. Chang, R. Ehlich, A. J. Hudson, J.C. Polanyi, and J. -X. Wang, J. Chem. Phys. 106, 3988 (1997).
4. J. Chen, T. H. Wong, Y. C. Cheng, K. Montgomery, and P. D. Kleiber, J. Chem. Phys. 108, 2285 (1998).
5. S. Yoshida, K. Daigoku, N. Okai, A. Takahata, A. Sabu, K. Hashimoto, and K. Fuke, J. Chem. Phys. 117, 8657 (2002).
6. X. Yang, Y. Hu, and S. Yang, J. Phys. Chem. A 104, 8496 (2000).
7. K. Ohshimo, F. Misaizu, K. Ohno, J. Chem. Phys. 117, 5209 (2002).
8. J. B. Foresman, M. Head-Gordon, J. A. Pople, and M. J. Frisch, J. Phys. Chem. 96, 135 (1992).

FABRICATION OF TWO-DIMENSIONAL AND THREE-DIMENSIONAL PLATINUM NANOCLUSTERS TO SERVE AS HIGH TECHNOLOGY CATALYSTS - CATALYTS CAPABLE OF 100% REACTION SELECTIVITY

G. A. SOMORJAI[a,b,*], R. M. RIOUX[a,b] and J. GRUNES[a,b]
[a]*Department of Chemistry, University of California, Berkeley and* [b]*Lawrence Berkeley National Laboratory, Materials Science Division, Berkeley, CA 94720*

Abstract

Electron beam lithography and photolithography, followed by size reduction lithography, are carried out to produce two-dimensional nanostructures in the 1–100 nanometer range. The development of size reduction lithography in Berkeley permits parallel formation of 10^{11} nanowires to provide 1 cm^2 surface area nanocluster catalyst that can be used in model studies of catalytic activity and selectivity for comparison with single crystal surfaces. Electron beam lithography, a series preparation technique can only produce 10^9 nanoparticles or 1 mm^2 metal surface area after one day. In most cases, active surface areas of 1 cm^2 or more are required for reaction selectivity studies. We shall review the fabrication, cleaning, and characterization of these two-dimensional nanostructure catalysts and their performance in hydrogenation and dehydrogenation reactions, using ethylene and cyclohexene. The metal–oxide interface may be important for several of the catalytic processes that were studied.

Three–dimensional nanoclusters with 10^{15} nanoparticles are prepared by stabilization of the nanoclusters on an inorganic mesoporous support. The large metal content coupled with the high surface-to-volume ratio of nanoclusters leads to 1 m^2 of metal surface area. Monodispersed platinum nanoparticles are prepared by alcohol reduction methods and then encapsulated in mesoporous silica, which is prepared by a hydrothermal reaction in the same aqueous solution. The encapsulated particles are reduced to the metallic state, making them active for catalysis. A second synthetic method produces well dispersed nanoclusters on mesoporous silica using a two-step method and low power sonication to facilitate nanocluster diffusion into the silica channels.

Two–dimensional and three dimensional nanoclusters which possess controlled spacing and monodispersed metallic nanoclusters, respectively, provide the opportunity to develop green catalysts that demonstrate *100%* reaction selectivity.

* corresponding author: somorjai@socrates.berkeley.edu

1. Catalysis in the 21st Century: 100% Selectivity for All Catalyst-Based Processes

As the 21st century begins the challenge of catalytic scientists, both academic and industrial is to develop a catalyst, whether synthetic or biological that is capable of 100% selectivity for the desired product.[1] At the end of the 20th century, our understanding of the molecular details of a catalyst that control activity was well developed. Understanding the catalyst features, which are instrinsically molecular in nature that control selectivity is a more difficult endeavor. Selectivity is a kinetic consequence which is determined by the difference in the activation energy barriers of competing reactions.[2] The relative heights of these barriers may be altered by changing properties of the catalyst, which in turn can influence selectivity if one barrier is altered more than the other. Most catalysts used in industrial processes are composed of a high surface area solid support material upon which small metallic or metal oxide particles are dispersed. These materials are complex, and a molecular level understanding of their parameters that control activity and selectivity has not been fully developed. An example of reaction selectivity and the effect of catalyst design on product distribution is the reforming of C_{6+} alkanes to reformate (high octane gasoline).[3] A reaction scheme for the reforming of *n*-hexane is shown in Figure 1. The goal of the chemistry is to produce aromatics, isomers and naphthenes by aromatization, isomerization and cyclization reactions, respectively, while avoiding C-C bond breaking (hydrogenolysis) products. Initial reforming catalysts suffered severely from catalyst deactivation thus requiring large hydrogen pressures and poor reaction selectivity. Modification of the reforming catalyst led to major improvements in reaction selectivity and catalyst lifetime, enabling reforming to become a viable industrial process. The introduction of an acidic function to the catalyst support increased isomer and cyclization product yields, while a bimetallic catalyst (Pt/Re, Pt/Ir, Pt/Sn) formulation increased catalyst lifetime by decreasing carbon deposition.

In some cases, a catalyst parameter such as surface structure can solely dictate the observed product selectivity. The role of surface structure of Ziegler-Natta catalysts has been examined for its effect on selectivity during the polymerization of propylene.[4] The selectivity of this reaction is stereospecific producing either actactic polypropylene (*a*PP), where the methyl groups are randomly arranged on both sides of the chain or isotactic polypropylene (*i*PP), where all methyl group are located on one side of the chain. With its superior mechanical properties and commercial applications, *i*PP is the preferred stereospecificity. Using model Ziegler-Natta catalysts, it was shown that the $TiCl_y$ basal plane was primarily responsible for the formation of *a*PP, while the non-basal plane was 100% selective to the desired *i*PP.[4]

2. Molecular Ingredients of Catalytic Activity and Selectivity

A number of features of the catalyst which influence activity and reaction selectivity have been discovered and the mechanisms by which they exert control have been investigated. These include 1) metal surface structure (*i.e.* metal particle size); 2) bonding modifier additives; 3) mobility of metal atoms in order to restructure and adsorbate mobility; 4) selective site blocking; 5) bifunctional catalysis; and 6) metal-oxide interfaces.

The influence of surface structure on catalyst activity is well known from studies on single crystals and supported small metal crystallites (1-5 nm).[5] H_2-D_2 exchange, a probe for H_2 dissociation occurs with unit probability on a Pt(775) surface containing atomic steps, while on a flat close-packed Pt(111) surface the dissociation of hydrogen is three orders of magnitude slower.[6] One of the most remarkable examples of the influence of surface structure on specific activity is the synthesis of ammonia on Fe single crystals. In Figure 2, it is shown that close-packed Fe surfaces have a higher turnover frequency than the more open surfaces.[7] Schematic representation of the Fe surface structures (Figure 2) demonstrates that the most active Fe surfaces ((111) and (211)) contain surface Fe atoms with seven nearest neighbors (C_7 sites). It is proposed that these sites are able to dissociate dinitrogen to molecular nitrogen with near zero activation energy. Boudart and co-workers reached the same conclusion studying ammonia synthesis on supported iron catalysts with Fe particle sizes of 1.5-30 nm.[8]

The addition of a bonding modifier additive can have profound implications on catalytic activity and selectivity by perturbing the adsorbate bonding to the surface. This generally leads to an increased or decreased heat of adsorption of the adsorbate. UHV studies have shown dissociative nitrogen chemisorption is promoted by potassium addition to iron. The addition of potassium to a Fe single crystal increases the rate of ammonia production by decreasing the activation energy for ammonia desorption. Figure 3 demonstrates that the inhibitory effect of ammonia during ammonia synthesis is decreased in the presence of potassium, most likely due to donor-donor interaction between NH_3 and K, which decreases the heat of adsorption of ammonia.[9]

Surface science studies of bare and adsorbate covered metal surfaces demonstrate that the metal atoms and adsorbates are in constant motion. Surface atoms with their intrinsic low coordination restructure to accommodate a lower surface energy configuration or to optimize bonding with an adsorbate.[10] The heat released upon adsorption, an exothermic process provides the energy required for metal-metal bond weakening, a requirement for atomic reconstruction. Adsorbates are diffusing rapidly about the surface during turnover, suggesting that their mobility is vital for catalysis. High pressure scanning tunneling microscopy (HP-STM) studies of CO poisoning of ethylene hydrogenation have shown that the ethylidyne and hydrogen covered surface is disordered, while the addition of CO orders the adsorbates and stops the reaction from turning over (Figure 4). This indicates that the role of a catalyst poison may extend beyond a simple site blocking explanation but may also inhibit adsorbate mobility.[11]

Selective site-blocking is one of the most efficient ways to influence activity and selectivity by eliminating the catalyst component that contributes to undesirable chemistry. For example, steps and kinks have a high activity for C-C bond breaking during the dehydrogenation of cyclohexane to benzene over Pt.[12] A self-induced site blocking can occur in the initial stages of the reaction when the most active metal sites are poisoned by the formation of an inactive carboneacous layer.[13] The transient nature and efficiency of this self-poisoning mechanism is highly dependent upon the catalytic chemistry. Most often, sites performing undesirable chemistry are intentionally poisoned by an adsorbate that forms a strong bond with a metal atom(s). Poisoning with sulfur is the most commonly utilized method. Sulfur is a selective poison, because it will adsorb to the metal surface atoms of highest energy (i.e. coordinatively unsaturated atoms).[14] Addition of small concentrations of gold to platinum eliminates the 3 or 4 high coordination platinum surface sites by substitution (ensemble effect).[15] Therefore the catalytic chemistry associated with these sites is eliminated thereby changing reaction selectivity.

Another method of site-blocking is obtained via shape control of either the active site or the geometry surrounding the active site. Control of the active site geometry is a primary mechanism for selectivity control in enzyme catalysis, while control of the geometry around the catalytic active site is the basis of shape selective zeolite catalysis. Reaction selectivity is imparted by restricting the entry channel to the internal zeolite structure to molecular diameters that are smaller than the diameter of some potential reactants.[16] Likewise, product molecules form in a selective manner which allows only the small size products to escape from the internal zeolite structure.

Catalysts are often composed of a support and an active species, which is usually metal nanoclusters. The support itself may also be active and promote chemical transformation in sequence or parallel with the chemistry occurring on the metallic surface.[17] A schematic representation of bifunctional catalysis is shown in Figure 5. The metal surface is primarily responsible for hydrogenation, dehydrogenation or breaking of strong chemical bonds, while the oxide promotes organic rearrangement reactions, such as isomerization, dehydrocylization and alkylation. The Pt/Al_2O_3 catalyst used in reforming is an example of a bifunctional catalyst. The acidic alumina is primarily responsible for the isomerization chemistry, while the dehydrogenation of the saturated cyclic products to aromatics occurs on the metal function.

The choice of catalyst support can have dramatic effects on the observed catalytic chemistry. It is well known that the support can influence metallic dispersion but also effect catalytic activity and selectivity beyond particle size effects. The boundary or metal-oxide interface can have significant impact on catalytic activity and selectivity. A most notable example is the metal–TiO_2 interface where it is suggested that reduced TiO_x species are responsible for enhanced activity and selectivity. Chemistry involving polar carbonyl bonds in aldehydes and ketones are extremely sensitive to this metal-oxide interface.[18] Metal-support interactions (MSI) have been observed over various metal/metal-oxide catalysts. Bartholomew and co-workers[19] have shown that the type of support has a dramatic effect on the activity and selectivity to C_{2+} hydrocarbons during the hydrogenation of CO over Ni catalysts. Figure 6 demonstrates that the Ni/TiO_2 catalysts are more active and selective to C_{2+} hydrocarbons than either Al_2O_3 or SiO_2 supported catalysts. It must be stressed that the influence of metal particle size on catalytic activity and selectivity must be known when accessing the role of the metal-oxide interface in the catalytic chemistry. If particle size effects are not accounted for, the observed difference in activity and/or selectivity may be due to structure sensitivity effects rather the metal-oxide interface.

3. Fabrication of High Technology Catalysts: 2-Dimensional and 3-Dimensional Catalysts Toward 100% Selectivity

Catalysts prepared by classical methods (i.e. incipient wetness, ion-exchange) lack the control necessary to develop a catalyst capable of 100% selectivity. In general, these methods produce catalysts with broad particle size distributions (1-20 nm), have minimal control of the particle location within the support architecture and most importantly, prevent the ability to rationally tune these parameters in order to understand their role in catalytic chemistry. Very broad particle distributions generally lead to a small fraction of the particles to dominate the chemistry because of their optimal atomic arrangement. Reaction selectivity requires catalyst design, where the influence of a number of parameters can be rationally tuned and studied systematically. To this end, we are fabricating 2-dimensional and three-dimensional nanocluster catalysts, whose properties can be altered systematically.

3.1 Fabrication and Characterization of 2-D Catalysts

The details of electron beam lithography (EBL) have been described previously.[20,21] The procedure is outlined in Figure 7 and is explained briefly. A highly collimated electron beam is used to expose sections of a 15 nm thick Al_2O_3 or SiO_2 covered Si(100) wafer upon which a thin layer of polymethylmethacrylate (PMMA) has been spin-coated. After electron irradiation, the PMMA which has been damaged by the beam is removed in developing solution. After which a 15 nm Pt film is deposited on the surface by electron beam evaporation. The remaining PMMA is removed by sonication in acetone. Figure 8 is an example of Pt/SiO_2 nanoparticle array. Electron diffraction of the Pt nanoparticle arrays reveal the polycrystalline nature of the Pt particles, but after heating in either vacuum, hydrogen or oxygen atmosphere, the Pt particles were single crystalline.[21] The inherent disadvantage of this "top-down" approach to catalyst development is the fabrication time and cost. EBL allows the user to prepare 10^9 nanoparticles in ~1 day, which amounts to a total metal surface are of ~1 mm^2. The study of low turnover reactions ($\leq 10^{-2}$ s^{-1}) requires approximately 1 cm^2 metal surface area or 10^{11} nanoparticles. Using EBL, this would require 100 working days, a project too time-consuming and costly.

Before the nanoparticle arrays could be used fro catalytic reactions, the surface had to be cleaned. The cleaning procedure has been detailed elsewhere.[21] By utilizing the strong oxidate NO_2, the major contaminant, carbon, is removed from the catalyst surface. The surface carbon is oxidized under mild conditions of 10^{-6} Torr NO_2 and 573K. Adsorbed oxygen on the surface is removed by titration with 10L CO, after which the catalyst is flashed to 573K to remove CO_2. Auger spectroscopy has shown that this procedure safely and reproducibly clean the nanoparticle array model catalysts as well as the Pt(111) single crystal. Catalytic reactions with high turnover frequencies can be studied on the 1 mm^2 nanoparticle arrays. Ethylene hydrogenation with a high turnover frequency at room temperature has been studied on the nanoparticle arrays and compared with results from a single crystal Pt surface. Both surfaces catalyze the hydrogenation of ethylene with an activation energy of ~10 kcal mol^{-1} and with similar rates at room temperature (~10 s^{-1}).[21,23] Significant differences are observed on the two model catalyst systems when ethylene hydrogenation is poisoned by CO.[24] Upon addition of 1 Torr CO to the gas phase, the apparent activation energy for ethylene hydrogenation increased by 10 kcal mol^{-1} on the Pt(111) single crystal, while addition of either 0.3 or 0.6 Torr CO had little effect on the apparent activation energy for the Pt nanoparticle array catalysts (see Figure 9). The primary difference in activation energy on the two model systems is attributed to the ability of metallic sites at the metal-oxide interface to remain free of CO in order for the ethylene to adsorb and react. The single crystal lacks these interfacial sites, and CO must desorb before ethylene can adsorb and react. These studies of ethylene hydrogenation and other high turnover reactions such as cyclohexene hydrogenation/dehydrogenation on Pt nanoparticles arrays[25] have demonstrated the ability of these catalysts to serve as model systems.

The limitations of EBL and the necessity of 1 cm^2 metal surface requires a high throughput, low cost technique. A new method called size reduction lithography (SRL)[26] has been developed in Berkeley which enables 7 nm features to be prepared from 600 nm photolithographically-prepared features. A schematic representation of the SRL method is shown in Figure 10. Several repetitions of this cycle enable the production of 7 nm silicon nanowires. Figure 11 shows electron microscopy images of the Si nanowire mold after three consecutive SRL cycles. Once the mold has been fabricated, the pattern is transferred into PMMA using nanoimprint lithography (NIL). The mold is pressed into PMMA under pressure and elevated temperatures, followed by plasma etching and metal deposition, which leads to the formation of transition metal nanowires or nanodots (Figure 12). Figure 13 is an example of the last steps of the SRL technique, pattern imprint into PMMA and Pt nanowire formation after metal deposition and liftoff. The nanowire catalysts are active for ethylene hydrogenation with turnover frequencies comparable to the Pt nanoparticle array catalysts.[27] The catalyst in Figure 13 possess 1 cm^2 metal surface which is sufficient for the study of low turnover reactions, such as *n*-hexane reforming and CO hydrogenation.

3.2 Fabrication and Characterization of 3-D Catalysts

High surface area supported transition metal catalysts generally possess metal surface areas of 1 $m^2\ g^{-1}$ or higher. A surface area of this magnitude amounts to $\sim 10^{15}$ surface atoms. The 2-dimensional top-down approach of lithographic methods is unable to produce metallic nanowires or particles of this number density. Metal surface areas of this size can only be obtained in three-dimensional structures. The objective of this type of catalyst structure is to design a material via a synthesis in which catalyst parameters can be rationally tuned. This has been achieved using two methods of catalyst fabrication. The first step in both fabrication methods is the synthesis of well defined metallic nanoclusters. Monodisperse Pt nanoparticles in the size range of 1.7–3.6 nm have been synthesized using modified alcohol reduction methods according to literature methods.[28,29] Larger Pt nanoparticles (~8 nm) have been synthesized using hydrogen reduction techniques.[30,31] Figure 14 is an example of TEM micrographs for 1.7-8 nm Pt nanoparticles stabilized in aqueous solution. The first method of catalyst synthesis involves the hydrothermal synthesis of SBA-15 silica in a solution containing polymer stabilized Pt nanoparticles.[32-34] This method is referred to as nanoparticle encapsulation (NE) because during growth of the 90 ´ diameter channel, Pt nanoparticles are incorporated into the channel. The second method of 3-dimensional catalyst synthesis is a two-step method where polymer stabilized Pt nanoparticles are sonicated in a water/ethanol mixture with SBA-15 silica.[35] This synthetic method is called capillary inclusion (CI) because Pt nanoparticles with diameters less than the SBA-15 silica diffuse into the channel primarily by capillary force and the mechanical effects of low power sonication. A schematic representation of both methods is shown in Figure 15. After synthesis, the catalysts are calcined and reduced to remove the stabilizing polymer and adsorbed oxygen, respectively. Figure 16 is a TEM micrograph of a 0.90% Pt(2.6 nm)/SBA-15 catalyst prepared by CI after calcination. The Pt nanoparticles are distributed throughout the entire SBA-15 matrix and do not agglomerate after calcination or reduction.

The CI-Pt/SBA-15 materials are characterized by a number of physical and chemical techniques.[36] X-ray diffraction (XRD) and low angle XRD confirm that the Pt nanoparticle size is not affected by sonication or catalyst pretreatment and the ordering of SBA-15 is not perturbed by the sonication procedure, respectively. Physical adsorption measurements confirm that the addition of Pt nanoparticles to pristine SBA-15 has little effect on the total surface area of SBA-15 suggesting that Pt nanoparticles do not block the pore entrance and diffuse into the pore interior.[35] This is confirmed visually in Figure 16.

Chemical adsorption of probe gases is used to measure the Pt dispersion or surface area. Chemisorption is a surface average probe of the accessible number of Pt atoms for catalysis, while TEM and XRD are bulk estimates of Pt particle size. A series of adsorption isotherms for a 0.95% Pt(2.9 nm)/SBA-15 catalyst is shown in Figure 17. Gas uptakes were extrapolated to zero pressure to obtain monolayer uptakes. Surface areas for ~1% Pt/SBA-15 catalysts ranged from 0.5–1 m^2 g^{-1} for supported 1.7-8 nm Pt particles. Ethylene hydrogenation was chosen as a test reaction to probe the activity of these catalysts for comparison with other model systems such as single crystals and the nanoparticle arrays discussed previously. Figure 18 is a series of Arrhenius plots for the low temperature hydrogenation of ethylene on the Pt/SBA-15 catalysts with particle size between 1.7 and 3.6 nm. The apparent activation energy is *ca.* 6.5 kcal mol^{-1}, slightly lower than that measured on single crystals[23] and nanoparticle arrays[21] (~10 kcal mol^{-1}). Specific activity of the Pt/SBA-15 materials at room temperature is comparable to activities measured on a number of supported Pt catalysts[36], and approximately an order of magnitude lower than rates measured on Pt single crystals and nanoparticle arrays.

Acknowledgments

This work is supported by the Director, Office of Energy Research, Office of Basic Energy Sciences, Materials and Chemical Sciences Divisions of the U. S. Department of Energy under Contract No. DE-AC03-76SF00098. R. M. R. would like to acknowledge the Ford Motor Company and the Berkeley Catalysis Center for financial support.

References

1. Future directions of catalysis science–workshop. *Catal. Lett.* **76**, 111-124 (2001).
2. Zaera, F., Outstanding mechanistic questions in heterogeneous catalysis. *J. Phys. Chem. B.* **106**, 4043-4052 (2002).
3. Mills, G. A., Heinemann, H., Milliken, T. H., Oblad, A. G., Catalytic Mechanism. *Ind. Eng. Chem.* 45, 134-137 (1953).
4. Kim S.H., Somorjai G. A., Correlation between catalyst surface structure and polypropylene tacticity in Ziegler-Natta polymerization system. *J. Phys. Chem B.*, **105**, 3922-3927 (2001).
5. Boudart, M., Heterogeneous Catalysis by Metals. *J. Mol. Catal.*, 30, 27-38 (1985).
6. Bernasek, S. L., Somorjai, G. A., Molecular-beam study of mechanism of catalyzed hydrogen-deuterium exchange on platinum single crystal surfaces. *J. Chem. Phys.*, **62**, 349-4161 (1975).
7. Spencer, N. D., Schoonmaker, R. C., Somorjai, G. A., Iron single crystals as ammonia-synthesis catalysts-effect of surface structure on catalyst activity. *J. Catal.*, **74**, 129-135 (1982).
8. Dumesic, J. A., Topsoe, H., Kammouma, S., Boudart, M., Surface, Catalytic and Magnetic properties of small Iron particles. 2. Structure Sensitivity of Ammonia Synthesis. *J. Catal.*, **37**, 503-512 (1975).
9. Strongin, D. R., Somorjai, G. A., The effects of potassium on ammonia-synthesis over iron single-crystal surfaces. *J. Catal.*, **109**, 51-60 (1988).
10. Somorjai, G. A. *Introduction to Surface Chemistry and Catalysis.* John Wiley & Sons, Inc. New York 1994.
11. Hwang, K. S., Yang, M. C., Zhu, J., Grunes, J. Somorjai, G. A., The molecular mechanism of the poisoning of platinum and rhodium catalyzed ethylene hydrogenation by carbon monoxide. *J. Mol. Catal. A Chem.* **204**, 499-507 (2003).
12. Herz, R. K., Gilliespie, W. D., Petersen, E. E., Somorjai, G. A. The Structure Sensitivity of Cyclohexane Dehydrogenation and Hydrogenolysis Catalyzed by Platinum Single Crystals at Atmospheric Pressure. *J. Catal.*, **67**, 371-386 (1981).
13. Zaera, F., Somorjai, G. A., Direct Determination of Blocking of Surface Defects by Carbonaceous Deposits during Hydrocarbon Reactions on Platinum Single Crystals. *Langmuir.* **2**, 686-688 (1986).
14. Hagen, J. *Industrial Catalysis: A Practical Approach.* Wiley VCH. New York 1999.
15. Sachtler, J. W. A., Somorjai, G. A., Influence of Ensemble Size on CO Chemisorption and Catalytic *n*-Hexane Conversion by Au-Pt(111) Bimetallic Single Crystal Surfaces. *J. Catal.* **81**, 77-94 (1983).
16. Weisz, P. B., Molecular Shape Selective Catalysis. *Pure Appl. Chem.*, **52**, 2091-2103 (1980).

17. Boudart, M., Djéga-Mariadassou, G. *Kinetics of Heterogeneous Catalytic Reactions*. Princeton University Press. Princeton 1984.
18. Vannice, M. A., The influence of MSI (metal-support interactions) on activity and selectivity in the hydrogenation of aldehydes and ketones. *Top. Catal.*, **4**, 241-248 (1997).
19. Bartholomew, C. H., Pannell, R. B., Butler, J. L., Support and crystallite effects in CO hydrogenation on nickel. *J. Catal.* **65**, 335-347 (1980).
20. Jacobs, P. W., Ribeiro, F. H., Somorjai, G. A., Wind, S. J. New model catalysts: Uniform platinum cluster arrays produced by electron beam lithography. *Catal. Lett.* **37**, 13-136 (1996).
21. Grunes, J., Zhu, J., Anderson, E. A., Somorjai, G. A. Ethylene hydrogenation over platinum nanoparticle array model catalyst fabricated by electron beam lithography: determination of active metal surface area. *J. Phys. Chem. B.* **106**, 11463-11468 (2002).
22. Tsirlin, T., Zhu, J., Grunes, J., Somorjai, G. A. AFM and TEM studies of Pt nanoparticle arrays supported on alumina model catalysts prepared by electron beam lithography. *Catal. Lett.* **19**, 165-170 (2002).
23. Zaera, F., Somorjai, G. A. Hydrogenation of Ethylene over Platinum (111) Single-Crystal Surfaces. *J. Am. Chem. Soc.* **106**, 2288-2293 (1984).
24. Grunes, J., Zhu, J., Yang, M. C., Somorjai, G. A. CO poisoning of ethylene hydrogenation over Pt catalysts: a comparison of Pt(111) single crystal and Pt nanoparticle activities. *Catal. Lett.*, **86**, 157-161 (2003).
25. Eppler A. S., Zhu J., Anderson E. A., Somorjai G. A. Model catalysts fabricated by electron beam lithography: AFM and TPD surface studies and hydrogenation/dehydrogenation of cyclohexene plus H_2 on a Pt nanoparticle array supported by silica. *Top. Catal.* **13**, 33-41 (2000).
26. Choi, Y. K., Zhu, J., Grunes, J., Bokor, J., Somorjai, G. A. Fabrication of sub-10-nm silicon nanowire arrays by size reduction lithography. *J. Phys. Chem. B.* **107**, 3340-3343 (2003).
27. Grunes, J., Zhu, J., Contreras, A., Choi, Y. K., Bokor, J. and Somorjai, G. A. Size Reduction Lithography (SRL) and Nanoimprint Lithography (NIL) for the Fabrication of Platinum Nanocatalysts: A Reaction Study. To be published in the proceedings of the 2nd International Conference on Nanoimprint and Nanoprint Technology (NNT) Boston, MA. (2003).
28. Teranishi, T., Hosoe, M., Tanaka, T. Miyake, M. Size Control of Monodispersed Pt Nanoparticles and Their 2D Organization by Electrophoretic Deposition. *J. Phys. Chem. B.* **103**, 3818-3827 (1999).
29. Wang, Y. Ren, J., Deng, K., Gui, L., Tang, Y. Preparation of Tractable Platinum, Rhodium, and Ruthenium Nanoclusters with Small Particle Size in Organic Media. *Chem. Mater.* **12**, 1622-1627 (2000).
30. Ahmadi, T. S., Wang, Z. L., Henglein, A., El-Sayed, M. A. Cubic Colloidal Platinum Nanoparticles. *Chem. Mater.* **8**, 1161-1163 (1996).
31. Ahmadi, T. S., Wang, Z. L., Green, T. C., Henglein, A., El-Sayed, M. A. Shape-Controlled Synthesis of Colloidal Platinum Nanoparticles. *Science.* **272**, 1924-1925 (1996).

32. Konya, Z., Puntes, V. F., Kiricsi, I., Zhu, J., Alivisatos, P., Somorjai, G. A. Novel two-step synthesis of controlled size and shape platinum nanoparticles encapsulated in mesoporous silica. *Catal. Lett.* **81**, 137-140 (2002).
33. Zhu, J., Konya, Z., Puntes, V. F., Kiricsi, I., Miao, C. X., Ager, J. W. Alivisatos, A. P., Somorjai, G.A. Encapsulation of metal (Au, Ag, Pt) nanoparticles into mesoporous SBA-15 structures. *Langmuir.* **19**, 4396-4401 (2003).
34. Konya, Z., Puntes, V. F., Kiricsi, I., Zhu, J., Alivisatos, A. P., Somorjai, G. A. Nanocrystal templating of silica mesopores with tunable pore sizes. *Nano Lett.* **2**, 907-910 (2002).
35. Song, H. Rioux, R. M., Hoefelmeyer, J. D., Somorjai, G. A., Yang. P., Combined Synthesis, Characterization, and Reaction Studies of Monodispersed Platinum Nanocrystals in Mesoporous Silica. Submitted to *J. Am. Chem. Soc.* (2004).
36. Rioux, R. M., Song, H., Hoefelmeyer, J. D., Yang, P., Somorjai, G. A. High Surface Area Catalyst Design; Synthesis, Characterization and Reaction Studies of Platinum Nanoparticles in Mesoporous SBA-15 Silica. Submitted to *J. Phys. Chem. B.* (2004).

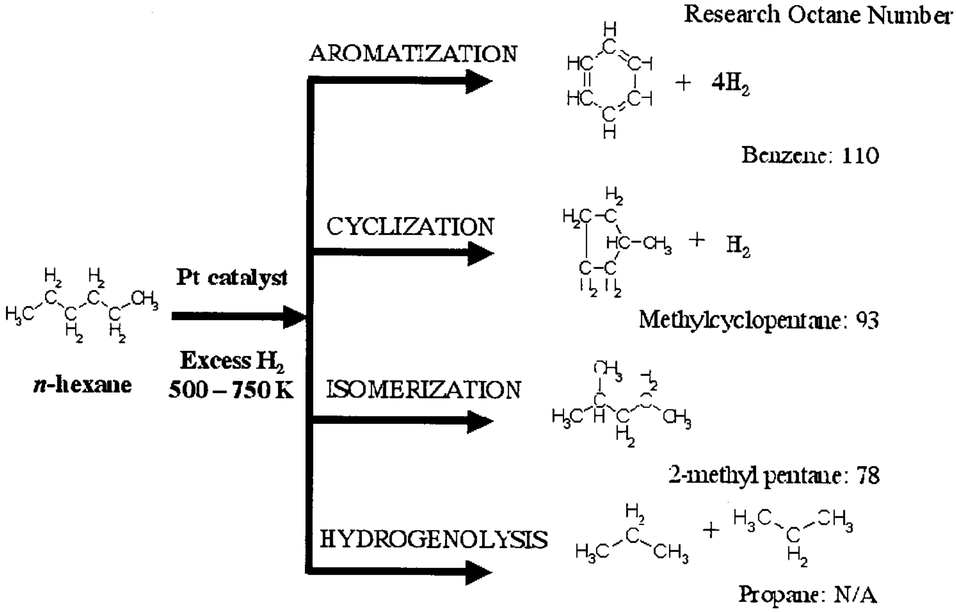

Figure 1. Reaction scheme for *n*-hexane reforming.

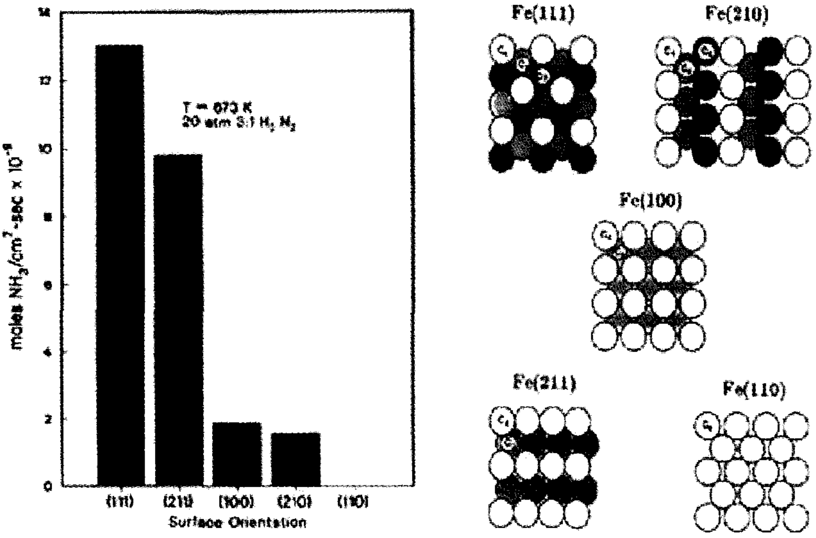

Figure 2. Specific activity over Fe single-crystal surfaces with different orientations and their respective surface structures.

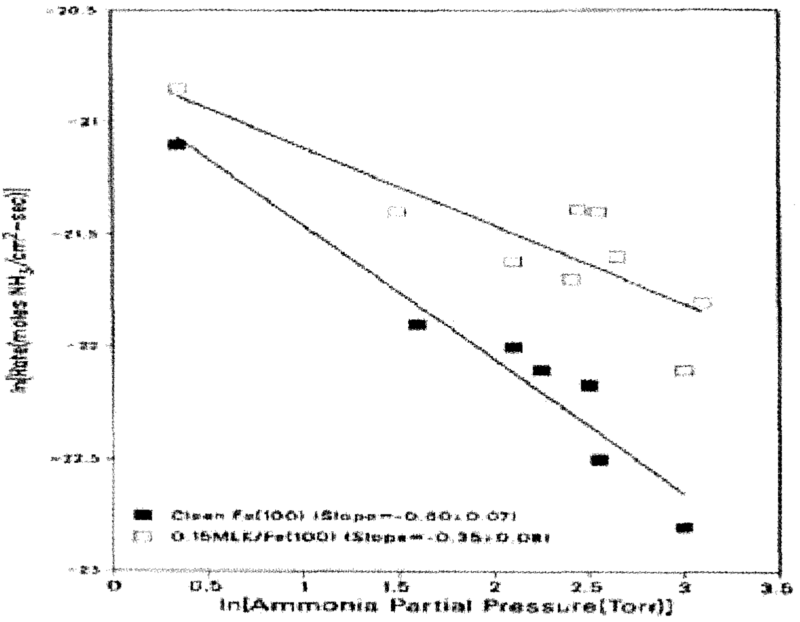

Figure 3. Apparent reaction order in ammonia during ammonia synthesis on a clean Fe(100) single crystal and K modified Fe(100) single crystal.

20 mTorr H_2

20 mTorr H_2
+
20 mTorr C_2H_4

$(100\ \text{Å})^2$ images

20 mTorr H_2
+
20 mTorr C_2H_4
+
5.6 mTorr CO

Figure 4. STM image of adsorbate induced ordering during CO poisoning of ethylene hydrogenation on Rh(111) surface.

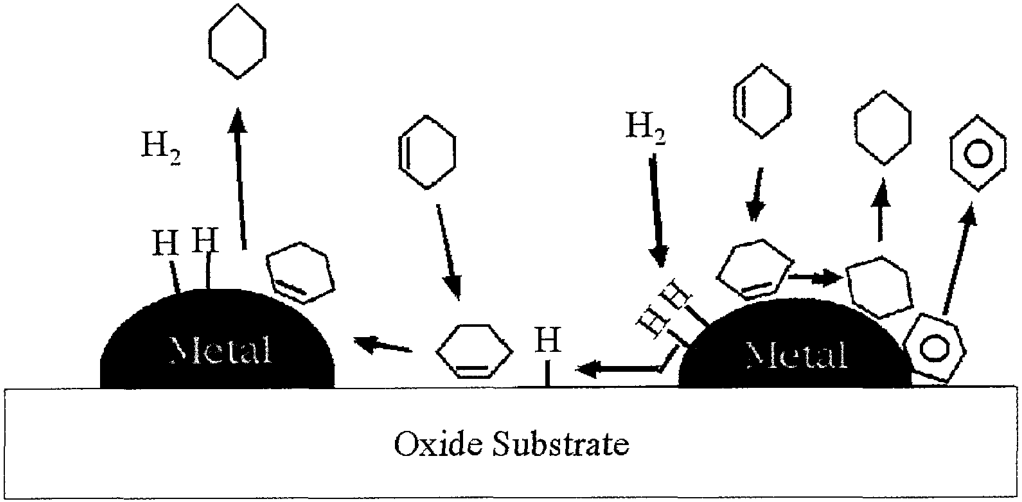

Figure 5. Schematic representation of bifunctional catalysis demonstrating the dual nature of the catalyst.

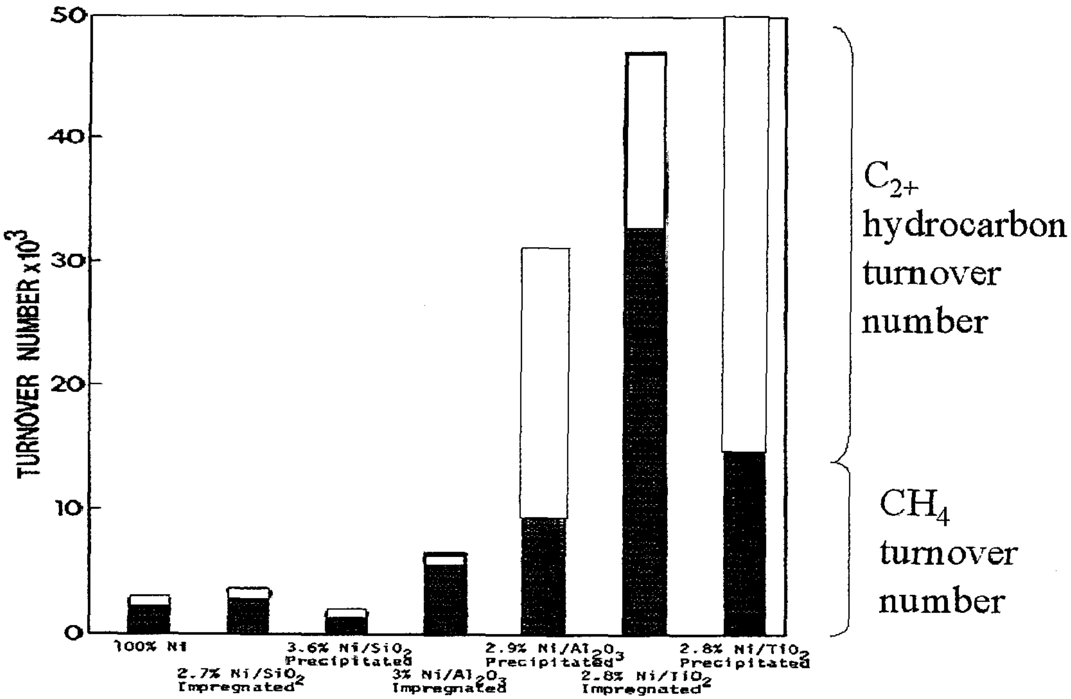

Bartholomew, C.H., Pannell, R.B., and Butler, J.L., *J. Catal.*, 65, 335 (1980)

Figure 6. Effect of support on the turnover frequency and selectivity to methane and C_{2+} hydrocarbons during CO hydrogenation over Ni supported catalysts. Reprinted from [19].

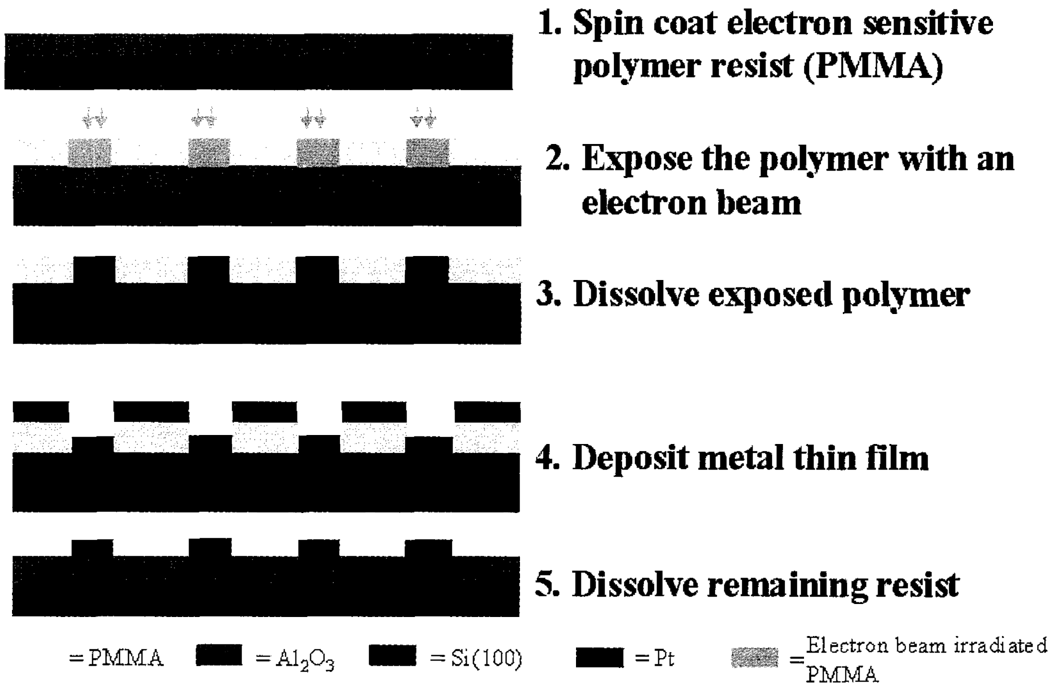

Figure 7. Schematic representation of the electron beam lithography (EBL) process used to fabricate 2-dimensional Pt nanoparticle array catalysts.

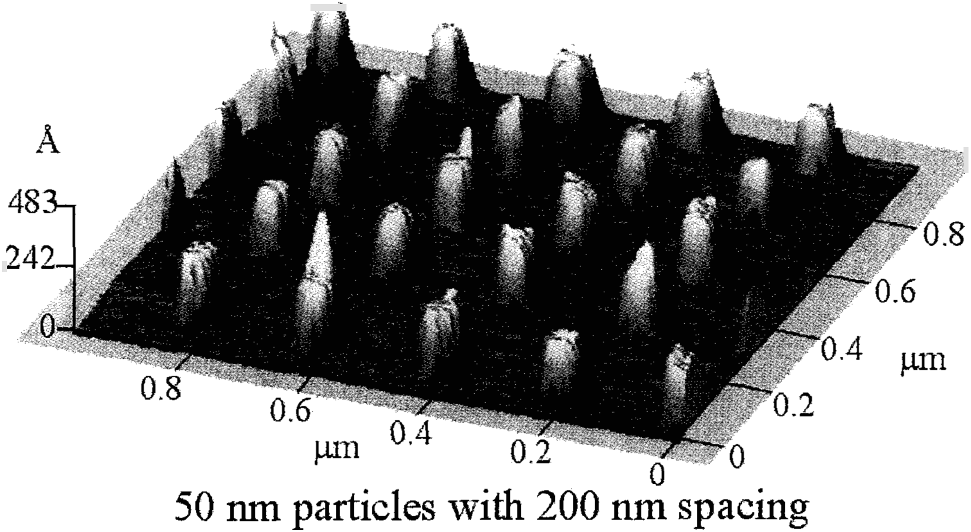

Figure 8. Atomic force microscopy (AFM) image of EBL fabricated 50 nm Pt particles with 200 nm spacing on SiO_2.

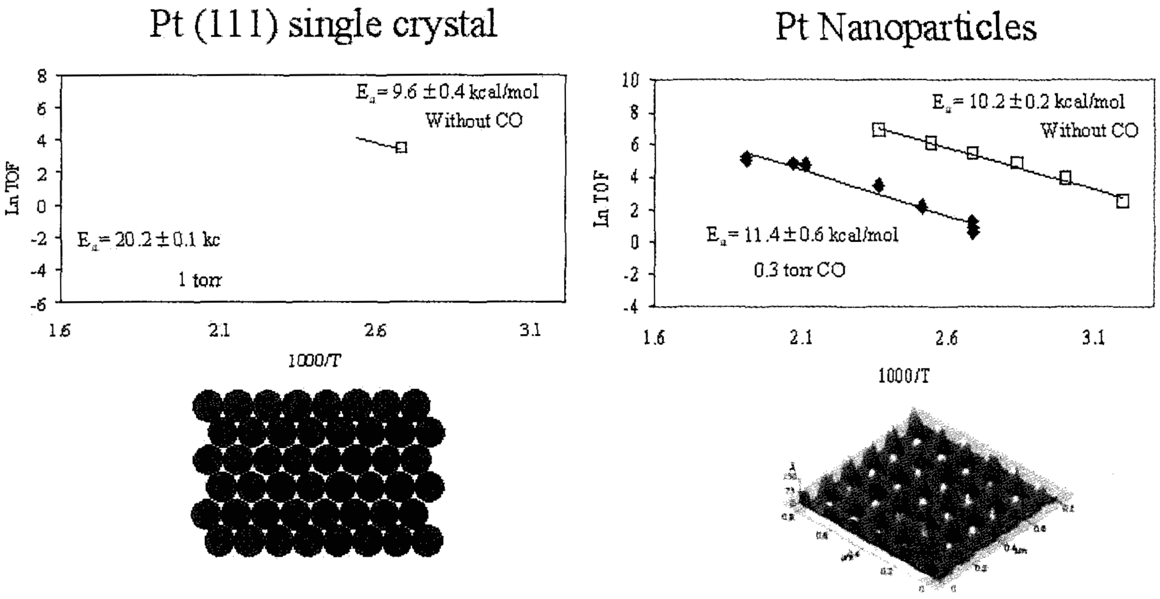

Figure 9. Arrhenius plot for ethylene hydrogenation in the presen e and absence of CO on (A) Pt(111) single crystal and (B) Pt nanoparticle array catalyst

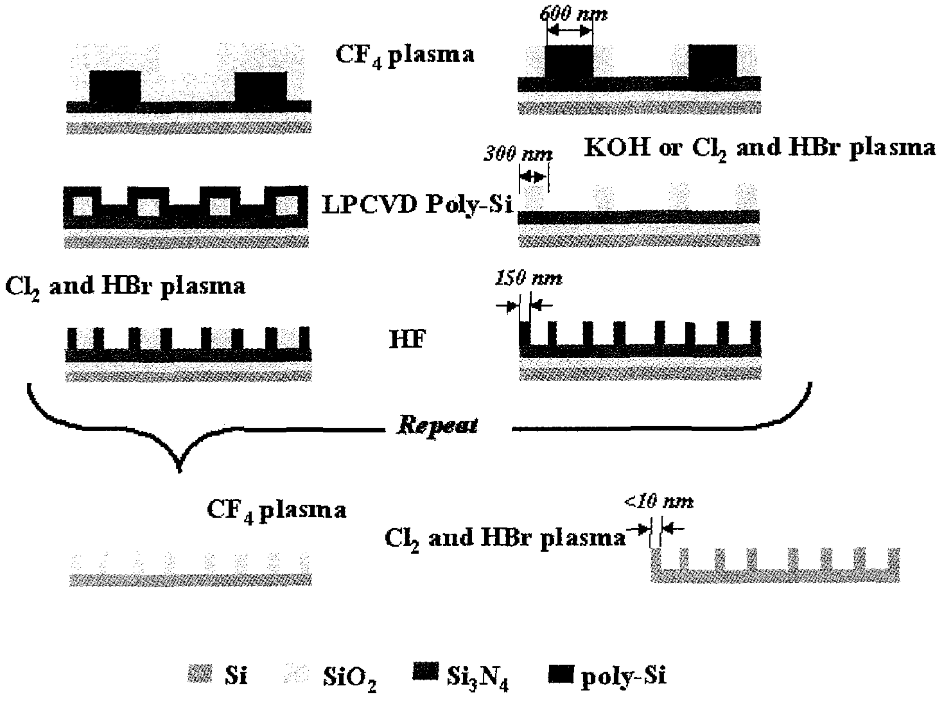

Figure 10. Overall scheme for multiple size reduction lithography (SRL).

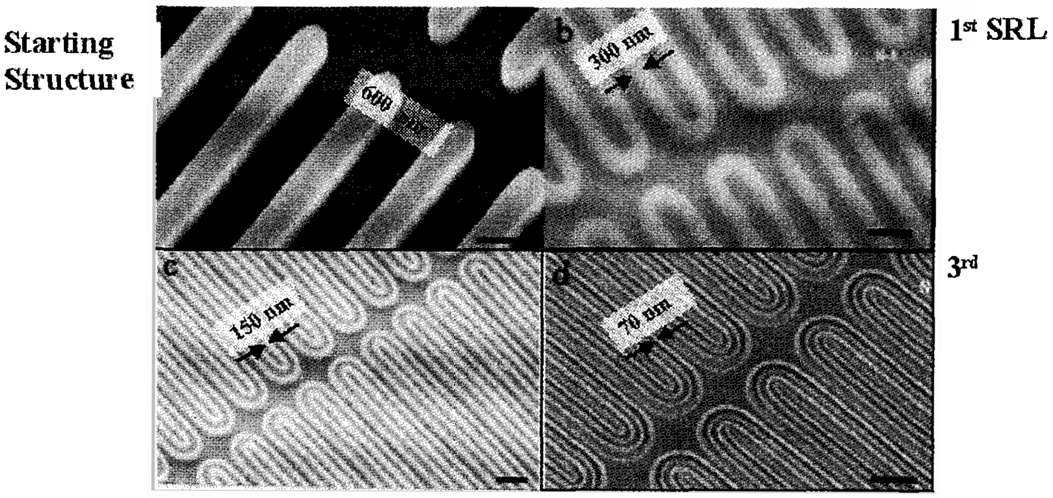

Figure 11. Field emission scanning electron microscopy (FESEM) images of pattern density multiplication by SRL. (a) after patterning sacrificial poly-Si layer, (b) after SiO_2 deposition, SiO_2 spacer etch by CF_4 plasma, and removal of sacrificial poly-Si by KOH, (c) after poly-Si deposition, poly-Si spacer etch by Cl_2 and HBr, and removal of SiO_2 by HF, and (d) after SiO_2 deposition, SiO_2 spacer etch by CF_4 plasma, and removal of sacrificial poly-Si by KOH. 8 ($=2^3$) lines were generated after 3 times size reduction lithography. Line width was 70 nm and space was 80 nm in (d). The scale bars are 1 μm.

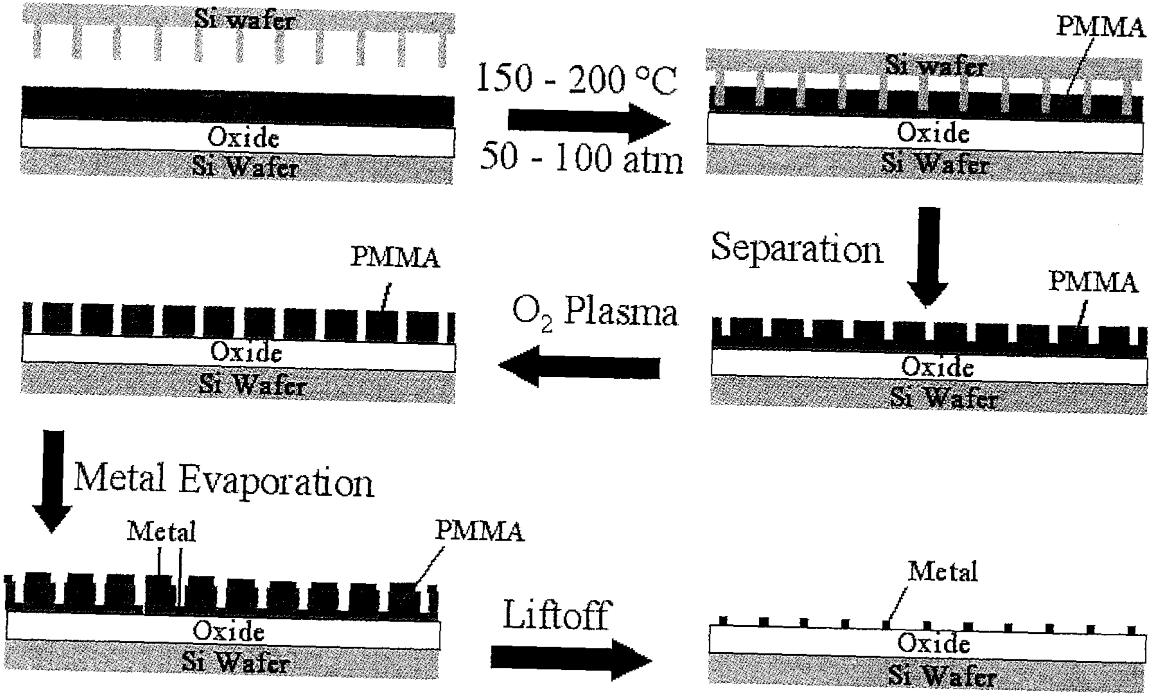

Figure 12. Preparation of Pt nanowire catalysts by nanoimprint lithography (NIL).

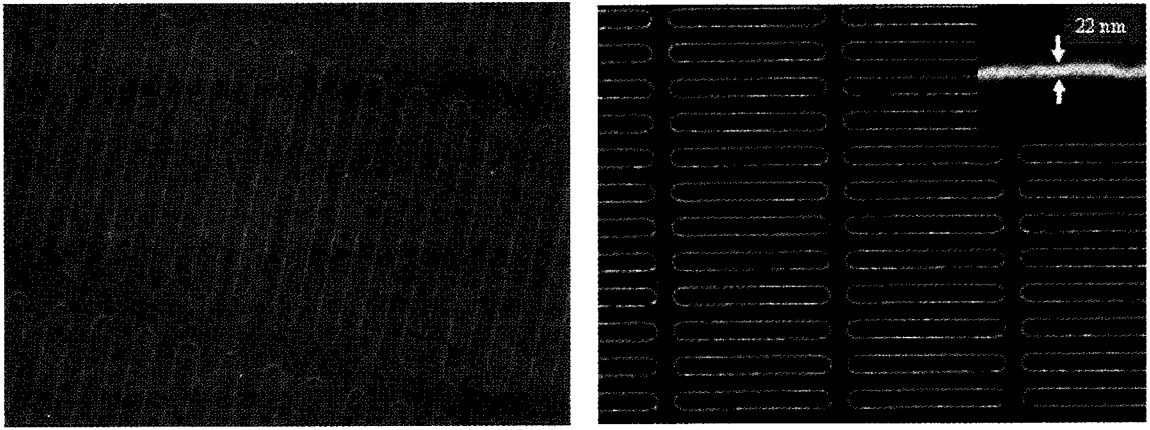

PMMA After Imprinting

22 nm Pt nanopattern after liftoff

Figure 13. Pattern transfer by NIL into (A) PMMA and (B) final nanowire catalyst after metal deposition and liftoff.

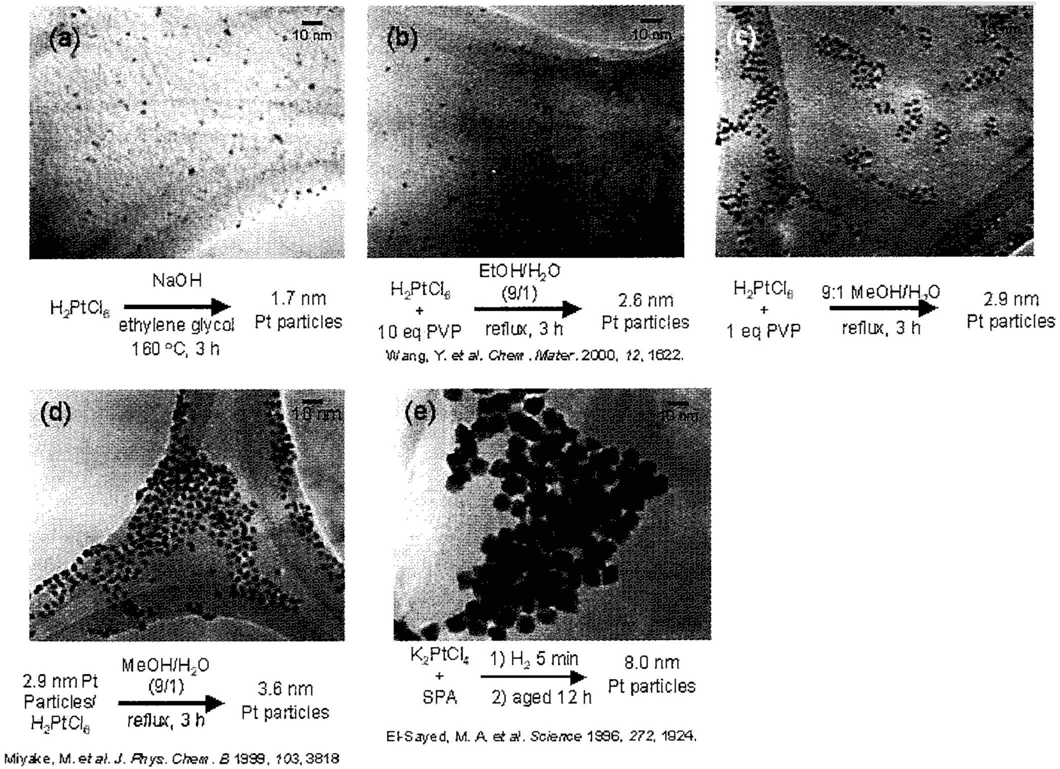

Wang, Y. *et al. Chem. Mater.* 2000, *12*, 1622.

Miyake, M. *et al. J. Phys. Chem. B* 1999, *103*, 3818

El-Sayed, M. A. *et al. Science* 1996, *272*, 1924.

Figure 14. TEM micrographs of polymer stabilized Pt nanoparticles in aqueous solution: (a) 1.7 nm; (b) 2.6 nm; (c) 2.9 nm; (d) 3.6 nm; and (e) 8 nm.

(a) Nanoparticle Encapsulation (NE):

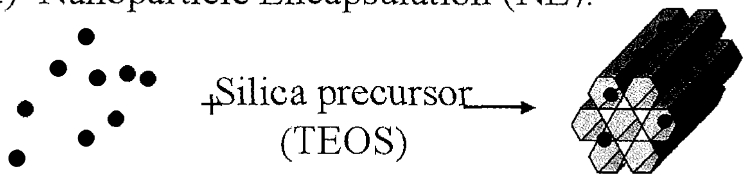

(b) Capillary Inclusion (CI):

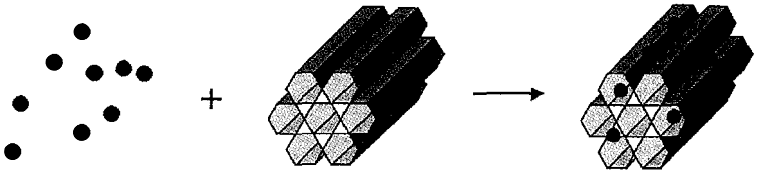

Figure 15. Synthetic methodologies for 3-dimensional high surface area metal nanocluster catalysts: (a) nanoparticle encapsulation (NE) and (b) capillary inclusion (CI).

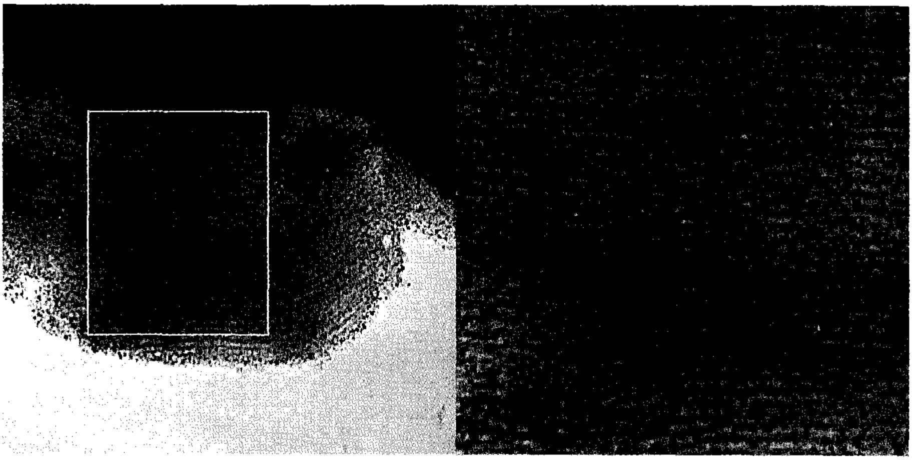

Figure 16. TEM image of a 0.90% Pt(2.6 nm)/SBA-15 catalyst synthesized by capillary inclusion (CI).

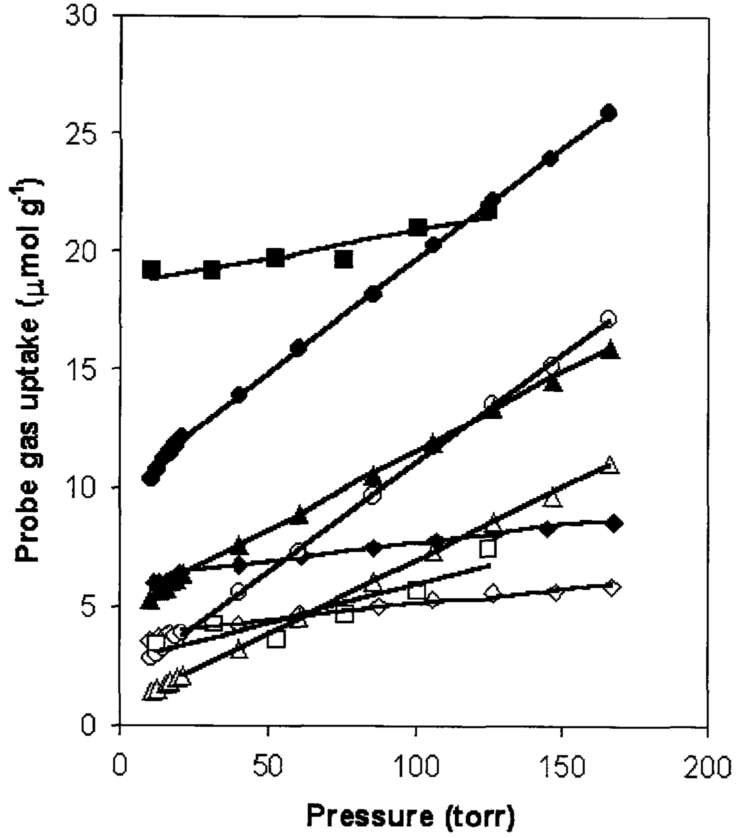

Figure 17. Adsorption isotherms for a 0.95% Pt(2.9 nm)/SBA-15 catalyst synthesized by capillary inclusion (CI). Monolayer uptakes are used to calculate metallic surface area. Solid data points; total adsorption, open data points; weak adsorption. (♦,◊) H_2; (●,○) CO; (▲,△) O_2; (■,□) H_2-O_2 titration.

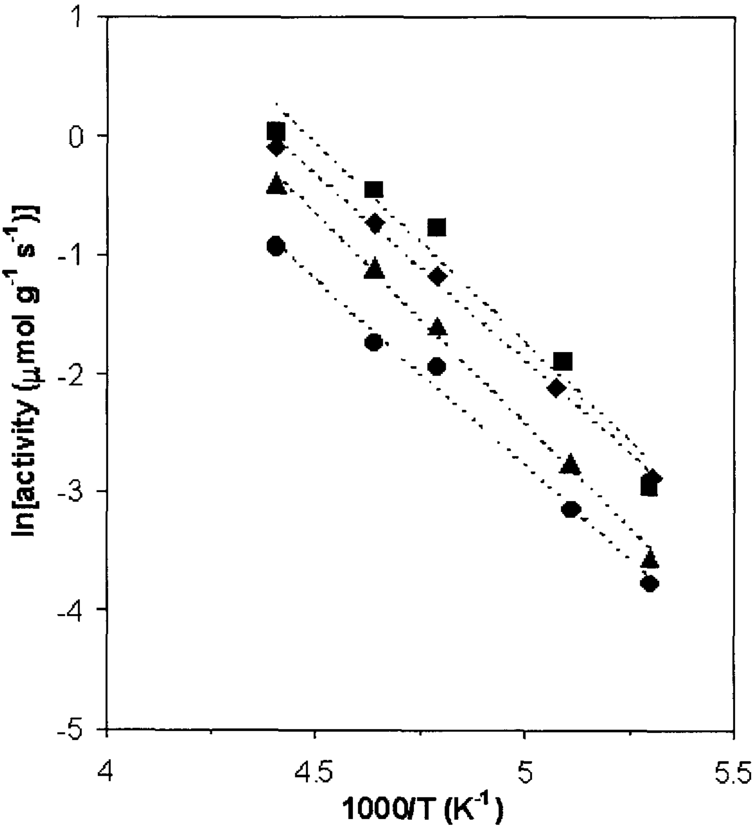

Figure 18. Arrhenius plots for low temperature ethylene hydrogenation on CI series Pt/SBA-15 catalysts. Reaction conditions were *10 Torr C_2H_4, 150 Torr H_2, and 188-228K.* All SBA-15 supported Pt catalysts had apparent activation energies of ~ 6.5 kcal mol^{-1}. (♦) 1.7 nm; (■) 2.6 nm; (●) 2.9 nm; (▲) 3.6 nm

ELUCIDATING MECHANISTIC DETAILS OF CATALYTIC REACTIONS UTILIZING GAS PHASE CLUSTERS

M. L. KIMBLE, D. R. JUSTES, N. A. MOORE, A. W. CASTLEMAN, JR.
Department of Chemistry and Physics, Pennsylvania State University, University Park, PA 16802, USA

Gas phase cluster ions have been shown to serve as useful models for the interactions occurring on catalytic surfaces. Results presented herein show that charge state, size, oxidation state, and stoichiometry have an effect on the reactions between CO and preoxidized gold cluster ions and propylene and vanadium oxide cations and niobium oxide cations.

1. Introduction

Establishing groundwork for developing catalysts that can influence the selectivity and activity of various reactions has become an area of increased interest in current catalysis research. Of particular interest in this context are nanoscale catalysts whose compositions may be customized to obtain the desired chemical properties, and cluster investigations are providing new insights into the prospects of achieving this objective. In fact, a study of cluster reactivity can be useful in catalyst development through elucidating the influence which various sizes, stoichiometries, charge states, and oxidation states have on reaction mechanisms.

Supported catalysts have received much attention in the recent past. However, the mechanisms and processes responsible for the size dependent interactions are not well understood. It has been proposed that the charge state [1] and a charge transfer from the support to the adsorbate play a crucial role in the activity [2] of supported particles. Recent studies have revealed that gas phase clusters are complementary to surface science by serving as models of the "cluster-like" assemblies of atoms on catalytic surfaces [3,4] and due to the similarity between their electronic structures [5] and those of free anionic clusters, it has been realized that a study of the reactions of free cluster anions can provide information useful in elucidating the role of degree of aggregation, charge state and stoichiometry on mechanisms involved in the catalytic oxidation of carbon monoxide by gold.

Current surface sensitive techniques often lack the ability to definitively determine the exact nature of the active site responsible for the catalytic activity, and the use of gas phase clusters to study industrially significant reactions is gaining acceptance as a valuable method for probing the active sites responsible for selected classes of reactions. Heiz, Landman, and coworkers propose that F-center defect sites are responsible for a charge transfer that promotes a reaction between molecular oxygen and carbon monoxide in the presence of gold [6]. This defect site, which contains an extra electron, may be modeled by gas phase gold cluster anions. Morever, this information may aid researchers in uncovering the mechanism governing certain catalytic processes, allowing for the development of more selective and efficient catalysts [7]. Furthermore, by viewing a metal oxide surface as a collection of clusters, as suggested by Muetterties and Witko *et al.*, the potential of gas phase clusters in elucidating catalytic reactions may be realized [8, 9].

In the context of unraveling mechanisms related to catalytic reactions, several research groups have devoted efforts to studying the reactions of gas phase clusters through experimental means [6,10-16], as well as theoretical calculations [17]. It is becoming increasingly recognized that electron density and even charge state can be significant factors to consider in unraveling the mechanisms of certain catalytic reactions, and gas phase cluster studies are especially amenable to investigating these issues. For example, in considering active sites, it has been suggested that OH^- and O^{2-} groups exist on γ-Al_2O_3 surfaces and that these sites are responsible for the nucleophilic behavior present in many catalytic oxidation processes [18]. Ionic active sites also have been proposed by Kung *et al.* [19, 20] and Kiely *et al.* [21] for the oxidation of CO on supported gold catalysts. Therefore, if charge is a characteristic of the active site, using cluster ions as models for the sites may provide insight which neutral studies are unable to produce. It has been suggested by Davis that further investigation into cationic single site systems would provide invaluable information on the catalytically active sites [22].

The study of gas phase cluster ions as active site models on catalytic surfaces has provided useful information on the possible mechanisms responsible for the interactions. Zamaraev *et al.* have shown that reactions of $Mo_xO_y^+$ clusters with methanol are similar to those occurring over molybdenum and oxygen containing surfaces in the condensed phase [3]. In addition, O'Hair *et al.* investigated molybdenum oxide anions to study the catalytic oxidation of methanol using a multi-stage mass spectrometer. They demonstrated the formation of formaldehyde as a collisionally activated process of $Mo_2O_6(OCH_3)^-$, and all the steps of their reaction cycle are those proposed as essential over industrial catalysts [23]. Furthermore, Wöste and coworkers have produced $Au_n(CO)_m(O_2)_x^-$ species through the reactions of carbon monoxide and oxygen with mass-selected gold cluster anions [24]. From these studies, they find that the appearance of the $Au_n(CO)_m(O_2)_x^-$ clusters has a temperature dependent behavior, appearing only at temperatures near 100K. Utilizing a rf-octopole ion trap, they also observed evidence for the formation of CO_2 inside the ion trap and obtained detailed kinetic and mechanistic information for the catalytic reaction [25]. Therefore, it has been demonstrated that full catalytic reaction cycles may be observed in the gas phase [23-25], thus providing further evidence for the value of gas phase cluster studies in describing catalytic reactions.

2. Experimental Methods

Reactions between carbon monoxide and gas-phase $Au_xO_y^{+/-}$ were carried out in a fast-flow reactor mass spectrometer. Described in detail previously [26-28], the preoxodized clusters are produced in a laser vaporization source by ablating a translating and rotating gold rod with the second harmonic of a Nd:YAG laser and passing a continuous flow of oxygen seeded in helium over the plasma. The clusters exit the source region through a conical nozzle and enter the flow tube where varying amounts of the CO are added at a reactant gas inlet located downstream. The clusters proceed to the end of the flow tube where most of the products and helium buffer gas are pumped away by a high volume roots pump. The surviving species are sampled through a 1 mm orifice and focused by electrostatic lenses into a quadrupole mass analyzer. The products are consequently detected utilizing a channel electron multiplier.

For the studies of propylene with $V_xO_y^+$ and $Nb_xO_y^+$, a guided ion beam apparatus coupled to a laser vaporization source was employed [29]. Briefly, the metal oxide cluster ions are generated in a laser vaporization source, similar to that discussed above, but with pulsed flow. At a predetermined time, oxygen seeded in helium (~8%) is passed over the rod using a pulsed valve. The clusters are formed through plasma reactions, cooled via supersonic expansion, and focused, via a skimmer and a set of electrostatic lenses and deflectors, into a quadrupole. The ion of interest is mass selected in the first quadrupole and guided through a second set of electrostatic lenses into the octupole, which functions as a reaction cell. The reactions conducted in the octopole are performed at near thermal energies, and the pressure of the propylene introduced into the system ranges from 0 to approximately 0.6 mTorr, effecting single as well as multiple collision conditions. The products generated in the reaction cell are focused through a third set of electrostatic lenses, mass analyzed using a second quadrupole, and detected with a channel electron multiplier.

3. Results and Discussion

3.1. *The Reactivity of Gas-Phase Gold Clusters for the Oxidation of CO*

By adding oxygen seeded in helium at the source, we form preoxidized gold clusters with oxygen in both the atomized and molecular forms. For the anions, we observe gold oxides with up to 3 oxygen atoms attaching to Au^-, while 4 and 5 oxygen atoms attach to Au_2^- and Au_3^-, respectively [28,30]. The cations have up to 5 oxygen atoms attached to both the monomer and dimer [31]. Therefore, we see that the interactions of gold clusters with oxygen are similar for both charge states. However, the oxidation reactions were found to be dramatically different.

Upon establishing the binding characteristics for oxygen to both the gold cluster anions and cations, the oxidation reactions were investigated. With oxygen added at the source and CO introduced at the reactant gas inlet, we observed the AuO^- and AuO_3^- peaks diminish in intensity. In fact, with 25 sccm (standard cubic centimeters per minute) of CO added, the AuO^- peak was found to completely disappear from the mass spectrum [28, 30] In contrast, the successive additions of CO appear to have no effect on AuO_2^-, while AuO_3^- also decreases in intensity, though not to the same extent as AuO^-.

The rates of reaction for AuO^- and AuO_3^- are also determined assuming pseudo-first order reaction kinetics and utilizing the following equation:

$$\ln\frac{I}{I_0} = -k[CO]t$$

Here, I and I_0 are the intensities of the ion with and without the CO reactant gas added, respectively, and t is the measured time the ion spends in the flow tube. From the reactions of the preoxidized gold anions with CO, we found the bimolecular reaction rate constant for AuO^- to be on the order of 10^{-11} cc/sec while that for AuO_3^- is 10^{-12} cc/sec [28].

We have also participated in a collaboration with the Bonačić-Koutecký research group at the Humboldt University in Berlin, Germany in order to elucidate the energetics and mechanisms for these reactions. Through this cooperation, we were able to predict the structures of the gold oxide anions and propose reaction mechanisms for the oxidation of CO in the presence of the atomic gold anion [28]. With the experimental results obtained in our laboratory, coupled to the theoretical calculations completed in Berlin, we propose a mechanism in which CO binds to preoxidized Au^- and allows CO_2 loss due to the facile cleavage of a Au-O or Au-C bond. The reactions of CO with $AuO_{1,3}^-$ progress via complex formation in which CO is bound to the oxygen atom. This is followed by either a complex rearrangement or by the breaking of the Au-O bond leading to a weakly bound CO_2 unit, which can easily be emitted.

We have also studied the CO oxidation reaction in the presence of the gas-phase Au_2^- and Au_3^- clusters [32]. From these investigations, Au_2O^-, $Au_2O_3^-$, $Au_2O_4^-$, Au_3O^-, and $Au_3O_4^-$ were found to promote the oxidation reaction to emanate CO_2. However, the reactions in the presence of each of these clusters were considerably slower than that for AuO^-. The bimolecular rate constants for Au_2O^-, $Au_2O_3^-$, $Au_2O_4^-$, and $Au_3O_4^-$ were found to be on the order of 10^{-13} cc/sec, while the rate constant for Au_3O^- was 10^{-12} cc/sec.

For the cations, as discussed previously, up to 5 oxygen atoms attach to Au^+ and Au_2^+, and with CO addition, all of the gold oxide cations disappear [31]. However, with the addition of CO to $Au_mO_n^+$, we observe reaction intermediates of the form $Au_nO_m(CO)_x^+$ ($n = 1\text{-}2$, $m = 0\text{-}3$, $x = 0\text{-}2$). This is similar to the results obtained by Wöste and coworkers and Wallace and Whetten for gas-phase anionic clusters [14, 33]. Wallace and Whetten propose a reaction cycle in which the formation of CO_2 depends on the appearance of peaks that correspond to $Au_nCO_mO^-$ [33]. Moreover, with the appearance of $Au_nCO_mO^-$ peaks, they also observe the recovery of $Au_n(CO)_{m-1}$ peaks. Wöste and coworkers have produced $Au_n(CO)_m(O_2)_x^-$ species through the reactions of carbon monoxide and oxygen with mass-selected gold cluster anions at temperatures near 100 K [14]. In contrast, we observe no intermediate products for the anion reactions, but we do see species of these forms for the cations. Furthermore, many of the intermediate species produced continue to react with further CO addition. These further reactions are especially interesting observations. For example, AuO_2CO^+ and AuO_3CO^+ increase in intensity with the initial addition of CO, but both also decrease in intensity with further CO addition. In fact, AuO_3CO^+ disappears completely from the mass spectrum. Similar trends are observed for the Au_2^+ intermediate species.

Reaction rate constants have not been determined for the reactions between the cations and CO due to the large number of products formed in these reactions. With the current experimental setup, it is difficult to ascertain the product/parent ion relationship. However, from these preliminary investigations, we are able to establish a difference in the reactivities due to charge state and stoichiometry.

3.2. *Reactions of Propylene with $V_xO_y^+$ and $Nb_xO_y^+$*

Gas phase ion molecule reactions were performed between propylene and vanadium and niobium oxide cluster ions using a guided ion beam mass spectrometer. The clusters were mass selected and varied by size, stoichiometry, oxidation state and composition. The results showed that these characteristics affected the reactivity of the cluster toward the preferred reaction pathway. The reaction products fell into two categories: charged hydrocarbons and molecular association to select metal oxide clusters. The hydrocarbon reaction products included $(C_3H_6)_{1\text{-}5}^+$, $(C_3H_6)_{1\text{-}4}CH_3^+$ and $(C_3H_6)_{1\text{-}3}C_2H_4^+$. There were also collision products that regularly occur with certain oxygen rich clusters. These are termed oxygen rich clusters because they lose oxygen at thermal energies under single collision conditions during collision induced dissociation experiments [29].

The effect of oxidation state and composition on the reactivity can be addressed by determining the branching ratios of MO_2^+, $M_3O_7^+$ and $M_5O_{12}^+$. Each of these clusters has the metal in the +5 oxidation state. It was found that VO_2^+ shows a strong association product channel, $V_3O_7^+$ shows a smaller but still evident association product, and $V_5O_{12}^+$ does not exhibit this pathway at all. The niobium analogues are relatively unreactive with $Nb_3O_7^+$ showing minor hydrocarbon products. This also demonstrates the effect that composition may have on the reactivity. These three vanadium oxide cluster ions were more reactive than their niobium analogues. The vanadium oxide cluster ions also show the effect of size on the reactivity. $V_5O_{12}^+$ was more unreactive than the VO_2^+ cluster. In addition, VO_2^+ and $V_3O_7^+$ exhibited molecular association as the dominant product at elevated pressure, whereas $V_5O_{12}^+$ only showed charged hydrocarbons.

The stoichiometry of the cluster may also impact the reactivity towards the reactant gas. VO^+ and VO_2^+ show different preferences for reaction pathways. VO^+ generates charged hydrocarbons whereas VO_2^+ attaches the propylene molecule. The vanadium tetramer series also demonstrates varying reactivities for each cluster, while $V_4O_9^+$ produces a significant amount of the propylene tetramer. $V_4O_{10}^+$ produces a small amount of several charged hydrocarbons. The main reaction product of $V_4O_{11}^+$ is loss of a single oxygen atom to yield $V_4O_{10}^+$.

4. Summary

Results obtained in our laboratory provide evidence for the value of gas phase cluster ions in elucidating the details of the interactions taking place on catalytic surfaces. It was found that the oxidation of CO takes place in the presence of select preoxidized gold cluster anions. Furthermore, we observed that interactions occur between $Au_nO_m^+$ and CO, with all peaks corresponding to preoxidized gold cluster cations disappearing from the mass spectrum with CO addition. For the reactions between propylene and $V_xO_y^+$ and $Nb_xO_y^+$, we observed hydrocarbon charging, molecular association of propylene to select metal oxide clusters, and collision products typical of oxygen rich clusters.

With these experiments, we have found that charge state, size, oxidations state, and stoichiometry effect the interactions taking place with gas phase cluster ions. From these results, insight into the kinetic and mechanistic aspects of catalytic systems may be gained.

Acknowledgments

We gratefully acknowledge the Department of Energy, Grant Number DE-FG02-97ER14258, for their financial support for the work on gold. For financial support for the experiments with propylene and vanadium oxide and niobium oxide, we also acknowledge the Air Force, Grant Number F49620-01-1-0122. We also acknowledge the Bonačić-Koutecký research group for the theoretical contributions.

References

1. D. M. Cox, R. Brickman, K. Creegan, and A. Kaldor, *Z. Phys. D* **19**, 353 (1991).
2. G. A. Somorjai, *Introduction to Surface Chemistry and Catalysis*; John Wiley and Sons: New York, (1994); p 369.
3. E. F. Fialko, A. V. Kikhtenko, V. B. Goncharov, and K. I. Zamaraev, *J. Phys. Chem. B* **101**, 5772 (1997).
4. G. A. Somorjai, *Introduction to Surface Chemistry and Catalysis*; John Wiley and Sons: New York, (1994); p 402.
5. D. Stolcic, M. Fischer, G. Ganteför, Y. D. Kim, Q. Sun, and P. Jena, *J. Am. Chem. Soc.* **125**, 2848 (2003).
6. A. Sanchez, S. Abbet, U. Heiz, W.-D. Schneider, H. Häkkinen, R. N. Barnett, and U. Landman, *J. Phys. Chem. A* **103**, 9573 (1999).
7. K. A. Zemski, D. R. Justes, and A. W. Castleman, Jr., *J. Phys. Chem. B*, **106**, 6136 (2002).
8. E. L. Muetterties, *Science* **196**, 839 (1997).
9. M. Witko, K. Hermann, and R. Tokarz, *J. Electron. Spectrosc. Rel. Phenom.* **69**, 89 (1994).
10. H. Koizumi, M. Larsen, P. B. Armentrout, and D. Feller, *J. Phys. Chem. A* **107**, 2829 (2003).

11. K. R. Asmis, M. Brümmer, C. Kaposta, G. Santambrogio, G. von Helden, G. Meijer, K. Rademann, and L. Wöste, *Phys. Chem. Chem. Phys.* **4**, 1101 (2002).
12. A. Fielicke, and K. Rademann, *Phys. Chem. Chem. Phys,* **4**, 2621 (2002).
13. A. Bérces, P. A. Hackett, L. Lian, S. A. Mitchell, and D. M. Rayner, *J. Chem. Phys.* **108**, 5476 (1998).
14. W. T. Wallace, and R. L. Whetten, *J. Am. Chem. Soc.* **124**, 7499 (2002).
15. H. Häkkinen, and U. Landman, *J. Am. Chem. Soc.* **123**, 9704 (2001).
16. M. Andersson, and A. Rosén, *J. Chem. Phys.* **117**, 7051 (2002).
17. B. Gzrzybowska-Świerkosz, *Appl.Catal. A: General* **157**, 409 (1997).
18. A. Bielański, and J. Haber, *Oxygen in Catalysis,* Marcel Dekker, Inc., New York (1991).
19. C. K. Costello, M. C. Kung, H.-S Oh, Y. Yang, and H.-H. Kung, *Appl. Catal. A* **232**, 159 (2002).
20. H.-S. Oh, C. K. Costello, C. Cheung, H.-H. Kung, and M. C. Kung, *Stud. Surf. Sci. Catal.* **139**, 375 (2001).
21. N. A. Hodge, C. J. Kiely, R. Whyman, M. R. H. Siddiqui, G. J. Hutchings, Q. A. Pankhurst, R. E. Wagner, R. R. Rajaram, and S. E. Golunski, *Catal. Today* **72**, 133 (2002).
22. R. J. Davis, *Science* **301**, 926 (2003).
23. T. Waters, R. A. J. O'Hair, and A. G. Wedd, *J. Am. Chem. Soc.* **125**, 3384 (2003).
24. J. Hagen, L. D. Socaciu, M. Elijazyfer, U. Heiz, T. M. Bernhardt, and L Wöste, *Phys.Chem. Chem. Phys,* **4**, 1707 (2002).
25. L. D. Socaciu, J. Hagen, T. M. Bernhardt, L. Wöste, U. Heiz, H. Häkkinen, and U. Landman, *J. Am. Chem. Soc.* **125**, 10437 (2003).
26. A. W. Castleman, Jr., K. G. Weil, R. E. Sigsworth, R. E. Leuchtner, and R. G. Keesee, *J. Chem. Phys.* **86**, 3829 (1987).
27. R. E. Leuchtner, A. C. Harms, and A. W. Castleman, Jr., *J. Chem. Phys.* **92**, 6527 (1990).
28. M. L. Kimble, A. W. Castleman, Jr., C. Bürgel, R. Mitrić, and V. Bonačić-Koutecký, *J. Am. Chem. Soc.* (submitted).
29. R. C. Bell, K. A. Zemski, D. R. Justes, and A. W. Castleman, Jr., *J. Chem. Phys.* **114**, 798 (2001).
30. M. L. Kimble, and A. W. Castleman, Jr., *Proceedings of Gold 2003: New Industrial Applications for Gold*, Vancouver (2003).
31. M. L. Kimble, and A. W. Castleman, Jr., *Int. J. Mass Spectrom.* (submitted).
32. M. L. Kimble, A.W. Castleman, Jr., R. Mitrić, C. Bürgel, and V. Bonačić-Koutecký, (in preparation).
33. J. Hagen, L. D. Socaciu, M. Elijazyfer, U. Heiz, T. M. Bernhardt, L. Wöste, *Phys. Chem. Chem. Phys.* **4**, 1707 (2002).

COMPUTATIONAL STUDY OF METAL ADSORPTION ON TiO_2 (110) SURFACE

RAJ GANESH S. PALA[1,2], THANH N. TRUONG[2] and FENG LIU[1]
[1]*Department of Material Science and Engineering,*
[2] *Department of Chemistry,*
University of Utah, Salt Lake City, UT 84112

Adsorption of K, Ni, Pd, Pt, Ir and Au on the TiO_2 (110) surface at 0.5ML coverage is studied by pseudopotential, plane-wave method in the density functional formalism within the generalized gradient approximation (GGA). Four high-symmetry binding sites have been compared for each metal adatom to determine the most stable binding site on the TiO_2 surface. For all the metal atoms considered except Au, the bridging oxygen position is favored, and Au has slightly greater affinity for surface Ti atoms. With increase of coverage to 1ML, the most stable binding site differs from that obtained at 0.5ML coverage. The effect of using local density approximation (LDA) was considered at 1ML coverage and the trends obtained with GGA and LDA differs qualitatively in some cases. The use of spin-polarization for 1ML adsorption does not qualitatively change the trends in metal adsorption.

1. Introduction

Metal clusters and films supported on TiO_2 are attracting wide attention due to their novel catalytic behavior [1, 2]. Prior to theoretically modeling clusters and metal films that do not have a clear epitaxial relationship with the oxide support, it is useful to investigate a structurally simpler but relevant system comprised of metal atom adsorbed on the surface. Also, before undertaking an extensive theoretical study on these systems, it is important to establish the dependence of adsorption properties on the theoretical approximations commonly used in first-principle calculations of condensed matter systems. We have performed total energy calculations to determine the energetics of half monolayer (ML) adsorption of K, Ni, Pd, Pt, Ir and Au on the TiO_2 (110) surface using density functional theory (DFT) within the generalized gradient approximation (GGA). The coverage dependence, the effect of local density approximation (LDA) and spin-polarization on adsorption is also analyzed.

2. Computational Methodology and Description of the Physical Model

Conjugate gradient energy minimizations were performed using a plane-wave basis set and ultra-soft pseudopotentials [3] within the DFT [4] using PW-91 GGA functional[5]. A cut-off of 400eV, and sixteen and thirty-two irreducible K-points mesh[6] were used for 0.5ML and 1ML adsorption studies respectively. The TiO_2 (110) surface was represented by a five-layer slab approximation[7]. Four different high-symmetry adsorption sites were considered to identify the most stable binding site (Fig.1) and the terminologies used to describe the high-symmetry sites are given in Table 1. Studies were performed at 0.5ML and 1ML coverage. There is no unambiguous way of defining coverage for systems like metal adatoms on oxide surface because the metal adatoms do not have a clear epitaxial relationship with the underlying oxide substrate. The definition adopted in the present study is the following: 1ML coverage has one metal adatom for every two fold coordinated bridging oxygen of the surface (Fig.2). For 0.5ML coverage, the conventional unit cell shown in Fig.2 is doubled along the [001] surface and in this adsorption geometry, the ratio of metal adatoms to the number of bridging oxygen atoms is 0.5. The energy of adsorption is defined in *the following manner:* $E_{ad} = ½(E_m - E_s - 2xE_a)$*, where* E_{ad} *is the adsorption* energy of the metal adatom, E_m is the energy of the metal-adsorbed TiO_2 slab, E_s is the energy of the metal adatom free TiO_2 slab, and E_a is the energy of free metal atom. The factor ½ comes about because of the addition of one metal adatom on either side of the slab in the calculation.

3. Results and Discussions

A. *Adsorption energetics at 0.5ML coverage using GGA functional*

The feasibility of extending a useful correlation observed in an embedded-cluster study[8] was tested. The previous study revealed that the metal atom having a lower (higher) ionization potential (IP) had higher (lower) E_{ad} on TiO_2[8]. The IP and E_{ad} of metal adatoms on the TiO_2 surface in each of the four high-symmetry binding sites are given in Table 2. The correlation between IP and E_{ad} does not seem to extend to the set of metal adatoms considered here. The possible reason behind this might be that the previous embedded cluster study models adsorption of an *isolated* adatom interacting with the surface, whereas the present periodic study models an *array* of atoms interacting with the surface. In the periodic calculations, the elastic and electronic interactions [9, 10] between the periodic cells are compounded on to the E_{ad}. We also observe that for all the metal atoms considered except Au, the bridging oxygen position is the favored binding site.

B. *Comparisons of metal adsorption energetics at 0.5 ML and 1ML coverage*

To analyze the importance of adatom-adatom interaction on adsorption, computations were performed at higher coverage of 1ML and compared with 0.5ML results. Comparing E_{ad} reported in Table 2 performed using GGA exchange correlation functional, we can see that increasing the coverage has influence on both the binding site preference and also on the quantitative value of E_{ad}. For Ni, Pd, Pt and Ir, with the increase in coverage, the O-top position becomes the most stable binding site. The increase in E_{ad} is especially drastic in the case of Au adsorption, where the E_{ad} increases from –0.35 eV at 0.5ML to –1.3 eV at 1ML. The important point is that the E_{ad} obtained at 0.5ML coverage is more indicative of the interaction between the metal adatom and TiO_2 surface and the increased 'adsorption energy' observed at 1ML coverage is due to greater co-ordination with other Au adatoms along the [001] direction of the surface.

C. *Adsorption trends obtained using GGA and LDA functional at 1ML coverage*

Comparison of energetic features of metal adsorption at 1ML coverage using LDA and GGA are consistent with the general feature of LDA to over-estimate binding energies and under estimate bond-lengths[11]. But the surprising features are the changes in binding preferences with different exchange correlation functional (Table.2). It is a general expectation that errors in calculations of exchange-correlation energy are 'systematically' cancelled out, and *trends* in binding energies computed are dependable irrespective of how exchange-correlation is computed and the present study shows these relative energies are very much dependent on whether one uses LDA or GGA.

D. *Effect of spin-polarization*

Spin-polarized calculations were performed for 1ML adsorption and both GGA and LDA give similar quantitative estimate of the stability of spin-polarized state. The spin-polarization at 0.5 ML coverage was performed at the most stable binding site and showed that for traditionally magnetic atoms like Ni and Ir have a greater spin-polarization and the increase in E_{ad} ~ 0.2 to 0.25 eV. For other adatoms the increase in stability due to spin-polarization is < 0.05 eV.

4. Conclusions

We have carried out a systematic DFT study of energetic features of adsorption of a range of metal atoms on the TiO_2 surface. The correlation between E_{ad} and IP observed in a previous study modeling isolated adatom adsorption does not extend to the set of metal adatoms considered in the present study. The possible reason for this might be the adatom-adatom interactions between the periodic arrays of atoms may become more important at moderate and high coverage. Increase of coverage from 0.5ML to 1ML affects metal adsorption in two ways, namely, in increasing the E_{ad} due to metal adatom-metal adatom interaction, and in changing the binding site preferences. The use of LDA was investigated for 1ML coverage. In all cases, the relative binding energies for the four different sites are different with GGA and LDA In some cases, there is also qualitative disagreement between the results obtained using LDA and GGA. The effect of spin-polarization is seen to be less important in determining trends in adsorption at 1ML coverage.

Table 1. Description of the four high-symmetry binding sites (also refer to Fig.1)

Terminology	Bonding geometry	As indicated in Fig.1
O-bridge	Metal atom adsorbed in between two bridging oxygens	A
O-top	Metal atom adsorbed on top of the bridging oxygen	B
Ti-bridge	Metal atom adsorbed in between the five-fold coordinated surface Ti atom	C
Ti-top	Metal atom adsorbed on top of the five- fold coordinated surface Ti atom	D

Table 2. Energetics of metal adsorption *(eV)

	K	Ni	Pd	Pt	Ir	Au
I.P.	4.34	7.63	8.33	8.96	9	9.22
0.5ML (GGA)						
O-bridge	**-2.23**	**-2.63**	**-1.4**	**-1.71**	**-2.30**	-0.13
O-top	-1.8	-1.55	-1	-1.3	-1.16	-0.36
Ti-bridge	-1.88	0.21	-0.21	0.03	0.61	-0.04
Ti-top	-1.86	0.18	-0.24	-0.91	-0.44	**-0.39**
0.5ML(SP-GGA)[†]	**-2.26**	**-2.83**	**-1.45**	**-1.74**	**-2.56**	**-0.44**
1ML (GGA)						
O-bridge	**-1.29**	-1.11	-1.48	-1.75	-1.94	-1.27
O-top	-0.94	**-2.28**	**-1.59**	**-2.65**	**-3.25**	-1.33
Ti-bridge	-0.87	-1.06	-0.88	-1.85	-2.02	-1.35
Ti-top	-0.81	-1.05	-0.88	-1.87	-2.00	**-1.37**
1ML (SP-GGA)						
O-bridge	**-1.25**	-1.4	-1.52	-1.86	-2.33	-1.31
O-top	-0.96	**-2.42**	**-1.62**	**-2.69**	**-3.31**	-1.37
Ti-bridge	-0.85	-1.36	-0.92	-1.94	-2.38	-1.38
Ti-top	-0.79	-1.3	-0.91	-1.96	-2.37	**-1.39**
1ML (LDA)						
O-bridge	**-1.86**	**-3.8**	**-2.53**	**-3.53**	-4.005	-1.99
O-top	-1.35	-3.17	-2.49	-3.49	-4.4	-2.17
Ti-bridge	-1.34	-2.99	-2.48	-3.48	**-4.43**	-2.22
Ti-top	-1.3	-1.83	-2.075	-3.075	-3.22	**-2.29**
1ML (SP-LDA)						
O-bridge	**-1.87**	**-3.85**	**-2.54**	-3.26	-4.13	-1.96
O-top	-1.36	-3.27	-2.52	**-3.71**	-4.42	-2.16
Ti-bridge	-1.35	-3.03	-2.44	-3.61	-4.43	-2.22
Ti-top	-1.31	-1.94	-2.04	-3.09	-3.3	**-2.28**

* Bold letters indicates values at the most stable site and I.P. refers to ionization potential

[†] E_{ad} calculated only at the most stable binding site using GGA functional with spin-polarization

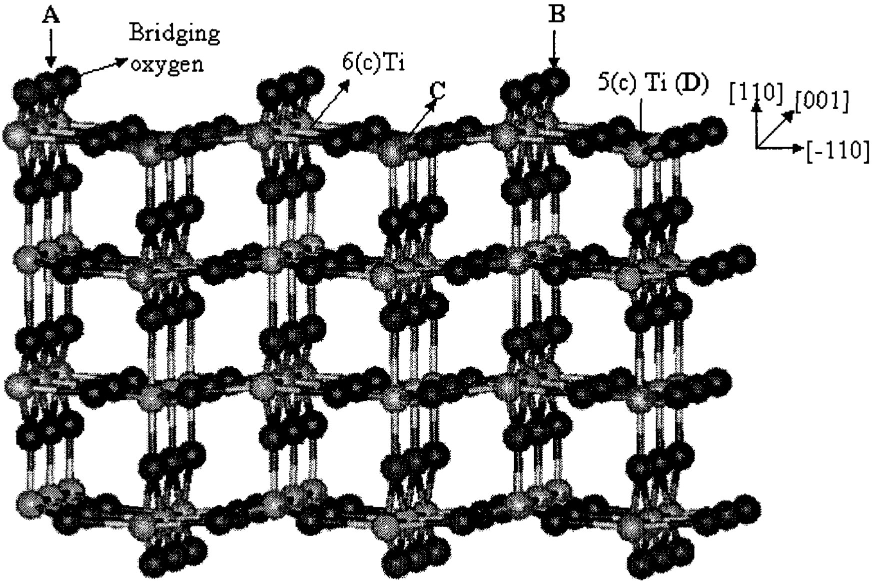

Figure 1: A perspective view of the TiO_2 (110) surface. Darker balls are the O atoms and grey balls are the Ti atoms. Five- and six-fold coordinated Ti are indicated as 5 (c) and 6(c) Ti respectively. The four high-symmetry positions that were considered for metal adsorption studies are indicated as A, B, C and D (also refer to Table 1)

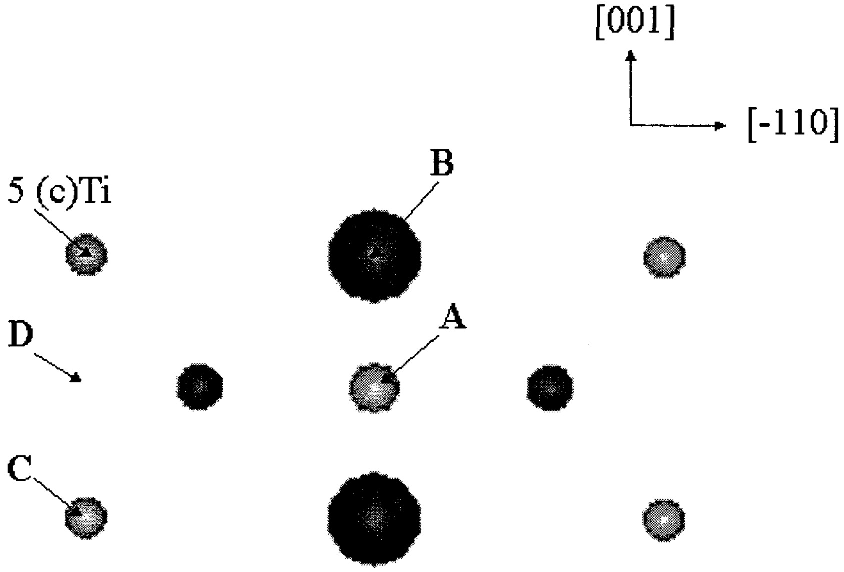

Figure 2: Top-view of a conventional 1x1 unit cell for 1ML coverage. The notations are same as in Fig. 1 and are explained in Table 1.

References

1. M. Haruta, Catalysis Today **36**, 153 (1997).
2. M. Valden, X. Lai, and D. W. Goodman, Science **281**, 1647 (1998).
3. D. Vanderbilt, Phys. Rev B **41**, 7892 (1990).
4. M. C. Payne, M. P. Teter, D. C. Allan, et al., Rev. Mod. Phys. **64**, 1045 (1992).
5. J. P. Perdew, J. A. Chevary, S. H. Vosko, et al., Phys. Rev. B **46**, 6671 (1992).
6. H. J. Monkhorst and J. D. Pack, Phys. Rev B **13**, 5188 (1976).
7. S. P. Bates, G. Kresse, and M. J. Gillan, Surf. Sci. **385**, 386 (1997).
8. L. Giordano, G. Pacchioni, T. Bredow, et al., Surf. Sci. **471**, 21 (2001).
9. K. H. Lau and W. Kohn, Surf. Sci. **65**, 607 (1977).
10. W. Kohn and K. H. Lau, Solid St. Comm. **18**, 553 (1976).
11. W.Koch and M.C.Holthausen, A Chemist's Guide to DFT. (2000).

QUANTUM DOTS AND QUANTUM DOT LATTICES: CORRELATIONS IN SMALL QUANTAL SYSTEMS*

M. BORGH, M. TOREBLAD, S. ÅBERG AND S.M. REIMANN
Deptartment of Mathematical Pysics,
Lund Institute of Technology, Lund University,
Sölvegatan 14A, Box 118, SE-221 00, Lund, Sweden

M. KOSKINEN AND M. MANNINEN
Department of Physics, University of Jyväskylä,
40351 Jyväskylä, Finland

Recently, Attaccalite *et al.* proposed a new expression for the exchange-correlation energy of the two-dimensional electron gas, based on quantum Monte Carlo calculations. We compare this functional with the established expression given by Tanatar and Ceperley for use in density functional calculations. As model systems serve a circular few-electron quantum dot and a square lattice of dots. For single dots, electronic structure calculations are performed using both energy functionals for the self-consistent solution of the Kohn-Sham equations. The results are compared with those of a numerical diagonalization of the many-body Hamiltonian.

1. Introduction

Quantum dots have been the subject of intense research in condensed matter physics in recent years[1]. A quantum dot is a nanometer scale, man-made structure, in which a number of electrons—ranging from a few to several hundreds—are trapped in a semiconductor heterostructure.

Quantum dots display several phenomena originating from the many-body physics governing the dynamics of the confined electrons. One prominent such feature of a quantum dot is shell structure[2], analogous to the shell structures seen in atoms and nuclei[3]. The shell structure of a few-electron quantum dot can be seen clearly from the so called addition energy spectrum[2]. Other many-body effects that occur in quantum dots include

---

*Work supported by the Swedish Research Council (VR), the Swedish Foundation for Strategic Research (SSF) and the Academy of Finland.

localization and spin polarization (see Ref. 1 for a review).

A topic of recent interest is the formation of so called spin density waves (SDW), where the total electron density can show circular symmetry, but the spin up and spin down densities do not[4]. Instead, the internal structure of the wave function can show antiferromagnet-like ordering of the spins. This was first predicted[4] by using the methods of spin density functional theory (SDFT) in the local spin density approximation (LSDA). There is an ongoing discussion whether the formation of SDW is an artefact[5] of SDFT, or is a consequence of strong correlations in the many-body ground state[6].

In the case of a 2D circular quantum dot with parabolic confinement containing N electrons, the many-body Hamiltonian is

$$H = \sum_{i=1}^{N} \left(\frac{\mathbf{p}_i^2}{2m^*} + \frac{1}{2} m^* \omega_0^2 \mathbf{r}_i^2 \right) + \sum_{i<j}^{N} \frac{e^2}{4\pi\epsilon\epsilon_0 |\mathbf{r}_i - \mathbf{r}_j|} . \tag{1}$$

Here, m^* denotes the effective mass of the electron in the semiconductor host material and ϵ the dielectric constant of the host. H is analytically solvable only for one or two particles. For all other cases, approximative and numerical methods must be used (see Ref. 1 and the references therein). The most straightforward method of solving the many-body problem is numerical, so-called exact diagonalization. For reasons of numerical feasibility, it is necessary to truncate the set of basis functions to be used in the diagonalization[7]. As the required matrix size increases rapidly with N, accurate calculations are restricted to small systems at not too large $r_s = a_B^*/\sqrt{\pi n}$, with a_B^* being the effective Bohr radius $a_B^* = \hbar^2 4\pi\epsilon\epsilon_0 / m^* e^2$ and n the particle density. Other methods to solve Eq. (1) are based on the mean field approach. The idea here is to rewrite the many-body problem in terms of a single-particle problem, where the interaction is approximated by a mean field potential in which the single particles move. We use the Kohn-Sham DFT method[8] in its spin-dependent form.

One of the central problems in (S)DFT calculations is to find the appropriate form of the exchange-correlation energy, E_{xc}, defined as the difference between the true energy and the Hartree solution. In general this is not known, and we have to make do with approximations. The most widely used approximation in condesed matter physics is the Local (Spin) Density Approximation (L(S)DA), wherein the assumption is made that locally, the exchange-correlation energy per particle, e_{xc}, can be approximated by that of the homogeneous 2D electron gas at the same spin densities.

2. The Tanatar-Ceperley and AMGB Functionals

In light of the above, it is evident that an accurate determination of the energy functional is of central importance to the research using (S)DFT. In the L(S)DA, this boils down to finding an accurate expression for the exhange-correlation energy of the 2D electron gas (2DEG). The standard choice of energy functional in SDFT calculations in the last ten years has been to use the expression for the exchange-correlation energy of the 2DEG given by Tanatar and Ceperley[9] in 1989. We will call this expression the Tanatar-Ceperley (TC) functional. Tanatar and Ceperley calculate the exchange-correlation energy of the 2DEG in the non-polarized and fully polarized cases ($\zeta = 0$ and $\zeta = 1$, respectively. ζ is the spin polarization $\zeta = (n_\uparrow - n_\downarrow)/n$, where $n_{(\uparrow,\downarrow)}$ are the spin densities obtained in SDFT and n is the total electron density). For intermediate values, the assumption is made that the correlation part of e_{xc} follows the same ζ-dependence as the exchange part (which is known from Hartree-Fock theory).

Since the TC functional is based on a relatively simple interpolation between no spin plarization and full spin polarization, it is reasonable to expect there to be room for improval. In 2002, Attaccalite *et al.*[10] published a new expression for the exchange-correlation energy of the 2DEG. Here, there is no assumption made regarding the polarization dependence of e_{xc}. Instead, quantum Monte Carlo calculations were also performed for intermediate spin polarizations. This results in an expression for e_{xc} which is slightly different from the one given by Tanatar and Ceperley. Attaccalite *et al.* separate e_{xc} into an exchange part and a correlation part, $e_{xc} = e_x - e_c$. They furthermore express the total density in terms of the coupling parameter r_s and write for the correlation energy:

$$e_c(r_s,\zeta) = \left(e^{-\beta r_s} - 1\right) e_x^{(6)}(r_s,\zeta) + \alpha_0(r_s) + \alpha_1(r_s)\zeta^2 + \alpha_2(r_s)\zeta^4, \quad (2)$$

where $e_x^{(6)}(r_s,\zeta)$ is the Taylor expansion of e_x beyond fourth order in ζ. The α_i are functions supplied in Ref. 10. In the following, we call Eq. (2) the "AMGB-functional" for simplicity.

3. Comparative Study

We seek to compare the TC and AMGB functionals for use in SDFT calculations on finite, 2D fermion systems. For this comparison, we choose the 2D circular quantum dot as our model system. We perform SDFT using both functionals. Whenever it is possible to do so, we also compare the SDFT results to those obtained by the exact diagonalization technique. The

AMGB functional was implemented from the original paper[a] by Attaccalite *et al.*[10]

We first note, that we obtain spin density wave (SDW)-like groundstates with both the TC and the AMGB functionals. This, first of all, shows that the SDW is not an artefact of the *interpolation* between fully- and non-polarized e_{xc} used in the TC functional. The formation of the SDW is most clearly examplified in the case of the six electron quantum dot (See Figure 1). In the results from the AMGB functional, the electron densities are circularly symmetric for both spin directions, and hence the total density has the same symmetry, for $r_s = 3a_B^*$ and below (i.e. at high densities). At $r_s = 4a_B^*$ the formation of the SDW can be seen clearly. The spin up and spin down densities both show three clear bumps and the two are rotated with respect to each other to form antiferromagnet-like order. The total density, however, still preserves the circular symmetry. At $r_s = 6a_B^*$ we see some localization in the total density. This pattern is repeated in the results obtained with the TC functional, but the SDW is formed at higher values of r_s, between $r_s = 6a_B^*$ and $8a_B^*$.

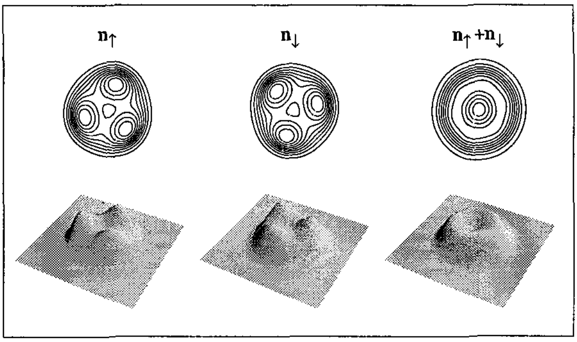

Figure 1. From left to right, the spin up, spin down and total electron density for a six-electron quantum dot at $r_s = 4a_B^*$. The spin densities form a SDW, while the total density is circularly symmetric. The AMGB functional was used for the calculations.

Exact diagonalization will always yield a solution with the same symmetry as the Hamiltonian. In our case, the "exact" N-particle state $|\Psi_N\rangle$

---

[a] In September 2003, an erratum to the paper by Attaccalite *et al.*[10] was published. We have implemented the corrected results of Ref. 10 and found no deviations from the original results for the r_s values considered here.

as well as the corresponding density $n(\mathbf{r})$ is axially symmetric as a result of the azimuthal symmetry of the confining potential. However, one means of probing the *internal* structure of the wave function is to study the pair correlation function[11], by requiring the density of the cloud to be non-zero at a specific reference point $\mathbf{r}_0$. This converts the circular symmetry of the single-particle density to a mirror symmetry with respect to the vector $\mathbf{r}_0$: $g_{\downarrow,\sigma}(\mathbf{r}_0,\mathbf{r}) = \langle\Psi_N|\hat{n}_\downarrow(\mathbf{r}_0)\hat{n}_\sigma(\mathbf{r})|\Psi_N\rangle$. Given the position of one (arbitrary) particle with a given spin, this function describes the probability of finding another. In the absence of correlations one should expect a homogeneous distribution; except at the position of the pinned electron with a given spin when we study the probability of finding an electron with like spin. This is due to the Pauli principle. For a system with internal structure, there will be maxima and minima in the pair correlation function. Indeed this is what we see in the exact diagonalization study for six electrons. Figure 2

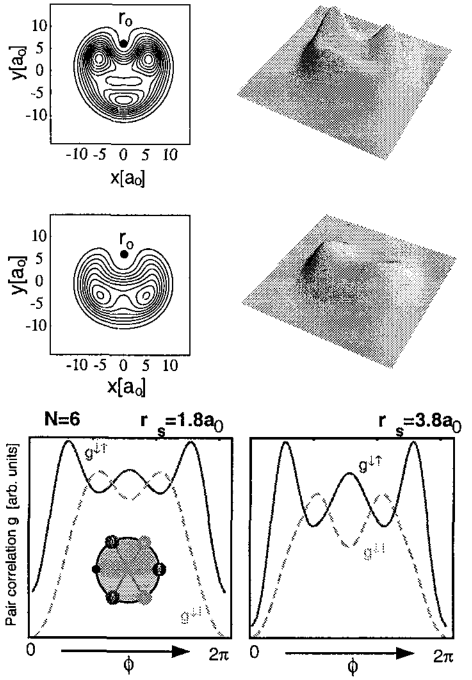

Figure 2. Pair correlations for a six-electron quantum dot. The upper panels show the $(\downarrow,\uparrow)$, the middle panels the $(\downarrow,\downarrow)$-correlations. The bottom panels compare $r_s = 1.8a_B^*$ and $r_s = 3.8a_B^*$.

shows $g(\mathbf{r},\mathbf{r}_0)$ for $N = 6$ and $r_s = 3.8a_B^*$. The upper panel shows the $(\downarrow,\uparrow)$-, and the middle panel the $(\downarrow,\downarrow)$-correlation. The antiferromagnet-like order in the internal structure of the wave function clearly resembles that of the SDW obtained in SDFT which we showed above. The bottom panel of Figure 2 compares $g_{\downarrow,\sigma}(\mathbf{r},\mathbf{r}_0)$ for $r_s = 1.8a_B^*$ and $r_s = 3.8a_B^*$, respectively. For simplicity, instead of calculating g for the whole mesh in (x, y), we determine the radius r_0 of maximum density and then calculate $g_{\downarrow,\sigma}((r_0,\phi),(r_0,0))$ as a function of the angle $\phi \in \{0, 2\pi\}$. Note that in contrast to the SDFT results, the exact diagonalization yields pronounced correlations already at rather small r_s. As r_s increases, the peaks in the pair correlation function become more pronounced.

In context of the above results, we refer to a recent paper by Wensauer and Rössler[12]. They find large deviations between the exact diagonalization e_{xc} and the SDFT e_{xc} at small r_s, typically $r_s < 1a_B^*$. The disagreement is larger for small spin polarizations. This means that, contrary to what might be expected the SDFT with LSDA may not work well at high densities, corresponding to very strongly confined systems.

The general trend in our comparison of the AMGB and TC functionals is that all features and phenomena are shifted towards lower r_s in the AMGB. In particular, in the case of the formation of the SDW, the AMGB comes closer to the results obtained by exact diagonalization.

4. Electronic Structure of Quantum Dot Lattices

Single quantum dots can be electrostatically coupled to form "artificial molecules" [13] or possibly even an extended superlattice[14]. In contrast to the real solid, where atomic bonding defines the band structure, the inter-dot coupling is tunable, and allows to design an "artificial crystal". It was suggested to use quantum dot arrays for fast processing and high-density storage of information[15]. In this context, it is essential to obtain information on the basic electronic and spin structures of dot lattices, as these form the basis for understanding their properties when placed in electronic circuits.

The interacting electrons in the dot lattice are assumed to be confined on an infinite two-dimensional (2D) plane with a *periodic* positive background charge distribution, described by the sum of Gaussians at lattice sites $\mathbf{R} = a(n_1, n_2)$, each carrying a charge N :

$$\rho_{\mathrm{B}}(\mathbf{r}) = \sum_{\mathbf{R}} \rho_{\mathrm{d}}(\mathbf{r}-\mathbf{R}) \; ; \quad \rho_{\mathrm{d}}(\mathbf{r}) = \frac{1}{\pi r_{\mathrm{s}}^2} e^{-r^2/N r_s^2} \, . \tag{3}$$

The quantity ρ_d is the background charge density of a single quantum dot and $\mathbf{R}$ is the lattice vector. The quantum dot lattice is determined solely by the number of electrons in a single quantum dot, N, the parameter r_s (here we chose $r_s = 2a_B^*$), and the lattice constant a. Again the SDFT-LSDA method was applied, using the TC e_{xc}-functional. Surprisingly, we found a rich but systematic magnetic behaviour of the dot lattices (see Fig. 4). While for small values of the lattice constant, all lattices are non-magnetic, at larger values the shell structure of the single dots determines the magnetism. At closed shells, $N = 2, 6, 12$, the lattices are non-magnetic insulators. At the beginning and the end of a shell, they become ferromagnetic and stay metallic up to large values of the lattice constant, while antiferromagnetism was observed only in the insulating phase at mid-shell ($N = 1, 4, (8), 9$). Square quantum dot lattices built of dots with half-filled electronic shells are special. They form antiferromagnetic insulators and are even more persistent against metallisation than lattices built of quantum dots with closed shells. At the beginning and the end of a shell, the quantum dot lattices mainly form ferromagnetic metals, turning into non-magnetic metals already at small values of the dot-dot overlap. In the light of the above discussion of the differences between the AMGB and TC e_{xc}-functionals, one should expect that the magnetism becomes even more pronounced when the AGMB functional is used instead[16].

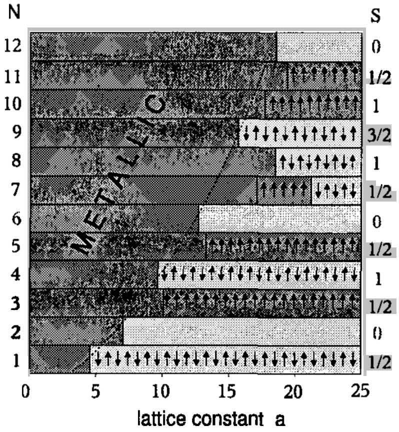

Figure 3. Magnetism (indicated by arrows) of square lattices of quantum dots with $N \leq 12$ electrons per dot, as a function of the lattice constant a (in a_b^*). The numbers on the right give the ground-state spin configuration of a single dot. The metallic phase (no band gap) is shown as dark grey and the insulating phase (band gap) as light grey. From Ref. 14.

5. Summary and Conclusions

We have made a comparison between the expression for the exchange-correlation energy of the 2D electron gas given by Attaccalite *et al.*[10] and the expression given by Tanatar and Ceperley[9], used within the SDFT-LSDA for small, parabolic quantum dots. The intensely debated phenomenon of spin density wave formation occurs with both functionals. We conclude from this that SDW formation is not an artefact of the assumption that the correlation energy follows the same polarization dependence as the exchange energy. This assumption was made when using the TC functional, but is not present in the AMGB functional. We investigate this also by studying the pair correlation function of the ground state obtained by exact diagonalization. We find that there are pair correlations down to very small r_s, corresponding to high electron densities, in contrast to the SDFT results.

The main difference between the results obtained with the AMGB functional and those obtained with the TC is that transitions such as changes in spin polarization, formation of SDW and localization happen at smaller r_s, i.e. at higher densities. These results are of importance also for the magnetism in dot lattices discussed above.

References

1. S.M. Reimann and M. Manninen, *Rev. Mod. Phys.* **74**, 1283 (2002).
2. S. Tarucha, D.G. Austing, T. Honda, R.J. van der Haage, and L. Kouwenhoven, *Phys. Rev. Lett.* **77**, 3613 (1996).
3. Å. Bohr, and B. R. Mottelson, *Nuclear Structure*, World Scientific (1975).
4. M. Koskinen, M. Manninen, and S.M. Reimann, 1997, *Phys. Rev. Lett.* **79**, 1389 (1997).
5. K. Hirose, and N. Wingreen, 1999, *Phys. Rev.* **B59**, 4604.
6. M. Koskinen, M. Manninen, S.M. Reimann, B. Mottelson, *Phys. Rev.* **B63**, 205323 (2001).
7. S.M. Reimann, M. Koskinen, and M. Manninen, *Phys. Rev.* **B62**, 8108 (2000).
8. Kohn, W., and L. J. Sham, *Phys. Rev.* **140**, A1133 (1965).
9. B. Tanatar, and D. M. Ceperley, *Phys. Rev.* **B39**, 5005 (1989)
10. C. Attaccalite, S. Moroni, P. Gori-Giorgi, and G. B. Bachelet, *Phys. Rev. Lett.* **88**, 256601 (2002) and err. *Phys. Rev. Lett.* **91**, 109902 (2003).
11. For pair correlations in strong magnetic field, see P.A. Maksym, Phys. Rev. B 53, 10 871 (1996).
12. A. Wensauer, and U. Rößler, *cond-mat/0307529*
13. W. G. van der Wiel, S. De Franceschi, J. M. Elzerman, T. Fujisawa, S. Tarucha, and L. P. Kouwenhoven *Rev. Mod. Phys. 75*, **1** (2003).
14. M. Koskinen, S. M. Reimann, and M. Manninen, *Phys. Rev. Lett.* **90**, 066802 (2003).
15. K. Shiraishi, H. Tamura and H. Takayanagi, *Appl. Phys. Lett.* **78**, 3702 (2001).
16. M. Borgh *et al.*, to be published.

SINGLE JOSEPHSON JUNCTIONS AS QUBITS*

J. R. ANDERSON[1,†], A. J. BERKLEY[1], A. J. DRAGT[1], S. DUTTA[1], M. GÓRSKA[1,2], M. A. GUBRUD[1], P. R. JOHNSON[1], C. J. LOBB[1], R. C. RAMOS[1], F. W. STRAUCH[1], F. C. WELLSTOOD[1], H. XU[1]

[1]*Department of Physics, University of Maryland, College Park, Maryland 20742, U.S.A.*

[2]*Institute of Physics, Polish Academy of Sciences, A. Lotników 32/46, 02-668 Warsaw, Poland*

The search for a quantum computer has been stimulated by the development of algorithms that would solve intractable problems (exponential time) if the massive parallel processing of the anticipated quantum computer were available. Foremost among these problems is the determination of the prime factors of a large integer. We discuss our studies of single Josephson junctions as the qubits of a quantum computer and present microwave spectroscopy results for both single and coupled pairs of Josephson junctions. In addition, we will give some preliminary results on escape rates from single and pairs of junctions. We will also briefly discuss the advantages and obstacles connected with the single Josephson-junction approach.

1. Introduction

Recently there have been estimates that the limit to Moore's Law [1] for classical digital computers, based on silicon, will be reached within the next decade. Although this time estimate has been extended almost yearly, it is clear that at nanometer dimensions we will not be able to make reproducibly silicon transistors whose properties depend upon added impurities. In addition, dissipating the heat produced by packing such small transistors closely will be extremely difficult. A quantum computer, based on entanglement of qubits, the equivalent of bits in a classical computer, would allow the parallel processing and speed such that exponential-time requirements of a classical computer could be reduced to polynomial times for certain problems. One example is the algorithm for finding the prime factors of large integers, which was proposed by Shor in 1994 [2]. Since public-key encryption, the basis of the security of electronically transmitted information, depends upon the difficulty in finding

---

* Research funded by National Security Agency, National Science Foundation, and the University of Maryland Center for Superconductivity Research

† e-mail: ja26@umail.umd.edu

prime factors with a classical computer, there is now an intensive effort, both theoretically and experimentally, to find a quantum computer.

Many solid-state systems have been suggested as qubits for quantum computing. These include semiconductors with appropriate impurities, quantum dots, and superconducting components based on flux, charge, or phase. The challenge is to find a system in which quantum states, acting as qubits, may be accurately identified and manipulated. Then we must be able to control the interactions between quantum states in a multiple-qubit system.

Recently we have been focusing on single Josephson junctions as phase-based qubits [3]. These qubits have several advantages, including:

1. Simplicity (each Josephson junction represents a qubit) and straightforward fabrication.
2. Easy state readout as a voltage signal.
3. Possible external control of qubit coupling.
4. Immunity to flux and charge noise.
5. Flexibility of design (wide range for selection of system parameters).
6. Theoretical studies and simulations are relatively straightforward.

There are, however, obstacles to the use of Josephson-junction qubits, for example:

1. Junctions are connected to electrical leads, major sources of decoherence, and junctions are susceptible to current noise. Thus coherence times are short.
2. Only fixed capacitance coupling, not switchable coupling has been demonstrated.
3. Only indirect evidence of entanglement by microwave spectroscopy has been demonstrated [4]. Demonstration of Bell's inequality test [5] and the Einstein –Podolsky-Rosen test [6] would be desired.
4. Working gates, such as CNOT and SWAP, have not yet been developed.
5. Scalability to a many-qubit system, seemingly straightforward, has not been demonstrated.
6. The overhead required for error correction must be established.
7. It is not known from direct experimental evidence if mesoscopic objects of millimeter dimensions can be treated as quantum mechanical systems.

It is clear that better isolation schemes are needed to overcome these obstacles.

In this report we summarize briefly our microwave spectroscopy measurements on single Josephson-junction qubits and coupled pairs of these qubits. Measurement of escape rates from the junctions is important in evaluating the success of our approach for decoupling junctions from their environment. Therefore, we will describe preliminary measurements of escape rates from single junctions and correlated escape rates from a pair of coupled junctions and compare these data with a model based on a slow ramp of the junction bias current. We will conclude with a summary of the direction we expect our research to take in the future.

2. Experiment

We have been measuring the I-V characteristics of Josephson junctions with and without the application of microwaves. Fig. 1 presents a schematic of a current-biased junction, shunted by a resistance R and capacitance C, (Fig. 1a) and the junction I-V characteristics (Fig. 1b) as well as the standard Josephson-junction washboard potential (Fig. 1c). The R and C represent a combination of resistance and capacitance of the junction and include the values from the rest of the circuit as seen by the junction. The washboard potential, with I_0 the critical current and γ the phase across the junction as shown in Fig. 1c, changes with bias current I (or I_b). As I_b increases, the potential difference between a well minimum and the next maximum becomes smaller and the separation between the metastable energy levels decreases. The bias current is ramped and at a certain time there is switching out of a metastable level to a free-running state, which is signaled by the appearance of a dc voltage signal. The time at which this voltage appears is recorded and the actual switching current is determined from a calibration of I_b vs. ramping time. The general approach is to ramp the bias current many times and record the values at which switching occurs as a histogram of switching current (I_{switch}) vs. the number of switching events (See Fig, 1d). In the presence of a microwave signal, peaks occur in the number of counts vs. I_b and these peaks can be correlated with the transitions between energy levels in the washboard potential well (Fig. 1c). Escape of the system to the voltage state with an applied microwave signal occurs at smaller bias currents than in the absence of microwaves. From the positions of the peaks in the histogram we can determine the energy level separations, and the peak widths provide information about lifetimes and decoherence effects.

We have carried out microwave spectroscopy measurements on both single junctions and pairs of coupled junctions. From these studies we have been able to extract energy levels of both the single and coupled junctions. In the qubit pair we have observed an avoided crossing of energy levels, which is evidence for actual entanglement [4].

Here, however, we will focus on our recent measurements of escape rates from a single junction and how these results can be applied to the determination of the junction-energy relaxation time, T_1, using a slow-ramp technique and different junction temperatures [7]. Fig. 2 shows a semi-log plot of the escape rate Γ vs. bias current I_b for a Nb/AlO$_x$/Nb junction with critical current I_0 (= 33.67 μA) at six different mixing-chamber temperatures between 35 mK and 320 mK. (We assume that the junction temperature is approximately the same as the temperature at the mixing chamber.) The escape rates are higher for higher temperatures as expected, but all the curves tend to the same limiting values as the bias current approaches I_0. The plot at the lowest temperature is almost linear on this semi-log plot, but we see that each of the higher –temperature plots has a distinct "shoulder".

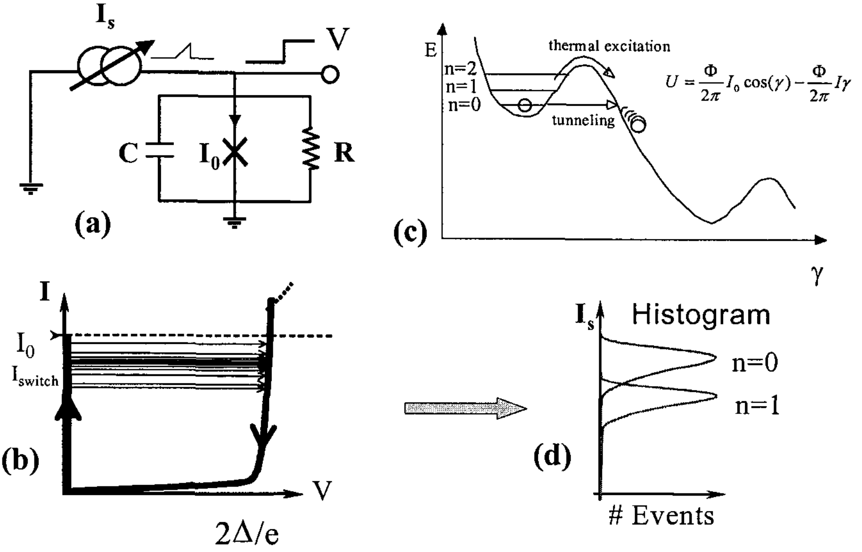

Figure 1. a. Schematic of current-biased Josephson junction with R and C shunts. b. I-V characteristics of the junction of part a. I_0 is the critical current, I_{switch} corresponds to the current at which the junction switches to the voltage state, Δ is the superconducting gap energy, and e is the electron charge. c. Washboard potential U of the Josephson junction. Metastable levels are shown for n = 0, 1, and 2. γ is the phase difference across the junction. d. Switching histogram corresponding to levels 0 and 1.

Simulations have been carried out using energy levels, inter-level transition rates, and tunneling rates, which were calculated with the Schrödinger equation on a grid using the standard washboard potential shown in Fig. 1c. In these calculations it is assumed that there is a wave incident on the barrier from the left and an exponentially damped wave emerging from the barrier on the right. We treat only two levels, n = 0 and 1, and neglect the influence of higher energy states including the continuum. Therefore, we describe the time evolution of our single junction system by the coupled differential equations:

$$\partial\rho_0/\partial t = -(\Gamma_0+\Gamma_U)\rho_0+\Gamma_D\rho_1 \qquad \text{and} \qquad (1)$$
$$\partial\rho_1/\partial t = \Gamma_U\rho_0-(\Gamma_1+\Gamma_D)\rho_1 \;.$$

Here ρ_0 and ρ_1 are the relative probabilities that the system is in the states |0> (n = 0) and |1> (n = 1), respectively, at time t. (The symbols Γ_0, Γ_1, Γ_U, and Γ_D represent the tunneling escape rate from state |0>, from state |1>, the rate of thermal excitation to state |1> from state |0>, and the spontaneous rate of transition from |1> to |0>, respectively). The sum of these relative probabilities, $\rho(t)$ (= $\rho_1(t) + \rho_0(t)$), does not equal 1 because there is also the probability that the system has "escaped" to the voltage state by time t. If we assume that these transition rates are independent of time, then Eq. 1 becomes two coupled linear differential equations which can be solved by assuming solutions $\rho_0 = C_0\, e^{\alpha t}$ and $\rho_1 = C_1\, e^{\alpha t}$, where C_0, C_1, and α are independent of time. The quantity α is negative, indicating a decrease in the probabilities with increasing time.

Solving Eqs. 1 in this linear two-level approximation, we find that

$$\alpha = \frac{-(\Gamma_1+\Gamma_D+\Gamma_0+\Gamma_U)+\sqrt{(\Gamma_1+\Gamma_D-\Gamma_0-\Gamma_U)^2+4\Gamma_D\Gamma_U}}{2}$$

and (2)

$$C_1 = C_0\,\frac{-(\Gamma_1+\Gamma_D-\Gamma_0-\Gamma_U)+\sqrt{(\Gamma_1+\Gamma_D-\Gamma_0-\Gamma_U)^2+4\Gamma_D\Gamma_U}}{2\Gamma_D}\,.$$

We define the probabilities, $P_0 = \rho_0/(\rho_0 + \rho_1)$ and $P_1 = \rho_0/(\rho_0 + \rho_1)$, which represent the probabilities that the system has not yet escaped from the states |0> and |1>, respectively. These probabilities are normalized such that their sum =1 and can be written as $P_0 = C_0/(C_0+C_1)$ and $P_1 = C_1/(C_0+C_1)$. The system makes a transition to the voltage state at a rate given by $\Gamma = -d \ln(\rho)/dt = \Gamma_0 P_0 + \Gamma_1 P_1$.

We now examine some limiting cases. From detailed balance we may write $\Gamma_U = \Gamma_D \exp[-\Delta E/(k_b T)]$, which is usually much less than Γ_D. ΔE is the energy difference between the states |1> and |0>, k_b is the Boltzmann constant, and T is the temperature. As $\Gamma_U \rightarrow 0$, $\alpha \rightarrow -\Gamma_0$, which is what one would expect since the |1> state is not being repopulated. In the same limit $C_1/C_0 \rightarrow \Gamma_U/(\Gamma_1 + \Gamma_D - \Gamma_0)$. In Table 1 we show the limiting values of the occupation probabilities for different bias currents.

Next we show from the plot of Fig. 2 how an approximate lifetime T_1 is extracted. In the range of bias currents shown in the figure, Γ_0 and Γ_1 depend approximately linearly on I_b, as we have found from our simulations. Thus we can write: $\log(\Gamma_0/10^4) \approx 3.235\text{x}10^7\, I_b - 1.08\text{x}10^3$ and $\log(\Gamma_1/10^4) \approx 3.0035\text{x}10^7\, I_b - 1\text{x}10^3$, with I_b expressed in amperes. In figure 2 the shoulder is evident for temperatures 75 mK and above and appears at a bias current of about 33.44 μA.

If we assume this value corresponds to the point at which $\Gamma_1 = \Gamma_D$, we find that $T_1 \approx 1/\Gamma_1 \approx 4.25$ ns.

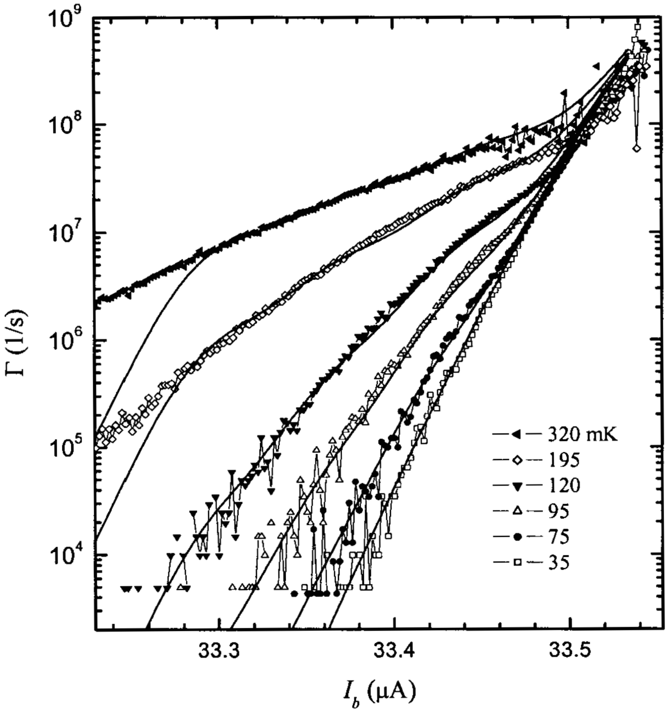

Figure 2. Total escape rate, Γ vs. I_b, for a single junction at 6 different temperatures. The sweep rate was 0.9 A/s. The solid lines are the results of model simulations using parameters, Γ_0, Γ_1, Γ_U, and Γ_D, which were calculated with the Schrödinger equation from the dependence of the washboard potential on I_b.

Table 1. Approximate probabilities of state occupancy for different bias current ranges.

Bias Current	P_0	P_1	Γ
Low I_b	$\Gamma_D/(\Gamma_D+\Gamma_U)$	$\Gamma_U/(\Gamma_D+\Gamma_U)$	$\Gamma_0+\Gamma_1(\Gamma_U/\Gamma_D)$
I_b ($\Gamma_D = \Gamma_1$)	$1-\Gamma_U/\Gamma_1$	Γ_U/Γ_1	$\Gamma_0 + \Gamma_U$
High I_b	$\Gamma_1/(\Gamma_1+\Gamma_U)$	$\Gamma_U/(\Gamma_1+\Gamma_U)$	$\Gamma_0 + \Gamma_U$

In this report we have briefly described our microwave spectroscopy measurements on single and coupled junctions; some of this work has already been published. Next we summarized our recent measurements of escape rates for single junctions from which we estimate a lifetime T_1 of about 4 ns, a result that is consistent with our other measurements. This type of lifetime measurement is relatively easy to carry out and would provide a check on other measurements of T_1 and T_2. Our future plans are to look for Rabi oscillations in these junctions and to prepare and measured coupled systems of three and more qubits.

Acknowledgements

We wish to acknowledge helpful discussions with Bruce Kane, Marc Manheimer, Keith Schwab, and Richard Webb. We also thank Richard Webb for loaning us a pump when one of ours failed.

References

1. See for example, P. Packan, "Pushing the Limits", *Science* **285**, 2079 (1999).
2. P. W. Shor, Proceedings, 35th Annual Symposium on Foundations of Computer Science, IEEE Press, Los Alamitos, CA. p. 124 (1994). S.I.A.M. Journal on Computing 26,1484 (1997).
3. R. C. Ramos, M. Gubrud, A. J. Berkeley, J. R. Anderson, C. J. Lobb, and F. C. Wellstood, *IEEE Trans. Appl. Supr.* **11**, 998 (2001).
4. A. J. Berkley, H. Xu, M. Gubrud, R. Ramos, F. W. Strauch, P. R. Johnson, J. R. Anderson, A. J. Dragt, C. J. Lobb, and F. C. Wellstood, Science **300**, 1548 (2003).
5. J. Bell, Physics **1**, 195 (1964).
6. A. Einstein, B. Podolsky, and N. Rosen, Phys. Rev. **47**, 777 (1935).
7. S. K. Dutta, H. Xu, A. J. Berkley, R. C. Ramos, M. A. Gubrud, J. R. Anderson, C. J. Lobb, and F. C. Wellstood – Manuscript in preparation.

ON THE ABSENCE OF KONDO RESONANCE FOR Co DIMERS ON A Cu (111) SURFACE

J.-L. HELFER, F. A. REUSE
Institut de Physique des Nanostructures, École Polytechnique Fédérale de Lausanne, CH-1015 Lausanne, Switzerland

S. N. KHANNA
Department of Physics, Virginia Commonwealth University, Richmond, Virginia 23284-2000, U.S.A.

The electronic structure and the magnetic properties of Co atoms and Co_2 adsorbed on a Cu(111) surface have been studied using an ab initio density functional approach that permits host and adatom relaxations. A single Co adatom is shown to be magnetic with a moment of 1.73 μB,as observed in recent experiments. The coupling between the adsorbed Co sites is shown to be ferromagnetic, and a Co_2 on the surface has a magnetic moment of 3.72 μB that is comparable to its value in a free molecule. However, the formation of the dimer is shown to result in an increased separation of the Co atoms from the underlying surface, leading to a reduction of the host-adatom interaction. This reduced coupling leads to the disappearance of the Kondo resonance, as observed experimentally at a temperature of 6 K for an analogous system, namely Co on Au(111).

1. Introduction

Of all the properties, the magnetic properties of nanoscale materials are probably the most unique. Atomic clusters can be considered as the ultimate nanoscale materials. It has been found that clusters of itinerant ferromagnetic solids like Fe, Co, and Ni exhibit super-paramagnetic behavior with enhanced moments [1], while free clusters of non-magnetic solids like Rh are found to be magnetic [2]. The magnetic coupling can also change with size. For example, it has been recently shown that small clusters of Mn undergo a ferromagnetic to ferrimagnetic transition around 7 Mn atoms [3]. These changes at the nanoscale occur because of the reduced size and the preponderance of the surface sites that changes the local environment of various atoms. These features get further amplified in a new area that is currently drawing considerable attention, namely the clusters deposited on surfaces. Here, the atomic arrangement and interactions in clusters can be further controlled by the substrate and this can lead to a novel class of behaviors.

In a recent paper, Chen *et al.* [4] reported the Kondo resonance for Co deposited on Au(111) surface. As the Co atoms are marked by localized d-states with unpaired electrons, the experiment enables one to investigate the interaction of the localized magnetic states with the delocalized electron gas of the Au substrate. Chen *et al.* looked for the Kondo resonance that detects the many-body ground state formed by the screening of the localized magnetic moment by the host electrons. As such, the resonance not only detects the presence of localized moments, but the Kondo temperature is a measure of the strength of interaction between the localized moment and the host electron gas. In the experiment by Chen *et al.*, in addition to the Kondo resonance for isolated atoms, the authors moved the Co atoms on the surface to form dimers. Such an experiment can provide information on how the Co atoms interact in the presence of the nearly free electron gas, and how the interaction between the localized moments and the electron gas changes as the moment becomes more extended. They observed an intriguing result. When the Co atoms were isolated on the surface, they observed a distinct resonance. However, as the atoms were moved to separations less than 6 Å, the Kondo resonance disappeared. Since a free Co_2 dimer is ferromagnetic with a moment of 2 μ_B/atom, it was surprising why the resonance could not be observed. Chen *et al.* proposed three possible explanations.

1. The magnetic moment on each Co atom is quenched during the dimerization.
2. The Co atoms remain magnetic but the coupling becomes antiferromagnetic. This could occur if the indirect coupling between the Co sites through the electron gas was antiferromagnetic and if it dominated over the direct interaction. The possibility of an anti-ferromagnetic Co_2 would be particularly attractive in view of the recent theoretical studies on a free Co_2 that indicate the possibility of an antiferromagnetic state [5].
3. The interaction between the Co and the surface is modified during the dimerization. In particular, there is reduced coupling between the conduction electrons and the localized moment at the Co sites. It is important to note that the experiments of Chen *et al.* were carried out at 6 K. The Kondo temperature is highly sensitive to the coupling and even a small reduction in coupling could drive the temperature to below the experimental temperature, leading to a disappearance of the signal.

In this paper, we have carried out detailed theoretical investigations to resolve the above paradox. It is important to realize that a complete investigation of the above problem requires theoretical studies that permit relaxation of the surface as the atoms are brought together to form dimers and yet permit treatment of the infinite surface. Most of the available codes are unable to perform both tasks and we have recently developed a new approach that permits studies of deposited clusters while relaxing the surface. However, the code is still non-relativistic and thus unable to accurately describe the Au surfaces. Recent experiments have nevertheless established that a similar Kondo resonance may be observed on other noble metal surfaces as well, in particular for isolated Co atoms on Cu(111) [6]. With this in mind, we have carried out studies on this analogous system, namely Co adsorbed on Cu(111). We show that the Co dimer on Cu(111) is indeed magnetic with a moment of 1.86 μ_B/atom compared to 2 μ_B/atom for a free Co_2. However, while isolated Co atoms are able to acquire deeper positions on the surface, the dimerization leads to a Co_2 where the Co sites are significantly elevated above the surface. This leads to a reduction of the coupling between the Co localized moments and the host conduction electrons, thereby leading to the disappearance of the Kondo resonance. Our studies highlight the importance of surface relaxations in these magnetic phenomena and show how the clustering can alter the cluster-surface interactions.

2. Method of Calculation

The theoretical studies were carried out using a code we have just developed. While the details will be published in a separate publication, we only give here the main technical characteristics of the calculation. The general framework is the Born-Oppenheimer approximation, in which nuclei are treated as classical point charges, and the electrons are treated quantum mechanically. The idea is to build a fictitious system with a finite number of electrons, whose electronic properties of interest approach those of a semi-infinite surface on which a small cluster of atoms is adsorbed. This fictitious system is chosen as a system of N electrons in a box with periodic boundary conditions in the x and y directions. The box is infinitely extended in the z direction. In the present case, its xy section consists of 4 primitive cells of the Cu(111) Bravais lattice (Fig. 1). Time and memory constraints prevented us from taking a larger box. Three monolayers of 4 Cu atoms each were chosen to model the Cu(111) surface. The Co atoms and dimers were adsorbed on both sides of the three Cu layers in order to restore the central symmetry of the system, which reduces the calculations. It was checked that the interaction between the two symmetric atoms or dimers is negligible across the three layers.

All electrostatic interactions (electron-electron, electron-nucleus, nucleus-nucleus) are described through the 2D periodic Ewald potential. Applying the adiabatic connection to this fictitious system allows one to obtain one-electron

Kohn-Sham type equations, which are solved self-consistently in a basis of periodized atomic gaussian type functions (DZVP2 [7], 15 gaussians of type s, 9 of type p, 5 of type d, for each atom). All calculations are performed at the all-electron level. The local spin-density approximation to the exchange-correlation potential was used.

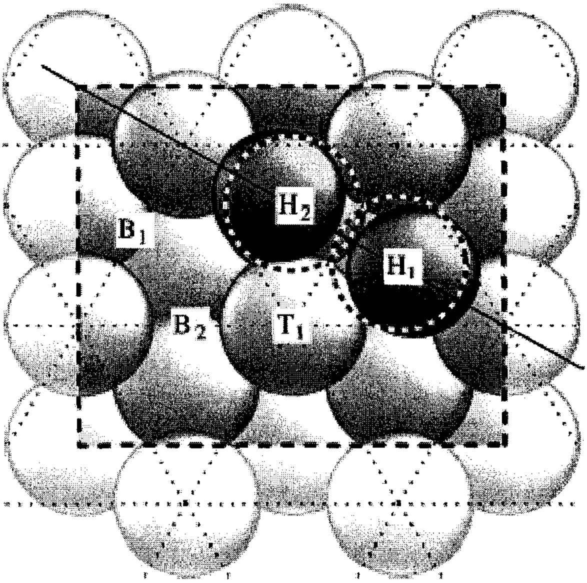

Figure 1. Equilibrium geometry of the Co dimer adsorbed on the Cu(111) surface. The dashed rectangle represents the box on the sides of which 2D periodic boundary conditions are imposed. The dashed circles indicate the starting geometry of the dimer, which was then fully relaxed. The sizes of the spheres representing atoms are arbitrary. The different adsorption sites for a single atom are labeled with respect to the triangular lattice of the upper Cu layer (dotted lines).

On the one hand, analytic recurrence relations are used to calculate the matrix elements of the kinetic energy operator and of the short-range nuclear potential operator. On the other hand, the electronic density is separated into atomic contributions, which are then expanded into multipoles up to $\ell=8$. The Poisson equation is solved numerically to obtain the Hartree potential on a mesh around each atom, constructed as the cartesian product of a 56 points radial mesh and a 110 points angular mesh. The same mesh is then used to calculate the matrix elements of the Hartree potential operator and of the long-range nuclear potential, taking care of the periodic nature of these potentials.

It should be emphasized at this point that the hamiltonian of the system is invariant under time reversal, which allows the use of real basis functions. Thus, the angular momentum will always be zero at this level of approximation. The magnetic properties thus reduce to the spin magnetic moment density, which is simply referred to as "the magnetic moment density" in the following. Indeed, it is known experimentally that the spin magnetic moment is the main contribution to the total magnetic moment [8].

3. Results and Discussions

We first investigated the adsorption of a single atom on the different symmetric sites of the Cu(111) surface, shown in Fig. 1: an on-top site T_1, two hollow sites H_1 and H_2 (depending on the presence of a Cu atom directly below in the second layer), and two bridge sites B_1 and B_2 (depending on the orientation of the bridge with respect to the periodicity box). The positions of all atoms were fully relaxed, but the displacements of the Cu atoms turned out to be negligible (less than 0.1 Å). The main results are summarized in Table 1. The adsorption energy E_{ads} is the difference in energy between the Cu surface with the adsorbed Co atom and the clean Cu surface with the Co atom far at infinity.

Table 1. Adsorption energy E_{ads}, adsorption distance d_{ads}, and magnetic moment μ of a Co atom on the Cu(111) surface for the different adsorption sites shown in Fig. 1.

Site	E_{ads} (eV)	d_{ads} (a.u.)	μ (μ_B)
hollow H_1	4.05	3.3	1.73
hollow H_2	4.24	3.3	1.73
bridge B_1	4.27	3.5	1.78
bridge B_2	3.86	3.5	1.77
on-Top T_1	3.39	4.0	1.91

The rather high adsorption energies are an artifact of LSDA. However, we did not use gradient corrections, since we are primarily interested in the magnetic properties and the inclusion of gradient corrections is not likely to change the magnetic properties. The results also show the effect of the size of the periodicity box on the calculated properties. For example, the calculated binding energy of the two hollow and bridge sites differ by 0.5 eV. This shows that one has to be careful in choosing the periodicity box in order to approach correctly the properties of the Cu surface. If one takes the most stable bridge and hollow sites, our studies indicate that the two sites have nearly equal binding energy. Recent experiments on Co atoms on Cu(111) indicate that the Co atoms probably occupy the hollow sites [6]. Our results are not inconsistent with that observation. However, we expect the magnetic properties of interest here to be much less sensitive to the size of the periodicity box, and the present calculations thus allows one to determine them with enough precision. Indeed, in Table 1 the difference in adsorption distance and magnetic moment between the two bridge sites and the two hollow sites is less than 1%. While there are no definite measurements of the magnetic moment of a single Co atom on Cu(111), our results are in agreement with the recent experiments of Kondo resonance for Co on Cu(111) [6] that confirm the presence of the local magnetic moment, and with numerical calculations for Co on Cu(001) as well [9].

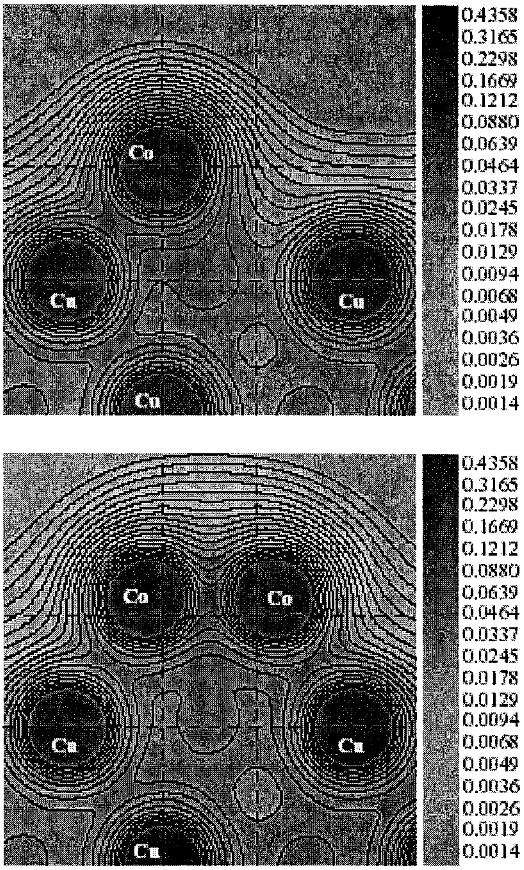

Figure 2. Contour plot of the electronic density along the plane perpendicular to the Cu surface through the solid line shown in Fig. 1. The color scale is logarithmic, shown on the right in electrons/a.u^3. On both plots, the dashed lines indicate the equilibrium position of the single Co atom on both hollow sites.

We now turn to the adsorption of the Co dimer. Following the experimental belief that hollow sites are energetically favored for a single Co atom [6], we started the calculations with an initial position of the Co dimer above two neighboring hollow sites, as shown with dashed lines in Fig. 1. Calculating the Hellmann-Feynman forces on all nuclei, we relaxed all Co and Cu nuclei positions, and obtained the equilibrium geometry shown in Fig. 1. The results for this geometry are summarized in Fig. 2 and Table 2. They allow us to assess the pertinence of the three explanations for the disappearance of the Kondo resonance as stated earlier:

1. Possible disappearance of the magnetic moment when the dimer is formed: our calculation shows a magnetic moment of 1.9 μ_B per Co atom in the dimer. Thus, this first reason is ruled out, at least in the case of Co on Cu(111). This result is consistent with other calculations (for Co atoms on Au(111) [11], for small Co clusters on Cu(001) [9,10], for Co monolayers on Cu(001) [12], for Co monolayers on Cu(111) [13]) and measurements (for small Co clusters on Pt(111) [8]) which show that Co atoms adsorbed on a metal have a very stable magnetic moment of about 1.6 to 2 μ_B, from single atoms to full monolayers.
2. Starting the calculation with an antiferromagnetic configuration of the dimer, the self-consistent procedure converges to the ferromagnetic configuration indicating that the antiferromagnetic solution is unstable. This is also consistent with the above cited calculations and measurements (see also [14]).
3. Considering the equilibrium geometries, we observe that the Co dimer lies higher above the surface (3.8 a.u.) than the single atom (3.3-3.5 a.u. for hollow and bridge sites). Furthermore, the bond length of the adsorbed dimer is almost identical to the bond length of the free Co dimer [5]. This suggests that a Co atom binds stronger to another Co atom than to the Cu surface. This fact is corroborated by the adsorption energy per Co atom E_{ads} of the Co dimer, defined here as

$$E_{\text{ads}} = (1/2)[E(\text{clean Cu slab}) + E(\text{free Co dimer}) - E(\text{Cu slab} + \text{adsorbed Co dimer})] \qquad (1)$$

   This energy being smaller than E_{ads} for a single Co atom, it shows that the dimer is less bound to the surface than the atom.

Table 2. Adsorption energy E_{ads} per Co atom defined by Eq. (1), adsorption distance d_{ads}, and magnetic moment μ of a Co dimer on the Cu(111) surface.

E_{ads}	d_{ads}	d_{bond}	μ
3.30 eV	3.8 a.u.	3.7 a.u.	1.86 μ_B

These facts suggest that the coupling between the Co atoms and the conduction electrons in the surface is reduced when they are moved close enough to form a dimer. To see how it affects the Kondo resonance, we show in Fig. 2 the total charge density for the case of single impurity and the dimer. Since the surface electronic density decays exponentially outside the surface, the local density of state of the surface electrons is considerably reduced at the Co atoms when the dimer is formed, since it is farther to the surface than the single Co atom. This would then lead to a reduction of the observed Kondo resonance.

4. Concluding Remarks

The present studies show that the isolated cobalt atoms as well as Co2 on a noble metal surface are indeed magnetic. For Co_2, the magnetic moment is close to that of free dimers. However, the interaction between the Co sites and the surface is weakened during the formation of the dimer, which explains the disappearance of the Kondo resonance in the experiments at 6 K. The fact that the dimer is magnetic, however, indicates that it should be possible to observe this resonance in carefully planned experiments at lower temperatures. We hope that the current work would inspire such experiments.

Acknowledgments

This work was supported by the Swiss National Science Foundation.

References

1. S. N. Khanna, S. Linderoth, Phys. Rev. Lett. **67**, 742 (1991).
2. I. M. L. Billas, A. Chatelain, and W. A. de Heer, Science **265**, 1682 (1994); B. V. Reddy, S. N. Khanna, and B. I. Dunlap, Phys. Rev. Lett. **70**, 3323 (1993); A .J. Cox, J. G. Louderback, and L. A. Bloomfield, Phys. Rev. Lett. **71**, 923 (1993).
3. M. B. Knickelbein, Phys. Rev. Lett. **86**, 5255 (2001); S. K. Nayak and P. Jena, Chem. Phys. Lett. **289**, 473 (1998); M. R. Pederson, F. Reuse, and S. N. Khanna, Phys. Rev. B, **58**, 5632 (1998).
4. W. Chen, T. Jamneala, V. Madhavan, and M. F. Crommie, Phys. Rev. B **60**, R8529 (1999).
5. G. L. Gutsev, S. N. Khanna, and P. Jena, Chem. Phys. Lett. **345**, 481 (2001).
6. N. Knorr, M. A. Schneider, L. Diekhöner, P. Wahl, and K. Kern, Phys. Rev. Lett. **88**, 096804 (2002).

7. N. Godbout, D. R. Salahub, J. Andzelm, and E. Wimmer, Can. J. Chem. **70**, 560 (1992).
8. P. Gambardella, S. Rusponi, K. Kern, H. Brune, S. S. Dhesi, I. Cabria, R. Zeller, P. H. Dederichs, A. Dallmeyer, and C. Carbone, submitted to Phys. Rev. Lett.
9. V. S. Stepanyuk, W. Hergert, P. Rennert, K. Wildberger, R. Zeller, and P. H. Dederichs, J. Mag. Mag. Mat. **165**, 272 (1997).
10. It should be emphasized that these calculations did not relax the geometry of the adsorbed Co dimer, as opposed to our work. This was shown in [15] to change radically the magnetic moment in the case of the vanadium dimer.
11. M. Weissmann, A. Saúl, A. M. Llois, and J. Guevara, Phys. Rev. B **59**, 8405 (1999).
12. R. Pentcheva and M. Scheffer, Phys. Rev. B **61**, 2211 (2000).
13. L. Zhong, M. Kim, X. Wang, and A. J. Freeman, Phys. Rev. B **53**, 9770 (1996).
14. P. Poulopoulos, P. J. Jensen, A. Ney, J. Lindner, and K. Baberschke, Phys. Rev. B **65**, 064431 (2002).
15. B. V. Reddy, M. R. Pederson, and S. N. Khanna, Phys. Rev. B **55**, R7414 (1997).

ENERGY SPECTRUM, PERSISTENT CURRENT AND ELECTRON LOCALIZATION IN QUANTUM RINGS

M. MANNINEN[1], P. KOSKINEN[1], M. KOSKINEN[1], P. SINGHA DEO[2], S.M. REIMANN[3], AND S. VIEFERS[4]
[1]*NanoScience Center, Department of Physics, University of Jyväskylä, Finland*
[2]*S.N. Bose National Centre of Basic Science, Kolkata 98, India*
[3] *Department of Mathematical Physics, Lund University of Technology, Sweden*
[4]*Department of Physics, University of Oslo, Norway*

Energy spectra of quasi-one-dimensional quantum rings with a few electrons are studied using several different theoretical methods. Discrete Hubbard models and continuum models are shown to give similar results governed by the special features of the one-dimensionality. The energy spectrum of the many-body system can be described with a rotation-vibration spectrum of a 'Wigner molecule' of 'localized' electrons, combined with the spin-state determined from an effective antiferromagnetic Heisenberg Hamiltonian. The persistent current as a function of magnetic flux through the ring shows periodic oscillations arising from the 'rigid rotation' of the electron ring. For polarized electrons the periodicity of the oscillations is always the flux quantum Φ_0. For nonpolarized electrons the periodicity depends on the strength of the effective Heisenberg coupling and changes from Φ_0 first to $\Phi_0/2$ and eventually to Φ_0/N when the ring gets narrower.

1. Introduction

Recent experimental developments in manufacturing quantum dots[1] and rings[2] with only a few electrons have made quantum rings an ever increasing topic of experimental and theoretical research. In a quantum ring the electrons move in a ring-shaped quasi-one-dimensional confinement. The one-dimensionality makes the electrons strongly correlated. Among the quantum effects seen in such systems are the Aharonov-Bohm oscillations[3] and persistent currents[4].

Many properties of the quantum rings can be explained with single-electron theory, which in a strictly one-dimensional (1D) system is naturally very simple. On the contrary, the many-particle fermion problem in 1D systems is surprisingly complicated due to enhanced importance of the Pauli exclusion principle. It is then customary to say that strictly 1D systems are not 'Fermi liquids' but 'Luttinger liquids' with specific collective excitations (for reviews see[5,6,7,8]).

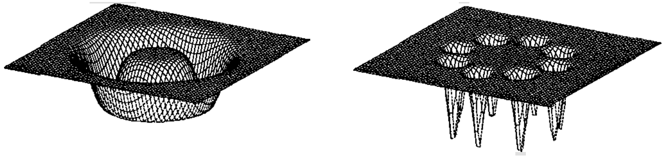

Figure 1. **Two models** of quantum rings, a continuum ring and a ring consisting of discrete lattice sites.

We consider two models for quantum rings. In the *continuum model* the electrons move in an external two-dimensional potential (shown schematically in Fig. 1a) usually considered to be harmonic:

$$V(r) = \frac{1}{2} m_e \omega_0^2 (r - R)^2, \tag{1}$$

where R is the radius of the ring and ω_0 the strength of the radial confinement. The electron-electron interaction is the normal long-range Coulomb interaction. If the number of electrons is small, the many-electron states in this external potential can be solved (numerically) exactly using standard configuration interaction (CI) methods[9,10,11].

Another theoretical approach[12,13,14] to quantum rings has been a model where the ring consists of discrete lattice sites, as shown in Fig. 1b. The many-particle Hamiltonian can be approximated with the Hubbard model[15,16]

$$H = -t \sum_{i=1}^{L} \sum_{\sigma} \left(e^{-i2\pi\phi/L} c_{i+1,\sigma}^{\dagger} c_{i,\sigma} + e^{i2\pi\phi/L} c_{i,\sigma}^{\dagger} c_{i+1,\sigma} \right) + U \sum_{i=1}^{L} \hat{n}_{i\uparrow} \hat{n}_{i\downarrow}, \tag{2}$$

where t and U are the Hubbard parameters determining the hopping between neighbouring sites and the on-site energy, L is the number of electrons and the number of sites, respectively, and ϕ is the magnetic flux through the ring (in units of the flux quantum $\Phi_0 = h/e$). The advantage of the discrete model is that the many-body problem is much easier than that of Eq. (1), and can be solved exactly in some limiting cases.

The two theoretical approaches, although seemingly very different, give in many cases qualitatively similar results. The aim of this work is to compare these models quantitatively and study the reasons for the similarities of these two approaches (for an introductory review see Ref.[17]).

2. Energy Spectra: Rotational and Vibrational States

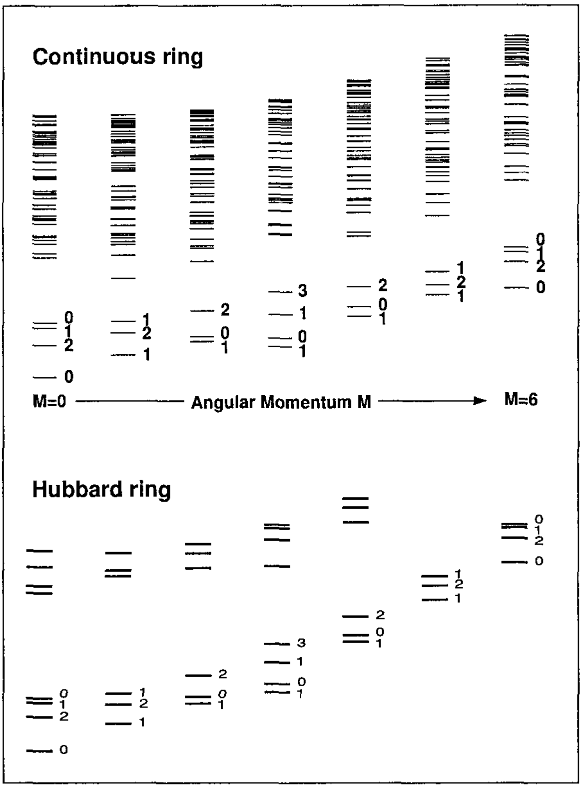

Figure 2. Many-particle spectra of six electrons in a continuum ring and in a Hubbard ring with eight sites. The numbers indicate the total spin of the state.

Figure 2 shows the energy spectra of quantum rings with six electrons, calculated from the continuum model and from the lattice model with eight sites. In both cases the excitation spectrum contains a low energy band of *rotational* states with energy increasing in the continuum model roughly as $\hbar^2 M^2/2I$, where M is the total angular momentum and I the moment of inertia $I = Nm_eR^2$. The low energy electron spectrum thus corresponds to rigid rotation of a ring of six electrons while the higher bands correspond to vibrational excitations. Moreover, the energy splitting (due to spin) can be quantitatively described with an antiferromagnetic Heisenberg model[11].

Thus one arrives at the following model Hamiltonian

$$H_{\text{eff}} = \frac{\hbar^2}{2I}\mathbf{M}^2 + J\sum_{\langle i,j\rangle} \mathbf{S}_i \cdot \mathbf{S}_j + \sum_{\nu} \hbar\omega_\nu n_\nu, \tag{3}$$

where the last term describes vibrational states of electrons localized on the ring (in Fig. 2 the vibrational states are the ones not marked with the spin number).

Figure 2 shows that nearly exactly the same low energy spectrum can be obtained from the Hubbard model with suitably chosen parameters. It is known that in the limit of large U the half-filled Hubbard model ($N = L$) approaches the antiferromagnetic Heisenberg model, explaining the correct spin structure of the model Hamiltonian above. However, the correspondence seems to go even further: If $L > N$ the rigid rotations and vibrational states also appear in agreement with the continuum model.

The similarity of the discrete lattice model with contact interaction and the continuum model with long-range interaction can be traced back to the special properties of one-dimensional systems. The strong contact interaction effectively prevents electrons to pass each other and the 'kinetic energy repulsion' makes the strong δ-function interaction look like a $1/r^2$ interaction as evident from the Calogero-Sutherland model[18,19,17]. Nevertheless, it is surprising that the similarity survives to quasi-one-dimensional rings considered in Fig. 2.

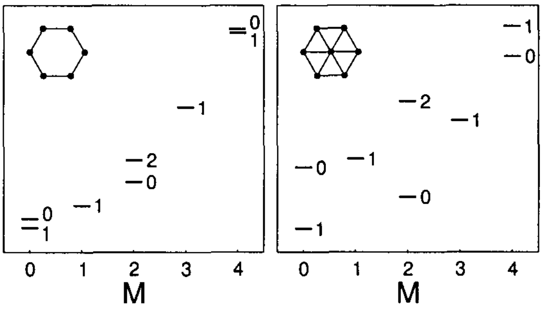

Figure 3. Many-particle spectrum of four electrons in a ring and a dot, shown in the insets ($U = 40t$).

The 'localization' of electrons along the ring happens at all electron numbers. Similar traces of electron localization can be found in the energy spectra of two-dimensional quantum dots[20]. Figure 3 shows the energy spectra of quantum rings and dots with four electrons. In both cases the classical localization geometry is a square. Indeed the low-energy spectrum is similar for a ring and for a dot. The Hubbard model gives again qualitatively the same spectra as the continuum model (not shown here)[11,17].

3. Periodicity of the Persistent Current

The persistent current of a quantum ring can be determined from the flux dependence of the total energy[17]

$$I(\Phi) = -\frac{\partial E}{\partial \Phi}, \tag{4}$$

where Φ is the magnetic flux through the ring. Since the discrete Hubbard model gives the same energy levels as the continuum model, we can use it to study the persistent current. The Hamiltonian (2) can be solved numerically for small number of electrons and sites. Due to the phase factors the energy levels, and consequently the persistent current, will be periodic functions of the flux.

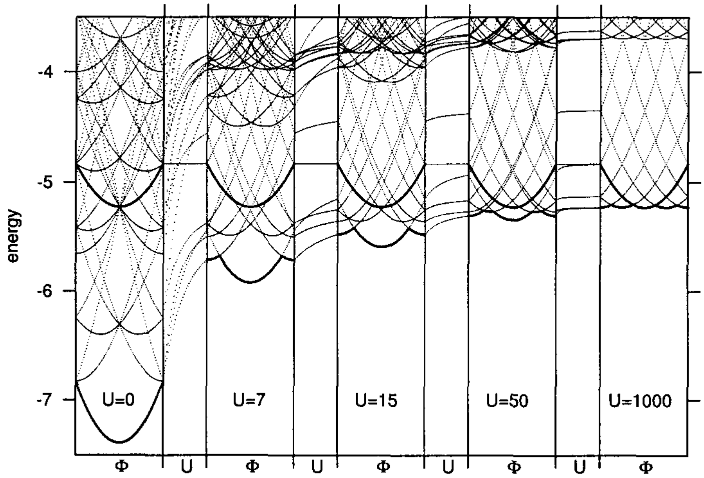

Figure 4. Flux-dependence of the many-particle spectrum of a Hubbard ring with eight sites and four electrons.

Figure 4 shows the spectrum of a Hubbard ring of four electrons in eight sites, as a function of Φ for different values of U. For $U = 0$ the ground state energy has a periodicity Φ_0. When U increases the period changes first to $\Phi_0/2$ and eventually to Φ_0/N. This happens at all electron numbers and in a similar fashion for continuum[21] and discrete[17] rings. The increase of the strength of the radial confinement, ω_0 in Eq. (1), of the continuum model corresponds to the increase of the on-site energy U of the Hubbard model. In both cases the ring becomes more strictly one-dimensional in the sense that electrons are prevented to pass each other.

Acknowledgements

This work has been supported by the Academy of Finland under the Finnish Centre of Excellence Programme 2000-2005 (Project No. 44875, Nuclear and Condensed Matter Programme at JYFL).

References

1. S. Tarucha, D.G. Austing, T. Honda, R.J. van der Haage, and L. Kouwenhoven, Phys. Rev. Lett. **77**, 3613 (1996).
2. A. Lorke, R.J. Luyken, Physica B **256** 424 (1998)
3. Y. Aharonov and D. Bohm, Phys. Rev. **115**, 485 (1959).
4. M. Büttiker, Y. Imry, and R. Landauer, Phys. Lett. A **96**, 365 (1983).
5. F.D.M. Haldane, in *Proceedings of the International School of Physics 'Enrico Fermi' Course CXXI*, North Holland (1994).
6. J. Voit, Rep. Prog. Phys. **57**, 977 (1994).
7. H.J. Schulz, in *Proceedings of Les Houches Summer School LXI*, ed. E. Akkermans, G. Montambaux, J. Pichard, et J. Zinn-Justin (Elsevier, Amsterdam, 1995).
8. E.B. Kolomeisky and J.P. Straley, Rev. Mod. Phys. **68**, 175 (1996).
9. T. Chakraborty and P. Pietiläinen, Phys. Rev. B **52**, 1932 (1995).
10. K. Niemelä, P. Pietiläinen, P. Hyvönen, and T. Chakraborty, Europhys. Lett. **36**, 533 (1996).
11. M. Koskinen, M. Manninen, B. Mottelson, and S.M. Reimann, Phys. Rev. B **63**, 205323 (2001)
12. A.A. Zvyagin, Fiz. Nizk. Temp. **16**, 1299 (1990), Sov. J. Low Temp. Phys. **16**, 745 (1990).
13. F.V. Kusmartsev, J. Phys.: Condens. Matt. **3**, 3199 (1991).
14. N. Yu and M. Fowler, Phys. Rev. B **45**, 11795 (1992).
15. J. Hubbard, Proc. R. Soc. London A **276**, 238 (1963).
16. R. E. Peierls, Z. Phys. **80**, 763 (1933).
17. S. Viefers P. Koskinen, P. Singha Deo, and M. Manninen, Physica E (in press), cond-mat/0310064.
18. F. Calogero, J. Math. Phys **10**, 2191 (1969); **10**, 2197 (1969); **12**, 419 (1971).
19. B. Sutherland, J. Math. Phys. **12**, 246 (1971); **12** 251 (1971).
20. M. Manninen, S. Viefers, M. Koskinen, and S.M. Reimann, Phys. Rev. B **64**, 245322 (2001).
21. P. Koskinen, M. Koskinen, and M. Manninen, Eur. Phys. J B **28**, 483 (2002).

GADOLINIUM NANOWIRE GROWTH ON HIGH-INDEX SILICON SURFACES

E. MORRIS, J.W. DICKINSON, M.L. WILLIS, and A.A. BASKI
Department of Physics, Virginia Commonwealth University, Richmond, VA 23284
E-mail: aabaski@vcu.edu

It is known that submonolayer coverages of rare earth metals such as Gd can form nanowires on the low-index Si(001) surface. This nanowire formation is presumably due to a close lattice match between the rare earth silicide and Si along the $[\underline{1}10]$ direction, and poor match perpendicular to it. In this study, we have used scanning tunneling microscopy (STM) to examine Gd growth on the high-index Si(113) and Si(5 5 12) surfaces. As expected, Gd also forms nanowires on these surfaces for annealing temperatures above 550°C. They are similar to those found on Si(001), but have a single orientation and incorporate (001) and (111) sidewalls. The optimal template for nanowire growth appears to be the Si(113) surface with growth temperatures above 600°C. Because the lattice periodicity along the nanowire direction is identical for the (001), (113), and (5 5 12) surfaces, the appearance of such nanowires on the high-index surfaces provides further evidence for a lattice mismatch mechanism.

1. Introduction

The continued drive toward device miniaturization has spurred efforts to create functional nanowires. One possible method is to employ the self-assembly of metals on semiconductor substrates. Recent scanning tunneling microscopy (STM) investigations of Gd on the low-index Si(001) surface have revealed the creation of nanowires and interesting surface reconstructions[1-2]. Regrettably, wires on the Si(001) surface grow in two perpendicular domains, reducing their utility for device applications. The formation of such nanowires is thought to be due to the small lattice mismatch (0.96%) between gadolinium silicide ($GdSi_2$) and the underlying silicon surface in the $[\underline{1}10]$ direction and the larger lattice mismatch (8.65%) in the perpendicular direction. Therefore, orientations of Si surfaces having the same lattice spacing in the $[\underline{1}10]$ direction should likewise be templates for Gd silicide nanowire growth. Such a family of template surfaces includes the high-index surfaces between Si(001) and Si(111), which are single-domain surfaces and should produce aligned nanowires.[3] The purpose of this study was to investigate the reaction of Gd on Si(113) and Si(5 5 12) and compare its growth behavior to that on Si(001).

2. Experimental Procedure

These experiments were carried out in an ultra-high vacuum chamber with facilities for sample heating, metal deposition, and characterization by low energy electron diffraction (LEED) and scanning tunneling microscopy (STM).

The Si samples were cut from commercial Si(5 5 12) and Si(113) wafers, which are oriented nominally 30.6° and 25.3° down from (001) towards (111). The samples were then cleaned *in situ* by briefly heating to ~1200°C. Gadolinium was evaporated from a tungsten basket onto DC-heated substrates, where the deposition rate was calibrated using a quartz crystal microbalance. Typical rates were below 1 ML/min, where 1 ML equals the atomic density of a reconstructed Si(001) surface. The samples were then annealed for 2-4 minutes at temperatures between 600 and 900°C. Nanowire growth was typically observed from ~0.5 to 1 ML. It should be noted that Gd did not completely desorb from the surface after a high temperature (~1200°C) anneal. Instead, it diffused into the bulk at elevated temperatures and then segregated to the surface upon cooling, leading to the formation of Gd-induced reconstructions on nominally "clean" surfaces. STM images were acquired at room temperature using a constant current (0.1 to 0.5 nA) and show the filled electronic states of the surface (-1.0 to -2.5 V sample bias).

3. Results

An overview of the Gd-induced nanowires grown on the Si(001), Si(113), and Si(5 5 12) surfaces is shown in Figure 1. As expected, the close lattice match of these surface orientations along $[\bar{1}10]$ with Gd silicide results in nanowire growth along this direction. A large lattice mismatch occurs in the perpendicular direction and is dependent upon the surface orientation. At low coverage, the nanowires have a similar appearance on all three surfaces, but there are two equivalent perpendicular orientations on the two-domain (001) surface and only a single orientation on the single-domain (113) and (5 5 12) surfaces. An additional distinguishing characteristic of each surface is the rearrangement of the terraces surrounding the nanowires. On the (001) surface, the terraces have been substantially disrupted after nanowire growth. In contrast, the terraces surrounding the nanowires on the (113) surface are well-ordered, which is due to a stable Gd-induced (113) 2×2 reconstruction (see Fig. 5b). This same

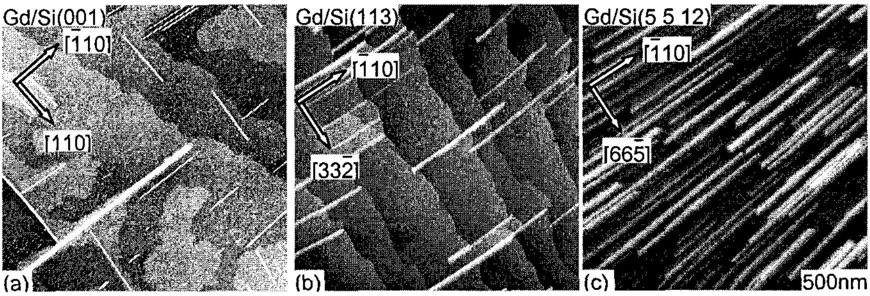

Figure 1: STM images of Gd silicide nanowires on (a) Si(001), (b) Si(113), and (c) Si(5 5 12). The image sizes are 500×500nm², as indicated in the lower right-hand corner.

reconstruction occurs on the (5 5 12) surface, but due to surface faceting results in a much rougher morphology.

3.1. *Gd/Si(001)*

Gd silicide nanowires grown on Si(001) have two orientations and significantly disrupt the surrounding terraces. As has been observed previously by other groups, the nanowires appear to have a high-energy barrier for crossing step edges and therefore cause steps to recede in front of them, with the removed Si being incorporated into the silicide.[1] Eventually, this leads to a limited nanowire length, as the receding step edges are halted by a perpendicular nanowire on a higher terrace. At the low coverage shown in Fig. 2a, Gd induces isolated long nanowires (~100 to 150 nm length, ~4 nm wide) and several short nanowires (<30 nm). Optimum growth occurs at ~650°C, where nanowires can be in excess of 400 nm long. As coverage increases, the wires grow in both length and width as well as begin to cluster together. At the highest coverages shown in Fig. 2c, the dense packing of nanowires restricts nanowire length as they intersect. The nanowires are rounded on top and are typically ~0.5 nm tall, but short islands can grow on the wires and increase their height to ~1 nm. With regard to the underlying terrace structure, a 2×7 reconstruction dominates at most coverages, but is only well ordered at low coverage.

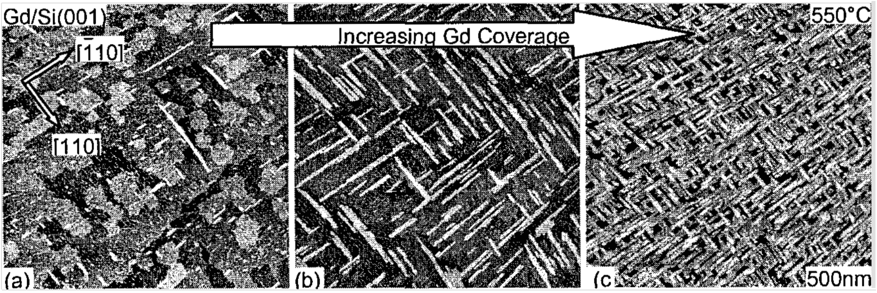

Figure 2: Coverage evolution of Gd silicide nanowire growth on Si(001) at ~550°C

3.2. *Gd/Si(113)*

The nanowires produced by Gd deposition on the Si(113) surface appear to be superior to those produced on Si(001). They preferentially nucleate along step edges and can cross multiple steps with minimal disruption of the nanowire and step edges. This may be due in part to the stability of a highly ordered 2×2 reconstruction found on the surrounding terraces, which hinders nucleation on the terraces. Fig. 3 shows the evolution of nanowire growth with increasing coverage. At the lowest coverage shown in Fig.3a, the nanowires are relatively short and typically cross only one step boundary. Higher Gd coverages result in more densely packed nanowires, where such wires can extend more than 500nm in length. In contrast to the nanowires grown on Si(001), there is not a strong tendency to form bundled nanowires. At the highest coverage shown in Fig. 3c, disordered 3-D islands also appear along the step edges. Such island growth again confirms the higher reactivity of the (113) steps with respect to the terraces.

The dimensions of the nanowires on Si(113) are similar to those found on Si(001), with a higher proportion being greater than 400 nm in length. Also, the islands formed on top of the nanowires can be up to 6nm tall, in contrast to the much shorter islands found on Si(001). With regard to topology, the nanowires on Si(113) are not as rounded as those observed on Si(001). Instead, their cross-sections are triangular, as evidenced by the line profile shown in Fig 5b. The sidewalls of the nanowires are consistent with the low-index (001) and (111) orientations. Occasionally, the (111)-oriented sidewall can be exposed below the plane of the terrace, as is evident in the image and line profile of Fig. 5b. The resulting trench supplies Si to the silicide structure.

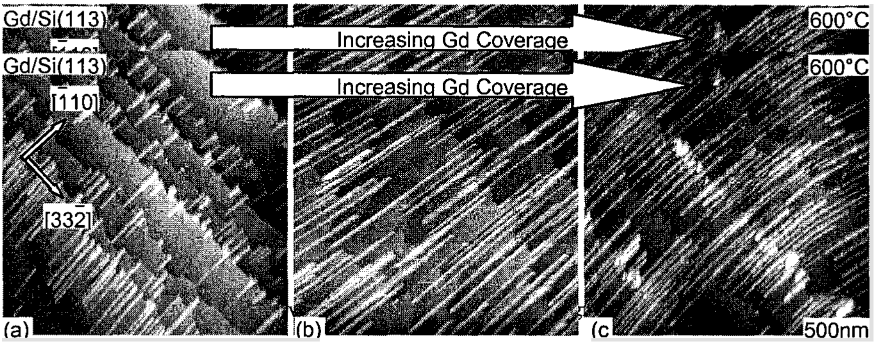

Figure 3: Coverage evolution of Gd silicide nanowire growth on Si(113) at ~600°C

3.3. *Gd/Si(5 5 12)*

Nanowires grown on the Si(5 5 12) surface have a single orientation as does Si(113), but on Si(5 5 12) produce a faceted morphology. As shown in Fig. 4, this faceting results in the rough surface morphology that surrounds the nanowires, which are found along facet edges. The (5 5 12) orientation is apparently not stable after Gd deposition and facets to the nearby (113) plane, which forms the well-ordered 2×2 phase mentioned earlier. To maintain the basal orientation in areas without nanowires, the (113) facets are countered by step bunches. It should be noted that a number of other metals cause faceting to the (113) plane after high temperature annealing (>500°C), including noble metals (Cu, Ag, and Au) and group IV Sn[4,5,6,7] The nanowires for the Gd/Si(5 5 12) system are typically 150 to 300 nm long, 15 to 35 nm wide, and 3 to 6 nm tall. Similar to the Gd/Si(113) system, these nanowires have a triangular cross section with (001) and (111) sidewalls (see Fig. 5c). In addition, the surrounding terrace is consistent with a (113)-oriented facet. Notice that the (111) planes are longer than the (001) planes on the Si(5 5 12) surface in order to maintain the basal orientation.

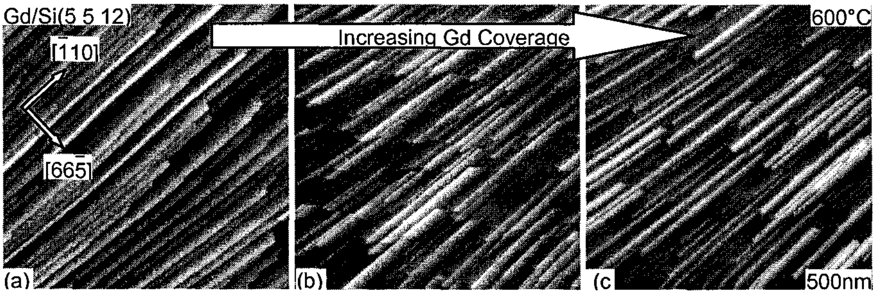

Figure 4: Coverage evolution of Gd silicide nanowire growth on Si(5 5 12) at ~600°C.

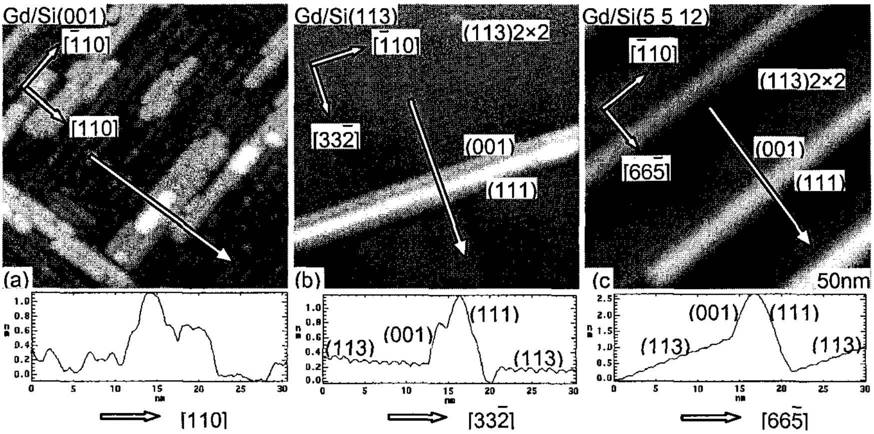

Figure 5: Higher resolution STM images and line profiles of the Gd silicide nanowires on (a) Si(001), (b) Si(113), and (c) Si(5 5 12). A Gd induced 2×2 reconstruction is present on the (113) terraces.

4. Summary

The proposed explanation for the highly anisotropic growth of Gd silicide nanowires on the Si(001) surface concerns the lattice mismatch between the silicide and Si substrate. Assuming that Gd forms the A_1B_2 hexagonal disilicide phase with $a = 0.387$ nm and $c = 0.417$ nm, the lattice mismatch with the Si(001) surface ($a = 0.384$ nm) is (0.96%) along the $[\underline{1}10]$ direction and 8.65% perpendicular to it. The disilicide therefore has a small lattice mismatch along $[\underline{1}10]$ that favors growth in this direction, and a large perpendicular mismatch that limits the nanowire width. Given that the family of high-index surfaces oriented between (001) and (111) have the same lattice constant along $[\underline{1}10]$, this lattice mismatch explanation is consistent with our results. The mismatch perpendicular to the nanowires for (113) and (5 5 12) surfaces is 35% ($b = 0.64$ nm) and 92% ($b = 5.35$ nm), respectively. The very high mismatch for the (5 5 12) surface may explain why Gd induces faceting to the nearby (113) plane in the vicinity of nanowires. In addition, the presence of (001) and (111) sidewalls on these high-index nanowires may be a mechanism for relieving the large stress occurring perpendicular to the growth direction. One feature unique to the high-index surfaces is the presence of well-ordered terraces surrounding the nanowires. It appears that, with appropriate optimization of the sample temperature and Gd coverage, higher quality nanowires with a single orientation can be grown on the Si(113) versus Si(001) surface.

References

1. Y. Chen, D.A.A. Ohlberg, and R.S. Williams, J. Appl. Phys. **91**(2001) pp. 3213-3218.
2. B.Z. Liu, J. Nogami, *Surf. Sci.* **540**(2001) pp. 136-144.
3. A.A. Baski, S.C. Erwin, L.J. Whitman, *Surf. Sci.* **392**(1997) pp. 69-85.
4. P.H. Woodworth, J.C. Moore, A.A. Baski, J. Vac. Sci. Technol. A **21**(2003) pp. 1332-1335.
5. H.H. Song, K.M. Jones, A.A. Baski, J. Vac. Sci Technol. A **17**(1999) pp. 1696-1699.
6. A.A. Baski, K.M. Saoud, K.M. Jones, Appl. Surf. Sci. **182**(2001) pp. 216-222.
7. I. Samanta, M.S. Thesis, Virginia Commonwealth University (2000).

THE EFFECT OF FUNCTIONALIZATION ON DOUBLE-WALLED NANOTUBE MATERIALS

S. J. V. FRANKLAND, G. M. ODEGARD
National Institute of Aerospace, 144 Research Drive,
Hampton, VA 23666, USA

T. S. GATES
NASA Langley Research Center, Mechanics and Durability Branch,
Hampton, VA 23681, USA

A double-walled nanotube is modeled in which the outer nanotube was chemically modified with n-propyl groups. Molecular dynamics simulations demonstrate that the Young's modulus of this system decreases with the degree of functionalization of the outer nanotube. Molecular dynamics simulations of nanotube pull-out also predict that functionalization impedes the slippage of nanotubes during telescopic motion.

1. Introduction

The use of chemically modified (functionalized) carbon nanotubes (NT) in the synthesis of polymer-NT composites is of current interest as a way to improve the composite mechanical properties by enhancing the load transfer between the NT and the surrounding polymer [1]. For composites made with double-walled carbon NTs (DWNT), the DWNTs have an advantage over single-walled NTs in that the outer NT of the DWNT may be cross-linked directly into the matrix, while mechanical stiffness and strength of the inner NT remains unaltered. However, nonfunctionalized multi-walled NTs may fail under axial mechanical load as the inner NTs pull out from one another with a telescopic motion [2-4]. It is assumed that the resistance to this telescopic motion may be increased in DWNT by roughening the outer NT via functionalization so that, not only does the outer NT cross-link into the composite matrix, but also the slippage of the inner NT is inhibited. One possible disadvantage of functionalizing NTs is the possibility that rehybridization will alter the structure to the extent that the NT weakens. As evidence of this, molecular dynamics (MD) simulations of individual functionalized NTs have shown that the functionalization will slightly reduce the axial stiffness of the NT [5,6]. In polymer-NT composites, a similar effect was observed using MD and equivalent continuum modeling [7].

In the present work, the objective is to focus on the NT-to-NT interaction and computationally predict the effect of functionalization on the axial Young's modulus and the telescopic motion of a DWNT under axial deformation. To this end, the outer NT of a DWNT was functionalized by the addition of varying amounts of n-propyl groups. The Young's moduli of these systems were computed from MD, and a description of the method is provided. In addition, MD simulations were performed of the inner NT being pulled through the functionalized outer NT under axial load, and the results were used to explore the effects of the induced surface roughness on relative motion of the NTs.

2. Molecular Modeling

The functionalized DWNT modeled in this work is illustrated in Figure 1. It consisted of an outer (15,15) NT, which has a radius of 1.02 nm, and an inner (10,10) NT of radius 0.68 nm. The outer NT was chemically functionalized with increasing numbers of n-propyl groups, as shown in Figure 1. The DWNT contains 2200 carbon atoms, not including the additional n-propyl groups, and is 5.4 nm long. The molecular system was equilibrated at 300 K with MD using the hydrocarbon Brenner potential to represent the chemical bonding [8]. This potential is capable of including the geometrical effects of rehybridization from the addition of the n-propyl groups. In addition, a SHAKE algorithm was used to constrain the bonding within the n-propyl groups and their bond to the NT. A harmonic valence angle potential describes the angles within the n-propyl units [9]. These additional potentials were superimposed on the Brenner potential to ensure the presence of the n-propyl groups throughout the simulation. The non-bonded interactions between the NTs were represented by the Lennard-Jones potential [10]. The time step during equilibration was 0.1 fs. Unless otherwise stated, the MD simulations were carried out with DL-POLY [11] to which the Brenner hydrocarbon potential had been added.

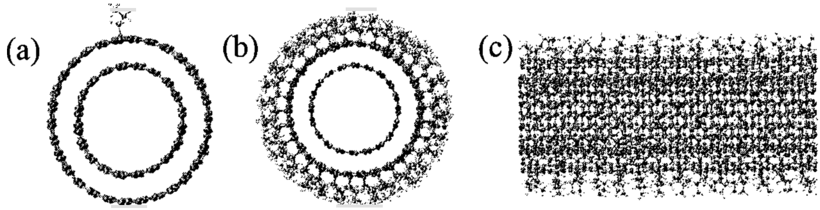

Figure 1. The DWNT with (a) 1 and (b) 210 n-propyl groups, cross-sectional and (c) side-view.

2.1. *Young's Modulus*

The axial Young's moduli (the direction parallel to the nanotube length axis) of the functionalized DWNT systems were determined using an equivalent-continuum modeling approach [12] in which the energies of deformation of the molecular model and an equivalent-continuum model were equated under identical axial deformations. For each MD-defined DWNT structure, the equivalent-continuum models were subsequently defined as a homogeneous, linear-elastic, solid cylinder with length and radii of 3.8 and 1.18 nm, respectively. The energies of deformation of the equivalent-continuum models were calculated using a previously derived expression [13] for a 1% axial strain while allowing a transverse Poisson contraction. The energies of deformation of the molecular models were determined using MD simulations. Initial, undeformed energies of each structure were first determined, followed by the energies of the structures after the 1% axial strain. The deformation was imposed on the model by prescribing the strain on the outer 8 Å of each end of the DWNT. The initial and deformed energies were calculated on the remaining length of the DWNT. The MD computations were performed with Tinker 3.9 [14] using the AMBER force field [9], converting input structures equilibrated with the Brenner potential. The parameters assigned to each atom are similar to those used in a previous study [7]. Before and after deformations, the molecular structures were simulated at 298 K for 3 ps. The energy values used in the Young's moduli calculations were an average over the final 400 fs of each simulation.

2.2. *Pull-through of the Inner Nanotube*

To examine the effect of NT rehybridization on the slippage of the inner NT relative to the outer NT, NT pull-through was modeled with MD guided by results from previous work [15,16]. In the current simulations, an axial load was applied to the inner NT, and its velocity and displacement were monitored as a function of time. These simulations were carried out until the inner NT had traversed at least 0.25 nm, about the length of a carbon ring. The loading rate was 0.0015 nN per 3000 steps at 0.1 fs each.

3. Results and Discussion

3.1. *Young's Modulus*

The computed Young's modulus of nine DWNT structures, with 0, 1, 4, 16, 30, 52, 70, 100, and 210 n-propyl groups added to the outer NT, are shown in Figure 2 as a function of the number (n) of functionalized groups. The size of the symbols in Figure 2 is larger than the standard error based on the average of the 400 time steps over which the Young's moduli were calculated. The percentage of carbon atoms directly bonded to n-propyl groups is included on the upper axis. Figure 2 indicates that there is a clear trend between the Young's moduli of the DWNTs and the number of functionalized groups in that as more groups are functionalized onto the outer NT, the Young's modulus decreases. Considering the nature of the force field that was used [9] and how the molecular structure at the functionalized sites was modeled [7], this trend is most likely due to the changes of the structure and properties of the NT carbon atoms at the sites that are functionalized. When functionalized, the NT carbon atom rehybridizes from sp^2 hybridization to sp^3, which forces the local structure of the NT to distort [7], and causes the local covalent bonding to become more compliant [9]. The results in Figure 2 are consistent with those obtained for a NT/polyethylene composite using a similar modeling approach [7].

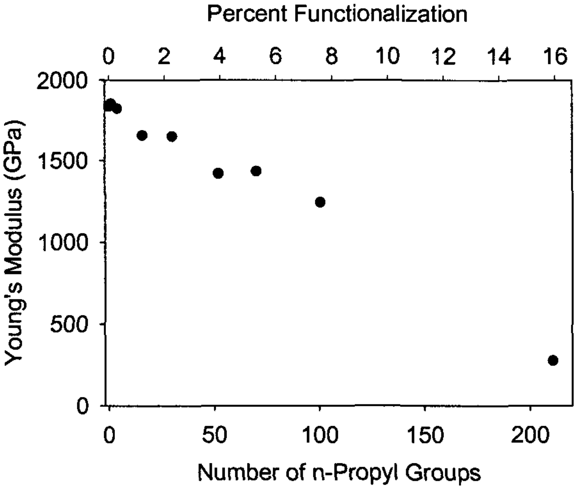

Figure 2 . Young's modulus of the functionalized DWNT.

3.2. *Pull-through*

Rehybridization of the outer NT also affects the degree of relative sliding of the inner NT with respect to the outer NT. In Figure 3, the velocity of the inner NT in response to the applied load and the resultant distance traveled by the inner NT are plotted as a function of time. Since there is no chemical bonding between the NTs, the effects observed in Figure 3 only result from the functionalization induced geometrical changes in the outer NT structure.

In general, the average velocity of the inner NT decreases as the amount of outer NT functionalization is increased. However, the correlation between NT motion and degree of functionalization may involve more than just the number of groups attached to the outer NT. Observing the velocity data in Figure 3(a) (shown for selected systems), the systems with the fastest to slowest moving inner NTs are in the following order: 0 > 1 > 4 > 30≈52 > 16 > 70 ≈ 100 ≈ 210. The distance data in Figure 3(b) gives the following sequence from most to least displaced: 0, 1, 4, 52, 30, 16, 100, 210, 70. These sequences indicate an overall, but imperfect, correlation of functionalization with resistance to NT motion. A second aspect of NT motion is also identifiable in Figure 3(b). In the systems with 16 or more n-propyl groups attached, the inner NT exhibits a form of stick-slip behavior as evidenced by the large increase in slope in the distance plots. In some cases, the NT may experience multiple sticking points, e.g. n = 16 or n = 210.

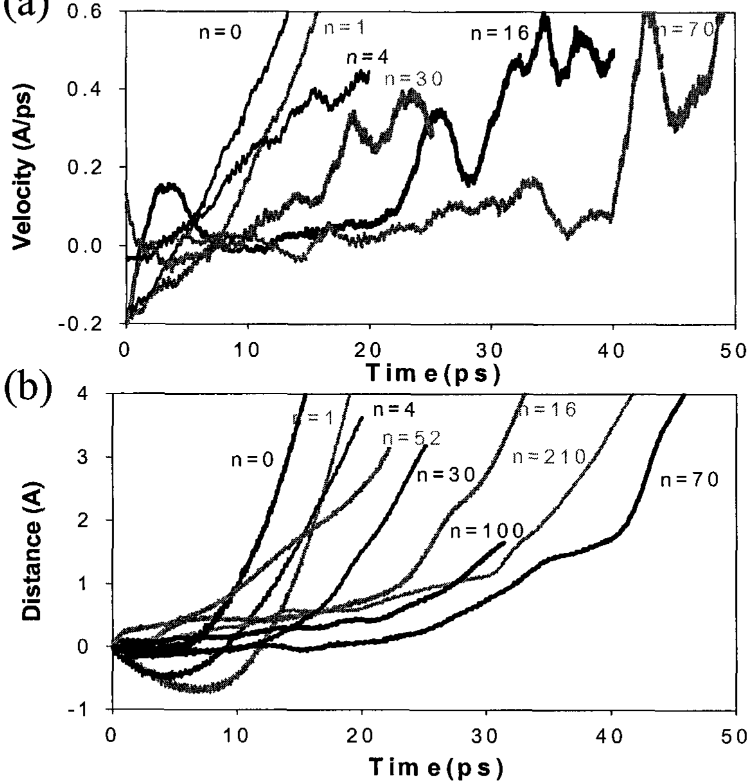

Figure 3. (a) Velocity of and (b) distance traveled by inner NT under axial load.

4. Conclusions

Molecular dynamics, coupled with an equivalent continuum method, have simulated the first-order effects of an n-propyl functionalized double-walled nanotube under axial load. The simulations have modeled the effects of nanotube rehybridization and shown that the axial Young's modulus of a double-walled nanotube decreases with the addition of more n-propyl groups (increased functionalization). The model also predicted that the inner nanotube showed an increased resistance to slippage relative to outer nanotube under axial load as more n-propyl groups were added to the outer nanotube. Results indicate that the effects of the geometrical changes resulting from functionalization of the outer NT may not vary directly according to the number of groups attached.

Acknowledgment

S.J.V. Frankland and G.M. Odegard gratefully acknowledge support from NASA Cooperative Agreement NCC-1-02043 with the National Institute of Aerospace.

References

1. S. B. Sinnott, *J. Nanosci. Nanotech.* **2,** 113 (2002).
2. M.-F. Yu, O. Lourie, M. J. Dyer, K. Moloni, T. F. Kelly and R. S. Ruoff, *Science* **287**, 637 (2000).
3. M.-F. Yu, B.I. Yakobson and R.S. Ruoff, *J. Phys. Chem. B* **104**, 876 (2000).
4. J. Cumings and A. Zettl, *Science* **289**, 602 (2000).
5. D. W. Brenner, O.A. Shenderova, D.A. Areshkin, J.D. Schall and S. J. V. Frankland, *Comp. Mod. Eng. Sci.* **3,** 643 (2002).
6. A. Garg and S. B. Sinnott, *Chem. Phys. Lett.* **295,** 273 (1998).
7. G. M. Odegard, S. J. V. Frankland, and T. S. Gates, AIAA-2003-1701.
8. D. W. Brenner, O. A. Shenderova, J. A. Harrison, S. J. Stuart, B. Ni and S. B. Sinnott, *J. Phys C: Condensed Matter* **14,** 783 (2002).
9. W.D. Cornell, P. Cieplak, C.I. Bayly, I.R. Gould, K.M. Merz, D.M. Ferguson, D.C. Spellmeyer, T. Fox, J.W. Caldwell and P.A. Kollman, *J. Am. Chem. Soc.* **117,** 5179 (1995).
10. M. P. Allen and D. J. Tildesley, *Computer Simulation of Liquids,* Clarendon Press, Oxford, 1987.
11. W. Smith and T. F. Forester, DL-POLY, Council for the Central Laboratory of the Research Councils, Daresbury Laboratory, Warrington, 1996.
12. G. M. Odegard, T. S. Gates, L. M. Nicholson and K. E. Wise, Comp. Sci. Techn. 62, 1869 (2002).
13. G. M. Odegard, T. S. Gates, K. E. Wise, C. Park, and E.J. Siochi, Comp. Sci.Techn. 63, 1671 (2003).
14. J.W. Ponder, TINKER:Software Tools for Molecular Design, Ver. 3.9. Washington University School of Medicine, 2001.
15. S. J.V. Frankland, A. Caglar, D. W. Brenner and M. Griebel, *J. Phys. Chem. B,* **106,** 3046 (2002).
16. S. J.V. Frankland and V. M. Harik, *Surf. Sci. Lett.* **525,** L103 (2003).

SPECTROSCOPY-BASED CHARACTERIZATION OF SINGLE WALL CARBON NANOTUBES

M. NAMKUNG[1], J. S. NAMKUNG[2], B. WINCHESKI[1], J. SEO[3] and C. PARK[4]

[1]NASA Langley Research Center, Hampton, VA, USA 23681
[2]Naval Air Warfare Center, Patuxent River MD, USA 20670
[3]Hampton University, Hampton, VA, USA 23668
[4]National Institute of Aerospace, Hampton, VA, USA 23666

We present the initial results of our combined investigation of Raman scattering and optical absorption spectroscopy in a batch of single wall carbon nanotubes (SWNTs). The SWNT diameters are first estimated from the four radial breathing mode (RBM) peaks using a simple relation of $\omega_{RBM} = 248cm^{-1}nm/d_t(nm)$. The calculated diameter values are related to the optical absorption peaks through the expressions of first interband transition energies, i.e., $E_{11}^S = 2a\gamma/d_t$ for semiconducting and $E_{11}^M = 6a\gamma/d_t$ for metallic SWNTs, respectively, where a is the carbon-carbon bond length (0.144 nm) and γ is the energy of overlapping electrons from nearest neighbor atoms, which is 2.9 eV for a SWNT. This analysis indicates that three RBM peaks are from semiconducting tubes, and the remaining one is from metallic tubes. The detailed analysis in the present study is focused on these three peaks of the first absorption band by determining the values of the representative (n,m) pairs. The first step of analysis is to construct a list of possible (n,m) pairs from the diameters calculated from the positions of the RBM peaks. The second step is to compute the first interband transition energy, E_{11}, by substituting the constructed list of (n, m) into the expression of Reich and Thomsen, and Saito et al. Finally, the pairs with the energies closest to the experimental values are selected.

1. Introduction

The two integer coefficients, (n, m), of the lattice unit vectors of two-dimensional graphite unit cell define the chiral vector and, consequently, the chirality. It has been shown that the major physical properties of SWNTs are determined by the chirality [1, 2], and the determination of the (n,m) pair(s) of a single SWNT (batch of SWNTs) comprises a nearly complete morphology characterization. The (n, m) characterization of carefully prepared SWNT samples has been accomplished by a number of authors in the past [3]. The procedures employed for the previous work begin, first, to examine the radial breathing mode (RBM) Raman peak positions that correspond to the SWNT diameters through a simple expression of $\omega_{RBM} = 248cm^{-1}nm/d_t(nm)$. The diameter of a SWNT, however, is a multi-valued function of (n, m). In addition, one has to allow a reasonable degree of errors in the experiments. Therefore, one normally establishes a list of possible (n, m) pairs by examining the Raman RBM peak positions. The subsequent steps involve detailed analysis to identify the most probable (n, m) pair from the list. This analysis is usually complex and the results can be subjective.

The present study is our first attempt to introduce a new method of determining the most probable pairs of (n, m) representing the chirality distribution in a batch of SWNTs. The unique element of this study is the inclusion of optical absorption spectroscopy. This technique directly measures the energies of interband transitions normally from three absorption bands, i. e., two for semiconducting and one for metallic tubes. In this study the analysis focuses on the details of three peaks in the first absorption band of semiconducting tubes in relation to the corresponding the Raman RBM peaks.

2. Experiments

The SWNT samples used in this study were synthesized by Carbon Nanotechnologies, Inc. through the HiPco process. A drop of SWNTs sonicated in water was deposited on an optically transparent plate and allowed to evaporate. The optical absorption spectra were obtained with a Cray Model 5E to collect data in a wide spectral range. A Digilab Fourier transform infrared (FT-IR) spectrometer with its resolution set to 8 cm^{-1} was used to measure the first absorption band from SWNTs. An AlmegaTM dispersive spectrometer, with a spectral resolution less than 1.8 cm^{-1}, was used with the laser wavelengths of 532 and 785 nm to obtain Raman spectra.

3. Results and Discussion

Fig.1 shows a spectrum obtained from the dispersive Raman spectrometer with an incident laser beam of $\lambda = 758$ nm. A spectrum obtained in this region with the incident laser beam of $\lambda = 512$ nm shows essentially the identical features. From the results in Fig. 1, we consider that those peaks at 268, 237, 232 and 210 cm^{-1} represent the major peaks in the tube diameter distribution of this batch of SWNTs. Using the expression of $d_t(nm) = 248cm^{-1}nm / \omega_{RBM}$, the corresponding tube diameters are calculated to be 0.925, 1.046, 1.069 and 1.187 nm. Applying $E_{11}^S = 2a\gamma / d_t$, the first interband transition energy in semiconducting SWNT, where a is the carbon-carbon bond length (0.144 nm) and γ is the energy of overlapping electrons from nearest neighbor atoms that is 2.9 eV in a SWNT, E_{11} values of 0.903, 0.798, 0.781 and 0.704 eV are obtained from the diameters calculated from the four RBM peaks of Fig. 1.

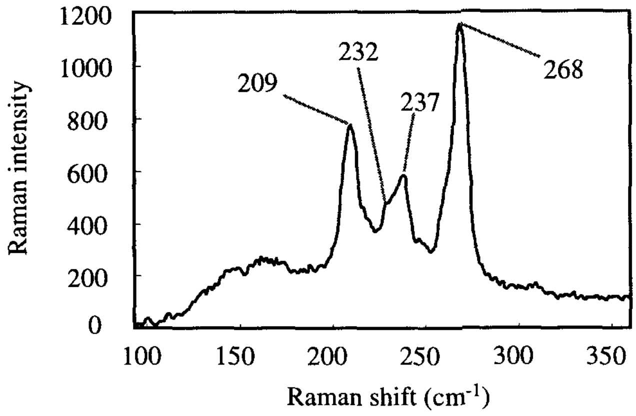

Figure 1. Breathing mode Raman scattering peaks obtained with an incident laser λ = 785 nm.

Fig. 2 shows the first absorption band from the same sample using the FT-IR spectrometer. Three absorption peaks are found at 0.93, 0.84 and 0.8 eV. The absorption peak at 0.84 eV deviates from the computed values of 0.798 eV but those at 0.93 and 0.8 eV agree well with the computed values of 0.903 and 0.781 eV.

Fig. 3 shows the IR absorption spectrum obtained using Cray Model 5E dispersive spectrometer. The spectrum of Fig. 3 provides very useful information, i. e., the range of E_{11}^M , the first transition energy in a metallic tube, which is seen to be between 1.7 to 2.2 eV. This means that the RBM peak at 210 cm^{-1} corresponding to E_{11}^M = $6a\gamma / d_t$= 2. 11 eV is well within the range of E_{11}^M in Fig. 3. Based on this, we conclude that three RBM peaks at 268, 237 and 232 cm^{-1} in Fig. 1 are from the semiconducting SWNTs and the one at 210 cm^{-1} is from the metallic SWNTs.

Using the expression $d_t = (\sqrt{3}/\pi)a\sqrt{n^2 + m^2 + nm}$ and allowing an error range, a list of (n,m) pairs for each RBM peak is constructed. Table 1 provides a list of the calculated parameters for the RBM at 268 cm^{-1} by allowing a 5% error range. Two pairs, (2, 10) and (6, 7), are seen to produce the values of E_{11}^S that are closest to the measured one of 0.93 eV. The actual analysis in this work uses an error range of 15 %. The second column shows the tube diameters corresponding to a given (n, m) pair. The third column provides E_{11} calculated using the expressions by Reich and Thomsen [5], and only the steps of application will be discussed.

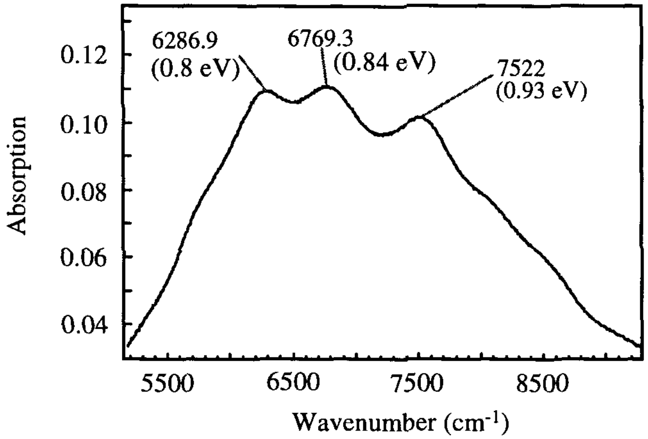

Figure 2. Three peaks in the first optical absorption band. The peak position at 0.84 eV deviates from the calculated value by 0.4 eV, but those of the other two peaks agree well with the calculated values.

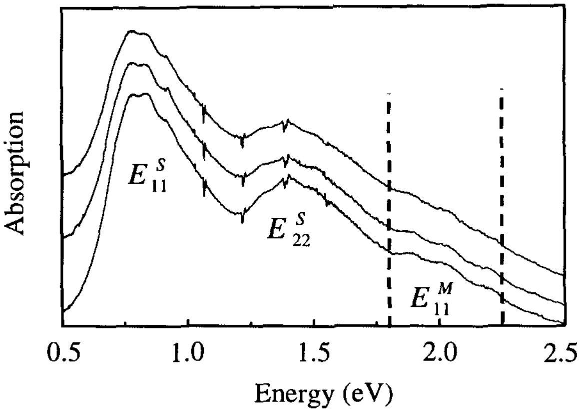

Figure 3. Optical absorption spectra collected from the SWNT sample at three different locations. These spectra provide important information on the range of E_{11}^{M} that is indicated by dotted vertical lines.

The allowed electron wave vector component perpendicular to the SWNT axis, k_T, is discrete due to the periodicity along the circumference, meanwhile that along the SWNT axis, k_z, is continuous. For given values of $\pm k_T$, the values of k_zs for which dE/dk_z vanishes, causing a Van Hove singularity in the density of states (DOS), are calculated. Two values of k_z result in two different energy values of singularity peaks for any SWNTs with an axial symmetry that is reduced from that of the armchair configuration, i. e., $n = m$. These two energies result in a split DOS peak structure. In the present work the energies for the split peaks are averaged since the experimental optical absorption peaks do not resolve the fine structures formed by the transitions among the split peaks. The values of E_{11} are calculated by using the nonzero minimum of k_T and the results are listed in the third column of Table 1. The fourth column lists the E_{11} values computed using $E_{11}^S = 2a\gamma / d_t$ and $E_{11}^M = 6a\gamma / d_t$ for semiconducting and metallic SWNTs, respectively, as given by Saito et al. We notice that for semiconducting SWNTs with, $n - m \neq 3q$, where q is an integer, the values of column 3 and 4 agree well. For metallic SWNT, satisfying the condition $n - m = 3q$, there is slight difference between the values of columns 3 and 4. As discussed earlier, the RBM peak at 268 cm^{-1} is identified as that from semiconducting SWNT, and, according to the results summarized in Table 1, (6, 7) is the most probable pair of (n, m) for the SWNTs producing this RBM peak.

Continuing the steps of analysis with the RBM peak found at 237 cm^{-1}, we find three pairs (n, m) resulting in E_{11} values close to the measured one of 0.84 eV as summarized in Table 2. The results for the RBM peak at 232 cm^{-1} are shown in Table 3. As clearly seen in these tables, several pairs of (n, m) result in E_{11} very close to the experimentally obtained value for a given RBM peak. It is therefore necessary to be able to analyze the second optical absorption band

Table 1. List of (n, m) pairs corresponding to the tube diameters within 5% of 0.925 nm computed from the RBM peak at 268 cm^{-1}. The third column shows the smallest E_{11} calculated for (n, m) using the expression by Reich and Thomsen. The fourth column lists E_{11} calculated using the expression by Saito et al. The pair (6, 7) gives the computed E_{11} value that is closest to the experimental values of 0.93 eV. The other pair (2, 10) is seen to produce a second closest E_{11} obtained using the expressions of (*) Reich and Thomsen, and (*) Saito et al. See text for more details.

n, m	diameter(nm)	E_{11} (eV)*	E_{11} (eV)**
0, 12	0.953	2.622	2.629
1, 11	0.952	0.912	0.915
2, 10	0.884	**0.944**	**0.945**
2, 11	0.963	2.284	2.602
3, 10	0.936	0.891	0.892
4, 9	0.916	0.91	0.912
5, 8	0.902	2.71	2.778
6, 7	0.895	**0.93**	**0.933**
6, 8	0.966	0.862	0.865
7, 7	0.963	2.539	2.602

Table 2. List of three (n, m) pairs for the RBM peaks 237 cm^{-1} that produce the E_{11} values close to the experimental value of 0.84 eV.

n, m	diameter(nm)	E_{11}(eV)	E_{11} (eV)
1, 12	0.995	0.839	0.84
5, 9	0.976	0.854	0.87
6, 8	0.966	0.862	0.865

Table 3. List of three (n, m) pairs for the RBM peaks 232 cm^{-1} that produce the E_{11} values close to the experimental value of 0.8 eV.

n, m	diameter(nm)	E_{11}(eV)	E_{11} (eV)
2, 12	1.041	0.802	0.802
5, 10	1.05	0.794	0.795
7, 8	1.03	0.807	0.809

for E_{22}^{S} to narrow down to a single most probable pair of (n, m) for each semiconducting SWNT RBM peak. Nevertheless, the critical element is to gain better understanding of the factors affecting the measurements, such as the effect of intertube interaction in a batch or bundles of SWNTs, which is estimated to increase the RBM peak position by as much as 10% from that of isolated tubes [6].

4. Summary and Conclusion

The results of present study clearly demonstrate that the feasibility of developing a simple method characterizing the representative (n, m) pairs of a batch of SWNT samples by combining the techniques of Raman scattering and IR absorption. To identify the true (n, m) pairs representing a batch of SWNTs, more progress in understanding of the effects of intertube interaction on the experiments and other potential factors is necessary.

References

1. See, for example, Carbon nanotubes, ed. Mildred Dresselhaus, Gene Dresselhaus and Phadeon Avon, Springer (Heidelberg, 2001).
2. R. Saito, G, Dresselhaus and M. S. Dresselhaus, Physical Propeties of Carbon Nanotubes, Imperial College Press (London, 2001).
3. A. Jorio et al., Phys. Rev. Lett. **86**, 1118 (2001).
4. R. Saito, G, Dresselhaus and M. S. Dresselhaus, Phys. Rev. B. **61**, 2981 (2000).
5. S. Reich and C. Thomsen, Phys. Rev. B. **62**, 4273 (2000).
6. Henrad et al., Phys. Rev. B. **64**, 205403 (2001).

ASSEMBLY AND APPLICATION OF CARBON NANOTUBE FIBRILS WITH CONTROLLED AND VARIABLE LENGTHS BY DIELECTROPHORESIS

JIE TANG†
Department of Physics and Astronomy, University of North Carolina, Chapel Hill, NC 27599, USA
National Institute for Materials Science, 1-2-1 Sengen, Tsukuba, Ibaraki 305-0047, Japan

GUANG YANG, JIAN ZHANG, HUAIZHI GENG, BAO GAO, LU-CHANG QIN, OTTO ZHOU
Department of Physics and Astronomy, University of North Carolina, Chapel Hill, NC 27599, USA

ORLIN D. VELEV
Department of Chemical Engineering, North Carolina State University, Raleigh, NC 27695, USA

In this paper we show that dielectrophoresis can be utilized as a general approach for guided-assembly of hierarchical structures of one-dimensional nano-materials. As a demonstration, pre-formed carbon nanotubes (CNTs) were assembled into sub-micron diameter fibrils anchored on a metal tip by dielectrophoresis. This method affords fine control of the fibril length and the potential for parallel processing. The CNTs within the fibril are bonded by van der Waals forces and are aligned along the fibril axis. The fibrils with 1~20 μm in length are sufficiently stiff for use as scanning probe microscope probes. Longer fibrils have also been drawn from the liquid. The fibrils are also stable electron field emitters.

1. Introduction

Carbon nanotube is a very good one-dimensional material. Carbon nanotubes have large aspect ratios, very small diameters, excellent mechanical and electronic properties [1]. They are hopeful to be the high resolution scanning tunneling microscope (STM) probes [2-7]. Until now, there have been many attempts to make carbon nanotube-based STM probes. The earlier approach is to pick and stick a multiwalled carbon nanotube bundle to the tips under an optical microscope [1] and electron microscopes [2,3,6]. With the chemical vapor deposition technique, important advances have been made to grow carbon

---

email: tang.jie@nims.go.jp

nanotubes on a catalyst-deposited metal tip surface [4,5]. Recently, electric field has been found that it is useful to align the carbon nanotubes [7].

It is highly desirable to develop a method that is easy to handle, a batch process, controllable and giving good alignment. Here we report an efficient approach for guided-assembly of carbon nanotubes. In this method, we use electrophoresis to assemble carbon nanotubes on the metallic tip with an applied alternating electrical field.

2. Experimental

The starting material is single-walled nanotubes and multi-walled carbon nanotubes. Single-walled carbon nanotube (SWNT) bundles were synthesized by laser ablation, purified to remove the impurity phases and processed to shorten the bundles by sonication in acid solution. The final material has about 90% SWNTs, bundle diameter 30 ~ 50 nm, and bundle length 0.5 ~ 4 μm with individual tubule diameter of about 1.4 nm. The multi-walled carbon nanotubes are prepared by microwave plasma-enhanced chemical vapor deposition and they aligned very well [8].

In the dielectrophorestic process, we use an alternating current circuit and a very sharp tungsten (W) tip. The suspension solution made of water and ETOH. The tungsten tip is used as one electrode and a small metal ring as the other. The two electrodes were mounted on separate translation stages under an optical microscope and were connected to a function generator. A droplet of the suspension was first placed on the metal ring, and an AC field was then applied to the electrodes. To begin the deposition, the tungsten electrode was moved to touch the surface of the suspension and after a fixed dwell time under the electric field, the tungsten electrode was moved away from the liquid surface to stop the deposition. By controlling the processing parameters, carbon nanotubes fibrils on the tungsten tip ranging from 1 μm to greater than 1 cm were fabricated.

3. Results and Discussions

3.1 Single-walled carbon nanotube fibrils

Figure 1 shows a single-walled nanotube fibril is on the apex of a very sharp tungsten tip. The surface of the fibril is very smooth. The diameter of the fibril is about 100 nm, but at the end of the fibril the diameter reduced to about 20 nm.

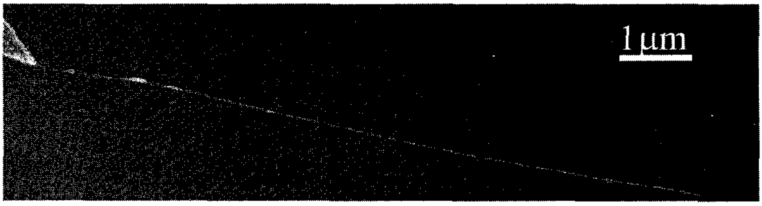

Fig. 1 Image of a single-walled carbon nanotube fibril on tungsten tip.

The controlled assembly of individual CNTs reported here results directly from the interaction between the polarizable CNTs and the applied AC field. The CNTs in water were first polarized and aligned along the electric field direction due to the force acting upon the induced dipole moments. When the first group of CNTs deposited to the apex of the W tip, they became the new outermost surface of the electrode where the next CNT group is deposited. With continuous migration and deposition of CNTs the structure grew along the field line towards the counter electrode [9-12].

In the electrophorestic process, when an AC field was applied, by controlling the carbon nanotube concentration of the suspension and the angle of tungsten tip entering the solution, the angle of alignment between the carbon nanotube fibril and the tungsten tip is determined. The distribution of the alignment angle of the carbon nanotube fibrils is shown in Fig. 2. The angles for most of them are less than 10 degrees. This process is simple and has controlled to make the carbon nanotube STM probes.

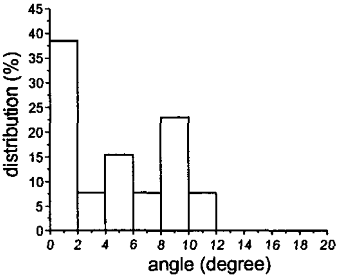

Fig. 2 Distribution of alignment angle between single-walled carbon nanotube fibril and tungsten tip.

3.2 Multi-walled carbon nanotube fibrils

With the same electrophorestic method, we can obtain not only a single-walled carbon nanotube fibril but also a multi-walled carbon nanotube fibril on the tungsten tip, as shown in Fig. 3(a). The fibril is a bundle and is coated on the apex of the tungsten tip. The length is less than 10 μm and the diameter about 100 nm. The fibril is aligned along the electrical field direction. Figure 3(b) shows the magnified area of the end of the fibril. It is observed that there are some protrusions of the individual multi-walled carbon nanotubes along the surface of the CNT fibril. This is because the multi-walled nanotubes grown from chemical vapor deposition are often curved and have kinks. The important factor to get the smooth surface of the carbon nanotube fibrils is to use high quality starting material.

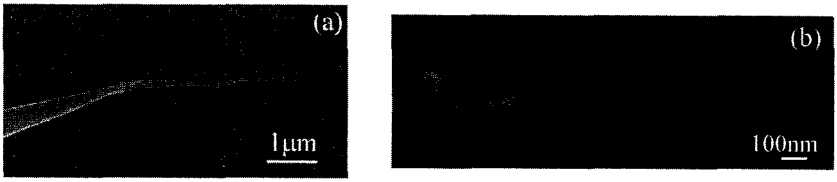

Fig. 3 (a) Image of a single-walled carbon nanotubes fibril on tungsten tip; (b) Image of the end of the fibril.

3.3 Application of carbon nanotube fibrils

The fibrils are stable electron field emitters. A stable emission current of 5 μA has been obtained from a single CNT fibril. From the current-voltage curve, we found that we did get field emission from CNT. The current can be up to 8 μA. From the current-time measurement, although the current fluctuates a little, in the whole range, the current stability is very good. We have kept the stable current more than 25 hours without break down.

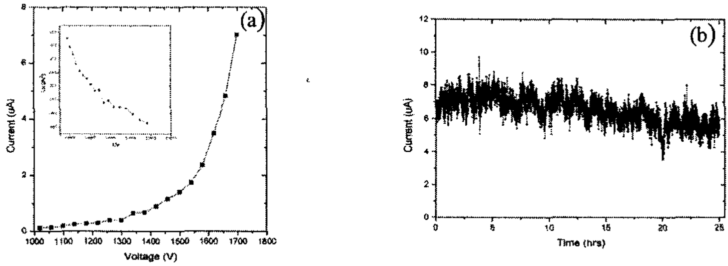

Fig.4 Field emission measurement of a single-walled carbon nanotube fibril on tungsten tip. (a) The current dependence on applied voltage to show the field emission property of carbon nanotube fibrils; (b) The current dependence on time to show that the carbon nanotube fibrils are stable electron field emitters.

Fig. 5 are the field emission images of carbon nanotube fibrils under different voltages from 1400 V to 1900 V recorded on a phosphor screen. A single emission spot was observed at all operating voltages. The intensity of the spot increases as the applied voltage increasing.

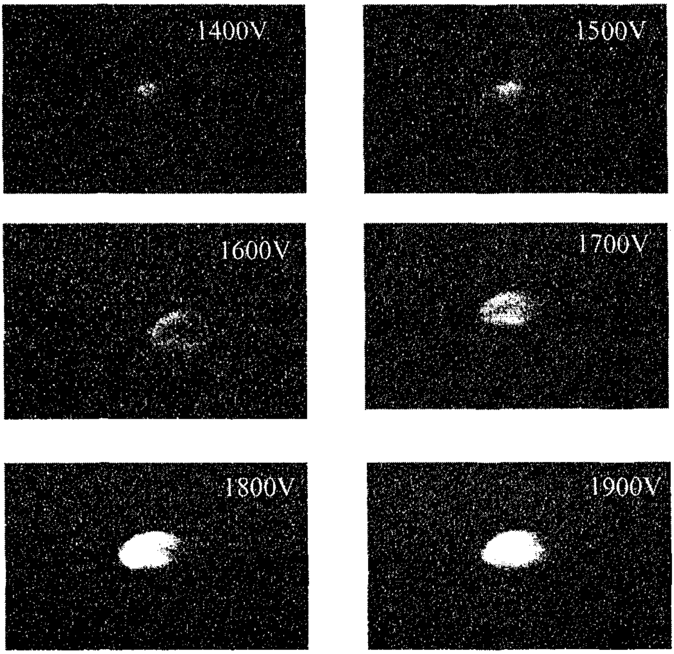

Fig. 5 Field emission images of carbon nanotube fibrils under different voltages from 1400 V to 1900 V at a phosphor screen.

4. Conclusions

We have developed an electrophorestic method to assemble carbon nanotube fibrils. The process is a liquid-phase deposition process at room temperature and it is very simple, reproducible, easy to control and can be automated for a high throughput parallel process. From the characterization, we found the fibril is composed of bundles of nanotubes and the nanotubes within the fibril are bonded by van der Waals forces and they are aligned along the fibril axis. The fibrils are good to use not only as scanning tunneling microscope probes but also as the stable electron field emitters.

Acknowledgments

This work was partially supported by grants from NASA (NAG-1-01061) and the Office of Naval Research (N00014-91-1-0597). The current address of B.G. is Applied Nanotechnologies, Inc., 308 West Rosemary St. Chapel Hill, NC 27516.

References

1. J. Hu, T.W. Odom, and C.M. Lieber, *Acc. Chem. Res.* **32**, 435 (1999).
2. H. Dai, J. H. Hafner, A. G. Rinzler, D. T. Colbert, and R. E. Smally, *Nature* **384**, 147 (1996).
3. S. Wong, E. Joselevich, A. Woolley, C. Cheung, and C. Lieber, *Nature* **394**, 52 (1998).
4. J. H. Hafner, C. L. Cheung, and C. M. Lieber, *Nature* **398**, 761 (1999).
5. J. Hafner, C. Cheung , and C. M. Lieber, *J. Am. Chem. Soc.* **121**, 9750 (1999)
6. H. Nishijima, S. Kamo, S. Akita, Y. Nakayama, S.C. Minne, T. Hunt, and C. F. Quate, *Appl. Phys. Lett.* **75**, 3566 (1999).
7. X.Q. Chen, T. Saito, H. Yamada, and K. Matsushige, *Appl. Phys. Lett.* **78**, 3714 (2001).
8. C. Bower, O. Zhou, W. Zhu, D.J. Werder, and S. Jin, *Appl. Phys. Lett.* **77**, 17 (2000).
9. L.X. Benedict, S.G. Louie, and M.L. Cohen, *Phy. Rev. B* **52**, 8541 (1995).
10. T.B. Jones, *Electromechanics of Particles*. Cambridge: Cambridge Univ Press. 1995.
11. K. Yamamoto, S. Akita, and Y. Nakayama, *J. Phys. D: Appl. Phys.* **31**, L34 (1998).
12. J. Tang, B. Gao, H.Z. Geng, O.D. Velev, L.-C. Qin, and O. Zhou, *Adv. Mater.* **15**, 1352 (2003).

THE MAGNETISM OF THE POLYMERIZED C_{60} MATERIALS

ANTONIS N. ANDRIOTIS
Institute of Electronic Structure and Laser, Foundation for Research and Technology-Hellas, P.O. Box 1527, Heraklio, Crete, Greece 71110

MADHU MENON
Department of Physics and Astronomy, University of Kentucky, Lexington, KY 40506-0055, U.S.A.

We present an analysis of the common features found in the magnetic properties of C_{60}-based polymers (as obtained in our recent work: Phys. Rev. Lett., **90**, 026801 (20003)) and the magnetic properties reported in other non-metallic ferromagnets (carbon- and/or non-carbon-based). Our analysis indicate that the magnetic phase of the C_{60}-based polymers appear to be a sub-class of a new class of non-metallic ferromagnetic materials appearing with the same features that lead to a common formation mechanism of ferromagnetism.

1. Introduction

The recent discovery of magnetic phase of the polymerized C_{60} materials [1,2], characterized by high Curie temperatures and small saturation magnetization values, has attracted the research interest from both theoretical and technological point of view. A pronounced characteristic of this new magnetic material is the experimentally found narrow windows, defined by pressure and temperature, within which magnetic C_{60}-based polymers can be found. These windows are approximately at the graphitization limit of the C_{60}-based polymers i.e., the limit at which the fullerene cages begin to break down, thus, justifying the assumption (see below) that the magnetic phase is associated with the appearance of structural defects in an otherwise (and experimentally verified) crystalline structure of these materials. It has also been verified that the magnetism of these samples is not influenced by the presence of the impurities. The determination of any structural differences, however, between magnetic and non-magnetic samples by conventional characterization methods has not been possible yet [1-3].

The explanation of the observed magnetism in these C_{60}-based polymers is a very challenging two-fold issue [4]. First, an explanation of the existence of unpaired spins is needed. This has to be followed by a theoretical justification of the the origin of the long range correlation that couples the unpaired spins into a ferromagnetic alignment.

As Makarova *et al.*, observed [3], the magnetism in the polymerized C_{60}-polymers cannot be seen independently of the graphitic magnetism. Other magnetic graphite-based magnetic materials discovered include, for example, the activated carbon fibers [5], the fluorinated graphite [6], the carbon foam [7], the TDAE-C_{60} [8], etc. At the same time, other organic and non-metallic magnetic materials have been discovered among which we mention the p-nitrophenyl-nitronyl-nitroxide (p-nnn) [9], the hexaborites [10-13], the oxides of rock-salt structure [14], the cation-substituted oxides (i.e. Co substituted cations in ZnO and TiO_2) [15], etc.

Based on a series of theoretical calculations, we have recently proposed a model for explaining the magnetic phase of the polymerized-C_{60} materials [4]. The basic assumption of our model is the existence of vacancies in an otherwise pristine crystalline structure as intimated by the experimental results of Makarova and collaborators [1-3]. Concurrently with our model, another vacancy-based model has also been reported in an effort to explain the magnetic phase of oxides of rock-salt structure (i.e., CaO) [14]. This work provided the necessary motivation for us to explore to see if such a property can be used in justifying the appearance of magnetism in the materials referred to in the above. A careful study of both classes of non-metallic magnetic materials, i.e., the carbon-based and the non-carbon based ones referred to in the above seem to reveal some common underlying features relevant to the nature of the associated magnetism in these materials. In the following discussion we will present our conclusions of such a study in an attempt to explain the magnetic phase of the polymerized-C_{60} materials.

2. Common Features of Carbon- and Non-Carbon-Based Non-Metallic Ferromagnets

The most pronounced common features in the non-metallic (carbon-based and non-carbon-based) magnetic materials are found to be the following:

- The presence of defects in an otherwise crystalline structure
- The development of significant charge transfer
- The existence of a degenerate ground state, and
- The presence of a resonant ground state

In the present work, the term "defect" is ascribed to any type of point and/or structural defects including vacancies [16], edge states [17], substitutional impurities [15], Stone-Wales defects in graphite-based materials [18], orientational changes (as for example among the C_{60} molecules in the C_{60}-based polymers) [8], adsorbed adatoms [19] etc. The role of the defects appear to be multiple. Firstly, they provide unpaired electrons and help in their delocalization. Secondly, they break locally the symmetry of the crystalline structure. This has, as a consequence, the development of intra-molecular charge and spin density transfers which results in the triplet ground state becoming energetically most favorable. It is worth mentioning that in carbon-based materials the defects are developing conditions found in the various levels of the proposed McConnell model [20-22] and create the *starred* and *un-starred* C-atoms (non Kekulè structures) extensively discussed within the Ovchinnikov's spin-polarization model [23].

The presence of defects seem to have an additional role. That is, they promote the triplet ground state so that it becomes comparable in energy with the singlet one. This is facilitated by a sufficient charge transfer which provides the required energy. In some cases this process is facilitated by the existence of a resonant ground state (as for example in the case of the TDAE-C_{60} [8] and the p-nnn [9] materials). Thus, it is observed that the formation of defects followed by charge and spin transfer result in a degenerate ground state. The flat bands at the Fermi level can be associated with this and in this sense allows us to relate the magnetism in the systems referred to in the above with the materials exhibiting the flat band magnetism [24,25].

3. Magnetic C_{60} Polymers

We have used the tight-binding molecular dynamics (TBMD) method [26] to study the two-dimensional (2D) rhombohedral-C_{60} (Rh-C_{60}) (Fig. 1a), the 2D-tetragonal system (Fig. 1b) and two types of one-dimensional (1D) C_{60}-polymers (Figs. 1c and 1d). The 2D and one of the 1D systems contain sp^2 and sp^3 bonded C-atoms, the latter originating from the formation of 2+2 cycloaddition mechanism linking the C_{60} molecules. The other 1D system contains only sp^2 bonded C-atoms (Fig. 1d). All these systems are of infinite size and were studied at the Hubbard-U level of approximation of the electron-electron (e-e) correlations [26]. More detailed and accurate information was obtained by performing ab initio calculations [27] on a C_{60}-C_{60} dimer with and without defects. According to our extensive study, the systems studied exhibit the following properties [4]:

- The introduction of defects (vacancies) provides additional unpaired electrons. This is in agreement with recent reports [8, 16-18, 28].

- The defect-free polymers do not exhibit magnetic ground state. For a magnetic ground state to appear the e-e correlations have to have a considerable value for all systems.
- When vacancies are introduced (one vacancy per C_{60} molecule), then a ferromagnetic (FM) ground state appears favorable for the systems that include sp^3 bonded C-atoms in the presence of small e-e correlations (much smaller than that required in the defect-free systems). The system for which the FM ground state appears more easily attainable is the defected-Rh-C_{60}. It is worth noting that the presence of defects in the 1D-system exhibiting only sp^2 bonding for all C atoms does not lead to its attaining a FM ground state (as compared to its corresponding defect-free state). All these findings are in very good agreement with the experimental reports [1, 2].
- The ground state of the defected-Rh-C_{60} is doubly degenerate. This is not the case for the 2D-tetragonal system.
- The defected-Rh-C_{60} system exhibits flat bands near the Fermi energy.
- The defected-Rh-C_{60} system exhibits intra-molecular charge transfer which leads to an accumulation of 0.5 electrons in the region of each cycloaddition bond and a corresponding accumulation of positive charge (of 0.5 electrons) in the region of each vacancy. This charge transfer develops a large electric dipole moment of 2.264 Debye per C_{60} molecule).

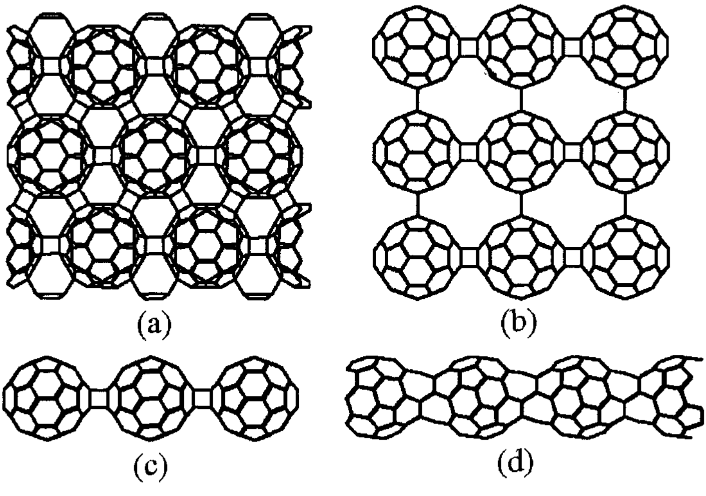

Figure 1. Various 2-D and 1-D polymeric solids formed from C_{60}. All structures are fully relaxed using the TBMD method. (a)-(c) contain mixed sp^2 and sp^3 bonded carbon atoms. Linear C_{60} polymer with only sp^2 bonding is shown in (d).

4. Discussion and Conclusions

It is apparent from Secs. II and III that the 2D-Rh-C_{60} exhibits all the main features of the non-metallic ferromagnets (carbon- or non-carbon-based). It appears that the presence of unpaired electrons (in the sp^3 orbitals) is a necessary condition for the appearance of the magnetic phase in the C_{60}-based polymers. However, this condition is not sufficient. In order for these unpaired spins to couple in a ferromagnetic alignment they need a FM-coupling-unit (FCU). This is provided by the defects which act via a multilevel process. The essential step in this process appears to be the development of a significant charge transfer which should be adequate to promote the triplet ground state so that it is now degenerate with the singlet one, the latter becoming energetically more favorable in the presence of e-e correlations. The large electric dipole moments that are developed help in this direction. At the same time the defects provide additional unpaired electrons and may act as a de-localizer of the existing unpaired electrons.

In conclusion, although the s-d ferromagnetism cannot be ruled out, the magnetic phase of the C_{60}-based polymers seems to be a sub-class of a new class of non-metallic ferromagnetic materials which appear with the same features which lead to a common formation-mechanism of ferromagnetism.

Acknowledgments

The present work is supported through grant by EU-GROWTH research project AMMARE (G5RD-CT-2001-00478), NSF (ITR-0221916), DOE (00-63857), NASA (00-463937), and the Kentucky Science & Technology Corporation (03-60214).

References

1. T.L. Makarova, B. Sundquist, R. Hohne, P. Esqulnazi, Y. Kopelevich, P. Scharff, V.A. Davidov, L.S. Kashevarova and A.V. Rakhmanlna, Nature **413**, 716 (2001).
2. T.L.Makarova in *Studies of High-T_c Superconductivity*, vol. 44-45, Ed. by A.Narlikar, abstract cond-mat/0207368.
3. T.L. Makarova, Elsevier Science, (in print) (2003).
4. A.N. Andriotis, M. Menon, R.M. Sheetz and L. Chernozatonskii, Phys. Rev. Lett. **90**, 026801 (2003).
5. Y. Shibayama, H. Sato and T. Enoki, Phys. Rev. Lett. **84**, 1744 (2000).

6. M. Panich, A.I. Shames and T. Nakajima, J. Phys. Chem. Solids **62**, 959 (2001).
7. K. Umemoto, S. Saito, S. Berber and D. Tomanek, Phys. Rev. B **64**, 193409 (2001).
8. B. Narymbetov, A. Omerzu, V.V. Kabanov, M. Tokumoto, H. Kobayashi and D. Michailovic, Nature **407**, 883 (2000).
9. K. Awaga and Y. Maruyama, Chem. Phys. Lett. **158**, 556 (1989).
10. D.P. Young , Nature **397**, 412 (1999).
11. K. Matsubayashi, M. Maki, T. Tsuzuki, T. Nishioka and N.K. Sato, Nature **420**, 143 (2003).
12. D.P. Young *et al.*, Nature **420**, 144 (2003).
13. R. Monnier and B. Delley, Phys. Rev. Lett. **87**, 157204 (2001).
14. I.S. Elfimov, S. Yonoki and G.A. Sawatzky, Phys. Rev. Lett. **89**, 216403 (2002).
15. Y. Matsumoto *et al.*, Science **291**, 854 (2001).
16. M. Hjort and S. Stafstrom, Phys. Rev. B **61**, 14089 (2000).
17. K. Harigaya, Chem. Phys. Lett. **340**, 123 (2001).
18. Y.-H. Kim, J. Choi, K.J. Chang and D. Tomanek, Phys. Rev. B **68**, 125420 (2003).
19. P.O. Lechtinen, A.S. Foster, A. Ayuela, A. Krasheninnikov, K. Nordlund and R.M. Nieminen, Phys. Rev. Lett. **91**, 017202 (2003).
20. H.M. McConnell, J. Chem. Phys. **39**, 1910 (1963).
21. H.M. McConnell, Proc. R.A. Welch Found. Chem. Res. **11**, 144 (1967).
22. R. Breslow, B. Jaun, R.Q. Kluttz and C-.Z. Xia, Tetrahedron **38**, 863 (1982).
23. A.A. Ovchinnikov and I.L. Shamovsky, J. Mol. Structure (Theochem) **251**, 133 (1991).
24. H. Tasaki, Prog. Theor. Phys. **99**, 489 (1998).
25. A. Mielke, J. Phys. A **24**, L73 and 3371 (1991).
26. A.N. Andriotis and M. Menon, Phys. Rev. B **57**, 10069 (1998).
27. Gaussian 98, Revision A.6, M. J. Frisch Gaussian, Inc., Pittsburgh PA, (1998).
28. K.Yoshiwaza, K.Okahara, T.Sato, K.Tanaka and T.Yamade, Carbon **32**, 1517 (1994).

BUILDING HIGH PERFORMANCE MAGNETIC MATERIALS OUT OF GAS PHASE NANOCLUSTERS

C. BINNS, S. H. BAKER, S. LOUCH, S. C. THORNTON
Department of Physics and Astronomy, University of Leicester, Leicester LE1 7RH UK

It has been known for over a decade that free magnetic nanoclusters display novel properties including enhanced magnetic moments in ferromagnetic metals, ferrimagnetism in antiferromagnetic metals and the appearance of magnetism in non-magnetic metals. A contemporary challenge is to build intrinsic novel behaviour into macroscopic materials. We have investigated the magnetic behaviour of supported Fe and Co nanoclusters from the simplest possible system of isolated clusters adsorbed on substrates in UHV to dense interacting assemblies. XMCD measurements of exposed mass-selected Fe clusters in the size range 180-700 atoms deposited in situ onto HOPG substrates reveal enhancements in both orbital and spin moments relative to the bulk. Increasing the surface density of Fe clusters to induce a significant interaction however reduces the orbital moment to its small bulk value. Coating the exposed Fe clusters with Co increases the spin moment still further without significantly changing the orbital moment. The anisotropy in isolated Fe and Co clusters embedded in Ag matrices is uniaxial with the anisotropy axes randomly oriented in three dimensions. Thick cluster films adopt a domainless correlated super-spin glass magnetic configuration resulting from the frustration between the inter-cluster exchange coupling and random anisotropy. This state is magnetically soft, which is a useful attribute in high-moment films.

1. Introduction

In the last decade a great deal of attention has been focused on the study of gas-phase magnetic nanoparticles containing a few to a few thousand atoms [1]. Partly this is due to a fundamental interest in nanomagnetism as gas-phase clusters afford the opportunity to study how magnetism develops in matter as it is built atom by atom from the monomer. It has been known for a decade that free clusters have novel magnetic properties such as a significant increase in the magnetic moment per atom relative to the bulk [2, 3], the appearance of magnetism in paramagnetic metals [4] and ferrimagnetism in antiferromagnetic materials [5]. It has since been discovered that substantially increased magnetic moments are retained in 3d transition metal clusters when they are deposited onto a surface [6-9] or embedded in a matrix [10].

In addition there is a growing realisation of the enormous potential of cluster-assembled films in the production of high-performance magnetic materials. A determined attempt to produce technologically useful materials using clusters raises the question of the macroscopic magnetic behaviour of films of strongly interacting clusters. The equipment in most of the established cluster laboratories enables the clusters to be co-deposited in conjunction with an atomic beam from a conventional MBE source so that they can be embedded in a matrix of choice. The technique produces granular films in which there is independent control over the grain size and volume fraction. In addition it enables the manufacture of granular mixtures of miscible materials [11], for example Fe grains in Co matrices, which are important for applications and cannot be produced by other fabrication techniques.

2. Experimental

2.1. *Cluster Production*

All Fe and Co cluster samples reported here were produced by a UHV-compatible gas aggregation source described previously [12]. Briefly clusters produced by thermal evaporation of the metal into a cooled He bath gas are ionised and mass-selected with a quadrupole filter that can pass masses up to 350,000 amu, corresponding to Fe clusters containing up to ~6,000 atoms (5 nm diameter). Lenses and steering plates beyond the mass filter focus and guide the ionised clusters onto the substrate. For the *in situ* experiments at synchrotron radiation facilities (ESRF, Grenoble, France and super-ACO, Orsay, France) the source was coupled directly to the endstations on the beamlines and clusters were deposited onto substrates in UHV conditions. During a typical deposition the substrate chamber pressure would rise to around 10^{-5} mbar of He but the partial pressure of contaminant gases mainly CO was in the 10^{-11} mbar region.

2.2. *X-Ray Magnetic Circular Dichroism (XMCD)*

This technique exploits the dichroism in L-edge (for transition metals) X-ray absorption when the angular momentum of circularly polarised X-rays is changed from parallel to anti-parallel alignment with the sample magnetisation. The geometry of the experiment is illustrated in Fig. 1 along with a typical pair of absorption spectra and their difference (dichroism) from a dilute (0.5Å) film of Fe clusters on HOPG. The orbital (m_L) and spin (m_S) contributions to the total magnetic moment can be determined independently and (in heterogenous systems) for each element by applying magneto-optical sum rules to the absorption spectra [13, 14]. All moment values are given per valence band hole, n_h, which may be different from the bulk value but can be determined by measuring the integrated (white line) L-edge absorption strength, which is proportional to n_h. A further complication is that the spin sum rule actually relates the value of $m_S + 7\langle T_z \rangle$ to dichroism intensities where $\langle T_z \rangle$ is the expectation value of the magnetic dipole operator:

$$T = \frac{1}{2}[\mathbf{S} - 3\hat{\mathbf{r}}(\hat{\mathbf{r}}.\mathbf{S})] \tag{1}$$

This averages to zero over all directions and does not appear in conventional magnetic measurements but since the X-rays sample a directional cut through the atomic electron density, the term must be included in the sum rule. It can be eliminated by averaging measurements over all X-ray incidence angles, making a single measurement on a polycrystalline sample or, for samples with rotational symmetry about the substrate normal, making a single measurement at the 'magic' angle of 55° off-normal [15,16].

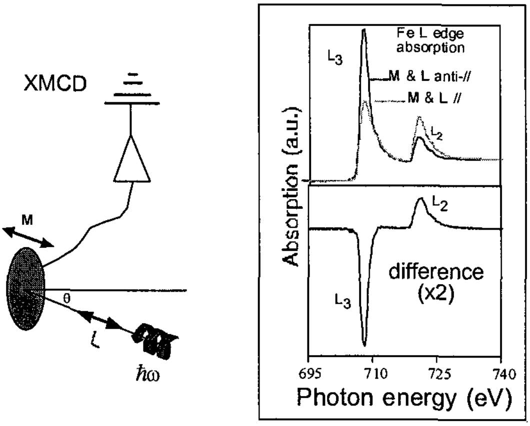

Figure 1. Geometry of X-Ray Magnetic Circular Dichroism (XMCD) measurements. The representative data shown is from 0.5Å equivalent thickness film of exposed 400-atom Fe clusters on HOPG.

All the XMCD data reported here were collected on beam line ID12B of the European Synchrotron Radiation Facility (ESRF) in Grenoble, France. The source is a helical undulator that can be phased to produce either helicity of circularly polarised X-rays with a polarisation of 85% to 90%. The X-ray absorption was obtained by measuring the sample drain current. Cluster samples were deposited *in situ* from the cluster source onto highly oriented pyrolitic graphite (HOPG) substrates held at 6-8K between the poles of a UHV cold-bore 5T magnet. The field direction was along the photon beam (parallel or anti-parallel to the photon spin). The moments in the isolated clusters were measured from films deposited to an equivalent thickness of 0.5-0.6 Å (~0.03 cluster monolayers). The filter window was set to ±50 atomic masses around the selected mass.

2.3. *Magnetometry Measurements*

Magnetometry measurements were made with a vibrating sample magnetometer (VSM) operating at fields up to 9T and temperatures down to 1.4K. The samples were prepared by depositing the cluster-assembled films in UHV onto polyetheretherketone (PEEK) foil, which has a very small diamagnetic response. Some films were prepared by depositing onto a PEEK rod that could be sealed *in situ* in a PEEK ampoule and transferred into the magnetometer in UHV conditions without breaking vacuum. Thus films could be measured without the need for a protective capping layer, which can significantly alter the magnetic behaviour [17].

3. Isolated Cluster Properties

3.1. *Exposed Clusters on Surfaces in UHV*

An exposed isolated cluster supported on a substrate is the fundamental building brick of a cluster-assembled material. Figs. 2a and 2b shows the spin and orbital moments in mass-selected Fe clusters deposited *in situ* onto HOPG substrates, held at 6K, to a coverage of ~0.03 cluster monolayers. The spin $m_S + 7m_T$ values are shown for data taken at normal incidence and with the sample rotated to the 'magic angle' of 55° incidence. At this latter angle the m_T contribution vanishes revealing the pure spin moment. The number of valence band holes (n_h) required to extract the values of m_S and m_L was obtained from the white light 3d absorption intensity.

The spin moment shown in Fig. 2a increases with decreasing cluster size and shows a 10% enhancement relative to the bulk value at the smallest size measured (181 atoms). Note how the data taken at 55° and normal incidence diverge revealing the increasing importance of the dipole contribution as the cluster size decreases. The bulk value for comparisons was obtained by XMCD from a 250Å thick conventional Fe film deposited in situ. The measured value, however, even after eliminating the effect of the dipole moment is 0.17 μ_B/atom lower than the accepted spin moment. This well-known systematic error is due to a number of factors such as band structure effects (XMCD sum rules are atomic) and the insensitivity to the small valence s-electron polarisation. Crudely we can compensate by simply adding 0.17 μ_B/atom to the measured spin moments. This is not stringent since the systematic error may be different in a cluster but is likely to produce a more accurate value than the uncorrected XMCD data.

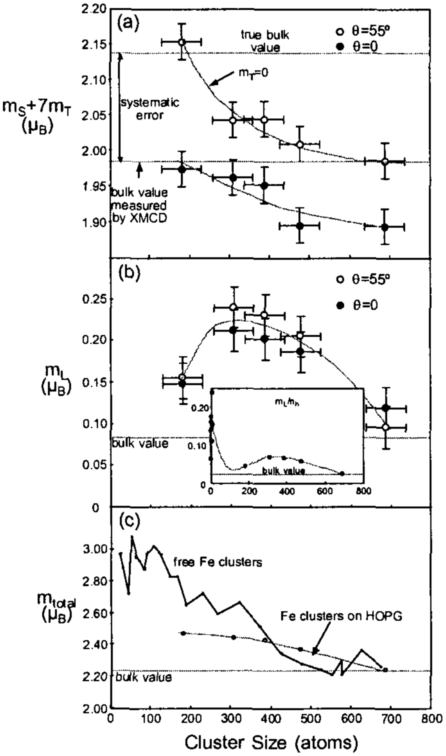

Figure 2. (a) $m_S + 7m_T$ values obtained by XMCD from isolated Fe clusters on HOPG as a function of size. Measurements at θ=0 (filled circles) and 55° (open circles) are displayed and $m_T = 0$ in the data at θ= 55° (the 'magic angle') revealing the pure spin moment. The measured bulk value was from a 250Å thick conventional Fe film and the difference between this spin value and the accepted value for bulk Fe reveals the systematic error in the XMCD meaurement. (b) m_L values obtained by XMCD showing a peak at ~300 atoms. There is no observable difference between the measurements at θ=0 (filled circles) and 55° (open circles) indicating that the orbital moment is isotropic. The inset compares the present data with the measurements of Lau *et al.* [18] for very small Fe clusters (n=2-9) on Ni substrates. The combined data reveals an oscillation in m_L with cluster size. (c) Total magnetic moment in isolated Fe clusters on HOPG as a function of size (open circles), after correcting for the systematic error in the spin moment, compared with gradient field deflection measurements of the total moments in free Fe clusters [2] (filled circles).

The orbital moment shown in Fig.2b also increases with decreasing cluster size and is enhanced by a factor of three relative to the bulk value for cluster sizes around 300 atoms. In the smallest clusters however it diminishes again, which may be due to the formation of a closed shell system, for example the 147-atom icosahedron. The inset in Fig. 2b compares our measurement of m_L/n_h from Fe clusters on HOPG with the values obtained by Lau *et al.* [18] for very small Fe clusters in the size range 2-9 atoms deposited on Ni substrates. It is clear from the combined data that there is a minimum in the orbital moment at cluster sizes around 100-150 atoms.

The total moments in the exposed Fe clusters are shown in Fig. 2c after correcting for the systematic error in the XMCD measurement of the spin moment. The gradient-field deflection measurements of the total moment in free Fe clusters is also shown for comparison and it is evident that the supported clusters have a significantly enhanced moment relative to the bulk (about half of which comes from the increased orbital moment) but the total moment in the adsorbed clusters is smaller than in the free clusters.

3.2. *Co-Coated Clusters on Surfaces*

Some of the exposed Fe cluster films on HOPG were coated with a Co film of thickness 8Å in situ and analysis of the magnetisation curves showed that the combined film consisted of Co islands with embedded Fe clusters [7]. The Fe clusters were exchange-coupled to the Co film and the magnetisation showed a strong in-plane shape anisotropy due to the Co islands. The fundamental orbital and spin moments localised in the Fe clusters could be extracted due to the chemical specificity of XMCD. Fig. 3a shows the measured size-dependent spin moment, after correcting for the systematic error discussed above, compared with the calculation by Xie and Blackman [19] for free Co-coated Fe clusters, with a composition of FeNCo1021-N. The agreement is good and demonstrates an increase in the spin moment of $\sim 0.2\mu_B$ relative to the exposed clusters. Fig. 3b reveals that over a significant fraction of the size range the total magnetic moment per atom measured in the supported Co-coated Fe clusters is as large as in free Fe clusters.

3.3. *Isolated Fe and Co Clusters in Ag Matrices*

To understand dense interacting films we not only need the magnitude of the moments in isolated clusters but other magnetic properties such as the magnitude of the magnetic anisotropy and its symmetry. These were determined by magnetometry measurements in dilute (1-2% volume fraction) Fe and Co clusters embedded in Ag matrices prepared by co-depositing the clusters and the matrix. In these samples clusters were not mass-filtered so the films contain the full size distribution of particles from the source. This is quantified below.

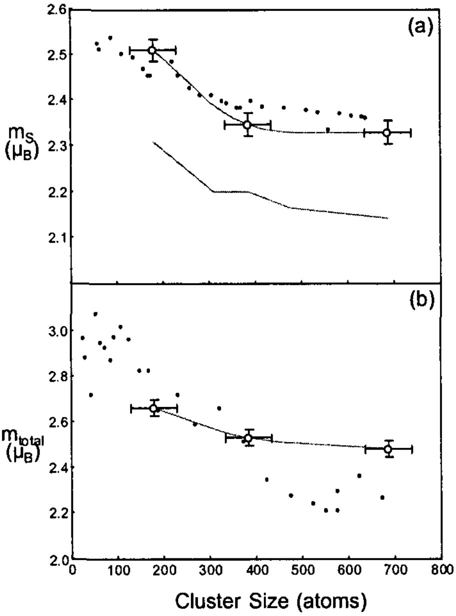

Figure 3. (a) Spin moment measured by XMCD (after correction for systematic error) in Co-coated Fe clusters on HOPG as a function of the Fe cluster size (open circles) compared with the calculated spin moment in free Co-coated Fe clusters with composition Fe_NCo_{1021-N} as a function of N [19] (filled circles). The grey line shows the measured spin moments in the exposed clusters prior to coating. (b) Total magnetic moment measured by XMCD in Co-coated Fe clusters on HOPG (open circles) compared with the free Fe cluster values measured by gradient field deflection [2] (filled circles).

To begin with it is important, in order to obtain the native properties of the isolated clusters, to verify that they are non-interacting and have not agglomerated. Magnetic Isotherms from an Fe_1Ag_{99} cluster-assembled film in the plane of the film at temperatures in the range 50-300K are shown in Fig. 4a (symbols). It has been shown previously that this magnetisation data scales with B/T and the film displays ideal super-paramagnetism in the range 50-300K [17,20]. The isotherm at each temperature was fitted by a set of Langevin functions with different moment values where the amplitude of each Langevin function was a fitting variable thus the cluster size distribution could be obtained. Ten size bins were used in the range 0.5 - 8nm and the average amplitude as a function of particle size (moment) after fitting all data sets is shown in the inset in Fig. 4a. The calculated curves are displayed as lines and the fit is excellent in every case. The size distribution is the usual asymmetric shape and fitting it to a log-normal distribution (inset) gives a most probable cluster size of 2.57nm with a standard deviation of 1.95 giving a median diameter of 3.0nm. This distribution is similar to those obtained by direct STM imaging of deposited cluster films. Thus we can confirm that the clusters are isolated in this film and don't interact.

At 2K most of the clusters in the Fe_1Ag_{99} sample are below the blocking temperature and as shown in Fig.4b the magnetic isotherm develops hysteresis. The remanence, M_r, of an assembly of blocked particles reveals the symmetry of the anisotropy axes and their distribution in space. For example uniaxial anistropy axes give $M_r/M_s=0.5$ if they are randomly distributed over three dimensions and $M_r/M_s=0.71$ if they are distributed over two dimensions in the plane of the applied field. The measured remanence is 0.4 and is thus closest to the case for uniaxial anistropy axes randomly distributed over 3D. The slight discrepancy may be due to the smallest clusters in the distribution remaining unblocked at 2K or a non-collinear alignment of atomic moments in the relaxed cluster. A uniaxial anisotropy of the individual clusters is expected as it will be produced by any incomplete atomic shell. Only clusters containing magic numbers of atoms are expected to have a cubic anisotropy but even in this case it is likely to be lost due to the (low energy) collision with the substrate.

For particles with a uniaxial anisotropy randomly oriented in 3D the magnetisation between saturation and remanence is obtained at each field value by minimising over all alignments of the anisotropy axes, the intra-particle energies:

$$E_\phi = KV\sin^2(\phi - \theta) - \mu B\cos\phi \qquad (2)$$

where K is the anisotropy constant, V is the particle volume and □and □ are the angles between the applied field and the anisotropy axis and particle magnetisation vector respectively. The inset in Fig. 4b compares the curve calculated thus with the data and it is evident that this simple model reproduces the data accurately. So in zero field the system is a collection of static, randomly aligned cluster giant moments each pointing along the local anisotropy axis. The anisotropy constant is a parameter of the fit and optimises at $K=2.63\times10^5$ Jm^{-3}, which is in reasonable agreement with the value of $K=2.3\times10^5$ Jm^{-3} obtained by a previous SQUID measurement of a similar sample [21], and is about 5 times the bulk value. A similar measurement perpendicular to the film plane reveals similar behaviour with a slightly higher anisotropy constant [20], which we attribute to a degree of 'flattening' of the clusters on landing. To a first approximation, however the clusters films are isotropic.

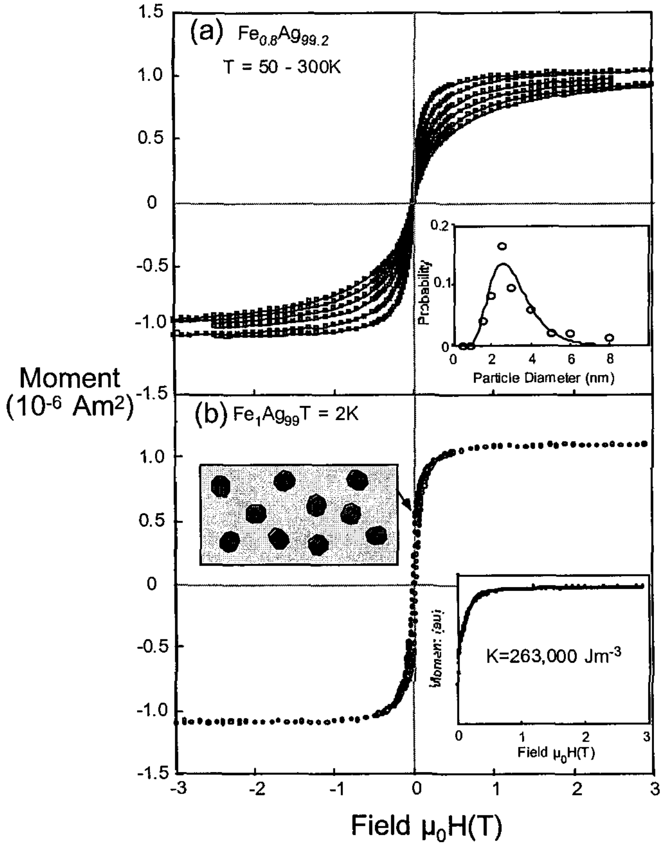

Figure 4. (a) Magnetisation isotherms in the range 50K-300K of Fe_1Ag_{99} cluster-assembled film (open squares) compared to fits by Langevin functions (line) with a size distribution represented by 10 size bins in the range 0.5 - 8 nm. The inset shows the average probability of each bin for the optimum fit to curves at temperatures >50K (open circles) and the corresponding log-normal distribution (line) with d_{max}=2.57nm and σ=1.95. (b) In plane magnetisation isotherms at 2K of Fe_1Ag_{99} sample: (full circles) Field sweeping down, (open circles) field sweeping up. The inset shows the decay from saturation (full circles) compared to a calculation (line) assuming a random distribution of uniaxial anisotropy axes (equation (2)). The best fit anisotropy constant is displayed in the inset.

Magnetic isotherms from a Co_2Ag_{98} cluster-assembled in the temperature range 50 - 300K are shown in Fig. 5a (symbols) along with the Langevin fits using the procedure described above (lines). In this case a departure from ideal super-paramagnetism is observed below about 150K [20], which we attribute to the higher anisotropy of the Co clusters (see below) requiring a higher temperature to reach the super-paramagnetic limit. Thus we can obtain the size distribution by Langevin fits as described above to the curves taken at 150K and above. The result along with the fitted log-normal distribution is shown in the inset in figure Fig. 5b and for the Co clusters the most probable size is 2.45nm with a standard deviation of 1.81 giving a median diameter of 2.8nm.

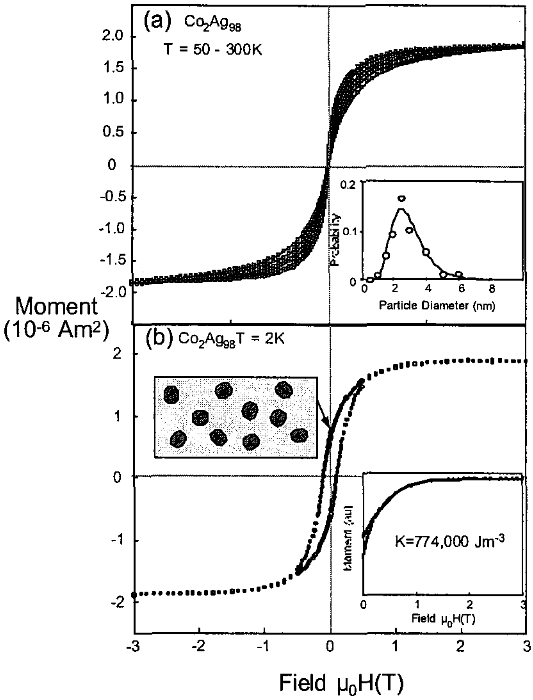

Figure 5. (a) Magnetisation isotherms in the range 50K-300K of Co_2Ag_{98} sample (open squares) compared to fits by Langevin functions (lines) with a size distribution represented by 10 size bins in the range 0.5 - 8 nm. The inset shows the average probability of each bin for the optimum fit to curves at temperatures >150K (open circles) and the corresponding log-normal distribution (line) with d_{max}=2.45nm and σ=1.81. (b) Out of plane magnetisation isotherms at 2K of Co_2Ag_{98} sample: (full circles) field sweeping down, (open circles) field sweeping up. The inset shows the decay from saturation (full circles) compared to a calculation (line) assuming a random distribution of uniaxial anisotropy axes (equation (2)). The best fit anisotropy constant is displayed in the inset.

The low temperature isotherms from the isolated Co clusters in Ag are shown in Fig.5b. Again the remanence is slightly less than 50% indicating that the clusters are randomly oriented over 3D and have a uniaxial anisotropy. The approach to saturation can thus be modeled using equation (2) and this is compared to the data in the inset in Fig. 5b. The anisotropy constant optimising the fit is 2-3 times larger than in the Fe cluster assembly.

4. Interacting Clusters

4.1. *Cluster-Cluster Interfaces in Interacting Cluster Films*

Having determined the detailed magnetic properties of isolated clusters, the next step is to elucidate the behaviour in dense cluster films in which there is significant interaction and an important consideration is the nature of the interface between clusters in contact. Fig. 6 shows an STM image of un-filtered Fe clusters deposited on Si(111) surfaces in situ in UHV [22] and it is observed that the clusters are randomly distributed, they are faceted and they tend to join along the facets. Metal to metal contact at the cluster interfaces will invoke a strong exchange coupling between neighbouring clusters.

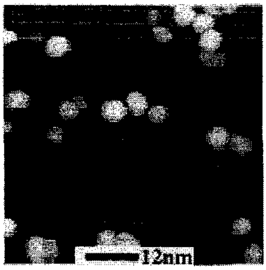

Figure 6. *In situ* STM image (40nm x40nm) of unfiltered Fe clusters deposited on Si(111) in UHV.

TEM images of Fe clusters embedded in amorphous carbon matrices at high volume fractions show that the film lattice planes randomly switch direction on the length scale of a cluster diameter [23]. It is reasonable to assume that in neighbouring clusters the anisotropy axes are randomly oriented as in the case of isolated clusters. Thus clusters in contact will try and align their magnetisation directions due to the exchange interaction but this will frustrate the anisotropy energy that requires the magnetisation vector in each cluster to lie along the local anisotropy axis. This frustration has important consequences for the mesoscopic magnetic configuration in interacting cluster films.

4.2. *Orbital and Spin Moments in Interacting Cluster Films*

Fig. 7 shows the orbital and spin moments measured by XMCD in unfiltered Fe clusters deposited on HOPG as a function of coverage [6], from isolated clusters to the 2D percolation threshold. The closed symbols show the values obtained from a low coverage mass-selected deposit with the filter set to the peak of the size distribution (400 atoms). The orbital moment decays towards the bulk value as the clusters come into contact. This efficient quenching indicates partial coalescence at the interfaces since a simple Fe-Fe interface will still break symmetry and produce an enhanced orbital moment.

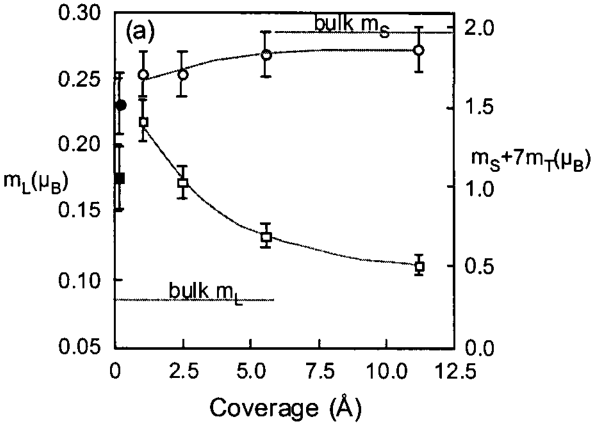

Figure 7. Variation of orbital (open squares) and spin (open circles) moments in unfiltered Fe clusters deposited *in situ* on HOPG as a function of coverage. The filled symbols indicate the values for a mass-selected deposit with the filter set to the mass of the peak of the distribution (400-atoms).

The XMCD data was taken at normal incidence so the spin moment has a non-vanishing dipole contribution. The small rise in the spin term observed in Fig. 7 is attributed to a decrease in the dipole moment (opposite to the spin) as the clusters come into contact thus it is difficult to extract the spin moment from the XMCD data. Previous MLDAD measurements on thick cluster films do however indicate that an enhanced spin moment ~5% larger than the bulk is maintained in the interacting cluster film [23].

4.3. *Macroscopic Magnetic Properties of Interacting Cluster Assemblies*

Magnetometry results on interacting Fe cluster assemblies in Ag matrices as a function of volume fraction have been reported previously [17]. Briefly, as the volume fraction is increased from isolated clusters, the behaviour of the assembly evolves from ideal super-paramagnetism to an interacting super-paramagnetic phase described by Allia *et al.* [24]. In this regime the clusters agglomerate into groups of exchange-coupled clusters and the groups interact with each other via dipolar forces. The main effect on the magnetic behaviour is a greatly enhanced initial susceptibility of the film.

Here we report on the magnetic behaviour at the extreme end of the volume fraction range consisting of pure cluster assemblies with no matrix. Two films will be described, that is, a pure Co cluster film of thickness 200Å and a pure Fe film of thickness 50Å. Both samples were prepared in the UHV sealable ampoule described in section 2.4 and were transferred into the magnetometer in UHV conditions without a protective capping layer. It has been shown previously that capping layers can significantly alter the magnetic behaviour of cluster films [17]. The behaviour was analysed using a random anisotropy (RA) model developed by several authors in the last two decades [25-29]. In the RA formalism, the magnetic ground state in a granular film is determined by the relative strength of a random anisotropy field:

$$H_r = \frac{2K_r}{M_s} \tag{3}$$

and an exchange field:

$$H_{ex} = \frac{2A}{M_s R_a^2} \tag{4}$$

where K_r is the (randomly oriented) anisotropy of the grains, M_s is their saturation magnetisation, A is the exchange constant for the interaction between the grains and R_a is the nanometre sized region over which the local anisotropy axis is correlated, i.e. the characteristic grain size. Their relative strength is given by the dimensionless parameter:

$$\lambda_r = \frac{H_r}{H_{ex}} = \frac{K_r R_a^2}{A} \tag{5}$$

The model was developed to describe amorphous films in which a local, randomly-oriented, anisotropy is due to local atomic order. It is even better suited to providing a description of the magnetisation in cluster-assembled films in which the distance R_a over which an anisotropy axis is correlated is well defined (i.e. the particle diameter).

For $\lambda_r > 1$ the magnetic correlation length at zero field is R_a, and the magnetic vector in each particle points along the local intra-particle anisotropy axis. Note that in an arrow representation this state would be identical to that in isolated non-interacting particles at absolute zero. This regime is illustrated in Fig. 8b. With increasing inter-particle exchange (or decreasing intra-particle anisotropy) the configuration becomes a correlated super spin glass (CSSG). In this state the magnetisation vector in neighbouring particles is nearly aligned but the random deviation from perfect alignment produces a smooth rotation of the magnetisation throughout the system with a magnetic correlation length that is a factor $1/\lambda_r^2$ larger than the particle diameter as illustrated in Fig. 8c.

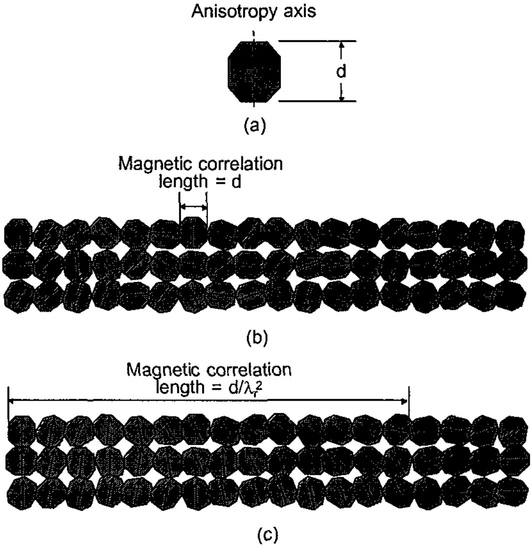

Figure 8. (a) Schematic representation of a magnetic nanoparticle with a uniaxial anisotropy axis (represented by a slight elongation). (b) and (c) a stack of particles with randomly oriented anisotropy axes. In (b) $\lambda_r > 1$ and the magnetisation vector points along the local anisotropy axis so the magnetic correlation length is a single particle diameter. In (c) $\lambda_r < 1$ and the magnetic vectors are nearly aligned. The random perturbation from perfect alignment results in a finite magnetic correlation length that is a factor $1/\lambda_r^2$ larger than a single particle.

The disordered CSSG state is fragile and application of a small field produces a 'ferromagnet with wandering axes' (FWA) [26]. The randomised nanoscale anisotropy results in a very high susceptibility of cluster-assembled films as illustrated in the left hand insets in Fig. 9a and Fig. 9b. These compare the magnetisation curves of pure cluster-assembled Fe and Co films (dots) at 300K with the magnetisation of isolated Fe and Co clusters embedded in Ag (lines).

According to Chunovsky [29] the approach to saturation of a system, whose ground state is a CSSG, is given by:

$$M = M_s\left(1 - \frac{1}{32}\frac{\lambda_r^2}{\sqrt{h_{ex}}}\int_0^\infty dx C(x) x^2 K_1\left[x\sqrt{h_{ex}}\right]\right) \qquad (6)$$

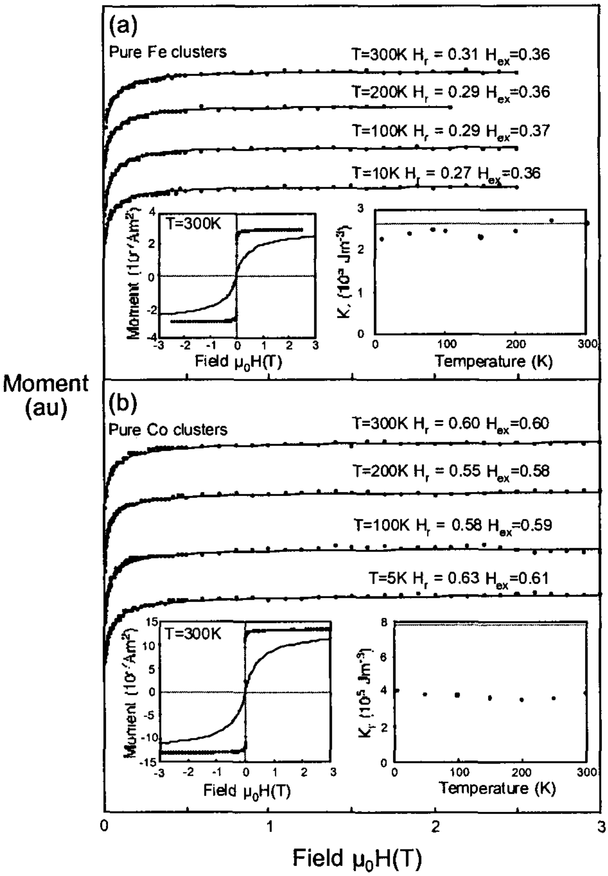

Figure 9. (a) Approach to saturation of 5nm thick pure Fe cluster film for temperatures in the range 10 -300K (full circles) compared to a calculation using the RA model with the parameters shown (lines). The left inset shows the full magnetisation curve (circles) of the dense cluster film compared to that of isolated clusters at 300K. The left inset shows the variation of the random anisotropy (evaluated from H_r and equation (3)) with temperature (full circles). The grey line shows the value for the isolated clusters. (b) As (a) but for the 20nm thick pure Co cluster film sample.

in two dimensions and

$$M = M_s\left(1 - \frac{1}{30}\frac{\lambda_r^2}{\sqrt{h_{ex}}}\int_0^\infty dx C(x) x^2 \exp\left[x\sqrt{h_{ex}}\right]\right) \qquad (7)$$

in three dimensions. In equations (6) and (7), $h_{ex} = H/H_{ex}$, K_1 is the modified Hankel function and $C(x)$ is the correlation function for the anisotropy axes with x in units of R_a. In an amorphous metal, $C(x)$ will be a smoothly decreasing function a characteristic decay distance of R_a while in a cluster-assembled film consisting of mono-sized particles it will be a step function cutting off at $x = 1$. Here we have rounded the step function by using $C(x) = \exp(-x^8/2)$ to simulate the narrow size distribution but visually there is no change to the fits if a simple step is used. We have used the 2D form (equation (6)) for the approach to saturation for Fe cluster sample as it is only two cluster layers thick whereas we have used the 3D form (equation (8)) for the much thicker Co cluster film.

The only independent parameters entering equation (6) and (7) are the exchange and random anistropy fields, H_{ex} and H_r. From the analysis of the isolated particles (Figs. 5 and 6) we can write the condition $K_r \leq. 2.6 \times 10^5$ for Fe and $K_r \leq. 7.7 \times 10^5$ for Co i.e. from (3), $H_r \leq 0.3$T for Fe and $H_r \leq 0.9$T for Co. The exchange constant, A, must be much smaller than the atomic value of $\sim 10^{-11}$ Jm^{-1} giving from (4) and the median cluster diameter, $H_{ex} << 1.3$T. In addition any coherent anisotropy field, H_c must be included in the fits by replacing H with $H+H_c$ [26]. In a previous report [20], we showed, by comparing the in-plane and out of plane behaviour of cluster films that the coherent anisotropy field is less than 0.1T.

Restricting all parameters to the ranges discussed above we have optimised the fits between the magnetisation data, in the range between $0.85M_s$ and M_s, and the calculated curve from equations (6) and (7) as a function of the parameters H_{ex}, H_r and H_c where the results for temperatures in the range 5-300K are shown in Fig. 10a and 10b. The first observation is the excellent agreement between the data and the RA model at all temperatures for both films reinforcing the assertion that the cluster layers form a CSSG in their ground state. It is found that in both cases the values of H_{ex} and H_r change little with temperature, which is just confirmation of the observation that the shape of the curves appears to be independent of temperature. The value of the random anisotropy, K_r, obtained from H_r and equation (3) is shown in the right insets and compared to the values for the isolated clusters. For the Fe cluster film, the random anisotropy is close to the isolated cluster value whereas for the Co cluster film it is significantly smaller. The exchange fields are ~0.36T and ~0.6T for the Fe and Co cluster films respectively, corresponding to an exchange constant (from equation (4)) of $A \sim 3 \times 10^{-12} \text{Jm}^{-1}$ for both films, which is much less than the bulk value as required. The coherent anisotropy field remains constant with temperature and is ~0.03T for Fe and ~0.01T for Co.

The fits indicate that the exchange and anisotropy fields are approximately constant but according to the model [29] both should increase slightly with decreasing temperature. The fact that this is not picked up by the analysis is not surprising given the looseness of the constraints on the parameters. The behaviour is however in sharp contrast to a previous observation of a pure Fe cluster film that was sandwiched between Ag buffer and capping layers [17]. In that case the film formed a CSSG state at 300K but a significant increase in the value of H_r with temperature was found. Below 50K, the aniotropy was sufficiently high to produce a transition from a CSSG to a simple spin glass state in which the moment in each cluster points along the local intra-cluster anisotropy axis just as in isolated clusters below the blocking temperature. This was ascribed to mechanical stress in the film, which was deposited at room temperature so that when cooling, the higher expansion coefficient of Ag would exert a pressure on the clusters. This is supported by the observation here, i.e. in uncapped films deposited on an organic substrate the variation of H_r with temperature is small.

Acknowledgements

We gratefully acknowledge support from the UK EPSRC grant GR/N66100 and EC contracts HPRI-CT-2001-50025 and GRD1-1999-11088 for this work.

References

1. C. Binns, Surf. Sci. Rep. 44 (2001) 1.
2. I. M. L. Billas, J. A. Becker, A. Châtelain, W. A. de Heer Phys. Rev. Lett. 71 (1993) 4067.
3. D. C. Douglass, A. J. Cox, J. P. Bucher, L. A. Bloomfield Phys. Rev. B 47 (1993) 12874.
4. A. J. Cox, J. G. Louderback, S. E. Apsel, L. A. Bloomfield Phys. Rev. B 49 (1994) 12295.
5. M. B. Knickelbein Phys. Rev. Lett. 86 (2001) 5255.
6. K. W. Edmonds, C. Binns, S. H. Baker, S. C. Thornton, C. Norris, J. B. Goedkoop, M. Finazzi, N. B. Brookes Phys. Rev. B 60 (1999) 472.
7. K. W. Edmonds, C. Binns, S. H, Baker, M. J. Maher, S. C. Thornton, O. Tjernberg, N. B. Brookes J. Magn. Magn. Mater. 231 (2001) 113.
8. K. W. Edmonds, C. Binns, S. H. Baker, M. J. Maher, S. C. Thornton, O. Tjernberg, N. B. Brookes, J. Magn. Magn. Mater. 220 (2000) 25.
9. S. H. Baker, C. Binns, K. W. Edmonds, M. J. Maher, S. C. Thornton, S. Louch, S. S. Dhesi J. Magn. Magn. Mater. 247 (2002) 19.
10. D. A. Eastham, I. W. Kirkman, J. Phys.: Condens. Matter 12 (2000) L525.
11. M. Negriér, PhD thesis, Université Claude Bernard, Lyon, 2000.

12. S. H. Baker, S. C. Thornton, K. W. Edmonds, M. J. Maher, C. Norris, C. Binns, Rev. Sci. Instr. 71 (2000) 3178.
13. B. T. Thole, P. Carra, F. Sette, G. van der Laan, Phys. Rev. Lett. 68 (1992) 1943.
14. . Carra, B. T. Thole, M. Altarelli, X. Wang, Phys. Rev. Lett. 70 (1993) 694.
15. J. Stöhr, H. König, Phys. Rev. Lett. 75 (1995) 3748
16. G. van der Laan, Phys. Rev. B 57 (1998) 5250.
17. C. Binns, M. J. Maher, Q. A. Pankhurst, D. Kechrakos, K. N. Trohidou, Phys. Rev. B 66 (2002) 184413.
18. J. T. Lau, A. Fölisch, R. Nietubyc, M, Reif, W. Wurth, Phys. Rev. Lett. 89 (2002) 057201.
19. Y. Xie and J. A. Blackman. Phys. Rev. B 66 (2002) 085410.
20. C. Binns and M. J. Maher, New J. Phys. 4 (2002) 85.1.
21. T. J. Jackson, C. Binns, E. M. Forgan, E. Morenzoni E, Ch. Niedermayer, H. Glückler, A. Hofer, H. Luetkens , T. Prokscha, T. M. Riseman, A. Schatz, M. Birke, J. Litterst, G. Schatz, H. P. Weber, J. Phys:Condens. Matt. 12 (2000) 1399.
22. M. D. Upward, B. N. Cotier, P. Moriarty, P. H. Beton, S. H. Baker, C. Binns, K. W. Edmonds, J. Vac. Sci. Technol. B 18 (2000) 2646.
23. C. Binns, S. H. Baker, S. Louch, F. Sirotti, H. Cruguel, P. Prieto, S. C. Thornton and J. D. Bellier, Appl. Surf. Sci. accepted, in press, available on-line.
24. P. Allia, M. Coisson, P. Tiberto, F. Vinai, M. Knobel, M. A. Novak, W. C. Nunes, Phys. Rev. B 64 (2001) 144420.
25. E. M. Chudnovsky, J. Mag. Magn. Mater. 40 (1983) 21.
26. E. M. Chudnovsky, W. M. Saslow and R. A. Serota, Phys. Rev. B 33 (1986) 251.
27. W. M. Saslow, Phys. Rev. B 35 (1987) 3454.
28. E. M. Chudnovsky, J. Appl. Phys. 64 (1988) 5770.
29. E. M. Chudnovsky, in *The Magnetism of Amorphous Metals and Alloys*, edited by J. A. Fernandez-Baca and Wai-Yim Ching (World Scientific, Singapore, 1995), Chap. 3.

MAGNETIC FIELD EFFECTS ON THERMAL FLUCTUATIONS OF CLUSTER MAGNETIC MOMENTS

KEYUR DESAI,[§] [*] AND S. D. MAHANTI[*]
Department of Physics and Astronomy, §Department of Electrical & Computer Eng., Michigan State University, East Lansing, MI 48824

S. N. KHANNA[†]
Department of Physics, Virginia Commonwealth University, Richmond, VA 23284

We have investigated the effects of magnetic field and temperature on the average magnetic moment of Gd_{13} atomic clusters using a classical Heisenberg model with competing interactions between atomic spins $\vec{S}_i$. Monte Carlo simulations were carried out at different temperatures (T) and field strengths (B) to obtain $M_1 = \sqrt{\sum_{i,j} < \vec{S}_i \bullet \vec{S}_j >}$ and $M_2 = \sum_i < S_{iz} >$, where the external magnetic field is along the z-direction. In the limit of vanishing B, the relationship between M_2 and M_1 was checked against fluctuation-dissipation theorem and its implication on the extraction of the temperature dependence of cluster magnetic moments in Stern-Gerlach measurements was investigated.

1. Introduction

The field of clusters and nano-scale materials is drawing considerable attention, as the physical, chemical, electronic, magnetic and optical properties are all found to change, as the size is reduced [1]. Of all the properties, the magnetic properties probably exhibit the most dramatic effects [2]. Clusters of itinerant ferromagnetic solids Fe, Co, and Ni are found to exhibit super-paramagnetic relaxations [3, 4], while clusters of non-magnetic solids like Rh are found to be ferromagnetic [5, 6]. Further, the atomic magnetic moments in Fe, Co, and Ni are enhanced in reduced sizes, largely due to reduced coordination thereby providing the hope that stronger magnets could be designed using smaller clusters. While the transition metal clusters exhibit enhanced moments, the clusters of rare earth elements Gd, Tb etc. are found to have magnetic moments

---

[*] Work partially supported by the Center for Fundamental Materials Research at Michigan State University.

[†] SNK was partially supported from the Department of Energy (#DE-FG02-96ER45579).

per atom that are far below the bulk values [7]. Since the atomic moments in these systems arise due to localized f-electrons, the observed reduction is quite surprising. Particularly for Gd, marked by valence configuration of $4f^7 5d^1 6s^2$, where the magnetic moment arises predominantly due to filled localized f shell, such a decrease would require pairing of the electrons in the f-states, which is highly unlikely. In fact, first principles density functional calculations on small Gd_n clusters did yield magnetic moments of around 7.5 μ_B per atom, far above the observed value [8]. The apparent conflict was resolved by Pappas et al. [8] who argued that it is the nature of the magnetic coupling and not the value of the atomic moments that was responsible for the observed behavior. They argued that the coupling between the localized f-moments was mediated by the RKKY interactions marked by oscillatory changes. Such behaviors are beyond the mean field framework of the current density functional approach. These authors, therefore, took a Heisenberg Hamiltonian with nearest neighbor ferromagnetic and next nearest neighbor anti-ferromagnetic couplings. They showed that while the local moments were high, the atomic spins in the ground state were ferrimagnetically arranged leading to a smaller overall moment.

Experimentally one usually gets information about the magnetic moment of a cluster by carrying out a Stern-Gerlach (SG) experiment. Here, the clusters are passed through a gradient magnetic field where the magnetic field tries to orient the cluster moments while the gradient field generates a net force. The resulting behavior, therefore, depends on the value of the cluster magnetic moment (CMM) and its dynamics as the cluster goes through the gradient field. For cases where the overall cluster magnetic moment is fixed, two kinds of behaviors namely the "frozen moment" or "locked moment" and "superparamagnetic" behavior are observed. To address these orientation and relaxation issue we had earlier studied, using Fokker-Planck equation and transition state theory, a simple model where the magnitude of the CMM was fixed but its orientation changed in the presence of a potential barrier [9]. Depending on the value of a dimensionless parameter $\alpha=\lambda\tau exp$ (λ is an internal orientational relaxation rate and τexp is an experimental time scale i.e. the time spent by the cluster in the field gradient region of the SG set-up), one extrapolates smoothly between the "frozen moment" and super- paramagnetic limits.

In this paper we investigate the same problem but allowing for both the magnitude and orientational fluctuations of the CMM as a function of temperature and magnetic field. Whereas, the former depends on the coupling between individual spins in a given cluster, the orientational fluctuations are reminiscent of the Super-paramagnetic relaxations. We show that the inclusion of global rotations in the Monte Carlo simulations is critical to describing the orientational fluctuations and hence the observed behavior in Stern Gerlach experiments. The particular system we have chosen is Gd_{13} cluster whose magnetic moment has been investigated experimentally by Gerion et al [10]. In sec. II, we discuss the model and describe briefly our simulation procedure. Sec. III gives our main results and Sec. IV gives a summary.

2. The Model

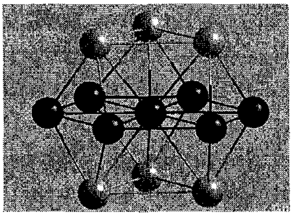

Figure 1: Gd_{13} Cluster

The physical system we have studied is a Gd_{13} cluster, where the Gd atoms are arranged in a hexagonal closed packed structure (see figure 1) consisting of a centered hexagon of seven atoms in the middle plane and three atoms above and three below this plane and arranged in a triangle. The magnetic moments are localized at the Gd sites and interact via indirect RKKY type interaction. The observed ground state moment, whose precise nature is not known, was explained by Pappas et al [8] within a Heisenberg model with competing ferro and antiferromagnetic interaction. The Hamiltonian for such a system in the presence of an external magnetic field $\vec{B} = B\hat{z}$ is given as:

$$H = J\left(- \sum_{<i,j>} \vec{S}_i \cdot \vec{S}_j + \gamma \sum_{<i,j>'} \vec{S}_i \cdot \vec{S}_j \right) - g\mu_B B \sum_{<i>} S_{iz} \ , \qquad (1)$$

where the nearest neighbor exchange given by the first term inside the bracket is ferromagnetic ($J > 0$). The non-nearest neighbor interactions given by the second term inside the bracket and parameterized by the dimensionless quantity γ are assumed to be the same for all pairs for simplicity and antiferromagnetic ($\gamma > 0$). We will measure energies in units of J and magnetic moments in units of $g\mu_B$.

2.1 *Magnetizations*

One can define the magnetic moment of a cluster in two ways.

$$M_1 = \frac{1}{N} < \sqrt{\sum_{(i,j)} \vec{S_i} \bullet \vec{S_j}} > \quad \text{and} \quad M_2 = \frac{1}{N} < \sum_i S_{iz} >, \tag{2}$$

where N is the number of spins in the cluster. Both M_1 and M_2 depend on temperature (T) and external magnetic field (B). According to the fluctuation-dissipation theorem and in the limit of small B, one has

$$M_2 = \frac{M_1^2}{3k_B T} B \tag{3}$$

where M_1 on the right hand side involves the zero field limit of M_1 given in Eq. (2). The degree to which Eq. (3) is satisfied using M_2 and M_1 from MC simulation is a measure of thermal equilibrium. In our previous study we observed M_1 for B=0 and found it to be strongly temperature dependent due to the competing nature of spin-spin interactions. Here our main focus is to see the interplay of intra-cluster thermal fluctuations vis-à-vis rotational motion of the spins in the presence of an external magnetic field, and their effects on M_1 and M_2.

3. Results

3.1. *Monte Carlo Simulations (local spin rotations)*

Finite temperature Monte Carlo simulations have been performed where the magnetic moment of each Gd atom is represented by its polar angle (θ) and azimuthal angle (ϕ) with magnitude unity (note $g\mu_B$=1). The simulation method consists of applying single spin Metropolis Monte Carlo steps (changing the spin orientation by ($\Delta\theta$, $\Delta\phi$)). Initially M_1 was computed for B=0 starting with high temperature and cooling down to low temperatures. The results for γ=0.4 are shown in figure 2(a); they are very similar to the one published in [11]. Equilibrium spin configurations obtained in this simulation have been used for evolving the system in the presence of an external magnetic field. The non-monotonic T-dependence of M_1 in figure 2(a) arises from the competing ferro and antiferro magnetic coupling between the spins. The ground state is a canted ferromagnetic state with average moment per atom less than the saturated value [8]. At finite T, thermal fluctuations mix in the ferromagnetic state (at low T) thereby enhancing the average magnetic moment [11].

Before presenting our simulation results for M_2 we would like to discuss the issue of spin orientations in thermal equilibration. Thermal equilibration is important while simulating model systems. Systems explore more configurations at higher temperature while at lower temperature it is hard for the system to make transition from one configuration to another. However, our simulation results show that in the absence of magnetic field, the single spin MC steps are sufficient to simulate the system even at low temperatures[1]. In the presence of an external magnetic field, we computed both M_1 and M_2 for different temperatures. The results are shown in figure 2(b). To ensure whether we have achieved thermal equilibrium or not, we checked to what extent simulated M_1 and M_2 values satisfied the fluctuation- dissipation theorem. To this end we define:

$$M_1^* = \underset{B\to 0}{}\sqrt{\frac{3k_B T M_2}{NB}} \tag{4}$$

If the system is in true thermal equilibrium, fluctuation dissipation theorem should be satisfied i.e. $M_1^*/M_1 = 1$, where M_1 (same as in figure 2(a)) is directly computed for given T using Eq. (2) with B=0. We found $M_1^*/M_1 \neq 1$; this indicates lack of thermal equilibrium. We then introduced an additional MC move to improve the equilibration process, as discussed below.

3.2. *Monte Carlo Simulations (with local & global spin rotations)*

Our extended MC simulation algorithm consists of both local rotations (single spin rotations) and global rotations (collective spin rotations while persevering the internal relative spin orientations). In the latter, we rotate all the spins simultaneously in such a way that the angle between each of them is preserved. When the external magnetic field is absent, these global rotations leave the energy of the system unchanged. However, when external magnetic field is present, the energy does not remain the same (see Eq. (1)) and hence the global move is accepted with certain probability. For the later discussions, we define a quantity called local to global MC rate (GR), which is the number of local rotation steps per one global rotation.

Now we present our results regarding M_2. Magnetic field dependence of magnetization M_1 and M_2 for a particular value of γ(=0.4) and T(=0.4) is given in figure 2(b). Magnetization M_2 is nearly 0 when B is 0. This is expected because when B=0 all the orientations and individual moment are uniformly distributed and hence the net moment in the z-direction turns out to be 0. With increase in B both M_1 and M_2 increase. Initially the rate of increase in M_2 is much faster than that of M_1 but at large B both achieve nearly the same value and saturate near the maximum possible value of 1. The effects of global spin rotations on M_2 were studied for two sample cases: (i) high temperature T(=0.4) and (ii) low

---

[1] Results in [11] were verified as equilibration results and we obtain very similar results (see Fig. 2(a)) for B=0.

temperature $T(=0.1)$. The Plots of M_2 *vs.* B for both cases are given in figure 2(c) and 2(d). At $T=0.1$ the values of M_2 at any given B are nearly the same (within an acceptable error-bar) for all values of GR, but for high temperature $T=0.4$, M_2 varies significantly with GR.

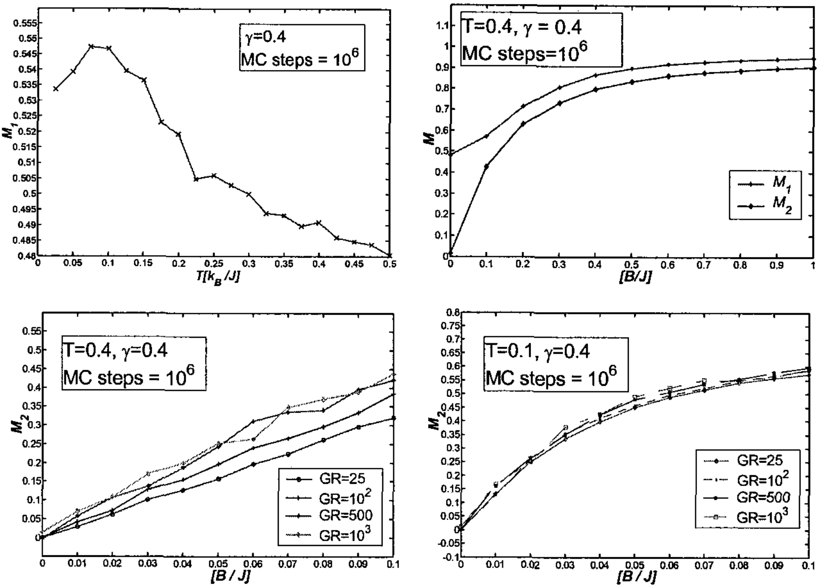

Figure 2: (a) Magnetization (M_1) vs. temperature; (b) Magnetization (M_1 & M_2) vs. external magnetic field; (c) M_2 vs. B for different global rotation rates (high temperature); (d) M_2 vs. B for different global rotation rates (low temperature).

Table 1: M_1^*/M_1 for various *T*s and GRs.

GR	$T=0.1$	$T=0.2$	$T=0.3$	$T=0.4$
25	0.9849	0.9975	1.0751	1.1198
10^2	1.0043	1.0250	1.1198	1.2011
500	1.0091	1.0869	1.1396	1.2750
10^3	0.9649	1.0799	1.1671	1.3000

Later, the relationship between M_1 and M_2 (Eq. (3)) as $B \rightarrow 0$ was checked. The values of M_2 at different GRs were used to compute M_1^* (Eq. (4)). Table 1 gives the values of the ratio M_1^*/M_1 for four different temperatures as a function of GR. With smaller values of GR, which implies more number of global rotations, the ratio M_1^*/M_1 approaches unity (Table 1). This implies that the system obeys the fluctuation dissipation theorem only when global spin rotations become more frequent particularly at higher temperatures.

4. Discussions

The present results show that a correct understanding of the observed magnetic behavior of the Gd_n clusters in Stern-Gerlach experiments through MC simulations requires the inclusion of both the local and global spin rotations. This is particularly important at high temperatures where the clusters undergo more fluctuations in global orientations. As mentioned before, the clusters are passed through a gradient magnetic field and one measures the deflection of the beam. The determination of the magnetic moment of the cluster, then proceeds via using a model that relates the deflection to the intrinsic moment of the cluster. For example, for clusters undergoing super-paramagnetic relaxations, the magnetic moment $<\mu_Z>$ is deduced using the paramagnetic equation,

$$d = L^2\,((1 + 2D/L)/2mv_x^2)\ \partial B/\partial z < \mu_Z>,$$

where d is the deflection, L is the length of the gradient magnetic field, D is the distance from the exit of the magnet to the time of flight mass spectrometer, and $\partial B/\partial z$ is the gradient of the magnetic field in z direction. As seen in our MC simulations, $<\mu_Z>$ is indeed the thermal average of the cluster magnetic moment provided; both local and global orientations of the spins are present in real cluster as they move through the Stern-Gerlach apparatus. This will of course depend on the intrinsic relaxation processes of the cluster and their time scales compared to the travel time of the cluster. We believe that the present work provides a framework for understanding the cluster magnetic moment in a Stern-Gerlach measurement. It also indicates the significance of orientational relaxations effect in identifying $<\mu_Z>$ as the super paramagnetic moment of a cluster. These issues will be addressed in a later publication.

References

1. "Clusters and nanostructure Interfaces" Ed. P. Jena, S. N. Khanna, and B. K. Rao, (World Scientific, 2000); "Quantum Phenomena in Clusters and Nanostructures", Ed. S. N. Khanna and A. W. Castleman, Jr., (Springer, New York, 2003).
2. D. D. Awschalom and D. P. Di Vicenzo, Physics Today, p. 43 (1995); J. Merikoski, J. Timonen, M. Manninen, and P. Jena, Phys. Rev. Lett. **66**, 938

(1991). S. K. Nayak and P. Jena, Chem. Phys. Lett. **289**, 473 (1998); M. R. Pederson, F. Reuse, and S. N. Khanna, Phys. Rev. **B58**, 5632 (1998).

3. W. A. de Heer, P. Milani, and A. Chatelain, Phys. Rev. Lett. **65**, 488 (1990); J. P. Bucher, D. C. Douglass, and L. A. Bloomfield, Phys. Rev. Lett. **66,** 3052 (1991).
4. S. N. Khanna and S. Linderoth, Phys. Rev. Lett. **67**, 742 (1991).
5. A. J. Cox, J. G. Louderback, and L. A. Bloomfield, Phys. Rev. Lett. **71**, 923 (1993).
6. B. V. Reddy, S. N. Khanna, and B. I. Dunlap, Phys. Rev. Lett. **70**, 3323 (1993).
7. D. C. Douglass, J. P. Bucher, and L. A. Bloomfield, Phys. Rev. Lett. **68**, 1774 (1992).
8. D. P. Pappas, A. P. Popov, A. N. Anisimov, B. V. Reddy, and S. N. Khanna, Phys. Rev. Lett. **76**, 4332 (1996)
9. S. Dattagupta and S. D. Mahanti, Phys. Rev. B **57**, 10244 (1998).
10. D. Gerion, A. Hirt, and A. Chatelain, Phys. Rev. Lett. **83**, 532 (1999)
11. V. Z. Cerovski, S. D. Mahanti, and S. N. Khanna, Eur. Phys. J. D **10**, 119 (2000).

MAGNETIC AND THERMAL PROPERTIES OF INTERACTING (Mn_xN) CLUSTERS

H. KHANG, S. D. MAHANTI*
Department of Physics & Astronomy, Michigan State University,
East Lansing, Michigan 48824, U.S.A

B. K. RAO, P. JENA
Physics Department, Virginia Commonwealth University,
Richmond, Virginia 23284-2000, U.S.A

We investigate the effect of clustering on the magnetic and thermal properties of (Mn_xN) clusters at finite temperature. The interaction between the clusters is treated using a mean-field approach while the intra-cluster exchange coupling parameters are obtained from density functional calculations. We show that there is a strong dependence of magnetization on temperature and external field, and high ferromagnetic transition temperatures are possible for reasonable strengths of the inter-cluster interaction, resulting from clustering effects.

1. Introduction

Ferromagnetism in Mn-doped semiconductors such as InAs, GaAs, and GaN has attracted considerable experimental and theoretical interest over last several years because of their potential implications in the area of spintronics [1,2]. The origin of ferromagnetism in these systems is commonly ascribed to exchange interaction between localized Mn moments via the itinerant conduction electrons (or holes) [3,4]. It has been recently suggested that clustering of Mn ions and subsequent local enhancement of ferromagnetic exchange coupling between neighboring Mn spins might indeed increase the ferromagnetic transition temperature of these diluted magnetic semiconductors [5,6]. For example, *ab initio* density-funtional theory studies carried out in (Mn_xN) clusters by two of us have indicated that these clusters can carry large magnetic moments at zero temperature, indicating intra-cluster ferromagnetic coupling between Mn moments [5]. The natural

---

*Corresponding author. *E-mail:* mahanti@pa.msu.edu

questions then are: whether these large moments survive thermal fluctuations and if so how they interact to give rise to enhanced ferromagnetic transition temperature. In this paper we address these questions by constructing model interacting quantum spin clusters and studying their magnetic properties.

2. Model

We use a quantum Heisenberg model to describe the interaction between Mn and N spins belonging to individual clusters and, for simplicity, we do not take into consideration the distribution in cluster sizes.

In a given (Mn_xN) cluster Mn spins do not interact directly because of large separation [5], but they interact with the spin of a common N neighbor. Furthermore, the clusters magnetic moments interact via long range interactions whose exact nature depends on the doping etc... In this paper, we treat this interaction using a mean field approach assuming the inter-cluster interaction to be ferromagnetic. Under these conditions, the effective single-cluster Hamiltonian is given by

$$H = -J_0 \sum_{i=1}^{x} \mathbf{S}_i.\mathbf{s} - J \sum_{i=1}^{x} < \mathbf{S}_i + \mathbf{s} > \sum_{i=1}^{x} (\mathbf{S}_i + \mathbf{s}) - g\mu_B \mathbf{B} \sum_{i=1}^{x} (\mathbf{S}_i + \mathbf{s}) \,, \quad (1)$$

where $\mathbf{S}_i$, $\mathbf{s}$ are Mn and N spins, respectively; J_0 gives the strength of the intra-cluster exchange interaction between Mn and N spins, and J is a measure of the inter-cluster ferromagnetic coupling. B is the externally applied field in z-direction; g is the g-factor and μ_B is the Bohr magneton. We have studied clusters with $x \leq 4$. For clusters with larger x it is not possible to represent the low energy excitations by Spin Hamiltonian given by (1).

In the following sections, we discuss the results of calculations of magnetization and magnetic susceptibility carried out exactly (numerically) for (Mn_2N) clusters. The results for other clusters will be discussed in a future publication. In case of (Mn_2N), the spin system consists of three spins $S_1 = S_2 = 5/2$ (for Mn) and $s = 1/2$ (for N). The value of intra-cluster coupling J_0 is obtained by knowing the energies of states with different z-component (S_z) of the total spin S given by density-functional method. These calculations were carried out using generalized spin density functional theory with GGA for exchange correlation potential. For example, the ground state of (Mn_2N) has $S_z = 9/2$ (in units of $\hbar$) with energy -262.64932 *Hartrees* and the first excited state with $S_z = 11/2$ and energy -262.64321 *Hartrees* [7]. From the energy difference between these two configurations we estimate J_0 to be $-30meV$. This implies that the N and Mn spins in a given cluster are antiferromagnetically coupled.

3. Results

3.1. *Non-interacting Clusters*

Several physical observables e.g. magnetization $M = -\frac{\partial G}{\partial B}$ and magnetic susceptibility $\chi = -\frac{\partial^2 G}{\partial B^2}$ can be calculated exactly for a single cluster once we know the magnetic Gibb's free energy G. G is given by

$$G = -k_B T \ln Z, \quad Z = \sum_n e^{-\beta E_n};$$

where E_n is the energy of the system given by (1).

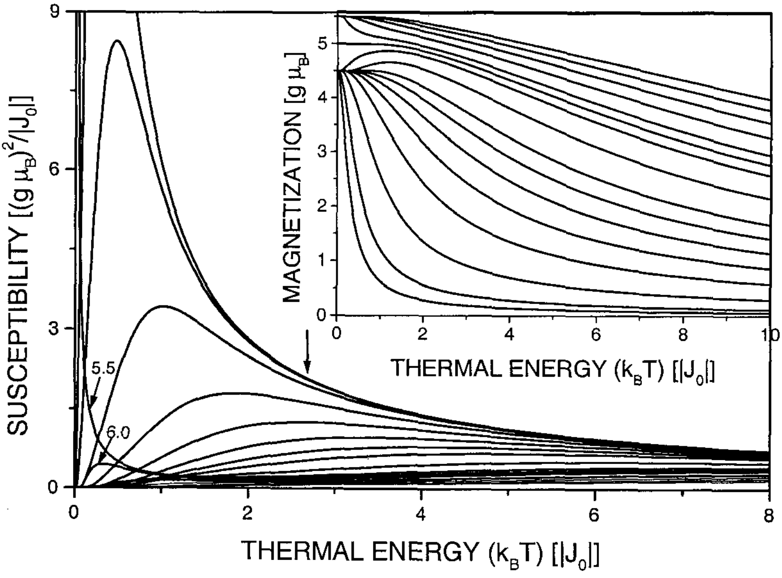

Figure 1. Magnetization (inset) and magnetic susceptibility (figure) of a single (Mn_2N) cluster with various values of the external magnetic field, $g\mu_B B/|J_0| =$ 0.1, 0.2, 0.5, 1.0, 1.5, 2.0, 2.5, 3.0, 4.0, 5.0, 6.0, 7.0, 8.0, 9.0, 10.0 from below (inset) or in the arrow's direction (figure).

Note that the eigenstates are characterized by the total spin S and S_z. Figure 1 shows the magnetization (inset) and the magnetic susceptibility (figure) of a single cluster as a function of T for different values of B, where $J_0 < 0$. As we see, the temperature dependence of M is strongly affected by B. The decrease of magnetization due to thermal fluctuations is rapid at low external fields, becoming slower as the field is increased. An interesting feature of Fig.1 is that the magnetization at zero temperature increases from 4.5 to 5 and then to 5.5. This means that the ground state of the system changes from a state of $S_z = 9/2$ to an intermediate state of $S_z = 10/2$ (at $g\mu_B B_0 = 5.5|J_0|$) and then to a state of $S_z = 11/2$. It is important to note that the state with $S_z = 10/2$ is not possible for the cluster of 3 spins (5/2,5/2,1/2). This state appears because at a particular magnetic field states with (S, S_z)=$(11/2, 11/2)$ and $(9/2, 9/2)$ become degenerate and we see the average value in the limit of zero T. We also see the effect of the transition from anti-ferromagnetic to ferromagnetic ordering in the ground state with increasing the external field as described above on χ. For all fields excepting the cross-over field B_0, $\chi \to 0$ as $T \to 0$. This is easily understood because the ground state in the presence of nonzero B (excepting $B = B_0$), is non-degenerate and $\chi \to \frac{1}{T} e^{-\frac{B}{T}}$. For the cross-over field however, due to the the degeneracy of the ground state, $\chi \to \frac{1}{T}$.

3.2. *Interacting Clusters*

To study the effect of the inter-cluster coupling on magnetic properties we assume that this interaction is ferromagnetic, $J > 0$. If, on the other hand, this interaction is anti-ferromagnetic or oscillatory (both ferro and antiferro), then the system will be a spin-glass. Since the thermodynamic average of the total spin of a cluster is proportional to its magnetization, the magnetization depends on itself via the energy function, i.e. we have to solve self-consistently an equation of the form:

$$M = f[B, T, M], \tag{2}$$

to find the magnetization of the interacting clusters.

For zero-field ($B = 0$), equation (2) has non-trivial solution when the following condition is satisfied,

$$\left. \frac{\partial f[B = 0, T, M]}{\partial M} \right|_{M=0} > 1\,. \tag{3}$$

From this equation we can find the critical temperature T_C for the transition from para- to ferro-magnetic phase of the interacting clusters.

The magnetic susceptibility of the interacting clusters is given by

$$\chi = \frac{\chi_0}{1 - \frac{J}{(g\mu_B)^2}\chi_0}, \quad \chi_0 = \frac{\partial f[B,T,M]}{\partial B}. \tag{4}$$

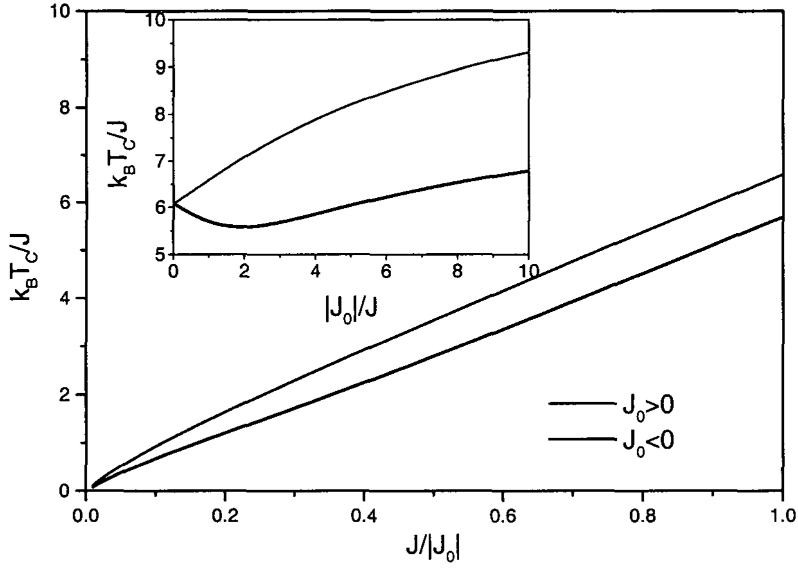

Figure 2. Critical temperature as a function of the interaction for the anti-ferro. ($J_0 < 0$, solid lines) and ferro. ($J_0 > 0$, dashed lines) cases.

Figure 2 shows the critical temperature of interacting clusters as a function of the inter-cluster coupling J (J_0 is kept fixed). For the sake of comparison we have shown results for both anti-ferromagnetic $J_0 < 0$ and ferromagnetic $J_0 > 0$ intra-cluster interactions. In both cases, T_C is almost linear in J except for very small values of J. In the inset, we show how T_C changes with the intra-cluster coupling J_0, keeping J fixed. In the anti-ferromagnetic case ($J_0 < 0$), interestingly, T_C decreases for small values of $|J_0|$ and then increases. This results from the competition between inter- and intra-cluster interactions. In this case, which is appropriate for the (Mn_2N) clusters, the critical temperature T_C is estimated to be about 240K for the choice of $J = 0.1|J_0|$. While we do not have a measure of J, this is a reasonable choice because the strength of inter-cluster interaction is likely to be considerably smaller than the intra-cluster coupling.

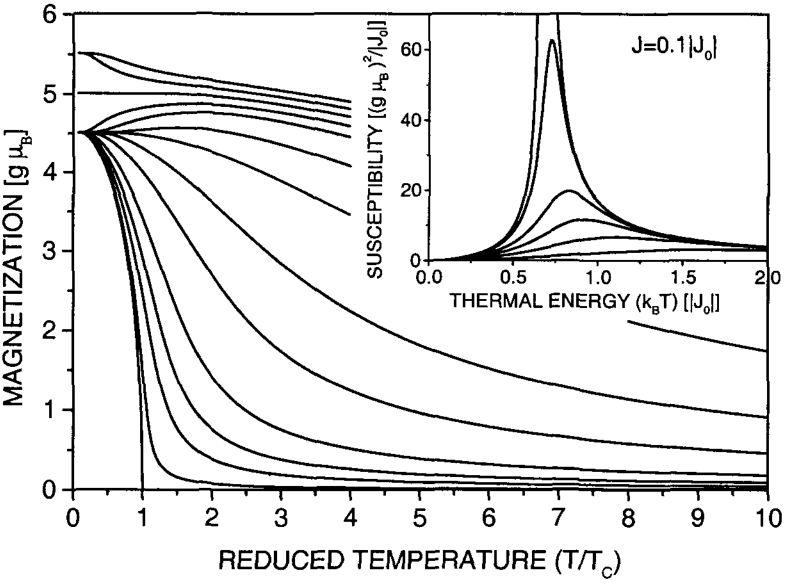

Figure 3. Magnetization (figure) and magnetic susceptibility (inset) of an interacting (Mn_2N) cluster at $J = 0.1|J_0|$ with various values of the external magnetic field, $T_C = 240K$; $g\mu_B B/|J_0|$=0.0, 0.01, 0.05, 0.1, 0.2, 0.5, 1.0, 2.0, 3.0, 4.0, 4.5, 5.0, 5.5, 6.0, from below (figure, up to 6.0) or from above (inset, up to 0.5).

Figure 3 shows the magnetization (figure) and the magnetic susceptibility (inset) of interacting (Mn_2N) clusters as a function of the reduced temperature (T/T_C) for $J = 0.1|J_0|$ and different values of B for $J_0 < 0$. We can see the jump in magnetization at zero temperature, from 9/2 to 10/2 (at $g\mu_B B = 5|J_0|$), and then to 11/2 corresponding to the change from anti-ferromagnetic to ferromagnetic ordering in the ground state with increasing B. In the inset, the magnetic susceptibility is seen to diverge at $T = T_C$ when $B = 0$. The divergence is supressed with increasing B.

4. Summary

In summary, we have constructed a simple model of ferromagnetically coupled magnetic (Mn_2N) clusters taking into account intra-cluster interactions obtained from *ab initio* electronic structure calculations and treating the inter-cluster interactions in a phenomenological (mean-field) approach. We find interesting non-monotonic (as a function of B) low-T response (due to anti-ferromagnetic coupling between Mn and N spins inside a cluster). Furthermore for reasonable choice of inter-cluster ferromagnetic coupling we estimate the transition temperature to be $\sim 250K$. Further work on larger clusters and the effect on cluster size distribution are under progress.

References

1. G.A. Prinz, *Science* **282**, 1660 (1998)
2. F. Matsukura *et al.*, *Phys. Rev.* **B57**, R2037 (1998)
3. M. Methfessel and D.C. Mattis, *Handb. Phys.* **18**(1), 389 (1968)
4. T. Dietl, H. Ohno and F. Matsukura, *Phys. Rev.* **B63**, 195205 (2001)
5. B.K. Rao and P. Jena, *Phys. Rev. Lett.* **89**, 185504 (2002)
6. K. H. Ploog *et al.*, *J. Vac. Sci. Technol.* **B21**(4), 1756 (2003)
7. B.K. Rao and P. Jena (unpublished)

SPIN FLUCTUATIONS AND “SPIN NOISE”

SANDIPAN PRAMANIK
Department of Electrical Engineering, Virginia Commonwealth University, Richmond, VA 23284, USA

SUPRIYO BANDYOPADHYAY
Department of Electrical Engineering and Department of Physics, Virginia Commonwealth University, Richmond, VA 23284, USA

We have theoretically studied the temporal fluctuations and the resulting kinetic noise in the average spin polarization of an electron ensemble drifting in a quantum wire under a high electric field. Electrons are initially injected in the wire from a ferromagnetic contact with all their spins polarized along the wire axis. The average spin polarization of the ensemble decays during transport because of D’yakonov-Perel’ relaxation caused by both Rashba and Dresselhaus interactions. Once steady state is reached, the average spin fluctuates randomly around zero. The time average of this fluctuation is zero. The autocorrelation function of this fluctuation approximates a Lorentzian and so does the spectral density. To our knowledge, this is the first study of spin fluctuations and “spin noise” in a nanostructure.

1. Introduction

“Spintronics” is a rapidly burgeoning field of science and technology dedicated to the development of electronic and optical devices that exploit the spin degree of freedom of charge carriers to elicit a myriad of storage and processing functions. A number of spintronic device proposals have appeared in the literature, e.g. spin-HEMTs[1], diodes[2], solar cells[3], filters[4], stub tuners[5], spin-coherent photodetectors[6] and quantum spin field effect transistors that transport a spin current in the absence of any charge current[7]. Modeling spin transport in *nanostructures* has gained particular importance since quantum confinement has been found to strongly suppress spin depolarization mechanisms, making spin polarization long-lived.

Spin transport in semiconductors has been treated in the past with a variety of models such as: (1) *single particle ballistic models* which are fully quantum mechanical but do not account for any scattering or spin dephasing effects[8, 9]; (2) *phase coherent quantum mechanical approaches* that treat spin dephasing via elastic scattering only[10]. These are more sophisticated than the ballistic models but do not account for inelastic (or phase-breaking) scattering mechanisms, which are important at high temperatures and electric fields; (3) *linear classical drift diffusion models*[11, 12] that cannot handle non-linear and non-local effects. More importantly, being classical, they cannot account for interference between orthogonal spin states (e.g. "spin-up" and "spin-down" states); and finally (4) *semi-classical non-linear models*[13-16] which couple spin density matrix evolution (based on a fully quantum mechanical Sturm-Liouville type equation) with the semi-classical Boltzmann transport equation. This approach can account for non-linear transport effects, as well as interference effects between orthogonal spin states. So far, these models have revealed surprising features of spin transport in semiconductor quantum wires. For instance, it has been shown that spin relaxation rate can be very anisotropic (spin injected along the wire is much longer lived than spin injected transverse to the wire axis) and the relaxation rate can be suppressed by at least an order of magnitude by quasi one-dimensional quantum confinement[13-15]. These models are ideal for studying spin relaxation due to D'yakonov-Perel'[17] and Elliott-Yafet[18] mechanisms. They are also capable of producing information about spin fluctuations since they are microscopic and deal with a *spin distribution function* unlike the drift diffusion models that deal only with ensemble averaged "moments" of the distribution function. In this paper, we have used such a model to study temporal spin fluctuations of a steady state electron ensemble drifting in a quantum wire under a high electric field when hot carrier effects (non-local and non-linear effects) are important. To our knowledge, this is the first study of spin fluctuation and noise in a nanostructure. We present results pertaining to the autocorrelation function of the fluctuations as well as the spectral density of the associated kinetic "spin noise".

2. Theory

We consider a "spin-valve" type quantum wire structure consisting of a GaAs quantum wire capped by half-metallic ferromagnetic contacts with 100% spin polarization. The wire has a rectangular cross section of 30 nm × 4 nm. The confining potential in the wire is slightly asymmetric which gives rise to a uniform electric field of 100 kV/cm transverse to the wire axis (y-axis, see Figure 1).

This field, which can be applied by an external gate contact as visualized in reference 1, causes a Rashba interaction in the wire, but does not perturb the energy levels in the wire significantly[14]. The ferromagnetic contact is magnetized along the axis of the wire and therefore injects electrons with their spins polarized along the wire. An electric field $E_x\hat{x}$ is applied along the axis of the wire ($\hat{x}$ axis) to drive transport. As the electrons traverse the wire, they experience momentum dependent spin-orbit coupling interactions due to the Rashba effect (structural inversion asymmetry) [19] and the Dresselhaus effect (bulk inversion asymmetry) [20]. As a result, the spin vector of each electron precesses around an effective magnetic field. This precession is randomized by inter-subband scattering between different subbands that have different Dresselhaus interaction strengths[14]. As a result, the *ensemble averaged spin* decays with time resulting in D'yakonov-Perel' type relaxation.

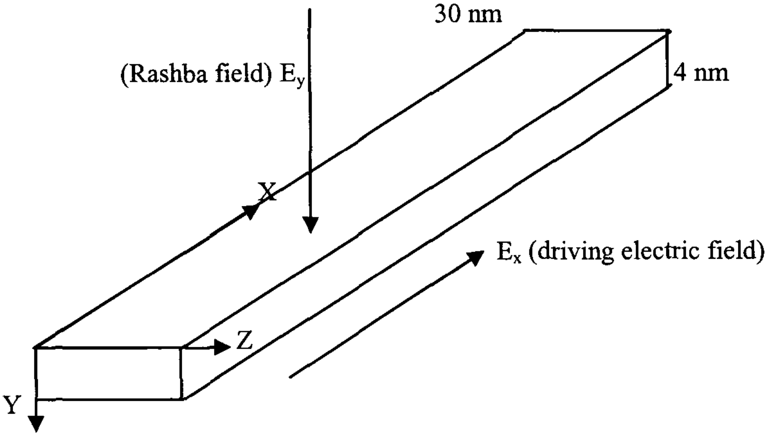

Figure 1. Geometrical structure of the quantum wire and axis designations.

We have considered a case where E_x = 2kV/cm and the lattice temperature T =30K. The details of the simulation approach (which is based on a Monte Carlo simulator modified to study spin transport) can be found in reference 15 and will not be repeated here. In the simulation, we consider only the D'yakonov-Perel' relaxation[17] and ignore the Elliott-Yafet[18], Bir-Aronov-Pikus[21] and all other relaxation mechanisms (including relaxation due to hyperfine interactions with the nuclei[22]), since these are insignificant compared to the D'yakonov-Perel' relaxation in the present case.

In Figure 2, we show that the ensemble average spin component along the wire axis $\langle S_x \rangle(t)$ decays to zero after 6 ns and thereafter continues to fluctuate around zero, signaling the onset of complete depolarization. We will study the nature of this spin fluctuation.

We define spin autocorrelation function as follows:

$$C(\tau) = \int_{t_0}^{\infty} \left[\langle S_x \rangle(t) - \langle S_x \rangle_{av}\right]\left[\langle S_x \rangle(t+\tau) - \langle S_x \rangle_{av}\right] dt \qquad (1)$$

where

$$\langle S_x \rangle_{av} = \int_{t_0}^{\infty} \langle S_x \rangle(t) dt \qquad (2)$$

and the variable τ is generally referred to as "delay time".
We observe from Figure 2 that $\langle S_x \rangle(t)$ varies randomly around zero for $t \geq t_0$ where t_0 is the time taken to reach steady state. Hence, $\langle S_x \rangle_{av} = 0$.

The noise spectral density is defined as the cosine transform of the autocorrelation function and is expressed as follows:

$$S(f) = \int_{0}^{\infty} \left[C(\tau)\cos(2\pi f \tau)\right] d\tau \qquad (3)$$

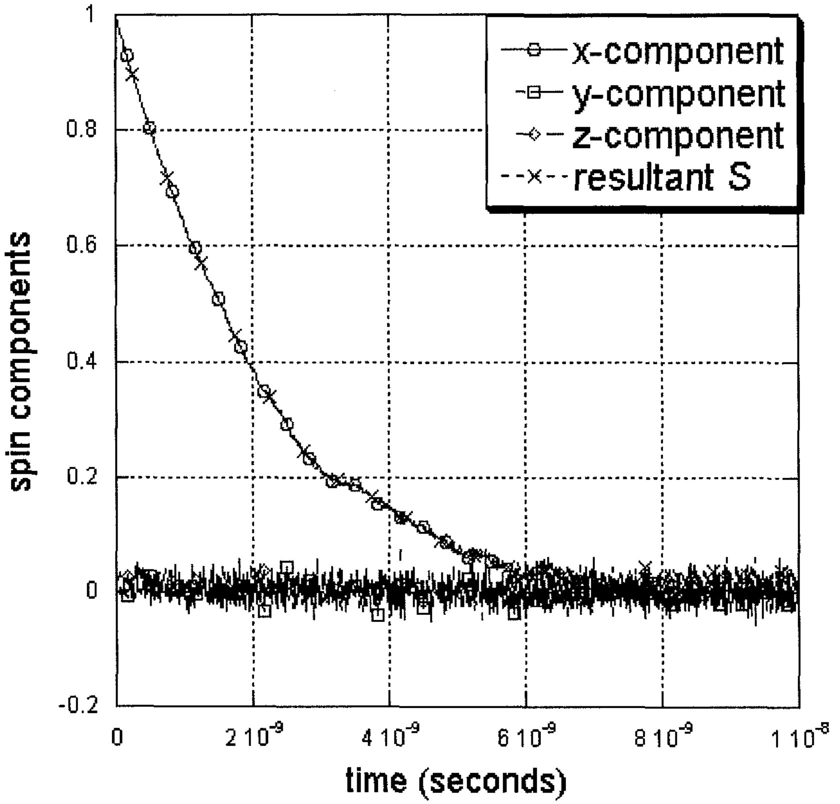

Figure 2. Temporal dephasing of the x, y and z components of ensemble average spin in the GaAs quantum wire at 30K. The driving electric field is 2kV/cm and the spins are injected with their polarization initially aligned along the wire axis (x-axis).

3. Results and discussion

Figure 3 shows the autocorrelation function of the spin fluctuations at a driving electric field of 2kV/cm and the lattice temperature of 30K. The autocorrelation function decays rapidly and becomes almost zero for τ = 0.375 ns. Beyond this point it shows very small fluctuation around zero.

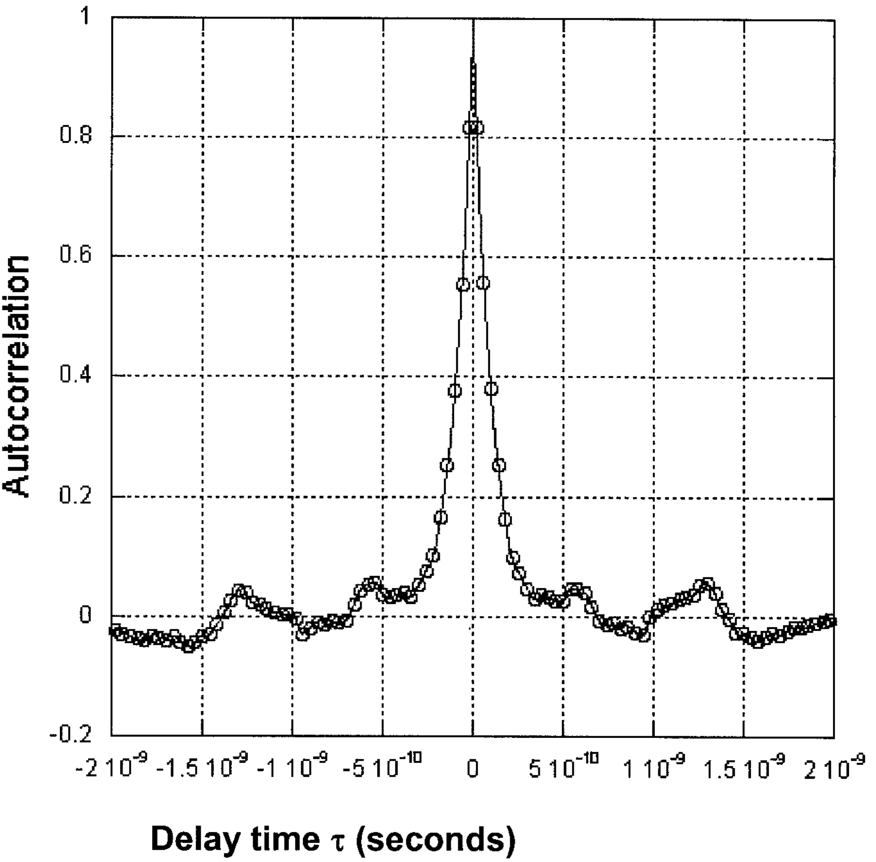

Figure 3. Autocorrelation function of the spin fluctuations in the GaAs quantum wire at a driving electric field of 2 kV/cm and at a lattice temperature of 30 K.

The associated noise spectral density is shown in Figure 4. It decays rapidly within 10 GHz.

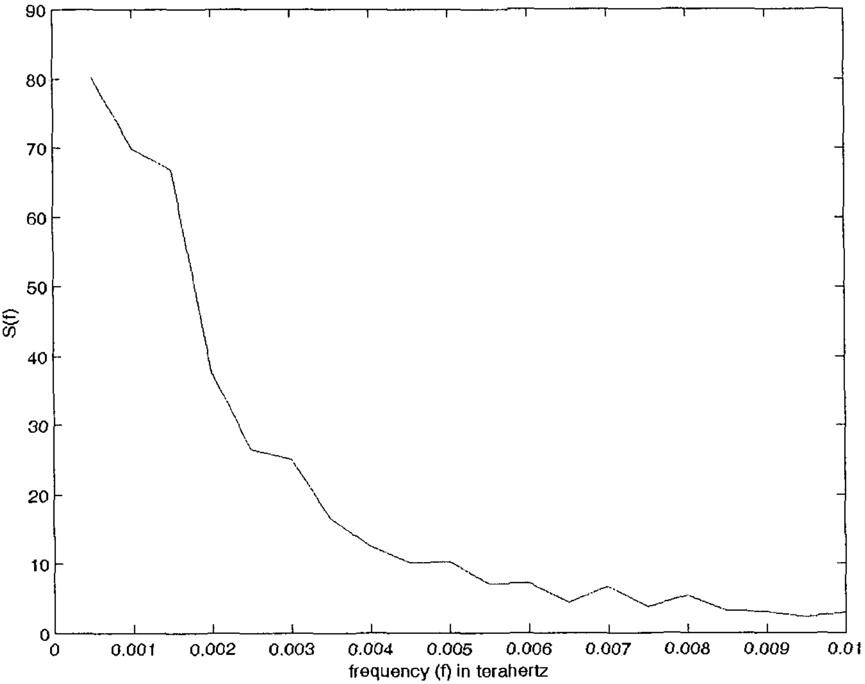

Figure 4. The spectral density of "spin-noise" in the quantum wire for driving electric field=2kV/cm and lattice temperature=30K.

4. Conclusion

In this paper we have studied, for the first time, "spin noise" in a semiconductor structure using a semi-classical approach. The autocorrelation function has no long-duration component indicating that once steady state is reached, there is no long-lived "memory" of the initial spin state in the fluctuations. The D'yakonov-Perel' relaxation is therefore an efficient relaxation mechanism that completely erases any long-lived memory of the initial spin state.

5. Acknowledgments

This work is supported by the US National Science Foundation under grant ECS-0196554. The authors are indebted to Prof. Marc Cahay for stimulating discussions.

References

1. S. Datta and B. Das, *Applied Physics Letters*, **56**, 665 (1990).
2. M.E. Flatte' and G. Vignale, *Applied Physics Letters*, **78**, 1273 (2001).
3. I. Zutic, J. Fabian, S. Das Sarma, *Applied Physics Letters*, **79**, 1558 (2001).
4. T. Koga, J. Nitta, H. Takayanagi and S. Datta, *Physical Review Letters*, **88**, 126601 (2002).
5. X.F. Wang, P. Vasilopoulos and F.M. Peeters, *Physical Review B*, **65**, 165217 (2002).
6. R. Vrijen and E. Yablanovitch, *Physica E*, **10**, 569 (2001).
7. B. Wang, J. Wang and H. Guo, *Physical Review B*, **67**, 092408 (2003).
8. F. Mireles and G. Kirczenow, *Physical Review B*, **64**, 024426 (2001).
9. Th. Schparers, J. Nitta, H. B. Heersche and H. Takayanagi, *Physica E*, **13**, 564 (2002).
10. M. Cahay and S. Bandyopadhyay, www.arXiv.org/*cond-mat/0305622, Phys. Rev. B (in press)*.
11. J. Fabian, I. Zutic and S. Das Sarma, *Physical Review B*, **66**, 165301 (2002).
12. Z. G. Yu and M. E. Flatte, *Physical. Review B*, **66**, 235302 (2002).
13. S. Pramanik, S. Bandyopadhyay and M. Cahay, *Proc. of IEEE-NANO 2003 (also www.arXiv.org, cond-mat/0306082)*.
14. S. Pramanik, S. Bandyopadhyay and M. Cahay, *www.arXiv.org/cond-mat/0310245*. Also *Applied Physics Letters*. (in press).
15. S. Pramanik, S. Bandyopadhyay and M. Cahay, *Physical Review B*, **68**, 075313, (2003).
16. S. Saikin, M. Shen, M. C. Cheng and V. Privman, *www.arXiv.org/cond-mat/0212610* and, *www.arXiv.org/cond-mat/0302395*; A. Bournel, V. Delmouly, P. Dollfus, G. Tremblay and P. Hesto, *Physica E* (Amsterdam), **10**, 86 (2001).
17. M. I. D'yakonov and V. I. Perel', *Soviet Physics Solid State*, **13**, 3023 (1972).
18. R. J. Elliott, *Physical Review*, **96**, 266 (1954).
19. Y. A. Bychkov and E. Rashba, *Journal of Physics C: Solid state Physics*, **17**, 6039, (1984).
20. G. Dresselhaus, *Physical Review*, **100**, 580 (1955).
21. G. L. Bir, A. G. Aronov and G. E. Pikus, *Soviet Physics JETP*, **42**, 705 (1976).
22. A. V. Khaetskii, D. Loss and L. Glazman, *Physical Review Letters*, **88**, 186802 (2002).

GEOMETRY DRIVEN INTERFACIAL EFFECTS IN NANOSCOPIC AND MACROSCOPIC SEMICONDUCTOR METAL HYBRID STRUCTURES: EXTRAORDINARY MAGNETORESISTANCE AND EXTRAORDINARY PIEZOCONDUCTANCE

S. A. SOLIN[†]

Department of Physics and Center for Materials Innovation, Washington University in St. Louis, St. Louis, MO, 63130, USA

The interface resistance between the metal and semiconductor components of a hybrid structure can be altered by external perturbations such as a magnetic or strain field. For selected geometries, such perturbations give rise to a redistribution of current flow in the metal and semiconductor that results in a large amplification of the effective resistance of the hybrid. Two examples of this general phenomenon, extraordinary magnetoresistance (EMR) and extraordinary piezoconductance (EPC) are presented.

1. Introduction

The recent discovery by Solin and co-workers of the phenomenon of extraordinary magnetoresistance (EMR) in hybrid structures of narrow-gap semiconductors and non-magnetic metals[1] portends considerable promise for impacting magnetic sensor technology for macroscopic, microscopic and nanoscopic applications.[2] It has been recently realized by Solin and his colleagues that the EMR phenomenon, is but one example of a broad class of geometry-based interfacial effects in hybrid structures formed from the juxtaposition of a semiconductor such as InSb, InAs[3] or $Hg_{1-x}Cd_xTe$[4] with a metal such as Au. Indeed, one can envision a number of other "EXX" interfacial effects in metal semiconductor hybrid structures where E = extraordinary and XX = photoconductivity, electroconductivity, thermoconductivity etc. and combinations of these such as magnetothermoconductivity. These new EXX effects form the basis for a number of new macroscopic and nanoscopic sensor devices analogous to those such as automobile ignition sensors and ultra-high-density read-head sensors, respectively, that derive from the discovery of the EMR phenomena. Here we first provide a discussion of the general principle of the EXX phenomena. We then illustrate the phenomena for macroscopic and

---

[†] Work partially supported by the US National Science Foundation under grant # ECS-0329347.

nanoscopic EMR devices. Finally we show proof of principle results for the newly discovered extraordinary piezoconductance, (EPC) effect.

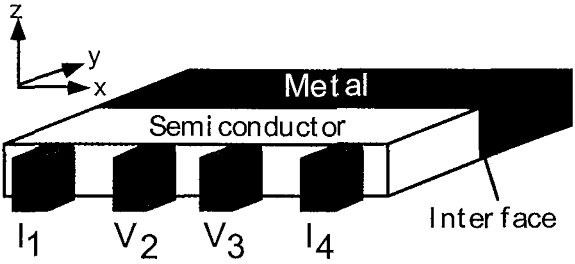

Figure 1. A schematic diagram of a hybrid semiconductor-metal structure configured for a 4-probe measurement. I and V refer, respectively to current and voltage probes.

2. Generalized EXX Phenomena

Consider a simple hybrid structure composed of a metal and semiconductor such as that shown in Figure 1. For historical reasons,[5] the construct in Fig. 1 is referred to as an externally shunted van der Pauw plate (hereafter vdP). The 4-probe effective resistance of this composite structure is $R_{eff} = V_{23}/I_{14}$, where I and V represent current and voltage probes, respectively. Now R_{eff} will depend on the relative conductivities of the metal and semiconductor (typically $\sigma_{metal}/\sigma_{semiconductor} > 1000$), on the interface resistance between them and on the specific placement of the current and voltage probes (e.g. on the geometry). In a non-perturbed state, the highly conducting metal acts as an effective current shunt, provided that the interface resistance is low, and R_{eff} of the composite structure can be close to that of the metal. If a relatively small external perturbation such as an applied magnetic field, electric field, strain, temperature change etc. significantly alters the interface resistance and, concomitantly, the current flow across the interface, this alteration can manifest itself as a large change in the effective resistance or, equivalently, in the output voltage (signal) of the "sensor" for that particular external perturbation. A concrete example, EMR, will facilitate the illustration of this point.

3. EMR in Macroscopic Structures

Solin *et al.* showed that in general,

$$EMR(\Delta H)=\frac{R^{eff}(\Delta H)-R_0^{eff}}{R_0^{eff}}=G_S(\Delta H)[\mu\Delta H]^2 \pm G_{AS}(\Delta H)[\mu\Delta H] \qquad (1)$$

where ΔH is the applied field normal to the plane of the device, $R^{eff}(\Delta H)$ is the effective field-dependent resistance measured in a 4-probe configuration, μ is the carrier mobility, $G_S(\Delta H)$ and $G_{AS}(\Delta H)$ are, respectively, symmetric and antisymmetric geometric factors which depend on the shape, location and physical properties of the shunt and contacts while $R^{eff}(0) = R_0^{eff}$. Clearly, narrow-gap high mobility semiconductors such as InSb are choice materials for EMR devices.

The EMR of a non-biased macroscopic (long dimensions ~ 0.5 mm) vdP plate formed from InSb and Au is shown in Fig. 2 as a function of the geometry of the metallic shunt and of the placement of the voltage and current leads. Two features are noteworthy: a) the room-temperature EMR is very large reaching values as high as 100% at a field of 500 Gauss. b) The EMR is asymmetric with respect to the applied field when the leads are placed asymmetrically on the rectangular narrow-gap-semiconductor plate. The latter feature constitutes a condition of self-biasing which is important for a number of applications in which the sign of the applied magnetic field must be determined.

The magnetotransport properties of the externally shunted vdP plate clearly depend strongly on the placement of the current and voltage leads, e.g. on lead geometry. These properties also depend strongly on the shape and relative dimensions of the semiconductor and metal components of the hybrid structure itself as can be seen from the dependence of the EMR in Fig. 2 on the width, W, of the shunt for a semiconductor region of fixed width.

The EMR phenomenon can be readily understood using a simple though non-intuitive classical physics analysis. There are two principal contributions to the magnetoresistance (MR) of any resistive device, namely a physical contribution and a geometric contribution.[6] The physical contribution derives from the dependence of intrinsic material properties such as carrier concentration and carrier mobility on the applied magnetic field. The geometric contribution is an extrinsic property that depends on the shape of the device, the placement and geometry of the (metallic) contacts and, the placement and geometry of any inhomogeneities that may be present. The geometric contribution to the MR also depends on the intrinsic physical properties of the inhomogeneities relative to those of the host material, e.g. on the conductivity ratio.[7] For most materials of current interest as MR sensors such as layered magnetic metals which exhibit giant MR (GMR)[8] or tunneling MR (TMR)[9] and the magnetic layered oxide manganites which exhibit colossal MR (CMR),[10] the physical contribution to the MR is dominant. In contrast, judiciously designed EMR hybrid structures can exhibit a room temperature MR that is not only dominated by the geometric contribution but also attains room temperature values of order 1,000,000%[1] which is several orders of magnitude higher than what has been achieved with conventional GMR, TMR or CMR devices.

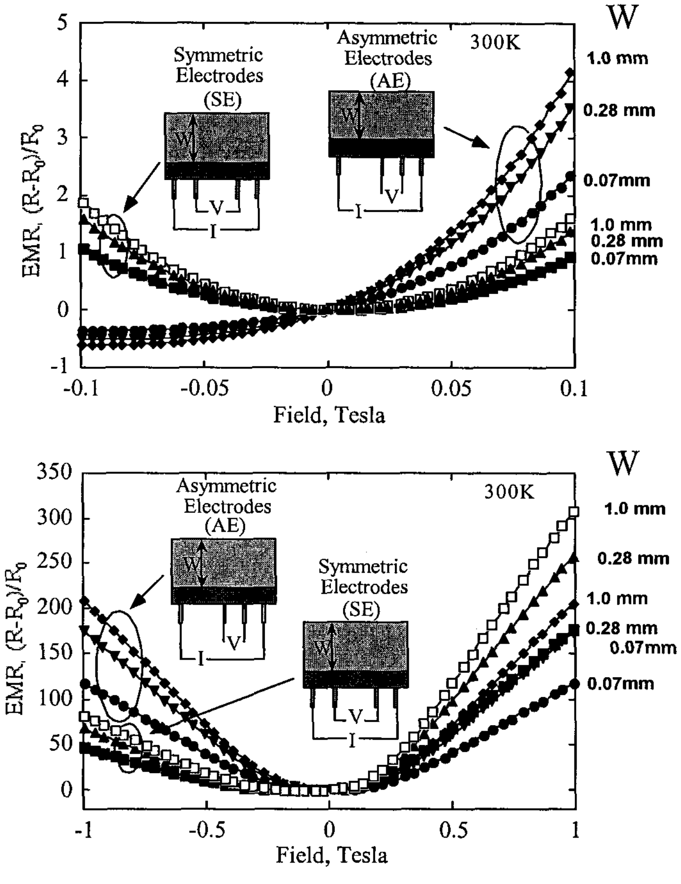

Figure 2. The low field (upper panel) and high field (lower panel) room temperature EMR of van der Pauw plates with symmetric and asymmetric electrode configurations as a function of the width, W, of the external shunt. The dark (light) rectangle represents Te:InSb (Au).

The magnetotransport properties of the macroscopic vdP structure shown in Fig. 2. can be quantitatively accounted for using the above equations together with both finite element analysis[11] and analytic techniques.[12] However, the EMR phenomenon can be readily understood using a simple though non-intuitive classical physics analysis. The components of the magnetoconductivity tensor

$\underline{\sigma}(H)$ for the semiconductor are $\sigma_{xx}(\beta)=\sigma_{yy}(\beta)=\sigma/\left[1+\beta^2\right]$, $\sigma_{zz}(\beta)=\sigma$, and $\sigma_{xy}(\beta)=-\sigma\beta/\left[1+\beta^2\right]=-\sigma_{yx}(\beta)$ with $\beta=\mu H$ and all others being zero. If the electric field on the vertical surface of the shunt is $\vec{E}=E_x\hat{x}+E_y\hat{y}$, the current density is $\vec{J}=\underline{\sigma}(H)\vec{E}$. The electric field is everywhere normal to the equipotential surface of a highly conducting shunt. At $H = 0$, $\underline{\sigma}(H)$ is diagonal so $\vec{j}=\sigma\vec{E}$ and the current flows into the shunt which acts as a *short circuit.* At high H ($\beta>1$), the off-diagonal components of $\underline{\sigma}(H)$ dominate so $\vec{J}=(\sigma/\beta)\left[E_y\hat{x}-E_x\hat{y}\right]$ and $\vec{J}\perp\vec{E}$. Equivalently, the Hall angle between the electric field and the current density approaches 90^0, and the current becomes tangent to, i.e. deflected from, the shunt which then acts as an *open circuit.* The transition of the shunt from short circuit at low H to open circuit at high H results in a geometric enhancement of the MR of the semiconductor even if its resistivity is field-independent (i.e. the physical MR is zero).

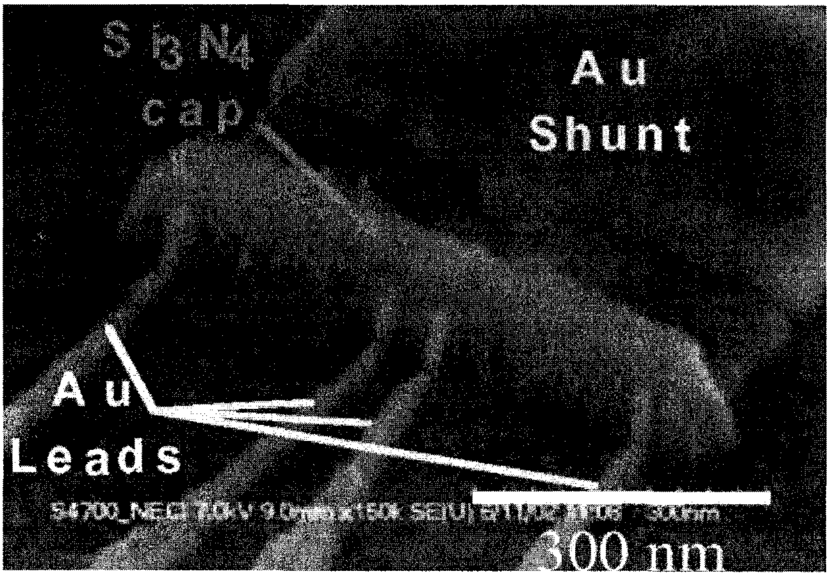

Figure 3. An electron micrograph of a hybrid nanoscopic van der Pauw EMR plate structure fabricated from an $InSb/In_{1-x}Al_xSb$ quantum well heterostructure shown in Fig. 3a. The current leads, voltage leads and external shunt are labeled as indicated. The floor of the etched mesa shown in the micrograph is parallel to the substrate and lies within the 25 nm $Al_{0.15}In_{0.85}Sb$ lower barrier. The four contacts shown in the micrograph extend along the mesa floor and up the side of the mesa to the upper 25 nm $Al_{0.15}In_{0.85}Sb$ barrier.

4. EMR in Nanoscopic Structures

Having established that extremely high values of EMR could be obtained from macroscopic semiconductor-metal hybrid structures, Solin and co-workers then faced the formidable challenge of scaling such EMR devices to the nanoscopic sizes required for ultra-high-spatial resolution and high sensitivity detection of magnetic fields. To meet this challenge, they used a quantum well structure, InSb/InAl$_{1-x}$Sb$_x$, and state of the art suspended mask e-beam lithography incorporating a new type of resist, calixarine, to fabricate the structure shown in Fig. 3. Details of the fabrication method are provided elsewhere[13] with one exception. The leads and shunt on the device shown in Fig. 3 were insulated from the floor of the mesa containing the quantum-well by an Al$_2$O$_3$ layer that extended to within 50 nm of the mesa sidewall.

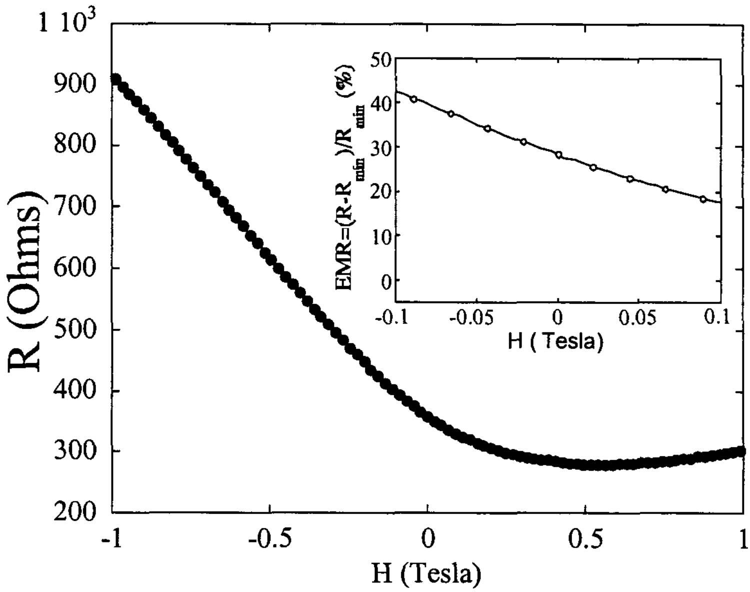

Figure 4. The field dependence of the resistance of the hybrid nanoscopic van der Pauw plate structure shown in Fig.3b. Inset - the extraordinary magnetoresistance (referenced to R_{min}) of the hybrid nanoscopic van der Pauw plate in the low field region.

The field dependence of the room temperature magnetoresistance of the externally shunted nanoscopic EMR device shown in Fig. 3 is shown in Fig. 4. As can be seen, the EMR reaches values as high as 5 % at a signal field of 0.05T. To our knowledge, this is the highest room temperature MR level obtained to date for a patterned magnetic sensor with this spatial resolution. Moreover, with a modest bias field of 0.2 T corresponding to the zero-field offset[14] in Fig. 4, the measured EMR is 35% at a signal field of 0.05 T. [The offset is associated with the asymmetric placement of the leads.] Also note that the device can be biased into a field region where the EMR response is linear with field, a feature that can simplify signal amplification. Equally significant is the fact that the current sensitivity, at a magnetic field bias of 0.2T has a large measured value of 585 Ohm/T at room temperature. It is this figure that enters directly into the calculation of the power signal to noise ratio which is found from the data of Fig. 4 to be 44.5 dB for a bandwidth of 200 MHz and a signal field of 0.05T at a bias of 0.2T.

5. EPC in Macroscopic Structures

In principle, any external perturbation which redistributes the current between the metallic shunt and the semiconductor, in the hybrid structure depicted in Fig. 1, will result in a large conductance change of that hybrid structure. In particular, it can be anticipated that uniaxial tensile strain along the x direction (see Fig. 1) will significantly perturb the interface resistance via perturbation of the barrier to current flow that gives rise to that resistance. For narrow-gap semiconductors such as InSb the room temperature interface resistance with noble metals such as Au is known to be low and of order 10^{-6} - 10^{-7} Ohm-cm^2.[15] This low resistance is a manifestation of the narrow gap of InSb and the ease with which carriers (electrons in this case) can be thermally excited over the barrier. Evidence suggests that such barriers are Schottky-like. However, whatever the detailed nature of the barrier that gives rise to the interface resistance, it can be reasonably anticipated that the barrier height will decrease with increasing longitudinal tensile strain. Since interface resistance varies exponentially with barrier height,[16] strain can be expected to significantly perturb the output of a vdP plate.

Confirmation of this expectation is provided in Fig. 5. which shows the piezoconductance (PC) of macroscopic thin film samples of Te doped (1.7 x 10^{17}/cm^3) InSb – Au hybrid structure vdP plates as a function of the plate geometry. The PC is defined through the 4–terminal effective resistance as $PC(\%) = [R_{eff}(\varepsilon,\alpha) - R_{eff}(0,\alpha)] / R_{eff}(0,\alpha)$ where ε is the strain and α is a filling factor. The parameter α is a quantitative specification of the plate geometry and, in the case of the vdP plate, is a complex but calculable function of the dimensions of the semiconductor and the metal. In general, the larger the filling factor, the larger the area of the metallic shunt relative to the area of the semiconductor assuming a constant thickness for both. Note: $\alpha = 0$ corresponds to a shuntless device and $\alpha = 1$ corresponds to an all-metallic device.

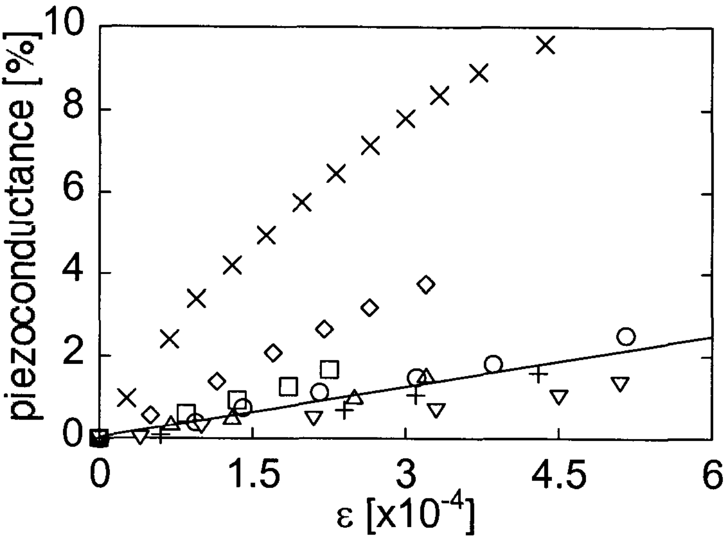

Figure 5. The room temperature piezoconductance versus strain for several different values of a. The symbols correspond to $16\alpha = 0$, O; 6, □; 8, ◇; 9, ×; 12, △; 13, ▽; 15, +; and homogeneous semiconductor alone (—). The uniaxial tensile strain is applied || the metal-semiconductor interface as indicated in fig. 1 and the four terminal resistance is measured according to the labels specified in that figure.

The hybrid structures used to obtain the data of Fig. 5 were fabricated using the same techniques employed in the fabrication of macroscopic EMR devices.[17] The data were acquired with the aid of a homemade piezo-magneto-opto-thermo cryostat insert[18] capable of applying bending-induced uniaxial stain to thin film metal-semiconductor hybrid structures deposited on a substrate which in this particular case was GaAs. The room temperature measurements of R_{eff} were carried out at a fixed current of 1 mA and the strain was gradually increased in the (001) crystal direction, parallel to the metal-semiconductor interface, until the substrate broke. The strain was measured with a resolution of 1.5×10^{-5} using a laser-based optical reflection technique.

Most noteworthy in the data of Fig. 5 is the dramatic increase in PC relative to that of the homogeneous semiconductor the latter being indicated by the solid line in the figure. This enhancement of the PC, which we designate as extraordinary PC or EPC, can be the basis for a new type of strain and/or pressure sensor. The figure of merit which is customarily used to characterize strain-based pressure sensors is the gain factor which is the slope of the quasi-linear PC vs. ε curve.[19] *For $\alpha = 9/16$, the gain factor is ~ 270 (see Fig.5),* *which greatly exceeds that of either metal foil gauges,* the gain factors of which are ~ 2,[19] or homogeneous silicon gauges the gain factors of which are typically 20 (but up to 100). It is clear that the PC of metal-semiconductor vdP hybrid structures exceed this limit of the homogeneous semiconductor via the interfacial enhancement, just as the EMR exceeds the Corbino limit.[20]

Acknowledgments

The author greatly acknowledges his colleagues, A.C.H. Rowe, D.R. Hines, Yu A. Pashkin, J. Shen Tsai, M. Santos and Tineke Thio without whose contributions, this work would not have been possible.

References

1. S. A. Solin, Tineke Thio, D. R. Hines and J. J. Heremans, Science **289**, 1530 (2000).
2. S. A. Solin, and D. R. Hines, *J. Magnetism. and Magnetic Materials*, **226 – 230**, 1976 (2000).
3. C. H. Moller, O. Kronenwerth, D. Grundler, W. Hansen, Ch. Heyn and D. Heitmann, *Appl. Phys. Lett.* **80**, 3988 (2002).
4. S. A. Solin, Tineke Thio, J. W. Bennett, and D. R. Hines M. Kawano, N. Oda, and M. Sano, *Appl. Phys. Lett.* **69**, 4105 (1996).
5. T. Zhou, D. R. Hines and S. A. Solin, *Appl. Phys. Lett.* **78**, 667 (2001).
6. R. S. Popovic, "Hall effect device*s* ", (Adam Hilger, Bristol, 1991).
7. Tineke Thio and S. A. Solin, *Appl. Phys. Lett.*, **72**, 3497 (1998).
8. W. F. Egelhoff, Jr., *et al.*, *J. Appl. Phys.* **78**, 273 (1995).
9. C. Mitra, P. Raychaudhuri, G. Kobernik,, K. Dorr, K. H. Muller, L. Schultzand and R. Pinto, *Appl. Phys. Lett.* **79**, 2408(2001).
10. S. Jin, M. McCormack, T. H. Tiefel and R. Ramesh, *J. Appl. Phys.* **76**, 6929 (1994).
11. J. Moussa, L. R. Ram-Mohan, J. Sullivan, T. Zhou, D. R. Hines, and S. A. Solin, *Phys Rev.* **B64**, 184410 (2001).
12. T. Zhou, D. R. Hines and S. A. Solin, *Appl. Phys. Lett.* **78**, 667 (2001).
13. Yu. A. Pashkin, Y. Nakamura, and J. S. Tsai, *Appl. Phys. Lett.* **76**, 2256 (2000).
14. S. A. Solin, Tineke Thio, J. W. Bennett, and D. R. Hines M. Kawano, N. Oda, and M. Sano, *Appl. Phys. Lett.* **69**, 4105 (1996).
15. C. Y. Chang and S. M. Sze, *Solid State Elect.* **13**, 727 (1970) and references therein.

16. S. M. Sze, *Physics of Semiconductor Devices* (John Wiley & Sons, New York, 1981).
17. S. A. Solin, Tineke Thio and D. R. Hines, Physica **B279**, 37 (2000).
18. A. C. H. Rowe. K. Fasanella, D. R. Hines, T. Zhou and S. A. Solin, *Rev. Sci. Inst.* **73**, 4270 (2002).
19. M. L. Nagy, C. Apanius, J. W. Siekkinen and H. V. Estrada, *Sensors Express*, June (2001).
20. R. S. Popovic, "Hall effect device*s*", (Adam Hilger, Bristol, 1991).

LIGHT TORQUED NANOMOTORS IN A STANDING WAVE

KEITH BONIN
Department of Physics, Wake Forest University,
Winston-Salem, NC 27109 USA

ANDREW SHELTON
Department of Physics, Wake Forest University,
Winston-Salem, NC 27109 USA

BAKHIT KOURMAN
Department of Physics, Wake Forest University,
Winston-Salem, NC 27109 USA

THAD WALKER
Department of Physics, University of Wisconsin,
Madison, WI 53706 USA

Light torques that use polarization are a novel and important way to control nanoparticles and to produce nanomotors. We briefly summarize results from previous experiments, where we applied light torques to glass nanorods in a single-beam optical trap, and we give a preliminary report on new experiments to apply torques using a dual-beam standing wave trap. A standing wave trap will enable us to study the effect of a nearby surface on the behavior of a rotating nanorod. Such investigations will help us to model and understand nanorheological phenomena that could be important factors in nanofluidics in both biological and inorganic systems.

1. Introduction

Light forces can control microscopic and nanoscopic particles, and light traps or optical tweezers have been applied to a wide variety of problems in physics, chemistry and biology[1]. Light torques were first observed by Beth a long time ago using lamps and birefringent quartz[2]. In recent years many clever schemes for applying light torques have been devised for particles on the microscopic and nanoscopic scale[3-14]. Here we briefly report on two related schemes for applying light torques to asymmetric nanoparticles. Both methods rely on rotating linearly polarized light to produce the torque on an induced dipole in the particle. We have generated nanomotors, that rotate at moderate speeds, and nanorockers, whereby the rodlike particles oscillate between two fixed angles. The rotation and rocking frequencies can change without modifying the trapping forces. We discuss a simple model to explain observed behavior and to predict what will happen in a standing wave optical trap.

The experiments were performed with an optical tweezers setup that had up to 20 mW of laser light at wavelength λ= 514 nm from an Ar+ laser. We trapped cylindrical borosilicate glass fibers (average diameter d = 260 nm and lengths of 1-5 μm). Single-beam optical tweezers used a 100x, NA=1.3 oil-immersed objective – see Fig. 1. The standing wave setup consisted of the same laser light split into two beams using a prism beamsplitter and two 100x, NA=1.25 NA oil objectives. The laser beam waist at focus was about 0.5 μm. In both setups, a half-wave plate was used to rotate the polarization of the laser light in a controlled fashion. A stepper motor could be used to continuously change the polarization axis of the light.

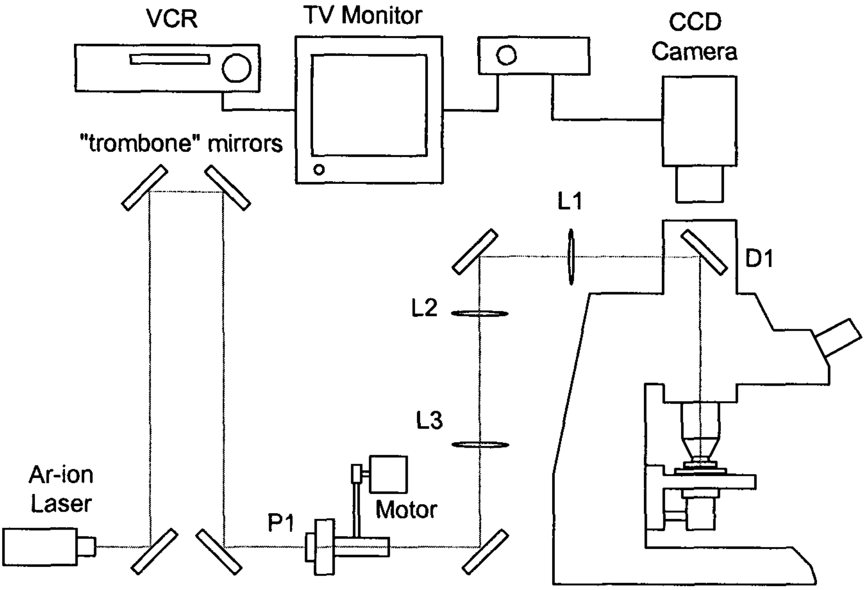

Figure 1. A sketch of the apparatus. The trombone mirrors allow for the beam to expand; L1 and L2 are beam expanding lenses to allow for fine adjustment of the size of the beam at the back focal plane of the objective. Lense L3 is to match the radius of curvature expected by the finite tube length objective. D1 is a dichroic that reflects laser light and transmits light at longer wavelengths than the laser. P1 is the half-wave plate, which is rotated using a stepper motor; this causes the linearly polarized light to rotate at twice the motor shaft rotation frequency.

2. Single Beam Results

The sample consisted of glass nanorods suspended in water between a glass microscope slide on the bottom and a microscope coverslip on the top. The sample was sealed with valap. It is important to note that if a nanorod was lifted above the bottom of the sample it would orient longitudinally (its long axis along the beam propagation direction). To hold the nanorods transversely in the trap, they must be kept within a rod length of the surface of the slide. Experiments involving microscopic particles, where $\lambda << d$, can be explained using ray optics.

In our case, the particle diameter $d < \lambda/2$, and so we will describe the light-particle interaction in the Rayleigh limit (where $d < \lambda/6$). An electric field **E** will induce a dipole moment $\mathbf{p} = \overleftrightarrow{\alpha}\mathbf{E}$ in the particle, where $\overleftrightarrow{\alpha}$ is the particle's polarizability tensor. A torque $\boldsymbol{\tau}$ is produced, where $\boldsymbol{\tau} = \mathbf{p} \times \mathbf{E}$ and this causes the dielectric glass nanorod to try to align its long axis along **E**. The magnitude of the torque depends on the polarizability difference $\alpha = \alpha_{\parallel} - \alpha_{\perp}$. Using this torque in Newton's second law gives rise to a nonlinear equation of motion

$$I\ddot{\theta} = U\sin[2(\Omega t - \theta)] - \gamma\dot{\theta} \qquad (1)$$

where the dot over a function indicates a time derivative; I is the moment of inertia; $U = -\alpha E_0^2/4$ is the trapping potential (time-averaged over one optical cycle); θ is the angle of the nanorod axis with respect to a fixed laboratory frame axis; Ω is the angular rotation frequency of the light polarization axis; and γ is the angular drag coefficient from Stokes law for rotation in a viscous medium[15]. Equation 1 ignores the important interaction of the nanorod with the nearby surface. In most cases the left hand side of Eq. 1 can be ignored (except in vacuum conditions, where the damping term is small). Under normal circumstances, at low Reynolds number[16], the drag torque exceeds the inertial term by 7-8 orders of magnitude.

The main single beam results consisted of saltatory (or interrupted) rotation – see Fig. 2(a), and nanorod rocking – see Fig. 2(b). Both of these behaviors occurred while the laser polarization was smoothly rotating at a set frequency. Sometimes the motion would switch from one type to the other. However, very stable rotation or rocking could be readily achieved. For instance, we started a nanorod rotating at a certain rate, left the laboratory for about 45 minutes, and when we returned the rod was still rotating as before. One critical clue about the condition that determines whether the rod will rock or rotate is the trapping point along the rod. A centered trapping point favors rotation, while an off-center trapping point will frequently favor rocking. The rate of rocking and rotation also depended on the rotation rate of the linearly polarized light. For example, the total angular range $\Delta\theta$ of the rocking motion decreased monotonically with rotation frequency.

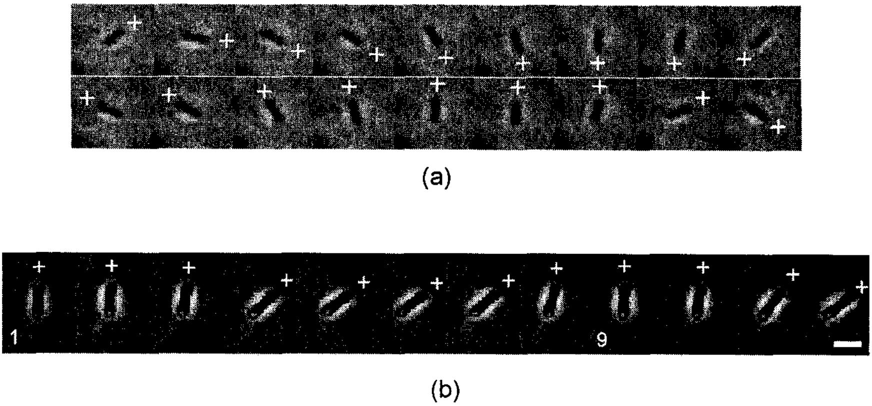

Figure 2. Image sequences showing two different types of motion. In each frame a + symbol labels the orientation of the rod. (**a**) Nanomotor behavior: the rod rotates in response to a rotating polarization light torque. Note the subsequence of frames in which the rod is not moving (or interrupted). Only every other frame from the original sequence is shown. (**b**) Nanorocker behavior: here the rod rocks in response to a rotating polarization light torque. In frame # 9, the nanorod has completed one full period of rocking.

The rotary motion was not smooth, but was interrupted by 'dead' times where the rod slowed down. This effect is clear from Fig. 2(a) and is illustrated in Fig. 3, where we have plotted the angular position versus time for several periods of a nanorod undergoing rotatory motion. Due to surface-rod interactions, the speed of rotation did not reach the speeds or the shape predicted by the model embodied in Eq. 1. Additional details about the motion in a single-beam trap can be found in Ref. [12].

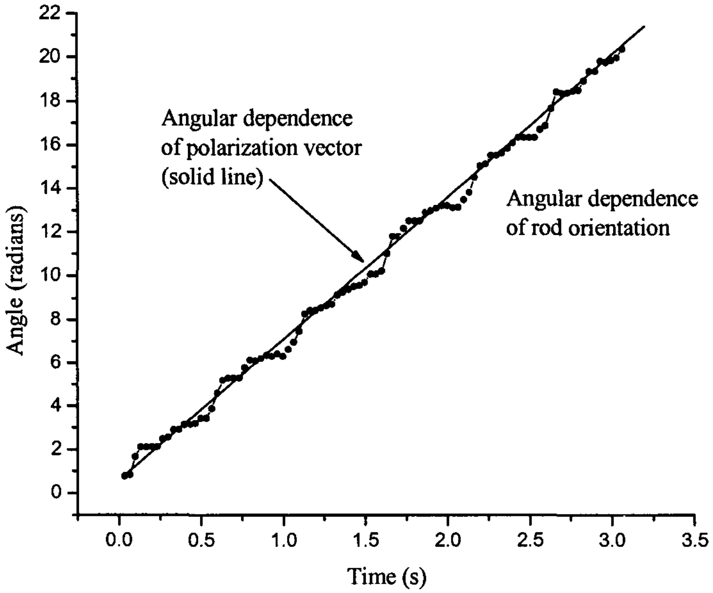

Figure 3. A plot of the rotation angle θ versus time for the motion corresponding to the sequence given in Fig. 2(a). The zero of angle is defined to be the positive y-axis, with positive angles measured with a clockwise rotation. The laser polarization rotation frequency was Ω=6.5 rads/s and the angle of the polarization vector is shown as the solid line in the figure. Note that the sequence of images in Fig.2(a) corresponds to slightly more than one period of the motion, whereas this plot goes significantly farther out in time.

3. Standing-Wave Optical Trap

It is not possible to model the motion of the single beam trapped nanorods in detail, due to a lack of knowing the rod-surface distance and due to the complex nature of the rod-surface interaction. For motion well away from the surface, Eq. 1 would predict an angular position versus time like that graphed in Fig. 4. In order to access this cleaner regime for the motion, that allows one to ignore surface effects, we are developing a standing wave optical trap. We expect that such a trap, when finally complete, will be able to trap a rod in a horizontal position (long axis parallel to the sample surface) at any depth in the sample. The rod diameter is less than a wavelength of light, and so it should become trapped in the region of an antinode of the standing wave beam.

Preliminary results of our attempts to trap in a standing wave show that the rods need to be small to be trapped well away from the surface. The ability to image such small rods is compromised by the use of another objective in place of the usual condenser lens, which normally guarantees the highest possible optical resolution. Results on a single nanorod trapped from below and from above simultaneously show that the standing wave can trap a rod. Initially we had the linearly polarized light rotating in opposite directions, so that the trapped rod did not rotate at all while the linearly polarized light was rotating. If we blocked the top beam (trapping by the bottom beam only), the nanorod rotated clockwise and if we blocked the bottom beam (trapping by the top beam only) the nanorod rotated counterclockwise. Trapping with just the bottom beam allowed the nanorod to rotate at much higher speeds than earlier single-beam results. However, the rods did not exactly follow the predicted curve in Fig. 4, and a more detailed analysis of the motion awaits future results, where the distances from both sample surfaces are known.

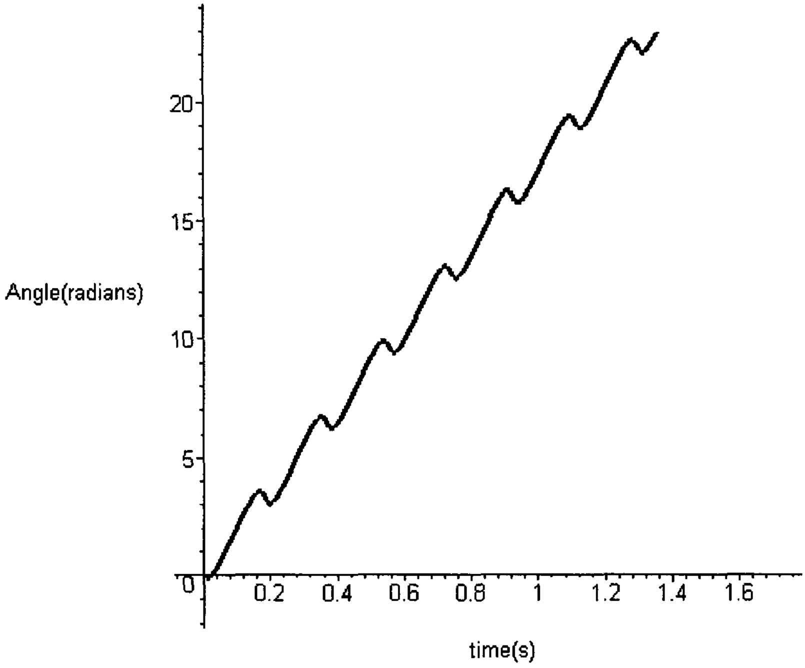

Figure 4. A theoretical plot of the rotation angle θ versus time for a nanomotor free of the surface and rotating at an angular frequency of Ω=34 rads/s. The curve is a plot of the solution to Eq. 1, for typical rotation rates and intensities available from the experimental apparatus.

The ability to control surface-rod distances will enable us to study nanorheological behavior near surfaces. Such nanorheological behavior can play an important role in nanofluidic flow due to the increased importance of surface effects in motion at the nanoscale. Microfluidic and nanofluidic regimes in biology, physics, and engineering are being increasingly explored in single cell experiments and with the use of biochips for protein assays. We hope that our studies of light-torqued nanorods will help elucidate the fundamental physics of flow at such small scales.

Acknowledgments

We thank the Johns-Manville Corporation for providing glass fibers. B. K. thanks Wake Forest University for their support; T.W. was partially supported by the NSF. We also thank Robert Morris; George Holzwarth, Jeff Weiner, and Robert Swofford for the loan of critical equipment.

References

1. A. Ashkin, *Proc. Nat. Acad. Sci.* **94**, 4853 (1997); A. Ashkin and J.M. Dziedzic, *Science* **235**, 1517 (1987).
2. R.A. Beth, *Phys. Rev.* **50**, 115-125 (1936).
3. L. Paterson, M.P. MacDonald, J. Arlt, W. Sibbett, P.E. Bryant, and K. Dholakia, *Science* **292**, 912 (2001).
4. M.P. MacDonald, L. Paterson, K. Volke-Sepulveda, J. Arlt, W. Sibbett, and K. Dholakia, *Science* **296**, 1101 (2002).
5. R.C. Gauthier, M. Ashman, and C.P. Grover, *Appl. Opt.* **38**, 4861 (1999).
6. A.T. O'Neil, M.J. Padgett, Opt. Lett. **27**, 743 (2002).
7. M.E.J. Friese, T.A. Nieminen, N.R. Heckenberg, and H. Rubinsztein-Dunlop, *Nature* **394**, 348 (1998).
8. E. Higurashi, H. Ukita, H. Tanaka, and O. Ohguchi, *Appl. Phys. Lett.* **64**, 2209 (1994).
9. T.B. Jones, *Electromechanics of Particles*, (Cambridge University Press, New York, 1995).
10. Z.-P. Luo, Y.-L. Sun, and K.-N. An, *Appl. Phys. Lett.* **76**, 1779 (2000).
11. Z. Cheng, PM Chaikin, and T.G. Mason, *Phys. Rev. Lett.* **89**, Art.No.108303 (2002).
12. K. Bonin, B. Kourmanov, and T. G. Walker, *Opt. Express* **10**, 984-989 (2002). http://www.opticsexpress.org/abstract.cfm?URI=OPEX-10-19-984
13. Peter Galajda and Pal Ormos, *Opt. Express* **11**, 446-451 (2003).
14. P. Galadja and P. Ormos, Appl. *Phys. Lett.* **78**, 249 (2001).
15. M.M. Tirado and J.G. de la Torre, *J. Chem. Phys.* **73**, 1986 (1980).
16. E. M. Purcell, *Am. J. Phys.* **45**, 3 (1977).

COMPARISON OF THE MIE SCATTERING OF Co, Ni and Fe MAGNETIC SPHERES

R.-J. TARENTO, P. JOYES
Laboratoire de Physique des Solides ,bât 510, Université de Paris-Sud, Orsay, 91405, Fr

K.-H. BENNEMANN
Institute for Theoretical Physics,Freie Universitat Arnimallee,14,D-14195 Berlin,Ger

The Mie scattering intensity of a magnetic sphere has been derived by extending the classical Mie scattering approach to a media where the dielectric constant is no more a real number but a tensor of gyromagnetic form. Using a perturbation method the equations of the electromagnetic field are derived. This model has been applied to Co, Ni and Fe spheres. For an incident plane wave the magnetization effect could be detectable in the special incident case where the magnetic field of the incident plane wave is polarized along the magnetization direction. This magnetization effect is most important for the finger pattern of the backscattering intensity. Magnetic Mie scattering is still significant for a magnetic sphere of radius larger than 10 nn for Co and 6 nm for Fe.

1. Introduction

Magnetic nanostructures are of growing interest, in particular due to their potential industrial applications to high density magnetic recording media. The conventional magnetic characterization techniques[1] are limited to the study of large clusters or to ensembles of particles[2]. Then the interpretation of the data is not so trivial due the shape and cluster size distribution. A recent experiment on the magnetic anisotropy of a single cobalt nanocluster used a new micro-Squid set up[3].

The determination of the magnetization of clusters has been the subject of many theoretical[4] and experimental[5] studies. The experimental studies are based on Stern and Gerlach deflection measurements. The aim of the present article is to show that magnetic effects can be detected by Mie scattering experiments. This would provide then an alternative way to determine the magnetization. It is well known that the interaction of an electromagnetic wave with a magnetic sphere is weak. However, as our calculation show the magnetization effects are detectable.

In Sec.2. we discuss the model and in Sec.3. we report the influence of the magnetization direction on the Mie scattering intensity profile of Co, Ni and Fe.

2. The Model

The classical Mie[6] scattering of an electromagnetic wave by a metallic nonmagnetic sphere is controlled by the Maxwell equations of the electromagnetic field

$$\Delta\vec{E}+k^2\vec{E}=0\,, \tag{1}$$

$$\Delta\vec{H}+k^2\vec{H}=0\,, \tag{2}$$

$$\left(\vec{E}_i+\vec{E}_{sc}-\vec{E}_{in}\right)\times\vec{e}_r=0\,, \tag{3}$$

$$\left(\vec{H}_i+\vec{H}_{sc}-\vec{H}_{in}\right)\times\vec{e}_r=0\,. \tag{4}$$

The 2 last equations are the boundary conditions, $\vec{E}_{i,sc,in}$ $(\vec{H}_{i,sc,in})$ are the incident, scattered and inner sphere electric (magnetic) fields, $\vec{e}_r$ the vector perpendicular to the sphere. k^2 is equal to $\omega^2\varepsilon\mu$. Here, ω is the wave frequency and ε and μ are the dielectric and magnetic constants of the media. In the magnetic case the dielectric constant is a tensor which has a gyromagnetic form ,i.e.for a magnetization along the z-axis. One has

$$\varepsilon=\begin{pmatrix}\varepsilon_o & \varepsilon_{xy} & 0\\ -\varepsilon_{xy} & \varepsilon_o & 0\\ 0 & 0 & \varepsilon_o\end{pmatrix} \tag{5}$$

The off-diagonal terms[7] in ε are linear functions of the magnetization M and are obtained from the magneto-optical Kerr effect[8] (ellipticity + rotation).Then ε can be written as $\varepsilon_0 I+\varepsilon'$. Here ε' is a matrix proportional to the magnetization M. Moreover, ε' is different from zero only in the inner sphere region. Therefore, the wave equations for the electromagnetic fields are written as:

$$\Delta\vec{E}+\omega^2\varepsilon_o\,\mu\,\vec{E}=-\omega^2\mu\,\varepsilon'\,\vec{E}^o\,, \tag{6}$$

$$\Delta\vec{H}+\omega^2\varepsilon_o\,\mu\,\vec{H}=-\omega^2\mu\,\varepsilon'\,\vec{H}^o \tag{7}$$

Here ε' can be regarded as a perturbation to ε. Thus, it seems natural to apply a perturbation approach. Hence, $\vec{E}$ and $\vec{H}$ are written as

$$\vec{E}=\vec{E}^o+\vec{E}^1+\vec{E}^2..,\tag{8}$$

$$\vec{H}=\vec{H}^o+\vec{H}^1+\vec{H}^2....\tag{9}$$

$\vec{E}^o$ and $\vec{H}^o$ are the fields without the magnetization given by the classical Mie scattering. The terms $\vec{E}^i$. and $\vec{H}^i$ result from the magnetization of the sphere in the ith order perturbation theory.

Let us investigate the first order field correction $\vec{E}^1$, $\vec{H}^1$ (the higher corrections are obtained similarly). It follows that

$$\Delta\vec{E}^1 + \omega^2\varepsilon_o\,\mu\,\vec{E}^1 = -\omega^2\mu\,\varepsilon'\,\vec{E}^o, \qquad (10)$$

$$\Delta\vec{H}^1 + \omega^2\varepsilon_o\,\mu\,\vec{H}^1 = -\omega^2\mu\,\varepsilon'\,\vec{H}^o\ . \qquad (11)$$

In Eqs.10 and .11 the terms $\omega^2\mu\,\varepsilon'\,\vec{E}^o$ and $\omega^2\mu\,\varepsilon'\,\vec{H}^o$ can be regarded as source terms. Therefore, $\vec{E}^1$, $\vec{H}^1$ can be obtained with the Green function method. Let us denote by $G_o^{(E,H)}(\vec{r},\vec{r}\,')$ the Green function for $\vec{E}$ and $\vec{H}$ if M=0 with the boundary conditions given by Eq.3-Eq.4. Thus, the first order contributions to the fields due to the magnetization are

$$\vec{E}^1(\vec{r}) = \iiint_{D_S} \varepsilon'\,\omega^2\,\mu\,\vec{E}^o_{in}(\vec{r}\,')\,G_o^{(E,H)}(\vec{r},\vec{r}\,')\,d\vec{r}\,', \qquad (12)$$

$$\vec{H}^1(\vec{r}) = \iiint_{D_S} \varepsilon'\,\omega^2\,\mu\,\vec{H}^o_{in}(\vec{r}\,')\,G_o^{(E,H)}(\vec{r},\vec{r}\,')\,d\vec{r}\,'. \qquad (13)$$

D_S is the inner volume of the sphere. Higher order perturbation contributions to the fields are obtained in a similar way.

3. Results

We apply our model to cobalt, nickel and iron spheres. Note, for radius larger than a critical radius a_{cr} the sphere is no more a monomagnetic domain(for cobalt a_c =30nm). Nevertheless an applied magnetic field may cause a single domain structure and will control the direction of the magnetization. The dielectric tensor is dependent on the frequency of the electromagnetic wave. We use the optical constant obtained by Johnson et al[11] and derive the off-diagonal part of the dielectric tensor from the bulk measurement of Kerr ellipticity and rotation done by Zeper et al[9] for cobalt and by Krinchnik et al[10] for nickel and iron. For Ni the off diagonal terms are smaller leading to smaller magnetization effects on the Mie scattering. The bulk value used are a good first guess for answering if the magnetization effect is significant or not.

The incident electromagnetic field ($\vec{E}_i$, $\vec{H}_i$) is a planar wave propagating along the z-axis with an electric field polarized along the x-axis and the magnetic field along the y-axis. The direction of the magnetization M is assumed to be arbitrary. From Eq.12-Eq.13 we notice that the field corrections $\vec{E}^1$ and $\vec{H}^1$ involve only integrations over a small volume of sphere. As a consequence the corrections are weak. Therefore, the magnetization has a weak effect on the value of the electromagnetic field and on the total Mie scattering cross section W:

$$W = \frac{1}{2}\mathrm{Re}\int_0^{2\pi}\int_0^{\pi} \mathrm{d}\theta\ \mathrm{d}\phi\ \mathrm{r}^2 \sin(\theta)^2 \times (E_{i\phi}H^*_{sc\theta} - E_{i\theta}H^*_{sc\phi} - E_{sc\theta}H^*_{i\phi} + E_{sc\varphi}H^*_{i\theta})$$

However, the magnetization effect could be detected for special directions of the differential cross section for which the contributions given by $\vec{E}^0$ and $\vec{H}^0$ are small. This is the case for the backscattering spectra displaying some finger pattern when the size of the cluster is of the same order as the light wavelength.

Now let us discuss the effect of the magnetization on the Mie scattering. Our calculation shows that the effect is detectable for special directions of the magnetization. This is the case if the magnetization is essentially along the $\vec{B}_i$ (i.e. along the Y-axis).

Let us first report the results for cobalt. In Fig.1 the Mie scattering intensity for different wave energies in the half plane X-Y (X>0) i.e. in the plane containing $\vec{E}$ and $\vec{k}$ is given. We use the polar representation and the axis units are arbitrary. The solid line is the classical Mie scattering curve (for H=0). We plot also

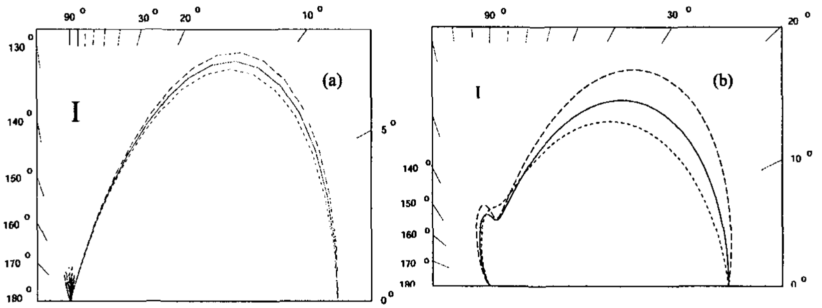

Figure 1. Cobalt angle-dependent magnetic Mie scattering intensity I. The angle refers to the polar coordinate in the Z X plane and the axis units are arbitrary. The cobalt sphere radius is 2600Å. The wave energy is E_ω=5 (1) eV in Fig.1.a(b). The dielectric tensor is derived from Ref.9-Ref.11.

the first order changes due to the magnetization (when $\vec{M}$ is along the positive Y-axis) ,(long-dashed curve), and in dashed when it is along the negative Y-axis.

The effect of the magnetization is maximal when $\vec{M}$ is parallel to the Y-axis. In fact, the boundary conditions Eq.3-Eq.4 give some relations for the normal components of the fields. These are increasing (decreasing) when M is along the positive (negative) Y-axis. The spectra are essentially modified for $\theta=\pi/4$. Note, for a wave energy E_ω=5eV the largest effect is nearly 10 percent, for E_ω=1eV it is 25

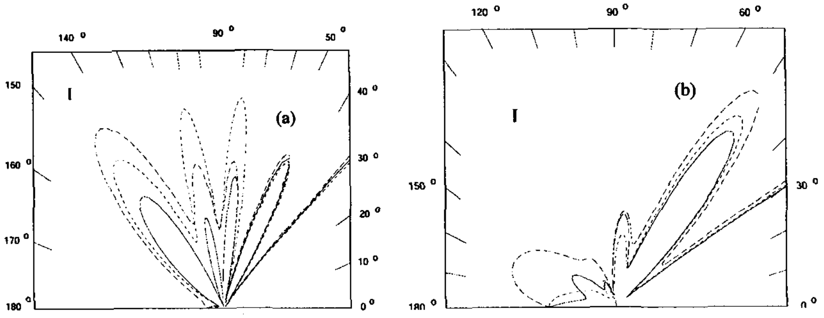

Figure 2. Finger Pattern of the cobalt angle-dependent magnetic Mie scattering intensity I. The angle refers to the polar coordinate in the Z X plane and the axis units are arbitrary. The cobalt sphere radius is 2600Å. E_ω=5 (1) eV in Fig.2.a(b).The dielectric tensor is derived from Ref.9-Ref.11.

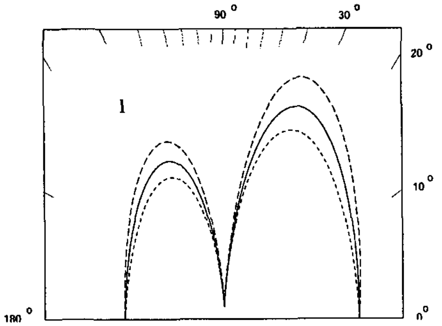

Figure 3. Cobalt angle-dependent magnetic Mie scattering intensity. I The angle refers to the polar coordinate in the Z X plane and the axis units are arbitrary. The cobalt sphere radius is 260Å. The wave energy is E_ω=5 eV. The dielectric tensor is derived from Ref.9-Ref.11.

percent. For $\theta=0$ (or π) the magnetization-effect does not occur. The corrections to the field are weak. The fingering pattern of the backscattered spectra is more modified and complex (Fig.2). The zeroth order is no more located between the ones obtained with $\vec{M}$ parallel or antiparallel to the Y-axis. Notice that for $\theta=\pi/2$ and E_ω=5eV the zeroth order intensity is very small, but the first order one due to magnetization is large.

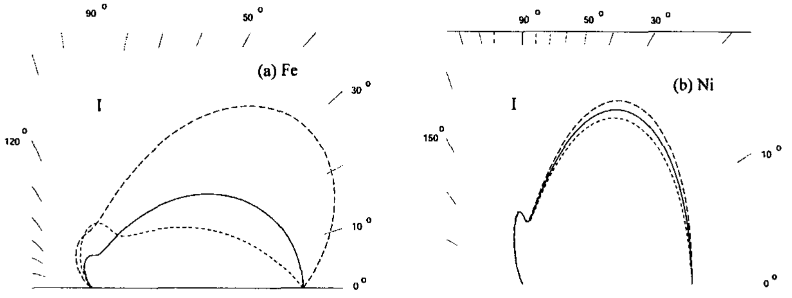

Figure 4 Angle-dependent magnetic Mie scattering intensity I. The angle refers to the polar coordinate in the Z X plane and the axis units are arbitrary. The sphere radius is 2600Å. The wave energy is $E_\omega=1$ eV Iron and Nickel case are shown in Fig.4.a(b). The dielectric tensor is derived from Ref.10-Ref.11.

For smaller cluster radius the finger pattern disappears. The spectra for a radius of 260Å display a significant effect due to magnetization for $\theta=\pi/4$ or $3\pi/4$ with changes of 25 percent for E_ω=5eV (Fig.3). For a radius of 150Å the effect is only to 8 percent and for 100Å only 4 percent.

In Fig.4, we report some results for the Mie scattering of iron and nickel spheres with a radius of 2600Å. For Nickel due to the low value of the off-diagonal dielectric tensor elements[10] the effect is detectable only for a wave energy E_ω of 1eV and the M-dependence is smaller than in the cobalt case. For iron the M effect is quite important, in fact it is still detectable for iron cluster radius of 60Å.

4. Conclusions

The Mie scattering reflects magnetization for special incident wave configuration and for a radius sphere larger than 100 Å. Characteristic differences are obtained for Co, Ni and Fe.

Acknowledgements

The authors thank Egide for support (Procope:03196UB)

References

1. Wernsdorfer W,Mailly D and Benoit A, *J.Appl.Phys* **87** (2000),5094-5096.
2. Kodoma R.H, J.Magn.Magn.Mater..**200** (1998), 359-372.
3. Jamet M,Wernsdorfer W, Thirion C, Mailly D, Dupuis V, Mélinon P and Pérez, *Phys.Rev Lett*. **86** (2001), 4676-4679.
4. Andriotis A.N and Menon M, *Phys.Rev*.. **B57** (1998),10069-10081.

5. Gerion D,Hirt A,Billas I.M.L,Chatelain A and de Heer A., *Phys.Rev..* **B62** (2000), 7491-7501.
6. Mie G.,*Ann.Physik.* **25** (1908), 377-445.
7. Bennett H.S and Stern E A,*Phys.Rev.* **137** (1965), A448-A461
8. Visnovsky S, Nyvlt M, Prosser V, Ferré J, Pénissard G, Renard D and Sczigel, *J.Magn.Magn.Mater* **128** (1993),179-189
9. Zeper W.B,Greidanus J.A:M, Garcia P.F and Fincher C.R, *J.Appl.Phys* **65** (1989),4971-4975
10. Krinchnik G.S and Artem'ev V.A, *J.E.T.P* **26** (1968),1080-1085
11. Johnson P.B and Christy.R.W, *Phys.Rev.* **B9** (1974), 5056-5070

This page intentionally left blank

C 1s CORE PHOTOEMISSION OF C_{60} AND $C_{59}N$

R.-J. TARENTO, P. JOYES, A. KORBA SABIHA and D.E. MEKKI
Laboratoire de Physique des Solides, bât 510 Université d'Orsay
91401 Orsay, France

We make a theoretical study of the shakeup structure of the 1s photoemission spectrum of C_{60}. The method takes into account the reactions of the .σ and π electrons which accompany the formation of the photoemission hole on one carbon atom. We analyse the origin of the satellite. The method has been applied to the $C_{59}N$ case.

1. Introduction

Heterofullerenes , which have one or more of the carbon atoms substituted by other elements such as boron and nitrogen have stimulated a great interest of researchers in physics and chemistry to investigate its structural[1], electronic ,optical[2] and other properties[3-4]. In particular, such material display rather strong non linear optical behavior[3]. The fact that the band gaps is easily modified with different substitute doping could be convenient in potential application in nanometer electronics[5].

Nitrogen heterofullerenes experiments have achieved great progress since the report on C_xN_y production by Rao[6]. Firstly $C_{59}N^+$,formed by fragmentation of iminofullerene has been detected by Hirsch and al[7] . $C_{59}N$ has synthesized and characterized by Yu and al[8]. The dimer $(C_{59}N)_2$ has been detected by Humelen et al[9]. Prassides at al succeed in the formation of intercalation compound of the heterofullerene salt $K_6C_{59}N$[10].

Theoretical studies on the $C_{59}N$ electronic structure have intensively been carried out[11-13]. In particular, Quantum molecular dynamics has been used to study stable structure of $C_{59}N$[14]. The deformation of the fullerene cage is limited to the environment impurity. The gap is small (.3 eV) and the molecule would act rather as a electron donor.

Synchroton-radiation and X-ray photoemission of the valence states bring some insight on the electronic structure. This technique has been applied firstly by J.H Weaver et al to C_{60}[15]. They perform evaporation of C_{60} molecules on GaAs or

InP substrates. They report seventeen distinct molecular features extending ≈ 23eV below the highest occupied molecular states (mention that their spectra analysis in terms of transition of molecular levels neglect the N-body electron shake up. Moreover the interaction between the substrate and the fullerene layers is important and has been investigated during the growth mode of chemisorption of C_{60} on a InP(100) [16] or GeS[17] surfaces and also for C_{70} on MoS_2[18]. The C 1s core photoemission spectra shape depends strongly on the fullerene coverage of the substrate and the annealing treatments. For large number of fullerene monolayer we could expect that the interaction with the substrate could be neglected. Such experiments on heterofullerene could be achieved in the next future.

Let us give some remarks on the photoemission theory. It is generally admitted that the many-electron effects govern the discrete X-ray line and photoemission spectra (Mahan-Nozières-de Dominicis theory)[19-20].This phenomenon has been studied in bulk metals where it is characterized by two effects: the Anderson orthogonality between the initial and final ground states and the $|E|^{\alpha_H-1}$ spectrum behavior , where E is the emitted particle energy defect (with respect to the one-electron energy) and α_H (with $0<\alpha_H<1$) an exponent related to the phase shift at the Fermi level due to the localized hole potential. A study on a limited media (close loop with N atoms) has shown that the overlap between the groundstates overlap tends to as N increases like the Anderson $N^{-\alpha_H/2}$ behavior[21]. Previous studies of the C 1s core photoemission has been performed for C_{60} , C_{110} and C_{20}[22-23] in a emitted particle energy defect range of 0-5eV; a Hückel Hamiltonian neglecting the σ electrons has been used in the calculation.

The part II describes the model which takes account of the shake up of the electron gas during the photoemission process. Sections 3 and 4 deals for the results for the C 1s core photoemission for C_{60} and $C_{59}N$.

2. The Model

The excitation probability of a system into a state of energy ε_f by a photo of energy ε_{ph} is given by:

$$\sigma(\varepsilon_f) \propto \sum_f \left\langle \Psi_i^o \middle| \sum_n \nabla_n . e \middle| \Psi_f \right\rangle^2 \delta(\varepsilon_f - \varepsilon_{ph} - \varepsilon_i^o) \tag{1}$$

where e is an unitary vector along the polarization direction, n labels the electrons ψ_i^o, ε_i^o and ψ_f , ε_f are the wavefunctions and energies of the system before and after the transition. The label o in ψ and ε refers to the initial state and f is a label which run over all the possible states of the final states after the transitions.

Let us introduce $|\phi_a\rangle$ and $|\phi_b\rangle$ the one-electron levels of the transition respectively for the initial deep level and the final free state. Let us be $|\phi_j\rangle$ and $|\phi_j^{'}\rangle$ the π and σ valence levels of the C_{60} or $C_{59}N$ molecule before and after the transition. (j=1…240). In eq(1) the sum over n can limited only to the main contribution (i.e: the dipolar moment is calculated between the states $|\phi_a\rangle$ and $|\phi_b\rangle$ and the others electrons are projected from $|\phi_j\rangle$ onto $|\phi_j^{'}\rangle$). Hence

$$\left\langle \Psi_i^o \left| \sum_n \nabla.\mathrm{e} \right| \Psi_f \right\rangle \approx \omega_{ab} \left\langle \tilde{\Psi}_i^o \middle| \tilde{\Psi}_f \right\rangle \tag{2}$$

with $\omega_{ab} = \langle \phi_a | \nabla.\mathrm{e} | \phi_b \rangle$. $|\tilde{\Psi}_i^o\rangle$ and $|\tilde{\Psi}_f\rangle$ are Slater determinants built up with the one-electron wavefunctions $|\phi_j\rangle$ and $|\phi_j^{'}\rangle$.

The energy of the photoelectron is fixed but it varies in an energy range which is small and we assume that ω_{ab} is a constant ($\omega_{ab} \cong \omega$). Let $\tilde{\varepsilon}_f$ ($\varepsilon_f = \tilde{\varepsilon}_f + \varepsilon_b$) be the energy associated to the state $|\tilde{\Psi}_f\rangle$. Eq(1) is recasted into:

$$\sigma(\varepsilon_b) \propto \omega^2 \sum_{\mathrm{f}} \left| \left\langle \tilde{\Psi}_{\mathrm{i}}^{\mathrm{o}} \middle| \tilde{\Psi}_f \right\rangle \right|^2 \delta\left(\tilde{\varepsilon}_f - \varepsilon_{ph} - \varepsilon_i^o + \varepsilon_b\right) \tag{3}$$

The maximal photoememission energy is obtained when the final state $|\tilde{\Psi}_f\rangle$ is the fundamental state $|\tilde{\Psi}_f^o\rangle$ what is not forbidden in finite system:

$$\varepsilon_{b,\max} = \varepsilon_i^o + \varepsilon_{ph} - \tilde{\varepsilon}_f^o \tag{4}$$

$$\sigma(E) \propto \omega^2 \sum_{\mathrm{f}} \left| \left\langle \tilde{\Psi}_{\mathrm{i}}^{\mathrm{o}} \middle| \tilde{\Psi}_f \right\rangle \right|^2 \delta\left(\tilde{\varepsilon}_f - \tilde{\varepsilon}_f^o + E\right) \tag{5}$$

3. The C_{60} Photoemission Spectra

Let us model the C_{60} molecule in the tight binding framework. The Hamiltonian H^o taking into account the σ and π electrons of the molecule is written as:

$$H^o = \sum_{\substack{i \neq j \\ \gamma,\mu,\sigma}} \beta^{ij}_{\gamma\mu} c^+_{\gamma i\sigma} c_{\mu j\sigma} + \sum_{i\gamma\sigma} E_\gamma c^+_{\gamma i\sigma} c_{\gamma i\sigma} \tag{6}$$

where γ,μ label the orbital components of $2s,2p_x,2p_y,2p_z$. The $\beta_{\gamma\mu}{}^{ij}$ are the hopping term between site i and .j. C_{60} has 240 electrons (120 ↑,120↓). Thus each C_{60} state is described with a Slater determinant which is the product of two determinants of size (120x120). The C_{60} one-electron levels obtained with H^o in the vicinity of the LUMO level shows that the gap is 2.15eV as for the experimental value is 1.73eV. The difference is due that we neglect the electronic correlation in H^o and as it has been shown the correlation effects reduce the gap value.

The photoemission process can be described by the Hamiltonian H

$$H = H^o + \sum_{\gamma\sigma} \Delta_\gamma \quad c^+_{\gamma 1\sigma} c_{\gamma 1\sigma} a a^+ \tag{7}$$

The second contribution in H is the apparition of attractive term (Δ_γ<0) due to the deep hole creation on site 1, a^+ is the creation of an electron site on the 1s level of site 1 (site 1 has been chosen arbitrary as all the sites are equivalent). Δ_γ is an effective term we derive it by comparison our calculated photoemission spectra with experiments to get the same ratio between the main line and satellite contributions in the photoemission spectra (Δ_p=- 4.16 eV, Δ_s= - 6.8eV).

Let us explain our computation. The determination of the photoemission spectra need the calculation of $\left\langle \tilde{\Psi}^o_i \middle| \tilde{\Psi}_f \right\rangle$. The initial state is single : it is the ground state we put the electrons on the 120 lowest energy states $\left| \phi_j \right\rangle$ for each spin direction. For the final state the number of possibility is tremendously huge. In fact for each spin direction we have to consider all the ways of distributing 120 electrons among 240 levels and the number is C^{120}_{240}, hence the number of final states is $\left(C^{120}_{240}\right)^2$. We limit our calculation to final states with only zero and one electron-hole pair .This assumption is valid for the bulk system. The number of such states with one electron-hole pair is still high 120x120 for one spin direction. A good criterion to control the assumption is given by a sum rule identity $\sum_f \left| \left\langle \tilde{\Psi}^o_i \middle| \tilde{\Psi}_f \right\rangle \right|^2$ which worth 1 if f runs on all the possible final states, in our calculation the sum worth 0.992. In Fig.1. we report the 33 Photoemission satellites in C_{60}. Note, the first satellite is at an energy of 2.10 eV which is the same value than the gap value in our calculation and like in experiments. Weaver et al[15] associate the peaks to 1-electron molecular transitions. In our calculation they are N-body transitions between C_{60} state and one state of C_{60} with a deep hole. In Table.1 the analysis the satellite transitions is reported. For each satellite several transitions are generally associated which could be ($\pi \to \pi^*$, $\pi \to \sigma^*$, $\sigma \to \pi^*$, $\sigma \to \sigma^*$) transitions. Note that for the first satellite the N-body transition is a $\pi \to \pi^*$ type between the (Humo-1) state of C_{60} and with the Lumo state of C_{60} with an deep hole. (it is not a Homo→Lumo transition).

4. The $C_{59}N$ Photoemission Spectra

We have applied our formalism to the case of $C_{59}N$. The 1s hole is always on the carbon atom. As a nitrogen atom is in the molecule the position of the hole with respect to the nitrogen atom is not unique they are 59 possibilities but some are equivalent by symmetry reasons. In Fig.1 we report the average on the hole position of the $C_{59}N$ photoemission spectra. In fact note, the main line centered at zero is larger than in the C_{60} case and also that the spectra is not null between –2eV and 0eV. The reason is due to the main line contributions of the individual spectra obtained with the hole as the nearest neighbor of the Nitrogen atom which are shifted. The spectrum is also smoother due some interference in the summation.

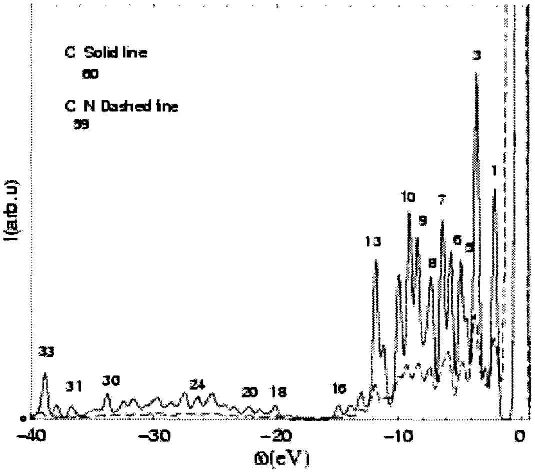

Figure 1. Shakeup structure of carbon 1s photoemission spectrum in C_{60} (solid line) and $C_{59}N$ (dashed)

Table 1. Analysis of the Nbody transition between C_{60} state and C_{60} with a deep hole involved in the satellite peaks of photoemission in C_{60} (see Fig.1). L and H stand for Lumo and Homo.

Peak	Transition $\pi\rightarrow\pi^*$	Transition $\pi\rightarrow\sigma^*$	Transition $\sigma\rightarrow\pi^*$
1	H-1→L		
2	H→L+3		
3	H-3→L		
4	H-2→L +3		
5	H-4→L , H→L +5		
6	H-5→L , H-3→L +3 , H→L +10		
7	H-4→L +3 , H-2→L +5 , H→L +3		
8	H-6→L , H-3→L +5 , H-2→L +10 , H→L +17		
9	H-7→L , H-5→L +3, H-4→L +5 , H-3→L +10		
10	H-6→L +3 , H-4→L +10, H-3→L +13		H-8→L
11	H-7→L +5 , H-6→L +10 , H-5→L +17		
12	H-6→L +5 , H-5→L +10		
13	H-7→L +5 ; H-6→L+10 ;H-5→L+17 ; H-4→L +21		
14	H-7→L +13 , H-6→L +17 , H-1→L +21		
15	H-7→L +17	H-2→L +34	
16	H-7→L +21		

Peak	Transition $\pi\rightarrow\sigma^*$	Transition $\sigma\rightarrow\pi^*$	Transition $\sigma\rightarrow\sigma^*$
17	H-7→L +34		
18		H-9→L +28	
19			H-9→L +35
20			H-12→L +29 , H-9→L +39
21		H-14→L +28	H-12→L +5
22			H-16→L +29
23		H-26→L +5 , H-17→L +28	
24		H-27→L +15, H-20→L +28	H-20→L +29, H-18→L +35 H-16→L +40
25		H-21→L +28	H-20→L +36, H-18→L +39 H-14→L +40
26		H-23→L +28	H-21→L +35
27		H-29→L +5, H-27→L +21 H-25→L +28	H-24→L +29, H-23→L +34 H-16→L +71
28		H-31→L +5	H-24→L +34, H-20→L +71
29			H-26→L +34
30		H-31→L +17	H-27→L +34
31			H-29→L +34
32			H-31→L +29, H-30→L +34
33			H-31→L +34

5. Conclusions

The calculation has analysed the origin of the satellites of the photoemission spectra in C_{60}. Each satellite is associated to transitions between N-body state of C_{60} and state of C_{60} with a hole. The $C_{59}N$ average spectra is smoother than the C_{60} one.

Acknowledgements

The authors thank the Egide for the support (Procope:03196UB)

References

1 Kroto H.W et al., *Chem.Rev.* **91**,(1991)1213-1243
2 Saito S and Oshiyama A, *Phys.Rev.Lett.* **66**,(1991)2637-2640
3 Blau W.Jet al., *Phys.Rev.Lett* **67**,(1991)1423-1425
4 Chen C.Tet al. ,*Nature* **352**(1991)603-605
5 Diener M.D. and Alford J.M, *Nature* **393**,(1998)668-671
6 Pradeep T et al, *J.Phys.Chem* **95**,(1991)10564-10565
7 Lampart I et al *Angew.Chem* **35**,(1995)2257-2259
8 Yu R, Zhan M et al *J.Phys.Chem* **99**,(1995)1818-1819
9 Hummelen J:C et al *Science* **269**,(1995)1554-1555
10 K. Prassides et al, *Science* **271**, (271)1833-1835
11 Chen Z, Zhao X and Tang A, *J.Phys. Chem.***A 103**, (1999)10961-10968
12 Dong,J.J, Jiang J et al , *Phys.Rev.***B 51**,1977 (1996)1977-1980
13 Wang S.H, Chen F et al *J.Phys.Chem* **99**,(1995)6801-6807
14 Androni W, Gygi F and Parinello MChem. *Phys. Lett* **190**,(1992)159-162
15 Weaver J.H et al, *Phys.Rev.Lett* **66**,(1991)1741-1744
16 Y. Chao, K. et al, *Phys.Rev.***B 64**,(2001)235331-23533
17 Genstterbierm G. et al*Phys.Rev.***B50**, (1994)11981-11995
18 Bo-ying Han et al *Phys.Rev* **B 51** (1995) 7179-7185
19 Mahan G.D , *Phys.Rev.***163**,(1967)612617
20 Nozières P and de Dominicis C.T, *Phys. Rev*,**178**, (1969)1097-1107
21 Joyes P ,Tarento R-J *Z.Phys.D***24**,(1992)235-239
22 Joyes P and Tarento R-J, *J.Phys.1 (France)* **2**,(1992)1667-1676

23 Joyes P, R, TarentoR-J and Van de Walle J, *in Cluster and Nanostructure Interfaces Edts P. Jena P, Khanna S.N and RaoB.K World Press*, (2000)371-374

A TUNABLE OPTICAL PARAMETRIC OSCILLATOR LASER SYSTEM FOR SINGLE PARTICLE MASS SPECTROMETRY

RAMKUBER T. YADAV[1], JOSEPH L. BANYASZ[2], KENNETH H. SHAFER[2], MOHAMMAD R. HAJALIGOL[2]

[1]Philip Morris USA Postgraduate Research Program
[2]Philip Morris USA Research Center, 4201 Commerce Road, P. O. Box 26583, Richmond VA 23261

Highly selective and sensitive methods are required for the on-line detection of organic products in incomplete combustion. One approach is time of flight measurement in conjunction with selective soft ionization. Resonance enhanced multi-photon ionization (REMPI) – time-of-flight mass spectrometry has proven to be well suited for the identification of organic components present in complex gas mixtures. In the present work we describe the integration of a pulsed (20 Hz) optical parametric oscillator (OPO) laser system and an aerosol time of flight mass spectrometer(ATOFMS). The OPO laser system is based on β-barium borate (BBO) crystals and is equipped with a frequency doubling option. This solid-state laser has a wide spectral tuning range of 220-1850 nm. The laser is designed to work at a fixed repetition rate to improve beam stability; the maximum allowable deviation in periodicity is 10%. We have designed an external triggering arrangement to facilitate the OPO operation in a random fashion, as required in single particle mass spectrometry. The applicability of the system will be demonstrated through measurements of aerosol particles generated by combustion of biomaterials. The goal of this work is to test how different wavelength affect the laser desorption/ionization process.

1. Introduction

Development of aerosol instruments capable of determining both size and chemical composition is an active area of research. Mass spectrometry is the technique of choice due to high sensitivity to minor components in the aerosols and its ability to provide on-line analysis. A number of mass spectrometer configurations1-6 developed in recent years primarily differ in terms of sampling techniques, particle sizing schemes and detection/ionization methods. In the present work, we focus on desorption/ionization. Many groups 1,2,3 use flash vaporization of the aerosol particles followed by electron impact ionization and quadrupole mass analysis of the resultant ions. This technique is relatively simple and quantitative. However, the limitation is that the quadrupole mass spectrometer can monitor only a single mass from any single aerosol particle. An alternative approach used by several researchers4,5,6 is based on laser ionization followed by time of flight mass spectrometry. Among various real-time single particle mass spectrometry instruments, an aerosol time of flight mass spectrometer7,8 (ATOFMS) can be used to determine both the size and the chemical composition of the individual aerosol particle. The major benefit is that this generates the entire mass spectrum in a single laser shot from a single multi-component aerosol particle.

To date, ATOFMS has been used primarily for studying atmospheric aerosols and source characterization studies. In such studies interpretation of the mass spectra corresponding to inorganic species is relatively straightforward. However, interpretation of organic particle mass spectra is quite challenging, because a single particle can be a complex organic matrix comprised of hundreds of different organic species. In addition, the increased fragmentation with increasing desorption/ionization laser power further complicates the interpretation of mass spectra. One of the primary objectives of laser based single particle mass spectroscopy is to develop a selective ionization scheme for enhanced sensitivity and quantification. In many designs, including ours, a laser operating at a fixed wavelength is used for both particle ablation and ionization. This approach simply and powerfully provides qualitative details on single aerosol particles, but it has limitations.

The application of these single wavelength UV lasers results in ion formation through multi photon ionization. The untapped advantage of the laser based desorption/ionization is its flexibility as a multi-photon, wavelength-tunable ionizing agent. For example, resonance enhanced multi-photon ionization (REMPI) is a useful tool for selective ionization and enhanced sensitivity for analysis of highly complex gas mixtures9. In this process, photon wavelength is varied to match the energy of particular molecular excited states. If the multi-photon absorption imparts energy greater than or equal to the ionization energy, photo ionization may occur. Appropriate tuning of the laser wavelength selectively excites electrons to higher energy levels, by absorption of incident photon radiation. The electron in the excited state can be ejected from the molecule by absorbing an additional photon resulting in ionization. Since, the arrangement of electrons in a given molecule is a unique feature of that particular molecule, this phenomenon enhances its ionization probability.

It is known10 that the dependence of laser desorption/ionization on the absorption characteristics of an individual particle suggests that ionization occurs most efficiently as a resonant process. In order to harness resonant phenomena for greater ionization efficiency, single particle mass spectrometry requires an ionization source that can be tuned to a variety of wavelengths.

The goal of this work is to test how different wavelength affect the laser desorption/ionization process. In this work, we report in brief the development of a tunable laser system and its integration to ATOFMS for single particle mass spectrometry. The complete details of this newly developed system will be published elsewhere11. The measurements, at two different wavelengths on cigarette smoke aerosols, demonstrate the capability of the system.

2. Experimental Details

Cigarette smoke particles are generated by drawing a 35 cc puff with a hypodermic syringe. The smoke is stored for 3 minutes in this syringe for aging. During this time, particles grow in size. The change in size occurs due to coagulation and evaporation of volatile and semi volatile components from the particle surface. These aerosol particles are then transferred to a dilution jar of 20-liter volume. Continuous dilution occurs during sampling by allowing the room air to enter into the dilution jar. Smoke aerosol particles are introduced into the ATOFMS system by coupling it with the dilution. The measurement system is comprised of the ATOFMS and the tunable laser system. The ATOFMS system (TSI, MN) has been described previously in detail7,8. This instrument typically uses the fourth harmonic of an Nd: YAG laser (266 nm) as the ablation laser.

In order to enhance the selectivity by varying the laser wavelength and also realizing the IR and UV outputs for two-step desorption/ionization processes, we have added an OPO (Optical Parametric Oscillator) solid-state laser system to the ATOFMS. This unit is a Spectra Physics (Ca) model MOPO-SL. The system covers a wavelength range of 220-1850 nm, with a small discontinuities arising from the presence of gap in the non-linear crystals used in the laser. The available output energies of the OPO system vary from a few mJ to tens of mJ per pulse, depending upon wavelength and pulse duration (~5-7 nanoseconds). Besides the output from the OPO, we have the capability to generate the fifth harmonic output (213 nm) using 1064 and 266 nm as the pump wavelengths in the fifth harmonic crystal. The energy from the fifth harmonic unit is ~30-40 mJ, which is sufficient to ionize species having large ionization potentials. The OPO has been used for the measurements reported here.

The basic mechanism for tunable wavelength generation based on the OPO principle is simple. A pump laser providing a specific wavelength (355 nm 3rd harmonic output from Nd:YAG in the present case) is incident on a non-linear crystal, which in our case is β-barium borate (BBO). Nonlinear processes in the BBO result in generation of two wavelengths, referred to as signal and idler. By the principle of energy conservation the sum of the energies of signal and idler is equal to the photon energy of the pump laser. The available wavelength range for the signal is 440-705 nm and 715-1850 nm for the idler. The UV range tuning is achieved by frequency doubling the signal beam in a non-linear crystal. In addition to the non-linear crystal, the signal beam also passes through a complex optical arrangement responsible for separating the parent beam from the frequency-doubled beam. The frequency doubling process provides UV output in the range of 220-440 nm.

In the present experimental configuration, the sampled particles pass through two continuous laser beams in the sizing region of ATOFMS as shown in figure 1. The particle size is determined based on the transit time of the particle, between these two continuous laser locations. The ionization laser is triggered based on the particle size, ensuring that the laser arrives at the ionization region at the same time as particle. Triggering the 1064 nm to produce the 266 nm (fourth harmonic) laser was simple from the optics perspective. However, there is a sampling rate limit for operation of an OPO based on triggering from a random event. Because of the effect of non-thermal equilibrium conditions on the optical behavior of the non-linear crystals and other components, these systems are designed to operate at a fixed repetition rate; in our case 20 Hz. Additionally, the pump laser, which delivers over 400 mJ/pulse at 355 nm, has its operational limitations at higher repetition rates. In order to integrate the tunable laser system with the ATOFMS so that the laser could be randomly triggered based on particle arrival time, we had to design a new triggering arrangement.

The new triggering arrangement is shown schematically in figure 2. The flash lamp trigger generated from the particle sizing part is connected to a Boolean processor (Siemens FM352-5) and an OR gate. The second input to the OR gate is the output from the Boolean processor. This Boolean processor generates a train of pulses at 20 Hz. The output from the OR gate is fed into a digital delay generator (SRS-DG535, Stanford Research Systems, Ca). The FM352-5 configuration ensures that on average the OPO laser is triggered at a repetition rate of around 20 Hz. It also ascertains that the periodicity of the pump laser is not shifted by more than 5 msec from its original anticipated pulse time based on a constant 20 Hz triggering, required for the normal OPO operation.

The output of the OPO reaches the ionization region after passing through reflective and focusing elements. The laser beam is directed to the ionization spot by uncoated right angle prisms along with combinations of reflecting mirrors. We present here the measurements on smoke aerosol using an OPO laser operating at 260 nm and 280 nm. The measured laser energies, at the exit port of the ionization region are 0.2 mJ/pulse and 0.6 mJ/pulse, respectively. The substantial loss in laser power is due to the large number of reflecting surfaces for redirecting the beam. The power loss is severe especially when multiple uncoated right angle prisms are used.

Results and Discussion:

The averaged mass spectra obtained at 260 nm are shown in figure 3 and figure 4 for positive and negative ions respectively. Figures 5 and 6 show the averaged mass spectra for positive and negative ions acquired using the 280 nm laser. In both the cases, more than 100 individual particle spectra were used for averaging. The general feature of all these spectra is that they exhibit a congested region at higher masse. This is due to the extremely complex nature of the chemical composition of tobacco smoke. The application of a more intense laser beam at these wavelengths can simplify the mass spectra by efficiently fragmenting ions with higher molecular weights. However, this approach is not desirable as all the information about the higher masses is embedded in the fragment ion signal. Since many molecular ions yield similar fragments, it would be a daunting task to identify parent ion based solely on the fragment distribution and intensities obtained at a given wavelength and energy. For simplicity, let us consider the broad features of the spectra for discussion purposes.

The most intense signal for the positive ion mass spectra is at m/z =39, associated with K+. This is as expected, as the photon energies used here exceed the first ionization potential of K, (4.34 eV) 12. In this case, a single photon is sufficient to ionize K, unlike other species requiring at least two photons. Another important factor is the difference in cross sections, in one photon and two photon ionization processes. Not all the ion intensity at m/z =41 corresponds to K+. Based on K isotopic mass distribution, only 7% of the total intensity at m/z =39 can be associated with it.

The measurement at 260 nm shows much more pronounced positive ion signal intensities than at 280 nm, as well as a distinct hump around m/z =200. This difference may be due to the characteristic absorption of 260 nm wavelength by a class of compounds. The other plausible cause could be the laser intensity differences in the two cases. However, if the difference were associated with the laser power, then the effect should be the opposite, since the laser power at 280 nm is 3 times higher than at 260 nm. Thus, the observed difference is associated with the laser wavelength. In smoke the higher mass species may be due to polycyclic aromatic hydrocarbons (PAHs), oils, waxes, carbohydrates etc. Since PAHs have high molar absorptivities at 260 nm, the increase in signal intensities is due to enhanced absorption from PAHs present in the particle. For example, in the case of PAHs and their heterocyclic analogues, the molar absorptivity at 266 nm lies in the range 103-105; larger ring systems, such as chrysene, can be even higher, exhibiting cross section greater than 106, 13. In addition, the presence of high mass peaks is largely from unfragmented or partially fragmented ions. Since the laser intensity was small, the desorption/ionization process was soft enough to give largely unfragmented or partially fragmented ions.

For the negative ion spectra, the one obtained at 260 nm has a large number of closely spaced peaks at higher masses compared to the one at 280 nm. This spectrum also shows strong wavelength dependence on the observed number of ions, especially at higher masses.

3. Conclusion

A brief description of the design and development of a new tunable laser system and its integration with the existing ATOFMS system has been provided in this work. The mass spectra corresponding to the positive as well as negative ion have strong wavelength dependences. These dependences are due to differences in the absorption characteristic of the molecular species present in the aerosol particles. In addition, the absorption properties of the particle as a whole, which lead to desorption/ionization, play critical roles. The presence of pronounced ion signals at higher masses in case of 260 nm measurements is due to the presence of PAHs on the particles, which have large molar absorptivities at this wavelength.

Acknowledgements

The authors would like to thank Jeremy Straight for his help in triggering electronics and Alan Goldsmith for help with manuscript. Also, the helpful discussions with Drs. D. Kane, Y. Pithawalla, P. Lipowicz and A. C. Lilly are acknowledged.

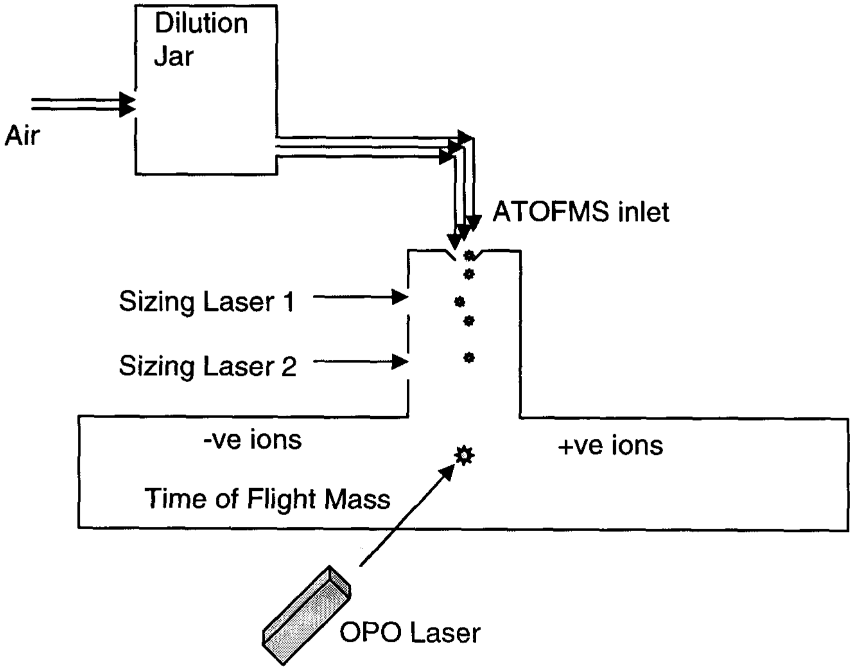

Figure 1. Schematic representation of Aerosol Time of Flight Mass Spectrometry System

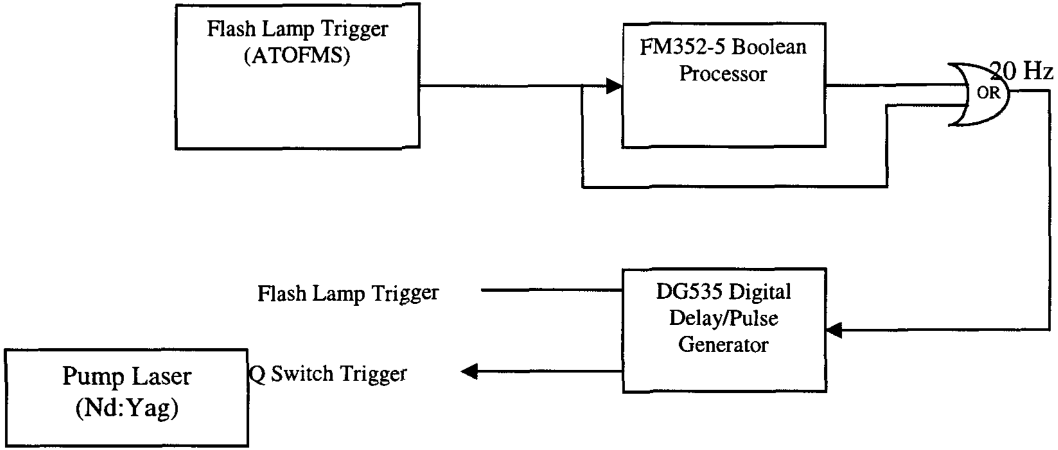

Figure 2. Pump laser-triggering arrangement. FM352-5 Boolean processor is from Siemens and DG535 delay generator is from Stanford Research Systems (SRS).

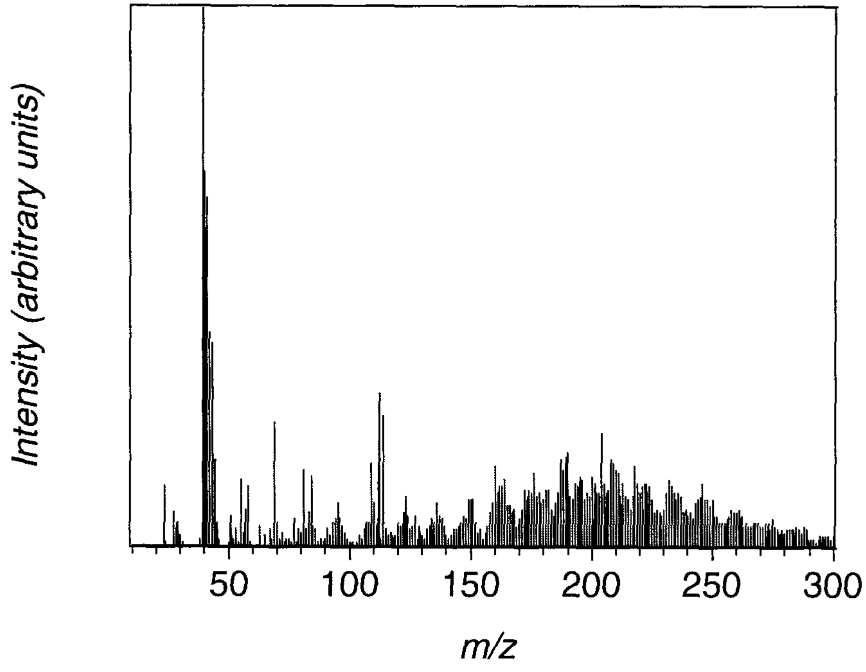

Figure 3. Average positive ion mass spectra obtained at OPO wavelength of 260 nm

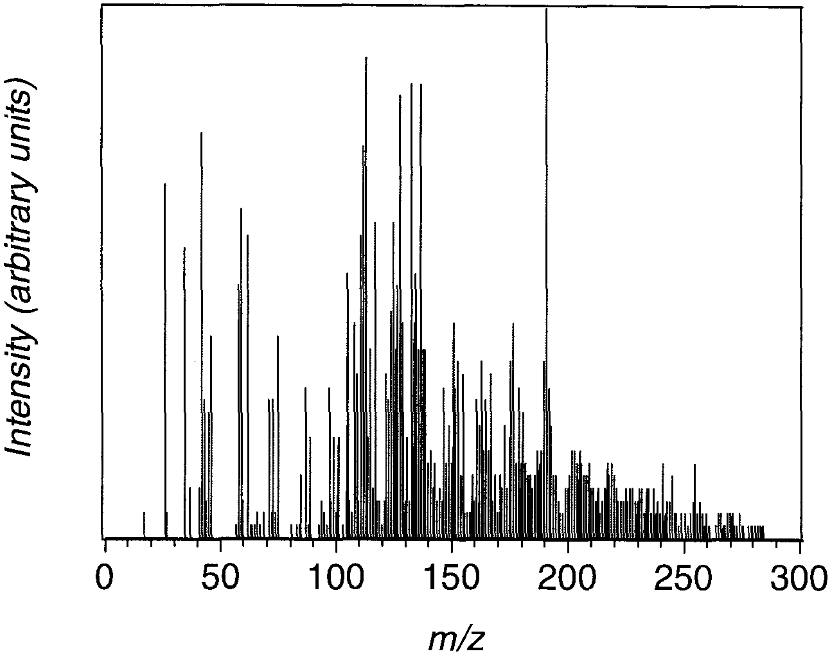

Figure 4. Average negative ion mass spectra obtained at OPO wavelength of 260 nm

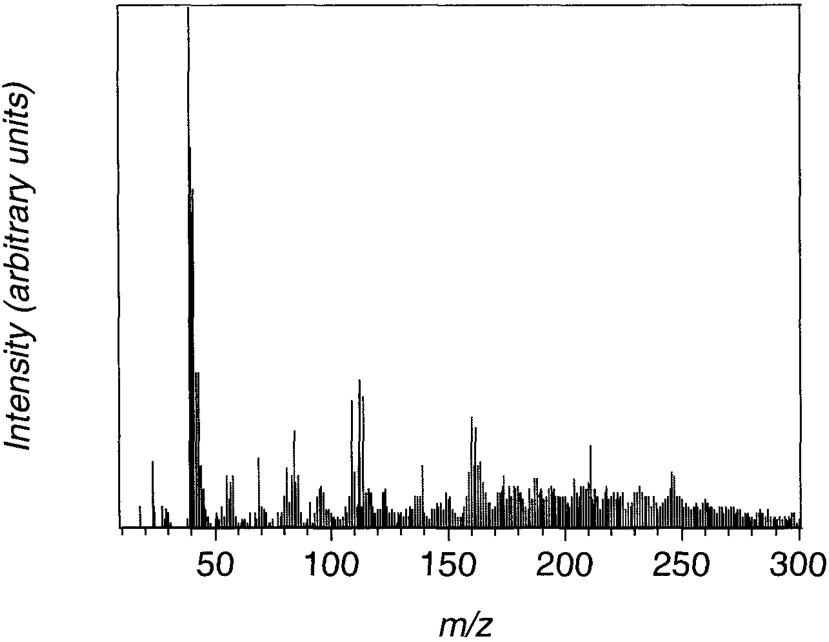

Figure 5. Average positive ion mass spectra obtained at OPO wavelength of 280 nm

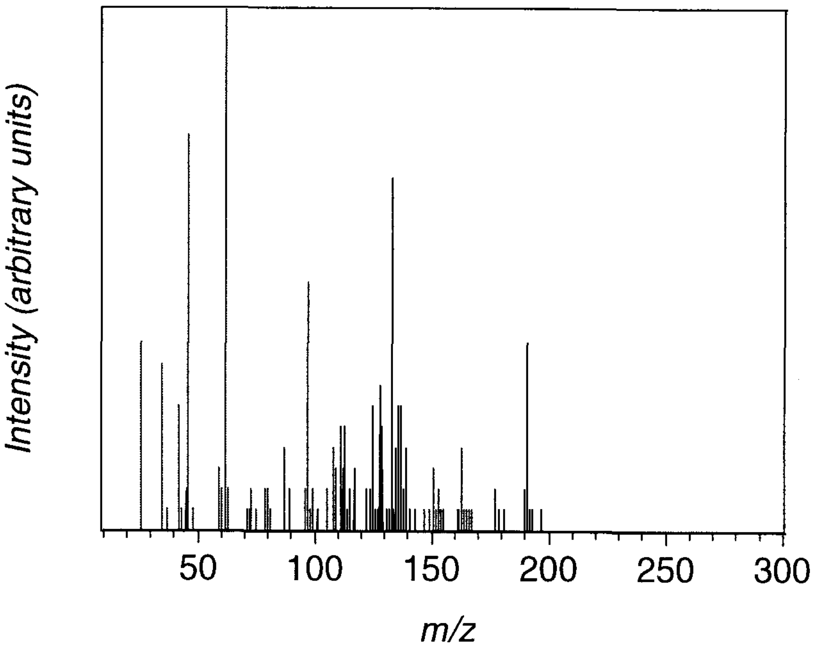

Figure 6. Average negative ion mass spectra obtained at OPO wavelength of 280 nm

Reference

1. Allen, J.; Gould, R.K. *Rev. Sci. Instrum.* **1981**, 52, 804-809.
2. Tobias, H. J.; Kooiman, P. M.; Docherty K. S.; Ziemann, P. J., *Aerosol. Sci. Technol.* **2000**, 33, 170-190.
3. Jayne, J. T.; Leard, D. C.; Zhang, X.; Davidovits, P.; Smith, K. A.; Kolb, C. E.; Worsnop, D. R. *Aerosol. Sci. Technol.* **2000**, 33, 49-70.
4. Prather, K. A.; Nordmeyer, T.; Salt, K. *Anal. Chem.* **1994**, 66, 1403-1407.
5. Murphy, D. M.; Thomson, D. S. *Aerosol Sci. Technol.* **1995**, 22, 237-249.
6. Carson, P. G.; Neubauer, K. R.; Johnston, M. V.; Wexler, A. S. *J. Aerosol Sci.* **1995**, 26, 535-545.
7. Nordmeyer, T.; Prather, K. A. K. *Anal. Chem.* **1994**, 66, 3540.
8. Yadav, R. T.; Saoud, K.; Rasouli, F.; Hajaligol, H.; Fenner, R. *J. Anal. Appl. Pyrol.* **2004** (In-press).
9. Zimmermann, R.; Heger, H. J.; Kettrup, A.; U. Boesl, U. *Rap. Comm. Mass Spectrom.* **1997**, 11, 1095.
10. Hunt, A. L.; Petrucci, G. A. *Trends in Anal. Chem.* **2002**, 21, 74-81.
11. Yadav, R. T.; Shafer, K. H.; Hajaligol, M. R. to be communicated.
12. *CRC Handbook of Chemistry and Physics*, 82nd Edition, Lide, D. R., Ed.; CRC Press (2001), **10**-175
13. Silva J. S., Prather, K. A., Anal. Chem. **2000**, 72, 3553-3562.

REVERSIBLE OPTICAL RECORDING ON A CdSe/ZnS NANOCRYSTAL THIN FILM*

TAKAFUMI UEMATSU†, JUNICHI KIMURA, SHINYA MAENOSONO,
YUKIO YAMAGUCHI

Department of Chemical Engineering, the University of Tokyo
Hongo 7-3-1, Bunkyo-ku, Tokyo 113-8656, Japan,

Here we report that reversible and multi-digital recording on a CdSe/ZnS core/shell nanocrystal (NC) thin film by using confocal laser scanning microscope. After a 7.4μm-squared area on the NC film was excited by strong light (11 to 1370 nW) under dry-N_2 atmosphere, a 60μm-squared area including the pre-excited region was scanned by weak light (ca. 0.6 nW) to visualize the photoluminescence (PL) intensity difference between pre- and non-excited regions. The PL intensity on pre-excited area increased with excitation energy, and finally saturated. The saturated increment of the PL intensity increases with decreasing the pre-excitation intensity. In addition, the PL increment reversibly changes with excitation intensity. The results imply that both the storage and clearing of data (i.e. PL intensity) can be operated by single excitation wavelength.

1. Introduction

CdSe nanocrystals (NCs) prepared by a high temperature organometallic synthesis have received a considerable attention because of tunability of photoluminescence (PL) spectra by varying NC size,[1-4] and various investigations regarding optical properties of CdSe NC have been reported.[5-15] As one of the interesting properties of CdSe NC, it has been presented that PL intensity of a close-packed CdSe NC film increases as a function of the irradiation time of UV light.[13-15] If one can control the PL intensity, this phenomenon can be applied to optical storage media. Our group has reported a possibility of high density storage system by using near field scanning optical microscopy (NSOM).[14]

Here we show that the PL intensity reversibly changes with decreasing the excitation intensity. The results imply that both the storage and clearing of data can be operated by single excitation wavelength.

---

[*] This work is supported by both "Nanotechnology Materials Program-Nanotechnology Particle Project" of the New Energy and Industrial Technology Development Organization (NEDO) and Grants-in-Aid for Scientific Research from the Ministry of Education, Culture, Sports, Science and Technology, Japan (MEXT).

[†] E-mail; taka@chemsys.t.u-tokyo.ac.jp

2. Experimental

CdSe/ZnS core/shell NCs capped with trioctylphosphine oxide (TOPO) were synthesized by known colloid chemical method.[2,3] The peak wavelength and half maximum full width of fluorescence spectrum of the CdSe/ZnS NCs in toluene solution was 550nm and 30 nm, respectively. By dispersing the NCs in toluene, a suspension of 1wt% solid concentration was obtained. The NC film was then fabricated on a cover glass by spin coating. The obtained NC film was dried in vacuum for one hour and subsequently preserved a desiccator (humidity 15±5%).

Microscopic fluorescent images were obtained by Leica TCS-SP2 confocal laser scanning microscope. The sample was observed in dry-N_2 atmosphere (the temperature; 25°C, relative humidity; under 3.0%). The cw Ar laser (488 nm) was used as an excitation light, and the PL intensity was detected at wavelengths from 500 to 600 nm. First, small area (7.4μm×7.4μm) on the NC film was repeatedly scanned by excitation light ranging in light intensity from 11 to 1370 nW (writing process). After the writing process, lager area (60μm×60μm) including the pre-excited region was scanned by weak light (ca. 0.6 nW) to visualize the difference in PL intensity between pre- and non-excited regions (read-out process). In order to achieve high signal-to-noise ratio, successively obtained six images were averaged. During the read-out process, the PL intensity enhancement was not significantly affected because of low irradiation energy (0.4 nJ). The cycle of both writing process and read-out process was repeatedly demonstrated on the same area of NC thin film.

The normalized PL intensity of pre-excited region I/I_0, where I represents the PL intensity of pre-excited region and I_0 is that of non-excited regions, was used as characterization factor of PL intensity enhanced by pre-excitation.

3. Results

The normalized PL intensity I/I_0 is plotted as a function of excitation energy as shown in Fig. 1. I/I_0 increased up and then saturated with excitation energy at all excitation intensity. The irradiation energy required for saturation was almost same for all excitation intensities (about 400 nJ), and the saturated PL intensity decreased with increasing excitation intensity.

This result shows that multi-digital storage is demonstrated on CdSe/ZnS core/shell NC thin film by controlling excitation intensity. It has great advantage of controllability because excitation intensity is easier to control by using an optical filter. In previous paper, we revealed a storage system by controlling of irradiation time.[13,14] However, it would be difficult to control irradiation time if a writing speed became faster and an irradiation time is less than millisecond order.

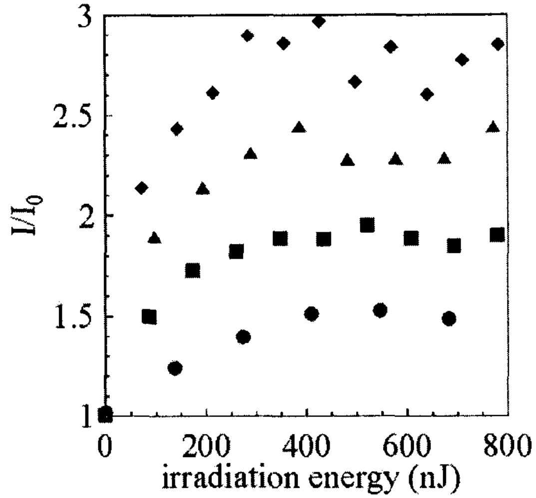

Figure 1. I/I_0 obtained after pre-excitation with each excitation intensity versus irradiation energy. Diamonds, triangles, squares, and circles reveal 11, 48, 217, and 1370 nW-intensity pre-excitation, respectively.

Interestingly, the PL increment that depended on the excitation intensity reversibly changed as shown in Figures 2 and 3. The PL intensity of the central pre-excitation area was clearly enhanced by 11 nW-intensity light (Fig. 2b), whereas PL intensity was homogeneous before the pre-excitation (Fig. 2a). After the PL intensity was enhanced to I/I_0=3.0 by 11 nW-intensity pre-excitation, the same area was excited by 1370 nW-intensity light. Then I/I_0=3.0 instantaneously attenuated to I/I_0=1.6 (Fig. 2c). After that, the region having I/I_0=1.6 was excited by 11 nW-intensity light once again, I/I_0 increases to I/I_0=3.0 (Fig. 2d). The behavior of I/I_0 during the alternating excitation was shown in Fig. 3.

These results suggest that the quantum efficiency reversibly changed with the excitation intensity, and that cleaning and re-writing of data (i.e. PL intensity) can be operated by using a single excitation wavelength.

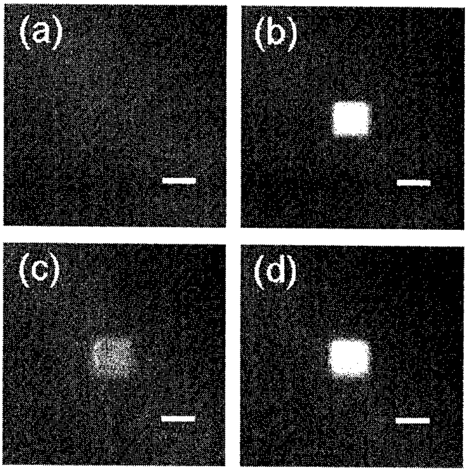

Figure 2. Fluorescent images obtained by alternating pre-excitation; before the excitation (a), after pre-excitation on the central area with 11 nW-intensity light (b), after pre-excitation with 1370 nW-intensity light following the 11 nW-intensity excitation (c), and after pre-excitation with 11 nW-intensity light following the 1370 nW-intensity excitation (d). Scale bars in all images reveal 7μm.

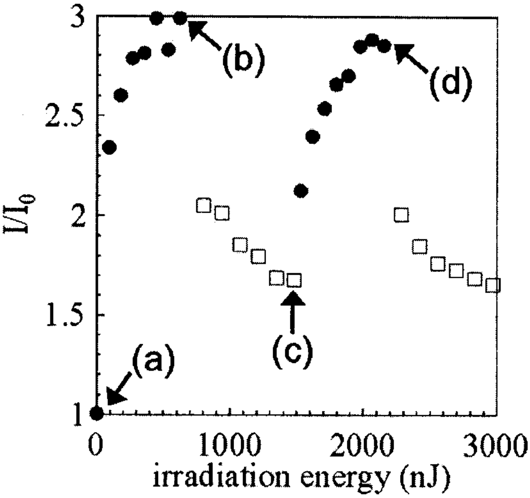

Figure 3. I/I_0 obtained by alternating pre-excitation with 11 nW-intensity light (filled circles) and 1370 nW-intensity light (open squares) plotted as a function of excitation energy. Fluorescent images that were obtained at the excitation energy revealed by the inserted alphabets were shown in Fig. 2, respectively.

In order to apply this phenomenon to optical storage media, the stability of PL intensity in dark condition is also important. In previous paper, we revealed that the PL intensity was stable for more than month in dark condition when SiO_2 was spattered on the CdSe film as a protective film.[13] The stability of PL intensity in this system was under investigation by the same experiment.

4. Discussion

The mechanism of the PL enhancement is considered as follows. First, irradiation of NC film increases both densities of exited-state NCs and ionized-state NCs. Then, the ionization probability of the remaining neutral NCs decreases due to the electrostatic potential produced by ionized-state NCs. As a result, the probability of radiative recombination of the remaining neutral NCs increases, that is, total emission efficiency enhances. When the electrostatic potential of the TOPO matrix surrounding NCs is saturated, the PL intensity is also saturated.

The excitation intensity dependence of increment of PL intensity can be explained by our hypothesis considering effect of Auger ionization of NC.[7,9] Auger ionization becomes to be dominant compared with thermally-driven ionization as excitation intensity increases. When NC film is excited by strong intensity light, Auger ionization increases the densities of ionized-state NCs against the suppression of ionization rate. Therefore, the increment of PL intensity due to the suppression of ionization rate becomes to be smaller. The reversibility of the increment of PL intensity can be also explained by the Auger ionization. When the region having I/I_0=3.0 by 11.1 nW-intensity pre-excitation was excited by 1370 nW-intensity light, the more and more NCs were ionized by Auger ionization, and it leads to the decreasing PL intensity of NC film. On the other hand, the reason of the second enhancement of PL intensity by 11.1 nW-intensity light is still not clear. The detailed mechanism is under investigation.

5. Conclusion

The PL intensity of CdSe/ZnS NC thin film increased as a function of total irradiation energy, and finally reached saturation. The saturated increment of PL intensity reversibly increased with decreasing excitation intensity. These results suggest that CdSe/ZnS NC film would be applied to reversible and multi-digital storage media. The system has great advantage because PL intensity can be controlled only by irradiation intensity using a single wavelength light.

The mechanism of PL enhancement can be explained by the suppression of ionization rate, which results from electrostatic potential produced by ionized-state NCs. In addition, the excitation intensity dependence of PL enhancement suggests Auger ionization is related to the phenomenon. The results also imply that the quantum efficiency of CdSe/ZnS NCs is sensitive to electrostatic potential of surrounding matrix.

References

1. 1.C. B. Murray, D. J. Norris, M. G. Bawendi, *J. Am. Chem. Soc.* **115**, 8706 (1993).
2. J. E. B. Katari, V. L. Colvin, A. P. Alivisatos, *J. Phys. Chem.* **98**, 4109 (1994).
3. X. Peng, J. Wickham, A. P. Alivisatos, *J. Am. Chem. Soc.* **120**, 5343 (1998).
4. M. Kuno, J. K. Lee, B. O. Dabbousi, F. V. Mikulec, M. G.. Bawendi, *J. Chem. Phys.* **106**, 9869 (1997).
5. M. Nirmal, B. O. Dabbousi, M. G. Bawendi, J. J. Macklin, J. K. Trautman, T. D. Harris, L. E. Brus, *Nature* **383**, 802 (1996).
6. S. A. Empedocles, M. G. Bawendi, *Science* **278**, 2114 (1997).
7. U. Banin, M. Bruchez, A. P. Alivisatos, T. Ha, S. Weiss, D. S. Chemla, *J. Chem. Phys.* **110**, 1195 (1999).
8. P. Michler, A. Imamoglu, M. D. Mason, P. J. Carson, G. F. Strouse, S. K. Bratto, *Nature* **406**, 968 (2000).
9. W. G. J. H. M. van Sark, P. L. T. M. Frederix, D. J. Van den Heuvel, H. C. Gerritsen, A. A. Bol, J. N. J. van Lingen, C. de Mello Donegá, A. Meijerink, *J. Phys. Chem. B* **105**, 8281 (2001).
10. G. Schlegel, J. Bohnenberger, I. Potapova, A. Mews, *Phys. Rev. Lett.* **88**, 137401 (2002).
11. Y. Ebenstein, T. Mokari, U. Banin, *Appl. Phys. Lett.* **80**, 4033 (2002).
12. M. Kuno, D. P. Fromm, S.T. Johnson, A. Gallagher, D. J. Nesbitt, *Phys. Rev. B* **67**, 125304 (2003).
13. S. Maenosono, C. D. Dushkin, S. Saita, Y. Yamaguchi, *Jpn. J. Appl. Phys.* **39**, 4006 (2000).
14. J. Kimura, S. Maenosono, Y. Yamaguchi, *Nanotechnology* **14**, 69 (2003).
15. S. R. Cordero, P. J. Carson, R. A. Estabrook, G. F. Strouse, S. K. Bratto, *J. Phys. Chem. B* **104**, 12137 (2000).

OBSERVING AND STEERING THE FORMATION OF COORDINATION COMPOUNDS ON SURFACES AT THE SINGLE-MOLECULE LEVEL

N. LIN, A. DMITRIEV, H. SPILLMANN, J. WECKESSER,
M. ABEL, P. MESSINA, K. KERN
Max-Planck-Institute for Solid State Research, Stuttgart, Germany

J. V. BARTH
Institut de Physique des Nanostructures, Ecole Polytechnique Fédérale de Lausanne, Switzerland

Towards the end of the 19th century Alfred Werner formulated the basics of coordination theory, which describes how a central transition metal atom interacts with a set of surrounding molecular ligands. Coordination compounds are of high scientific interest: they play an important role in many biological processes and are employed in the synthesis of novel supramolecular architectures and materials. A rich variety of three-dimensional molecular nanostructures and architectures with well-defined shape and geometry have been obtained using transition metal centers and concepts from coordination chemistry. However, efforts to implement this concept to low-dimensional systems are scarce. In order to gain direct insight into the nature of coordination compounds at surfaces, we have carried out single-molecule level investigations using scanning tunneling microscopy (STM) to analyse compound formation and structure, and to develop recipes for controlled metal-organic assembly.

In our studies both molecular ligands and metal centers are provided by vacuum deposition of organic molecules/metals from molecular beam evaporators onto an atomically clean single crystal Cu(100) surface, giving precise control of both absolute and relative concentrations of the resprective constituents. Also the substrate temperature is well defined by a cooling/heating stage to control of reaction kinetics and to achieve thermodynamic equilibrium. STM characterization was performed in situ under ultra-high vacuum conditions to avoid contaminations from ambient gases or dusts.

Dynamics of single chemical reactions and quantification of reaction energetics. When 1,3,5-tricarboxylic acid (tma) molecules are deposited on the substrate held at room-temperature, their carboxylic groups are deprotonated. The resulting reactive molecular ligands readily interact with naturally occuring Cu adatoms (under the employed conditions there is a gas of highly mobile Cu adatoms on the surface which are evaporated from atomic steps). In sequences of STM images the process of individual complexation reactions could be monitored. Fig. 1 shows the displacements and rotations of single molecules and records how a Cu atom (red dot) is trapped by four tma molecules and subsequently released again. Thus single events of association and dissociation of cloverleaf-shaped Cu(tma)$_4$ coordination compounds were directly observed.

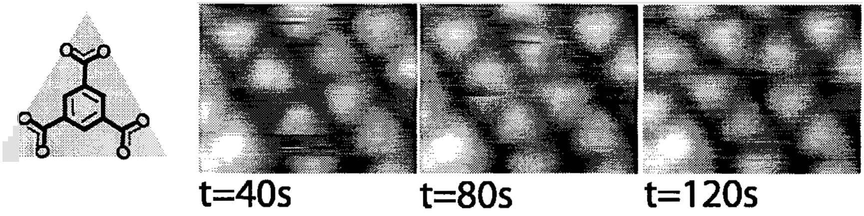

Figure 1: *tma-molecules bond in a flat adsorption geometry at a Cu(100) surface and are resolved as equilateral triangles in STM. The sequence of STM images reveals how the thermal motion of molecules at the surface proceeds. Following rotational motions and displacements a Cu adatom (red dot) is captured whereupon a cloverleaf-shaped Cu(tma)$_4$ coordination compound evolves (second image for t = 80 s; see also http://www.mpi-stuttgart.mpg.de/kern/Res_act/supmat_2.html).*

From an analysis of STM image sequences recorded with high scanning velocities (9 seconds per frame) at various temperatures, the temperature-dependent average lifetimes of isolated cloverleaves are determined. The inversion of these values provides the mean dissociation rates. These rates obey an Arrhenius law from which an energy barrier of 0.31±0.08 eV for the dissociation reaction is deduced. Note that this value is smaller than typical binding energies of related compounds in the gas phase.

Furthermore it turned out that the lifetime of the compounds depends crucially on the local chemical environment. For instance, with two compounds neighboring each other the average lifetime is typically more than three times longer than that of an isolated species. This suggests different reactivity, i.e., two neighboring species are more stable than isolated ones. Similarly increased lifetimes were observed for compounds at step edges. Since all measurements were made at the same temperature, this variation of reactivity is associated with steric effects depending on the specific local conditions of individual reactions.

It is important to note that the nature of the coordination bond is expected to be modified in the presence of the electrons from the Cu conduction band. Therefore, it is important to note that the Cu(tma)$_4$ compound cannot be regarded as an isolated entity as the coordination bonding and the electronic states of both Cu and tma are affected by the presence of the metal surface electrons effectively screening charged adsorbates. Thus an isolated deprotonated tma molecule should not be considered as $(\mathrm{tma}_{\mathrm{ad}})^{3-}$, but rather as neutral tma/Cu(100) configuration. As a consequence the oxidation state of the Cu in the $\mathrm{Cu(tma)_4/Cu(100)}$ compound cannot be determined unambiguously.

Creating chiral compounds out of achiral molecules. A chiral object is not superimposible onto its mirror image. Chirality is encountered at different levels, from single molecules and supramolecular assemblies to living organisms. Chiral molecules play an important role in biology and pharmacology. We succeed in creating chiral coordination compounds from achiral reactants - iron atoms and tma molecules. Again the reaction took place with the constituents adsorbed at the Cu(100) surface where a cloverleaf-shaped $\mathrm{Fe(tma)_4}$ compound evolves. However, a stronger interaction between the central Fe atom and the carboxylato ligands is encountered in this system. As a consequence there is an increased thermal stability and a more compact compound structure.

It can be seen in Fig.2 that in a compound the tma molecules do not point straight towards the center Fe. Rather, their triangular envelope is rotated by 22.5° clockwise or counterclockwise with respect to the principal axes of the compound.

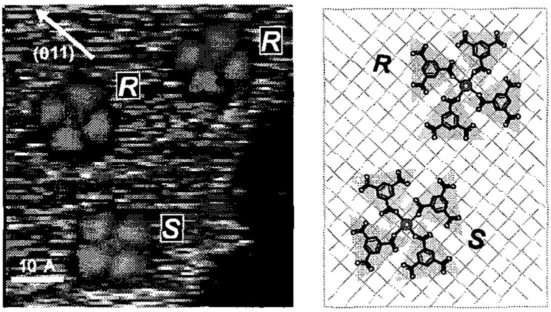

Figure 2: *Synthesis of $\mathrm{Fe(tma)_4}$ compounds at a copper substrate. There is a unidentate bonding and a correlated orientation of the four tma molecules surrounding the central Fe atom. As a consequence two mirror-symmetric compounds can be formed, designated with R and S, i.e., the system is chiral in two dimensions.*

This is associated with a unidentate Fe-carboxylate bond, where one of the oxygen atoms of the carboxylate group involved in the bonding comes significantly closer to the central Fe atom than the other. In addition there is a strict correlation of the rotation in any given complex. As a result of this symmetry breaking two distinct compounds exist (labeled *R* and *S*) which cannot be superimposed onto each other by translation or rotation on the surface. They are mirror-symmetric configurations with respect to the [011] direction of the substrate and thus represent two Fe(tma)$_4$ enantiomers on Cu(100). This represents the first observation of a chiral coordination compound at a surface.

Modular assembly of surface-supported coordination networks. For many applications the controlled realization of metal-organic architectures with specific topologies and a high structural stability at well-defined substrates is desirable. We succeeded in developing a new strategy to fabricate surface-supported coordination networks by modular assembly of 1,2,4-benzenetricarboxylic acid molecules (tmla) and Fe atoms at a surface. The networks are stabilized by relatively strong lateral metal-organic coordination bonds and consist of regularly spaced nanocavities of identical size and shape. The precise control of the concentration ratio of the components allows for the assembly of distinct architectures. This approach opens up new possibilities for the bottom-up fabrication of low-dimensional functional materials.

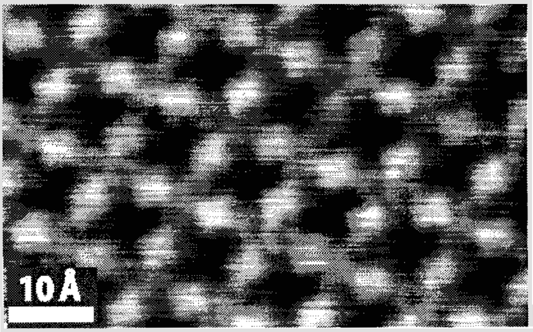

Figure 3: *STM topograph showing a regularly ordered metal-organic network structure comprising nanocavities. Single protrusions (highlighted in green) at the network's points of intersection are associated with Fe atoms, laterally coordinated by tmla carboxylato moieties.*
(I guess showing the corresponding model might help to understand what's actually going on)

In the STM image reproduced in Fig. 3 we demonstrate an example of a regular coordination network assembled at the Cu(100) surface: pairs of Fe atoms (highlighted by green dots) are linked to tmla molecules, which gives rise to an extended open network architecture comprising cavities with a well-defined shape. These cavities have a size of 5 Å × 5 Å and are regularly spaced forming an array with a 10 Å periodicity.
It is interesting to address the potential functionality of the networks. Firstly, the periodically arranged magnetic atoms which are mediated by organic linkers represent a nanoscale magnetic system. On the other hand, the well-defined nanocavities may find an application in selective molecular or ion adsorption.

Finally, the long-range order provides potential templates for three-dimensional molecular architectures, such as nanoporous frameworks.

These research efforts represent first steps in the exploration of the nature and bonding mechanisms in coordination compounds at surfaces, a research field where our current knowledge is rather limited. In view of the remarkable structures obtained such as the chiral cloverleaf compounds and the metal-organic networks, it is expected that a systematic understanding of the underlying chemistry and physics will be of significant value for the deliberate synthesis of surface-supported functional supramolecular architectures and nanostructures.

THE INTERACTION OF A LITHIUM ATOM WITH A GRAPHITE SURFACE

B. E. F. CONSTANCE AND B. K. RAO
Department of Physics, Virginia Commonwealth University, Richmod, VA 23284-2000, U. S. A.

Ab initio density functional calculations including gradient correction has been performed to study the interaction of a lithium atom with various sites on the surface of graphite. Bulk graphite has been modeled by a limited two-layer system which appears to be sufficient to obtain bulk-like behavior. The results indicate that the Li atom prefers to attach to an open site at the center of the six-member carbon rings. The interaction of the valence s-electron of Li atom with the π electrons above the graphite layer has been found to be the the main reason for this attachment. These results compare very well with similar calculations performed with transition metal atoms interacting with benzene molecule. The attached Li site is expected to provide an activation site where hydrogen atoms and molecules can eventually bind.

1. Introduction

Absorption of hydrogen for possible uses has been the object of research for a long time. Various types of metallic as well as non-metallic surfaces have been used to study the efficiency of this process. Graphite is one such surface which has been studied in detail. It is very well known that when a plasma of carbon atoms is deposited on a surface to produce a diamond film, one needs to put in a layer of hydrogen first [1] so that the diamond film will adhere to the surface and will grow efficiently. This happens because diamond structure prefers to terminate in hydrogen while graphite does not like to do so [2-4]. The differences in the electronic structures of the bulk graphite and diamond cause this contrast between these two forms of bulk carbon. It is known from the work of other researchers [5] that there is no binding between hydrogen and the open site of graphite. From our work [6] we have also concluded that in the case of a pristine graphite surface even the on-top site and the electron rich bridge site will not bind hydrogen.

There are many references to the physisorption of hydrogen on graphite in the literature. The modification of the pristine surface could support the physisorption of hydrogen. This is the prevailing situation in experiments that report the physisorption of hydrogen on graphite. Nijkamp *et al.* [7] have found that hydrogen adsorption on synthetic graphite is zero while activated graphite surfaces physisorbs as much as 36ml/gram. Bercu and Grecu [8] give estimates of the binding energy of molecular hydrogen on graphite in the range of −44meV to almost zero. For clean and hydrogenated diamond and graphite surfaces Kern [9] has reported adsorption energies of −0.82 eV for the β-site and −1.0 eV for the α-site. However, this was referenced against the surface and two hydrogen atoms, and his final statements on this have mentioned that the hydrogenated graphite surface was unstable against desorption of H_2 molecules. Therefore, we conclude that there is sufficient theoretical and experimental evidence for pristine graphite being unable to bind a hydrogen atom or a hydrogen molecule. Activation of the graphite surface for hydrogen absorption can be done through deposition of foreign atoms. These atoms can provide defect sites where the hydrogen atoms/molecules can attach.

In the current work we have studied the interaction of lithium atoms with graphite surface as Li has been proved to be effective in intercalation and may possibly perform equally well in low density deposition on the surface.

2. Graphite as a Surface

When clusters interact with a surface very strongly, as when the surface and the cluster are made of the same atoms, the cluster would not retain its identity. Therefore, any useful property of that cluster arising out of size effect would be lost. Calculations by Dederichs *et al.* [10, 11] and Nayak *et al.* [12] have shown that metal surfaces usually provide strong interaction and change the properties of the deposited clusters. These calculations have used the long-range order for the simulation of the bulk surface. Ray *et al.* [13] have demonstrated that clusters reacting strongly with a surface do not grow as free clusters do. They follow the geometry of the underlying surface and the resulting magic numbers are different from what is observed for free clusters. Experimentally this has also been observed by Poelsema *et al.* [14] Therefore, the next step should be aimed at a study where the cluster or the surface would be relatively less reactive.

Graphite can provide a surface that should be less reactive towards metallic clusters. Graphite consists of planes of carbon atoms stacked above each other. The distance between consecutive planes is 3.4Å. Each plane of graphite is characterized by a pattern of 6-membered hexagonal rings of carbon atoms. The rings are flat, and each atom in the ring is covalently bonded to each other. The carbon-carbon bond of the graphite layer is formed by sp^2 hybridization of the valence orbitals. Bonding between the layers is weak and allows for the slippage of the layers over each other. This structure is, to a considerable extent, chemically inert, with the majority of its electron density lying within the plane.

We expect that it might be possible to deposit a cluster on this surface without significantly changing the electronic structure of the cluster.

We plan to study the interaction of a limited model of graphite surface with Li atoms. We are interested in the answers to the following questions. What force will the lithium atom experience at different sites? Will it bind at any point of the surface? Is there an energy barrier? Where on the surface would a lithium atom like to sit in relation to the atoms that make up the surface? Would the lithium atom like to sit close to the surface, below the surface or does it prefer to be far from the surface? Would the presence of a lithium atom influence the charge distribution of the surface? Is it a local or a long-range effect? What other adsorbates will be expected to duplicate the behavior of lithium on graphite? The answers to these will eventually be required to study the interaction of hydrogen atoms and molecules with graphite surface where Li atoms have been deposited. This part of the study will be conducted at a later stage.

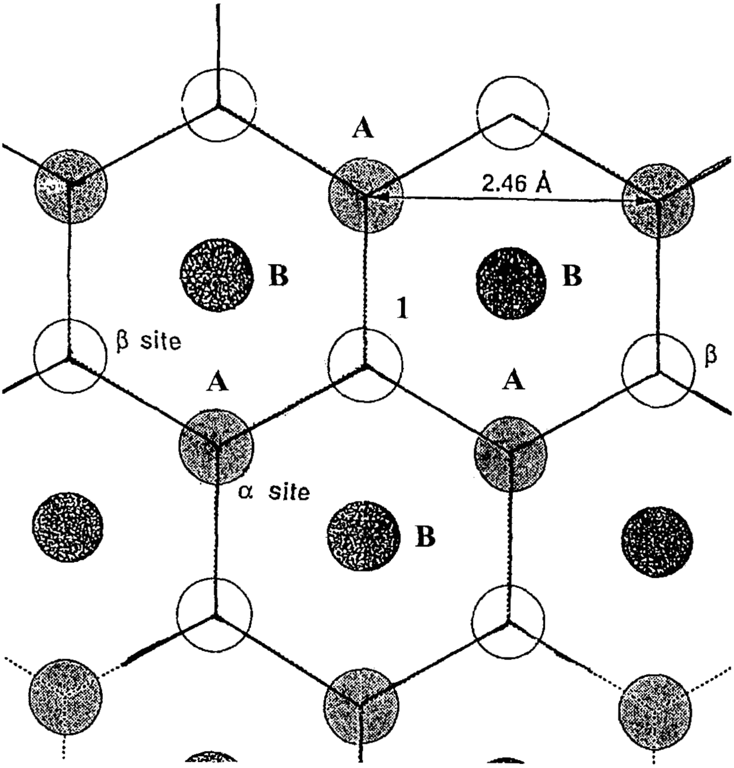

Figure 1. Schematic representation of bulk graphite as seen from the top of the surface.

3. The Model for Graphite

A segment of the geometry of two layers of bulk graphite is shown in Fig. 1. In the figure the atoms "A" are exactly above carbon atoms in the lower layer while those marked "B" are the atoms of the lower layer. The carbon atoms in the α positions are those that have a carbon atom immediately below them while the β-carbon atoms do not. Using this information the graphite surface will be modeled by a two-layer system (Fig. 2). The topmost layer will be represented by 13 carbon atoms arranged so as to represent 3 hexagonal rings. The otherwise dangling bonds of the edges of the system are terminated by 9 hydrogen atoms. A second layer will be represented by 6 carbon atoms and arranged to form a single hexagonal ring with the dangling bonds terminated by 6 hydrogen atoms. The quenching of the dangling bonds by hydrogen atoms is a convenient means of avoiding strain in the calculations. This has been found [15, 16] to be very helpful while studying covalent systems. The distance between the layers will be fixed at 3.35Å. The carbon-carbon distance within a plane will be fixed at the characteristic value of graphite, 1.42 Å. The second layer, however limited, is an absolute necessity because in the absence of this layer the behavior of the π electrons [17] above the top layer will not be similar to what is expected in bulk graphite.

4. Interaction with the Lithium Atom

The Li atom will be brought from infinity towards the upper layer. There are three possible sites on the graphite surface that the atom will be required to approach. These are (1) the on top site, which corresponds to the adsorbate directly above a carbon atom, (2) the bridge site, which corresponds to the adsorbate above the center of the carbon bond, and (3) the open site, which corresponds to the adsorbate above the center of the six-member ring (Fig. 2). As shown in the figure, the atom will be far away from the edges of the upper surface such the edge effects will not influence the results. The approach of the Li atom to the surface will be carried out in a series of steps. At each step, the total energy of the system will be calculated using density functional theory with gradient correction through Becke-Perdew-Wang formulation (BPW91) [18-21]. These results will allow us to observe how the energy of the system changes as the Li atom gets closer to the surface along different paths of approach. The information obtained from this process will yield the shape of the potential energy profile of the interaction. This will give us information on the heights of energy barriers, their position and shapes for example, and whether the curve is flat over a large region, or are there many local maxima and minima. Through a natural bond analysis the electron distribution of the adsorbates may be monitored as they approach the surface: thus allowing us to discern changes in the electronic properties as they develop.

5. Results and Discussions

In the calculations, the first step was to optimize the part of the geometry that does not belong to bulk graphite. As mentioned earlier, the positions of the carbon atoms are prefixed following the bulk graphite geometry. Thus the optimization was performed for the C-H bond length and its angle with nearest neighbor carbon atoms. The dihedral angle for the position of the H atoms was also optimized to determine if the atoms stayed in the plane of the carbon atoms. The optimized C-H bond length was obtained as 1.082Å. The accepted carbon-hydrogen single bond length is 1.07Å.

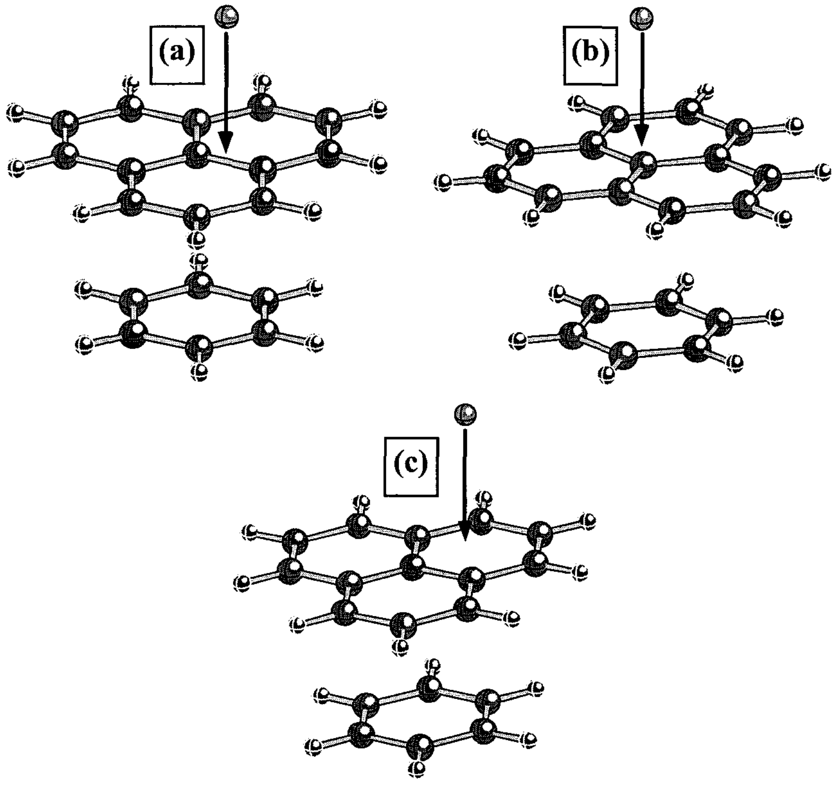

Figure 2 (a) Bridge site, (b) On-top site, and (c) Open site for approach of a Li atom.

A natural bond analysis showed that all the terminating hydrogen atoms lost a slight amount of electronic charge. All carbon atoms had a slight excess of electrons. In the case of the lower layer, the excessive charge on each carbon can be attributed to the loss of charge from their associated terminating hydrogen. The average loss of electronic charge from each of these hydrogen atoms is 0.22e. The gain in electron charge on each carbon atom in the lower layer is 0.22e. As is the case with the lower layer, each hydrogen atom in the upper layer donates some of its electronic charge to the closest carbon atom. However, β-carbons got slightly less charge than the hydrogen-terminated α-carbons, each of which had an excess electronic charge of about 0.2e. The non-terminated carbons had very little excess charge. The central carbon of the upper layer, carbon 1, had the smallest excess charge.

The small amount of excess charge of the non-terminated carbon atoms compared to the more substantial charges on the terminated carbon atoms may be considered to be a weakness of the model. It may be argued that the model should have been representative of a more extensive region of the surface, say an additional outer layer of hexagonal rings. This would necessitate an additional twenty-two carbon atoms in the upper layer only. Consequently the computational cost could be prohibitive. As the optimization did yield the correct C-H bond length and perfect hexagonal planes of the benzene-like rings in the planes and the charge difference discussed about was actually insignificant, it was decided to use the model of graphite as proposed.

5.1. *Lithium Atom Approaching the On-Top Site*

Total energy of the system was calculated with a lithium atom approaching towards the on-top site of the graphite surface. Starting at distance of 4 Å from the surface the atom was brought down in steps towards carbon 1 (Fig. 1) and for each step the total energy of the system was calculated. When the Li atom moved closer to the surface, it caused a gradual reduction in the total energy of the system eventually achieving a minimum when the lithium atom was 2.0 Å above the surface. As the lithium atom came even closer the energy of the system rose steeply due to repulsive force between the lithium atom and carbon atom1. Therefore, the Li atom was taken below the carbon atom and was then moved slowly away vertically. The energy of the system decreased until the lithium was 1.8 Å below the surface where it attained a minimum. As the lithium atom moved further below the surface the energy of the system began to rise again.

The binding energy of the Li atom with graphite is defined as

$$E_b = E(\mathrm{Li} + \mathrm{Graphite}) - E(\mathrm{Graphite}) - E(\mathrm{Li}).$$

In this definition, the system for which the energy is obtained is given in the parenthesis. Thus, when E_b is negative, there is a binding between the Li atom and the graphite. It is interesting to notice that the binding energy corresponding to the second minimum (below the surface) is more than the first binding energy (corresponding to the energy minimum above the surface) by 0.27 eV.

The energy minimum above the surface is easy to understand. As the Li atom comes closer to carbon 1, the overlap between their orbitals increases and binding occurs at a height of 2.0 Å. This is comparable to the usual Li-C bond length of 1.86 Å. However, when the atom moves closer, Coulomb repulsion results in a sharp increase of the energy. When the atom moves away below carbon 1, it should have created the second minimum at exactly the same distance as seen above, i.e. 2.0 Å. However, the Li atom is moving in a direction that would take it though the center of the ring formed by the carbon atoms of the lower layer. This causes a slight amount of repulsion from these atoms and therefore, the minimum occurs at a slightly shorter distance.

The bound condition of a lithium atom on top the carbon atom above the surface is characterized by the lithium atom's complete loss of its outmost electron to the surface. The electron charge is redistributed mainly to hydrogen terminated β-carbon atoms. These account for 2/3 of the redistributed charge. However, the on-top carbon atom acquires the most charge (0.162e) for any individual carbon atom. The α-carbon atoms show a slight increase in charge. The hydrogen-terminated α carbons reflect a very small loss of electron charge. There is no significant change in the charge distribution of the lower layer.

Examination of the natural population analysis shows that increased electron occupation of the on-top carbon and the hydrogen terminate in β-carbon atoms was the result of increased occupation of the $2p_z$ orbital of these atoms. These orbitals are orientated perpendicular to the surface. The transfer of electron charge to the surface, leaving the lithium atom with a net positive charge, suggests that the binding condition between the lithium atom and the surface is ionic in character. This is in keeping with principles of general chemistry, which *teaches that a bond is about 50% ionic in character if the difference in electro*-negativity of the two species involved is 1.7. Lithium has an electro-negativity of 1.0 while carbon has an electro-negativity of 2.5. The difference in electro-negativity between carbon and lithium suggest that the Li-C bond is slightly less than 50% ionic in character.

As previously stated, a minimum configuration exists when the lithium atom is 1.8 Å below the on top site. The following describes the distribution of charge at this minimum. As is the case when the lithium atom is above the surface, here the lithium has lost almost all its outer electron. However, the extent of the loss is less when compared to the loss when the lithium atom is at the minimum above the surface. The central carbon atom C1 gained the most charge for any individual atom, about 0.17e. Generally the charge distribution of the upper layer is much like the case when the lithium atom is above the surface. However, the occupancies are slightly lower and the central carbon atom C1 gained more charge when the lithium atom is below the surface than when it is above the surface. The lower layer responded by increasing electron charge on the carbon atoms, this increase is comparable to the increase of charge on the α-carbons of the upper layer while the electron charge on the terminating hydrogen atoms were further reduced.

5.2. *Lithium Atom Approaching the Bridge Site*

As the lithium atom descended towards the bridge site of the graphite surface this was modeled by its approach to the mid-point between carbon atom 1 and the nearest carbon atom (Fig. 2(a)). The energy of the system gradually decreased and it entered a shallow, bound region extending between the heights 2.8 Å and 1.6 Å from the surface. The lowest energy of the system occurred at a height of 2.0 Å above the surface. At this point the binding energy of the Li atom with the surface is 0.97 eV. Interestingly, this is also the height at which the best binding occurred as the lithium atom approached the on-top site.

The binding energy E_b, for different heights of the Li atom is given in Fig. 3. As mentioned before, a negative value of E_b means that the Li atom is bound to the graphite. As the lithium atom is moved below the bridge site, the system goes through an energy minimum at a distance of 1.7 Å below the bridge site. Here it is bound by 0.74 eV, which is less favorable than the minimum energy configuration for the lithium atom above the surface. Further movement towards the lower layer causes the energy of the system to increase.

As in the case of lithium over the on-top site, the lithium atom has a net positive charge and has essentially lost its outermost electron to the top layer of the surface. The effect on the lower layer is insignificant. However, whereas the charge transfer to the surface in the case of the on-top site went mainly to the $2p_z$ orbital of the central β-carbon atoms, the charge redistribution when lithium is over the bridge site is not as straightforward. About 0.23e was donated to carbon atom 1 and carbon atom 2 most of which occupied the $2p_z$ orbitals. Carbon atom 3 acquired the most charge for any individual carbon atom but this charge occupied the $2p_x$ orbital. The other hydrogen-terminated β-carbon except carbon atom 13 showed increase occupancy of their $2p_z$ orbital. This was accompanied by a small loss of charge from their $2p_x$ orbitals. The other carbon atoms showed increased electronic charge, with more of it going to the α-carbon atoms.

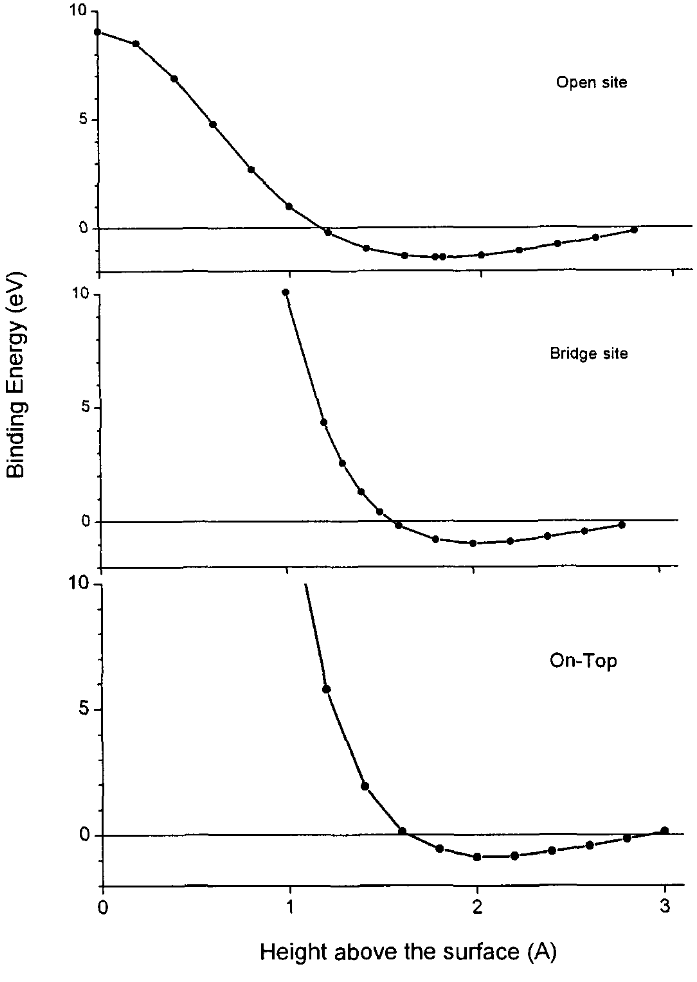

Figure 3. Comparison of binding energies of the Li atom at various sites.

The lithium atom gave up slightly less charge when placed at the minimum configuration below the surface. Like the case of lithium above the surface, substantial amount of charge occupy the $2p_z$ orbitals of C1 and C2, the atoms from the C-C bridge. This time, however, C1 has the highest increase of charge. The charge distribution of the upper layer is similar to the situation described for the lithium atom above the bridge site except that the quantities of charge are somewhat reduced. The intercalated lithium has considerable effect on the charge distribution of the lower layer. It made the hexagonal ring more electronegative, which drew more charge from the terminating hydrogen atoms. There were small increases of charge on the atoms below open sites but those below α-carbons and further from the interacting bridge site loose electronic charge.

5.3. *Lithium Atom Approaching the Open Site*

The approach of the lithium atom towards the open site of the graphite surface is associated with a steady decline in the total energy of the system. This decrease in energy continues until the lithium atom is 1.76 Å above the surface. If the lithium atom moves closer to the surface the energy of the system rises until it achieves its greatest value when the lithium atom is lying in the surface of the graphite ring. Once again, the energy of the system decreases as the lithium atom moves through the surface towards the lower layer. This decrease continues until the lithium atom is 1.48 Å below the surface where an inter-planar minimum is obtained. Further movement towards the lower layer leads to an increase of energy. Details of these data are presented in Fig. 3. The charge distribution of the system when it was in its minimum configuration, characterized by the lithium atom 1.76Å above the surface, can now be compared with the charge distribution of the bare surface. The results show that there was no significant redistribution of charge in the lower layer. However, this is not the case for the upper layer where changes in orbital occupancy were made to accommodate the presence of the outer electron yielded up by the lithium atom.

Of the atoms that bound the open site, the hydrogen-terminated β-carbons show the largest increase of electronic charge due to the presence of the lithium atom. In both cases about two thirds of the increased charge occupied the $2p_z$ orbital and about 1/3 of it occupied the $2p_x$ orbital. The two α-carbons showed small increase in electron occupancy. This was mainly confined to the $2p_z$ orbital. The atom C1 increased its electronic charge by a value comparable to the increase on the α-carbons and likewise, the excess charge occupied the $2p_z$ orbital. Though the geometry and species of the boundary of the hole site is symmetrical, the charge redistribution due to the presence of the lithium atom does not have the symmetrical qualities that one might expect. This must be due to the different environment of the individual carbon atoms that constitute boundary of the open site.

The charge distribution when the lithium atom is in the minimum configuration below the open site is similar to the distribution with the lithium atom above the open site. However, in this case the charge on the atoms that bound the open site is slightly less. This may be due to the lithium atom losing more charge when it is above the surface than when it is below the surface. Unlike the situation when the lithium atom is above the surface, there is a substantial increase of charge on the carbon atoms of the lower layer. Most of this charge occupies the $2p_y$ orbital of the carbon atom directly below the open site. The α-carbon atoms that are the nearest to this atom have a slight increase in charge and the one further away and the carbon atoms below the other open sites have lost charge. The terminating hydrogen atoms of the lower layer have become more positive.

Table 1. Comparison of the positions where the Li atom binds in its approaches to various sites.

Approach	Above the surface		Below the surface	
	Height (Å)	E_b (eV)	Height (Å)	E_b (eV)
On-top site	2.00	-0.87	-1.80	-1.15
Bridge site	2.00	-0.97	-1.70	-0.74
Open site	1.76	-1.38	-1.40	-1.44

5.4. *Comparison of the Results from Different Sites*

The results (see Table 1 above) show that the lithium atom can be attached to any of the sites studied. However, the open site was the most favorable one either above the surface or below the surface. When the Li atom is placed in a symmetric position with respect to the benzene-like carbon ring, its valence electron finds it easier to bind with the system through interaction with the π electrons that are almost delocalized. In any other situation, it needs to interact with only one (on-top) or two (bridge) carbon atoms. Since these carbon atoms are covalently bonded to one another, displacing their charge to share with the Li atom is energetically less favorable. Moreover, the Li-C bond, when formed, is a strong bond. Therefore, a Li atom prefers to bind with six carbon atoms placing itself in a symmetric position with respect to 6-atom ring, i.e. the open site. This is also noticeable from Fig. 3 showing a comparison of the binding energies of the Li above various sites. Even though the nature of the minima seems to be the same, in the case of the open site the binding energy does not go up above the $E_b = 0.0$ baseline as rapidly as in the other two cases. From the positions of these minima one notices that for all the cases the Li-C distance is almost the same indicating that the Li-C binding has been maximized for the open site. The preference of the symmetric open site has also been observed in the case of transition metal atoms interacting with a benzene molecule when the atom has very few valence electrons (Sc, V) [22, 23] as compared with the situation when the d-shell is almost filled (Ni) [24].

Acknowledgment

This work was partially supported by a grant from the U. S. Department of Energy.

References

1. J-Y Raty, G. Galli, C. Bostedt, T. W. van Buuren, and L. J. Terminello, Phys. Rev. Lett. **90**, 037401 (2003).
2. L. L. Regel and W. R. Wilcox, J. Mat. Sc. Lett. **19**, 455 (2000).
3. N. Ali, W. Ahmed, Q. H. Fan, and C. A. Rego, Thin Solid Films **377-378**, 208 (2000).
4. B. V. Spitsyn, L. L. Bouilov, and B. V. Derjaguin, J. Cryst. Growth **52**, 219 (1981).
5. M. S. Dresselhaus, K. A. Williams, and P. C. Ecklund, MRS Bulletin **24**, 45 (1999).
6. BFC thesis
7. M. S. Nijkamp, J. E. M. J. Raaymakers, A. J. van Dillen, and K. P. de Jongh, Appl. Phys. A **72**, 619 (2001).
8. M Bercu and V. Grecu in *Romanian Conference of Theoretical Physics* (http:// www.theory.nipne.ro/ctp2002/abstracts/a32.html).
9. Georg Kern, Ph. D. Dissertation (Technische Universität, Vienna, 1998).
10. K. Wildberger, V. S. Stepanyuk, P. Lang, and P. H. Dederichs, Phys. Rev. Lett. **75**, 509(1995).
11. P. Lang, V. S. Stepanyuk, K. Wildberger, R. Zeller, and P. H. Dederichs, Solid State Commun. **92**, 755 (1994).
12. S. K. Nayak, S. E. Weber, P. Jena, K. Wildberger, R. Zeller, P. H. Dederichs, V. S. Stepanyuk, and W.Hergert, Phys. Rev. B **56**, 8849 (1997).
13. A. K. Ray, B. K. Rao, and P. Jena, Phys. Rev. Lett. **76**, 2878 (1996).
14. G. Rosenfeld, A. F. Becker, B. Poelsema, L. K. Verheij, and G. Comsa, Phys. Rev. Lett. **69**, 917 (1992).
15. S. K. Nayak, S. E. Weber, P. Jena, K. Wildberger, R. Zeller, P. H. Dederichs, V. S. Stepanyuk, and W.Hergert, Phys. Rev. B **56**, 8849 (1997).
16. J. H. McCreery and G. Wolken, Jr., J. Chem. Phys. **63**, 6 (1975).
17. M. A. Fox and J. K. Whitesell, *Organic Chemistry* (Jones and Bartlett, Boston, 1994), p. 27-29 and p. 544.
18. J. P. Perdew, Phys. Rev. B **33**, 8822 (1986).
19. J. P. Perdew and Y. Wang, Phys. Rev. B **45**, 13244 (1992).

20. A. D. Becke, J. Chem. Phys. **98**, 1372 (1993).
21. *Gaussian 98*, Revision A.7, M. J. Frisch, G. W. Trucks, H. B. Schlegel, G. E. Scuseria, M. A. Robb, J. R. Cheeseman, V. G. Zakrzewski, J. A. Montgomery, Jr., R. E. Stratmann, J. C. Burant, S. Dapprich, J. M. Millam, A. D. Daniels, K. N. Kudin, M. C. Strain, O. Farkas, J. Tomasi, V. Barone, M. Cossi, R. Cammi, B. Mennucci, C. Pomelli, C. Adamo, S. Clifford, J. Ochterski, G. A. Petersson, P. Y. Ayala, Q. Cui, K. Morokuma, D. K. Malick, A. D. Rabuck, K. Raghavachari, J. B. Foresman, J. Cioslowski, J. V. Ortiz, A. G. Baboul, B. B. Stefanov, G. Liu, A. Liashenko, P. Piskorz, I. Komaromi, R. Gomperts, R. L. Martin, D. J. Fox, T. Keith, M. A. Al-Laham, C. Y. Peng, A. Nanayakkara, C. Gonzalez, M. Challacombe, P. M. W. Gill, B. Johnson, W. Chen, M. W. Wong, J. L. Andres, C. Gonzalez, M. Head-Gordon, E. S. Replogle, and J. A. Pople, (Gaussian, Inc., Pittsburgh PA, 1998).
22. T. Kurikawa, K. Takeda, M. Hirano, K. Judai, T. Arita, S. Nagao, A. Nakajima, and K. Kaya, Organometallics **18**, 1430 (1999).
23. P. Weis, P. R. Kemper, and M. T. Bowers, J. Phys. Chem. **101**, 8207 (1997).
24. B. K. Rao and P. Jena, J. Chem. Phys. **117**, 5234 (2002).

CLUSTER STUDY OF THE DISSOCIATION OF H_2 ON Cu AND Ni (100) AND (111) SURFACES

B. E. F. CONSTANCE, B. K. RAO,[†] AND P. JENA

Department of Physics, Virginia Commonwealth University, Richmond, VA 23284-2000 U. S. A.

Ab initio calculations have been performed to study the microscopic details of the interaction of H_2 molecules with copper and nickel metal surfaces using a cluster model. Finite number of metal atoms placed at their corresponding bulk sites have been chosen to represent the metal surface. Dependence of the interaction of H_2 upon the size of these clusters as well as the symmetry of the metal surfaces has been investigated. Results on molecular physisorption, molecular chemisorption, and dissociative chemisorption are presented.

1. Introduction

Dissociative chemisorption of hydrogen molecules occurs on the surfaces of most metals. This process has important influence on technology and therefore, economy. Use of fine particles of metals as catalysts in various reactions involving hydrogen is dependent upon the H_2 molecule being chemisorbed on the surface of the particle after dissociation and then atoms reacting with other reagents available in the environment.

Many recent studies of metal-hydrogen interactions [1,2] have been initiated by the fact that small atomic clusters show strong size dependence on the properties and it is expected that the reactivity and the binding energy of hydrogen on metal clusters would depend strongly on the size and composition of the clusters. The nature of this interaction should be different from that on bulk metal surfaces. As small metal clusters are mostly composed of surface atoms and the interaction occurs at the surface of bulk metals, the difference in behavior requires fundamental understanding. One needs to find out if the flexibility of the cluster geometry lowers the barrier against the interaction. Such a study can have important influence on the potential of hydrogen being used as a clean fuel.

Theoretical tools have been available to study the interaction of atomic clusters with H_2 with great accuracy. As the interaction of a hydrogen molecule with metal surface is limited to only a few atoms of the surface, it may be

---

[†] Electronic mail: bkrao@vcu.edu

possible to use the same accurate theoretical methods to study the nature of the interactions in the case of bulk metal surface.

For such a study the choice of the model is very important for obtaining information on the electronic structure at the atomic level. It must be extensive enough to incorporate the physical character of the system while it must also be simple enough to use the *ab initio* theoretical method with sufficient accuracy to obtain meaningful results. The study should include (1) physisorption, (2) associative and dissociative chemisorption, (3) energy barriers, and (4) equilibrium sites occupied by hydrogen atoms following dissociation. It is expected that as a hydrogen molecule approaches the metal surface, electrons from the metal would be transferred to the anti-bonding orbital of the hydrogen molecule, thus weakening the H-H bond, which would eventually break. The two free hydrogen atoms may then bond to the metal atoms on the surface or in some cases, may diffuse into the bulk metal and occupy preferred sites. The interaction of hydrogen with transition metal surface is complicated by the presence of holes in the d-states, which may act as sinks for the s-state electrons of the approaching hydrogen molecule.

2. Choice of the Model

We shall use a small cluster of metal atoms to represent the corresponding bulk metal [3, 4]. The atoms will be fixed to the lattice sites at the bulk geometry and the interactions of the H_2 molecule will be studied with the metal cluster so chosen using *ab initio* theoretical methods.

Bulk copper and nickel both have face centered cubic (fcc) structure. A small segment of a crystal with fcc structure is presented in Fig. 1 with two cubes only. Four nearest neighbor atoms on the (100) surface and the (111) surface lattice are shown in Figs. 1(b) and (c) respectively.

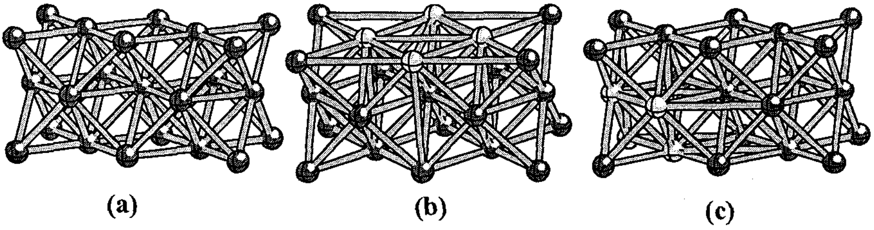

Figure 1. Model of (a) a face centered cubic structure showing (light shaded atoms) the four nearest neighbor atoms on (b) the (100) surface and (c) the (111) surface.

It is noticed that the spaces between the atoms of the (100) surface are larger than the spaces between the atoms of the (111) surface. The surface atoms of the fcc (100) surface have four-fold symmetry while those of the (111) surface have three-fold symmetry.

If one uses only two metal atoms to model the surface one will have to follow the model given in Fig. 2 below. Here the distance between the two metal atoms (M) is fixed at the bulk value for the chosen surface of the metal. The H_2 molecule will be brought down symmetrically step by step, and for each value of Z, the distance between the center of the H_2 molecule and that of the metal dimer, the total energy will be calculated for different values of d, the H-H bond length. This will provide a complete picture of the reaction channel.

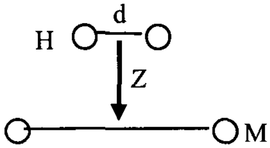

Figure 2. Model for interaction of H_2 with a metal surface represented by 2 metal atoms (M).

When four atoms are used to model the surface of the metal, the symmetries of the chosen group of atoms will change from the (100) surface to the (111) surface. This will lead to different approaches to the two surfaces.

3. Calculations and Results

Using these models the interactions of a hydrogen molecule with the (100) and the (111) surfaces of Cu and Ni have been studied. Self-Consistent Field Molecular Orbital theory (SCF-LCAO-MO) [5] has been used with unrestricted Hartree-Fock approximation (UHF) to calculate the total energies of the systems at the configurations mentioned. Split-valence double zeta 6-31G basis set has been used to represent the atomic wave functions. In each case, correlations corrections has been applied through the use of Möller-Plesset perturbation theory [6].

There are two basic questions that need to be answered. (1) Does an associative chemisorption occur and does it depend upon the cluster size chosen to represent the metal surface? (2) Does the energy barrier against dissociation exist in the entrance channel or the exit channel? As a matter of detail, in some cases we have also investigated more than one spin configuration for the systems to determine if there is a crossover between different spins at specific configurations.

3.1. *Cu_2H_2 and Ni_2H_2 Systems*

Using the model in Fig. 2 and choosing the proper value for the M-M distance for Cu or Ni (for example, for Cu this distance is 2.57 Å) the H_2 molecule was brought down stepwise and the total energy was calculated for various values of d for each fixed value of Z. The value of d was varied from 0.4 Å to 2.4 Å in steps of 0.1 Å. The value of Z was varied between 1.0 Å and 3.0 Å in steps of 0.1 Å. In Fig. 3 below we plot the constant energy contours as H_2 descends on Cu (Fig. 3(a) and Ni (Fig. 3(b)). For this plot the energies were calculated at 400 points as mentioned and later interpolated using a spline fit. The energies are shown in eV with respect to the reacting systems as $\Delta E = nE(M) - 2E(M) - 2E(H) + E(M_nH_2)$, where E is the total energy of the entity given in the parenthesis and n is the number of metal atoms (M) used in the study. $\Delta E > 0$ indicates that the formation of M_nH_2 is not favored.

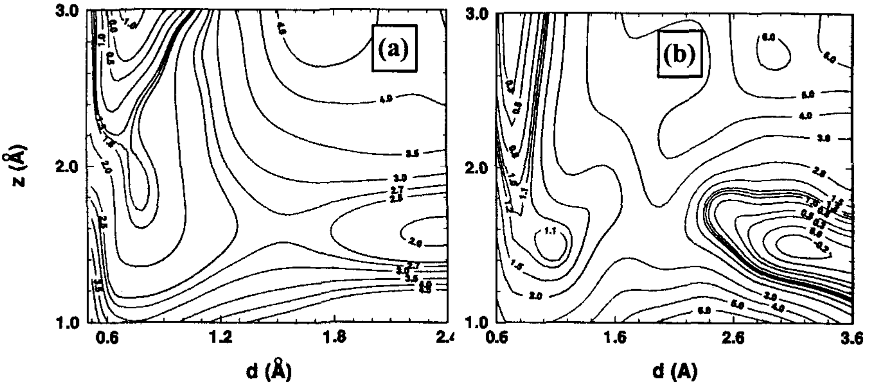

Figure 3. Constant energy contours for H_2 interacting with (a) Cu (100) surface and (b) Ni (100) surface. In each case there are two metal atoms used to represent the bulk. The energies are given in eV with respect to the interacting systems as defined above.

For Cu, it is seen that for Z > 3 Å, there is a molecular physisorption minimum and for Z ≈ 1.5 Å, the H_2 dissociates into a chemisorption minimum. There is a secondary minimum at Z ~ 2 Å where the hydrogen atoms remain in the molecular form. It is important to note that a large energy barrier separates the molecular chemisorption and the physisorption minima from each other. There is also a significant barrier between the molecular chemisorption and the dissociative chemisorption minima. Thus the H_2 encounters energy barriers in both the entrance as well as the exit channels.

The corresponding results for Ni show that the physisorption minimum is at Z > 3 Å and the chemisorption minimum at Z ≈ 1.5 Å is actually a local minimum with high energy. The molecular chemisorption minimum is separated from the dissociated minimum by a barrier of about 1.0 eV. Here, unlike the case of Cu, the dissociative minimum site is bound with respect to Ni_2 and H_2.

3.2. *Cu_4H_2 Systems for Cu(100) and Cu(111) Surfaces*

In order to check the cluster size effect we have studied the interaction of H_2 molecules with the Cu (100) surface being represented by 4 copper atoms (Fig. 1(b)). The same level of theory was used to calculate the total energy of the system with Z and d representing the same parameters as defined in Fig. 2. The results of this search are presented in Fig. 4(a) below.

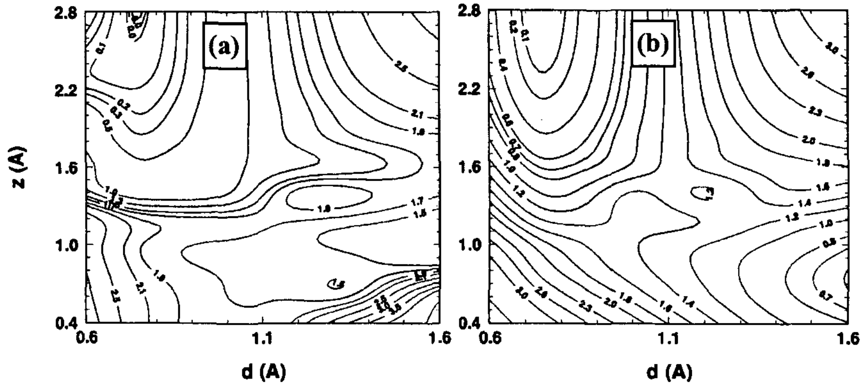

Figure 4. Constant energy contours for H_2 interacting with (a) Cu (100) surface and (b) Cu (111) surface represented by 4 Cu atoms. The energies are given in eV.

To examine if the presence/absence of molecular chemisorption is due to a surface orientation effect we have repeated the calculations for H_2 approaching the Cu_4 (111) surface. The results are shown in Fig. 4(b) above for H_2 coming down on the long diagonal (Fig. 2(c)). The energies along the short diagonal were consistently higher than this case. Once again, there is no evidence for the molecular chemisorption states. The energy surface is characterized by physisorption and a dissociative chemisorption minimum separated by an energy barrier of more than 1.0 eV. The surface orientation does not appear to be important.

3.3. *Ni_4H_2 Systems for Ni(100) and Ni(111) Surfaces*

Having observed the success of four metal atoms in describing the interaction of H_2 with bulk metal surface, it is natural to extend the study to the case of the Ni surface. Results for the Ni_4 (100) and Ni_4 (111) surfaces are presented in Fig. 5 with the H_2 coming down on the long diagonal (Fig. 2(c)). These are very much similar in nature to the contours given for Ni_2H_2 (Fig. 3(b)). It is therefore, clear that four nickel atoms are sufficient to model the metal surface effectively. In each case, the molecular chemisorption minimum is actually a high energy local minimum. The dissociative chemisorption minimum occurs at about the same height ($Z \approx 1.5$ Å) as in the case of Ni_2H_2. However, the value of d for the dissociative minimum is now approximately 1.5 Å. As observed here, others have also found that energy hypersurface for the case of H_2 interacting with Ni showed more structures than what was observed for the case of copper. It is expected because of the richness of the one-electron levels of Ni atoms due to the unfilled d shell.

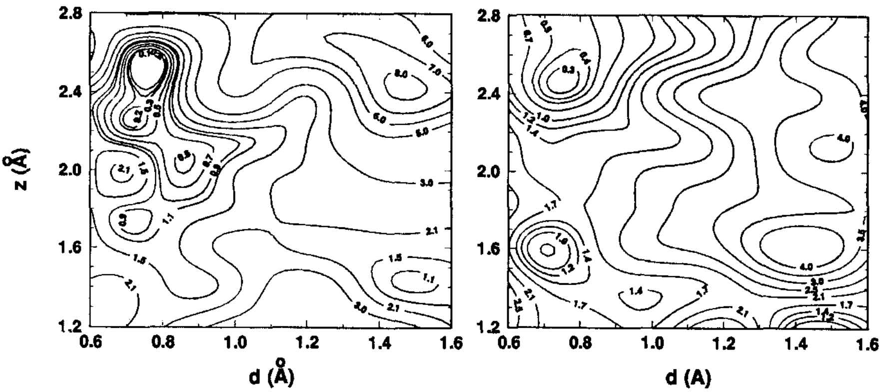

Figure 5. Constant energy contours for H_2 interacting with (a) Ni (100) and (b) Ni (111) surface represented by four nickel atoms. The energies are given in eV.

4. Cu_4H_2 Revisited

To examine if the minor discrepancy between the results of Cu_2H_2 and the Cu_4H_2 can be removed using a different method for calculation and with a much more extended basis set, we have repeated our calculations with density functional theory [7] and gradient correction (BPW91) [8] and split valence triple zeta basis set including polarization functions (6-311g**).

It was observed that when the H_2 molecule descended towards the short diagonal of the $Cu_4(111)$ surface, the molecular physisorbed region was only 0.02 eV deep at approximately 2.8 Å above the surface. This position is very close to what was observed for the cases of Cu studied with HF-MP2. When the H_2 molecule was allowed to descend towards the long diagonal, the position of the physisorbed region remained almost unchanged. However, the depth of the minimum increased to 0.1 eV. No molecular chemisorbed state was found either along the short diagonal or the long diagonal. The dissociative chemisorbed state along the long diagonal is situated at a height of 0.66 Å when the H-H bond stretches to 1.76 Å. Clearly the molecule has dissociated in this position. These observations can be seen clearly in the energetics presented in Fig. 6 below.

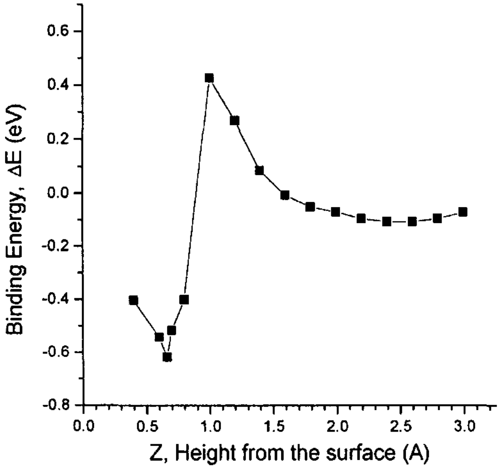

Figure 6. Plot of the binding energy (ΔE) for optimized H-H distance versus height (Z) with H_2 descending towards the long diagonal of $Cu_4(111)$ surface. The barrier between the two minima is quite sharp.

We have calculated Mulliken charges on the atoms to examine the details of the electronic structure during the interaction at various positions of the H_2 molecule. From the physisorbed configuration to the dissociative chemisorbed state we have observed a net increase of the electronic charge density on the hydrogen atom. Meanwhile, the Cu atoms on the long diagonal, which started with an excess charge, lose this charge to eventually experience a deficit at the chemisorbed minimum. With respect to the charge distribution of the Cu_4 fragment, the changes of charge experienced by the atoms on the long diagonal are the following: (i) a loss of 1.8% at the physisorbed minimum, (ii) a loss of 7% at the activation barrier, and (iii) a loss of 56% at the chemisorbed minimum. Each Cu atom on the short diagonal began with a deficit of about 17% of an electron. At the physisorbed configuration, the charge on H comes mainly from the Cu atoms on the short diagonal but about one third of it originates on the Cu atoms on the long diagonal. The same holds true for the activation barrier with the exception that slightly less than a half of the excess charge on H comes from the atoms on the long diagonal.

The situation at the chemisorbed minimum is dramatically different. Each H atom gained about 35% of an electron and each Cu atom on the short diagonal gained about 21% of an electron at the expense of the Cu atoms on the long diagonal each of which lost a little more than half an electron.

5. Concluding Remarks

It is seen that even with a few metal atoms placed at the corresponding lattice sites, one can get information about the nature of interaction of hydrogen molecules with bulk metal surface. In each case, there is molecular physisorbed state and a dissociated chemisorbed state separated by a barrier. In the case of metals with d electrons, the height of the barrier is expected to decrease because the d holes serve as sinks for the s electrons and the Pauli repulsion between the valence s electrons of the metal atoms and the hydrogen molecule gets reduced. At the dissociation minimum, the H_2 molecule gets electrons transferred to its anti-bonding state and the H-H bond breaks. The physisorbed minimum is characterized by the repulsion between the metal atoms and H_2. Beyond the barrier, the repulsion is between MH and MH dimers.

Acknowledgments

This work was partially supported by a grant from the Department of Energy.

References

1. P. Siegbahn, M. Blomberg, I. Panas, and U. Wahlgren, Theo. Chim. Acta **75**, 143 (1989).
2. M. Jo, M. Onuchi, and M. Nishijima, Surf. Sci. **154**, 417 (1985).
3. J. Harris and S. Andersson, Phys. Rev. Lett. **55**, 1583 (1985).
4. T. Rantala and R. M. Nieminen, Phys. Scripta **37**, 141 (1988).
5. A. Szabo and N. S. Ostlund, *Modern Quantum Chemistry: Introduction to Advanced Electronic Structure Theory* (Macmillan, New York, 1982).
6. C. Möller and M. S. Plesset, Phys. Rev. **46**, 618 (1934).
7. P. Hohenberg and W. Kohn, Phys. Rev. **136**, B864 (1964); W. Kohn and L. J. Sham, Phys. Rev. **140**, B1133 (1965).
8. J. P. Perdew, Phys. Rev. B **33**, 8822 (1986); J. P. Perdew and y. Wang, Phys. Rev. B **45**, 13244 (1992); A. D. Becke, J. Chem. Phys. **98**, 1372 (1993).

COMPUTATIONAL INVESTIGATION OF THE EFFECT OF CLUSTER IMPACT ENERGY ON THE MICROSTRUCTURE OF FILMS GROWN BY CLUSTER DEPOSITION

AVINASH M. DONGARE, DEREK D. HASS, and LEONID V. ZHIGILEI
Department of Materials Science & Engineering, University of Virginia,
Charlottesville, Virginia 22904-4745
E-mail: davinash@virginia.edu

The microstructure of thin film growth during low-energy cluster beam deposition is studied in a series of molecular dynamics simulations. The films are grown by depositing Ni clusters on a Ni (111) substrate at room temperature. The deposition of a single Ni cluster is first studied, followed by a detailed analysis of the effect of the impact velocity of the deposited clusters on the microstructure of the growing film. The observed differences in the microstructure are related to the differences in the impact-induced processes. In the case of the lower incident energy only a partial transient melting of a small contact region between the incoming cluster and the film takes place. Epitaxial growth is seen to occur for the first few layers of the clusters in contact with the substrate, above which the clusters largely retain their crystal structure and orientation. The films grown by deposition of low-energy clusters have a low density (~50% of the density of a perfect crystal) and a porous "foamy" structure with a large number of interconnected voids. The higher-energy impacts lead to the complete melting and recrystallization of the whole cluster and a large region of the film, leading to the epitaxial growth, smaller number of localized voids, and a higher overall density of the growing film.

1. Introduction

Cluster deposition is one of the major methods used in fabrication of nanostructured materials with unique range of optical, magnetic, mechanical and catalytic properties [1]. One of the commonly used nanofabrication techniques is the low-energy cluster beam deposition (LECBD) method, in which the materials are grown by a controlled deposition of clusters with a narrow size distribution, typically in the range from 1 to 10 nm. Different techniques used for generation of clusters beams, such as multiple-expansion cluster source (MECS) [2], gas segregation technique [3], electron beam direct vapor deposition (EB-DVD) [4], and laser vaporization cluster source [5], offer different degrees of control over the cluster size and energy distributions. From the point of view of fabrication of nanostructured materials it is often desirable to retain the characteristic length-scale and high surface/volume ratio of the deposited clusters in the cluster-assembled material and, at the same time, to form a continuous and mechanically stable material. To achieve the desired properties of the growing films, the parameters of the deposition process should be chosen based on the understanding of the fundamental atomic-level processes leading to the formation of the final microstructure.

The Molecular Dynamics (MD) simulation technique has been demonstrated to be capable of providing insights into the mechanisms of cluster-substrate interaction [6,7,8,9,10] as well as the relation between the parameters of the deposited clusters and the microstructure of the deposited films [10,11,12,13,14]. It has been observed that the final state of a deposited cluster depends on the size and the incident energy of the cluster, with partial "contact epitaxy" characteristic for low-energy "soft landing" of large clusters and complete epitaxy characteristic for smaller and/or more energetic clusters [7,8,9,10]. Simulations of the film growth by cluster deposition revealed a strong dependence of the morphology of the growing film on deposition parameters. In particular, Haberland, Insepov and Moseler [11] investigated the structure of thin films grown by deposition of 1043-atomic Mo clusters. They observed a transition from a porous film with multiple voids to a dense epitaxial film with a nearly bulk density as the incident energy increased from 0.1 eV/atom to 1 eV/atom and to 10 eV/atom. More recently Hou et al. performed MD simulations of film growth by deposition of Ni_3Au clusters on Ni and Al substrates with an impact energy of 0.25 eV/atom [13] and observed only a minor epitaxy with the substrates. Kang et al. studied film growth by deposition of small 177-atomic Al and Cu clusters and observed formation of epitaxial films at sufficiently high impact energies [14].

While the first MD simulations of cluster deposition clearly indicate that the impact energy of the deposited clusters has a strong effect on the structure and density of the growing film, further progress is needed in understanding of the dependence of the morphology and defect structures in the deposited films on the parameters of the deposited cluster. One question of a particular interest is the possibility to generate dense nanocrystalline films by cluster deposition. In this work we report the results of a series of MD simulations aimed specifically at the transition regime from the cluster assembly into an open low-density structure to a compact film with the density approaching that of the bulk. The impact-induced processes are analyzed and related to the density, morphology and microstructure of the growing films. Computational model used in the present study and parameters of the simulations are described below, in Section 2. The results on the film growth by cluster deposition are presented in Section 3 and summarized in Section 4.

2. Computational Model

We simulate deposition of Ni clusters on Ni (111) surface. The clusters are ~3 nm in diameter (532 atoms), which is a typical size of clusters in LECBD experiments [5]. The initial cluster is created by cutting a sphere of the desired radius from an fcc bulk crystal. The substrate is represented by eight atomic Ni (111) planes, each consisting of 1152 atoms. Periodic boundary conditions are applied in the directions parallel to the surface. Two bottom atomic layers of the substrate are kept rigid. The atoms in a stochastic region adjacent to the rigid layers experience the forces due to the interaction potential as well as friction and stochastic forces via the Langevin equation method [15]. The stochastic region is used for maintaining the constant temperature of the substrate and for an effective simulation of the dissipation of the energy deposited by cluster impacts due to the fast electronic heat conduction. The thickness of the stochastic region is increasing as the thickness of the film growth during the deposition process. The atoms in the topmost region of the system are experiencing only forces due to the interatomic interaction, described in this work by the Embedded Atom Method (EAM) potential in the form and parameterization suggested by Johnson and co-workers [16].

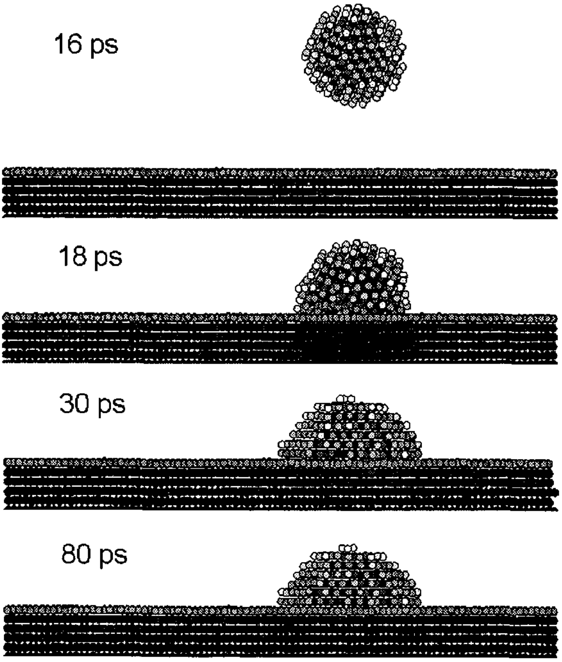

Figure 1. Snapshots from a simulation of the deposition of a single Ni cluster on a Ni (111) substrate at an impact velocity of 1000 m/s. The gray scale corresponds to the potential energy of each atom, from 3.25 eV for white color to 4.43 eV for black color (cohesive energy of the EAM Ni fcc crystal is 4.45 eV).

Prior to the deposition, both cluster and the substrate are equilibrated at 300 K for 10 ps. The positions of the deposited clusters are chosen at random in the x-y plane. The orientation of the cluster with respect to the substrate is also chosen at random. The z coordinate of the cluster is chosen so that the top atoms of the growing film do not interact with the cluster being deposited. The clusters are directed towards the substrate at different impact velocities representing three different cases studied in this work. Simulations are performed for impact velocities of 250 m/s (0.01 eV/atom), 500 m/s (0.076 eV/atom), and 1000 m/s (0.3 eV/atom). The time between the depositions of two consecutive clusters is chosen so that the substrate and the deposited cluster can relax completely and the temperature of the impact region stabilizes at 300 K.

The time between the cluster depositions is decided by investigation of cluster-substrate interaction in deposition of the first cluster, as shown in Figure 1 for a simulation performed for the incident velocity of 1000 m/s. As the cluster impacts the substrate, melting occurs in the cluster and in a part of the substrate as shown in the snapshot for 18 ps. Recrystallization of the substrate and the cluster occurs within the next 10 ps and the deposited cluster material forms an epitaxial island on the substrate, as apparent from the snapshot shown for 30 ps. Similar observations of the epitaxial regrowth of a cluster melted upon impact have been reported for deposition of energetic Au [9,10] and Cu [7] clusters. Only partial epitaxy has been reported for large clusters deposited at low impact energies [8,9]. We find that the tendency to form an epitaxial island also depends on the potential used in the simulation. For the conditions illustrated in Figure 1 we observe only partial epitaxy in a simulation performed with a pair-wise Lennard-Jones potential parameterized for Ni [17].

Comparison of the snapshots shown in Figure 1 for 30 ps and 80 ps indicate that the active processes of atomic rearrangements are finished by the time of 30 ps and the temperature of the impact region has decreased down to the temperature of the substrate, 300 K. The mobility of atoms and clusters on the surface can be neglected at 300 K [10,11] and further relaxation of the deposited atomic configurations should not lead to any significant changes in the morphology and microstructure of the deposited films. Therefore, the time between depositions of clusters in simulations of film growth described in the next section is chosen to be 40 ps.

3. Results and Discussion

Simulation results reported in this paper are obtained for three different impact velocities, 250 m/s (0.01eV/atom), 500 m/s (0.076 eV/atom), and

1000 m/s (0.3 eV/atom). The time between cluster depositions is chosen so that the growing film is completely relaxed after each cluster deposition, as discussed above, in Section 2. The total number of the deposited clusters is chosen so that the thickness of the film would be sufficient to perform analysis of the microstructure and density of the growing material. The visual pictures of the final deposited films and density distributions are shown in Figures 2, 3 and 4 for the three impact velocities.

Figure 2(a) shows the atomic configuration of the film created by the deposition of 55 clusters at a velocity of 250 m/s (0.01 eV/atom). A mere visual inspection of the atomic configuration indicates that the deposited film has an open "foamy" structure with a large number of interconnected voids separated by polycrystalline material with characteristic size comparable to the size of the deposited clusters. Epitaxial ordering of the deposited atoms can be identified only in the first few monolayers of the deposited material adjacent to the substrate (~3-5 nm). While the deposited clusters do not melt or disintegrate upon impact, they tend to reorient and adjust to the existing facets, forming crystallites that are larger than the size of an individual cluster. Large number of crystal defects, such as stacking faults, twinning planes, and grain boundaries, can be identified in the atomic configuration. The voids that are created by random deposition of clusters do not collapse with the deposition of the following incoming clusters. The overall density of the film grown at this low-impact velocity is ~50% of the density of the perfect fcc crystal, as can be seen from Figure 2(b).

Figure 3(a) shows the morphology of a film created by the deposition of 55 clusters at a higher velocity of 500 m/s (0.076 eV/atom). It can be seen that as the impact energy of the deposited clusters increases, the porosity of the film decreases. While relatively large voids are observed in the atomic configuration, they are less connected with each other and are separated by solid regions that are significantly thicker as compared to the size of the deposited clusters. Epitaxial growth is seen to occur for a greater thickness (~7-8 nm) as compared to the lower-energy simulation illustrated in Figure 2(a). The formation of a more compact film can be related to the higher energy of the deposited clusters, sufficient to induce melting of a significant part of the cluster and cause substantial atomic rearrangements in the vicinity of the impact region. The size of the voids created by random cluster deposition is decreasing due to the atomic rearrangements induced by the subsequent cluster depositions. Similarly to the films deposited at a lower impact energy of 0.01 eV/atom, a high density of defects can by identified in the atomic configuration shown in Figure 3(a). The density distribution of the film is shown in Figure 3(b). After formation of a thin ~2 nm high-density layer adjacent to the substrate, the density of the growing film stabilizes at ~60% of the density of the bulk crystal.

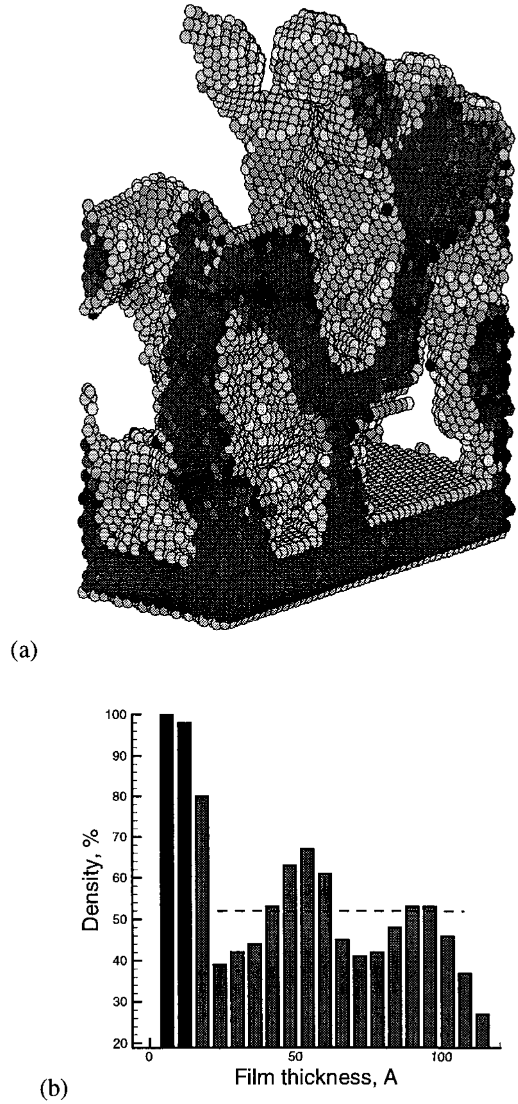

Figure 2. (a) Atomic structure of the film grown by deposition of 55 Ni clusters on the Ni (111) substrate with an impact velocity of 250 m/s. The gray scale corresponds to the potential energy of each atom, from 3.25 eV for white color to 4.43 eV for black color (cohesive energy of the EAM Ni fcc crystal is 4.45 eV). (b) The density distribution of the deposited film. The first two columns (black) correspond to the original substrate. Dashed line shows the average density of the deposited film.

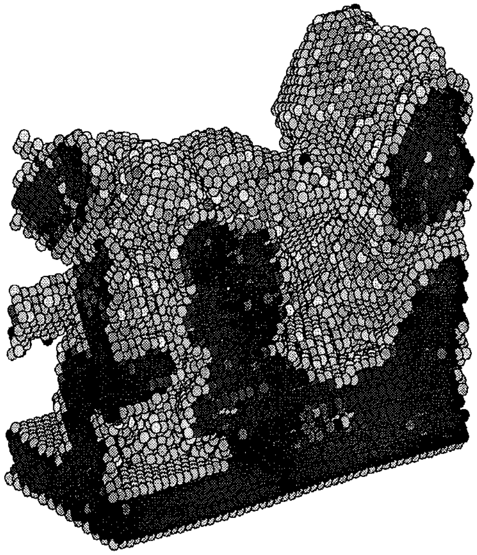

(a)

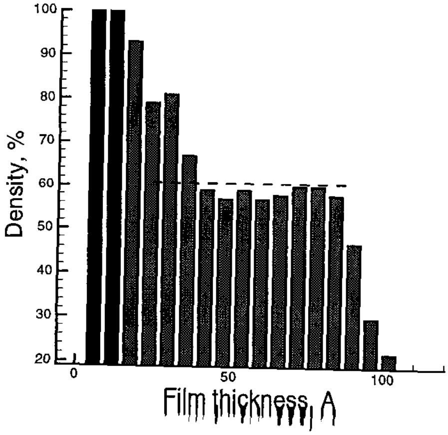

(b)

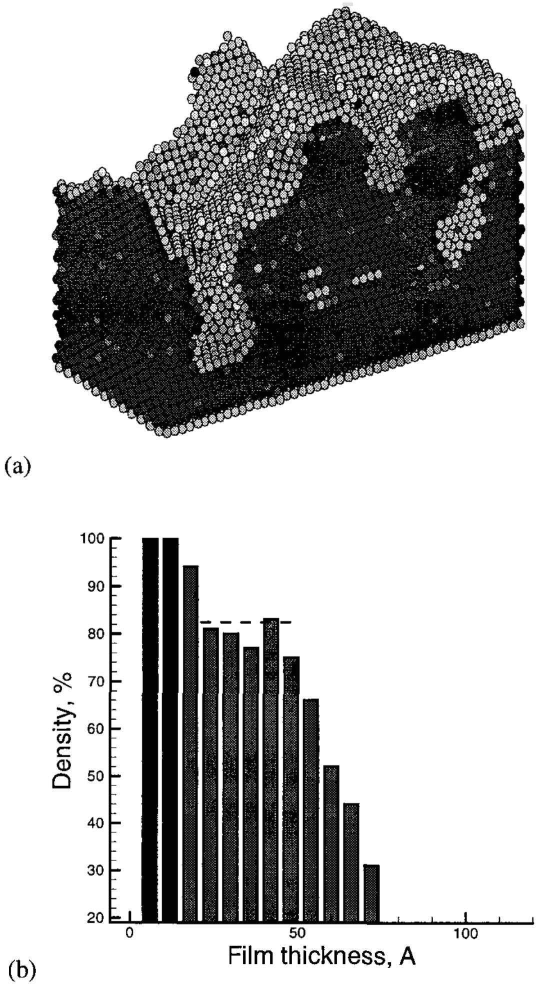

Figure 4. (a) Atomic structure of the film grown by deposition of 45 Ni clusters on the Ni (111) substrate with an impact velocity of 1000 m/s. The gray scale corresponds to the potential energy of each atom, from 3.25 eV for white color to 4.43 eV for black color (cohesive energy of the EAM Ni fcc crystal is 4.45 eV). (b) The density distribution of the deposited film. The first two columns (black) correspond to the original substrate. Dashed line shows the average density of the deposited film.

Figure 4(a) shows the morphology of the film after the deposition of 45 clusters at a velocity of 1000 m/s (0.3 eV/atom). At this deposition velocity almost complete epitaxy is observed, which is consistent with earlier observations for films produced by high-energy cluster deposition [11,14]. The higher-energy impacts lead to the complete melting of the whole cluster and a large region of the film, leading to the epitaxial regrowth of the surrounding crystalline material. As a result, the epitaxial ordering can be observed in the whole deposited film and only several relatively small isolated voids are present in the atomic configuration. The density of the growing film is ~85% of the density of the perfect crystal as can be seen from Figure 4(b). While significant number of low-energy defects (stacking faults and twin boundaries) can be identified in the atomic configuration, the original orientation of (111) planes in the substrate is retained throughout the deposited film.

4. Conclusions

The effect of the impact velocity of the deposited clusters on the morphology and microstructure of the growing films is studied in a series of MD simulations. We find that low-energy deposition results in the formation of open structures with a large number of interconnected voids and large surface-to-volume ratio. The crystalline regions have crystallographic orientation independent from the one of the original substrate and have characteristic sizes comparable to (and somewhat larger then) the size of the deposited clusters. The increase of the cluster impact energy leads to the formation of more compact/dense films with increasingly large epitaxial region adjacent to the substrate and with smaller voids that become isolated from each other. The density of the deposited films is increasing from ~50% to ~60% and to ~85% as the impact energy of the deposited clusters increases from 0.01 eV/atom to 0.076 eV/atom and to 0.3 eV/atom.

The observed difference in the microstructure of the growing films is a reflection of the difference in the impact-induced processes. In the case of the lower incident energies (250 m/s and 500 m/s) only a partial transient melting of a contact region between the incoming cluster and the film takes place and clusters tend to retain their crystal structure and orientation. The voids that are formed by random cluster deposition do not collapse with the deposition of more clusters at these low energies. On the contrary, the higher-energy impacts (1000 m/s) lead to the complete melting and recrystallization of the whole cluster and a large region of the film, leading to the epitaxial growth, smaller number of voids, and higher overall density of the growing film. Formation of a compact/dense nanocrystalline material appears to be hardly achievable by the direct cluster deposition.

The investigations of cluster deposition performed for a fixed size of the deposited clusters and impact energy can provide first useful insights into the mechanism of thin film growth. In experiments, however, the deposited clusters typically have a range of sizes and impact velocities, e.g. [5,18]. Moreover, the clusters are often co-deposited with monomers. On the modeling side, this calls for application of multiscale computational approaches, where the processes of cluster formation are investigated and the parameters of the deposited clusters (velocity and size distributions, internal temperatures of the clusters) are used as a realistic input in simulations of film growth. Multiscale computational approach for simulation of cluster formation in laser ablation/vaporization and subsequent film deposition has been recently discussed [19,20]. The processes responsible for cluster generation in laser ablation can be investigated in a combined MD – Direct Simulation Monte Carlo (DSMC) simulations [21,22]. The parameters of the ejected ablation plume can be used in MD simulations of film deposition, providing a direct connection between the parameters of the ejected clusters and laser irradiation conditions.

Acknowledgement

Partial financial support of this work was provided by the National Science Foundation through the Materials Research Science and Engineering Center for Nanoscopic Materials Design at the University of Virginia.

References

[1] P. Jensen, Rev. Mod. Phys. **71**, 1695 (1999)

[2] D. M. Schaefer, A. Patil, , R. P. Andres, and R. Reifenberger, Phys. Rev. B **51**, 5322 (1995)

[3] C. G. Granqvist and R. A. Buhrman, J. Appl. Phys. **47**, 2200 (1976)

[4] D. D. Hass and H. N. G. Wadley, in preparation.

[5] L. Bardotti, B. Prével, P. Mélinon, A. Perez, Q. Hou, and M. Hou, Phys. Rev. B **62**, 2835 (2000)

[6] H.-P. Chen and U. Landmann, J. Phys. Chem. 98, 3527 (1994)

[7] H. L. Lei, Q. Hou, and M. Hou, J. Phys.: Condens. Matter **12**, 8387 (2000)

[8] M. Yeadon, M. Ghaly, J. C. Yang, R. S. Averback, J. M. Gibson, Appl. Phys. Lett. **73**, 3208 (1998)

[9] M. Hou, Nucl. Instrum. Methods Phys. Research B **135**, 501 (1998)

[10] Q. Hou, M. Hou, L. Bardotti, B. Prével, P. Mélinon, and A. Perez, Phys. Rev. B **62**, 2825 (2000)

[11] H. Haberland, Z. Insepov, and M. Moseler, Phys. Rev. B **51**, 11061 (1995)

[12] C. L. Kelchner and A. E. DePristo, Nanostruct. Mat. **8**, 253 (1997)

[13] M. Hou, V. S. Kharlamov, E. E. Zhurkin, Phys. Rev. B **66**, 195408 (2002)

[14] J. W. Kang, K. S. Choi, J. C. Kang, E. S. Kang, K. R. Byun, and H. J. Hwang, J. Vac. Sci. Technol. A **19**, 1902 (2001)

[15] M. Berkowitz and J.A. McCammon, Chem. Phys. Lett. **90**, 215 (1982)

[16] X. W. Zhou, H. N. G. Wadley, R. A. Johnson, D. J. Larson, N. Tabat, A. Cerezo, A. K. Petford-Long, G. D. W. Smith, P. H. Clifton, R. L. Martens, and T. F. Kelly, Acta Mater. **49**, 4005 (2001)

[17] T. Halicioğlu and G. M. Pound, Phys. Stat. Sol. **30**, 619 (1975)

[18] L. V. Zhigilei, Appl. Phys. A **76**, 339 (2003)

[19] H. Mizuseki, Y. Jin, Y. Kawazoe, and L. T. Wille, Appl. Phys. A **73**, 731 (2001)

[20] L. V. Zhigilei and A. M. Dongare, Computer Modeling in Engineering & Sciences **3**, 539 (2002)

[21] L. V. Zhigilei, E. Leveugle, B. J. Garrison, Y.G. Yingling, M. I. Zeifman, Chem. Rev. **103**, 321 (2003)

[22] M. I. Zeifman, B. J. Garrison, and L. V. Zhigilei, J. Appl. Phys. **92**, 2181 (2002)

This page intentionally left blank

METAL-BENZENE COMPLEXES WITH INSERTED METAL ATOMS AND THE POSSIBILITY OF GENERATING MAGNETIC NI-BENZENE CLUSTERS

ANIL K. KANDALAM, N. O. JONES, S. N. KHANNA, and P. JENA
Physics Department, Virginia Commonwealth University
Richmond, VA 23284-2000

It is shown that a new class of structures where a metal atom is inserted in the benzene ring is more stable than the previous ground state reported for a single Ni-benzene anion. Our studies based on first principles density functional formalism indicate that the formation of such inserted structures may require overcoming a barrier. The new structure is characterized by high transition energies to the neutral clusters and some of the peaks in the existing negative ion photo-detachment spectra on $Ni_n(Bz)_m$ anions could be due to the existence of these species.

1. Introduction

The study of transition metal atoms supported on organic complexes in gas phase has attracted considerable attention over the past few years. On the one hand, such studies provide a convenient way to study the interaction between the metal atoms and organic complexes without having to deal with the effect of solvents, e.g. interaction between transition metal atoms and the benzene molecules provides an excellent example of interaction of the d-electrons with π-orbitals. On the other hand, supporting transition metal atoms or clusters on molecular templates may provide novel ways of generating cluster assembled materials. Over the past few years, numerous such complexes have been reported. For example, it is possible to deposit single or multiple transition metal atoms on a single template. A recent example is the multiple Fe atoms deposited on a single coronene[1]. Another class of systems that has attracted considerable attention is transition-metal-benzene complexes [$M_n(Bz)_m$]. Using laser vaporization techniques, Kaya and co-workers have reported[2] generating $M_n(Bz)_m$ complexes containing *3d*-transition metal atoms. Their mass-spectra on $Ni_n(Bz)_m$ are of special interest. They found that the spectra exhibits multiple peaks at (n,m) = (1,2), (2,2), (3,2); (2,3), (3,3), (4,3), (5,3), (6,3); (6,4), (7,4), (8,4), (9,4), (10,4), and (10,5). These studies have motivated numerous theoretical studies[3-6] to investigate their atomic configurations, electronic structure and the magnetic properties. These studies[5, 6] indicate that the benzene molecules cage the metal atoms. As an example, the ground state of $Ni_3(Bz)_2$ is a structure where the three Ni atoms occupy sites between the two benzene molecules. These investigations also bring out certain interesting results. For example, the investigations on anionic clusters suggest that the $NiBz^-$ and $Ni(Bz)_2^-$ anions are unstable against auto-detachment of the extra electron. Corresponding experimental studies[7] on negative ion photoelectron spectra do not detect the Ni(Bz) anions thereby confirming the theoretical suggestions.

The existing theoretical studies[5, 6] on metal-benzene complexes have always focused on structures where the metal atom occupied sites above the benzene molecule. In this paper, we present results of the theoretical studies on a NiBz molecule where we investigate the possibility of the metal-atom inserting in the benzene molecule. For a single NiBz anion, we demonstrate that a structure where the Ni atom is inserted in a C-H bond is more stable than the previously reported ground state where the Ni atom occupies sites above the benzene molecule. Further, the inserted anion structure is stable against the auto-detachment of the electron. The insertion of the Ni atom, however, has a reaction barrier that has to be overcome and this accounts for the inability of the existing experiments to observe this structure. What is even more interesting is that the inserted structure is less stable than the Ni-on-the-surface structures for the neutral NiBz systems. The inserted neutral NiBz, however, has a spin multiplicity of 3 as opposed to the singlet ground state of the neutral non-inserted structure. Note that if the stable NiBz anions with inserted Ni atoms could be generated, one could form the neutral NiBz inserted structures by detaching the extra electron. Further, since the insertion of the Ni has a barrier, once generated, the inserted neutral structures would be meta-stable. The fact that the neutral NiBz has a high spin multiplicity may provide novel ways of forming magnetic NiBz complexes where the Ni maintains its atomic magnetic moment.

In this paper we present the first theoretical study that examines the geometries, electronic properties, magnetic moments, and stability of a NiBz with an inserted metal atom. We show that, aside from the possibility of spin moments, the detachment energy of the electron from the inserted anions is much higher than in non-inserted structures. Such high transition energies have actually been observed in experiments on $Ni_2(Bz)_2$ anions and it has not been possible to explain these observations using the non-inserted structures. We believe that the inserted structures may be able to account for these observations. In this paper, we only focus on anionic and neutral NiBz molecule.

2. Computational Procedure

The theoretical studies were carried out using a linear combination of the atomic orbitals molecular orbital approach (LCAO-MO) and Density Functional Theory (DFT). The Generalized Gradient Approximation (GGA) to DFT was used in all these calculations. The gradient corrected exchange functional due to Becke[8], combined with gradient corrected Perdew – Wang[9] correlation functional (BPW91) is employed here. The actual calculations were carried out using the Gaussian98[10] code. The geometry optimization for various spin states was carried out on different NiBz structural configurations using 6-311G** basis set without any symmetry constraints. Vibrational frequency calculations were carried out for all the structural isomers to confirm their stability.

3. Results and Discussion

Figure 1 shows the low energy configurations of a NiBz anion. The ground state is the inserted structure (Fig 1(a)) where the Ni atom is inserted in one of the C-H bonds of the benzene molecule. Also marked are the energies of the various structures relative to the inserted structure. For the non-inserted case, the lowest energy configuration corresponds to the Ni bound to three C atoms of the benzene molecule (Fig 1(b)). As seen from Fig. 1, this state is 1.08 eV less stable than the current ground state. In addition, there are two other meta-stable configurations, one corresponding to a Ni bound to two carbon sites (from now on termed as bridge structure), and the other to a hollow configuration where the Ni is located above and along the C_6 axis of the benzene ring (ΔE = 1.34 eV). The C_{6v} configuration is similar to the previously reported[3-5] ground state geometry of $NiBz^-$. In all cases, the C-C bonds are around 1.40 Å. It has to be noted here that two non-inserted $NiBz^-$ geometries (Fig 1(b) and 1(c)) are energetically degenerate within the accuracy of our calculations. The other non-inserted structure, namely the C_{6v} configuration (Fig 1(d)) is also very close in energy (ΔE= 0.26 eV) with these non-inserted structures. This near equality implies a very flat potential energy surface. We have also investigated the localization of the extra electron in various structures. In Figure 2 we show the charge density of the highest occupied molecular orbital in the inserted and non-inserted ground state. Note that in the ground state, the charge is localized around the Ni site.

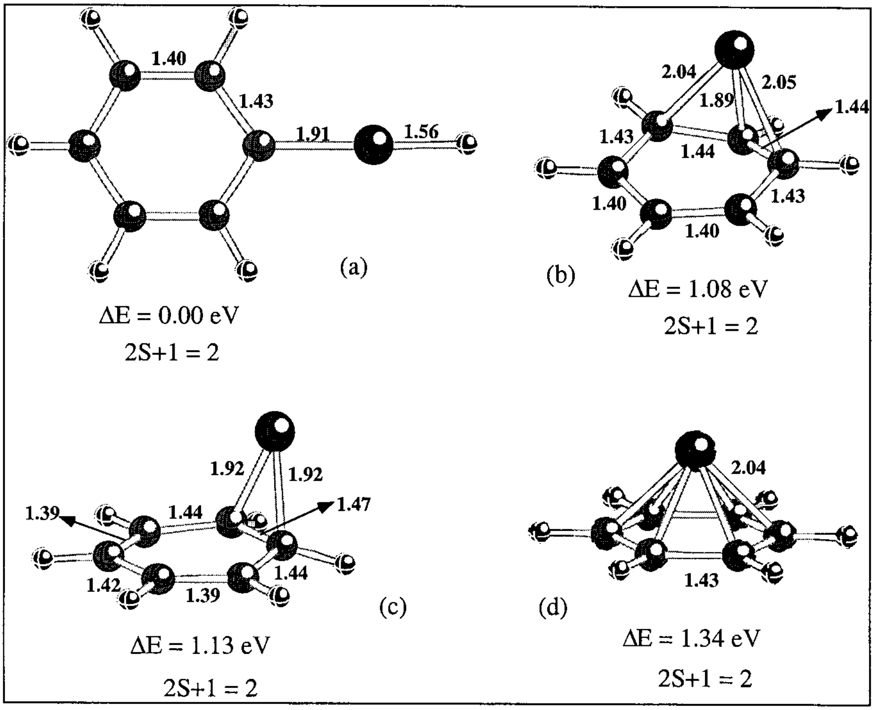

Figure 1: The optimized geometries, relative energies (ΔE), and the spin multiplicities of different structural isomers of anionic NiBz complex

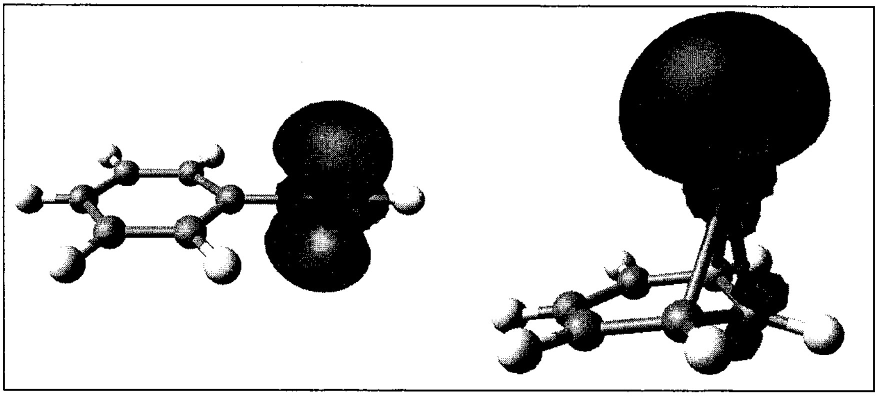

Figure 2: HOMO of the inserted and Non-inserted ground state geometries of Anionic NiBz complex

The relative stability of the various structure changes as the extra electron is removed to form the neutral clusters. Figure 3 now shows the ground state of the corresponding neutral structures. Also shown are the binding energies defined as

$$\text{B. E.} = -\,[E(\text{Ni}) + E(\text{Bz}) - E(\text{NiBz})]$$

where E(Ni) and E(Bz) are the ground state energies of the free Ni atom and the benzene molecule respectively and E(NiBz) is the total energy of the NiBz cluster.

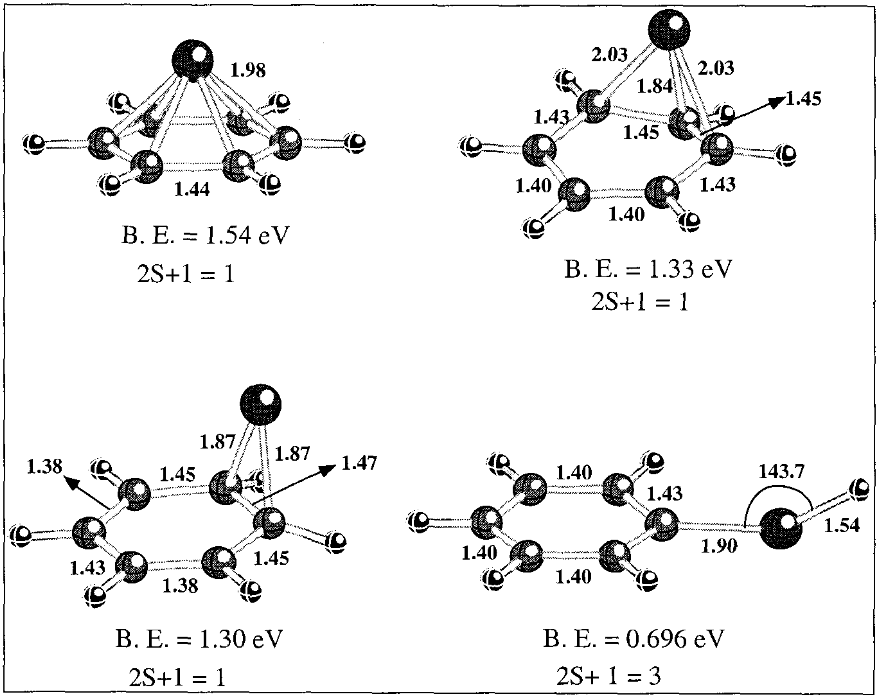

B. E. = 1.54 eV
2S+1 = 1

B. E. = 1.33 eV
2S+1 = 1

B. E. = 1.30 eV
2S+1 = 1

B. E. = 0.696 eV
2S+ 1 = 3

Figure 3: The Optimized geometries, binding energies, and spin multiplicities of neutral NiBz complex

Note that the ground state now corresponds to a C_{6v} configuration and the inserted structure is almost 0.85 eV less stable than the C_{6v} ground state. What is interesting is that whereas the ground state (C_{6v} configuration) is a spin singlet, the inserted structure has a spin multiplicity of three and hence the Ni atom maintains its magnetic spin of the free atom.

The stability of the inserted structure in the anion does raise interesting possibilities. Since the insertion of the metal atom involves breaking of the C-H bond, the formation of the inserted structures has a barrier. Note that if the anions are formed by attaching electrons to the neutral clusters, then since the ground state of the neutral has a C_{6v} configuration, attaching of the electron will not generate the inserted anion. One therefore has to resort to alternate mechanisms. On the other hand, once the inserted anion is formed, the presence of barrier will protect the structure even after the electron is detached. Before we address the formation and the barriers, let us examine if there exist electronic features that are characteristic to inserted structures. This could be important to explore if such structures exist in larger sizes. So we have examined the excitations from the anions to the corresponding neutral species. Such excitations can be probed in the negative ion photo-detachment spectra. In these spectra, an anionic cluster is irradiated with a laser of given frequency and one measures the energy of the detached electrons. The difference between the energy of the photon and the detached electron is then a measure of the vertical transition from the anion to the neutral cluster. Suppose then that the anion has a spin multiplicity of M. When an electron is removed, the neutral cluster can have the spin multiplicities of M ± 1. The calculated energy difference between the anion and the neutral clusters with multiplicity M ± 1 can then be compared with experimental spectra. For $Ni_n(Bz)_m$ clusters, such spectra have already been measured by Bowen et al.[7], and these may provide the testing grounds to some of the calculations.

For the various minimum energy configurations in Fig. 1, we calculated the energies of the neutral clusters with one higher and one lower multiplicity than the anion cluster maintaining the fixed geometry. The results of these investigations are given in Figure 4. The anionic C_{6v} configuration is found to be unstable against the auto-detachment of the extra electron; hence transition energies for the C_{6v} isomer are not given here. Note that the lowest transitions in the non-inserted structures are very small and are around 0.1 eV. In view of the current level of our computational accuracy, these transition energies are so negligible that the non-inserted $NiBz^-$ can be considered unstable against the auto-detachment. This instability of the non-inserted $NiBz^-$ is consistent with the previously reported theoretical and experimental results. However, the lowest transition energy in the inserted structure is significantly different from that in the non-inserted structures and is around 2.1 eV. This high transition energy implies that the inserted $NiBz^-$ is highly stable against the auto-detachment of the extra electron.

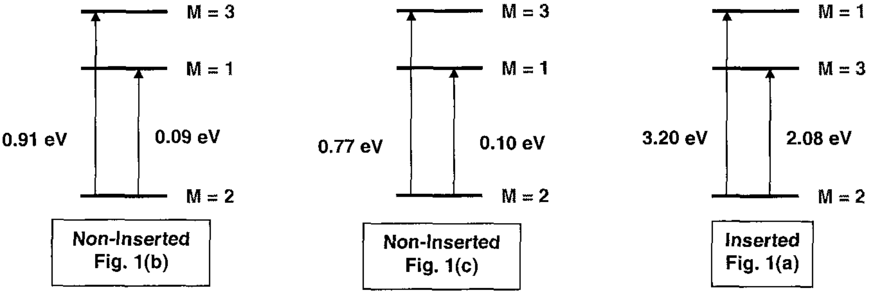

Figure 4: Transition energies from the anion NiBz complex to the corresponding neutral species at the same geometry as the anion

While the current experiments do not detect the inserted structure in NiBz$^-$, one must note that the inserted structure is characterized by large transition energy of 2.1 eV. To this end, it is interesting to note that the experimentally observed spectra for $Ni_2(Bz)_2$ does exhibit the first peak at 2.3 eV as opposed to 0.44 eV predicted by the theoretical studies on non-inserted structures. Since the transition energies for the inserted structures are around 2.1 eV, it is possible that it is the inserted structures of $Ni_2(Bz)_2$ that are seen in these experiments. We are currently investigating the possibility of such structures in these complexes.

4. Summary

To summarize, we have shown that the ground state of a NiBz anion is actually an inserted structure where a single C-H bond breaks to accommodate the Ni atom. Such structure is however, stable only for an anion and their formation requires overcoming a barrier. When an electron is detached, the inserted structure forms a high energy neutral state that has a high spin multiplicity as opposed to the singlet multiplicity for the non-inserted ground state. It may therefore be possible to form magnetic $Ni_n(Bz)_m$ assemblies by first forming the anions in their ground state and then removing the electron. The inserted anions are characterized by high transition energies to the neutral form and observed high transition energies in $Ni_2(Bz)_2$ may be an indication that such structures are present at higher sizes. We are currently investigating the barriers to the formation of such structures in a single NiBz cluster and this along with the structures at higher sizes will be reported in coming publications.

References

1. B. P. Pozniak, R. C. Dunbar, *J. Am. Chem. Soc.* 119, **(1997)** 10439
2. Kurikawa, T.; Takeda, H.; Hirano, M.; Judai, K.; Arita, T.; Nagao, S., Nakajima, A.; Kaya, K., *Organometallics* 18, **(1999)** 1430
3. R. Pandey, B. K. Rao, P. Jena, and J. M. Newsam, *Chem. Phys. Lett.* 321, **(2000)** 142
4. R. Pandey, B. K. Rao, P. Jena, and M. A. Blanco, *J. Am. Chem. Soc.* 123, (**2001**) 3799
5. **a)** B. K. Rao and P. Jena, *J. Chem. Phys.* 116, **(2002)** 1343. **b)** *J. Chem. Phys.* 117, **(2002)** 5234
6. G. E. Froudakis, A. N. Andriotis, and M. Menon, *Chem. Phys. Lett.* 350, **(2001)** 393
7. W. Zheng, J. M. Nilles, O. C. Thomas, and K. H. Bowen (unpublished)
8. A. D. Becke, *Phys. Rev. A.* 38, **(1988)** 3098
9. J. P. Perdew, Y. Wang, *Phys. Rev. B.* 45, **(1992)** 13244
10. Frisch, M. J.; Trucks, G. W.; Schlegel, H. B.; Scuseria, G. E.; Robb, M. A.; Cheeseman, J. R.; Zakrzewski, V.G.; Montgomery, J. A.; Stratmann, R. E.; Burant, J. C.; Dapprich, S.; Millam, J. M.; Daniels, A. D.; Kudin, K. N.; Strain, M. C.; Farkas, O.; Tomasi, J.; Barone, V.; Cossi, M.; Cammi, R.; Mennucci, B.; Pomelli, C.; Adamo, C.; Clifford, S.; Ochterski, J.; Petersson, G. A.; Ayala, P. Y.; Cui, Q.; Morokuma, K.; Malick, D. K.; Rabuck, A. D.; Raghavachari, K.; Foresman, J. B.; Cioslowski, J.; Ortiz, J. V.; Stefanov, B. B.; Liu, G.; Liashenko, A.; Piskorz, P.; Komaromi, I.; Gomperts, R.; Martin, R. L.; Fox, D. J.; Keith. T.; Al-Laham, M. A.; Peng, C. Y.; Nanayakkara, A.; Gonzalez, C.; Challacombe, M.; Gill, P. M. W.; Johnson, B. G.; Chen, W.; Wong, M. W.; Andres, J. L.; Head-Gordon, M.; Replogle, E. S.; Pople, J. A. *Gaussian 98*; Gaussian Inc., Pittsburgh, PA, **1998**

INFLUENCE OF STRUCTURAL RELAXATION ON THE OPTICAL AND ELECTRONIC PROPERTIES OF Ge and Si NANOCRYSTALS

HANS-CHRISTIAN WEISSKER, JÜRGEN FURTHMÜLLER,
FRIEDHELM BECHSTEDT
Institut für Festkörpertheorie und Theoretische Optik, Friedrich-Schiller-Universität,
Max-Wien-Platz 1, 07743 Jena, Germany

A proper account of the structural relaxation is found to be indispensable for the calculation of the electronic and optical properties of nanocrystals. While the average bond lengths are reduced as compared with the respective bulk bond lengths, the individual bond lengths show a strong variation. While they are shortened near the surface, they are enlarged at the center of the crystallite. For Ge crystallites, the radiative lifetimes are strongly reduced. Ge is predicted to be better for light-emitting applications than Si.

1. Introduction

Though much effort has been put into the description of the properties of nanocrystals (NCs), ab initio calculations of such systems are still a demanding task. They are, however, necessary in view of the sizes of the NCs in order to obtain complete physical understanding. The electronic-structure calculations for crystallites of up to a few hundred atoms are now common practice for a number of groups. The ionic degrees of freedom, i.e., the structural relaxation, have only recently become amenable to ab initio methods for larger clusters because of the large computational effort [1-3].

The ionic relaxation is a twofold problem. First, there is the purely technical problem of finding reasonable model structures for the crystallites. This involves the question of the influence of the ground state structural relaxation on the desired quantities. The possibility to "switch on" structural relaxation and to compare the results of the respective calculations with those of the ideal structures permits to infer quantitatively the influence of the relaxation on the electronic and optical properties.

Second, there is the physical question as to what is the structural relaxation pattern, and what are the properties of the relaxed structure. Often relaxation has been neglected. Several approaches have taken into account the structural relaxation in some way, be it within the force field model, classical-potential relaxation, and, recently, using *ab initio* relaxation. A detailed consideration of the limits of the respective approaches has rarely been given. In the present contribution we show the nature of the relaxation pattern in quasi-spherical NCs as well as the vital importance of taking relaxation into account.

2. Model and Computational details

Density-functional theory (DFT) calculations are performed in local-density approximation (LDA). The VASP program package [4] is used. We use the projector-augmented wave (PAW) method in order to both alleviate the high numerical efforts treating large cells and to obtain all-electron wave functions for the calculation of the optical matrix elements. Approximately spherical crystallites are constructed by starting from one atom and adding its nearest neighbors, thereby assuming the tetrahedral coordination of the respective cubic bulk material. We treat free, hydrogen-terminated crystallites. These are considered both a model for real free crystals, but also as a model of crystallites embedded in a matrix with a very large band gap [5]. Excitation energies can be calculated for them by means of the ΔSCF method [6].

The model crystallites are constructed as bulk fragments, bulk interatomic distances are assumed. Hydrogen atoms saturate the outermost bonds. After that, ab initio relaxation is carried out for all atoms, keeping, however, in most cases the Td symmetry constraint.

We use the supercell method with simple-cubic cells, the size of which corresponds to 216, 512, or 1000 atoms of bulk material, depending on the size of the nanocrystal in question. The calculation of the dielectric function is done on the level of the Ehrenreich-Cohen formula, i.e., neglecting non-linear and -local-field effects [5].

3. Results

The average bond lengths of both the Ge and the Si NCs are shortened as compared to the bulk bond lengths, which is shown in Fig. 1. From this it seems that the NCs are already fairly close to the bulk limit in the range of more than, say, 250 atoms. However, this assumption is proven wrong by the individual bond length distribution. As shown in Fig. 2, at the surface of the NCs, bond length reduction takes place. However, this is not the case for the interior of the NCs. In fact, at the center of the NCs the bond lengths are longer than in the respective bulk material. This is consistent with the findings about the average bond lengths, because there are fewer bonds at the center than close to the surface. While the contraction might be explicable in terms of surface-tension-like effects, the adverse effect at the center certainly is not.

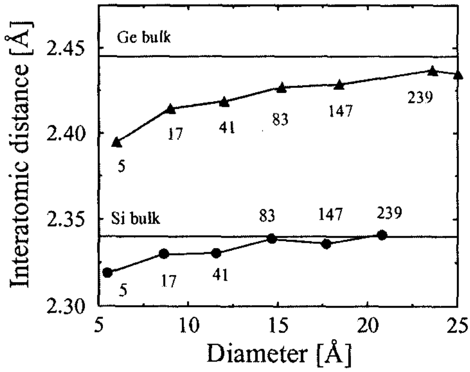

Figure 1. Average bond lengths after ionic relaxation for Si (circles) and Ge (triangles). The numbers indicate the number of atoms in the NCs, the horizontal lines represent the bulk bond lengths.

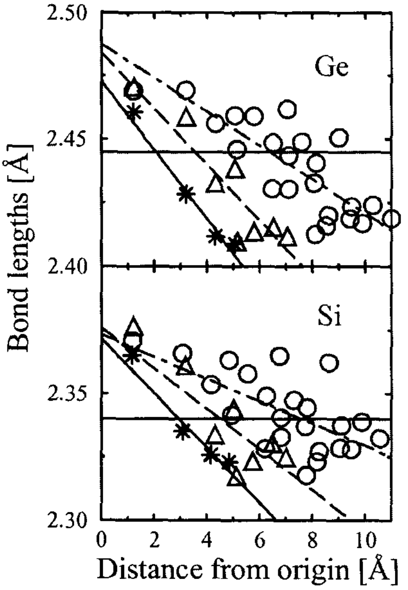

Figure 2. Individual bond lengths. Shown are the values for NCs of 239 atoms (circles), 83 atoms (triangles), and 41 atoms (stars) of Ge and Si. The horizontal lines indicate the bulk bond lengths.

The spatial symmetry of the NCs is prescribed in the calculation. However, for the ground-state calculations this is no restriction because the charge distribution in the electronic ground state likewise is of T_d symmetry.

For both the ideal and the relaxed structure, we calculate the radiative lifetimes as thermodynamically averaged transition probability [7]. The lowest transitions are the most important. Fig. 3 presents the lifetimes for both Ge and Si NCs. Apart from the very smallest NCs which present quasi-molecular structures rather than NCs, the lifetimes are drastically reduced for the Ge NCs, showing that ionic relaxation must be properly taken into account in the calculation of the optical properties. The extreme changes can be traced back to a change in the energetical order of the states around the HOMO and the LUMO states. After relaxation, in all the Ge NCs the HOMU-LUMO transition is very strong [1]. For the lifetimes of the Si NCs there are also strong changes, but the picture is not as consistent. In any case, the lifetimes of the Ge crystallites are much shorter as compared to the Si crystallites, indicating that Ge should be better for light-emission applications than Si NCs. This is a consequence of the strong transitions at or near the HOMO-LUMO gap which occur only in the Ge NCs, not for Si [1]. They are a consequence of the strong contributions of Γ-like wavefunctions to the LUMO [8].

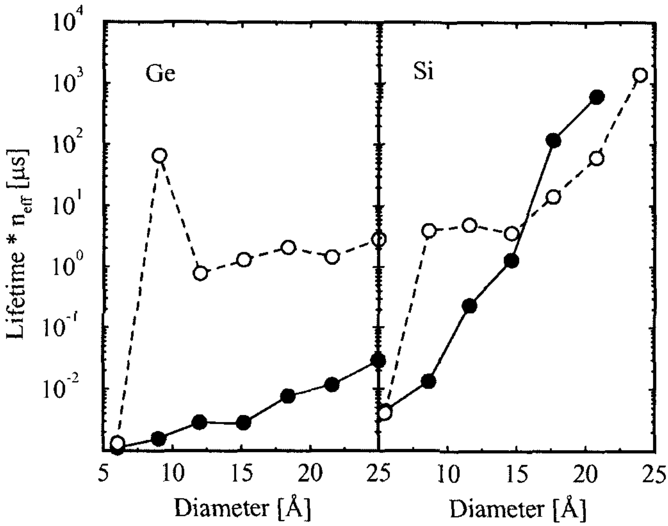

Figure 3. Radiative lifetimes as calculated for using the unrelaxed (empty) and the relaxed (filled) structure. The refractive index remains unspecified.

4. Conclusion

The structural relaxation pattern is complex. While the average bond lengths indicate a contraction of the NCs, the individual bond lengths show shortening near the NC surface, while they are longer at the center. We have shown that a proper account of the structural relaxation is indispensable if realistic results for the optical properties are desired. Especially the energetic order of the states and, hence, the radiative lifetimes, prove very sensitive with respect to the relaxation. The lifetimes in Ge NCs are, in general, much shorter than in Si NCs, which leads us to predict that Ge is better in order to achieve luminescence from NCs than Si.

Acknowledgments

One of us (HCW) is grateful for support for the participation at the ISCANA conference, Richmond 2003, from the ISCANA conference. We acknowledge financial support from the Deutsche Forschungsgemeinschaft (Project No. Be1346/12-1) and from the European Community in the framework of the Research Training Network NANOPHASE (contract HPRN-CT-2000-00167).

References

1. H. -Ch.Weissker, J. Furthmüller, and F. ~Bechstedt, Phys. Rev. B **67**, 245304 (2003).
2. I. Vasiliev, S. Ögüt and J. R.Chelikowsky, Phys. Rev. Lett. **86**, 1813 (2001).
3. A. Puzder, A. J.Williamson, J. C.Grossman, and G. Galli, J. Am. Chem. Soc. **125**, 2786 (2003).
4. G. Kresse and J. Furthmüller, Comput. Mater.Sci. **6**, 15 (1996); Phys. Rev. B **54**, 11169 (1996).
5. H. -Ch.Weissker, J. Furthmüller, and F. Bechstedt, Phys. Rev. B **65**, 155328 (2002).
6. H. -Ch.Weissker, J. Furthmüller, and F .Bechstedt, submitted to Phys. Rev. B.
7. D. L. Dexter, Solid State Phys. **6**, 360 (58).
8. H. -Ch.Weissker, J. Furthmüller, and F. Bechstedt, Mat. Sci. Eng. B **101**, 39 (2003).

SELF-ASSEMBLED NANOWIRES USING POROUS ALUMINA TEMPLATES

C.-G. STEFANITA, S. PRAMANIK, A. BANERJEE, S. BANDYOPADHYAY
Department of Electrical Engineering, Virginia Commonwealth University
Richmond, Virginia, 23284 USA
cstefanita@vcu.edu

The occurrence of unusual electronic, magnetic and optical properties displayed at the nanoscale provides an incentive to explore innovative routes to nanosynthesis. The nanoporous structure of anodized alumina is a convenient template for self-assembly of nanowires using simple beaker chemistry. In our laboratory, we routinely self-assemble extremely well regimented arrays of metallic and semiconductor nanowires (e.g. CdS, ZnSe, Cu, Ni, Fe, Co) of diameter 10 nm or 50 nm using anodized alumina templates. By depositing aluminum on a substrate of choice (e.g. silicon) and subsequently anodizing it, one can obtain the porous structure on a sturdy substrate. Nanowires are then produced by filling the pores with the material of interest. This is an inexpensive nanosynthesis technique that produces device quality materials with high throughput.

1. Introduction

Conventional fabrication technologies are often not synergistic with nanosynthesis because of high cost, slow throughput and low yield. As a result, non-traditional techniques, drawing upon chemical methods, have emerged as serious competitors to nanolithography and other traditional technologies. Here, we describe an electrochemical technique to fabricate nanowire arrays. Nanowires are the staple of nanoelectronic and nanophotonic devices. For instance, a variety of materials such as Bi [1], Ti [2], Ag [3], Ni [4], Co [5], Si [6], or III-V [7], II-VI [8-9] and IV-VI [6,10] semiconducting compounds have been fashioned into nanowires for novel devices such as nanolasers [11], nanophotodetectors [12], or magnetic nanomanipulators [13]. These nanoscale systems constitute promising building blocks for next generation devices in information storage [14], computing [15], communications [16], photonics [17], as well as biotechnology [18] and medicine [19].

Nanowire fabrication using anodized alumina templates is now a well-established technique. In the process of anodization, we transform an aluminum film into a porous alumina matrix with a hexagonal close packed array of nanopores, and subsequently fill the pores with a material. This results in the formation of a regimented array of nanowires in an insulating matrix. The insulating matrix can be removed after filling the pores; however this may not always be necessary, depending on the application. Although the technique is now quite old and widely investigated [20], it still holds a few challenges. For example, porous anodic alumina templates are usually created on thin sheets of aluminum. In many instances, the underlying aluminum is dissolved after obtaining the template to allow electrical access to the pores from the top and bottom. Unfortunately, alumina templates are brittle, quite often posing limitations on further processing. To eliminate this shortcoming, the aluminum film can be deposited on a robust conducting substrate and then processed into a nanoporous template. The advantage of this approach is that the conducting substrate provides mechanical stability to the structures, without impeding electrical function. For optical applications, the substrate will be non-conducting to prevent absorption losses.

2. Background

Anodization of aluminum has been studied for more than fifty years in the context of corrosion prevention [20]. A thin layer of aluminum oxide (about 3 nm) forms naturally when aluminum is exposed to oxygen or pure water, due to the following spontaneous chemical reactions:

$$2Al + \frac{3}{2}O_2 \rightarrow Al_2O_3 \qquad (1)$$

or

$$2Al + 3H_2O \rightarrow Al_2O_3 + 3H_2 \qquad (2)$$

When in contact with acids, aluminum oxide can dissolve as follows:

$$\begin{aligned} &Al_2O_3 + H_2O + 2H^+ \rightarrow 2Al(OH)_2^+ \\ &Al(OH)_2^+ + H^+ \rightarrow Al(OH)^{2+} + H_2O \\ &Al(OH)^{2+} + H^+ \rightarrow Al^{3+} + H_2O \end{aligned} \qquad (3)$$

These two processes of oxidation and dissolution are used in anodization. Generally, an anodization cell is filled with sulfuric, phosphoric, or oxalic acid. A dc voltage is applied between the aluminum film and a counter-electrode. The supplied electrical energy ensures that oxidation and dissolution occur continuously.

The current density is monitored during the anodization process. Two current contributions can be distinguished: a current density j_b associated with formation of an initial alumina barrier at the interface with the underlying aluminum metal, and a current density j_p responsible for the subsequent nucleation of pores [21]. When the alumina barrier is completely formed, the current density j_b is known to decrease abruptly. On the other hand, j_p increases during pore development until the latter becomes stable. The combined effect of these two contributions leads to the overall current behavior shown in Fig. 1. By monitoring the current during anodization, we can determine if pore formation is proceeding correctly.

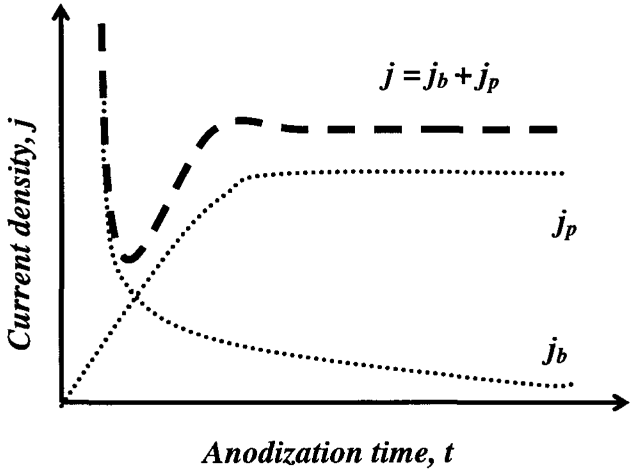

Fig. 1. Sketch of anodization current density j as a function of anodization time t. Two contributions to the net current density can be distinguished: a current density j_b due to barrier layer growth, and current density j_p as a result of pore growth.

3. Fabrication

In this section, we describe the technique to form nanowires on an arbitrary robust substrate.

The substrate we choose is an n-type <111> single-side polished Si wafer, with a resistivity of ~ 1Ω·cm. A 2-micron aluminum film is deposited using thermal evaporation in several runs. Prior to aluminum deposition, a thin layer of Ti (10 nm) is deposited by e-beam evaporation directly onto the Si surface. This intermediate step is performed to increase the adhesion of the aluminum metal to the substrate. To further improve the homogeneity of the aluminum layer, rapid thermal annealing is performed on the finished Al/Ti/Si structure at ~350°C.

Prior to anodization, aluminum films are sometimes electropolished to reduce surface roughness [22]. This is necessary if a commercially available aluminum foil is used as the substrate. However, if the aluminum film is evaporated on a substrate, then electropolishing is not required since the surface is already smooth as long as evaporated aluminum is a few microns thick. In any case, electropolishing is not possible on evaporated aluminum films since the electropolishing process consumes several tens of microns of aluminum and will therefore completely remove any evaporated film which is necessarily limited to a few microns in thickness.

Anodization is carried out as described in the previous section. When the process is complete, a porous alumina film forms on the surface of aluminum. It contains a regimented array of pores. The factors that determine pore regularity are anodization voltage, anodization time, and most importantly the number of anodization steps. The pores formed during the first anodization are usually irregular. Therefore, the alumina film formed in the first anodization step is stripped off in hot phosphoric/chromic acid and the process of anodization is repeated. After a few iterations, an extremely well ordered array of scallops develops on the surface of aluminum. Once they form, the next anodization step will result in a porous film with almost a periodic array of nanopores. Usually three or four iterations are sufficient for this to happen.

The appropriate value for the anodization voltage depends on the electrolyte used. In our laboratory we employ 40 V dc for anodization in 3% oxalic acid, or 20 V dc for 15 % sulfuric acid. (e.g. [23]). Fig. 2 shows an atomic force microscope (AFM) topographical image of the porous alumina film taken after completion of five iterations. The estimated length of the pores depicted in Fig. 2 is ~1 µm, and the average pore diameter is ~50 nm. The pores are of uniform diameter and open at one end. They usually develop parallel to each other and perpendicular to the substrate surface. Furthermore, their height can be increased with anodization time.

At the bottom of the pores, an insulating alumina barrier separates the pores from the underlying aluminum film (or the titanium film if all of the aluminum is converted to alumina). This is the barrier whose formation was discussed in Section II. Additional processing steps are required to remove this barrier layer. This is necessary because after the pores are filled, the resulting nanowires need to be contacted electrically from both the bottom and the top for current transport. A common procedure for removing the barrier is etching. For porous alumina structures obtained on a substrate such as silicon, the silicon substrate with the alumina pores is soaked in 5% phosphoric acid for up to 2 hours to remove the barrier completely. However, it is also possible to remove the barrier layer at low voltage with reverse bias in a KCl solution, as described in [25]. This is not the preferred technique since it can degrade the pore morphology.

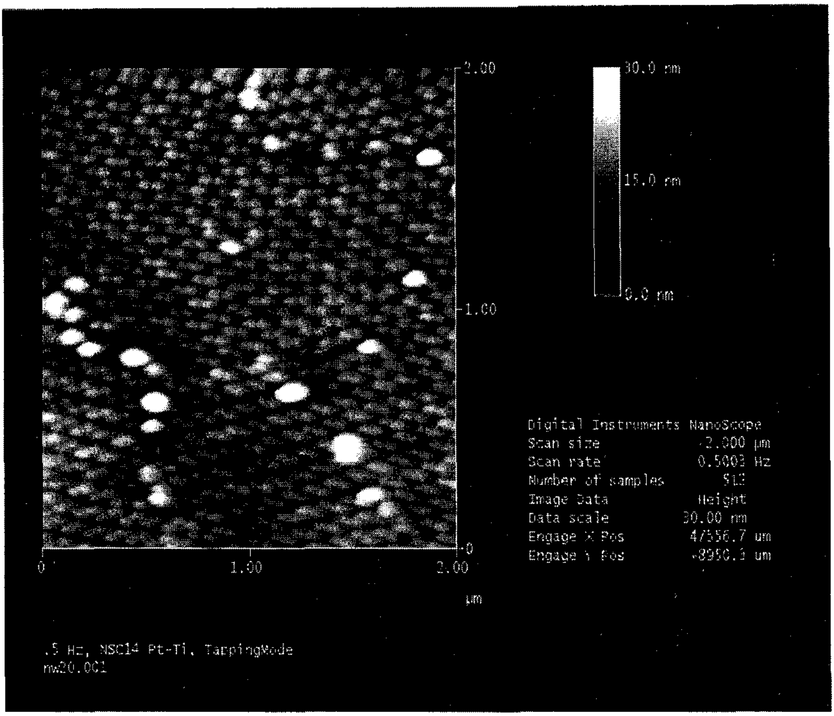

```
Digital Instruments NanoScope
Scan size                 2.000 µm
Scan rate                0.5003 Hz
Number of samples           512
Image Data               Height
Data scale             30.00 nm
Engage X Pos          47556.7 um
Engage Y Pos          -8950.3 um
```

```
.5 Hz, NSC14 Pt-Ti, TappingMode
nw20.001
```

Fig. 2. AFM topographical image of a porous alumina film after following a five step processing procedure described in [24].

To make nanowires, the pores are filled with the nanowire material by electrodeposition. For most metals, this is carried out in noncyanide baths that do not attack alumina. An ac current is passed at a suitable rms voltage between the substrate containing the alumina porous structure and a second electrode while immersed in an aqueous bath. The bath contains a soluble salt of the metal that ionizes to produce the metal ion. During the cathodic half-cycle, the metal ion is reduced to zero-valent metal and deposited within the pores. During the anodic half-cycle, the zero-valent metal is not re-oxidized back to a cation since alumina is a valve metal oxide. Selective deposition of metal within the pores takes place because the pores offer the least impedance paths for the electrodeposition current to flow. For compound semiconductors, often a non-aqueous solution is used for electrodeposition. The cation is deposited by ac electrolysis and the anion is incorporated by reaction with the cation in a boiling solution containing the anion [22]. However, the procedure generally followed in our group for preparing AX semiconductor nanowires (A = Cd, Pb, Zn and X = S, Se, Te) consists of electrodeposition in a nonaqueous electrolyte containing a salt of A and elemental X [12], [24].

The pores are filled non-uniformly so that not every pore is filled to the brim and not every wire is exposed at the top for electrical contacting. Dilute phosphoric acid is used to slightly etch the surface of the porous film and expose the tips of *some* of the nanowires (only the ones that are longest). A thin gold layer (~20 nm) is evaporated on the top surface to electrically contact the exposed nanowires. As long as the substrate is conducting, a back contact to the substrate produces the other contact for completing an electrical circuit.

4. Applications

Nanowires obtained by self-assembly in porous alumina templates exhibit a range of interesting properties such as room temperature single electron charging [26], negative differential resistance [9], giant photoresistivity and room temperature infrared photodetection [12], as well as electronic bistability [27]. We have studied a number of these effects and their potential for device applications. A somewhat comprehensive review of the device aspects can be found in ref. [28].

5. Conclusion

This work has summarized an electrochemical approach to the self-assembly of nanowires on an arbitrary substrate. These nanowires have exhibited intriguing device properties and may find applications in ultrafast and ultra-low-power electronic/optical devices.

This work is supported by the US National Science Foundation under grant ECS-0196554 and by the US Office of Naval Research under grant N00014-02-1-0929.

References

[1] M. S. Dresselhaus, Y.M. Lin, O. Rabin, A. Jorio, A.G. Souza Filho, M.A. Pimenta, R. Saito, G. G. Samsonidze, G. Dresselhaus *Mat Sci Eng* C, 23, 129 (2003).
[2] B.L. Wang, G. H. Wang, X. S. Chen, J.J. Zhao *Phys Rev B,* 67 (19), 193403 (2003).
[3] J.J. Zhao, C.L. Buia, J. Han, J.P. Lu *Nanotechnology,* 14 (5): 501 (2003).
[4] R. Ferre, K. Ounadjela, J.M. George, L. Piraux, S. Dubois *Phys Rev B,* 56, 14066 (1997).

[5] G.H. Zeng, A. Shakouri, C. La Bounty, G. Robinson, E. Croke, P. Abraham, X.F. Fan, H. Reese, J.E. Bowers *Electron Lett,* 35, 2146 (1999).
[6] A.M. Morales, C.M. Lieber *Science,* 279, 208 (1998).
[7] X. Duan, J. Wang, C.M. Lieber *Appl Phys Lett,* 76, 1116 (2000).
[8] D. Xu, Y. Xu, D. Chen, G. Guo, L. Gui, Y. Tang *Adv Mater,* 12, 520 (2000).
[9] K. Karahaliloglu, S. Balkir, S. Pramanik, S. Bandyopadhyay *IEEE T Electron Devices* 50 (7), 1610 (2003).
[10] X. Duan, C.M. Lieber *Adv. Mater,* 12, 298 (2000).
[11] M.H. Huang, S. Mao, H. Feick, H. Yan, Y. Wu, H. Kind, E. Weber, R. Russo, P. Yang *Science,* 292,1897 (2001).
[12] N. Kouklin, L. Menon, A.Z. Wong, D.W. Thompson, J.A. Woollam, P.F. Williams, S. Bandyopadhyay *Appl Phys Lett,* 79 (26), 4423 (2001).
[13] D.H. Reich, M. Tanase, A. Hultgren, L.A. Bauer, C.S. Chen, G.J. Meyer *J Appl. Phys,* 93 (10), 7275 (2003).
[14] V. Balzani *Photoch Photobio Sci* 2 (5): 459 (2003); Q.L. Wang, D.Z. Liao *Prog Chem,* 15 (3), 161 (2003).
[15] A. Jacobson *Comput Sci Eng,* 5 (3), 8 (2003).
[16] E. Yablonovitch, H.W. Jiang, H. Kosaka, H.D. Robinson, D.S. Rao, T. Szkopek *Proc IEEE,* 91 (5), 761 (2003).
[17] M. Ohtsu, K. Kobayashi, T. Kawazoe, S. Sangu, T. Yatsui *IEEE J Sel Top Quant,* 8 (4), 839 (2002).
[18] R.J. Mumper, Z.R. Cui, M.O. Oyewumi *J Disper Sci Technol.,* 24 (3-4): 569 (2003).
[19] M.C. Roco *Curr Opin Biotech* 14 (3): 337 (2003).
[20] M. Moskovits, International Patent 5202290 (1993); P. Czokan, in “Advances in Corrosion Science and Technology”, M.G. Fontana and R.W. Staehle (eds.), Plenum, New York, vol. 7, p 239 (1980); F. Keller, M.S. Hunter, D.L. Robinson *J Electrochem Soc* 100: 411 (1953).
[21] Q. Huang, W.-K. Lye, D.M. Longo, M.L. Reed, *Mat. Res. Soc. Symp. Proc.* 636: D9.49.1 (2001).
[22] S. Bandyopadhyay, A.E. Miller, in “Handbook of Advanced Electronic and Photonic Materials and Devices”, H.S. Nalwa (ed.), Academic, New York, vol. 6: *Nanostructured Materials*, p 1 (2001).
[23] O. Jessensky, F. Muller, U Gosele *Appl. Phys. Lett.* 72 (10):1173 (1998).
[24] C.-G. Stefanita, F. Yun, H. Morkoc, S. Bandyopadhyay “Self-assembled quantum structures using porous alumina on silicon substrates” in *Recent Research Developments in Physics,* Transworld Research Network, ed. S.G. Pandalai, Kerala, India (in press 2003).
[25] O. Rabin, P.R. Herz, S. B. Cronin, Y.-M. Lin, A. I. Akinwande, M.S. Dresselhaus, *Mat. Res. Soc. Symp.* 636: D4.7.1 (2001).
[26] N. Kouklin, L. Menon, S. Bandyopadhyay, *Appl. Phys. Lett.* 80 (9): 1649 (2002).

[27] N. Kouklin, S. Bandyopadhyay, S. Tereshin, A. Varfolomeev, D. Zaretsky, *Appl Phys Lett* 76 (4): 460 (2000).
[28] S. Bandyopadhyay, N. Kouklin and L. Menon, in *Quantum Dots and Nanowires*, Eds. S. Bandyopadhyay and H. S. Nalwa, (American Scientific, Stevenson Ranch, CA, 2003) Chapter 9.

CERIA-ZIRCONIA-ALUMINA MIXED OXIDES PREPARED BY THE ORGANIC-FREE SOL-GEL TECHNIQUE

E. FROLOVA[1*], M. IVANOVSKAYA[1], V. PETRANOVSKII[2], S. FUENTES[2],
E. TYAVLOVSKAYA[3]
[1]*Research Institute for Physical Chemical Problems, BSU, Minsk, Belarus*
[2]*CCMC, UNAM, Ensenada, B.C. 22800 Mexico*
[3]*Institute of Electronics, National Academy of Sciences of Belarus, Minsk, Belarus*

The structural composition and the cause of the thermal stability of the obtained structure in the Ce:Zr:Al (7.5:7.5:85 molar ratio) oxides nanosystem, prepared by the organic-free sol-gel technique were investigated by XRD, FTIR and XPS. According to the XRD analysis, the Ce:Zr:Al sample calcined at 1100 °C in air, presents a nanosystem with dispersion of C-$Zr_XCe_{1-X}O_2$ S.S.(~10 nm) nanoparticles in nanocrystalline γ-Al_2O_3 (~4 nm) matrix. This system remained stable during further heating up to 1200°C during 8 h in air. A strong chemical interaction between the components of ceria-zirconia nanoparticles on the phase boundary with alumina matrix with formation of charge transfer complexes [$Zr^{n+\delta}$ - O - $Al^{m-\delta}$] and [$Ce^{n+\delta}$ - O - $Al^{m-\delta}$] could explain the quenching of nanocrystalline state in this system, that "freeze" crystallization even at high temperatures.

Ceria-based materials, especially ceria-zirconia mixed oxides, are essential promoter components in the automotive three-way catalysts (TWC) system [1]. Catalytic activity of ceria is conditioned by cerium capability for switching between the Ce^{3+}/Ce^{4+} oxidation states. Usage of pure ceria is limited by thermal ageing and subsequent deactivation of catalysts. Enhanced oxygen storage capacity is the main reason for the usage of ceria-zirconia mixed oxides. It has been suggested that both zirconia-stabilized defects in ceria and structural modifications of ceria mediated by zirconia are responsible for the improvement of catalytic properties. Combination of CeO_2-ZrO_2 mixed oxides with Al_2O_3 greatly enhances thermal stability of the resultant material [2]. However, both the nature of the structural defects underlying such growth of catalytic activity and the nature of element interactions in the above system remain to be determined [3].

In this study, we investigated the thermal stability of ceria-zirconia-alumina mixed oxides obtained by organic-free sol-gel method, the chemical state of the elements as well as the crystallinity of the obtained products.

1. Experimental

The samples were prepared by two techniques: (a) co-precipitation (CP) from aqueous solutions of ZrO^{2+}, Ce^{3+}, Al^{3+} nitrates with molar ratio Zr:Ce:Al =

7.5:7.5:85. Precipitating agent was NH_4OH. After precipitation the samples were washed with distilled water, dried at 50°C and calcined at elevated temperatures in air. This method yielded powder sample. (b) Inorganic variety of sol-gel (SG) method, which differs from CP by that the after washing the precipitates were peptized to sol (colloidal solution) by HNO_3, and then dried at 50°C and calcined at elevated temperatures in air. This method yielded glassy samples.

X-ray powder diffraction data (XRD) of the samples were obtained with HZG 4A powder diffractometer (CoK_α radiation). XPS studies were performed with ES-2401 spectrometer. Sample surface etching with Ar^+ was employed. Core level energies were calibrated by the C 1s line with Eb = 284.6 eV.

2. Results and Discussion

XRD

According to the XRD data, the crystallization for the CP sample started after calcination at 500°C instead of 900°C for the SG sample (data not shown). The most evident finding in this XRD patterns for both CP and SG samples (according to the reflections positions and their relative intensities) is the appearance of the cubic $Zr_XCe_{1-X}O_2$ solid solution with fluorite structure (JCPDS 38-1439). It can be seen from the XRD patterns (Fig. 1.) that even after calcinations at high temperatures the reflections are steel quite broad for all samples and that can indicate the fine particle nature of the product. The particle size, D_{XRD} was calculated according to the Scherer equation [4]. The reflection from the (111) plane (100% *I*), occurring at $2\theta = 34.0°$, was used to calculate the

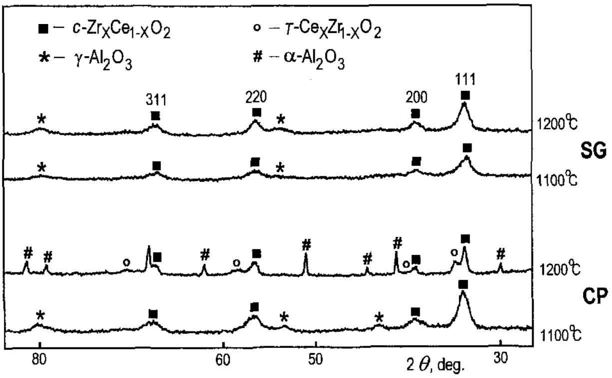

Fig. 1. XRD patterns of the CP and SG samples heated in air at 1100 and 1200 °C showing structural compositions of the samples (indicated) and *hkl* for c-$Zr_XCe_{1-X}O_2$ solid solution.

crystallite size. The particle size determined from the broadening curve for both samples is about ~10 nm in $Zr_XCe_{1-X}O_2$ solid solution. No evidence for extra reflections due to non-incorporated ZrO_2 was observed in any XRD patterns of Ce-Zr-Al-O samples. The lack of free ZrO_2 was also confirmed by FTIR-spectroscopy (data not shown). Since the composition in both samples is equal, the reason for crystallization inhibition must be in the sol-gel process steps [5]. Detailed examination of XRD patterns of CP and SG samples calcined at 1100°C in air (Fig. 1.), shows hardly visible very broad reflections, which can be assigned to the γ-Al_2O_3 (JCPDS 10-0425). It is known, that this phase remains stable only until ~900-1000°C and than the slow transition to corundum at 1000°C occurs [6]. The reflection from the (400) plane (100% *I*), occurring at $2\theta = 79.8^\circ$, was used to calculate the crystallite size. According the reflections width in more crystalline CP sample, which was calcined at 1100°C, a grain size of the γ-Al_2O_3 crystalline phase is around ~ 4 nm. No structural changes occurred during further heating of the SG sample up to 1200°C during 8 h in air (Fig. 1.). In contrast the CP sample presented a three-phase system which contains: *c*-$Zr_XCe_{1-X}O_2$, τ-$Ce_XZr_{1-X}O_2$ and α-Al_2O_3 (Fig. 1.).

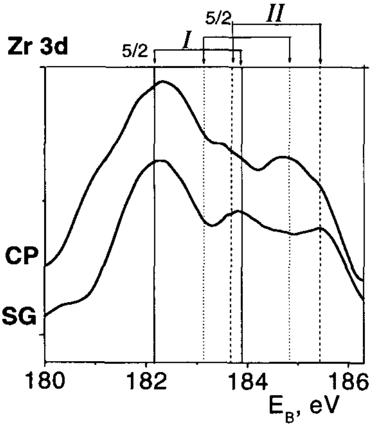

Fig. 2. Zr 3d core level XPS spectra for CP and SG samples, heated in air at 900°C.

XPS

Figure 2 illustrates a zirconium 3d spectra multiplet (analysis) of CP and SG samples heated at 900°C in air. The shapes of the Zr 3d photoelectron doublets very differ from those described in the Ref. [7] for CeO_2-ZrO_2 systems prepared differently. As can be seen in this figure the Zr 3d spectra is broadened to higher binding energies. The Zr $3d_{5/2}$ line (Fig.2., *I*-state) for SG sample appeared at 182.1 eV in good agreement with Ref. [8] (Fig.2, the solid vertical line) but the position of the second component (Zr $3d_{3/2}$) is difficult to determine. According to the assumption that the spin-orbit splitting for Zr $3d_{5/2}$ and $3d_{3/2}$ doublet is 1.7 eV [8] that line must be around 183.8 eV. The band broadening, indicative of the coexistence of non-equivalent Zr(IV)-states, is manifested by an increased intensity in the region between the two spin-orbit split components, which is absent in pure ZrO_2. In addition, a second doublet (Fig.2., *II*-state) can be noticeable at around 183.7 eV and 185.4 eV for Zr $3d_{5/2}$

and 3d$_{3/2}$, respectively. This position of the Zr 3d doublet can be assigned to the Zr(IV) cation in the salt-like compound ($ZrOCl_2$ [8]). This result indicate a chemical shift of ~ 1.6 eV. This binding energy shift is due to the relatively less electron-donating nature (i.e., more electronegative (EN)) of the second nearest-neighbor – M (a Zr-O-M bond arrangement) relative to zirconium (a Zr-O-Zr bond arrangement). According to these data, the EN for Ce, Zr and Al are 1.1, 1.3 and 1.5 respectively, the aluminum as the M (electron overdraw) can be assumed. The shape of the CP spectra is less broadened and more intense, indicating that in CP sample the charge transfer takes place at a lesser extent.

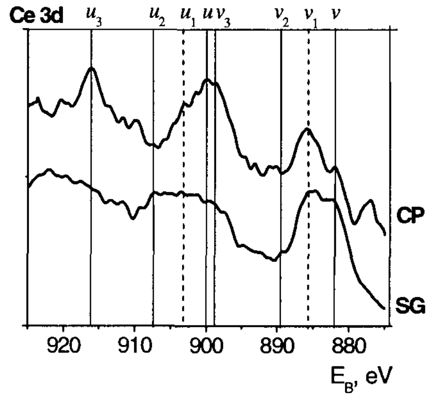

Fig. 3. Ce 3d core level XPS spectra for CP and SG samples, heated in air at 900°C.

The cerium spectra show the presence of many satellites, owing to the hybridization of the 4f level with O 2p states and to the `final` state effects caused by the creation of a core hole [9], the real origin of which is still a matter of controversy. The primary spin-orbit doublets are named *v* (~ 882.5 eV) and *u* (~900.6 eV) for 3d$_{5/2}$ and 3d$_{3/2}$ for Ce^{4+}/CeO_2 , respectively. The predicted shake-up peaks could occur around the region of v_1, v_2 (~ 885.6, 889.4 eV) and u_1, u_2 (~ 903.9, 907.7 eV). It has been known that v_1 and u_1 belong to unique photoelectron features from Ce^{3+} state. The v_3 (~ 898.7 eV) and u_3 (~ 916.6 eV) peaks are supposed to be the shake-down features or the charge transfer from the ligand (O 2p) to the metal (Ce 4f). Moreover, it is well accepted [3] that the main peaks characteristic for Ce 3d and specific to pure CeO_2 (i.e. Ce^{4+}) are situated at BE = 882.5 and 916.6 eV. The appearance of a strong peak at BE = 885.6 eV and the decrease in the intensity of the peaks at BE = 882.5 and 916.6 eV are an indication of the reduction of Ce^{4+} to Ce^{3+}. In Figure 3, we show the cerium 3d$_{5/2}$ and 3d$_{3/2}$ core levels of a SG and CP samples heated at 900°C in air. The spectra of CP sample show (Ce^{4+})-like features with the presence of six lines (noted and for the 3d$_{5/2}$ and 3d$_{3/2}$ transitions, respectively) with an exception, that the intensity of *v* (882.2 eV) line is much lower than expected for the Ce^{4+} state. The spectrum of the SG sample is not typical of pure CeO_2 [9]. The high intensity of the *v* (882.2 eV) line can be the evidence of Ce^{4+} state if it were not the lack of the u_3 line. A similar situation was described in [10] for CeO_2-TiO_2 system but not for CeO_2-ZrO_2 system. It was observed for two CeO_2-TiO_2 samples with different degree of homogeneity. More homogeneous samples lead to the highest contrast in CeO_2-TiO_2 and CeO_2 XPS spectra. The reason for the similarity between photoelectron spectra for CeO_2-TiO_2 and CeO_2-ZrO_2-Al_2O_3 systems might be related to the close EN value of Ti and Al – 1.5. The absence of the shake-down satellites can be the evidence of a stronger bond between the electron, oxygen and the second nearest-neighbor – aluminum.

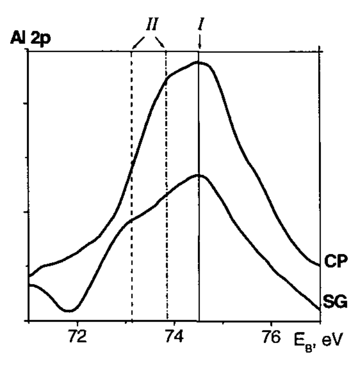

Fig. 4. Al 2p core level XPS spectra for CP and SG samples, heated in air at 900°C

Indeed, the Figure 4 demonstrates the Al 2p core levels of SG and CP samples heated at 900°C in air where the shapes of the photoelectron lines differ from those described in the Ref. [11] for Al_2O_3 systems. Both spectra show broadening of the Al 2p lines and a shift to lower binding energies. As is seen from this figure, the more evident peak appeared at 74.5 eV and can be attributed to the Al(III) in γ-Al_2O_3 [8], which is in a good agreement with XRD data. According to the assumption that the "full width at half maximum" (FWHM) is constant and for Al 2p it's equal – 1.1, the existence of second aluminum state can be predicted. The second line is located at around 73.3 eV and can be attributed to the Al(III) in the salt-like compound ($NiAl_2O_4$ [8]), as a member of the anion. This binding energy shift is likely due to the relatively more electron-donating nature (i.e., less EN) of the second nearest-neighbor – Zr or Ce (Al-O-Zr or Al-O-Ce bond arrangement) relative to aluminum (Al-O-Al bond arrangement). The shape of CP spectra is less broadened and more intense indicating that in the CP sample the charge transfer occurred in less degree.

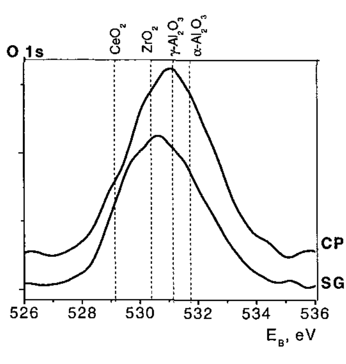

Fig. 5. O 1s core level XPS spectra for CP and SG samples, heated in air at 900°C.

Figure 5 demonstrates the oxygen 1s core levels of SG and CP samples heated at 900°C in air. The corresponding binding energies for individual oxides are shown as a dotted vertical line. The spectra of both CP and SG samples show the broadening of the respective lines. FWHMs of O 1s are 3.6 and 3.4 eV for SG and CP samples, respectively, instead of 2.0 eV for the most oxides [8]. According to this fact, the O 1s spectra for both samples holds peaks for all contained oxides. For CP sample, the O 1s peak located at 531.0 eV and for SG at 530.6 eV, which is an arithmetical mean for three individual oxides. However, the Al content in the samples is much higher that Zr and Ce (Ce:Zr:Al = 7.5:7.5:85 mol %), and the position of O 1s peak typical for Al_2O_3 (531.2 eV) could be expected. The above result indicates that in this sample the chemical shift of ~ 0.6 eV for the SG sample is due to surplus electron density on oxygen.

3. Conclusions

According to the XRD data, the crystallization of the SG sample started after calcination at 900°C instead of 500°C detected for the CP sample. This would indicate that the conversion of precipitates into colloidal solution could lead to the crystallization inhibition in the samples. Based on the analysis of the XPS spectra, one could conclude that the conversion into colloidal solution favors the shift of electron density from zirconium and cerium to aluminum. Strong mutual influence upon electronic state of the components leads to the formation of charge transfer complexes $[Zr^{n+\delta} - O - Al^{m-\delta}]$ and $[Ce^{n+\delta} - O - Al^{m-\delta}]$. A strong chemical interaction between the components of ceria-zirconia nanoparticles on the phase boundary with alumina matrix could explain the quenching of nanocrystalline state in this system that "freeze" crystallization even at high temperatures.

Acknowledgements

E. Frolova and E. Tyavlovskaya – to Belarusian FRF (Project X03-318) and NANOTEX. S. Fuentes – to CONACYT (Project 41331-Y). E. Frolova thanks Dr. L. Ivashkevich for assistance in XRD studies and Dr. V. Gurin for technical support. S. Fuentes – to E. Flores for technical help.

References

1. Bozo C., Gaillard F., Guilhaume N., *Applied Catalysis A:* **220** (2001) 69.
2. Ozaki T, Masui T., Machida K. et al, *Chem. Mater.* **12** (2000) 643.
3. Craciun R., Daniell W., Knözinger H.,*Applied Catalysis A:* **230** (2002) 153.
4. H.P.Klug, L.E.Alexander, X-Ray Diffraction Procedures, Wiley, NY. 1974.

5. M. Ivanovskaya, E. Frolova, D. Orlik, V. Gurin, *Proc. 4th Int. Conf. Mater. for Microelectronics & Nanoengineering, Hanasaari*, June 2002, 259.
6. Wells A.F., Structural inorganic chemistry, Clarendon Press, Oxford, 1986.
7. Martinez-Arias A., Fernandez-Garcia M., Hungria A.-B., Conesa J. and Munuera G., *J. Phys. Chem B.* **107** (2003) 2667.
8. Nefedov V.I., Photoelectron spectroscopy of chemical compounds, Khimiya, Moscow, 1984. (in Russian)
9. Xiao W., Guo Q., Wang E., *Chemical Physics Letters*, **368** (2003) 527.
10. Dauscer A., Hilaire L., Le Normand F., Müller W., Maire G. and Vasquez A., *Surface & Interface Analysis*, **16** (1990) 341.
11. Datta A., *J. Phys. Chem.* **93** (1989) 7053.

LIGHT INDUCED METAL NANOPARTICLE FORMATION (M=Ag, Au, Cu, Pd, Pt) IN AQUEOUS SOLUTIONS AND POLYMER FILMS COMPOSED OF SPEEK-PVA

A. S. KORCHEV, M. SARTIN, G. MILLS
Department of Chemistry, Auburn University,
Auburn, AL 36849, USA.

B. L. SLATEN
Department of Consumer Affairs, Auburn University,
Auburn, AL 36849, USA.

W. F. GALE
Materials Research and Education Center, Auburn University,
Auburn, AL 36849, USA.

Formation of Ag, Au, Cu, Pd and Pt nanoparticles has been observed in solutions containing sulfonated poly (ether-ether) ketone and poly (vinyl alcohol) upon irradiation with 350 nm photons. Alternatively, crosslinking of the polymers allowed fabrication of thin films that possess high light-sensitivity and ion exchange capabilities. Adsorbed Ag^+ ions are efficiently photoreduced in films, producing metal nanoparticles. In both films and solutions, reduction of metal ion precursors by polymeric alcohol radicals was the origin for the particle generation process. The polymer radicals were produced via photochemical H-abstraction from PVA molecules by the excited carbonyl groups of SPEEK. The chemical nature of the metal ion plays a crucial role in the development kinetics of the metal crystallites.

1. Introduction

Generation of nanometer-sized metal particles within polymer matrices is an attractive way to stabilize the crystallites from uncontrolled growth. This process is also relevant to the preparation of metallized plastics, which are of technological significance in a number of areas including the automotive, microcircuits and space industries. Efficient generation of metallic crystallites or structures within polymers requires preparation of composites, consisting of metal ion precursors present inside appropriate macromolecular solids, which respond effectively to illumination. Our earlier studies have shown that systems based on poly (vinyl alcohol), PVA, are interesting candidates as host materials because this polymer can serve as a hydrogen donor, and can be manufactured in the form of transparent films and fibers [1]. For instance, light-induced formation of silver nanoparticles has been achieved in blends of PVA and poly (acrylic acid), PAA, doped with Ag+ ions. However, an important drawback of the PVA/PAA systems is that they require the presence of light-sensitive metal ions (such as Ag (I) or Au (III) complexes) that can initiate the photochemical formation of metal crystallites.

Herein, we report a conceptually new approach involving photochemically active ($\lambda \leq 360$ nm) polymer matrices that consist of sulfonated poly (ether etherketone), SPEEK, combined with PVA. Light-induced reactions between the polymers allow conversion of photons into chemical energy, which drives the metal ion reduction. As a result, the blends have been used to photogenerate a variety of metal crystallites from light-inactive metal precursors. A summary of the reduction processes of $AgClO_4$, $HAuCl_4$, $CuSO_4$, Na_2PdCl_4 and K_2PtCl_6 in aqueous solutions initiated by the polymers is presented here, along with results on the silver nanoparticle generation in solid SPEEK/PVA films.

2. Metal Reduction in Solutions

The structures of the polymer units of SPEEK and PVA, shown in Figure 1, illustrate the presence of benzophenone (BP) groups in the SPEEK backbone.

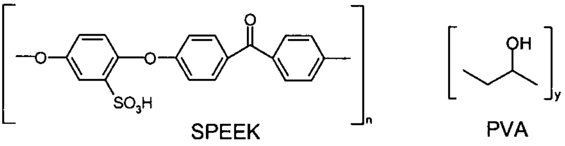

Figure 1. Chemical structure of the SPEEK and PVA polymers.

Generally speaking, SPEEK – PVA blends can be considered as polymeric analogues of one of the classical photochemical system consisting of BP and 2-propanol. It is well known that excitation of BP (λ_{max}=360 nm) leads to formation of a triplet state, which is highly reactive toward the hydrogen abstraction reaction [2], shown in reaction (1),

$$(C_6H_5)_2CO^* + RH \longrightarrow (C_6H_5)_2\dot{C}(OH) + R^\bullet \qquad (1)$$

The products of reaction (1) are a benzophenylketyl (BPK) radical and an isopropyl alcohol radical when RH represents 2-propanol. Thus, a similar reaction between PVA and light-excited SPEEK is expected to occur upon illumination. In fact, evidence that polymeric BPK radicals (or SPEEK radicals) form through photolysis of the polymer blends has been obtained using UV-Vis and EPR techniques, which demonstrate that a process analogous to reaction (1) takes place in SPEEK-PVA systems. Interestingly, SPEEK radicals exhibit a long lifetime in air-free solutions at room temperature since their absorption band centered at 565 nm can still be detected after 10-20 minutes of irradiation.

The presence of metal ions changed the UV-Vis spectrum significantly since the signal of the SPEEK radical was no longer detected. Instead, optical signals characteristic of small metal particles developed upon irradiation of solutions containing metal ions with 350 nm light. Growth of the surface plasmon band of Ag crystallites stopped after illuminating a degassed solution containing 6 x 10^{-5} M $AgClO_4$ for 70 s, indicating that complete reduction of the silver ions was achieved in that time. However, the signal of the SPEEK radicals at 565 nm appeared at the end of the Ag^+ photoreduction. If a solution of SPEEK and PVA (without silver ions) is irradiated first to produce SPEEK radicals, and then Ag^+ ions are added, a rapid decay of the radical absorption band occurs synchronously with the appearance of the Ag surface plasmon, see Figure 2.

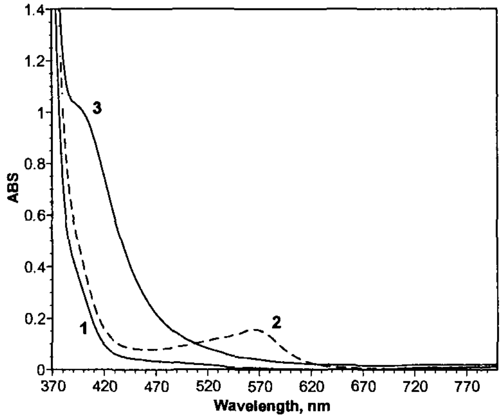

Figure 2. Reaction of photogenerated SPEEK radicals with Ag^+ ions followed using UV-Vis spectroscopy: 1) spectrum of an air-free SPEEK-PVA aqueous solution before irradiation; 2) spectrum after 1 min irradiation; 3) spectrum after injection of a degassed solution of $AgClO_4$.

Transmission electron microscopy (TEM) coupled with electron diffraction measurements confirmed that spherical Ag particles with an average size of 7 nm were generated. Based on the available evidence we assume that reaction 2 between SPEEK radicals and silver ions represents the reduction of Ag^+.

$$\left[\ldots\!-O-C_6H_4-\dot{C}(OH)-C_6H_4-\right]_n + Ag^+ \longrightarrow Ag + \left[\ldots\!-O-C_6H_4-CO-C_6H_4-\right]_n + H^+ \quad (2)$$

An interesting feature of this process is that scavenging of the polymer radicals by metal ions reforms the BP functions of SPEEK, therefore allowing further metal ion reductions to occur at the same reaction center. The net result of the process is Ag^+ reduction and oxidation of PVA. Systems able to sustain an efficient generation of particles require a PVA concentration two orders of magnitude higher than that of SPEEK. Evidence exists that 2-propanol radicals reduce several metal complexes in solution [3]. These radicals are good models for PVA radicals, which are expected to form simultaneously with SPEEK radicals. PVA radicals may contribute to formation of metal, either by reduction of the metal ions or of BP functions of SPEEK, yielding further polymeric BPK radicals.

Formation of Au nanoparticles is observed upon photolysis of aqueous solution containing $HAuCl_4$, SPEEK and PVA. Two distinct transformations are noticed: bleaching of the Au(III) complex takes place in the first step, followed by development of gold nanoparticles. No absorption signal centered at 565 nm is detected during either of these steps, which points to the involvement of SPEEK radicals in the metal ion reduction process. The photogenerated Au crystallites exhibit particle sizes in the range of 2-3 nm.

Photolysis of degassed solutions containing $CuSO_4$, SPEEK and PVA yields copper crystallites. As in the case of gold, formation of Cu particles occurs through a two-step process. The first reaction entails a one-electron reduction of Cu^{2+} to Cu^+; *the latter ion is detected optically via an absorption centered at* 460 nm. We assign this signal to Cu^+ ions complexed to polymer groups. The complex is stable for 24 h, but decays fast when exposed to air. Formation of Cu^+ slows down after 3 minutes of irradiation and a new band emerges at 570-580 nm with simultaneous disappearance of the 460 nm absorption. The signal at longer wavelengths corresponds to the well-known surface plasmon of Cu crystallites, which increases in intensity upon irradiation. These observations imply that the second step ($Cu^+ \rightarrow Cu^0$) is initiated by light as well. As in the case of the Cu^+ species, copper particles are oxidized in the presence of O_2. The resulting colloids exhibit the broadest size distribution of all prepared materials, with particle diameters ranging from 5 to 40 nm. Electron diffraction experiments confirmed that the crystallites consisted of fcc Cu.

Pd and Pt colloids are obtained by irradiation of solutions containing the polymers and Na_2PdCl_4 or K_2PtCl_6. Metal particles formation is accompanied by development of a broad absorption that extends over the entire visible range and increases in intensity with decreasing wavelengths. The final UV-Vis spectra of the solutions resemble those of "typical" Pd and Pt colloids prepared via addition of strong reducing agents to solutions of the metal salts. Since no distinct absorption signals are detected for these metals in the visible range, metal formation was followed at 500 nm.

The particle formation kinetics of Pd is drastically different from that of Pt since illumination for 10 s yields optical evidence that the former metal is forming. In contrast, the first sign of generation of metallic Pt can be detected only after 3 min of irradiation. Moreover, plots of Pd formed vs. time yield sigmoidal curves, with maximum rates occurring at the initial stages of the photoreaction. Pt formation curves are S-shaped, which result from the above mentioned induction period combined with a step of fast metal generation. Such a behavior is probably a consequence of: 1) generation of Pt species with several oxidation states that possess varying chemical properties; 2) catalytic reduction of platinum ions induced by the present metal. It should be noted that the optical signal of SPEEK radicals is not detected during generation of either metals. This absorption is noticed only in the case of Pd once the photoreduction is completed. Occurrence of an electron transfer from the macromolecular radicals to the platinum particles can explain the absence of the signal at 565 nm in the Pt systems. The proposed reaction is similar to the redox process that takes place when BPK radicals are photo-generated in the presence colloidal solutions of platinum [4].

In summary, the light-induced reaction between SPEEK macromolecules and PVA can be used to generate reducing radicals in solution. This approach succeeded at forming nanometer-sized colloidal particles of several metals.

3. Silver Reduction in Polymer Films

Solution casting of blends made from PVA, poly (acrylic acid) and glutaraldehyde (GA) as a cross-linker followed by drying at 55^0C resulted in transparent, flexible polymer films [1]. The same procedure can be employed for the presently used polymers, yielding crosslinked PVA matrices containing entrapped SPEEK macromolecules. Optimization of the GA concentration and thermal treatment enables to produce films that are flexible, water insoluble and optically transparent above 380 nm. The polymer matrices are light sensitive, producing the absorption band at 565 nm of SPEEK radicals upon illumination with 350 nm photons. This finding suggests that reaction (1) takes place in the solid-state as well. Another property of the films is their ion-exchange capability induced by presence of strongly acidic sulfoxy group in the SPEEK chains. For instance, cations such as Ag^+ can be absorbed into the films from aqueous solutions. Irradiation of Ag^+-doped polymer film with 350 nm light induces formation of the Ag plasmon at about 395 nm. The absence of the optical signal from SPEEK radicals implies that silver is generated in the films through reaction (2). Silver atoms or clusters most probably coalesce into particles. Figure 3 is a TEM image from a microtomed film photolyzed for 8h showing that the particle sizes range between 10 and 15 nm.

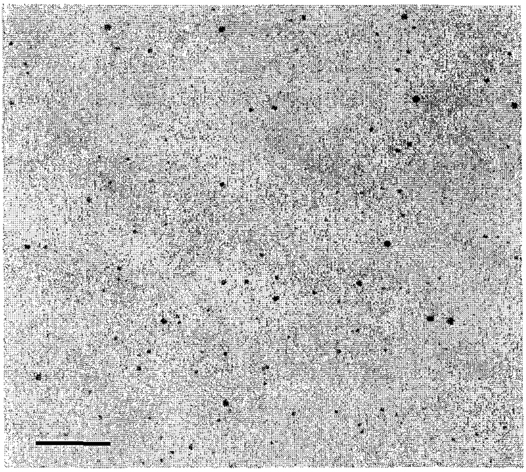

Figure 3. TEM image of the microtomed Ag^+ doped SPEEK-PVA film after being irradiated (a bar is 200 nm).

The rate of silver crystalline formation in films and solutions is linearly dependent on the light intensity which 1) is consistent with reaction (1); 2) allows the use intense beams to efficiently drive metal generation in polymer systems. The approach described here, based on the utilization of macromolecular radicals as reducing agents, has been recently employed by us for the direct photopatterning of polymer films with metal nanoparticles [5].

Acknowledgments

The authors would like to thank M. Miller for the sectioning and imaging of polymer films, R. Leibfried (Victrex USA Inc.) for the generous gift of PEEK and DOC/NTC for partial finding of this project.

References

1. G. A. Gaddy, J. L. McLain, E. S. Steigerwalt, R. Broughton, B. L. Slaten, G. Mills, *J. Cluster Sci.* **12**, 457 (2001)
2. N. J. Turro, in the book "Modern Molecular Photochemistry", Benjamin/ Cummings Pub. Co., (1978)
3. See, for example: Y. Yonezawa, T. Sato, S. Kuroda, K. Kuge, *J. Chem. Soc. Faraday Trans.* **87**, 1905 (1991)
4. C. K. Grätzel, M. Grätzel, *J. Am. Chem. Soc.* **101**, 7741 (1979)
5. A. S. Korchev, M. J. Bozack, B. L. Slaten, G. Mills, submitted to *J. Am. Chem. Soc.*

This page intentionally left blank

LAMB-MOESSBAUER FACTORS IN NANOCRYSTALS

KESHAV N. SHRIVASTAVA[1,2] and PUNIT BOOLCHAND[1]
[1]*Department of Electrical, Computer Engineering & Computer Science, University of Cincinnati, Cincinnati OH 45221-0030 and*
[2]*School of Physics, University of Hyderabad, Hyderabad 500046 India.*

Lattice vibrations in a nanocrystalline solid, in contrast to bulk crystalline solid, will have an additional contribution from surface scattering. Mean square displacement (msd) of atoms in a nanocrystal is calculated using such an additional contribution. The zero-point vibrational correction to the msd is found to vary as the inverse square of a nanocrystal size (L). Furthermore, the temperature dependent term of the msd is found to vary as exp(-1/TLk), where k is a constant. Since a structural distortion of a nanocrystalline solid can be expected to set in, at a particular temperature, we introduce a gap in phonon dispersion. Calculations of the LM factors with a gap in dispersion show that f(T) shows a global maximum at a threshold temperature (T_{th}). Thermal expansion is expected to occur at $T<T_{th}$, while thermal contraction should result at $T>T_{th}$ with increasing T. The gap is the result of a size dependent phonon scattering. We compare calculated f(T) and thermal expansion with measured results of these observables on nanometer-sized Au particles.

1. Introduction

Recently there has been a lot of interest in nanocrystals as nanosize particles embedded in a matrix and as independent particles in a powder. In some problems, one starts with the known nanocrystal size and calculates the adsorption energies or any other physical property. In other problems, the physical properties are first measured and from that the nanocrystal size is determined. The understanding of the physical properties of the nanocrystals is very important because of their application in the device fabrication. In the modern times, the components are often of the size of a few microns. If these components can be made within the size of a few nm, there will be a gain of a factor of 10^3. The much smaller currents can perform the same function which was previously performed by much larger currents. We have calculated the Moessbauer recoilless fraction for a fractal [1-3] and for a superconducting lattice [4,5]. We have calculated [6-9] the effect of lattice vibrations on the isomer shift which has been observed [10,12].

In this work, we calculate the mean-square displacement of an atom in a nanocrystal due to scattering of phonons of wave length of the order of the size of the nanocrystal. The recoilless fraction is nontrivial because of two terms with different slopes so that there is apparent "thermal contraction".

2. Theory

We consider that the material consists of an ensemble of nanocrystals. The size of the nanograin is d. The sound waves are scattered by the nanograin if the distance between two sides of a grain is an integer multiple of the wave length. In the case of x-rays, the diffraction is determined by the Bragg's law. The distance between atoms is of the order of the wave length, λ, so that the scattering occurs at, $2d \sin \theta = n\lambda$, where θ is the angle which the incident ray makes from the normal to the surface parallel to which the next atomic layer is located at a distance, d, from the first surface and n is an integer. We consider the sound waves or phonons in the solid which are scattered by the surface boundaries of the nanocrystals. The wave length of the phonons or that of the sound waves is, $\lambda = v/\nu$, where v is the sound velocity and ν is the frequency of the lattice wave. The phonon frequency which is scattered by the nanograin is, $\omega = 2\pi n v/2d \sin \theta$. The lower value of the phonon frequency is obtained by taking $\sin \theta = 1$ as, $\omega_l = \pi v/d$ where v is the sound velocity, $v \approx 5 \times 10^5$ cm/s. For the frequency of $\nu = 10^{12}$ Hz, we get 5π nm for the particle size. The high frequency can be cutoff by replacing sine θ by an average value, $<\sin \theta> = 1/2$ so that the upper cutoff frequency becomes, $\omega_2 = 2\pi v/d$. Thus we have determined the range of frequencies introduced by the nanocrystal in addition to the usual phonon frequency spectrum in the bulk crystal. This type of phonon scattering within the nanocrystal may be called the "phonon confinement". The effect of such a scattering is to produce a particle size dependence in the specific heat[13].

In a harmonic oscillator, the displacement of an atom is given by,

$$\delta R = (\hbar/2M\omega_k)^{1/2}(a_k + a_{-k}^{\dagger}) \tag{1}$$

so that the phonon correlation factor becomes (2n+1) which gives the zero-point as well as the temperature dependent terms in the mean-square displacement (msd). Using the Debye cutoff frequency, we find,

$$<u^2> = 3\hbar\omega_D{}^2/(16\,\pi^2\rho v^3) + (3\hbar/2\pi^2\rho v^3)(k_B T/\hbar)^2 \int_o^X x(e^x-1)^{-1}dx \tag{2}$$

where ρ is the mass density. Therefore, the msd varies as T^2 at low temperatures in a three dimensional solid. In the case of scattering from the boundaries the msd for a nanocrystal is given by,

$$<u^2>_{nano}(0) = [3\hbar/(8\pi^2\rho_n v_n{}^3)](\omega_2{}^2 - \omega_l{}^2)\ . \tag{3}$$

We substitute the values of the two limiting frequencies from the above to obtain,

$$<u^2>_{nano}(0) = 9\hbar/(8\rho_n v_n d^2). \tag{4}$$

Therefore, for $v = v_n$, the above expression shows that the mean-square displacement of atoms is proportional to the inverse square of the nanoparticle size, d. The largest term in the temperature dependent contribution, added to the above expression gives the msd in the form,

$$<u^2>_{nano}(0) + <u^2>_{nano}(T) = a_1/d^2 + a_2(T/d)\exp\{-a_3/(Td)\} \quad (5)$$

where $a_1=9\hbar/8\rho_n v_n$, $a_2=3k_B v/2\pi\rho_n v_n^3$ and $a_3=\hbar\pi v/k_B$. This msd varies as $1/d^2$ at low temperatures and then there is a term of the form of $(T/d)\exp(-a_3/Td)$. Thus the particle size plays an important role at low temperatures. At high temperature, $x << 1$, so that the integral can be simplified and the msd becomes,

$$<u^2>_{nano}(0) + <u^2>_{nano}(T) = a_1/d^2 + a_4(T/d) \quad (6)$$

where $a_4 \approx 3k_B/2\pi\rho_n v_n^2$. Thus, the msd varies as $1/d^2$ and there is a temperature dependent term which varies as 1/d. If there is a gap in the phonon dispersion, ω_l works like a gap corresponding to lattice distortion at this frequency.

Melting point

We use Lindemann criterion to determine the melting temperature of a nanocrystal. It is assumed that the lattice melts when,

$$<u^2> = c\, a_o^2 \quad (7)$$

where a_o is the usual lattice constant and $c \approx 0.1$. We apply (7) to (6) so that by ignoring the quantum mechanical zero-point term, we obtain the melting point as,

$$T_{nm}= 0.1 a_o^2 d/a_4 \quad (8)$$

which means that the larger crystals have larger melting temperatures. Let us consider the zero-point contribution also. Then, by using the Lindemann criterion we obtain,

$$c a_o^2 - (a_1/d^2) = (a_4/d)T_{nm} \quad (9)$$

for the melting temperature of a nanocrystal. Now the value of T_{nm} is slightly reduced compared with the value given by (8). Whereas T_{nm} versus d is linear in (8), in (9) it is slightly bent from the linear behavior. This kind of linear dependence as well as bending predicted here from the surface scattering is in accord with the melting found experimentally in Si, Bi and CdS.

Recoilless fraction

The recoilless fraction is written as $f = \exp(-4\pi^2\langle u^2\rangle/\lambda^2)$ where λ is the wave length of the γ ray. The recoilless fraction in a nanocrystal is given by,

$$f= \exp[-4\pi^2(\langle u^2\rangle + \langle u^2\rangle_{nano})/\lambda^2] \tag{10}$$

which can be written as,

$$f = f_c f_n \tag{11}$$

where f_c is the value in a crystal and f_n in a nanocrystal. From (8) the above can be written as,

$$f= f_c f_n(0) f_n(T)\ . \tag{12}$$

When the frequency increases by means of extra scattering at the surface of the nanocrystal, we expect u^2 to increase compared with that in the crystal but the interpretation is nontrivial. The mass density in a nanocrystal is slightly smaller than in the bulk crystal. It is like a "negative pressure" in going from the bulk solid to a nanocrystal. In the study of specific heat it has been shown that there are new modes due to nanometer size of the particles. The application of this mode gives the correct interpretation of recoilless fraction in Au. Usually, the recoilless fraction is as given above eq.(10), and the mean-square displacement is $u^2=(\hbar/2M\omega)(2n+1)$. Considering only the n=0 term, the msd becomes $u^2(0) =(\hbar/2M\omega)$. The mode found in the nanocrystal has the frequency of $\omega= \pi v/d$. Substituting this value of the frequency in the mean square deviation gives $u^2(0)= (\hbar d/2M\pi v)$. The recoilless fraction now depends on d, the size of the crystal as,

$$f=\exp(-4\pi^2\hbar d/2M\pi v\lambda^2). \tag{13}$$

In this expression, smaller particles have larger f. This prediction is in agreement with the experimental observation of recoilless fraction in Au. This means that the vibrations at the frequency $\pi v/d$ play a dominant role in nanocrystals than the usual phonon continuum.

Thermal expansion. Usually a material expands due to anharmonic forces in the solid. The size of the unit cell is measured by using x-ray diffraction or a high resolution microscope as a function of temperature. As the temperature is increased, the unit cell expands. In the nanocrystals, there is a vibrational mode which depends on the size, d, of the crystal. The frequency of this mode is predicted to be about $\pi v/d$. It is of interest to study the effect of excitation of this mode on the unit cell size. As the system is warmed, at a particular temperature, the size dependent mode acquires sufficient population to dominate over the usual phonon continuum. Therefore, the thermal expansion of the unit cell switches from the phonon continuum to the size-dependent mode. This type of switching occurs at a particular temperature which may be called the "switching temperature" and hence detectable by x-ray measurements. We assume that there is no kinetic energy and hence the potential energy is given by,

$$U(x) = cx^2 - g\,x^3 - fx^4. \tag{14}$$

We suppose that the thermal expansion arises from the gx^3 type anharmonicity and ignore the x^4 type anharmonicity. The cx^2 is the usual harmonic potential. The thermal expansion is determined by,

$$\langle x\rangle = \int x\,dx\,\exp(-\beta U)/\int dx\,\exp(-\beta U) \tag{15}$$

where $\beta = 1/k_BT$. We assume that cx^2 is much larger than x^3 and x^4 type terms so that,

$$\langle x\rangle_{bulk} = (3g/4c^2)k_BT \tag{16}$$

which increases with increasing anharmonicity and reduces by increasing harmonic force constant. As the temperature is increased, the harmonic force in the frequency domain is described by $c = m\omega^2/2$ with frequency $\omega = \pi v/d$ where v is the sound velocity and d is the size of the nanocrystal,

$$\langle x\rangle = 3gk_BT/(m^2\omega^4). \tag{17}$$

If the nanograins are spherical, it is sufficient to use only one value of ω so that the above expression gives,

$$\langle x\rangle_{nano} = 3gd^4k_BT/(\pi^4v^4m^2) \tag{18}$$

which varies as d^4. As the temperature is increased the thermal expansion switches from $\langle x\rangle_{bulk}$ to $\langle x\rangle_{nano}$ so that there is a peak in $\langle x\rangle(T)$. At low temperatures $\langle x\rangle$ expands with increasing T with slope given by $\langle x\rangle_{bulk}$. At a particular temperature the surface mode becomes important and the slope of $\langle x\rangle_{bulk}$ becomes irrelevant and then the slope is determined by $\langle x\rangle_{nano}$. This means that dx/dT has a positive sign at low temperatures as well as at high temperatures but in the intermediate range of temperatures, it has negative sign so that there is "thermal contraction" in addition to "thermal expansion" at low and high temperatures. This thermal contraction is characteristic of the nanocrystals. This predicted behavior agrees with experimental observation of thermal contraction in Au nanoparticles.

3. Experimental Data

^{196}Pt is irradiated by neutrons to produce ^{197}Pt from which the neutron decay produces ^{197}Au which gives 77 keV γ ray with a half life of 18 h. The Moessbauer measurements of this γ ray have been performed by Marshall and Wilenzick [14] and more recently by Vieger and Trooster [15]. From these measurements it is obvious that smaller particles have larger recoilless fraction as predicted by eq.(13). The thermal expansion of Au particles of size 4 nm has been measured by Li et al[16]. The cell parameter is about 0.4067 nm at zero temperature. As the temperature is increased, it expands to 0.4081 nm at 125 K but it reduces as the temperature is further increased becoming about 0.4054 at 400K. This kind of thermal "contraction" can arise from two mechanisms of expansion if the system switches from one mechanism to another. Therefore, the data is consistent with the theory. It means that below 125 K usual phonon anharmonicity gives the thermal expansion but above this temperature the phonon mode with size dependent frequency becomes important.

4. Conclusions

We conclude that there are new phonon modes in nanocrystals which are related to the scattering at the surface. At low temperatures the usual lattice dynamics determines the lattice properties but at a particular temperature the system switches from the bulk dynamics to the surface dynamics. Therefore, the recoilless fraction is dominated by the particle size. Similarly, the thermal expansion is determined by the anharmonicity but above a particular temperature, switches to that from the surface anharmonicity which depends on the particle size.

References.

[1]. K. N. Shrivastava, J. Phys. C 19, L389 (1986).
[2] K. N. Shrivastava and S. K. Misra, Solid State Commun. 65, 597 (1988).
[3] K. N. Shrivastava, Phys. Stat. Solidi B 153, 547 (1989).
[4] L. S. Lingam and K. N. Shrivastava, J. Phys.: Condens. Mat 7, L 231 (1995).
[5] L. S. Lingam and K. N. Shrivastava, Mod. Phys. Lett. B 10, 1491 (1996).
[6] K. N. Shrivastava, Phys. Rev. B 1, 955 (1970).
[7] K. N. Shrivastava, Phys. Rev. B7, 921 (1973).
[8] K. N. Shrivastava, Phys. Rev. B 13, 2782 (1976).
[9] K. N. Shrivastava, Hyperfine Interact 24-26, 817 (1985).
[10] W. Potzel, A. Forster, J. Moser and G. M. Kalvius, Phys. Lett. A 88, 307 (1982).

[11] C. Schafer et al, Phys. Rev. B 37, 7247 (1988)
[12] Y. Wu, S. Pradhan and P. Boolchand, Phys. Rev. Lett. 67, 3184 (1991).
[13] K. N. Shrivastava, Nano Lett. 2, 21 (2002); 2, 519 (2002).
[14] S. W. Marshall and R. M. Wilenzick, Phys. Rev. Lett. 16, 219 (1966).
[15] M. P. A. Vieger and J. M. Trooster, Phys. Rev. B 15, 72 (1997).
[16] W. H. Li, S. Y. Wu, et al, Phys. Rev. Lett. 89, 135504 (2002).

INTRACLUSTER ANIONIC POLYMERIZATION INDUCED BY ELECTRON TRANSFER FROM ALKALI METAL ATOM TO UNSATURATED HYDROCARBON MOLECULES

HIRONORI TSUNOYAMA, KEIJIRO OHSHIMO, ARI FURUYA,
WAKANA NAKAGAWARA, FUMINORI MISAIZU[†], AND KOICHI OHNO

Department of Chemistry, Graduate School of Science, Tohoku University, Aramaki, Aoba-ku, Sendai 980-8578, Japan

Size dependent stability and intracluster reactions have been investigated by photoionization mass spectrometry for alkali metal atom M (M=Na, K, and Cs)-methyl propiolate (HC≡CCOOCH$_3$; MP) clusters. The cluster ions with n=3 were predominantly observed in the M$^+$(MP)$_n$ series. This intensity anomaly can be explained by a stable benzene derivative formation in intracluster anionic polymerization reaction induced by electron transfer from the metal. From the measurement of photoionization efficiency curves for Cs(MP)$_n$, two different ionization threshold energies were obtained for Cs(MP)$_3$. These two thresholds are concluded to correspond with the ionization energies of solvation type isomer and reaction product, from the results of quantum chemical calculations.

1. Introduction

In recent years, anionic polymerization of vinyl compounds in bulk solution has received much attention as a method to obtain various useful materials [1]. Additionally polymerization of acetylene derivatives have also been investigated in the past several decades concerning with conducting polymers [2]. It has been established that electron transfer from strong bases, such as alkali metal, initiates anionic polymerization of unsaturated hydrocarbons with electron withdrawing groups, such as cyano and carboxyl groups. A pair of negative ion of unsaturated hydrocarbon and its counter ion is expected to be produced in the initial step of anionic polymerization. In the bulk solution the ion pair is subsequently separated as a result of solvation. Then the ion pair and/or separated carbanion reacts with another monomer to produce a propagating species.

Intracluster ionic polymerization is regarded as a microscopic model of initial step in polymerization reaction in the condensed phase. Several groups have extensively investigated cluster anions [3] and cations [4-6] for the model of anionic and cationic polymerization, respectively. In the mass spectra of acetylene and methylacetylene cluster positive ions, magic number behavior at

---

[†] Electronic mail: misaizu@qpcrkk.chem.tohoku.ac.jp

n=3 was observed, and this behavior was explained by intracluster polymerization reaction producing benzene derivatives [4]. Similar cyclic compound formations were also investigated in acrylonitrile (CH_2=CHCN; AN) cluster negative ions [3] and alkali metal-AN clusters [7].

In the present paper, we have investigated clusters containing an alkali metal atom M (M=Na, K, and Cs) and methyl propiolate (HC≡CCOOCH$_3$, MP) molecules by photoionization mass spectrometry. Intracluster polymerization reaction induced by electron transfer from a metal atom to molecules were discussed from size distribution of obtained mass spectra and ionization threshold values for Cs(MP)$_n$ clusters.

2. Experimental Section

Details of the experimental setup have been described in previous publications [7]. Briefly, the system is composed of three-stage differentially evacuated chambers, which contain a cluster source and an angular-type reflectron time-of-flight mass spectrometer (TOF-MS). Clusters of alkali metal atom-MP clusters were generated by pick-up source [7,8] with a combination of pulsed supersonic expansion and two types of alkali metal atom sources. We used laser vaporization (for Na, and K) or a high temperature pulsed valve [9] (for Cs) as alkali metal source. Generated neutral clusters were collimated with a conical skimmer and were introduced to the acceleration region of TOF-MS. Clusters were then ionized by frequency-doubled output of a dye laser pumped by Nd:YAG laser. To avoid multiphoton processes the laser fluence was kept under4 mJ/cm^2 throughout measurements. Photoionized clusters were accelerated to ~3.0 keV by static electric fields. After traveling field-free region these ions were reflected back to an ion detector by reflection fields. The mass separated ions were detected by a dual microchannel plate and output signals were stored in a digital oscilloscope.

3. Results and Discussion

3.1. *Photoionization mass spectra*

Typical mass spectra of M(MP)$_n$ (M= Na, K, and Cs) ionized at 5.64-eV photon energy are shown in Fig. 1. A series of M$^+$(MP)$_n$ cluster ions were predominantly observed in the mass spectra. Additionally several side peaks assignable to M$^+$(MP)$_n$(H$_2$O)$_m$ ions were observed for Na and K systems, which are due to water impurity in MP sample. Ions of M(MP)$_3$ were more strongly observed than adjacent cluster sizes. This intensity anomaly was commonly observed at 4.9-5.6 eV photon energies. Another common feature is that fragment ions assignable to a loss of CH_2 from $M(MP)_n$ were mainly observed for n=2.

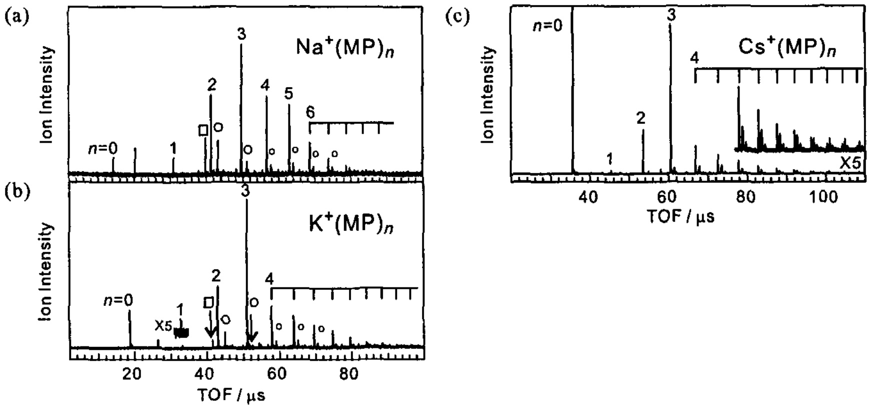

Figure 1. Typical photoionization mass spectra of (a) $Na(MP)_n$, (b) $K(MP)_n$, and (c) $Cs(MP)_n$ obtained by 5.64-eV laser irradiation. Cluster ions assigned to $M(MP)_n(H_2O)$ and fragment ions assignable to a loss of CH_2 from n=2 were denoted by circles and squares, respectively.

3.2. *Intensity anomaly at $M(MP)_3$*

There are three factors determining size distribution in photoionization mass spectrum of the metal atom-molecules clusters as discussed in a previous paper [7]: (1) Relative stability of neutral clusters depending on cluster size, n, (2) ionization efficiency of neutral clusters depending on n, and (3) evaporation processes after ionization. From the results of photoionization efficiency (PIE) curves shown below, ionization efficiency of clusters is expected to be almost independent of n at 5.64-eV photon energy. Intensity anomaly was also observed at 4.9-eV photon energy, which is less than 0.8 eV above the determined ionization thresholds for n=2 and 3, whereas binding energies between M^+ and MP were estimated to be 0.9-1.3 eV for M=Na and K from the quantum chemical calculations. Thus the evaporation processes after ionization do not contribute sensitively to the intensity enhancement. In addition, there was no intensity enhancement in a mass spectrum of $K^+(MP)_n$ produced by ion (K^+)-molecule (MP) reaction in the cluster source. We can assume that the photoionized clusters have different structures from the nascently produced ions. After all, intensity enhancement observed in the photoionization mass spectra is concluded to be due to relative stability of neutral clusters.

Next we discuss the possible structures of neutral $M(MP)_n$ clusters. Clusters consisting of a metal atom and solvent molecules have been extensively studied as a microscopic model for solvation in electrolyte solution [8,10,11]. These clusters are supposed to have solvation type structures, in which one metal atom is solvated by some solvent molecules, and relative stabilities of these clusters are expected to depend on the formation of solvation shell structures. These stabilities depend sensitively on the atomic radii of centered metal atoms. Same intensity enhancements were observed in all M-MP systems although three different metal atoms have different atomic radii (1.86 A for Na, 2.27 A for K, and 2.66 for Cs) [12]. Therefore the present intensity enhancement cannot be explained by the solvation structures. Clusters containing an alkali atom and unsaturated hydrocarbon with electron withdrawing groups can be regarded as a microscopic model for anionic polymerization as noted above. Intracluster anionic polymerization producing polymers with cyclic structure was investigated in alkali metal-vinyl compounds systems in our group [7]. This reaction is known to be induced by electron transfer from the metal atom to unsaturated hydrocarbons. From the results of quantum chemical calculations for M(MP) 1:1 complexes, electron transfer efficiently occurs in all M-MP systems. Methyl propiolate is also known to have reactivity towards anionic polymerization in bulk solution. Thus the reaction is also expected to proceed in the present cluster systems.

We subsequently consider the relative stability of the product in intracluster anionic polymerization. Polymerized products may have ring and/or linear structures with π-conjugated electrons in the present system. Relative stabilities of linear products are expected to change smoothly with cluster size *n* because their resonance energy and geometrical stability almost independent of *n*. However, stabilities of ring products depend sensitively on *n* because of their aromaticity. The ring product for *n*=3, benzene derivative, has more aromatic nature than adjacent *n* clusters. Thus it is expected that the benzene derivative is efficiently produced in intracluster anionic polymerization. After all we can conclude that the intensity enhancement at *n*=3 is due to intracluster anionic polymerization reaction producing benzene derivative (trimethyl 1,3,5-benzenetricarboxylate) [figure 2]. However we cannot exclude the possibility

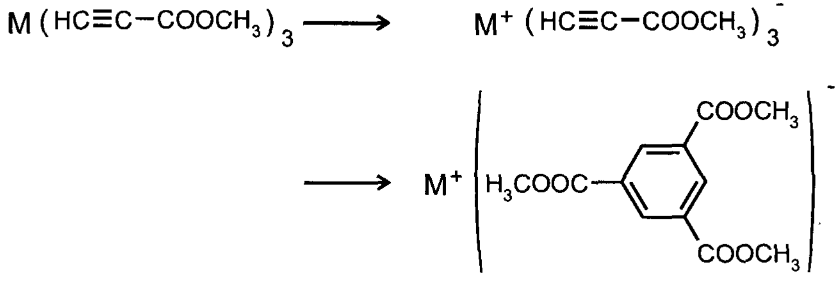

Figure 2. Intracluster anionic polymerization in M(MP)3 cluster (M=Na, K, and Cs)

that isomers having solvation structure coexist in $M(MP)_n$ clusters.

3.3. *Structural isomers of $M(MP)_3$*

Figure 3 shows PIE curves for $Cs(MP)_n$ (n=2 and 3). There were two rising steps in $Cs^+(MP)_3$ PIE curve, whereas that of $Cs^+(MP)_2$ showed monotonically increasing tendency with ionization laser energy. We have concluded that two ionization threshold energies (IE), 4.78 and 4.13 eV, correspond to two types of isomers of n=3 cluster as discussed below. From the consideration of intracluster reaction, we can assume that mainly two isomers coexist in $M(MP)_3$ cluster; one is unreacted, solvation-type isomer $M(MP)_3$ and another is reacted isomer M(trimethyl 1,3,5-benzenetricarboxylate). From the results of theoretical calculations for Na-MP clusters, we found that ionization energy of reacted isomer (4.25 eV) is 0.73 eV larger than solvation-type isomer (3.52 eV) at B3LYP/3-21G level.[‡] Same tendency was also obtained for the calculation of K-MP system. Furthermore, the energy difference between two IE values for $Cs(MP)_3$ in Fig. 3(b), 0.65 eV, is comparable with that of the two isomers calculated for $Na(MP)_3$. Thus the reacted isomer of $Cs(MP)_3$ is predicted to have a higher ionization threshold than unreacted isomer, although no quantitative data for the ionization energy of $Cs(MP)_3$ was available at present. Finally we can assign the IEs for the reacted isomer, Cs(trimethyl 1,3,5-benzenetricarboxylate), and for the solvation-type isomer, $Cs(MP)_3$ to be 4.78 eV and 4.13 eV, respectively. From these results, these two isomers are concluded to coexist in the $M(MP)_n$ clusters in the present experimental condition. In addition, the relative abundance of reacted isomer is found to be larger than that of unreacted one from the PIE measurement. Thus the intracluster anionic polymerization producing benzene derivative is suggested to proceed efficiently in M-MP systems.

[‡] We found two stable structures for Na(trimethyl 1,3,5-benzenetricarboxylate); (i) more symmetric structure in which sodium atom is located at on-top position of a benzene ring, (ii) less symmetric structure in which the sodium atom is positioned near one of carboxyl oxygen of benzene derivative. For the optimization of solvation type isomer, we start calculation from a more symmetric structure where each Na-MP portion has a similar structure to the most stable isomer of Na(MP) 1:1 complex [13].

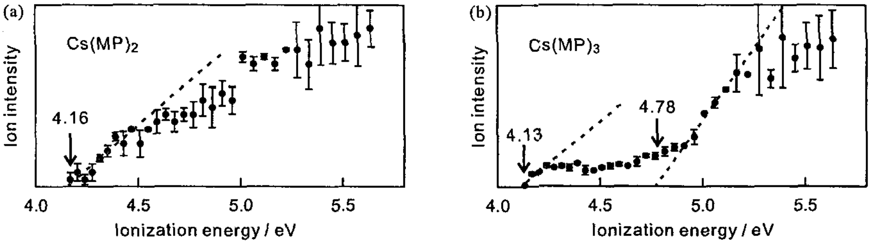

Figure 3. Photoionization efficiency curves of $Cs(MP)_n$ (a) for n=2 and (b) for n=3.

Acknowledgments

The authors thank to the Computer Center of the Institute for Molecular Science for the use of Fujitsu VPP5000 computer. This work has been supported in part by a Grant-in-Aid for Science Research from the Japanese Ministry of Education, Science, Sports and Culture. Financial support from Mitsubishi Foundation is also acknowledged. H. T. and K. Ohshimo are supported by the Research Fellowship of the Japanese Society for the Promotion of Science for Young Scientists.

References

1. T. E. Hogen-Esh and J. Smid, Recent Advances in Anionic Polymerization, Elsevier, New York (1987).
2. S. Patai (Ed), Supplement C2: The chemistry of triple-bonded functional groups, Wiley, Chichester, 1994.
3. T. Tsukuda and T. Kondow, *J. Am. Chem. Soc.* **116**, 9555 (1994).
4. M. T. Coolbasugh, S. G. Whitney, G. Vaidyanathan and J. F. Garvey, *J. Phys. Chem.* **96**, 9139 (1992).
5. J. F. Garvey, W. R. Peifer and M. T. Coolbasugh, *Acc. Chem. Res.* **24**, 49 (1991), and references theirin.
6. M. S. El-Shall and Z. Yu, *J. Am. Chem. Soc.* **118**, 13058 (1996).
7. K. Ohshimo, F. Misaizu and K. Ohno, *J. Chem. Phys.* **117**, 5209 (2002).
8. C. P. Schulz, R. Haugstatter, H. U. Tittes and I. V. Hertel, *Phys. Rev. Lett.* **57**, 1703 (1986).
9. M. Okunishi, K. Yamanouchi and S. Tsuchiya, *Chem. Lett.* 393 (1989).
10. C. P. Schultz and I. V. Hertel, In Clusters of Atoms and Molecules II, H. Haberland (Ed) Springer-Verlag, Berlin-Heidelberg (1994).
11. K. Fuke, K. Hashimoto and S. Iwata, *Adv. Chem. Phys.* **110**, 431 (1999).
12. J. Emsley, The Elements, 3rd ed. Oxford University Press, New York (1998).
13. H. Tsunoyama, K. Ohshimo, F. Misaizu and K. Ohno, *Int. J. Mass. Spectrom.* submitted.

DYNAMICS OF GAS PHASE OLIGONUCLEOTIDES

ALLISON S. DANELL, RYAN M. DANELL, JOEL H. PARKS
Rowland Institute at Harvard, 100 Edwin H. Land Boulevard, Cambridge, MA 02142, USA

The dynamics of biomolecule conformations in gas phase have been studied by applying methods which measure laser-induced fluorescence from trapped ions. The fraying of duplex terminal base pairs has been identified by measuring the donor fluorescence as a function of temperature from an oligonucleotide duplex labeled with a pair of FRET dyes. The degree of end terminal fraying observed for 14-mer duplexes is consistent with gas phase calculations. During these studies, the autodetachment of electrons from double- and single-stranded oligonucleotide anions was observed. This process is not observed to occur for oligonucleotides in solution phase and it is important to understand how it impacts the interpretation of gas phase dynamics. A strong dependence of the autodetachment rate on base composition has been identified. FRET measurements were performed as a function of charge state to measure the relative extension of the single strands as a function of charge state and were consistent with preliminary calculations of the single strand conformation. Finally, the redesigned optical apparatus and CW laser excitation will be discussed. The capability to obtain fluorescence data from a single trapped ion will be demonstrated.

1. Introduction

Ion trap instrumentation developed in our laboratory[1] has been used to carry out fluorescence measurements of trapped ions, and recently has been used to measure fluorescence resonance energy transfer (FRET) in trapped oligonucleotide ions.[2, 3] The extension of FRET methods from solution studies[4] to gas phase studies provides the opportunity to *directly* correlate changes in fluorescence intensity with changes in the average conformation of biomolecules. The combination of mass spectrometry with fluorescence will allow the differentiation between fluorescence changes caused by conformational change and those caused by dissociation or fragmentation. As will be shown in section 2.2, this capability not only helps to clarify data interpretation, but also helps the association of oligonucleotide fragmentation patterns with conformation.

These experimental methods have exploited the ability to store ions for long periods at thermal equilibrium. As shown in Section B.3, this capability has led to the surprising observation that electrons on multiply charged oligonucleotide anions undergo sequential autodetachment in gas phase. Initial analysis suggests that the autodetachment process is related to fluctuations of the oligonucleotide conformation.

2. Experiments

2.1. *Experimental Setup*

Unmodified, desalted oligonucleotides were obtained commercially (Synthegen Modified Oligonucleotides, Houston, TX). Solutions were prepared of 5 to 10 μM in 70/20/10 Methanol/Water/Trifluoroethanol. Oligonucleotides derivatized with fluorophore molecules were obtained commercially (Synthegen). The donor fluorophore was BODIPY-Tetramethylrhodamine (BODIPY-TMR) and the acceptor fluorophore was BODIPY-Texas Red (BODIPY-TR) (Molecular Probes, Eugene, OR). Measurements of BODIPY-TMR and BODIPY-TR displayed minimal spectral change with solvent polarity and <10% change in relative quantum yields with increasing temperature up to 60°C.[2] Structures and absorption and emission data for the BODIPY fluorophores are available elsewhere.[2,5] The sequences obtained were BODIPY-TR-5'-AAAAAAAGGCCGGC-3' and 5'-GCCGGCCTTTTTTT-3'-BODIPY-TMR. To form the oligonucleotide duplexes, the complementary single strands were combined at a concentration of 50μM in a 50mM ammonium acetate solution and annealed for 8 min. at ~ 90°C. Final concentrations for these nESI solutions of derivatized, annealed oligonucleotides were 5 to 10 μM in 50/50 methanol/water or 60/20/20 acetonitrile/isopropyl alcohol/water.

Experiments were conducted in a custom-built quadrupole ion trap described previously.[1] The trap electrodes and He gas inlet are seated in a copper housing which is resistively heated up to a maximum temperature of 170°C (Model 965 temperature controller, Watlow) with a temperature precision of ~1 °C. The He bath gas pressure was ~0.4 mTorr and was pulsed to ~1 mTorr before loading ions into the ion trap. Isolated parent ions were held in the ion trap for a variable time period, and all ions were ejected at q_z =0.908 and detected. A residual gas analyzer (Quadrex 200, Leybold, Export, PA) also is mounted on the vacuum system for detection of very low *m/z* species.

Fluorescence analysis in the quadrupole ion trap has been described in detail previously.[1] The bandpass filter used for these experiments passes wavelengths 535 to 580 nm, corresponding to the donor fluorescence bandwidth.[2] Thus, only the donor fluorescence was detected.

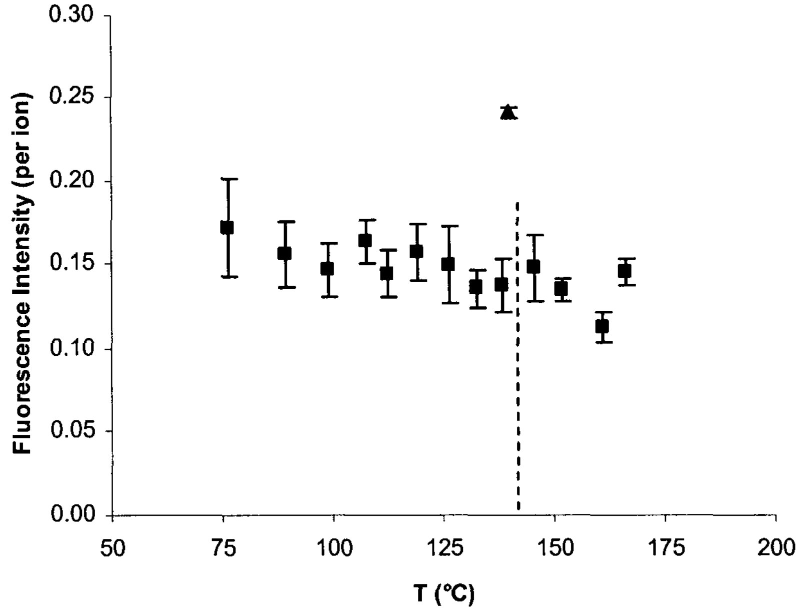

Figure 1. (■) Donor fluorescence intensity from the 7- charge state of the duplex BODIPY-TR-5'-AAAAAAAGGCCGGC-3' and 5'-GCCGGCCTTTTTTT-3'-BODIPY-TMR. Error bars represent standard deviation for triplicate measurements. At temperatures above the dashed line, fragment ions appeared in the mass spectrum acquired at the end of the 90 s irradiation periods. (▲) Donor fluorescence intensity from the 6- charge state of 5'-GCCGGCCTTTTTTT-3'-BODIPY-TMR.

2.2. *Fraying Dynamics*

FRET measurements of the distances between the fluorophores conjugated to the strands of a 14-mer duplex, BODIPY-TMR-5'-AATTAATCCGGCCG-3' and 5'-CGGCCGGATTAATT-3'-BODIPY-TR, have been found to correlate with the thermal dissociation pattern.[3] When the 7- charge state ions of another 14-mer duplex, BODIPY-TR-5'-AAAAAAAGGCCGGC-3' and 5'-GCCGGCCTTTTTTT-3'-BODIPY-TMR, were isolated and irradiated for 90 s periods as a function of temperature, the separation between the fluorophores was found to be constant. This is demonstrated in Fig. 1, in which the fluorescence intensity per ion obtained from fluorescence measurements is plotted as a function of temperature. The fluorescence intensity at ~ 140°C from a single-strand labeled with the TMR donor is also shown in Fig. 1. This intensity is taken to be constant over the entire temperature range since it has been observed that BODIPY-TMR quantum yields do not vary significantly as a function of temperature.[2]

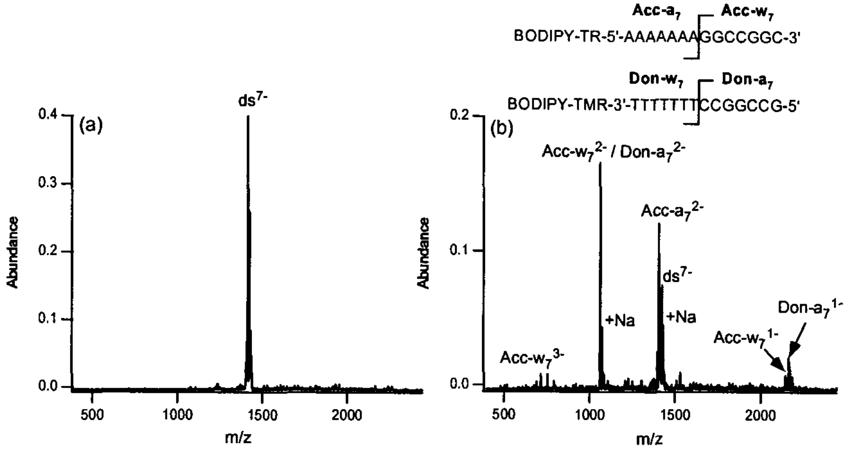

Figure 2. Thermal dissociation spectrum of the 7- charge state of the duplex BODIPY-TR-5' AAAAAAAGGCCGGC-3' and 5'-GCCGGCCTTTTTTT-3'-BODIPY-TMR after 20 min. heating at 160°C.

The 7- duplex ions reached the fragmentation threshold for 90 s heating periods at 140°C (dashed vertical line). Above this threshold, it is observed that all fragment ions are due to cleavage of bonds between the A-T portion and G-C portion of the oligonucleotides, i.e. the formation of 7-mer strands. The isolated mass spectrum is shown in Fig. 2(a) and the MS/MS spectrum is shown in Fig. 2(b), in which the peaks are identified as noted in the inset.

Based on the donor fluorescence intensities shown in Fig. 2 and assuming a Förster distance of ~52Å based on solution phase measurements,[6] the ensemble averaged separation between the fluorophores was estimated to be ~ 55Å.[3] If the duplex were to adopt a conformation in which only the G-C portion of the sequences were paired, the maximum distance between the fluorophores would ~ 60Å, which is sufficiently close to the distance (~ 55Å) estimated from fluorescence to conclude that the A-T section of the duplex is almost completely unpaired. Both the estimated fluorophore separation, as well as the fragmentation of the duplex between the A-T and G-C segments, support the conclusion that the distance between the fluorophores is large over the entire temperature range studied in the gas phase. The mass spectra acquired at the end of each irradiation period were crucial to verify that the duplex ions were intact, and that the distance between the fluorophores arose from the fraying of the A-T bonds.

Molecular dynamics simulations of 12-mer and 16-mer DNA have recently been performed[7] to investigate conformations both for gas phase and solution phase environments. In these simulations, A-T bonds are broken when water is removed but G-C bonds remain intact. This is consistent with our FRET measurements which imply that all the A-T bonds are broken in gas phase, and also with hydration studies[8] which found that A-T base pairs take up more water than G-C base pairs on formation. It has been shown by X-ray and NMR studies[9-13] that water molecules form an ordered structure in the minor groove of A-T base pairs in contrast to G-C base pairs. If these water molecules are important for the stability of A-T base pairs in solution, then the instability relative to G-C pairs observed in these gas phase experiments would be expected.

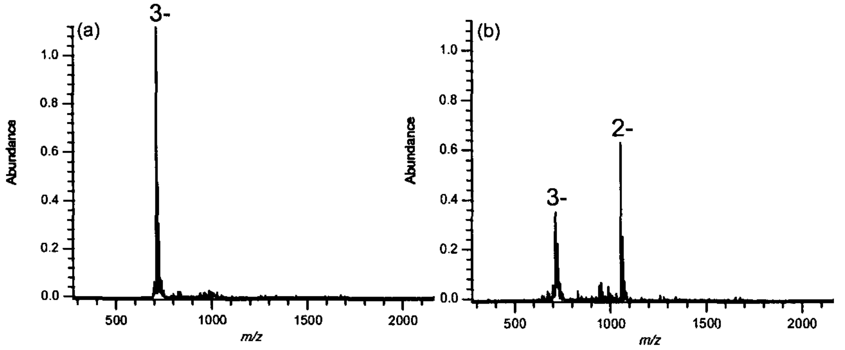

Figure 3. Mass spectra of A_7 at various heating times at 102°C. (a) 0 s (isolation of 3- charge state); (b) 240 s.

2.3. *Electron Autodetachment*

The conversion of a single isolated charge state, M^{n-}, of double-stranded oligonucleotides to the next lowest charge state, $M^{(n-1)-}$, was observed when ions were held in the ion trap under the heating and temporal conditions used in the FRET measurements.[3] The charge loss phenomenon also was found to occur for underivatized oligonucleotides.[3] Fig. 3 shows an example of the charge loss from $(A_7)^{3-}$. The isolation of $(A_7)^{3-}$ is shown in Fig. 3(a), and the resulting spectrum acquired after holding $(A_7)^{3-}$ in the ion trap for 240 s at 102°C is shown in Fig. 3(b). The two mass spectra in Fig. 3 are plotted on the same absolute intensity scale. Thus, the ion population is conserved during the change in charge state population, which negates the possibility of additional fragment ions appearing outside the detected m/z range.

We have attributed the charge loss phenomenon to electron autodetachment. Several pieces of evidence support this conclusion: (1) The deconvoluted mass spectra display no evidence of change in molecular weight for the newly formed lower charge state ions. (2) No additional fragment ions appear in the mass spectrum that could be a result of an electron-abstraction or other ion-molecule reaction involving the higher charge state ion of the oligonucleotide. (3) Residual gas analyzer measurements showed no presence of hydrocarbons up to 200 amu in the vacuum system, and no significant changes in background gas pressures (CH_2/N, CO/N_2, O_2) at room and elevated temperatures.

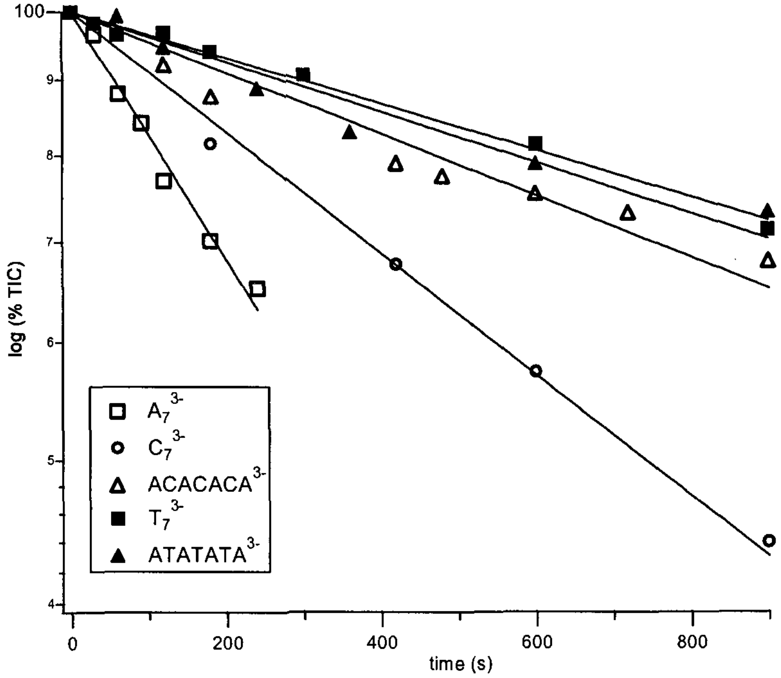

Figure 4. Change in ion intensities of 3- charge states of 7-mers as a function of heating time at 102°C. Solid lines are curves fitted to data.

The rates of electron autodetachment were determined for $(A_7)^{3-}$, $(T_7)^{3-}$, $(ATATATA)^{3-}$, $(ACACACA)^{3-}$, and $(C_7)^{3-}$. Fig. 4 shows the decrease in the percent total ion current (plotted as log %TIC) for these 7-mers as a function of the time the ions were held in the ion trap at 102°C at $q_z = 0.38$. The electron autodetachment rates for the five 7- mers analyzed were determined over the temperature range 102 ~ 150°C, and also were observed to vary as a function of the oligonucleotide sequence.

Fig. 5 shows that different charge states and different base compositions display Arrhenius plots having similar slopes. The linear fits of these data yield enthalpy barriers for electron loss of ΔH ~ 0.95 to 1.05 eV. The more significant variation in the temperature dependence of the rates appears to be determined by the entropic contribution related to the intercepts in Fig. 5. The Arrhenius prefactors for different sequences derived from the intercepts are $1.2\text{x}10^{11}$ s^{-1} for ATATATA; $1.6\text{x}10^{12}$ s^{-1} for A_7; $9.7\text{x}10^{12}$ s^{-1} for T_7; $8.7\text{x}10^{13}$ s^{-1} for C_7; $1.8\text{x}10^{15}$ s^{-1} for ACACACA.

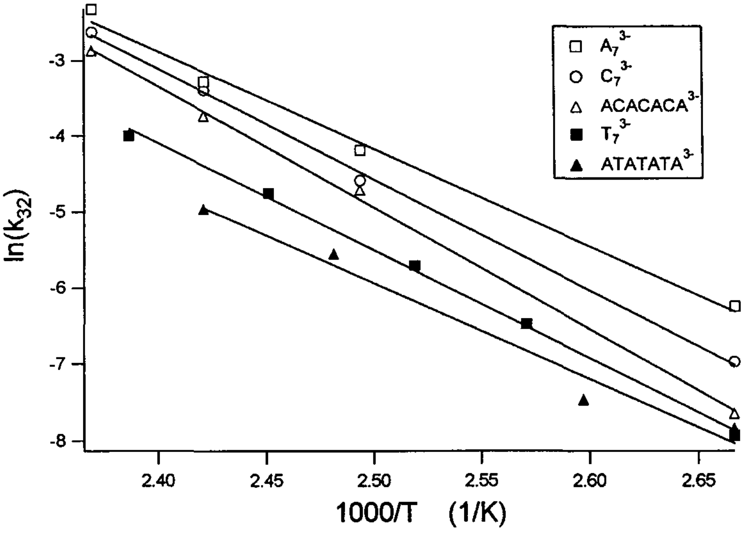

Figure 5. Rates of electron autodetachment of 3- charge state of 7-mers as a function of temperature.

The observed similarity of the barrier for different base compositions could be related to the vibronic state dynamics of the phosphates. A preliminary DFT calculation[14] of the electronic charge distribution of a charged poly(A)-poly(T) duplex indicates that the electronic charges are localized on the phosphates. Assuming this localization occurs for single-strand oligonucleotides, the phosphate anions will then be common to the detachment process independent of charge state and base composition. The similarity of the slopes for different base sequences could then be associated with the phosphate moiety of the nucleotide. It is interesting to note that the rates derived from the prefactors show much greater variation. This suggests that the phase space pathways to the transition state for electron loss may rely on the molecular dynamics of a greater portion of the oligonucleotide than simply the phosphate.

Experimental measurements of electron auto-detachment processes have been carried out for small organic molecules[15-18] and atomic clusters[19, 20] Theoretical calculations of the non-adiabatic processes associated with electronic curve-crossings[21-23] have been applied to describe the transfer of vibration to electronic energy in these smaller molecules. The electron auto-detachment from single strand oligonucleotides presumably involves similar vibration to electronic transfer processes. The thermal excitation of higher vibrational states of the phosphate anion would increase the rate of electron loss consistent with the observed temperature dependence, assuming the non-adiabatic curve crossing associated with the detachment transition occurs at higher vibrational levels.

Photoelectron spectroscopy studies of small, multiply charged anions have measured[24] the electron detachment energies. In contrast to these rigid molecules, the oligonucleotide structure for a single strand can be quite flexible depending on the charge state, temperature and base composition. This flexibility increases the probability that structure fluctuations could reduce a charge pair separation sufficiently for Coulomb repulsion to eject an electron. Preliminary molecular dynamics simulations[25] have indicated the single strand structure can vary from linear to globular conformations depending on the distribution of charges on the phosphates.

Although the electron affinity of the phosphate group is approximately 5 eV, from measurements[26] and calculations[27] of the dihydrogen phosphate anion, in the presence of reduced charge separations the detachment energy can be significantly lowered as a result of increased Coulomb repulsive forces. This suggests that the electron auto-detachment of a multiply charged oligonucleotide anion is correlated with conformation by comparing auto-detachment data with the predicted structures derived from molecular dynamic simulations.

Data have been obtained for the dependence of the FRET donor fluorescence on charge state by attaching fluorophores to the end termini of the single strand 14-mer sequence BODIPY-TMR-5'-T_{14}-3'- BODIPY-TR. These results, shown in Fig. 6, include large fluctuations but indicate that the fluorescence increases with charge state from 2- to 6- as might be expected to result from increased Coulomb repulsive forces acting to increase the distance between termini. These data reinforce the conformation dependence on charge state which will be the basis for further investigations.

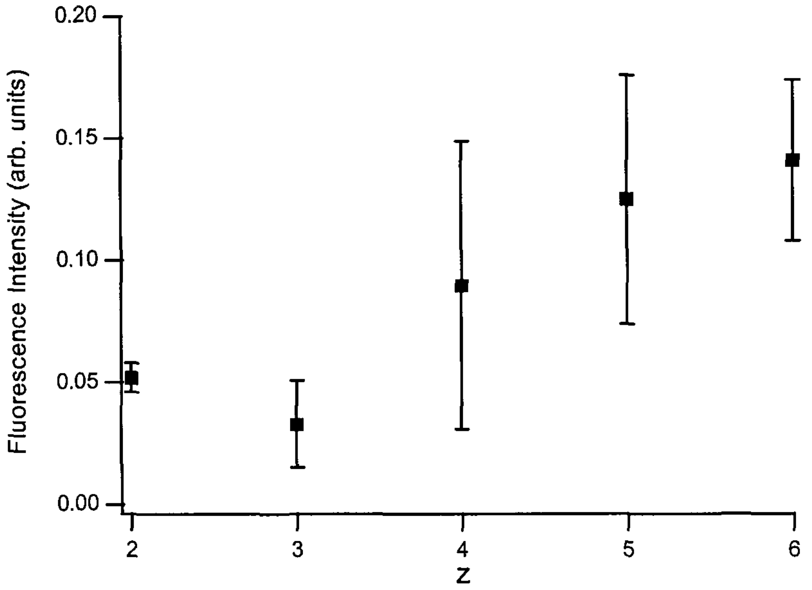

Figure 6. Donor fluorescence intensities from BODIPY-TMR-5'-T_{14}-3'-BODIPY-TR as a function of charge state. Error bars represent standard deviations for triplicate measurements.

Calculations are underway to investigate the autodetachment process: (a) extensive molecular dynamic simulations[28] to determine the distribution of charge separations for the oligonucleotides at relevant temperatures; and (b) applying the simulation results to estimate the Coulomb interactions and the charge-induced perturbations of the phosphate electronic states leading to detachment;[25] and (c) DFT calculations to determine the character of charge localization on partially charged single strands.

3. New Experimental Apparatus

3.1. *Laser Optics*

The new fluorescence excitation and detection apparatus is shown in Fig. 7(a). The excitation laser (Spectra Physics Millenia Vis-J series) is a diode pumped device that delivers a Gaussian beam of up to 6 W at 532 nm in a beamwidth of ~2.3 mm. The beam expander (Special Optics) and 50 cm focal length lens produces a beamwidth which can be varied over the range 50 - 400 μm. The Rayleigh range (~2 - 5 cm) is much greater than the ion cloud dimension

(<1mm). These beam properties will be sufficient to excite the trapped ion cloud with an intensity distribution whose interaction volume can be reliably modeled in the fluorescence analysis. The positioning of several iris apertures along the laser path which are required to reduce the laser forward scattering from the various optical elements. Data control and acquisition are accomplished by a computer system using LabView software which controls ion trap operation and synchronizes the fluorescence detection.

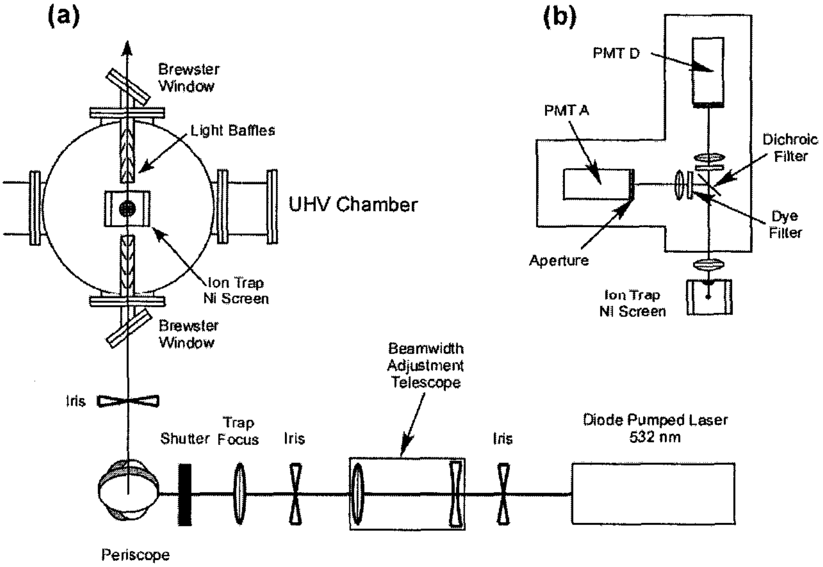

Figure 7. Diagram of the improved optics components which focus the laser through the trapped ion cloud. The laser is linearly polarized in the plane of the drawing.

3.2. *Two Channel Fluorescence Detection*

Fig. 7(b) shows a schematic of the detection optics and detectors. The fluorescence is collected by a 25mm dia. triplet lens close coupled to the trap but external to the UHV system. The dichroic beam splitter and dye filters (Chroma) in each channel were designed to optimally isolate the fluorescence bandwiths of the FRET donor and the acceptor dyes. Each filter attenuates scattered background at the laser wavelength by a factor of $\leq 5 \times 10^{-5}$. The doublet lenses (f = 95 mm) after the beam splitter focuses the fluorescence onto a 1 mm diameter pinhole before the photomultiplier. The focused fluorescence spotsize depends on the ion cloud size but will be ≤ 0.5 mm diameter. These optics will collect fluorescence within a solid angle of $\delta\Omega = 0.6$ st and focus the fluorescence well within the pinhole diameter.

The new collection optics were optimized using the ZEMAX lens design program (Focus Software Inc.). The triplet collection lens and the doublet focusing lenses are the principle aberration producing elements. This system will focus an ion cloud of 0.3 mm diameter. The GaAs photomultiplier (Hammamatsu H7421) has a detector surface of 5 mm diameter and a Quantum Efficiency of ≥40% at both donor and acceptor bandwiths. These detectors operate in pulse counting mode providing an output of TTL pulses to counting boards (National Instruments PCI-6602). A dedicated computer running LabView software synchronously processes and stores pulse counts for both the donor and acceptor fluorescence channels for subsequent data reduction and analysis.

3.3. *FRET Fluorescence Measurements*

Initial measurements of the fluorescence from Rhodamine 640 ions were performed to evaluate the laser background scattering detected by the new collection optics and the detection electronics (without the use of the new cylindrical trap). Although the dielectric filters were not optimized for the Rhodamine 640 fluorescence band, these measurements provide an important preliminary evaluation of the sensitivity and laser background scattering. The results of these measurements are displayed in Fig. 8 which plots the detected counts per second (CPS) as a function of the number of interacting ions. The number of ions in the trapped cloud which interact with the Gaussian beam cross section are derived from a calculation of the ion trajectories. This simulation includes both ion-neutral and ion-ion collisions and is performed for the experimental trapping parameters and the total ion number detected. The number of ions interacting with a Gaussian beam propagating in the x direction is given by

$$\langle N \rangle_{\text{inter}} = \left\langle \sum_{1}^{N} \exp[-(y_i^2 + z_i^2)/\sigma^2] \right\rangle_T \tag{1}$$

where $y_i(t)$ and $z_i(t)$ are the trajectory positions at time t, σ is the halfwidth at $1/e^2$, N is the total number of trapped ions and the sum is averaged over total simulation time T. Measurements shown in Fig. 8 were obtained for a laser power of 100 mW and $\sigma = 238\mu$m.

The data shown in Fig. 8 exhibit two important results. The FRET fluorescence sensitivity can be extended to single or few ion measurements. The background is low (~50±3 CPS) and adds insignificantly to the fluorescence standard deviation. The signal to noise ratio is S/N~5 for $<N>_{inter} \geq 4$. These results demonstrate that FRET measurements can be obtained for sufficiently few ions ($<N>_{inter} < 5$) to minimize the effects of ensemble averaging. In particular, $<N>_{inter} \approx 1$ will be required to identify intermediate conformation states by analyzing the transfer efficiency.[29-31]

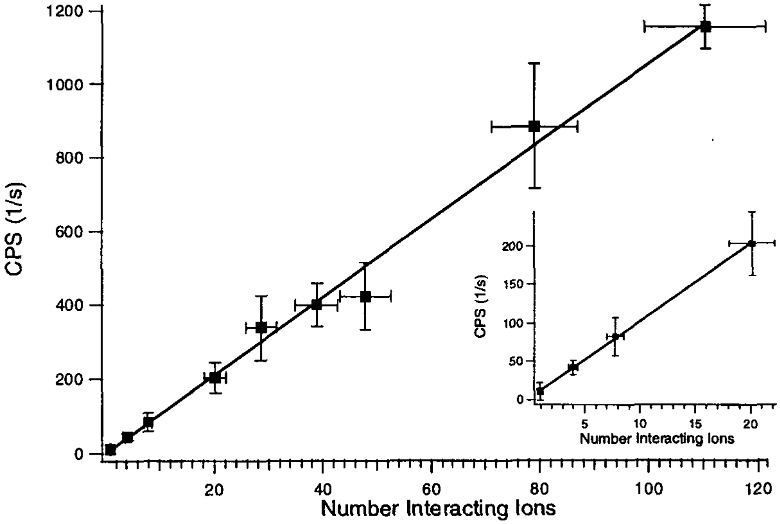

Figure 8. The fluorescence signal counts per second (CPS) corrected for background vs the number of interacting ions within the laser beamwidth. Solid lines are linear fits to the data (solid squares).

4. Experimental Plans

This research will investigate the opening dynamics as a function of temperature for sequences which avoid the ambiguities introduced by fragmentation. In addition to the ratiometric FRET analysis, the rate equation model[2] can be used to extract an equilibrium constant for the opening dynamics. The 14-mer duplex composed of AAAAAAAGGCCGGC and its complement exhibited broken A-T bonds at all temperatures which suggests the possibility that hydration may be an interesting experiment. Are these bonds still open with water hydrating the oligonucleotide? Finally the 16-mer duplex which has been calculated to significantly elongate in vacuum[7] is a candidate for FRET analysis of the presence of such predicted behavior.

Continued study of electron auto-detachment in multicharged oligonucleotide anions is planned to establish a basis for the dependence on base composition and sequence and understand the degree to which conformation fluctuations play a role. Molecular dynamics simulations and electronic curve crossing calculations of the phosphate anion will continue in collaborations underway.

Acknowledgments

This work has been funded by an NSF (CHE-0304359) and The Rowland Institute at Harvard. J.H.P. thanks Tom Cheatham, Jack Simons and James Lewis for discussions and calculations which have helped formulate an understanding of the electron auto-detachment process.

References

1. Khoury, J. T.; Rodriguez-Cruz, S. E.; Parks, J. H. *J. Am. Soc. Mass Spectrom.* **2002**, *13*, 696-708.
2. Danell, A. S.; Parks, J. H. *Int. J. Mass Spectrom.* **2003**, *229*, 35-45.
3. Danell, A. S.; Parks, J. H. *J. Am. Soc. Mass Spectrom.* **2003**, *14*, 1330-1339.
4. Selvin, P. R. *Nature Struct. Biol.* **2000**, *7*, 730-734.
5. Molecular Probes website, accessed May, **2003**.
6. Ha, T.; Enderle, T.; Ogletree, D. F.; Chemla, D. S.; Selvin, P. R.; Weiss, S. *Proc. Natl. Acad. Sci.* **1996**, *93*, 6264-6268.
7. Rueda, M.; Kalko, S. G.; Luque, J.; Orozco, M. *J. Am. Chem. Soc.* **2003**, *125*, 8007-8014.
8. Kankia, B. I.; Marky, L. A. *J. Phys. Chem. B.* **1999**, *103*, 8759-8767.
9. Drew, H. R.; Dickerson, R. E. *J. Mol. Biol.* **1981**, *151*, 535-536.
10. Kopka, M. L.; Fratini, A. V.; Drew, H. R.; Dickerson, R. E. *J. Mol. Biol.* **1983**, *163*, 129-146.
11. Alexeev, D. G.; Lipanov, A. A.; Skuratovskii, I. Y. *Nature.* **1987**, *325*, 821-823.
12. Kubinec, M. G.; Wemmer, D. E. *J. Am. Chem. Soc.* **1992**, *114*, 8739-8740.
13. Shui, X.; McFail-Isom, L.; Hu, G. G.; Williams, L. D. *Biochemistry* **1998**, *37*, 8341-8355.
14. Lewis, J. **2003**.
15. Foster, R. F.; Tumas, W.; Brauman, J. I. *J. Chem. Phys.* **1983**, *79*, 4644-4646.
16. Meyer, F. K.; Jasinski, J. M.; Rosenfeld, R. N.; Brauman, J. I. *J. Am. Chem. Soc.* **1982**, *104*, 663-667.

17. Woodin, R. L.; Foster, M. S.; Beauchamp, J. L. *J. Chem. Phys.* **1980**, *72*, 4223-4227.
18. Wight, C. A.; Beauchamp, J. L. *J. Am. Chem. Soc.* **1981**, *103*, 6499-6501.
19. Amrein, A.; Simpson, R.; Hackett, P. *J. Chem. Phys.* **1991**, *95*, 1781-1800.
20. Amrein, A.; Simpson, R.; Hackett, P. *J. Chem. Phys.* **1991**, *94*, 4663-4664.
21. Clary, D. C. *Phys. Rev. A.* **1989**, *40*, 4392-4399.
22. Acharya, P. K.; Kendall, R. A.; Simons, J. *J. Am. Chem. Soc.* **1984**, *106*, 3402-3407.
23. Simons, J. *J. Am. Chem. Soc.* **1981**, *103*, 3971-3976.
24. Wang, L.-S.; Wang, X.-B. *J. Phys. Chem. A.* **2000**, *104*, 1978-1990.
25. Simons, J., Personal Communication, **2003**.
26. Wang, X.-B.; Vorpagel, E. R.; Yang, X.; Wang, L.-S. *J. Phys. Chem. A.* **2001**, *105*, 10468-10474.
27. Kuo, I.-F.; Tobias, D. J. *J. Phys. Chem. B.* **2001**, *105*, 5827-5832.
28. Cheatham III, T. E., Personal Communication, **2003**.
29. Dahan, M.; Deniz, A. A.; Ha, T.; Chemla, D. S.; Schultz, P. G.; Weiss, S. *Chem. Phys.* **1999**, *247*, 85-106.
30. Ying, L.; Wallace, M. I.; Balasubramanian, S.; Klenerman, D. *J. Phys. Chem. B.* **2000**, *104*, 5171-5178.
31. Deniz, A. A.; Dahan, M.; Grunwell, J. R.; Ha, T.; Faulhaber, A. E.; Chemla, D. S.; Weiss, S.; Schultz, P. G. *Proc. Natl. Acad. Sci.* **1999**, *96*, 3670-3675.

THEORETICAL AND EXPERIMENTAL ASPECTS ON TRAPPING AND DETECTION OF SINGLE AND FEW MOLECULES BY USING NANOPROBES

M. WILLANDER, Z. CHIRAGWANDI, E. MAMOMTOV, O. NUR, N. CALANDER,
Physical Electronics and Photonics, Department of Physics and Engineering Physics,
Gothenburg University and Chalmers University of Technology
SE-412 96 Gothenburg, Sweden

RALPH HÖLZEL AND FRANK F. BIER
Fraunhofer-Group of Medical Biotechnology, Department of Molecular Bioanalyticaly
and Bioelectronics, Bergholz-Rehbruke, Germany

Here we give our recent results on optical trapping and electrical trapping of molecules in water. We show particularly the electrical trapping in a structure we call the water transistor. Water transistor is characterized in itself. Finally we briefly discuss transport of particles in an aqueous solution.

1. Introduction

Trapping and detection of small molecules in aqueous solutions has attracted a lot of interest recently. Here we start with brief theoretical discussion of trapping and sensing single molecules using sharp metal particles or electrodes with application to intercellular probe and lab on a chip technology. Then we continue with showing experimental results using a very sharp electrode which makes it possible to make single molecule trapping in aqueous solutions. Using dielectric forces and the so called water transistor a new sort of nano-chemistry is made possible. An important part is also the diffusion of molecules in a small water volume. We finalize by summing up our results in this field.

2. Optical Trapping in Aqueous Solutions

A classical approach has been compared to a quantum mechanical model for trapping molecules [1]. Unfortunately the quantum mechanical approach, which is the most realistic, shows the poorest trapping potential. Still, there is trapping, and the force can be either attractive or repulsive depending on the wavelength. The trapping potential is not very precise in frequency in the quantum mechanical approach.

Figure 1 shows the principal behavior of the probing. A molecule is attracted and trapped to the hot spot, where its properties are monitored, using SER(R)S or single molecule fluorescence spectroscopy. When done, the molecule is disposed by repulsive optical forces by changing the optical frequency.

Probes of the kind described above, could be introduced into cells, to perform intracellular proteomics displays, see Fig.2. The probe could be controlled by optical tweezers. The tweezing capacity is enhanced by the plasmon resonance.

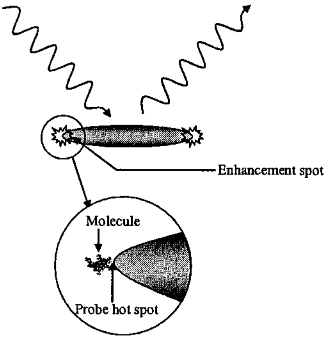

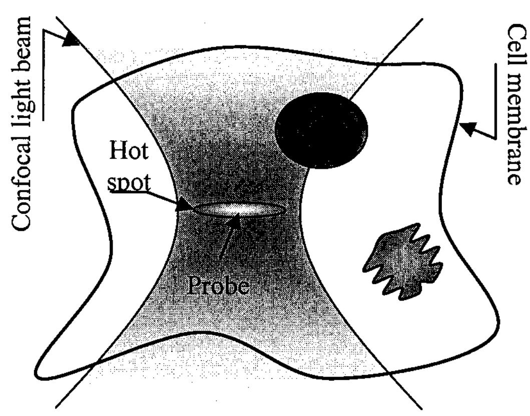

Figure 1 (left): Molecules are attracted and trapped at the hot spots of the surface plasmon resonant particle, when illuminated. By changing the frequency, repulsive forces are achieved, and the molecule is disposed.

Figure 2 (right): The probe is trapped by the strongly focused light beam of the optical tweezers. The cell is surveyed by the probe, of resonant (fluorescent) molecules.

Molecules are attracted and trapped to the hot spots, and disposed by changing the frequency such that repulsive forces are achieved. In this way the cell is surveyed by the optical probe. The molecules could either be natural fluorophores, or tagged by fluorescent probes.

Figure 5 (see section below) shows four electrodes for electrical and optical manipulation and analysis of single molecules. The local pH is controlled by other electrodes nearby. The electrodes also act as antennas, by enhancing the optical field in between, by the plasmon resonance. The optical enhancement between the electrodes should be possible to optimize considerably because the treatment above is limited to the prolate spheroidal structure only, and here we could have a narrow gap between the electrodes. The parameters used to optimize/tune the capture; manipulation and analysis of the single molecule are the geometry of the electrodes, the frequency of the optical field, the polarization, the angle of incidence, and the low-frequency electrical signals across the electrodes, and the pH.

When captured to the most sensitive spot at the nanoelectrodes, the single molecule could be analyzed by using the optical field enhancement for SE(R)RS measurements. The Raman spectrum is rather detailed and lots of information can be gained. After the analysis, the molecule can be disposed by repulsive optical forces, by changing the frequency, and a new molecule can be attracted.

- 3. Trapping of molecules in aqueous solutions by dielectric forces

Spatial manipulation of objects in the micrometer scale by AC elektrokinetics is well established [2-4]. In an inhomogeneous electric field (Fig. 3), polarizable particles experience a lateral force towards the regions of highest field strength.

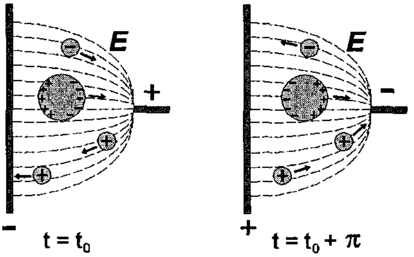

Figure 3: Basic mechanism of the dielectrophoresis. In inhomogeneous electric fields polarizable objects experience a force towards regions of highest field strength. It depends on the particle's electric properties and size, and on the electric field strength and its gradient. The use of AC field leaves permanent charges unaffected.

This so-called dielectrophoretic force depends on the dielectric properties of both the particles and their surroundings. By using alternating fields electrophoretic effects are avoided and permanent charges remain unaffected. Objects that are smaller than about a micrometer have come into focus only in recent years. This is because the dielectrophoretic effect is proportional to the cube of the particle's radius [5], while the impact of the Brownian motion increases with decreasing particles size [6]. Therefore very high electric field strengths, around 1MW/m and more, are needed, which, on the other hand, lead to disturbance by heating and electro hydrodynamic effects [7]. This dilemma is solved by working in low conductive media and by using electrodes with gap widths of only a few micrometers or less. Recently electric properties of viruses and polystyrene microspheres have been determined by studying their edges or dielectrophoretic response at different field frequencies [6]. Macromolecules of some micrometers length like DNA has been concentrated at the electrode have been aligned in parallel to the electric filed [8-11]. Figure 4 show a fluorescence micrograph of double standard DNA oriented between interdigitated aluminum electrodes on a quartz substrate. The molecule's theoretical length pf 2.2 µm exceeds the gap width of 1.4 µm. Therefore the molecules doesn't span the interelectrode gap in the shortest possible way, but are titled relative to the electric filed lines. However, in aqueous solution DNA molecules usually are coiled with persistence length around 80 nm [12]. Thus the final observable length of the molecule depends on the actual dielectrophoretic force.

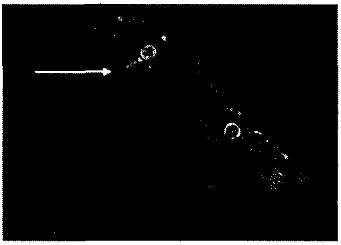

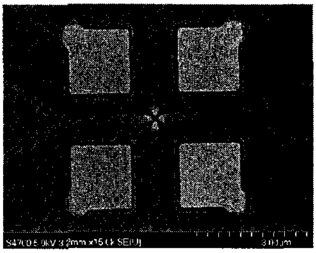

Figure 4 (left): Dielectrophoretic alignment of DNA. Linearized M13 phage DNA with nominal length of 2.2 µm was stained with the intercalating fluorescent dye Pico Green. Dissolved in ultra pure water it was then placed on interdigitated electrode of 1.4 µm gap. Collection and orientation was performed with an electric filed of 1 MHz and 2 V (RSM) electrode voltage.

Figure 5 (right): SEM of the nano-chip used in this work, large rectangles are pH control electrodes, and the small nano-electrodes appearing in the middle are the sense and control electrodes.

In order to manipulate smaller molecules, especially more compact ones like proteins, even higher electric field strengths or higher field gradients, respectively, are necessary. Interdigitated electrodes with thickness of typically 100 nm exhibit a gradient almost only in the z-direction. Thus sharp electrodes with a shape similar to needles help to increase dielectrophoresis. Field strength can be increased by using higher voltage or smaller electrode distances. Side effects like heating can be reduced by decreasing the volume of high fields. This is achieved by shrinking the active volume by reducing electrode distances and by confining the region of highest field strength to a small region by, again, sharp electrode tips. Such electrodes are shown in Fig. 5 with a distance of only 200 nm. They were manufactured by electron beam lithography on a silicon substrate. The outer, large square electrode is for monitoring purposes only. Nearly the complete surface except the active electrode area is electrical isolated by a photo resist. Experiments were performed on fluorescently labled IgG antibody molecules with a molecular weight of 150 kDa, corresponding to a diameter of about 8 nm. The ''north'' and ''south'' electrodes were activated by 3 V (RMA) at 100 kHz. Figure 6 shows fluorescence micrograph after 1, 2, 5, and 8 minutes field exposure at an antibody concentration of 30 nM in ultra pure water. The increase in the fluorescence intensity in the interelectrode space

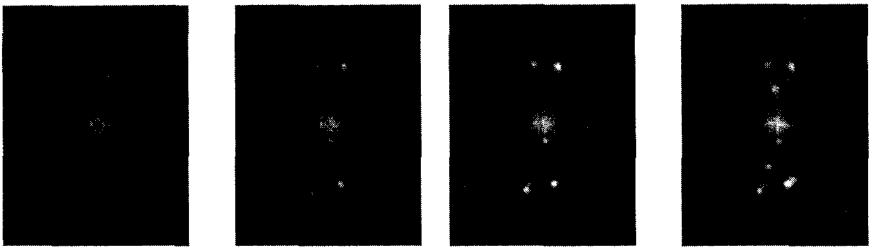

Figure 6: Short term response of antibody dielectrophoresis. The field has been switched on at t = 2 s and has been switched off 16 s later. Fluorescence has been taken from photomicrograph after background subtraction.

clearly is discernible. Interestingly some bright spots can be found at bends of the electrode strips which produce additional filed inhomogeneities. This shows that such experiments are also possible with an isolating layer between electrodes and solution due to capacitive coupling when using AC fields. Whether molecules are in close contact to the surface or are just trapped in a dielectrophoretic potential well is not discrnible due to the limited optical resolution (250 nm). The temporal course (not shown) of fluorescence was found to increase exponentially with a time constant of 70 s. This time course presumably depends on the diffusion coefficient and concentration of the molecules as well as on the shape and size of the interelectrode space. Switching on and off the filed leads to a nearly instantaneous increase and fall of fluorescence.

3. The Nano-Scale Water Transistor

Electrolyte transistor realized with water as the base element may present several potential advantages for industrial processes and sensor technology. In addition and due to the wide presence and usage of water in biological systems devices that use water is of importance and technological impact. With the main goal of developing a nano-device in which water is used as the main element, we have realized a nanoscale water based transistor based on the variation of the pH of water through a voltage applied to the base. The device composed of a nano-scale emitter and collector metallic electrodes with a small gap between them (15 -200 nm), and pH control electrodes with different size and distance with respect to the emitter-collector region. The device surface is covered by insulating layer (electron beam resist), except for a small part of the emitter-collector, and the pH electrodes which compromise the base of the device. Different device configurations were fabricated. The variation in the device configuration includes different nano-gap spacing for sensing (15nm-200nm), and the size and of the pH electrodes in addition to their proximity to the emitter-collector region.

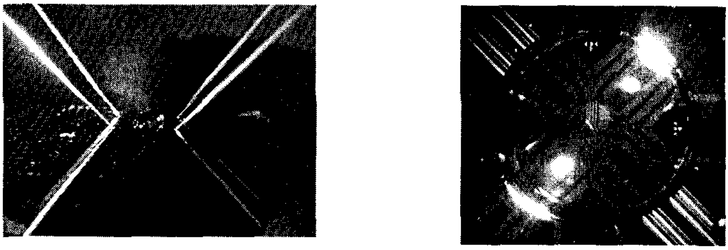

Figure 7: Left: Image showing the nano-scale water transistor under measurement with the water drop appearing in the middle. Right: Magnified micrograph showing the water drop and the large pH electrodes.

Figure 7 shows the water transistor under measurement. The theory and more description of this device can be found in [13]. We have also compared the experimental results with simulation results and we obtained consistency between the results. When the voltage applied to the pH electrodes is varied, different emitter to collector I-V curves are obtained. Such a device will find wide variety of applications (e.g. trapping of molecules, see section 2) since water is widely used and available in biological systems and experiments.

4. Problems and Results in Transport Modeling of Bioparticles in Solutions

Manipulation of biological particles, i.e. living cells and related molecules, includes various operations, for instance, separation of a group of the particles from a more general bioparticle population, i.e. biofluid, and trapping of a bioparticle or a few bioparticles. The corresponding physics is not very simple. One of the problems is that, generally speaking, populations of bioparticles cannot be described with common tools of theoretical physics. The reasons are the following.

Statistical mechanics (SM), classical or quantum, assumes that a fluid includes a *fixed*, time-independent number (normally, a few units) of mutually different fluid components each of which (i) comprises *statistically large* number of *identical* particles of a *negligibly small* particle volume and (ii) is located in a *macroscopically big* domain. The condition of the statistically large number of particles in a macroscopically big domain stems from the thermodynamic-limit (TDL) assumption. Generally, none of the aforementioned five assumptions (typed in italic) holds in living fluids. For instance, it is not uncommon in manipulation of biofluids that all the fluid particles are pair wise different. Subsequently, the number of the fluid components is equal to the number of the fluid particles, and each component includes exactly one particle. Obviously, the TDL assumption is inapplicable to this case. Moreover, SM does not take into account a *living* nature of the cells, i.e. their inherently non-equilibrium, nonlinear, time-dependent internal parameters which perform a kind of stable self-oscillations of the "birth-life-death" behavior.

The above problems attract attention of research community. We point out a few examples of the corresponding developments.

Book [14] and survey [15] underlie the results discussed below. Papers [16] and [17] (see also [24]) develop both the equilibrium and non-equilibrium versions of nonlinear stochastic mechanics free from the TDL assumption. They show how, by means of nonlinear stochastic differential equations, one constructs the random mechanics where the domain containing the fluid particles need not be macroscopically big and the particle number need not be statistically large. The latter can be arbitrary (e.g. from any number down to only one). The treatment generalizes Maxwell's derivation of the velocity probability density for a *single* particle. The results are applicable to macroscopic problems and those mesoscopic problems where the Schrödinger-wave effects are not dominating (e.g., see [17 or 24] for an example of the specific criterion). The related computational aspects including parallel computing are analyzed in work [18]. Paper [18] applies the *generalized-kinetics* (GK) ideas (e.g., [19, Section 10.3], [19]) to eliminate the SM limitation that the particles in each component of the fluid must be identical. The resulting treatment is highly flexible and allows for the mixtures of particles where the particles are disparate and the component number is time-varying rather than fixed. In particular, the fluid where all the particles are pairwise different and, thus, each component includes exactly one particle can be modelled. These results are illustrated in work [22] with the application to fluids of the particles with the spin mixture. This work shows the relevance to the experimental results difficult to interpret in other ways and introduces the notion of a composon, the spin-mixture particle physically more consistent than a quon. The notion of quon was proposed in [23]. Paper [24] overcomes the SM limitation that the particles must be of a negligibly small volume. This is consistently done by the dedicated, volume-scaling method (VSM) and in a close connection with the Heisenberg uncertainty principle (HUP), a fundamental experimental result. Work [24] also includes the extension of the above TDL-free treatment [15, 18] to the relativistic effects which can be important in the electronic parts of the biofluid-manipulation problems. This extension employs the notion of Rayleigh's dissipation function [25]. A particular version of the above VSM for simple biofluids is reported in paper [26] together with the numerical results on red blood cells in human blood. A special advantage of the approach of [24] is that it allows for the fact that HUP, as is shown by the advanced experiments in [26], holds for fairly "classical", i.e. (comparatively) big and heavy, particles. Notably, HUP turns out to be even more involved in the *classical* phenomena. For instance, paper [28] proves that the diffusion constant of a particle of a nonzero mass is bounded from below by a positive quantity (dependent on Planck's constant and the particle mass), and hence can never be zero. This stresses the fundamental nature of diffusion. Work [29] presents the most recent part of the above development. It focuses on the physical modelling of those properties of biological cells which determine the cells as living units. Work [29] is the first step towards a combination of the aforementioned advantages with the inherently non-equilibrium, nonlinear, time-dependent internal parameters of the living-fluid particles performing stable self-oscillations of the "birth-life-death" behavior. This treatment can be viewed as a substantial, based on the GK theory extension of common physical modelling to living fluids.

References

[1] N Calander and M Willander, Phys. Rev. Lett. 89, 143603 (2002).
[2] R. Peting and G. H. Max, *Wiley Chichester* (1979).
[3] P. T. Lynch, and M. R. Davey, *Chapman and Hall*, (1996).
[4] U. Zimmermann and G. A. Neil, *CRC Press*, Boca Raton, (1996).
[5] X.-B. Wang, Y. Huang, R. Hölzel, R. Burt, R. Pething, *J. Phy. D: Appl. Phys.* **26**, 312 (1993).
[6] H. Morgan, N. G. Green, *Biophysical J.* **15**, 516 (1999).
[7] A. Ramos, H. Morgan, N. G. Green, and A. Castellanos, *J. Phys. D: Appl. Phys.* **31**, 2338 (1998).
[8] M. Washizu, and O. Kurosawa, *IEEE Trans. Ind. Phys.* **26**, 1165 (1990).
[9] H. Kabata, O. Kurosawa, I. Arai, M. Margarson, S. A. Glass and N. Shimamoto, *Science* **262**, 1561 (1993).
[10] C. L. Asbury, A. H. Diercks, and G. van den Engh, *Electrophoresis* **23**, 2658 (2002).
[11] R. Hölzel, N. Gajovic-Eichelmann, F. F. Bier, *Biosensors and Bioelectronics* **18**, 555 (2003).
[12] N. C. Stellwagen, Y. J. Lu, and B. Weers, *Biophysical J.* **82**, 619 (2002).
[13] Z. Chiragwandi, O. Nur, M. Willander and N. Calander Appl. Phys. Lett, to appear on 22 December (2003).
[14]Y. V. Mamontov and M. Willander, *High-Dimensional Nonlinear Diffusion Stochastic Processes. Modelling for Engineering Applications.* World Scientific River Edge (2001)
[15] Y. V. Mamontov and M. Willander, (Invited Paper) *Int. J. Nonlinear Modelling in Science and Engineering* **1**, 1 (2001).
[16] Y. V. Mamontov, M. Willander, and J. Weiland, *Mathl Comput. Modelling* **36**, 889 (2002).
[17] Y. V. Mamontov and M. Willander, In: *13th Workshop on Physical Simulation of Semiconductor Devices*. Leeds University, Leeds (2002); ISBN 0-85316-229-8.
[18]E. Mamontov, M. Willander, and N. Calander, *Int. J. Nonlinear Modelling in Science and Engineering* (2003), accepted.
[19] N. Bellomo, E. Mamontov, and M. Willander, *Mathl Comput. Modelling* (2003), in press.
[20] N. Bellomo and M. Lo Schiavo, *Lecture Notes on the Mathematical Theory of Generalized Boltzmann Models*. World Scientific, Singapore, 2000.
[21] L. Arlotti, N. Bellomo and E. De Angelis, *Math. Models Methods Appl. Sci.* **12**, 567 (2002).
[22] N. Bellomo, N. Calander, E. Mamontov, and M. Willander, *Comptes Redus Mecanique* 331, 461 (2003).
[23] O. W. Greenb erg, *Phys. Rev. D* 43, 4111 (1991).
[24] E. Mamontov and M. Willander, *Mathl Comput. Modelling 38*, 637 (2003). Ed.
[25] J. W. Strutt, Lord Rayleigh, Some general theorems relating to vibrations, *Proc-London Mathematical Society* 4 (June 12), 357-368 (1873).
[26] E. Mamontov and M. Willander, *Acta Biotheoretica* **51**, 173 (2003).
[27] O. Nairz, M. Arndt and A. Zeilinger, *Phys. Rev. A* **65**, 032109/1 (2002).
[28] E. Mamontov and M. Willander, *Modern Physics Letters B* **16**, 467 (2002).
[29] M. Willander, E. Mamontov, and Z. Chiragwandi, Accepted *Math. Models Methods Appl. Sci.* (2003).

COMPUTATIONAL MODELS OF THE SEVEN-HELIX TRANS-MEMBRANE HUMAN MELATONIN RECEPTOR MT1, ONE OF NATURE'S COMMON NANO-ASSEMBLIES

CHARLES M. CASTEVENS AND DONALD D. SHILLADY

Departments of Physics and Chemistry, Virginia Commonwealth University, Richmond, VA 23284, USA

In recent years it has been discovered that nature uses slight variations in a common nano-assembly of seven nearly parallel alpha-helix structures across cell membranes to transmit biological signals. Over seventy of these seven-helix structures are now known and within that group up to 70 percent of the amino acid sequence is conserved; only slight modifications of the amino acid sequence provides a wide variety of functions. This work models the human melatonin receptor MT1. Melatonin is a hormone produced by the pineal gland at night, and regulates sleep in humans and other animals. Theoretical research is being done to find a quick and inexpensive computational model of the trans-membrane (3300+ atoms) receptor and the ligands that bind to it as a way to guide experimental work. The SYBYL-HINT computer programs were used to study this nano-assembly of over 300 amino acids. Good agreement was found relating the computational binding energies and experimental equilibrium dissociation constants over six orders of magnitude for melatonin and twenty-four similar compounds.

1. Introduction

While modern research is being carried out to develop nano-technology to create devices at the molecular level, discoveries are still being made as to how natural biochemical machinery works in detail. A recent review by Ray [1] shows that there are whole families of cellular trans-membrane receptors with a variety of functions, but with a common structural feature of seven, nearly parallel, alpha helices perpendicular to the cell wall. Ray points out that as much as 1-3% of the human genome codes for such G protein-coupled receptors (GPCRs) and they make up the largest known superfamily of plasma membrane receptors. Many of these receptors function with a stereo-specific pocket on the outside of the cell intended to accept a hormone or other relatively small biological messenger molecule. Then some sort of (usually unknown) conformational trigger transmits a signal through the cell wall to smaller G-proteins within the cell for some biochemical purpose. Fig. 1 shows only the helices with outer protein stripped away and melatonin in the pocket. Studying trans-membrane receptors is limited at present by the lack of crystallographic structures for such complex structures, but usually the sequence of amino acids for the receptor can be determined and molecular modeling can be used to determine a probable structure. On the other hand, it may be that the basic seven-alpha-helix array is only a common structural feature with many complicated modifications related to receptor-pocket shape and biochemical function of the transmitted biochemical signal so that the biochemical mechanisms are very different for each receptor pocket.

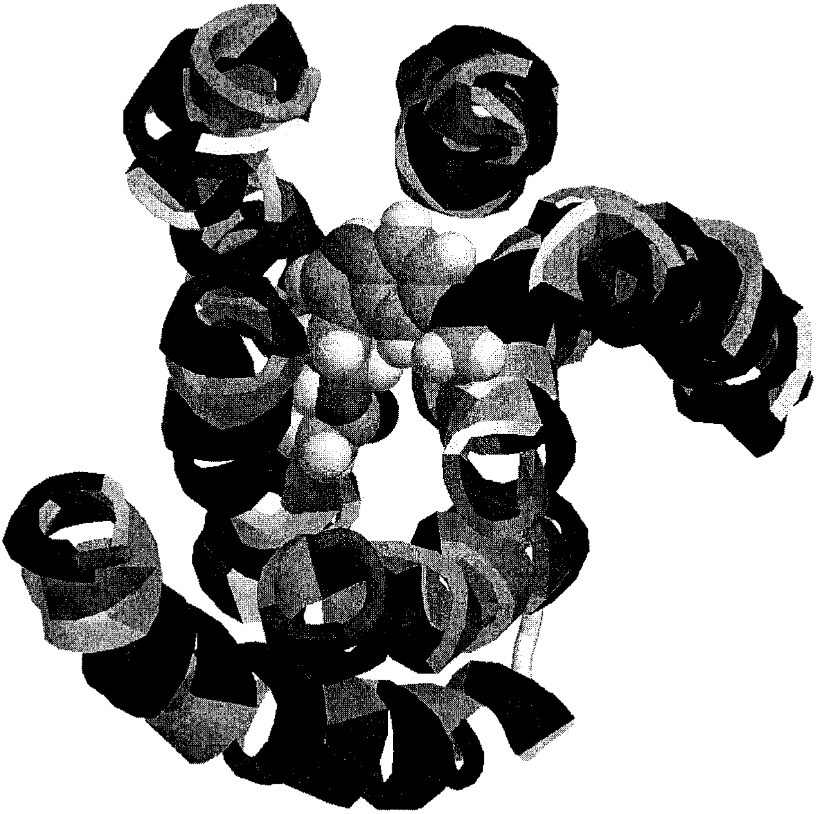

Figure 1. Model showing the structure of melatonin in the active site of MT1 helices.

This work is a preliminary attempt to understand some of the mechanistic features of the external receptor pocket of the human melatonin receptor MT1 using computer modeling compared to experimental data for binding of molecules similar to melatonin, a hormone believed to be a sleep-inducing messenger molecule. Other melatonin receptors are known in animals and there may be other human melatonin receptors, but this work is focused on the MT1 receptor. In this initial work the main emphasis is to understand how melatonin can fit into the receptor site and yet not become permanently attached. This is important for the daily day/night cycle effect of melatonin; it must fit the receptor site in a special way in terms of orientation and yet not become permanently attached or embedded in the receptor site. This is an especially complex problem because melatonin is not a rigid molecule and has a flexible alkylamide side chain as well as a rotating methoxy group in the 5-position of the indole moiety.

2. Procedure

The structure of MT1 (with melatonin in the receptor site) was adopted from that reported by Pogozheva and Mosberg [2]. Attempts were made to dissect the structure and calculate the interactions of each of the seven alpha-helix substructures with the melatonin molecule using *ab initio* and semi-empirical orbital calculations, but no conclusive trends were found with these methods and treatment of the entire protein by such methods was beyond the capability of computing facilities available at this laboratory. However, the SYBYL [3] molecular dynamics program was able to treat the entire protein with and without a molecule in the receptor site to estimate binding energies. SYBYL was used to calculate the energy of a geometry-optimized structure consisting of MT1 with a ligand molecule bound to it. Then the energies of the optimized MT1 structure and ligand structure alone were calculated, and the binding energy E_b =E(MT1 + ligand) - E(MT1) - E(ligand). Starting with the MT1 and melatonin coordinates, the melatonin was successively replaced with different ligands. SYBYL was then used to geometry-optimize the new MT1 and ligand coordinates with 10,000 minimization steps using Powell optimization [4] with a non-bonded cut-off distance of 8 angstroms, an effective dielectric constant of 8.0, a minimum energy change of 0.01 kcal/mole, Gasteiger-Hückel charges [5] and a Tripos force field [6]. Increasing the number of iterations from 10,000 to 20,000 only minimally affected the energy gradient that was typically 0.01 kcal/mole for the entire protein complex. The wall-clock time for each 10,000-step optimization was approximately 18 hours on a SGI O2 R5000 180 MHz workstation or 10.5 hours on a SGI O2+ RM5271 300 MHz workstation.

The Mosberg MT1 structure [2] includes a bound melatonin molecule, which is an agonist for the MT1 receptor. Other agonists bind to the MT1 receptor site, competing with melatonin, and cause the same biochemical effects as the native ligand. Agonists turn the receptor on. Antagonists have comparable binding affinity to the same receptor but do not cause the same biochemical reactions that agonists do. Antagonist ligands turn the receptor off. Large lists of both agonists and antagonists for the MT1 receptor have been studied by both Sicsic *et al.* [7] and by Dubocovich [8, 9]. With the goal of trying to understand how melatonin interacts with MT1, this work only included seventeen compounds from the list by Sicsic *et al.* [7] with substituted indole ring systems similar to melatonin. A few non-indole compounds with measured pKi values were included such as 8-M-ADOT, 8-M-CADOT, 8-M-PDOT and S20098 as given in Table 1. Others were not included even though they exhibited some binding with the receptor as not being near optimum fits. Eight other compounds were added from the work by Dubocovich [8,9] to bring the total to a set of twenty-five.

An option available in the Tripos SYBYL program is a procedure developed by G. Kellogg [9] which measures "hydropathic interactions" (HINT). It is well known that while the Gibbs free energy, G=H-TS, is the best way to evaluate chemical interactions, it is difficult to estimate the entropy term S. Fortunately the S term is usually small and approximately constant over a variety of enzyme active sites (to within about +/- 50%). Thus the HINT subroutine uses an approximation that the (T ΔS) term is about 14 kcal/mol and constant. This permits ΔG to be related to a calculated ΔE value using:

$$\Delta G = -2.303\ RT \log_{10} K_i = \Delta E - 14\ \text{kcal/mol} \qquad (1)$$

Here the K_i value is an experimentally measured equilibrium constant for the amount of a ligand bound to MT1 in the presence of the free ligand as available from the data of Sicsic [7] or Dubocovich *et al.* [8,9] and R is the Ideal Gas constant. The two data sets were merged approximately by taking the ratio of each pKi value to the pKi value of melatonin in that data set and multiplying by the average of the pKi values of melatonin in the two data sets. The HINT method has been documented extensively by Kellogg *et al.*[10-14] and it calculates an approximation to ΔG and includes a Van der Waals (Lennard-Jones 6-12) interaction, a term dependent on solvent accessible surface area, an exponential range factor and a logic function sensitive to acid-acid and base-base interactions within the protein matrix. The HINT method permits plotting of pK_i values ($pK_i = -\log_{10} K_i$) versus calculated ΔE values from calculation of binding energies; assuming the ΔS term is approximately constant. The HINT score is defined so that a higher positive number indicates stronger binding. Thus twenty-four substituted indole molecules similar to melatonin and two conformers of melatonin were each treated with 10,000 energy optimization steps using the Tripos SYBYL force field and the resulting binding energies were related to experimental pK_i values using equation (1). Labels such as "C13" relate to the numbering scheme given in reference [7] as compound-13 in that list. Fig. 2 shows two conformations of the 5-methoxy group of melatonin. The binding energy and the HINT score clearly favor the upper conformer of melatonin in the receptor pocket (E_b = –40.732 kcal/mol, upper versus –36.775, lower and HINT = 199.441, upper versus 93.108, lower). While there is only a very small energy barrier to rotation of this methoxy group relative to the plane of the indole ring, these calculations indicate that the upper conformation is more likely in the receptor pocket and all further binding energy calculations used this conformation of the 5-methoxy group.

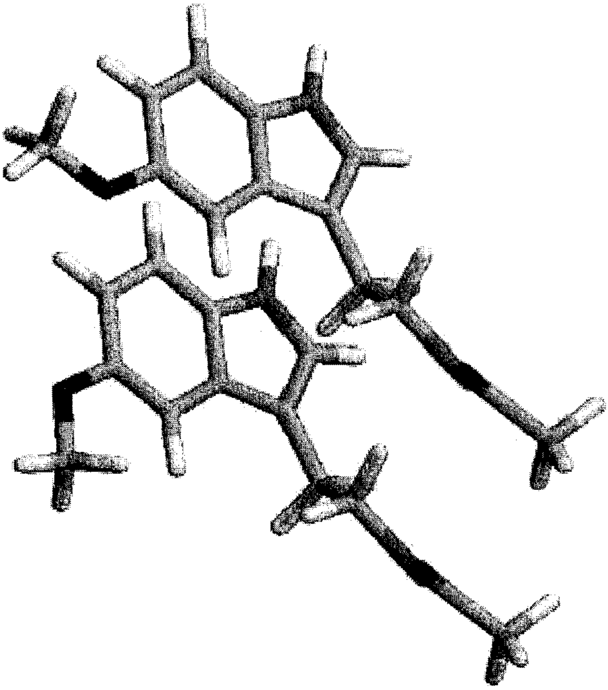

Figure 2. Two conformations of the 5-methoxy group of melatonin.

3. Results and Conclusions

A more detailed analysis of the binding of various compounds will be published elsewhere with emphasis here on the unusual success of relating the pK_i data to the binding energies (E_b) and the HINT score values. Although there are some outlying values, the correlation coefficient of the linear regression of 0.907 is surprisingly good for a relationship between calculated binding energies and experimental biological data. This bodes well for further use of the SYBYL-HINT analysis of other agonist and antagonist molecules. Perhaps this good fit to the data is partially due to the fact that for a single receptor (MT1 here), the entropy term ΔS is indeed approximately constant which leads to a more direct relationship between the calculated binding energies and the experimental pK_i values.

Table 1. Interactions of Ligands with MT1 Receptor [15].*

Ligand	HINT score	Exp. pK_i	E_b
2-iodomelatonin	191.668	10.2247	-42.659
5-methoxytrypyamine	73.298	3.6335	-30.293
6-chloromelatonin	240.623	7.9400	-39.012
6-chloro-2-methylmelatonin	282.391	8.9269	-42.273
6,7-diCl-2-methylmelatonin	292.633	8.3631	-44.378
6-fluoro-N-acetyltryptamine	305.232	6.7587	-32.009
8-M-ADOT [15]	568.429	7.0110	-36.261
8-M-CADOT [15]	507.370	8.3190	-38.964
8-M-PDOT [15]	588.993	7.2660	-38.843
C11 [7]	381.897	9.6799	-44.188
C13 [7]	706.856	9.8587	-44.602
C15 [7]	624.450	7.4732	-37.088
C16 [7]	912.952	7.9809	-38.101
C17 [7]	778.560	6.4900	-35.583
C22 [7]	512.487	8.7155	-40.399
C23 [7]	749.685	8.5160	-40.732
C27 [7]	868.511	9.2020	-43.051
C37 [7]	304.913	6.6288	-31.852
C38 [7]	287.556	6.6688	-35.407
C46 [7]	551.103	6.5599	-32.402
C47 [7]	226.364	5.6844	-31.659
Melatonin, 5-OCH_3 toward 6H	199.441	9.1073	-40.732
N-acetyltryptamine	298.715	6.5100	-31.665
N-acetylserotonin	43.620	6.6923	-34.497
S20098 [15]	657.781	9.1177	-40.799

Least-Squares Line: pKi = (-0.3029713) Eb -3.7488622; r = -0.907

---

* 8-M-ADOT = 8-methoxy-2-acetammidotetraline
8-M-CADOT= 8-methoxy-2-chloro-acetamidotetralin
8-M-PDOT= 8-methoxy-2-propion-amidotetralin
S20098 = N-[2-(7-methoxy-1-naphthalenyl)ethyl]acetamide

The most important and outstanding result of this work [15] is the finding that while the binding energy of melatonin is only different by about 4 kcal/mol for the two alternate orientations of the 5-methoxy group, the HINT score clearly shows that interactions with the receptor pocket strongly favor the orientation with the 5-methoxy group rotated toward the 6-H position rather than toward the 4-H position. With the 5-methoxy group oriented toward the 4-H position (lower conformer in Fig. 2) the correlation coefficient for a similar graph to that below (Fig. 3) drops to about 0.72 which shows the importance of the orientation of the 5-methoxy group as in the upper conformer. The improvement of the correlation between the HINT score (related to ΔG) and the calculated binding energies with the rotation of the 5-methoxy group is important for future studies of agonists/antagonists of MT1 and is the major finding of this work.

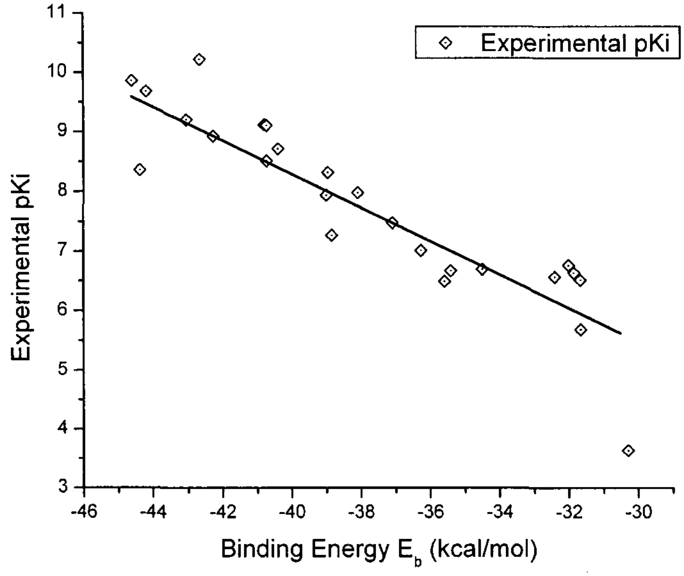

Figure 3. Experimental pKi versus the computed binding energies with the upper conformation of melatonin (Fig. 2). The least squares fit is also shown by the straight line.

Acknowledgements

Funding for chemicals and other consumables came from NSF grants CHE-0076290 and DGE-0086320. Thanks are due to Prof. Greg Buck, Director of the

Center for the Study of Biological Complexity for support of Mr. Castevens and to Mr. J. Michael Davis, Systems Programmer of the Department of Academic Technology for use of several computers. Discussions with Prof. Glen Kellogg of the VCU Department of Medicinal Chemistry were especially helpful in the use of the SYBYL-HINT program. Mr. Doug Shillady assisted in preparation of the graphics for the manuscript.

References

1. K. Ray, Int. Arch. Biosci., 1027 (2001).
2. A. L. Lomize, I. D. Pogozheva and H. I. Mosberg, J. Computer-Aided Mol. Design **13**, 325 (1999).
3. SYBYL 6.8, Tripos Inc., 1699 S Hanley RD, St. Louis, MO 63144.
4. M. J. D. Powell, Mathematical Programming **12**, 241 (1977).
5. J. Gasteiger and M. Marsali, Tetrahedron **36**, 3219 (1980).
6. M. Clark, R. D. Cramer III, and N. Van Opdenbosch, J. Comp. Chem. **10**, 982 (1989).
7. S. Sicsic, I. Serraz, J. Andrieux, B. Bremont, M. Mathe-Allainmat, A. Poncet, S. Shen and M. Langlois, J. Med. Chem. **40**, 739 (1997).
8. M. L. Dubocovich, J. Pharmacol. Exp. Ther. **246**, 902 (1988).
9. J. M. Jansen, S. Copinga, G. Gruppen, E. J. Molinari, M. L. Dubocovich and C. J. Grol, Bioorg. Med. Chem. Lett. **4**, 1321 (1996).
10. F. C. Wireko, G. E. Kellogg and D. J. Abraham, J. Med. Chem. **34**, 758 (1991).
11. G. E. Kellogg, S. F. Semus and D. J. Abraham, J. Comput.-Aided Mol. Design **5**, 545 (1991).
12. G. E. Kellogg, G. S. Joshi and D. J. Abraham, Med. Chem. Res. **1**, 444 (1992).
13. D. Abraham, G. E. Kellogg, J. M. Holt, and G. K. Ackers, J. Mol. Bio. **272**, 613 (1997).
14. G. E. Kellogg and D. J. Abraham, Eur. J. Med. Chem. **35**, 651 (2000).
15. C. M. Castevens, "Ligand Binding Energies and Magnetic Circular Dichroism of the Human Melatonin Receptor MT1", Ph.D. Thesis, Department of Chemistry, Virginia Commonwealth University (2003).

ULTRAHIGH MAGNETIC MOMENTS OF CORE-SHELL NANOCLUSTERS FOR BIOMEDICAL APPLICATIONS *

YOU QIANG,[†] JIJI ANTONY, CHANDRA S. KAKARAPARTHI AND SWETA PENDYALA
Department of Physics, University of Idaho, Moscow, ID 83844-0903, USA

Magnetic nanoparticles with suitable biocompatible coatings are becoming increasingly important for several biomedical applications in tagging, imaging, sensing and separation in recent years. Most magnetic particles or beads used in biomedical applications are based on ferromagnetic iron oxides with very low magnetic moment (between 20 and 80 emu/g). Here we report a new approach to synthesize monodispersive core-shell nanostructured clusters with ultrahigh specific magnetic moments above 250 emu/g. The Fe nanoclusters with size range from 2 nm to 100 nm are produced from a newly developed cluster source and go to a deposition chamber, where a chemical reaction starts and the nanoclusters are coated with Fe oxides before depositing on surface. HRTEM images show the coatings are very uniform. The core-shell nanoclusters are superparamagnetic at room temperature for the size less then 15 nm. These nanoclusters with ultrahigh moments can enhance dramatically the contrast for MRI, or reduce the concentration of magnetic particle needs for cell separation, or make drug delivery possible with much lower magnetic field gradients.

1. Introduction

Magnetic nanoparticles are being used in many biomedical applications, such as magnetic resonance contrast enhancement, cell and DNA separation, drug delivery, and gene cloning. These applications require the nanoparticles be superparamagnetic at room temperature, high magnetic moment and monodispersive for uniform biodistribution, bioelimination and high contrast effects. This is because they promise to greatly improve the performance of biomedical treatments and analyses.

Ferrite particles (such as Fe_3O_4) coated with compounds such as dextran or starch for biocompatibility, are now widely used. [1-5] Ferrite nanoparticles are biocompatible and easy to synthesize. But specific magnetic moment of ferromagnetic iron oxide particles is very low (< 80 emu/g). Iron has a greater specific magnetization than any iron oxide. The problem is that pure metallic iron nanoparticles are highly sensitive to oxidation and to corrosion, and not biocompatible. If iron nanoparticles were passivated with a very thin ion oxide-coated shell and keep high magnetic moments of pure iron core, they could enhance dramatically the contrast for MRI, or reduce the concentration of

---

[*] This work is supported by NSF Idaho-EPSCoR, ONR and DOE/PNNL.
[†] Contact information: Tel: 208-885-7558, e-mail: youqiang@uidaho.edu.

magnetic particle needs for cell separation, or make drug delivery possible with much lower magnetic field gradients.

To realize this goal, we apply a new approach to synthesize monodispersive, ultrahigh specific magnetic moment core-shell nanostructured clusters.

2. Experiment

The samples were prepared by our newly developed nanocluster deposition system, based on the earlier two generations of cluster deposition system built by Y. Qiang at the University of Freiburg, Germany, and the University of Nebraska, Lincoln, US. [6-10] The details information about this new system will be described elsewhere. Fe nanoclusters of a variable mean size of diameters from 1 to 100 nm are generated by a nanocluster source, which combines an improved high-pressure magnetron-sputtering gun with a gas-aggregation tube cooled by chilled water. We can control the cluster size by changing the flow rate of Ar gas, and the flow rate of He gas, and the cluster growth length L. For preparation of Fe oxide-coated Fe clusters, we introduced oxygen gas of the flow rate about 4 sccm through a nozzle set behind the skimmer into the deposition chamber, where a chemical reaction starts to form iron oxide shells covering the Fe clusters before depositing them on the substrate. The clusters land softly on the surface of substrates at room temperature to keep the original shape of clusters. This process ensures that all Fe clusters are uniformly oxidized before the cluster films are formed.

Three kinds of substrates are used for the core-shell cluster deposition: transmission electron microscopy (TEM) microgrids for high-resolution TEM observations, silicon wafers for scanning electron microscopy (SEM) observations, and polyimide films for magnetic measurement. The film thickness of deposited clusters was estimated using a quartz crystal thickness monitor, and we also measured the weight of the deposited cluster films by a microbalance. Magnetic measurement was performed using a superconducting quantum interference device magnetometer (SQUID of MPMS XL-7, Quantum Design Inc.) between 5 and 300 K with the maximum field of 70 kOe.

3. Results and Discussion

Figure 1 shows a SEM image of the core-shell Fe cluster assemblies deposited on the surface of Si wafer. Using image-analysis software, we estimated the size distributions (inset of Fig. 1) of the clusters recorded by a slow scan charge coupled device camera. One example as shown here, the mean cluster diameter (D) is 10.1 nm. The standard deviation is less than 8%. The distribution can be fitted very well to a lognormal function with a very narrow size distribution.

Figure 2 shows high-resolution TEM (HRTEM) overviews of 4 single core-shell structured nanoclusters with the size change from 3 nm to 85 nm deposited on the carbon film of microgrids. The nanoparticles appear almost spherical, and those that have a crystal axis oriented along the electron beam direction show two contrasts, a dark iron core region and a light-gray oxide shell. The electron diffraction pattern (not shown here) obtained from a large sample area tells us the core has the bulk bcc lattice structure of α-Fe with the lattice fringe 0.203 nm, while the lattice fringes 0.253 nm shown in the shell of Fe_3O_4 or Fe_2O_3 phase. These results also indicate that the oxide-coated Fe clusters were covered uniformly with the Fe_3O_4 or Fe_2O_3 shells composed of very small crystallites.

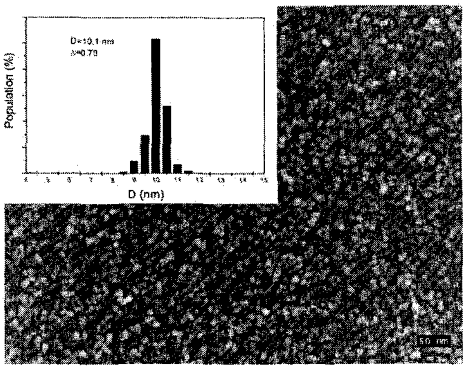

Fig.1. TEM image and size distribution of Fe/Fe oxide clusters prepared on a carbon microgrid.

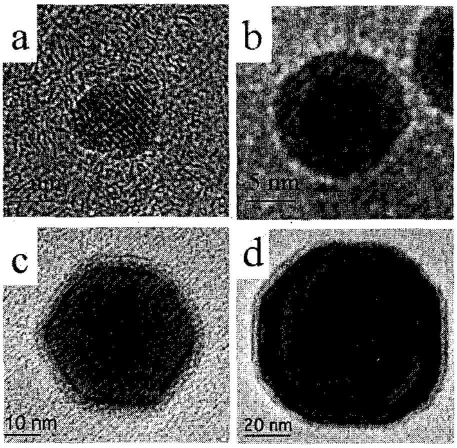

Fig. 2. HRTEM micrographs of the oxide-coated Fe clusters with the diameter from about 3 nm to 85 nm prepared on carbon microgrids.

The iron oxide shell has a thickness of about 2.5 nm that is independent of the nanoparticle size. We have observed that the core-shell nanoclusters were very stable against further oxidation according to our measurements after long time exposure to air or heating at high temperature of about 450 K for a few hours. For those sizes smaller than 5 nm there are no core-shell structures (Fig2-a) because the oxidation goes through the whole nanoparticles.

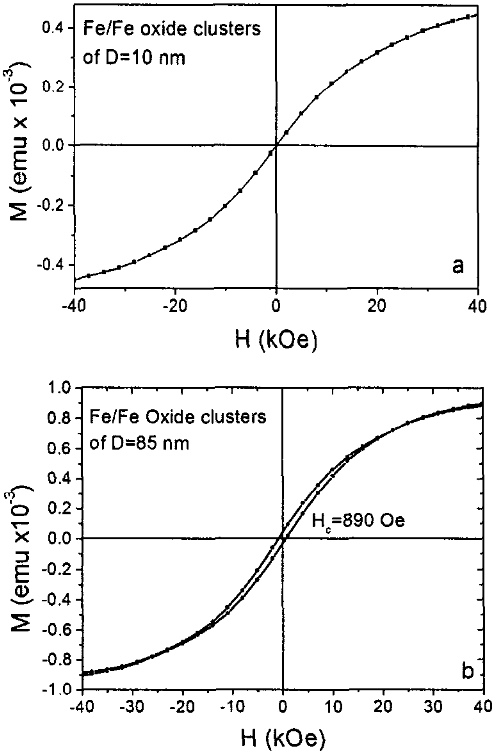

Fig. 3 Hysteresis loops of Fe oxide-coated Fe clusters with (a) D = 10 nm and (b) D = 85 nm at room temperature.

Fig. 3 shows some typical hysteresis loops of Fe oxide-coated Fe nanoclusters at room temperature. The samples with the size of cluster less than 15 nm are superparamagnetic at room temperature without coercivity. Fig. 3-a is one example of cluster size of 10 nm. It is clear that it has a superparamagnetic behavior. When the sizes of clusters are larger than 15 nm, they become ferromagnetic nanoparticles. The coercivity increases from 35 Oe for 16 nm size clusters to about 1 kOe of 100 nm clusters. Fig. 3-b shows a typical hysteresis loop of 85 nm diameter clusters with H_c = 890 Oe. All the samples at low temperature (5 K) are magnetically ordered with large hysteresis loops. H_c is about 1.5 kOe. Since the nanoclusters are superparamagnetic, for getting a saturated magnetization (M_s), we have to obtain it by high-field fit to the expression $M = M_s (1-A/H^2)$, where A is a constant. The results of M_s divided by the weight of cluster films yield the specific magnetic moment with a unit of emu/g.

Figure 4 shows a curve of the specific magnetic moment versus the nanocluster size. It can be seen that it increases as cluster size increases from 3 nm to 85 nm. When the size less than 10 nm, the specific magnetic moment is around 90 emu/g, similar to the value of ferromagnetic iron oxides. This information is consistent with the HRTEM image (Fig. 2-a), which shows the whole nanocluster is oxidized to form the ferromagnetic iron nanoparticle. If the cluster size is larger than 10 nm, the value of specific magnetic moments is increasing dramatically at above 250 emu/g when the cluster size reaches to 85 nm, but much less than the pure bulk Fe value. The detail explanation about this will be further studied and published elsewhere.

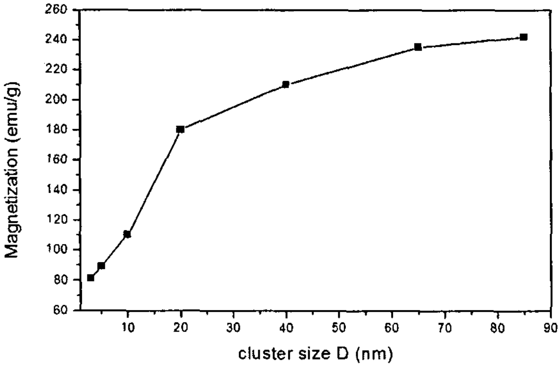

Fig. 4. Size dependent specific magnetic moments of Fe oxide-coated Fe nanoclusters.

4. Conclusion

In summary, monodispersive core-shell nanostructured clusters with ultrahigh specific magnetic moments (> 250 emu/g) are synthesized by a new approach of nanocluster deposition system. The size of core-shell nanoclusters can be changed easily from 1 nm to 100 nm by controlling the growth parameters. HRTEM images show the coatings are iron oxides and very uniform covered on the Fe cores. The nanoclusters are superparamagnetic at room temperature for the size less then 15 nm, and become ferromagnetic with increasing size of nanoclusters. The specific magnetic moment of core-shell nanoclusters is size dependent, and increases rapidly from about 80 emu/g at the cluster size of about 3 nm to over 250 emu/g at the size of 85 nm. This can enhance dramatically the contrast for MRI, or reduce the concentration of magnetic particle needs for cell separation, or make drug delivery possible with much lower magnetic field gradients if the high magnetic moment nanoclusters are used for biomedical applications.

Acknowledgments

Financial support for purchasing a SQUID instrument (MPMS XL-7, Quantum Design, Ins) from the Idaho NSF-EPSCoR project is gratefully acknowledged. Acknowledgment is also made to the Research Office of the University of Idaho, ONR and DOE through PNNL. TEM data were collected at EMSL, a user facility sponsored by the DOE and operated by Battelle. Dr. Chongmin Wang at PNNL is thanked for high valuable TEM assistance.

References

1. G. P. Hatch and R. E. Stelter, "Magnetic design considerations for devices and particles used for biological high-gradient magnetic separation systems", *J. Magn. Magn. Mater.*, 225 (2001) 262-276.
2. Do K. Kim, M. Mikhaylova, Y. Zhang anfd M. Muhammed, "Protective coating of superparamagnetic iron oxide nanoparticles", *Chem. Mater*, 15 (2003) 1617-1627.
3. D. H. Rich, *et. el.*, "Biological applications of multifunctional magnetic nanowires", *J. Appl. Phys.*, vol.93, 7275-7280 (2003)
4. M. Tada, S. hatanaka, H. Sanbonsugi, N. Matsushita and M. Abe, "Method for synthesizing ferrite nanoparticles ~30 nm in diameter on neutral pH condition for biomedical applications", *J. Appl. Phys.*, vol.93, 7566-7568 (2003).
5. M. Chen, S. Yamamuro, D. Farrell and S.A. Majetich, "Gold-coated ironnanoparticles for biomedical applications", *J. Appl. Phys.*, vol.93, 7551-7553 (2003).
6. Y. Qiang, R. F. Sabiryanov, S. S. Jaswal, Y. Liu, H. Haberland, and D. J. Sellmyer, "Magnetism of Co nanocluster films", *Phys. Rev.* B 66, 064404 (2002).
7. Y. Qiang, R. Morel, E. Eastham, J.M. Meldrim, J. Kraft, A. Fert, H. Haberland, D.J. Sellmyer, "Magnetic properties of cobalt clusters embedded in a nonmagnetic matrix (Ag, Cu, SiO2) ", *Cluster and Nanostructure Interfaces*, ed. By P. Jena, S.N. Khanna and B.K. Rao, Would Scientific, 2000.
8. Y. Xu, Z. Sun, Y. Qiang, and D. Sellmyer, "Magnetic Properties of L10-FePt and FePt:Ag Nanocluster Films", *Journal of Applied Physics,* 93, 10 (2003) 8289.
9. Y. Qiang, Y. Thurner, Th. Reiners, O. Rattunde and H. Haberland, "TiN and TiAlN coatings deposited at room temperature by Energetic Cluster Impact (ECI)", *Surface and Coatings Technology,* 101/1-3, 1998, p. 27-32
10. J. M. Meldrim, Y. Qiang, D.J. Sellmyer, H. Haberland, "Magnetic properties of cluster-beam synthesized Co-noble metal films", *J. Appl. Phys.* 87, 9 (2000) 701

ORGANIZATION

Chairman: P. Jena (U.S.A.)
Secretary: S. N. Khanna (U.S.A.)
Treasurer: B. K. Rao[*] (U.S.A.)

INTERNATIONAL ADVISORY BOARD

R. S. Berry (University of Chicago, Chicago, U.S.A.)
D. Bimberg (Technische Universität, Berlin, Germany)
L. E. Brus (Columbia University, U.S.A.)
C. Brechignac (CNRS, Orsay, France)
A. W. Castleman, Jr. (Pennsylvania State University, University Park, U.S.A.)
S. Datta (Purdue University, U.S.A.)
M. Dresselhaus (Massachusetts Institute of Technology, Cambridge, USA)
S. Iijima (NEC Corporation, Tsukuba, Japan)
J. Jortner (Tel Aviv University, Tel Aviv, Israel)
C. Mirkin (Northwestern University, U.S.A.)
H. Ohno (Tohoku University, Japan)
C. N. R. Rao (Jawaharlal Nehru Institute for Advanced Scientific Research, Bangalore, India)
M. C. Roco (National Science Foundation, U.S.A.)
R. W. Siegel (Rensselaer Polytechnic Institute, Troy, U.S.A.)
R. E. Smalley (Rice University, Houston, U.S.A.)
V. Vogel (University of Washington, U.S.A.)
M. Willander (Chalmers University of Technology, Sweden)
G. M. Whitesides (Harvard University, Cambridge, U.S.A.)
R.N. Zare (Stanford University, U.S.A.)
A.H. Zewail (California Institute of Technology, U.S.A.)

LOCAL ORGANIZING COMMITTEE

J. R. Anderson (University of Maryland)
A. S. Arrott (Virginia State University)
S. Bandyopadhyay (Virginia Commonwealth University
A. Baski (Virginia Commonwealth University
L. A. Bloomfield (University of Virginia)
K. Bonin (Wake Forest University)
S. C. Deevi (Philip Morris USA)
M. S. El-Shall (Virginia Commonwealth University)
A. Guiseppi-Elie (Virginia Commonwealth University)
T. Huff (Virginia Commonwealth University)
P. Jena (Virginia Commonwealth University)

D. Johnstone (Virginia Commonwealth University)
S. N. Khanna (Virginia Commonwealth University)
A. C. Lilly (Philip Morris, U.S.A.)
H. Morkoc (Virginia Commonwealth University)
M. Namkung (NASA)
B. K. Rao* (Virginia Commonwealth University)
C. E. Stronach (Virginia State University)

*Deceased

PARTICIPANTS

Victor M. Abdelsayed
8311 Jack Burd Lane, Apt. A
Richmond, VA 23294, USA
Tel: (804) 827-1222
szvmabde@mail1.vcu.edu

Hector Alonso, VP
Product Development and Technology
Philip Morris USA
PO Box 26603
Richmond, VA 23261, USA

Edreese H. Alsharaeh
4119 Townhouse Road, Apt. M
Richmond, VA 23228, USA
Tel: (804) 827-1222
ehalshar@vcu.edu

J. Robert Anderson
Department of Physics
University of Maryland
College Park, Maryland 20742
Tel: (301) 405-6142
Fax: (301) 314-9465
ja26@umail.umd.edu

Mats Andersson
Department of Experimental Physics
Chalmers University of Technology
Göteborg University
Göteborg, SE-41296
Sweden
Tel: +46 31 772 3277
Fax: +46 31 772 3496
mats.andersson@fy.chalmers.se

Antonis N. Andriotis
Professor in Research
Institute of Electronic Structure and Laser (IESL)
Foundation of Research and Technology - Hellas (FORTH)
P.O.Box 1527
Vassilika Vouton
71 110 Heraklion Crete
Greece
Tel: ++30-2-810-391812
Fax: ++30-2-810-391305
andriot@iesl.forth.gr

Jean-Marie Antonietti
Abteilung für Oberflächenchemie
Und Katalyse
Universität Ulm
D-89069 Ulm
Germany
Tel: 7315025454
Fax: 7315025452
jean-marie.antonietti@chemie.uni-ulm.de

Anthony S. Arrott
Department of Physics
Virginia State University
Petersburg, VA 23806, USA
Tel: (804)524-5915
Fax: (804) 524-5914
arrott@vsu.edu

Timothy M. Ayers
Chemistry Department
The University of Georgia
Athens, GA 30602, USA
Tel: (706) 542-2015
Fax: (706) 542-1234
tayers@chem.uga.edu

Sheryl D. Baldwin
1720 Hanover Avenue
Richmond, VA 23220, USA
Tel: (804) 353-5805
sdbaldwin@earthlink.net

Supriyo Bandyopadhyay
Electrical Engineering
Virginia Commonwealth University
Box 843072
601 W. Main St./Eng 238
Richmond, VA 23284-3072, USA
Tel: (804) 827-6275
Fax: (804) 828-4269
sbandy@vcu.edu

Ansuman Banerjee
Electrical Engineering
Box 843072
601 W. Main St.
Richmond, VA 23284-3072, USA
Tel: (804) 828-0181
banerjeea@mail1.vcu.edu

Tunna Baruah
Naval Research Laboratory
Code 6392
Bldg. 28
Washington, DC 20057, USA
Tel: (202) 404-1181
Fax: (202) 404-7546
baruah@dave.nrl.navy.mil

Alison Baski
Physics Department
Virginia Commonwealth University
Box 842000
Richmond, VA 23284-2000, USA
Tel: (804) 828-8295
Fax: (804) 828-7073
aabaski@vcu.edu

Jack L. Beauchamp
Chemistry Department
CALTECH
Mail Code 210-41
1200 E. California Blvd.
Pasadena CA 91125, USA
Tel: (626) 395-6525
jlbchamp@caltech.edu

Marcela R. Beltran
Inst. De Investigaciones en Materials
A.P. 70-360 CP 04510
Mexico D.F. 04510
Mexico
Tel: 5255 56224624
Fax: 5255 56161251
mbeltran@servidor.unam.mx

Denis E. Bergeron
Penn State University
152 Davey Lab
University Park, PA 16802, USA
Tel: (814) 863-3583
Fax: (814) 865-5235
deb223@psu.edu

Thorsten M. Bernhardt
Freie Universität
Fachbereich Physik
Inst. Für Experimentalphysik
Arnimallee 14
D-14195 Berlin-Dahlem
Germany
Tel: +49/30/838.56122
Fax: +49/30/838.55567
tbernhar@physik.fu-berlin.de

R. Stephen Berry
Dept. of Chemistry
University of Chicago
5735 S. Ellis Avenue
Chicago, IL 60637, USA
Tel: (312) 702-7021
Fax: (773) 834-4049
berry@uchicago.edu

Chris Binns
Depart. of Physics & Astronomy
Univesity of Leicester
Leicester, LEL7RH, UK
Tel: +44 (0)116 2523585
Fax: +44 (0)116 2522770
cb12@le.ac.uk

Louis A. Bloomfield
Department of Physics
University of Virginia
382 McCormick Road
P.O. Box 400714
Charlottesville, VA 22904-4714, USA
Tel: (434) 924-6595
Fax: (434) 924-4576
bloomfield@virginia.edu

Daniel E. Blumling
Penn State University
152 Davey Lab
University Park, PA 16802, USA
Tel: (814) 863-3583
Fax: (814) 865-5235
deb254@psu.edu

Kiran Boggavarapu
EMSL
Pacific Northwest National Laboratory
Po Box 999 MS: K8-91
Richland, WA 99352, USA
Tel: (509) 376-2723
Fax: (509) 375-6631
kiran@pnl.gov

Keith Bonin
Department of Physics
Wake Forest University
Winston-Salem, NC 27109, USA
Tel.: (336) 758-4962
Fax: (336) 758-6142
bonin@wfu.edu

Magnus Borgh
Dept. of Mathematical Physics
Lund Institute of Technology
Box 118
Lund S-22100
Sweden
Tel: +46 46 2229088
Fax: +46 46 2224416
magnus@matfys.lth.se

Kit H. Bowen, Jr.
Department of Chemistry
Johns Hopkins University
34th and Charles Sts.
Baltimore, MD 21218, USA
Tel: (410) 516-8425
Fax: (410) 516-4679
kitbowen@jhunix.hcf.jhu.edu

Michael T. Bowers
Department of Chemistry
Univ. of California-Santa Barbara
Santa Barbara, CA 93106, USA
Tel: (805) 893-2893
Fax: (805) 893-4120
bowers@ultra.chem.ucsb.edu

Gary A. Breaux
Department of Chemistry
Indiana University
800 E. Kirkwood
Bloomington, IN 47404, USA
Tel: (812) 219-8729
Fax: (812) 855-8331
gbreaux@indiana.edu

Catherine Brechignac
Lab Aime Cotton
CNRS II
Campus D'Orsay Bat 505
91405 Orsay Cedex, France
T:(33)169352002
F:(33)169352004
catherine.brechignac@lac.u-psud.fr

Simon A. Brown
Department of Physics
University of Canterbury
Christchurch, New Zealand
Tel: 64-3-3642507
Fax: 64-3-364-2469
simon.brown@canterbury.cc.nz

Jeff M. Byers
Code 6344
Naval Research Laboratory
4555 Overlook Road S.W.
Washington DC 20375, USA
Tel.: (202) 767-6147
FAX: (202) 767-1697
byers@foucault.nrl.navy.mil

Albert W. Castleman, Jr.
Department of Chemistry
152 Davey Laboratory
PA State University
University Park, PA 18803, USA
Tel: 814-865-7242
Fax: 814-865-5235
awc@psu.edu

Chatterjee, Bappaditya
311 W. Franklin St., Apt. #911
Richmond, VA 23220, USA
Tel: (804) 648-1239
bchatterjee@vcu.edu

Yok Chen
U.S. Department of Energy
Office of Basic Energy Sciences
SC-131 Germantown Building, Rm F-4
100 Independence Avenue, SW
Washington, DC 20585-1290, USA
Tel: (301) 903-4174
Fax: (301) 903-9513
Yok.chen@science.doe.gov

Margaret S. Cheung
IPST Room 2116
University of Maryland
College Park, MD 20742-2431, USA
Tel: (301) 405-7568
Fax: (301) 314-9404
mscheung@ipst.umd.edu

Robert N. Compton
Department of Chemistry
University of Tennessee
Knoxville, TN 37996, USA
T: (423) 974-9513
F: (423) 974-3454
rcompton@utk.edu

Brian Constance
Physics Department
Virginia Commonwealth University
Richmond, VA 23284-2000, USA
Tel: (804) 828-1818
Fax: (804) 828-7073
bfconstance@vcu.edu

Scott R. Crittenden
Physics Department
Purdue University
525 Northwestern Avenue
West Lafayette, IN 47907, USA
Tel: (765) 494-3018
Fax: (765) 494-0706
scott@physics.purdue.edu

Kevin M. Davis
Penn State University
152 Davey Lab
University Park, PA 16802, USA
Tel: (814) 863-3583
Fax: (814) 865-5235
kmd268@psu.edu

Sarojini Deevi
Research Center
Philip Morris USA
PO Box 26583
Richmond, VA 23261, USA
Tel: (804) 274-2767
Fax: (804) 274-4778
Sarojini.deevi@pmusa.com

Seetharama.C.Deevi
Senior Principal Scientist
Research, Development and Engineering
Philip Morris USA
4201 Commerce Road, Door 17
Richmond, VA 23234, USA
Tel: (804) 274-1934
Fax: (804) 274-2891
seetharama.c.deevi@pmusa.com

Dr Walt A de Heer
Ga Inst of Technology
Physics Dept
Atlanta, GA 30307, USA
Tel: (404) 894-7879
deheer@electra.physics.gatech.edu

Troy E. Dermota
Penn State University
152 Davey Lab
University Park, PA 16802, USA
Tel: (814) 863-3583
Fax: (814) 865-235
ted131@psu.edu

Keyur H. Desai
4261 Biomedical and Physical Sciences Bldg.
Department of Physics & Astronomy
Michigan State University
East Lansing, MI 48824, USA
Tel: (517) 355-9200 x 2246
Fax: (517) 432-6191
desaikey@msu.edu

Jonathan Dickinson
Physics Department
Virginia Commonwealth University
1020 W. Main St., Box 842000
Richmond, VA 23284-2000, USA
Tel: (804) 828-7353
Fax: (804) 828-7073
jwdicken@vcu.edu

Avinash M. Dongare
Materials Science & Engineering
University of Virginia
116 Engineer Way
Charlottesville, VA 22904, USA
Tel: (484) 825-4338
davinash@virginia.edu

Michael A. Duncan
Department of Chemistry
University of Georgia
Athens, GA 30602, USA
Tel: (706) 542-1998
Fax: (706) 542-1234
maduncan@uga.edu

Pulak Dutta
Dept. of Physics & Astronomy
Northwestern University
Evanston, IL 60208-3112, USA
Tel: +1-847-491-3477
Fax: +1-847-491-9982
pdutta@northwestern.edu

M. Samy El-Shall
Chemistry Department
Virginia Commonwealth University
Box 842006
Richmond, VA 23284-2006, USA
Tel: (804) 828-3518
Fax: (804) 828-8599
mselshal@vcu.edu

John B. Fenn
Chemistry Department
Virginia Commonwealth University
Box 84-2006
Oliver Hall, RM 3046 3040
Richmond, VA 23284-2006, USA
Tel: (804) 828-7511
jbfenn@vcu.edu

Andrew T. Fischer
3125 Kim Lane
Knoxville, TN 37917, USA
Tel: (865) 521-6626
afischer@utk.edu

Sarah-Jane V. Frankland
National Institute of Aerospace
144 Research Drive
Hampton, VA 23666, USA
Tel: (757) 864-4049
Fax: (757) 766-1855
sjvf@nianet.org

Hans Frauenfelder
CNLS
Los Alamos National Lab, MS B258
Los Alamos, NM 87545, USA
Tel: (505) 665-2547
Fax: (505) 665-2659
frauenfelder@lanl.gov

Ferruccio Gadani
Philip Morris USA
Po Box 26583
Richmond, VA 23261, USA
Tel: (804) 274-3146
Fax: (804) 274-2891
Ferruccio.gadani@pmusa.com

Giulia Galli
L-415 P.O. Box 808
Lawrence Livermore National Lab
Livermore, CA 94551, USA
Tel: (925) 423-4223
Fax: (925) 422-9655
Galligygi1@llnl.gov

Gerd Ganteför
University of Konstanz
Faculty of Physics
Konstanz 78457
Germany
Tel: (49) 7531-88-2067
Fax: (49) 7531-88-3091
gerd.gantefoer@uni konstanz.de

Lin Gao
Penn State University
152 Davey Lab
University Park, PA 16802, USA
Tel: (814) 863-3583
Fax: (814) 865-5235
jennylin@psu.edu

Shalva Gedevanishvil
Philip Morris USA
4201 Commerce Road
Richmond, VA 23234, USA
Tel: (804) 274-2258
Fax: (804) 274-4778
Shalva.Gedevanishvili@pmusa.com

William A. Goddard III
139-74 Beckman Inst., CALTECH
1201 E. California Blvd.
Pasadena, CA 91125, USA
Tel: (626) 395-2731
Fax:(626) 585-0918
wag@wag.caltech.edu

Justin S. Golightly
Penn State University
152 Davey Lab
University Park, PA 16802, USA
Tel: (814) 863-3583
Fax: (814) 865-5235
jsg210@psu.edu

Margaret Gorska
Institute of Physics
Polish Academy Of Ssiences
Al Lotnikof 32/46
02-668 Warsaw, Poland
gorska@ifpan.edu.pl

David E. Grove
Penn State University
152 Davey Lab
University Park, PA 16802, USA
Tel: (814) 863-3583
Fax: (814) 865-5235
deg160@psu.edu

Anthony Guiseppi-Elie
Chemical Engineering
Virginia Commonwealth University
Box 843028
601 W. Main St. 408
Richmond, VA 23284-3028, USA
Tel: (804) 827-7016
Fax: (804) 828-4269
guiseppi@vcu.edu

Irfan Gunduz
5033 Tippecanoe Dr.
Newburgh, TN 47630, USA
Tel: (804) 274-4568
Irfan.gunduz@pmusa.com

Mohammad R. Hajaligol
Philip Morris USA
PO Box 26583
Richmond, VA 23261, USA
Tel: (804) 274-2419
Fax: (804) 274-2891
hajaligm@pmusa.com

Naomi J. Halas
ECE Department
Rice University
PO Box 1892 MSS 366
Houston, TX 77251-1892, USA
Tel: (713) 348-5611
halas@rice.edu

Wolfgang Harbich
IPE
PHB-Ecublens
1015 CH Lausanne
Switzerland
Tel: 0041-21-693-4415
Fax: 0041-21-693-3604
wolfgang.harbich@epfl.ch

Masatake Haruta
Natl Inst AIST
Res Inst Green Technol
Tsukuba, Ibaraki 3058569
Japan
Tel: 0298-61-8204
Fax: 0298-61-8204
m.haruta@aist.go.jp

Fred M. Hawkridge
Chemistry Department
Virginia Commonwealth University
Box 842006
Richmond, VA 23284-2016, USA
Tel: (804) 828-1298
Fax: (804) 828-8599
fmhawkri@vcu.edu

Lei He
Electrical Engineering
Virginia Commonwealth University
601 W. Main St., Box 843072
Richmond, VA 23220, USA
Tel: (706) 302-2107
Fax: (804) 828-4269
lhe@vcu.edu

Andreas J. Heinrich
IBM Almaden Research Center
650 Hary Rd., D1
San Jose, CA 95120, USA
Tel: (408) 927 1978
Fax: (408) 927 2510
heinrich@almaden.ibm.com

Kristian Helmerson
MS 8424 NIST
100 Bureau Dr.
Gaithersburg MD 20899-8424
Tel: (301) 975-4266
kristian.helmerson@nist.gov

Robert E. Hetrick
25629 Wilson Dr.
Dearborn Hgts, MI 48127, USA
(313) 563-4112

Khang Hoang
Department of Physics & Astronomy
Michigan State University
East Lansing, MI 48824, USA
Tel: (517) 355-9200 x 2348
Fax: (517) 432-6191
hoang@pa.msu.edu

Thomas F. Huff
Vice Provost Life Science
Virginia Commonwealth University
Box 842030
1000 W. Cary St.
Richmond, VA 23284-2030, USA
Tel: (804) 827-5600
tfhuff@vcu.edu

Darren P. Hydutsky
Penn State University
152 Davey Lab
University Park, PA 16802, USA
Tel: (814) 863-3583
Fax: (814) 865-5235
dph142@psu.edu

Yehia M. Ibrahim
4123K Townhouse Rd.
Richmond, VA 23228, USA
Tel: (804) 261-0850
yibrahim@vcu.edu

Quazi T. Islam
Philip Morris USA
PO Box 26583
Richmond, VA 23261, USA
Tel: (804) 274-3681
Fax: (804) 274-4778
quazi.t.islam@pmusa.com

Shaheen M. Islam
Virginia Union University
1500 N. Lombardy Street
Richmond, VA 23220, USA
Tel: (804) 257-5661
Fax: (804) 257-5890
sislam@vuu.edu

Martin F. Jarrold
Chemistry Department
Indiana University
800 E. Kirkwood Avenue
Bloomington, IN 47405, USA
Tel: (812) 856-1182
Fax: (812) 855-8300
mfj@indiana.edu

Puru Jena
Physics Department
Virginia Commonwealth University
Box 842000
Richmond, VA 23284-2000, USA
Tel: (804) 828-8991
Fax: (804) 828-7073
pjena@vcu.edu

Wei Jiang
126 Monte Vista
Apt. #A
Charlottesville, VA 22903, USA
Tel: (434) 293-9804
wj2c@mail.phys.virginia.edu

Chuck E. Jones
Penn State University
152 Davey Lab
University Park, PA 16802, USA
Tel: (814) 863-3583
Fax: (814) 865-5235
cej119@psu.edu

Naiche O. Jones
Physics Department
Virginia Commonwealth University
Richmond, VA 23284-2000, USA
Tel: (804) 828-1818
Fax: (804) 828-7073
nojones@vcu.edu

Dina R. Justes
Penn State University
152 Davey Lab
University Park, PA 16802, USA
Tel: (814) 863-3583
Fax: (814) 865-5235
drj120@psu.edu

Anil K. Kandalam
Department of Physics
Virginia Commonwealth University
Richmond, VA 23228, USA
Tel: (804) 828-7079
Fax: (804) 828-7073
akkandalam@vcu.edu

Manfred M. Kappes
Institut für Physikalische Chemie II
Universität Karlsruhe
Karlsruhe D-76128, Germany
Tel: +49-721-6082094
manfred.kappes@chemie.uni-karlsruhe.de

Klaus Kern
MPI fuer Festkoerperforschung
Heisenbergssstr 1
D-70569 Stuttgart
Germany
Tel: +49 711 689-1660
Fax: +49 711 689-1662
klaus.kern@fkf.mpg.de

Shiv N. Khanna
Physics Department
Virginia Commonwealth University
Richmond, VA 23284-2000, USA
Tel: (804) 828-1820
Fax: (804) 828-7073
snkhanna@vcu.edu

Mikhail Khoudiakov
Applied Research Center
Old Dominion University
12050 Jefferson Avenue
Newport News, VA 23606, USA
Tel: (757) 269-6067
Fax: (757) 269-5644
Misha@jlab.org

Michele L. Kimble
Penn State University
152 Davey Lab
University Park, PA 16802, USA
Tel: (814) 863-3583
Fax: (814) 865-5235
mlk255@psu.edu

Kenneth L. Knappenberger
Penn State University
152 Davey Lab
University Park, PA 16802, USA
Tel: (814) 863-3583
Fax: (814) 865-5235
klk260@psu.edu

Andriy S. Korchev
179 Chemistry Blvd.
Auburn University
Auburn, AL 36849, USA
Tel: (334) 844-6932
Fax: (334) 844-6959
korchan@auburn.edu

Mattias Kordel
Universität Karlsruhe
Postfach 3640
Karlsruhe D-76021, Germany
Tel: 00497247826965
Fax: 00497247826368
mattias.kordel@int.fzk.de

Vitaly V. Kresin
Dept. of Physics & Astronomy
University of Southern California
Los Angeles, CA 90089-0484, USA
Tel: (213) 740-0868
Fax: (213) 740-6653
kresin@usc.edu

Nicole H. Levi
Wake Forest University
650-E Rugby Row
Winston Salem, NC 27106, USA
Tel: (336) 577-0925
Levin3@wfu.edu

Hong Mei Li
Penn State University
152 Davey Lab
University Park, PA 16802, USA
Tel: (814) 863-3583
Fax: (814) 865-5235

Xiang Li
Chemistry Dept.
Johns Hopkins University
3400 N. Charles St.
Baltimore, MD 21218, USA
Tel: (410) 516-7454
Fax: (410) 516-8420
shawnli@jhu.edu

James Lightstone
Brookhaven National Laboratory
Chemistry Department
Bldg 555
Upton, NY 11973-5000, USA
Tel: (631) 344-7607
Fax: (631) 344-5815
lightstone@bnl.gov

A. Cliff Lilly
4201 Commerce Road
Philip Morris USA
Richmond, VA 23234, USA
Tel: (804) 274-5074
Fax: (804) 274-3982
a.cliff.lilly@pmusa.com

Peter Lipowicz
Research Center
Philip Morris USA
Richmond, VA 23234, USA

Feng Liu
122 South Central Campus Drive
EMRO-313
Salt Lake City, UT 84112, USA
Tel: (801)-587-7719
Fax: (801)-581-4816
fliu@eng.utah.edu

Jin Liu
210 Maury Avenue
Apt. 10
Charlottesville, VA 22903, USA
Tel: (434)293-5619
jl3af@virginia.edu

Lesley Denise Lloyd
School of Chemistry
University of Birmingham
Edgbaston, Birmingham B15 2TT
UK
Tel: 44 (o) 121 414 4388
Fax: 44 (o) 121 414 4403
lesley@tc.bham.ac.uk

Steven G. Louie
Department of Physics
University of California-Berkeley
Berkeley, California 94720, USA
Tel: (510) 642-1709
Fax: (510) 643-9473
sglouie@uclink.berkeley.edu

Jun Lu
University of Chicago
5735 S. Ellis Avenue
Mail Box 237
Chicago, IL 60637, USA
Tel: (773) 702-7052
Fax: (773) 834-4049
junlu@uchicago.edu

Matti Manninen
Department of Physics
University of Jyvaskyla
PO Box 35
Fin-40351
Jyvaskyla, Finland
Tel: 358 14 2602362
Fax: 358 14 2602351
manninen@phys.jyu.fi

Susan R. McKay
Department of Physics & Astronomy
The University of Maine
5709 Bennett Hall
Orono, ME 04469-5709, USA
Tel: (207) 581-1019
Fax: (207) 581-3410
Susan-McKay@umit.maine.edu

Hans R. Micklitz
II. Physikalisches Institut
Universtiaet zu Koeln
Zuelpicherstrasse 77
Koeln 50937
Germany
Tel: (449) 221-470 3658
Fax: (449) 221-470 3658
micklitz@ph2.uni-koeln.de

Fuminori Misaizu
Department of Chemistry
Tohoku University
Aramaki, Aoba-ku
Sendai 980-8578
Japan
Tel: +81 22-217-6577
+81 22-217-6580
misaizu@qpcrkk.chem.tohoku.ac.jp

Indu B. Mishra
CPIA
Johns Hopkins University
10630 Little Patuxent Pkwy, #202
Columbia, MD 21044, USA
Tel: (410) 992-9951 x 209
Fax: (410) 730-4969
imishra@cpia.jhu.edu

Carlo D. Montemagno
Biomedical Engineering
Dept of Mechanical & Aerospace Eng.
Box 951597
University of CA-Los Angeles
Los Angeles, CA 90095-1597, USA
Tel: (310) 794-7270
Fax: (310) 794-5956
cdm@seas.ucla.edu

Nelly A. Moore
Penn State University
152 Davey Lab
University Park, PA 16802, USA
Tel: (814) 863-3583
Fax: (814) 865-5235
nam187@psu.edu

Takao Mori
National Inst. For Materials Science
Advanced Materials Laboratory
Tsukuba 305-0044
Japan
Tel: #81-29-860-4323
Fax: #81-29-851-6280
MORI.Takao@nims.go.jp

Tsugno Morisato
Physics Department
Virginia Commonwealth University
Richmond, VA 23284-2000, USA
(804) 828-1818
(804) 828-7073
tmorisato2@vcu.edu

Hadis Morkoç
Electrical Engineering
Box 843072
601 W. Main St. 338
Richmond, VA 23284-3072, USA
Tel: (804) 827-3765
Fax: (804) 828-4269
hmorkoc@vcu.edu

Martin Moskovits
Dept. Chemistry & Biochemistry
Univ. of CA-Santa Barbara
Santa Barbara, CA 93106, USA
Tel: (805) 893-5024
Fax: (805) 893.2441
mmoskovits@ltsc.ucsb.edu

Randall S. Murch
Institute for Defense Analyses
4850 Mark Center Drive
Alexandria, VA 22311-1882, USA
Tel: (703) 578-2812
Fax: (703) 931-7792
rmurch@ida.org

Min Namkung
Mail Stop 231
NASA Langley Research Center
Hampton, VA 23681, USA
m.namkung@larc.nasa.gov

Saroj K. Nayak
Physics Department
Rensselaer Polytechnic Institute
Troy, NY 12180, USA
Tel: (518) 276-2932
Fax: (528) 276-6680
nayaks@rpi.edu

Risto Nieminen
COMP/Laboratory of Physics
Helsinki University of Technology
FIN-02150 Espoo, Finland
Tel: 358 (9) 4513105
Fax: 358 (9) 4515067
rni@fyslab.hut.fi

Mike Nilles
Chemistry Dept.
Johns Hopkins University
3400 N. Charles St.
Baltimore, MD 21218, USA
Tel: (410) 516-7454
Fax: (410) 516-8420
Jmn1@jhu.edu

Arthur J. Nozik
The Journal of Physical Chemistry
Department of Chemistry, 215 UCB
University of Colorado, Boulder
Boulder, CO 80309, USA
Tel: (303) 735-1565
Fax: (303) 735-2350
jpc@colorado.edu

Hideo Ohno
Res. Inst. of Electric Commun.
Tohoku University
Katahira 2-1-1
Sendai 980-85, Japan
Tel: +81-22-217-5553
Fax: +81-22-217-5555 or 5553 (direct)
ohno@riec.tohoku.ac.jp

Jose N. Onuchic
Dept. of Physics 0319
University of California-San Diego
9500 Gillman Dr.
La Jolla, CA 92093-0319, USA
Tel: (858) 534-7067
jonuchic@ucsd.edu

Ray Ottenbrite
Department of Chemistry
Virginia Commonwealth University
Richmond, VA 23284, USA
Tel: (804) 828-7513
ottenbrite@vcu.edu

RajGanesh S. Pala
Material Science and Engineering
University of Utah
122 S. Central Campus Dr., Rm 304
Salt Lake City, UT 84112-0610, USA
Tel: (801) 585-9711
Fax: (801) 582-9613
pala@chpc.utah.edu

Sohini Paldey
RD&E
Philip Morris USA
4201 Commerce Road
Richmond, VA 23234, USA
Tel: 804-274-2305
Fax: (804) 274-4778

Richard E. Palmer
School of Physics and Astronomy
The University of Birmingham
Edgbaston, Birmingham B15 2TT, UK
Tel: (+44) (0)121 414 4653
F: (+44) (0)121 4147327
r.e.palmer@bham.ac.uk

Kyungwha Park
Center for Computational Materials Science
Naval Research Laboratory
Code 6392
Washington, DC 20375, USA
Tel: (202) 767-0691
Fax: (202) 404-2806
park@dave.nrl.navy.mil

Joel H. Parks
Senior Rowland Fellow
Rowland Institute at Harvard
Harvard University
100 Edwin H. Land Blvd.
Cambridge, MA 02142, USA
Tel: 617-497-4653
Fax: 617-497-4627
parks@rowland.harvard.edu

Ranjit Pati
Department of Physics
Rensselaer Polytechnic Institute
Troy, NY 12180, USA
(518) 276-2932
patir@rpi.edu

Forrest W. Payne
550-B Stagecoach Road
Charlottesville, VA 22902, USA
Tel: (434) 295-1761
fwp8c@virginia.edu

Samuel J. Peppernick
Penn State University
152 Davey Lab
University Park, PA 16802, USA
Tel: (814) 863-3583
Fax: (814) 865-5235
sjp185@psu.edu

William D. Phillips
Atomic Physics Division
NIST, 100 Bureau Drive, Stop 8424
Gaithersburg, MD 20899-8424, USA
Tel: (301)975-6554
Fax: (301) 975-8272
william.phillips@nist.gov

Sandipan Pramanik
Electrical Engineering
Box 843072
601 W. Main St.
Richmond, VA 23284-3072, USA
Tel: (804) 827-7040
pramaniks@vcu.edu

You Qiang
Physics Department
EP Building #321
University of Idaho
Moscow, ID 83844-0903, USA
Tel: (208) 885-7558
Fax: (208-885-4055
youqiang@uidaho.edu

Lucia G. Quagliano
Consiglio Nazionale delle Ricerche
Inst. For Nanostructured Materials
Area della Ricerca di Roma 1
PO Box 10, via Salaria km.29,300
00016 Monterotondo Scalo (Roma)
Italy
Tel: +39-06-90672214
Fax: +39-06-90672316
Lucia.quagliano@mlib.cnr.it

Dunja Radisic
Chemistry Dept.
Johns Hopkins University
3400 N. Charles St.
Baltimore, MD 21218, USA
Tel: (410) 516-7454
Fax: (410) 516-8420

Roberto C. Ramos
9308 Cherry Hill, RD #110
College Park, MD 20740, USA
Tel: (301) 405-7654
Fax: (302) 405-3779
ramos@squid.umd.edu

Bijan K. Rao
Physics Department
Virginia Commonwealth University
Richmond, VA 23284-2000, USA
Tel: (804) 828-1613
Fax: (804) 828-7073
bkrao@vcu.edu

Firooz Rasouli
1807 Gildenborough Ct.
Midlothian, VA 23113, USA
Tel: (804) 274-6260
Fax: (804) 274-4207
firooz.rasouli@pmusa.com

Budda V. Reddy
Philip Morris USA
Richmond, VA 23234, USA
Tel: (804) 274-2200
Fax: (804) 274-4778
budda.v.reddy@pmusa.com

Daniel H. Reich
Department of Physics & Astronomy
Johns Hopkins University
3400 N. Charles St.
Baltimore, MD 21218, USA
Tel: (410) 516-7899
Fax: (410) 516-7239
reich@jhu.edu

Ron Reifenberger
Department of Physics
Purdue University
W. Lafayette, IN 47907, USA
Tel: (765) 494-3032
Fax: (765) 494-0706
rr@physics.purdue.edu

Stephanie Reimann
Mathematical Physics
Lund Institute of Technology
PO Box 118, S-22100
Lund, Sweden
Tel: +46 46 222 9086
Fax: +46 46 222 4416

Mihail C. Roco
National Science Foundation
4201 Wilson Blvd.
Arlington, VA 22230, USA
Tel: (703) 292-8301
Fax: (703) 292-9013
mroco@nsf.gov

Arne Rosen
Department of Physics
Chalmers University of Technology
Goteborg, SE-41296
Sweden
Tel: 0046-31-7723295
Fax: 0046-31-7723496
arne.rosen@fy.chalmers.se

Alan Rosenbloom, M.D.
Carnegie Mellon University
4400 Fifth Avenue
Pittsburgh, PA 15213, USA
Tel: (412) 268-3461
Fax: (412) 268-6571
rosenbloomaj@ccm.upmc.edu

Philip J. Rous
Department of Physics
University of Maryland Baltimore County
Baltimore, MD 21250, USA
Tel: (410) 455-2598
Fax: (410) 455-1072
rous@umbc.edu

Jeffrey Rufinus
Widener University
Science Division
1 University Place
Chester, PA 19013, USA
Tel: (610) 499-4015
Fax: (610) 499-4496
rufinus@cs.widener.edu

Chhanda Samanta
Physics Department
Virginia Commonwealth University
Richmond, VA 23284-2000, USA
Tel: (804) 828-1818
Fax: (804) 828-7073
csamanta@mail1.vcu.edu

Darryl Sasaki
U.S. Department of Energy
Office of Basic Energy Sciences
SC-131 Germantown Building, Rm F-422
100 Independence Avenue, SW
Washington DC 20585-1290, USA
Tel: (301) 903-4174
Fax: (301) 903-9513
Darryl.sasaki@science.doe.gov

Donald D. Shillady
Chemistry Department
Virginia Commonwealth University
Richmond, VA 23284, USA
Tel: (804) 828-7508
Fax: (804) 828-8599
ddshillady@mail1.vcu.edu

Keshav N. Shrivastava
Department of ECECS
University of Cincinnati
Cincinnati, OH 45221-0030, USA
Tel: (513) 556-4790
Fax: (513) 556-4790
shrivast@ececs.uc.edu

Richard W. Siegel
Dept. of Materials Science and Engg.
Rensselaer Polytechnic Inst.
110 8th Street
Troy, NY 12180, USA
Tel: (518) 276-6373
Fax: (518) 276-8554
rwsiegel@rpi.edu

Mohamed A. Sobhy
Penn State University
152 Davey Lab
University Park, PA 16802, USA
Tel: (814) 863-3583
Fax: (814) 865-5235
mas665@psu.edu

Stuart A. Solin
Dept. of Physics
CB1105
Washington University
1 Brookings Dr.
St. Louis, MO 63130, USA
Tel: (314) 935-5605
Fax: (314) 935-5983
solin@wuphys.wustl.edu

Gabor A. Somorjai
Chemistry Department
University California-Berkeley
Berkeley, CA 94720, USA
Tel: (510) 642-4053
Fax: (510) 643-9668
somorjai@socrates.berkeley.edu

Josh Spradlin
Electrical Engineering
Virginia Commonwealth University
601 W. Main St., Box 843072
Richmond, VA 23284, USA
Tel: (804) 827-7040 x 639
s2jkspra@mail1.vcu.edu

Jason R. Stairs
Penn State University
152 Davey Lab
University Park, PA 16802, USA
Tel: (814) 863-3583
Fax: (814) 865-5235
jrs420@psu.edu

Carmen G. Stefanita
Electrical Engineering
Box 843072
Richmond, VA 23284-3072, USA
Tel: (804) 827-7040
cstefanita@vcu.edu

Sarah Stokes
Chemistry Dept.
Johns Hopkins University
3400 N. Charles St.
Baltimore, MD 21218, USA
Tel: (410) 516-7454
Fax: (410) 516-8420
sstokes4@jhu.edu

Carey E. Stronach
Physics Department
Virginia State University
Box 9325
Petersburg, VA 23806, USA
cstronac@vsu.edu

Qiang Sun
Physics Department
Virginia Commonwealth University
Richmond, VA 23284-2000, USA
Tel: (804) 828-7079
Fax: (804) 828-7073
qsun@vcu.edu

Rodney J. Sullivan
3200 Sutherland Avenue, Apt. K-12
Knoxville, TN 37919, USA
Tel: (865) 946-4454
rsulliva@utk.edu

Rangaraj S. Sundar
Philip Morris USA
4201 Commerce Road
Richmond, VA 23261, USA
Tel: (804) 274-2262
Fax: (804) 274-4778
rangaraj.s.sundar@pmusa.com

G. Bruce Taggart
Division of Materials Research
Room 1065
National Science Foundation
4201 Wilson Boulevard
Arlington, VA 22230, USA
Tel: (703) 292-4941
Fax: (703) 292-9035
gtaggart@nsf.gov

Jie Tang
National Inst. For Materials Science
1-2-1 Sengen
Tsukuba, Ibaraki 305-0047
Japan
Tel: 81-298-59-2728
Fax: 81-298-59-2701
Tang.jie@nims.go.jp

René-Jean Tarento
Laboratoire Physique des Solides
Universite Paris-Sud
Batiment 510, Centre Universitaire
91405 Orsay Cédex
France
Tel: (33) 1 69 15 53 79
Fax: (33) 1 69 15 60 86
tarento@physol.lps.u-psud.fr

Michael F. Thorpe
Bateman Physical Sciences PSF 359
Arizona State University
Tempe, AZ 85287-1504, USA
Tel: (480) 965-3085
Cell: (602) 463-1042
Fax: (775) 599-7188
mft@asu.edu

Peter Toennies
Max-Planck Inst.
Stroemungsf, Bunsenstr 10
D-37073 Gottingen
Germany
Lab. Tel: 011-49-551-5176-600,
Home Telephone: 011-49-551-57176.
Fax: 011-49-551-5176-607.
jtoenni@gwdg.de

Maria G. Toreblad
Department of Mathematical Physics
Lund Institute of Technology
Box 118, Lund, S-22100
Sweden
Tel: +46 46 222 9088
maria@matfys.lth.se

Steven Lee Tripp
Purdue University
1509 Shining Armor Lane
West Lafayette, IN 47906, USA
Tel: (765) 497-2393
tripp@purdue.edu

Barry Trotter
Chemistry Dept.
Johns Hopkins University
3400 N. Charles St.
Baltimore, MD 21218, USA
Tel: (410) 516-7454
Fax: (410) 516-8420
btrotter2@msn.com

Hironori Tsunoyama
Department of Chemistry
Tohoku University
Aoba-ku, Sendai 980-8578
Japan
Tel: +81 22-217-6578
Fax: +81 22-217-6580
tsuno@qpcrkk.chem.tohoku.ac.jp

Takafumi Uematsu
University of Tokyo
Dept. of Chemical Systems Engineering
Eng. 5-622
Hongo 7-3-1, Bunkyo-ku
Tokyo 113-8656
Japan
Tel: +81-3-5841-2324
Fax: +81-3-5841-7279
taka@chemsys.t.u-tokyo.ac.jp

Jaroslav Vacek
J. Heyrovsky Inst. of Physical Chemistry
Prague 18223
Czech Republic
Tel: +420-2-6605-3266
+420-2-8658-2307
vacek@jh-inst.cas.cz

Viola Vogel
Department of Bioengineering
University of Washington
Box 351721
Bagley Hall, Room 422B
Seattle, WA 98195, USA
Tel: (206) 543-1776
vvogel@u.washington.edu

Qian Wang
Physics Department
Virginia Commonwealth University
Richmond, VA 23284-2000, USA
Tel: (804) 828-7079
Fax: (804) 828-7073
qwang@vcu.edu

Hans-Christian Weissker
IFTO
Universität Jena
Max-Wien-Platz 1
Jena 07743
Germany
Tel: ++49-3641-947164
Fax: ++49-3641-947152
hcw@ifto.physik.uni-jena.de

Hollis Wickman
Condensed Matter Physics Program
National Science Foundation
Arlington, VA 22230, USA
Tel: (703) 292-4929
Fax: (703) 292-9035
hwickman@nsf.gov

Magnus Willander
Dept. of Microelectronics & Nanoscience
Chalmers Univ. of Technology
S412 96 Goteborg, Sweden
Tel: +46-31-772-2093
mwi@fy.chalmers.se

Elvira S. Williams
Shaw University
118 E. South St.
Raleigh, NC 27601, USA
Tel: (919) 546-8395
Fax: (919) 546-8258
e.s.Williams@larc.nasa.gov

Phillip A. Williams
NASA Langley Research Center
Mail Stop 231, 4 Langley Blvd.
Hampton, VA 23681, USA
Tel: (757) 864-4988
Fax: (757) 864-4914
p.a.williams@larc.nasa.gov

Russell A. Wincheski
Mail Stop 231, NASA Larc
Hampton, VA 23881, USA
Tel: (757) 864-4798
Fax: (757) 864-4914
Russell.a.wincheski@nasa.gov

Huizhong Xu
Department of Physics
University of Maryland
082 Regents Drive
College Park, MD 20742, USA
Tel: (301) 405-7581
Fax: (301) 314-9541
hzhxu@physics.umd.edu

Ramkuber T. Yadav
Research Center
Philip Morris USA
4201 Commerce Road
Richmond, VA 23261, USA
Tel: (804) 274-5687
Fax: (804) 274-1994
ramkuber.t.yadav@pmusa.com

Weitao Yang
Department of Chemistry
Duke University
Durham, NC 27708-0346, USA
Tel: (919) 660-1562
Fax: (919) 660-1605
weitao.yang@duke.edu

Zuyin "Frank" Yang
R&D, Philip Morris USA
615 Maury Street
Richmond, VA 23261-6583, USA
Tel: (804) 752-5737
Fax: (804) 752-5600
Zuyin.yang@pmusa.com

Songbai Ye
205-B Valley Road
Charlottesville, VA 22903, USA
Tel: (434) 295-4079
sy8K@virginia.edu

Guoping Zhang
Department of Physics
Indiana State University
Terre Haute, IN 47809, USA
Tel: (812) 237-2044
Fax: (812) 237-4396
gpzhang@indstate.edu

Wei-Jun Zhang
Philip Morris USA
4201 Commerce Road
Richmond, VA 23235, USA
Tel: (804) 274-2320
Fax: (804) 274-4778
weijun.zhang@pmusa.com

Yiming Zhang
Physics Department
Rensselaer Polytechnic Institute
110 8th St.
Troy, NY 12180, USA
Tel: (518) 892-1687
Fax: (518) 276-6680
zhangy4@rpi.edu

Weijung Zheng
Chemistry Dept.
Johns Hopkins University
3400 N. Charles St.
Baltimore, MD 21218, USA
Tel: (410) 516-7454
Fax: (410) 516-8420
zhengwj@jhu.edu

Otto Zhou
Department of Physics
CB 3255 Phillips Hall
University of North Carolina
Chapel Hill, NC 27599, USA
Tel: (919) 962-3297
Fax: (919) 962.0480
zhou@physics.unc.edu

AUTHOR INDEX

SUBJECT INDEX

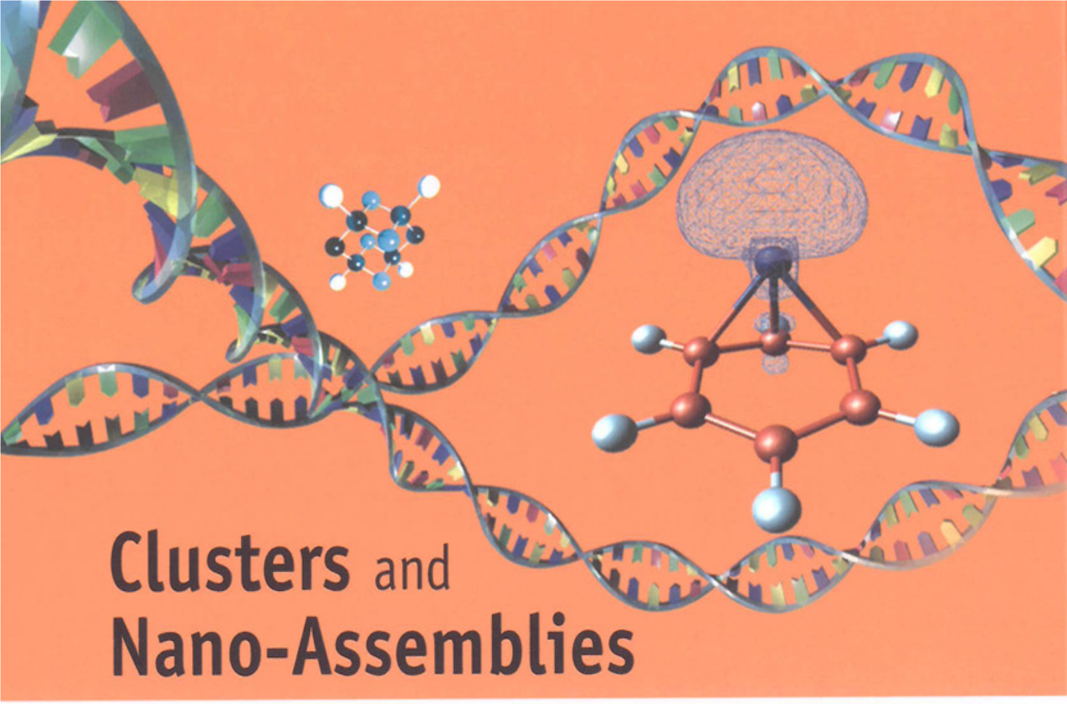

Clusters and Nano-Assemblies

Physical and Biological Systems

While the field of clusters and nano-structures in the physical sciences has been actively pursued only over the past two decades, nature has known the benefits of the nanoscale for a very long time. The focus of the International Symposium on *Clusters and Nano-Assemblies: Physical and Biological Systems* was to explore ways in which an understanding of the unique properties of nano-scale biological systems such as proteins, enzyme reactions, RNA, and DNA can help us design novel materials composed of inorganic nano-scale systems, and how techniques developed in the physical sciences can lead to a fundamental understanding of biological systems. Bringing together the expert contributions from the conference, this book deals with the fundamental science and technology of atomic clusters, nano-structures and their assemblies in physical and biological systems. It explores in fascinating detail the manner in which finite size, low dimensionality, and reduced symmetry affect the properties of nano-assemblies.

World Scientific
www.worldscientific.com
5826 hc

ISBN 981-256-331-8
9 789812 563316